W.P. Halperin, editor

Progress in Low Temperature Physics

Quantum Turbulence

VOLUME XVI

M. Tsubota, volume editor

Progress in Low
TEMPERATURE PHYSICS: QUANTUM TURBULENCE

VOLUME **XVI**

This page intentionally left blank

Progress in Low
TEMPERATURE PHYSICS: QUANTUM TURBULENCE

VOLUME **XVI**

Edited by

M. TSUBOTA
Department of Physics, Osaka City University,
Osaka, Japan

W. P. HALPERIN
Chairperson, Department of Physics and Astronomy,
Northwestern University, Evanston, IL, USA

For information on all Elsevier publications
visit our website at elsevierdirect.com

Working together to grow
libraries in developing countries

www.elsevier.com | www.bookaid.org | www.sabre.org

ELSEVIER   BOOK AID
            International   Sabre Foundation

The present volume, the 16th in the series *Progress in Low Temperature Physics*, collects seven articles reviewing the recent developments in quantum turbulence. Turbulence of superfluid ^{4}He was discovered in the mid-1950's. Since then, considerable experimental and theoretical effort has been devoted to the understanding of thermal counterflow. Superfluid turbulence is often called quantum turbulence, because it is strictly constrained by quantum mechanics. Any rotational motion of a superfluid must be sustained by quantized vortices. A quantized vortex is a definite topological defect with quantized circulation created by the appearance of the order parameter. A quantized vortex is very different from an eddy in a classical fluid. Quantum turbulence, comprised of quantized vortices, is expected to be much simpler than conventional turbulence and can serve as a prototype. Since the mid-1990's, the focus of investigations on quantum turbulence has evolved. Studies are no longer largely limited to thermal counterflow. Quantum turbulence has been studied intensively in superfluid ^{4}He, superfluid ^{3}He, and recently in atomic Bose–Einstein condensates.

Turbulence has long been one of the great mysteries in nature and a great challenge in technology, dating back to the time of Leonardo da Vinci. The study of quantum turbulence promises the real possibility of a breakthrough in understanding turbulence. This book is the first attempt to systematically review this fascinating problem.

In chapter 1, Makoto Tsubota and Michikazu Kobayashi review the issue of energy spectra in quantum turbulence. For nonlinear and other complicated phenomena, it is very important to monitor the statistical properties. Kolmogorov's law for energy spectra is the essential statistical law governing turbulence. This chapter discusses the energy spectra of quantum turbulence and how energy is transferred from large to small scales to sustain the self-similar inertial range. This problem is closely related with the issue of how quantum turbulence mimics classical turbulence.

In chapter 2, Vladimir Eltsov *et al.* review their studies of quantum turbulence in superfluid ^{3}He and ^{4}He under rotation. In their work, they observed the behavior of quantized vortices by NMR. They discuss the onset of turbulence, the dissipative mechanism and decay as a function of temperature. Of particular interest is the dissipative mechanism at very low temperatures where the normal fluid component is negligible and mutual friction does not occur.

Another important contribution to quantum turbulence in ^{3}He is reviewed in chapter 3 by Shaun Fisher and George Pickett. They have created turbulence by vibrating a wire or a grid and used quasiparticle excitations to probe the superfluid flow field in turbulence. This research features the direct measurement of Andreev reflection from quantized vortices. The technique is effective at very low temperatures and complements the NMR experiments described in chapter 2.

A recent trend in generating quantum turbulence is to use vibrating structures such as spheres, grids and wires. This technique is reviewed in chapter 4 by Ladik Skrbek and William Vinen. Quantum turbulence is induced in superfluid helium when the velocity of a vibrating object is increased above a critical velocity. The transition to turbulence is almost independent of the detailed geometry of the object, showing both similarities and differences with classical turbulence. Related experimental, theoretical and numerical works are reviewed in this chapter.

Recent remarkable developments have been made in the experimental technique of flow visualization in superfluid hydrodynamics. Steve Van Sciver and Carlo Barenghi review this technique experimentally and theoretically in chapter 5. The technique of particle image velocimetry (PIV) has been found to be very effective. However, it is not trivial to determine how micron-scale particle tracers move in the system. To address this problem, a better understanding of the interactions between small particles and quantized vortices is required. This chapter considers the theoretical and numerical determination of these interactions. The latter part of the chapter is devoted to the visualization of the velocity field in a counterflow and the direct visualization of quantized vortices.

German Kolmakov *et al*. review capillary turbulence on the surface of a quantum fluid in chapter 6. This phenomenon is very interesting as a typical example of wave turbulence, showing a cascade and energy spectra different from that of bulk turbulence. This chapter discusses recent typical experimental results using quantum fluids and theoretical considerations.

In chapter 7, Kenichi Kasamatsu and Makoto Tsubota review the physics of quantized vortices in atomic Bose–Einstein condensates. Since the discovery of the Bose–Einstein condensation of atomic gases in 1995, this field has become one of the most active fields in physics. A Bose–Einstein condensate has advantages over helium systems for the study of quantized vortices. Firstly, the density and the phase of the order parameter can be directly visualized by modern laser technology, making accessible some interesting physics of quantized vortices not available in helium research.

As can be seen, the field of quantum turbulence is very active. However, there are many unresolved problems. It is our hope that this volume will attract the interest of scientists, not only those working in low temperature physics but also from other fields, and that it will contribute to further developments and progress in low temperature physics.

Bill Halperin
Makoto Tsubota
November, 2008

This page intentionally left blank

CONTENTS

This page intentionally left blank

Volumes I-VI, edited by C.J. Gorter

Volume I (1955)

Volume II (1957)

Volume III (1961)

Volume IV (1964)

Volume V (1967)

Volume VI (1970)

Volumes VII-XIII, edited by D.E. Brewer

Volume VII (1978)

Volume VIII (1982)

Volume IX (1985)

Volume X (1986)

Volume XI (1987)

Volume XII (1989)

Volume XIII (1992)

Volume XIV (1995)

Volume XV (2005)

Energy Spectra of Quantum Turbulence

Makoto Tsubota* and **Michikazu Kobayashi***

Contents

Abstract

We review recent developments in the physics of quantum turbulence. Quantum turbulence is comprised of quantised vortices that are definite topological defects, giving a prototype of turbulence much simpler than the conventional model. Recent studies have shown clear similarities and differences between quantum and classical turbulence. Following a general introduction of this field,

* Department of Physics, Osaka City University, Sugimoto 3-3-138, Osaka, Japan

this chapter discusses the energy spectrum at very low temperatures. A key issue is the transfer of energy from large to small scales. At scales larger than the mean vortex spacing, the energy spectrum obeys the Kolmogorov law, and the energy is transferred through a Richardson cascade of quantised vortices, which is confirmed by numerical analysis using the vortex filament model and the Gross–Pitaevskii model. This range is considered classical. At scales smaller than the mean vortex spacing, the discreteness of vortices becomes significant, and the energy is transferred by a Kelvin-wave cascade caused by nonlinear interactions between different wavenumber modes of Kelvin-waves excited along a single vortex. This range is considered quantum. The crossover between the quantum and classical regions is discussed.

1. INTRODUCTION

Nature is filled with fluid flow, which in general can be laminar or turbulent. For high flow velocity or Reynolds number, flow is generally turbulent, and in fact, most flow observed in nature is turbulent. Over the centuries, turbulence has been studied as an important unresolved problem not only in basic science, such as physics and mathematics, but also in applied science, such as fluid engineering and aeronautics. Although turbulence has been studied intensely in many fields, it is still not yet well understood. This is chiefly because turbulence is a complicated dynamical phenomenon with strong nonlinearity and nonequilibrium. Vortices are a key issue for understanding turbulence. For example, Leonardo da Vinci observed the turbulent flow of water and drew many sketches showing that turbulence had a structure comprising of vortices with different sizes. However, vortices are not well defined in a typical classical fluid, and the relation between turbulence and vortices is not clear.

Turbulence in superfluid helium has been studied in the field of low temperature physics. Liquid ^{4}He enters a superfluid state below the λ point (2.17 K) with Bose–Einstein condensation of the ^{4}He atoms (Tilley and Tilley, 1990). Characteristic phenomena of superfluidity were discovered in the 1930s experimentally by Kapitza (Kapitza, 1938) and Allen et al. (Allen, 1938). The hydrodynamics of superfluid helium is well described by the two-fluid model, for which the system consists of an inviscid superfluid (density ρ_s) and a viscous normal fluid (density ρ_n) with two independent velocity fields $\mathbf{v}_s$ and $\mathbf{v}_n$. The mixing ratio of the two fluids depends on temperature. As the temperature is reduced below the λ point, the ratio of the superfluid component increases, and the whole fluid becomes a superfluid below about 1 K. The Bose-condensed system exhibits the macroscopic wave function $\Psi(\mathbf{x}, t) = |\Psi(\mathbf{x}, t)|e^{i\theta(\mathbf{x},t)}$ as an order parameter. The superfluid velocity field is given by $\mathbf{v}_s = (\hbar/m)\nabla\theta$ with boson mass m, representing the potential flow. Since the macroscopic wave

function should be single-valued for the space coordinate **x**, the circulation $\Gamma = \oint \mathbf{v} \cdot \mathrm{d}\ell$ for an arbitrary closed loop in the fluid is quantised by the quantum $\kappa = h/m$. A vortex with such quantised circulation is called a quantised vortex. Any rotational motion of a superfluid is sustained only by quantised vortices.

A quantised vortex is a topological defect characteristic of a Bose–Einstein condensate and is different from a vortex in a classical viscous fluid. First, the circulation is quantised, which is contrary to a classical vortex that can have any value of circulation. Second, a quantised vortex is a vortex of inviscid superflow. Thus, it cannot decay by the viscous diffusion of vorticity that occurs in a classical fluid. Third, the core of a quantised vortex is very thin, of the order of the coherence length, which is only a few angstroms in superfluid ^{4}He. Because the vortex core is very thin and does not decay by diffusion, it is always possible to identify the position of a quantised vortex in the fluid. These properties make a quantised vortex more stable and definite than a classical vortex.

Early experimental studies on superfluid hydrodynamics chiefly focused on thermal counterflow, in which the normal fluid and superfluid flow in opposite directions. The flow is driven by injected heat current, and it was found that the superflow becomes dissipative when the relative velocity between the two fluids exceeds a critical value (Gorter and Mellink, 1949). Feynman (1955) proposed that this is a superfluid turbulent state consisting of a tangle of quantised vortices. Vinen (1957a,b,c). later confirmed Feynman's proposition experimentally by showing that the dissipation comes from mutual friction between vortices and the normal flow. Subsequently, many experimental studies have been made on superfluid turbulence (ST) in thermal counterflow systems, and have revealed a variety of physics (Tough, 1982). Since the dynamics of quantised vortices is nonlinear and nonlocal, it has not been easy to understand vortex dynamics observations quantitatively. Schwarz (1985, 1988) clarified the picture of ST consisting of tangled vortices by a numerical simulation of the quantised vortex filament model in thermal counterflow. However, as thermal counterflow has no analogy with conventional fluid dynamics, this study has not helped clarify the relation between ST and classical turbulence (CT). ST is also often called quantum turbulence (QT), which emphasises the fact that it is comprised of quantised vortices.

A comparison of QT and CT reveals definite differences, demonstrating the importance of studying QT.

Turbulence in a classical viscous fluid appears to be comprised of vortices, as pointed out by Da Vinci. However, these vortices are unstable, repeatedly appearing and disappearing; the circulation is not conserved and is not identical for each vortex. QT consists of a tangle of quantised vortices which have the same conserved circulation. Hence, QT is an easier system to study than CT and gives a much simpler prototype of turbulence than CT.

Based on this consideration, QT research has tended toward a new direction since the middle of the 1990s. A chief interest is to understand the relation between QT and CT (Vinen and Niemela, 2002; Vinen, 2006), typically through the energy spectrum. The energy spectrum of fully-developed CT is known to obey the Kolmogorov law in an inertial range. The energy transfer in an inertial range is believed to be sustained by the Richardson cascade process in which large eddies are broken up self-similarly to smaller ones. Recent experimental and numerical works support the Kolmogorov spectrum in QT. The dissipative mechanism in QT is another phenomenon of similar interest.

This chapter reviews such important problems in QT as the energy spectra, the energy transfer and the dissipative mechanism etc. The contents of this chapter are as follows. After reviewing classical fluid dynamics and turbulence, Section 1 presents the problems to be solved and an overview of the present understanding of the energy spectrum of QT. New studies of QT follow the pioneering experiments supporting the Kolmogorov spectrum, which is described in Section 2. These experiments were made at finite temperatures where the normal fluid component is not negligible, though the coupled system of two fluids is difficult to treat. Thus, most of this chapter is devoted to QT at very low temperatures because it is easier to understand than QT at finite temperatures. We briefly comment on the system at finite temperatures in Section 8. The numerical approach is a powerful tool for studying turbulence and describing QT by the dynamics of quantised vortices. Section 3 describes two typical models for the numerical approach, the vortex filament model and the Gross–Pitaevskii (GP) model, and numerical simulations using these models. For QT at very low temperatures, it is necessary to consider the possible dissipation mechanism, which is reviewed briefly in Section 4. In Section 5, we discuss in detail the numerical studies of the energy spectrum by both the vortex filament model and the GP model to show that the spectrum obeys the Kolmogorov law under a Richardson cascade of quantised vortices. This semiclassical region is limited to scales larger than the mean vortex spacing ℓ. Energy transfers below ℓ are effected by a Kelvin-wave cascade, which is the topic of Section 6. How the energy spectrum continues between the Richardson and Kelvin-wave cascades is a mystery, the present understanding of which is reviewed in Section 7. Section 8 is devoted to a summary and discussions.

Experimental studies of QT have been made for superfluid ^{4}He and ^{3}He. Most of this chapter is about ^{4}He. For further information on ^{3}He, readers should refer to the chapters of Skrbek et al. (2008), Fisher et al. (2008) and Eltsov et al. (2008) in this volume. Another important quantum degenerate system is the atomic Bose–Einstein condensate (Pethick and Smith, 2002). Recent numerical simulations show that this system also can exhibit QT and obeys the Kolmogorov spectrum (Kobayashi and Tsubota, 2007) though the research is still in its infancy.

1.1 Energy Spectra in CT

Before considering QT, we briefly review classical fluid dynamics and the statistical properties of CT (Frisch, 1995).

Classical viscous fluid dynamics is described by the Navier–Stokes equation:

$$\frac{\partial}{\partial t}\mathbf{v}(\mathbf{x}, t) + \mathbf{v}(\mathbf{x}, t) \cdot \nabla\mathbf{v}(\mathbf{x}, t) = -\frac{1}{\rho}\nabla P(\mathbf{x}, t) + \nu\nabla^2\mathbf{v}(\mathbf{x}, t), \qquad (1)$$

where $\mathbf{v}(\mathbf{x}, t)$ is the velocity of the fluid, $P(\mathbf{x}, t)$ is the pressure, ρ is the density of the fluid and ν is the kinematic viscosity. The time development of $\mathbf{v}(\mathbf{x}, t)$ is dominated by Equation (1). The flow of this fluid can be characterised by the ratio of the second term of the left-hand side of Equation (1), hereafter called the inertial term, to the second term of the right-hand side, hereafter called the viscous term. This ratio is the Reynolds number:

$$R = \frac{\bar{v}D}{\nu}. \qquad (2)$$

Here, $\bar{v}$ and D are the characteristic velocity of the flow and the characteristic scale, respectively. When $\bar{v}$ increases to the point that the Reynolds number exceeds a critical value, the system changes from a laminar to a turbulent state in which the flow is highly complicated with many eddies.

Such turbulent flow comprised of eddies is known to show characteristic statistical behaviour (Kolmogorov, 1941a,b). We consider a steady state of fully-developed turbulence of an incompressible classical fluid. The energy is injected into the fluid with a rate ε, which is at a scale comparable to the system size D in the energy-containing range. In the inertial range, this energy is transferred to smaller scales without being dissipated. In this range, the system is locally homogeneous and isotropic, which leads to the statistics of the energy spectrum known as the Kolmogorov law:

$$E(k) = C\varepsilon^{2/3}k^{-5/3}. \qquad (3)$$

Here, the energy spectrum $E(k)$ is defined as $E = \int dk E(k)$, where E is the kinetic energy per unit mass and k is the wavenumber from the Fourier transformation of the velocity field. The spectrum of Equation (3) is easily derived by assuming that $E(k)$ is locally determined by only the energy flux ε and k. The energy transferred to smaller scales in the energy-dissipative range is dissipated at the Kolmogorov wavenumber $k_K = (\epsilon/\nu^3)^{1/4}$ through the viscosity of the fluid with dissipation rate ε in Equation (3), which is equal to the energy flux Π in the inertial range. The Kolmogorov constant C is a dimensionless parameter of order unity.

The Kolmogorov spectrum is confirmed experimentally and numerically in turbulence with high Reynolds numbers.

The inertial range is thought to be sustained by the self-similar Richardson cascade in which large eddies are broken up into smaller ones through many vortex reconnections. In CT, however, the Richardson cascade is not completely understood because it is impossible to definitely identify each eddy.

The Kolmogorov spectrum is based on the assumption that the turbulence is homogeneous and isotropic. However, actual turbulence is not necessarily homogeneous or isotropic, and hence the energy spectrum deviates from the Kolmogorov form. This phenomenon is called intermittency and is an important problem in modern fluid dynamics (Frisch, 1995). Intermittency is closely related with a coherent structure which may be represented by vortices. Research into QT can shed light on this controversial issue also.

1.2 Problems to be Solved

In this following, we present the problems dealt with in this chapter. Since turbulence is a complicated dynamical phenomenon with many degrees of freedom, it is very useful to consider the statistical properties, such as the energy spectrum. However, studying energy spectra has several associated problems. Our concerns can be generally classified into those at zero temperature and at finite temperatures.

1.2.1 Energy Spectra at Zero Temperature

Since there is no normal fluid component at zero temperature, the first problem is the nature of the energy spectrum of turbulence for the pure superfluid component. If QT has a classical analogue, the energy spectrum is expected to obey the Kolmogorov law and have an inertial range in which the energy is transferred self-similarly from large to small scales. In QT at zero temperature, any rotational motion should be carried by quantised vortices. Since quantised vortices are definite topological defects, the cascade can be attributed directly to their dynamics, which is rather different from the case for CT.

The second problem is how the energy is transferred from large to small scales. There is no dissipative mechanism at large scales. However, some dissipative mechanism should operate at small scales, as described below. A vortex tangle has a characteristic scale ℓ which is defined by the mean spacing between vortex lines. At scales larger than ℓ, a Richardson cascade should transfer the energy through the breakup of vortices. However, the Richardson cascade becomes ineffective at small scales, especially less than ℓ. What operates in that case?

The third problem is the dissipation in this system. What happens to QT at small scales? The first possibility is acoustic emission at vortex reconnections. In classical fluid dynamics, it is known that vortex reconnections cause acoustic emission. In quantum fluids, numerical simulations of the GP equation for the macroscopic wave function Ψ shows acoustic emission at every reconnection event (Leadbeater et al., 2001). However, this mechanism is thought to not be important because of the very short coherence length. The second possible mechanism is the radiation of sound (phonons) by the oscillatory motion of vortex cores. We will return to these mechanisms, as well as other possibilities, in more detail in Section 4.

1.2.2 Energy Spectra at Finite Temperatures

Experimental studies of the energy spectrum of QT at finite temperatures support the Kolmogorov spectrum directly (Maurer and Tabeling, 1998) or indirectly (Stalp et al., 1999). The problem here is what is the nature of the velocity field that gives rise to the observed energy spectrum. Vinen (2000) considered the situation theoretically and proposed that it is likely that the superfluid and normal fluid are coupled by mutual friction at scales larger than the characteristic scale ℓ of the vortex tangle. If so, the two fluids behave as a one-component fluid at the scales, where mutual friction does not cause dissipation. Since the normal fluid is viscous, the two coupled fluids can be turbulent and obey the Kolmogorov spectrum. The observation of the energy spectrum by Maurer and Tabeling (1998). and Stalp et al. (1999). should support the idea of the coupled dynamics of two fluids; this behaviour is confirmed numerically too (Kivotides, 2007). At small scales, the two fluids should be decoupled so that both mutual friction and normal fluid viscosity operate. It is important to ask what then happens to the energy spectrum. Although theoretical consideration has been given to this problem (L'vov et al., 2006), it is still controversial and not yet certain. While this is an important problem, it is not pursued in this chapter.

1.3 Overall Picture of the Energy Spectrum

Here we summarise the overall picture of the energy spectrum of QT at zero temperature from theoretical and numerical studies (Figure 1). QT is comprised of a tangle of quantised vortices. If the tangle is homogeneous and isotropic, it should have two characteristic length scales: the mean spacing ℓ between vortices, given by $\ell = L^{-1/2}$ with the line length density L (the vortex line length per unit volume), and the coherence length ξ corresponding to the size of the vortex core. Usually ℓ is much larger than ξ, and the wavenumber range is characterised by these scales. Since there
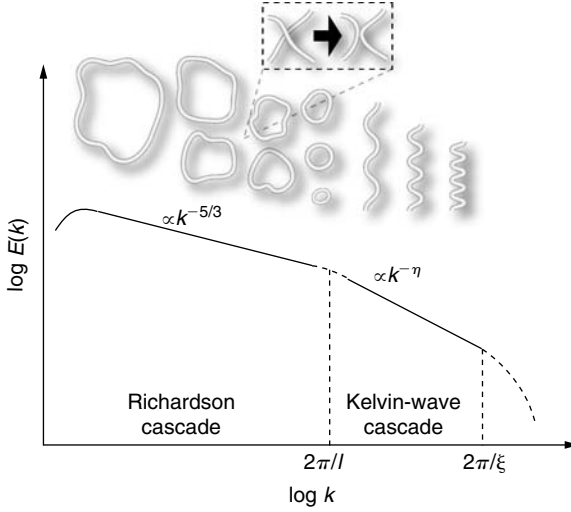
FIGURE 1   Overall picture of energy spectrum of QT at zero temperature. The properties of the cascade depend on the scale, and changes are observed at about the scale of the mean spacing ℓ between vortices. When the wavenumber k is smaller than $2\pi/\ell$, a Richardson cascade of quantised vortices transfers the energy from small to large wavenumbers, maintaining the Kolmogorov spectrum $E(k) = C\epsilon^{2/3}k^{-5/3}$. When k exceeds $2\pi/\ell$, a Kelvin-wave cascade becomes dominant; the nonlinear interaction between different wavenumbers of Kelvin-waves excited along a vortex line transfers the energy. Eventually, the energy should be dissipated at small scales, probably by acoustic emission.

is no normal fluid component, mutual friction does not operate. Some dissipation could occur at small scales, such as acoustic emission after a Kelvin-wave cascade, as described below. If QT exhibits a self-similar cascade process at large scales, however, the resulting energy spectra should be irrelevant to the detail of the dissipation, which may work only at small scales.

When the wavenumber k is smaller than about $2\pi/\ell$, the energy spectrum $E(k)$ obeys the Kolmogorov form $E(k) = C\varepsilon^{2/3}k^{-5/3}$. This is confirmed by numerical studies using the vortex filament model (Araki et al., 2002) and the GP model (Kobayashi and Tsubota, 2005a,b). There are no experimental works which directly observe the Kolmogorov spectrum at such low temperatures. At this scale, quantised vortices reconnect frequently, sustaining a Richardson cascade process that transfers energy from large to small scales without dissipating energy. Hence, QT exhibits quasi-classical behaviour in this region. The detailed structure and discreteness of quantised vortices are not important to the statistical properties of turbulence. However, it should be noted that this Richardson cascade of quantised

vortices is genuine, which is different from the schematic case of CT. The Kolmogorov constant C is not necessarily equal to the CT value (1.4–1.8); the Kolmogorov constant may depend on the system. The energy spectrum in this region will be discussed in Section 5.

If the wavenumber exceeds $2\pi/\ell$, vortex reconnection, which sustains the Richardson cascade, is no longer effective, and the quantised property of each vortex appears, giving rise to a Kelvin-wave cascade. This cascade process has been confirmed by the numerical and theoretical works of Vinen et al. (2003) and Kozik and Svistunov (2004, 2005a). The Kelvin-wave cascade will be described in Section 6.

A serious problem is how the spectrum of the Richardson cascade changes to that of the Kelvin-wave cascade over the transitional region of the order of $k \sim 2\pi/\ell$. A theoretical possibility based on the bottle-neck effect has been proposed by L'vov et al. (2007). Kozik and Svistunov (2008) have shown that the transitional region is comprised of three subcas-cades depending on the reconnections of vortex bundles. Section 7 reviews briefly the present understanding of this issue.

2. EXPERIMENTAL STUDY OF THE ENERGY SPECTRUM

Most older experimental studies on QT were devoted to thermal counter-flow. Since this flow has no classical analogue, these studies did not greatly contribute to the understanding of the relation between CT and QT. In the middle of 1990s, important experimental studies were published on QT not featuring thermal counterflow, differing significantly from previous studies.

2.1 Turbulence by Counter-Rotating Disks

The first experimental observation of the Kolmogorov spectrum in super-fluid ^{4}He was made by Maurer and Tabeling (1998). A turbulent flow was produced in a cylinder, 8 cm in diameter and 20 cm high, by driving two counter-rotating disks. The authors observed the local pressure fluctua-tions to obtain the energy spectrum. It should be noted that this technique works only at scales smaller than the spatial resolution of the pressure tube. The experiments were made at three different temperatures 2.3 K, 2.08 K and 1.4 K. Both above and below the λ point, the Kolmogorov spectrum was confirmed, as shown in Figure 2. The observed behaviour above the λ point is not surprising because the system is a classical viscous fluid. However, it is not trivial to understand the Kolmogorov spectrum below the λ point. The ratio of the superfluid component ρ_s/ρ is about 0.05 at 2.08 K and about 0.9 at 1.4 K. This result appears to show a cas-cade process that is independent of the relative ratio between ρ_s and ρ_n,
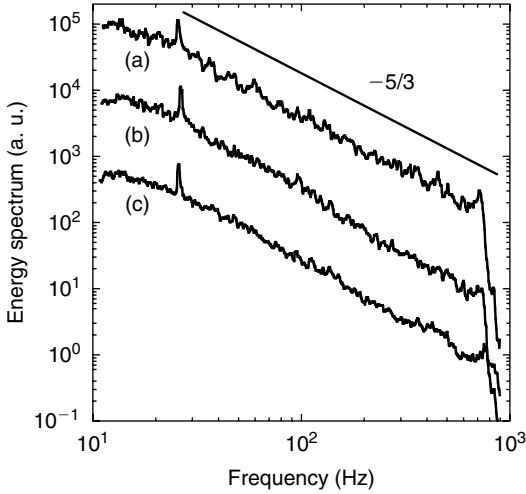
FIGURE 2　Energy spectra obtained for counter-rotating disks at (a) 2.3 K, (b) 2.08 K and (c) 1.4 K (Reproduced with permission of P. Tabeling from Figure 3 in Maurer and Tabeling (1998)).

which is a mystery because the dissipative mechanism should depend on temperature. We can understand this observation by the idea that the two fluids are coupled by mutual friction and behave like a one-component fluid (Vinen, 2000). Maurer and Tabeling (1998) investigated the distribution of the velocity increments in the inertial range to confirm intermittency.

2.2 Grid Turbulence

Flow through a grid is usually used for generating turbulence in classical fluid dynamics (Frisch, 1995). At sufficient distance behind the grid, the flow displays a form of homogeneous isotropic turbulence. This method has also been applied to superfluid helium.

A series of experiments were performed for superfluid ^{4}He above 1 K by the Oregon group (Smith et al., 1993; Stalp et al., 1999, 2002; Skrbek et al., 2000; Skrbek and Stalp, 2000). The helium was contained in a channel with a square (1 cm × 1 cm) cross-section, along which a grid was pulled at a constant velocity. A pair of second-sound transducers was set into the walls of the channel. When a vortex tangle appeared in a channel, it was detected by second-sound attenuation (Vinen and Niemela, 2002). The decay of the vorticity of the tangle created behind the towed grid was observed by the pair of transducers.

In combining the observations with the decay of the turbulence, the authors made some assumptions. In fully-developed turbulence, the energy dissipation rate can be shown to be given by

$$\epsilon = \nu \langle \omega^2 \rangle, \tag{4}$$

where $\langle \omega^2 \rangle$ is the mean square vorticity (rot $\mathbf{v}$) in the flow (Hinze, 1975). The Oregon group assumed that a similar formula applies in superfluid helium above 1 K. They noted that the quantity $\kappa^2 L^2$ would be a measure of the mean square vorticity in the superfluid component. Hence, they assumed that in grid turbulence, the dissipation rate is given by

$$\epsilon = \nu' \kappa^2 L^2 \tag{5}$$

with an effective kinematic viscosity ν'.

In order to combine Equation (5) with the observations of second-sound attenuation for grid turbulence, the authors furthermore assumed that a quasi-classical flow appears at length scales much larger than ℓ. The flow is thought to come from a mechanism coupling the superfluid and the normal fluid by mutual friction, causing the fluid to behave like a one-component fluid (Vinen, 2000). By choosing suitable values of ν' as a function of temperature (Stalp et al., 2002), it was found that κL decays as $t^{-3/2}$.

This characteristic behaviour can be understood based on a classical model using the Kolmogorov spectrum. We will here present the argument given in the review chapter (Vinen and Niemela, 2002). We assume that a turbulent fluid obeys the Kolmogorov spectrum of Equation (3) in the inertial range $D^{-1} < k < k_d$ with $D^{-1} << k_d$. The total energy is approximately given by

$$E = \int_{D^{-1}}^{k_d} C\varepsilon^{2/3} k^{-5/3} \approx \frac{3}{2} C\varepsilon^{2/3} D^{2/3}. \tag{6}$$

If the turbulence decays slowly with time and the dissipation rate ε is assumed to be time-dependent, we can write

$$\varepsilon = -\frac{\mathrm{d}E}{\mathrm{d}t} = -C\varepsilon^{-1/3} D^{2/3} \frac{\mathrm{d}\varepsilon}{\mathrm{d}t}. \tag{7}$$

The solution gives the time-dependence of ε:

$$\varepsilon = 27 C^3 D^2 (t + t_0)^{-3}, \tag{8}$$

where t_0 is a constant. Combining Equation (8) with Equation (5) gives the decay of L:

$$L = \frac{(3C)^{3/2}D}{\kappa \nu'^{1/2}}(t + t_0)^{-3/2}. \tag{9}$$

This behaviour has been observed, and a quantitative comparison with observations at any temperature gives ν' as a function of temperature. Thus, the decay behaviour of the vortex line length density is closely related to the energy spectrum. The observation of the decay $L \sim t^{-3/2}$ supports the conclusion that the Kolmogorov spectrum applies in turbulence though it is not necessarily a direct proof. However, it should be noted that this simple analysis is only applicable once the maximum length scale of the turbulent energy saturates at the size of the channel. For the complete dynamics, a more complicated decay of vortices has been observed and found to be consistent with the classical model of the Kolmogorov spectrum (Stalp et al., 1999; Skrbek et al., 2000; Skrbek and Stalp, 2000). This type of decay is observed also in turbulence induced by an impulsive spin down for superfluid ^{4}He (Walmsley et al., 2007) and in grid turbulence for superfluid ^{3}He (Bradley et al., 2006), both at very low temperatures.

3. NUMERICAL ANALYSIS OF THE DYNAMICS OF QUANTISED VORTICES

Since the early studies on ST, many experimental studies have been devoted to thermal counterflow, revealing many important properties (Tough, 1982). However, the nonlinear and nonlocal dynamics of vortices have delayed progress in the microscopic understanding of the vortex tangle. Schwarz (1985, 1988) overcame these difficulties by developing a direct numerical simulation of vortex dynamics connected with dynamical scaling analysis, enabling the calculation of physical quantities such as the vortex line density, anisotropic parameters and the mutual friction force. The observable quantities obtained by Schwarz agree well with the experimental results of the steady state of the vortex tangle.

The numerical approach is very useful in studying the energy spectrum in QT. Two formulations are generally available. One is the vortex filament model (Schwarz, 1985) and the other is the GP model. We will briefly review these two formulations.

3.1 Vortex Filament Model

As described in Section 1, a quantised vortex has quantised circulation. The vortex core is extremely thin, of the order of atomic size in helium II, much smaller than other characteristic scales in vortex motion. These properties

allow a quantised vortex to be represented as a vortex filament. The vortex filament model for a quantised vortex was pioneered and developed by Schwarz (1985, 1988). In classical fluid dynamics (Saffman, 1992), the vortex filament model is only a convenient idealisation; the vorticity in a realistic classical flow rarely takes the form of clearly discrete vorticity filaments. However, the vortex filament model is accurate and realistic for a quantised vortex in superfluid helium.

The vortex filament formulation represents a quantised vortex as a filament passing through the fluid, having a definite direction corresponding to its vorticity. Except for the thin core region, the superflow velocity field has a classically well-defined meaning and can be described by ideal fluid dynamics. The velocity at a point $\mathbf{r}$ due to a filament is given by the Biot–Savart expression:

$$\mathbf{v}_s(\mathbf{r}) = \frac{\kappa}{4\pi} \int_{\mathcal{L}} \frac{(\mathbf{s}_1 - \mathbf{r}) \times d\mathbf{s}_1}{|\mathbf{s}_1 - \mathbf{r}|^3}, \tag{10}$$

where κ is the quantum of circulation. The filament is represented by the parametric form $\mathbf{s} = \mathbf{s}(\xi, t)$ with the one-dimensional coordinate ξ along the filament. The vector $\mathbf{s}_1$ refers to a point on the filament, and the integration is taken along the filament. Helmholtz's theorem for a perfect fluid states that the vortex moves with the superfluid velocity. Calculating the velocity $\mathbf{v}_s$ at a point $\mathbf{r} = \mathbf{s}$ on the filament causes the integral to diverge as $\mathbf{s}_1 \to \mathbf{s}$. To avoid this divergence, we separate the velocity $\dot{\mathbf{s}}$ of the filament at the point $\mathbf{s}$ into two components (Schwarz, 1985):

$$\dot{\mathbf{s}} = \frac{\kappa}{4\pi} \mathbf{s}' \times \mathbf{s}'' \ln \left(\frac{2(\ell_+ \ell_-)^{1/2}}{e^{1/4} a_0} \right) + \frac{\kappa}{4\pi} \int_{\mathcal{L}}' \frac{(\mathbf{s}_1 - \mathbf{r}) \times d\mathbf{s}_1}{|\mathbf{s}_1 - \mathbf{r}|^3}. \tag{11}$$

The first term is the localised induction field arising from a curved line element acting on itself, and ℓ_+ and ℓ_- are the lengths of the two adjacent line elements after discretisation, separated by the point $\mathbf{s}$. The prime denotes differentiation with respect to the arc length ξ. The mutually perpendicular vectors $\mathbf{s}'$, $\mathbf{s}''$ and $\mathbf{s}' \times \mathbf{s}''$ point along the tangent, the principal normal and the binormal at the point $\mathbf{s}$, respectively, and their magnitudes are 1, R^{-1} and R^{-1} with the local radius R of curvature. The parameter a_0 is a cutoff corresponding to the core radius. Thus, the first term represents the tendency to move the local point $\mathbf{s}$ along the binormal direction with a velocity inversely proportional to R. The second term represents the nonlocal field obtained by integrating the integral of Equation (10) along the rest of the filament except for the neighbourhood of $\mathbf{s}$.

Neglecting the nonlocal terms and replacing Equation (11) by $\dot{\mathbf{s}} = \beta \mathbf{s}' \times \mathbf{s}''$ is called the localised induction approximation (LIA). Here, the

coefficient β is defined by $\beta = (\kappa/4\pi) \ln (c\langle R\rangle/a_0)$, where c is a constant of order 1 and $(\ell_+\ell_-)^{1/2}$ is replaced by the mean radius of curvature $\langle R\rangle$ along the length of the filament. Most of Schwarz's numerical studies on vortex tangles used the LIA because this approximation can greatly reduce computation times. The method is effective for analysing dense tangles (due to cancellations between nonlocal contributions). However, since the LIA does not properly include the intervortex interaction, it is not appropriate for studying the cases for which this interaction is essential, for example, for a vortex tangle sustaining the Kolmogorov spectrum (Araki et al., 2002) or a vortex array under rotation (Tsubota et al., 2003a).

A better understanding of vortices in a real system results when boundaries are included in the analysis. For this, a boundary-induced velocity field $\mathbf{v}_{s,b}$ is added to $\mathbf{v}_s$ so that the superflow can satisfy the boundary condition of an inviscid flow, that is, that the normal component of the velocity should disappear at the boundaries. If the boundaries are specular plane surfaces, $\mathbf{v}_{s,b}$ is simply the field due to an image vortex made by reflecting the vortex onto the plane and reversing its direction of vorticity. To allow for another, presently unspecified, applied field, we include $\mathbf{v}_{s,a}$. Hence, the total velocity $\dot{\mathbf{s}}_0$ of the vortex filament without dissipation is

$$\dot{\mathbf{s}}_0 = \frac{\kappa}{4\pi}\mathbf{s}' \times \mathbf{s}'' \ln \left(\frac{2(\ell_+\ell_-)^{1/2}}{e^{1/4}a_0} \right) + \frac{\kappa}{4\pi} \int_{\mathcal{L}}' \frac{(\mathbf{s}_1 - \mathbf{r}) \times d\mathbf{s}_1}{|\mathbf{s}_1 - \mathbf{r}|^3}$$

$$+ \mathbf{v}_{s,b}(\mathbf{s}) + \mathbf{v}_{s,a}(\mathbf{s}). \tag{12}$$

At finite temperatures, it is necessary to take account of mutual friction between the vortex core and the normal flow $\mathbf{v}_n$. Including this term, the velocity of $\mathbf{s}$ is given by

$$\dot{\mathbf{s}} = \dot{\mathbf{s}}_0 + \alpha\mathbf{s}' \times (\mathbf{v}_n - \dot{\mathbf{s}}_0) - \alpha'\mathbf{s}' \times [\mathbf{s}' \times (\mathbf{v}_n - \dot{\mathbf{s}}_0)], \tag{13}$$

where α and α' are temperature-dependent friction coefficients (Schwarz, 1985), and $\dot{\mathbf{s}}_0$ is calculated from Equation (12).

The numerical simulation method based on this model is described in detail elsewhere (Schwarz, 1985, 1988; Tsubota et al., 2000). A vortex filament is represented by a single string of points separated by a distance $\Delta\xi$. The vortex configuration at a given time determines the velocity field in the fluid, thus moving the vortex filaments according to Equations (12) and (13). Both local and nonlocal terms are represented by line elements connecting two adjacent points. As the vortex configuration develops and, particularly, when two vortices approach each other, the distance between neighbouring points can change. Then it is necessary to add or remove points to retain sufficient local resolution. Through the cascade

process, a large vortex loop can break up through many reconnections, eventually becoming a loop that is comparable to the space resolution $\Delta\xi$. The simulations cannot follow the dynamics beyond this resolution, so these vortices are eliminated numerically. This cutoff procedure works effectively as dissipation even for a simulation at zero temperature (Section 5.1).

It is important to properly include vortex reconnection when simulating vortex dynamics. A numerical study of a classical fluid shows that the close interaction of two vortices leads to their reconnection, chiefly because of the viscous diffusion of the vorticity (Boratav et al., 1992). Schwarz (1985, 1988) assumed that two vortex filaments reconnect when they get within a critical distance, and showed that the statistical quantities such as vortex line density were not sensitive to how the reconnections occur. Even after the Schwarz's work, it was still unclear whether quantised vortices can actually reconnect. However, Koplik and Levine (1993) solved directly the GP equation to show that two close quantised vortices reconnect even in an inviscid superfluid. More recent simulations show that reconnections are accompanied by emissions of sound waves of wavelength the order of the healing length (Leadbeater et al., 2001; Ogawa et al., 2002).

There are several controversial arguments of how effective the vortex filament model is for understanding CT. It is impossible to review the whole discussion here and readers should refer, for example, to Section 8.9 of Frisch's book (Frisch, 1995). The filament-like structure is confirmed in experimental and numerical studies, as well as the old observations by Da Vinci. The essential question is whether the vortex filaments are the 'dog' or the 'tail' for turbulence. In the former case, they would be indispensable for understanding the statistical properties of CT. The latter case would mean that they are only marginal signatures in CT. There are different opinions on both sides, and the issue is controversial. A discussion of the energy spectra will be described in Section 5.1. The greatest difficulty is that vortex filaments have not been definitely identified in classical flow. Studies of QT could overcome this difficulty because QT is by nature comprised of quantised vortex filaments.

Thus the vortex filament model is very useful for QT, though it cannot describe phenomena directly related with vortex cores as reconnection, nucleation and annihilation. These phenomena can be analysed only by the GP model.

3.2 The GP Model

In a weakly interacting Bose system, the macroscopic wave function $\Psi(\mathbf{x}, t)$ appears as the order parameter of Bose–Einstein condensation, obeying

the GP equation (Pethick and Smith, 2002):

$$i\hbar\frac{\partial\Psi(\mathbf{x},t)}{\partial t} = \left(-\frac{\hbar^2}{2m}\nabla^2 + g|\Psi(\mathbf{x},t)|^2 - \mu\right)\Psi(\mathbf{x},t). \qquad (14)$$

Here, $g = 4\pi\hbar^2 m/a$ represents the strength of the interaction characterised by the s-wave scattering length a, m is the mass of each pchapter and μ is the chemical potential. Writing $\Psi = |\Psi|\exp(i\theta)$, the squared amplitude $|\Psi|^2$ is the condensate density, and the gradient of the phase θ gives the superfluid velocity $\mathbf{v}_s = (\hbar/m)\nabla\theta$, which is a frictionless flow of the condensate. This relation causes quantised vortices to appear with quantised circulation. The only characteristic scale of the GP model is the coherence length defined by $\xi = \hbar/(\sqrt{2mg}|\Psi|)$, which gives the vortex core size.

The GP model can explain not only the vortex dynamics but also phenomena concerned with vortex cores such as reconnection and nucleation. However, strictly speaking, the GP equation is not applicable to superfluid ^{4}He, which is not a weakly interacting Bose system. The GP model does not feature, for example, short-wavelength excitations such as rotons which are present in superfluid ^{4}He. The GP equation is applicable to Bose–Einstein condensation of a dilute atomic Bose gas (Pethick and Smith, 2002).

4. POSSIBLE DISSIPATION MECHANISM AT VERY LOW TEMPERATURES

It is appropriate to begin this section by reviewing the present understanding of the possible dissipation mechanisms of QT at very low temperatures in which the normal fluid component is so negligible that mutual friction does not occur. In this case, there is no dissipation at relatively large scales, and dissipation can only occur at small scales. Energy at large scales should be transferred to smaller scales by a Richardson cascade and then a Kelvin-wave cascade until the dissipation becomes effective. The description here is only schematic. Please refer to other papers for a more detailed discussion (Vinen, 2000; Vinen and Niemela, 2002).

Dissipation of QT at zero temperature was first proposed by Feynman (1955). Feynman suggested that a large vortex loop should be broken up into smaller loops through repeated vortex reconnections, which is essentially identical to the Richardson cascade. Feynman thought that the smallest vortex ring having a radius comparable to the atomic scale must be a roton, though this idea is not currently accepted. Later, Vinen (1975c) considered the decay of ST in order to understand his experimental

results for thermal counterflow, leading him to propose Vinen's equation. Although the experiments were done at finite temperatures, the physics is important for studying the decay of QT, so we describe it here briefly. Vortices in turbulence are supposed to be approximately evenly spaced with a mean spacing $\ell = L^{-1/2}$. The energy of the vortices then spreads from the vortices of wavenumber $1/\ell$ to a wide range of wavenumbers. The overall decay of the energy is governed by the characteristic velocity $v_s = \kappa/2\pi\ell$ and the time constant ℓ/v_s of the vortices of size ℓ, giving

$$\frac{\mathrm{d}v_s^2}{\mathrm{d}t} = -\chi\frac{v_s^2}{\ell/v_s} = -\chi\frac{v_s^3}{\ell}, \tag{15}$$

where χ is a dimensionless parameter generally dependent on temperature. Rewriting this using L, we obtain

$$\frac{\mathrm{d}L}{\mathrm{d}t} = -\chi\frac{\kappa}{2\pi}L^2. \tag{16}$$

This is called Vinen's equation. The original Vinen's equation included also a term of vortex amplification, which is not shown here. This equation describes the decay of L. The solution is

$$\frac{1}{L} = \frac{1}{L_0} + \chi\frac{\kappa}{2\pi}t, \tag{17}$$

where L_0 is L at $t = 0$. The thermal counterflow observations are well described by this solution, which gives the values of χ as a function of temperature (Vinen, 1957c). The decay at finite temperatures is due to mutual friction. The value of χ at zero temperature is obtained by a numerical simulation of the vortex filament model (Tsubota et al., 2000).

What causes the different kinds of decay of $L \sim t^{-3/2}$ of Equation (9) and $L \sim t^{-1}$ of Equation (17)? This comes from different structures of vortex tangles in QT. When the energy spectrum of a vortex tangle obeys the Kolmogorov law, the tangle is self-similar in the inertial range and most energy is in the largest vortex. Then the line length density decays like $L \sim t^{-3/2}$ as described in Section 2.2. If a vortex tangle is random and has no correlations, however, the only length scale is $\ell = L^{-1/2}$, yielding the decay of $L \sim t^{-1}$ as described in the last paragraph. Hence the observations of how L decays help understand the structure of vortex tangles in QT.

However, these studies do not explain what happens to QT at zero temperature at small scales. There are several possibilities. The first is acoustic emission at vortex reconnections. In classical fluid dynamics, it

is known that vortex reconnections cause acoustic emission. In quantum
fluids, numerical simulations of the GP model show that acoustic emis-
sion occurs at every reconnection (Leadbeater et al., 2001; Ogawa et al.,
2002). The dissipated energy during each reconnection is about 3ξ times
the vortex line energy per unit length. We can estimate how L decays
by this mechanism. The number of reconnection events per volume per
time is of the order of $\kappa L^{5/2}$ (Tsubota et al., 2000). Since each reconnection
should reduce the vortex length by the order of ξ, the decay of L can be
described by

$$\frac{dL}{dt} = -\chi_1 \xi \kappa L^{5/2} \tag{18}$$

with a constant χ_1 of order unity. The solution is

$$\frac{1}{L^{3/2}} = \frac{1}{L_0^{3/2}} + \frac{3}{2}\chi_1 \xi \kappa t. \tag{19}$$

In superfluid helium, especially ^{4}He, ξ is so small that decay due to
this mechanism should be negligible. This dissipation mechanism might
be important for dilute atomic Bose–Einstein condensates in which ξ is
generally close to the system size (Pethick and Smith, 2002).

   The second possible mechanism is the radiation of sound (phonons)
by oscillatory motion of a vortex core. The characteristic frequencies of
vortex motion on a scale ℓ are of order κ/ℓ^2, which is too small to cause
effective radiation (Vinen, 2000). In order to make the radiation effective,
the vortices should form small-scale structures, which would be realised
by two consecutive processes. The first process is due to vortex recon-
nections (Svistunov, 1995). In a dense isotropic tangle, vortex reconnec-
tions occur repeatedly with a rate of order κ/ℓ^5 per unit volume (Tsubota
et al., 2000). When two vortices become close, they twist themselves so
that they become locally antiparallel and reconnect (Schwarz, 1985). They
then move apart leaving a local small-scale structure. However, even such
local structures created by single reconnection events are not sufficient
to cause effective acoustic radiation. The next process occurs due to a
Kelvin-wave cascade (Kozik and Svistunov, 2004, 2005a,b; Vinen, 2001;
Vinen et al., 2003). Kelvin-waves, which are helical waves excited along
the vortex cores, can transfer energy to smaller scales through the non-
linear interaction between different wavenumbers until acoustic emission
can occur. The Kelvin-wave cascade will be discussed in detail in Section 6.

   In actual experiments, the effects of vortex diffusion must be considered
though it is not dissipation. A vortex tangle is sometimes inhomogeneous
or local, and the probe observing the vortex tangle can be local too. When
a vortex tangle escapes from the observable region, it may appear to decay.

For example, a vortex tangle produced by a vibrating structure applies in this case. Using the vortex filament model, Tsubota et al. (2003b) numerically studied how an inhomogeneous vortex tangle diffuses. The obtained diffusion of the line length density $L(\mathbf{x}, t)$ was well described by

$$\frac{\mathrm{d}L(\mathbf{x}, t)}{\mathrm{d}t} = -\chi \frac{\kappa}{2\pi} L(\mathbf{x}, t)^2 + D \nabla^2 L(\mathbf{x}, t). \tag{20}$$

Without the second term in the right side, this is Vinen's equation (16) describing the decay of a homogeneous vortex tangle (Vinen, 1957c). The second term represents the diffusion of a vortex tangle. The numerical results show that the diffusion constant D is about 0.1κ. The dimensional argument indicates that D must be of order κ (Tsubota et al., 2003b).

5. ENERGY SPECTRUM AT ZERO TEMPERATURE

The energy spectrum of QT at zero temperature is not a trivial problem specifically, whether the QT obeys the Kolmogorov spectrum. No experimental studies have yet addressed this issue directly, though several numerical studies have been made of the energy spectrum at zero temperature. As described in Section 3, we have two formulations for studying the dynamics of quantised vortices in QT. The problem of the energy spectrum has been approached using both formulations.

   The first study was done by Nore et al. (1997a,b) using the GP model. They solved numerically the GP equation starting from Taylor–Green vortices and followed the time development. The quantised vortices become tangled, and the energy spectra of the incompressible kinetic energy seemed to obey the Kolmogorov law for a short period though eventually deviating from it. The second study was made by Araki et al. (2002) using the vortex filament model. They also made a vortex tangle arising from Taylor–Green vortices and obtained an energy spectrum consistent with the Kolmogorov law. As the third trial, Kobayashi and Tsubota (2005a,b) made a numerical analysis of the GP model with a dissipation term which works only at scales smaller than the healing length. This method enabled them to overcome the difficulties of Nore et al. (1997a,b) and to obtain spectra consistent with the Kolmogorov law. This section reviews these works.

5.1 Energy Spectra Obtained by the Vortex Filament Model

The energy spectrum is calculated by the Fourier transform of the fluid velocity $\mathbf{v}(\mathbf{r})$. The superfluid velocity field $\mathbf{v}_s(\mathbf{r})$ is determined by the configuration of quantised vortices in the vortex filament model. Therefore, the energy spectrum can be calculated directly from the configuration of

the vortices. This is an advantage of this formulation because it makes the numerical calculation of the spectrum less time-consuming than a method using $\mathbf{v}(\mathbf{r})$. Using the Fourier transform $\mathbf{v}_s(\mathbf{k}) = (2\pi)^{-3}\int d\mathbf{r}\, \mathbf{v}_s(\mathbf{r})\exp(-i\mathbf{k} \cdot \mathbf{r})$ and Parseval's theorem $\int d\mathbf{k}|\mathbf{v}_s(\mathbf{k})|^2 = (2\pi)^{-3}\int d\mathbf{r}|\mathbf{v}_s(\mathbf{r})|^2$, the kinetic energy of the superfluid velocity per unit mass is

$$E = \frac{1}{2}\int d\mathbf{r}|\mathbf{v}_s(\mathbf{r})|^2 = \frac{(2\pi)^3}{2}\int d\mathbf{k}|\mathbf{v}_s(\mathbf{k})|^2. \tag{21}$$

The vorticity $\omega(\mathbf{r}) = \mathrm{rot}\mathbf{v}_s(\mathbf{r})$ is represented in Fourier space as $\mathbf{v}_s(\mathbf{k}) = i\mathbf{k} \times \omega(\mathbf{k})/|\mathbf{k}|^2$ so that we have $E = \left((2\pi)^3/2\right)\int d\mathbf{k}|\omega(\mathbf{k})|^2/|\mathbf{k}|^2$. The vorticity is concentrated on the vortex filament, represented by

$$\omega(\mathbf{r}) = \kappa\int d\xi \mathbf{s}'(\xi)\delta(\mathbf{s}(\xi) - \mathbf{r}), \tag{22}$$

which can be rewritten as

$$\omega(\mathbf{k}) = \frac{\kappa}{(2\pi)^2}\int d\xi \mathbf{s}'(\xi)\exp(-i\mathbf{s}(\xi) \cdot \mathbf{k}). \tag{23}$$

Using the definition of the energy spectrum $E(k)$ from $E = \int_0^\infty dk E(k)$, these relations yield

$$E(k) = \frac{\kappa^2}{2(2\pi)^3}\int \frac{d\Omega_k}{|\mathbf{k}|^2}\int\int d\xi_1 d\xi_2 \mathbf{s}'(\xi_1) \cdot \mathbf{s}'(\xi_2)$$

$$\times \exp(-i\mathbf{k} \cdot (\mathbf{s}(\xi_1) - \mathbf{s}(\xi_2))), \tag{24}$$

where $d\Omega_k = k^2\sin\theta_k d\theta_k d\phi_k$ is the volume element in spherical coordinates. This formula connects the energy spectrum directly with the vortex configuration.

Starting from a Taylor–Green vortex in a 1-cm sized cube and following the vortex motion under the full Biot–Savart law without mutual friction, Araki et al. (2002) obtained a roughly homogeneous and isotropic vortex tangle. This is a decaying turbulence, dissipated by the cutoff of the smallest vortices whose size is comparable to the space resolution $\Delta\xi = 1.83 \times 10^{-2}$ cm. Initially, the energy spectrum has a large peak at the largest scale where the energy is concentrated. The spectrum changes as the vortices become homogeneous and isotropic. The time dependence of the energy dissipation rate ϵ shows that $d\epsilon/dt$ becomes small after about 70 s and artifacts of the initial state disappear. Similarly, the isotropic parameters introduced by Schwarz (1988) indicate a nearly isotropic
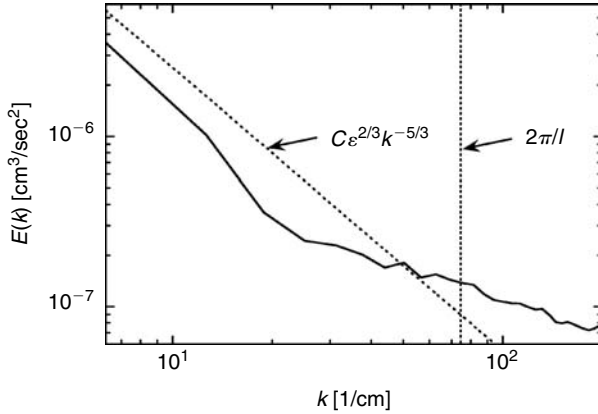
FIGURE 3 Comparison of the energy spectrum (solid line) numerically obtained at a late stage with the Kolmogorov law (dotted line) with $C = 1$ and $\epsilon = 1.287 \times 10^{-6}$ cm^2/sec^3 (Araki et al., 2002, reproduced with permission. Copyright (2002) by the American Physical Society).

vortex tangle after 70 s. Figure 3 shows that the energy spectrum of the vortex tangle at 70 s agrees quantitatively with the Kolmogorov spectrum in the small k region. The dissipative mechanism due to the cutoff works only at the largest wavenumber $k \sim 2\pi/\Delta\xi = 343$ cm^{-1}. However, the energy spectrum in the small k region is determined by this dissipation rate. By monitoring the development of the vortex size distribution, the decay of a tangle is found to be sustained by a Richardson cascade process (Tsubota et al., 2000). These results support the quasi-classical picture of the inertial range in QT at very low temperatures. The power of the spectrum changes from $-5/3$ to -1 at about $k \sim 2\pi/\ell$. The k^{-1} spectrum arises from the contribution of the velocity near each single vortex. However, the spectrum beyond $2\pi/\ell$ is controversial, as discussed in Section 7. This simulation may not have sufficient resolution to describe properly the spectrum in this region.

This problem of studying the energy spectrum by the vortex filament model is important in asking whether the picture of vortex filaments is essential for understanding turbulence. When estimating the energy spectrum of Equation (24), we may use the Gaussian model of a vortex tangle (Nemirovskii, 1997) and assume fractal structures of vortices with fractal dimension D. The Gaussian model assumes that the statistics of a vortex filament is Gaussian. This approach yields $E(k) \propto k^{D-2}$ (Nemirovskii et al., 2002). Because D should satisfy $1 < D < 3$, the spectrum never obeys the Kolmogorov $-5/3$ law. The worst scenario might be that the vortex filaments are only 'tail', namely marginal signatures in turbulence. However, the most probable reason for failing to yield the Kolmogorov law would be that the Gaussian model does not include the interaction between vortices.

5.2 Energy Spectra Obtained by the GP Model

We consider the normalised GP equation:

$$i\frac{\partial}{\partial t}\Phi(\mathbf{x},t) = [-\nabla^2 - \mu + g|\Phi(\mathbf{x},t)|^2]\Phi(\mathbf{x},t), \tag{25}$$

which determines the dynamics of the macroscopic wave function:

$$\Phi(\mathbf{x},t) = f(\mathbf{x},t)\exp[i\phi(\mathbf{x},t)]. \tag{26}$$

The GP equation is obtained from the Hamilton–Jacobi equation for the Hamiltonian:

$$H = \int d\mathbf{x}\left[|\nabla\Phi(\mathbf{x},t)|^2 - \mu|\Phi(\mathbf{x},t)|^2 + \frac{g}{2}|\Phi(\mathbf{x},t)|^4\right], \tag{27}$$

where μ is the chemical potential, g is a coupling constant, $|\Phi(\mathbf{x},t)|^2 = f(\mathbf{x},t)^2$ is the condensate density, and the superfluid velocity $\mathbf{v}(\mathbf{x},t)$ is given by $\mathbf{v}(\mathbf{x},t) = 2\nabla\phi(\mathbf{x},t)$. The total number of condensate particles is $N = \int d\mathbf{x}|\Phi(\mathbf{x},t)|^2$. The vorticity $\omega(\mathbf{x},t) = \mathrm{rot}\mathbf{v}(\mathbf{x},t)$ vanishes everywhere in a single-connected region of the fluid, and thus all rotational flow is carried by quantised vortices. In the core of each vortex, $\Phi(\mathbf{x},t)$ vanishes so that the circulation around the core is quantised by 4π. The vortex core size is given by the healing length $\xi = 1/f\sqrt{g}$.

It should be noted that the hydrodynamics described by the GP model is compressible, which is different from the case of the vortex filament model. The total energy of Equation (27),

$$E(t) = \frac{1}{N}\int d\mathbf{x}\,\Phi^*(\mathbf{x},t)\left[-\nabla^2 + \frac{g}{2}f(\mathbf{x},t)^2\right]\Phi(\mathbf{x},t), \tag{28}$$

is represented by the sum of the interaction energy $E_{int}(t)$, the quantum energy $E_q(t)$ and the kinetic energy $E_{kin}(t)$ (Nore et al., 1997a,b):

$$E_{int}(t) = \frac{g}{2N}\int d\mathbf{x} f(\mathbf{x},t)^4,$$

$$E_q(t) = \frac{1}{N}\int d\mathbf{x}\,[\nabla f(\mathbf{x},t)]^2,$$

$$E_{kin}(t) = \frac{1}{N}\int d\mathbf{x}\,[f(\mathbf{x},t)\nabla\phi(\mathbf{x},t)]^2. \tag{29}$$

The kinetic energy is furthermore divided into a compressible part $E_{kin}^c(t)$ due to compressible excitations and an incompressible part $E_{kin}^i(t)$ due to vortices:

$$E_{kin}^c(t) = \frac{1}{N} \int d\mathbf{x} \, [\{f(\mathbf{x}, t)\nabla\phi(\mathbf{x}, t)\}^c]^2,$$

$$E_{kin}^i(t) = \frac{1}{N} \int d\mathbf{x} \, [\{f(\mathbf{x}, t)\nabla\phi(\mathbf{x}, t)\}^i]^2. \tag{30}$$

Here, $\{\cdots\}^c$ denotes the compressible part $\nabla \times \{\cdots\}^c = 0$, and $\{\cdots\}^i$ denotes the incompressible part $\nabla \cdot \{\cdots\}^i = 0$. Numerically, the compressible part $\mathbf{A}^c(\mathbf{x})$ and the incompressible part $\mathbf{A}^i(\mathbf{x})$ of an arbitrary vector field $\mathbf{A}(\mathbf{x})$ are given by

$$\mathbf{A}^c(\mathbf{x}) = \sum_\mathbf{k} \frac{\mathbf{k} \cdot \tilde{\mathbf{A}}(\mathbf{k})}{k^2} \mathbf{k} \exp(i\mathbf{k} \cdot \mathbf{x}), \ \mathbf{A}^i(\mathbf{x}) = \mathbf{A}(\mathbf{x}) - \mathbf{A}^c(\mathbf{x}), \tag{31}$$

where $\tilde{\mathbf{A}}(\mathbf{k})$ is the Fourier component of $\mathbf{A}(\mathbf{x})$. If the Kolmogorov spectrum is observed, it should be for the incompressible kinetic energy $E_{kin}^i(t)$, which comes from the Richardson cascade of quantised vortices.

Pioneering work on the GP model was made by Nore et al. (1997a,b). Starting with Taylor–Green flow, they followed the dynamics through the GP model. The initial vortices become tangled. They calculated numerically the time development of the incompressible kinetic energy spectra $E_{kin}^i(k, t)$, and by using the fit $E_{kin}^i(k, t) \sim k^{-n(t)}$, they obtained the exponent $n(t)$ as a function of time. As a tangle forms, $n(t)$ decreases to about $5/3$ for a short period. However, this behaviour is broken at later stages of tangle formation. We should note that this is a decaying turbulence. Although the total energy $E(t)$ is conserved, $E_{kin}^i(t)$ decreases with increasing $E_{kin}^c(t)$. This is attributable to that fact that many compressible excitations are created through repeated vortex reconnections (Leadbeater et al., 2001; Ogawa et al., 2002) and disturb the Richardson cascade of quantised vortices even at large scales. If the emission of the compressible excitations is effectively suppressed, the Richardson cascade may be preserved to lead to the Kolmogorov law. This expectation has yielded the following studies.

Kobayashi and Tsubota (2005a,b) overcame the difficulties of Nore et al. (1997a,b). and obtained the Kolmogorov spectra in QT and clearly revealed the energy cascade. The object of their work was to introduce dissipation that occurs only at small scales and effectively depress compressible excitations. Kobayashi and Tsubota (2005a,b) made numerical calculation for

the Fourier transformed GP equation:

$$i\frac{\partial}{\partial t}\tilde{\Phi}(\mathbf{k},t) = [k^2 - \mu]\tilde{\Phi}(\mathbf{k},t)$$

$$+ \frac{g}{V^2}\sum_{\mathbf{k}_1,\mathbf{k}_2}\tilde{\Phi}(\mathbf{k}_1,t)\tilde{\Phi}^*(\mathbf{k}_2,t) \times \tilde{\Phi}(\mathbf{k}-\mathbf{k}_1+\mathbf{k}_2,t), \quad (32)$$

where $\tilde{\Phi}(\mathbf{k},t)$ is the spatial Fourier component of $\Phi(\mathbf{x},t)$ and V is the system volume. The healing length is given by $\xi = 1/|\Phi|\sqrt{g}$. The problem here is suppressing the compressible excitations; Equation (32) needs a dissipation mechanism. Since the wavelength of the excitations emitted through vortex reconnections is of the order of the coherence length, the dissipation should work at such small scales. On the other hand, the dissipation should not work for vortices at larger scales. Thus, a dissipation is introduced:

$$(i - \tilde{\gamma}(\mathbf{k}))\frac{\partial}{\partial t}\tilde{\Phi}(\mathbf{k},t) = [k^2 - \mu(t)]\tilde{\Phi}(\mathbf{k},t)$$

$$+ \frac{g}{V^2}\sum_{\mathbf{k}_1,\mathbf{k}_2}\tilde{\Phi}(\mathbf{k}_1,t)\tilde{\Phi}^*(\mathbf{k}_2,t)$$

$$\times \tilde{\Phi}(\mathbf{k}-\mathbf{k}_1+\mathbf{k}_2,t). \quad (33)$$

Here, the dissipation should have the form $\tilde{\gamma}(\mathbf{k}) = \gamma_0\theta(k - 2\pi/\xi)$ with the step function θ, which satisfies the above conditions. Introducing a dissipative term conserves neither the energy nor the number of particles. However, for studying the hydrodynamics of turbulence, it is realistic to assume that the number of particles is conserved. Hence, we allow the chemical potential $\mu(t)$ to be time dependant so that the total number of particles N can be conserved. This form of dissipation can be justified by the coupled analysis of the GP equation for the macroscopic wave function and the Bogoliubov–de Gennes equations for thermal excitations (Kobayashi and Tsubota, 2006a).

5.2.1 Decaying Turbulence

By a numerical analysis of Equation (33), Kobayashi and Tsubota confirmed the Kolmogorov spectrum for both decaying (Kobayashi and Tsubota, 2005a) and steady turbulence (Kobayashi and Tsubota, 2005b). Details of the numerical procedures are described in their paper (Kobayashi and Tsubota, 2005b). To solve the GP equation numerically with high accuracy, they used a pseudo-spectral method in space with periodic boundary conditions in a box with a spatial resolution consisting of

$N_{grid} = 256^3$ grid points. The length scale was normalised by the healing length ξ, and the system was a cube of volume L^3 with $L = 32$. Calculations were made for $g = 1$, space resolution $\Delta x = 0.125$ and wavenumber resolution $\Delta k = 2\pi/L \simeq 0.196$. The numerical time evolution was calculated using the Runge–Kutta–Verner method with time resolution $\Delta t = 1 \times 10^{-4}$.

The first analysis was made for decaying turbulence. To obtain a turbulent state, they started the calculation from an initial configuration in which the density $f^2 = 1$ was uniform and the phase $\phi_0(\mathbf{x})$ had a random spatial distribution. The initial velocity $\mathbf{v}(\mathbf{x}, t = 0) = 2\nabla\phi_0(\mathbf{x})$ given by the initial random phase was also random. As a result, the initial wave function was dynamically unstable and soon developed to fully developed turbulence with many quantised vortex loops. A typical simulation was done for $\gamma_0 = 1$. The dissipation is shown in Figure 4, showing the time development of $E(t)$, $E_{kin}(t)$, $E_{kin}^c(t)$ and $E_{kin}^i(t)$ for (a) $\gamma_0 = 0$ and (b) $\gamma_0 = 1$. Without dissipation, the compressible kinetic energy $E_{kin}^c(t)$ increases in spite of the total energy conservation (Figure 4a), consistent with the simulation by Nore et al. (1997a,b). The dissipation suppresses $E_{kin}^c(t)$ and thus causes $E_{kin}^i(t)$ to be dominant in Figure 4b.

The spectrum $E_{kin}^i(k, t)$ of the incompressible kinetic energy was calculated. Initially, the spectrum significantly deviates from the Kolmogorov power-law. However, it approaches the power-law of $k^{-5/3}$ as turbulence develops. The authors also calculated the energy dissipation rate $\varepsilon = -\partial E_{kin}^i(t)/\partial t$ and compared the results quantitatively with the Kolmogorov law. Figure 5 shows a vortex tangle in developed turbulence
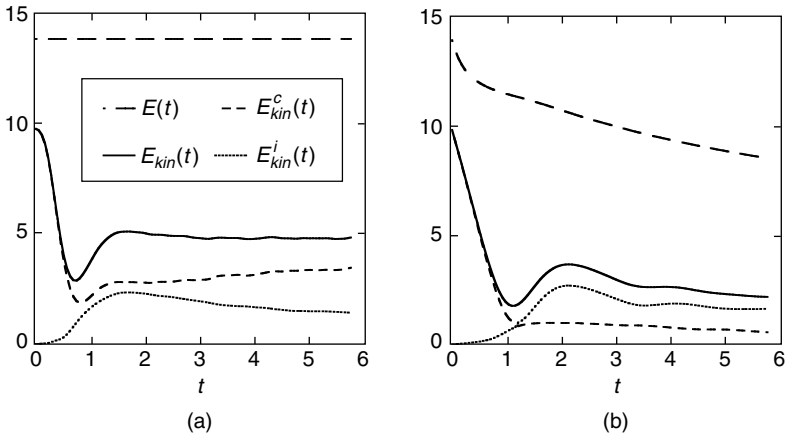
FIGURE 4   Time development of $E(t)$, $E_{kin}(t)$, $E_{kin}^c(t)$ and $E_{kin}^i(t)$ for (a) $\gamma_0 = 0$ and (b) $\gamma_0 = 1$ (Kobayashi and Tsubota, 2005a, reproduced with permission. Copyright (2005) by the American Physical Society).
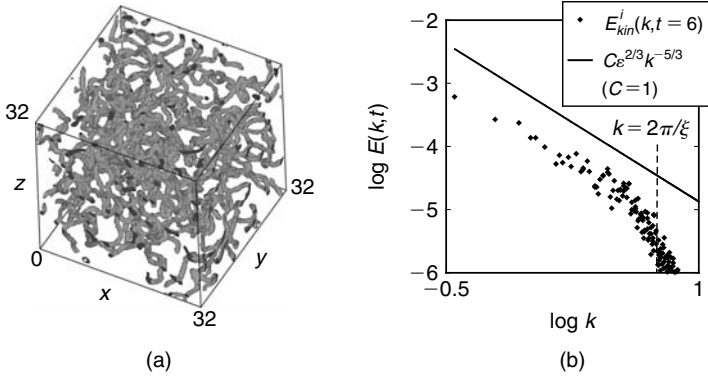
FIGURE 5   Simulated configuration of quantised vortices and the energy spectrum at
$t = 6$. (a) Configuration. (b) Energy spectrum obtained from an ensemble average of
20 initial states. The solid line indicates the Kolmogorov spectrum (Kobayashi and
Tsubota, 2005b).

and the energy spectrum of the ensemble average. Since the numerically
obtained ε was used for the black solid line, the energy spectrum was
found to be in quantitative agreement with the Kolmogorov law. The
Kolmogorov constant was estimated to be $C = 0.32 \pm 0.1$, smaller than
the value $1.4 \lesssim C \lesssim 1.8$ known for CT. Araki et al. (2002) obtained the
Kolmogorov constant $C \simeq 0.7$ by the vortex filament model, which is
also smaller than that in CT. This small Kolmogorov constant may be
characteristic of QT.

5.2.2 Steady Turbulence

A more elaborate analysis was made for steady QT by introducing energy
injection at large scales as well as energy dissipation at small scales
(Kobayashi and Tsubota, 2005b). The advantages of steady QT over decay-
ing QT are the following. First, steady QT gives a clearer correspondence
with the Kolmogorov law because the original statistics in the inertial range
have been developed for steady turbulence. Second, it enables confirma-
tion of the energy-containing range, inertial range and energy-dissipative
range of QT, which also exist in CT. Third, in all ranges, we can obtain
the time-independent energy flux in wavenumber space. Consequently,
it is possible to reveal the cascade process of QT, which is made only by
quantised vortices and short-wavelength excitations.

Energy injection at large scales was effected by moving a random
potential $V(\mathbf{x}, t)$. Numerically, Kobayashi and Tsubota (2005a,b) placed
random numbers between 0 and V_0 in space-time $(\mathbf{x}, t)$ at every distance
X_0 for space and T_0 for time, and connected them smoothly by using a

four-dimensional spline interpolation. The moving random potential exhibited the Gaussian two-point correlation:

$$\langle V(\mathbf{x}, t) V(\mathbf{x}', t') \rangle = V_0^2 \exp\left[-\frac{(\mathbf{x} - \mathbf{x}')^2}{2X_0^2} - \frac{(t - t')^2}{2T_0^2} \right]. \qquad (34)$$

This moving random potential had a characteristic spatial scale X_0. Small vortex loops were nucleated by the random potential, growing to the scale X_0 by its motion obeying Equation (34). The wavenumber $2\pi/X_0$ may be defined as separating the energy-containing range and the inertial range. The wavenumber $2\pi/\xi$ between the inertial range and the energy-dissipative range is defined as for decaying turbulence. Therefore, steady QT has an energy-containing range $k < 2\pi/X_0$, inertial range $2\pi/X_0 < k < 2\pi/\xi$ and energy-dissipative range $2\pi/\xi < k$.

   A typical simulation of steady turbulence was performed for $V_0 = 50$, $X_0 = 4$ and $T_0 = 6.4 \times 10^{-2}$, which are suitable numerical parameters to create fully-developed turbulence. The dynamics started from the uniform wave function $\Phi(\mathbf{x}, t = 0) = f_0 = 1$. Figure 6 shows the time development of each energy component. The moving random potential nucleates sound waves as well as vortices, but both figures show that the incompressible kinetic energy $E_{kin}^i(t)$ due to vortices is always dominant in the total kinetic energy $E_{kin}(t)$. As shown in Figure 6b, the four energies are almost constant for $t \gtrsim 25$ and steady QT was obtained.

   The steady QT is sustained by competition between energy injection at large scales and energy dissipation at small scales, which enables us to investigate the energy cascade. In this state, we expect an energy
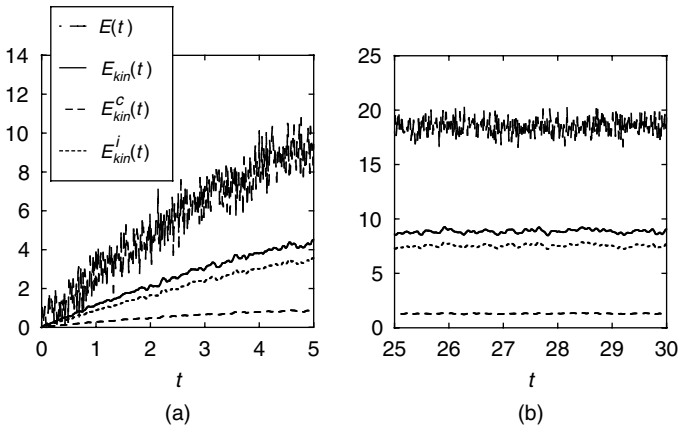
FIGURE 6   Time development of $E(t)$, $E_{kin}(t)$, $E_{kin}^c(t)$ and $E_{kin}^i(t)$ at (a) the initial stage $0 \leq t \leq 5$ and (b) a later stage $25 \leq t \leq 30$ (Kobayashi and Tsubota, 2005b).
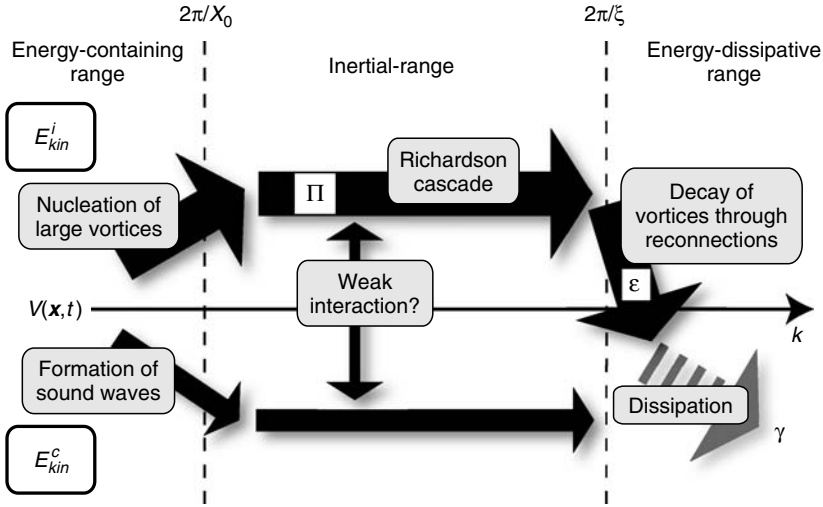
FIGURE 7 Flow of the incompressible kinetic energy $E^i_{kin}(t)$ (upper half of diagram) and compressible kinetic energy $E^c_{kin}(t)$ (lower half) in wavenumber space (Kobayashi and Tsubota, 2005b).

flow in wavenumber space similar to that in Figure 7. The upper half of the diagram shows the kinetic energy $E^i_{kin}(t)$ of quantised vortices and the lower half shows the kinetic energy $E^c_{kin}(t)$ of compressible excitations. In the energy-containing range $k < 2\pi/X_0$, the system receives incompressible kinetic energy from the moving random potential with effective 'nucleation' of large quantised vortex loops. During the Richardson cascade process of these quantised vortices, the energy flows from small to large k in the inertial range $2\pi/X_0 < k < 2\pi/\xi$. In the energy-dissipative range $2\pi/\xi < k$, the incompressible kinetic energy transforms to compressible kinetic energy through reconnections of vortices or the disappearance of small vortex loops. The moving random potential also creates long-wavelength compressible sound waves, which are another source of compressible kinetic energy and also produce an interaction with vortices. However, the effect of sound waves is weak because $E^i_{kin}(t)$ is much larger than $E^c_{kin}(t)$, as shown in Figure 6. Moreover, sound waves of long wavelength have a small scattering cross-section with vortex cores of the order of ξ.

This cascade can be confirmed quantitatively. It is important whether the energy dissipation rate ε of $E^i_{kin}(t)$ is comparable to the flux of energy $\Pi(k,t)$ through the Richardson cascade in the inertial range. First, the energy dissipation rate ε of $E^i_{kin}(t)$ in steady QT can be equated to $\varepsilon = -\partial E^i_{kin}(t)/\partial t$ after switching off the moving random potential. The
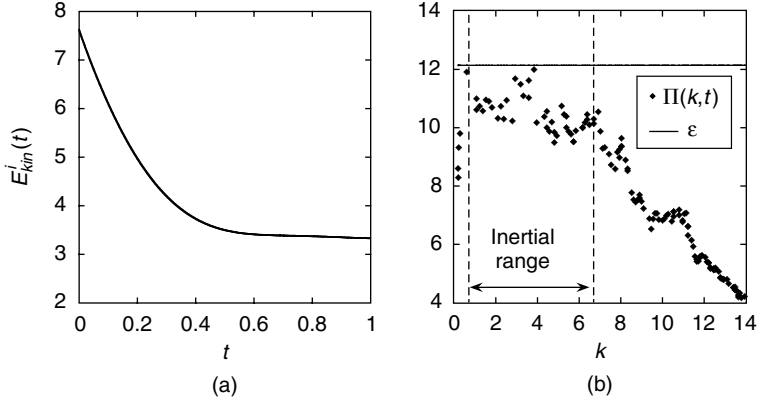
FIGURE 8   (a) Time development of the incompressible kinetic energy $E_{kin}^i(t)$ after switching off the moving random potential in steady QT. (b) Dependence of the energy flux $\Pi(k, t)$ on the wavenumber k. The energy flux was calculated from an ensemble average of 50 randomly selected states at $t > 25$. The solid line is the energy dissipation rate ε calculated from Figure 8 (a) (Kobayashi and Tsubota, 2005b).

incompressible kinetic energy decays to the energy of compressible short-wavelength excitations through dissipation. Figure 8a shows one example of the time development of $E_{kin}^i(t)$ after switching off the moving random potential. Initially, $E_{kin}^i(t)$ decreases almost linearly at a rate giving $\varepsilon \simeq 12.5 \pm 2.3$. Second, the energy flux $\Pi(k, t)$ of the incompressible kinetic energy in QT can be calculated by considering the scale-by-scale energy budget equation as well as CT (Frisch, 1995). The mathematics is complicated and is described in Appendix A. The obtained energy flux $\Pi(k, t)$ in Figure 8b is nearly constant at $\Pi(k, t) \simeq 11 \pm 1$ and consistent with the energy dissipation rate ε in the inertial range. These results show that the incompressible kinetic energy steadily flows in wavenumber space through the Richardson cascade at a constant rate Π and finally dissipates to compressible excitations at the rate $\varepsilon \simeq \Pi$. This energy flow is shown in the diagram of Figure 7. The energy flux Π is slightly smaller than the energy dissipation rate ε, which may be attributable to the weak interaction between vortices and sound waves.

The picture of the cascade process can be completed by calculating the energy spectrum $E_{kin}^i(k)$ as shown in Figure 9. The energy spectrum is quantitatively consistent with the Kolmogorov law in the inertial range $2\pi/X_0 < k < 2\pi/\xi$, which is equivalent to $0.79 \lesssim k \lesssim 6.3$. This inertial range is slightly narrower than that of the decaying turbulence because the moving random potential sets the energy-containing range. The resulting Kolmogorov constant C is $C = 0.55 \pm 0.07$, which is smaller than that in CT as well as that for decaying turbulence.
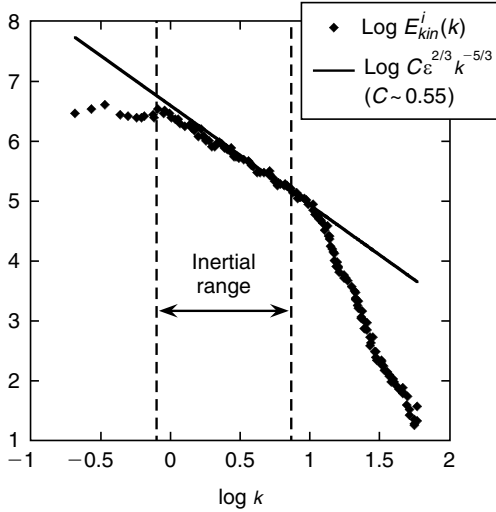
FIGURE 9   Energy spectrum $E_{kin}^i(k,t)$ for QT. The plotted points are from an ensemble average of 50 randomly selected states at $t > 25$. The solid line is the Kolmogorov law (Kobayashi and Tsubota, 2005b).

Kobayashi and Tsubota (2006b) studied the decay of QT under the same formulation. After obtaining a steady tangle, they switched off the motion of the random potential and found that L decayed as $t^{-3/2}$.

6. THE KELVIN-WAVE CASCADE

The arguments in the last section were chiefly limited to the large scale, usually larger than the mean spacing ℓ of a vortex tangle, in which the Richardson cascade of quantised vortices transfers the energy from large to small scales through reconnections. However, what happens at smaller scales for which the Richardson cascade should be less effective? The most probable scenario is the Kelvin-wave cascade. A Kelvin-wave is a deformation of a vortex line into a helix with the deformation propagating as a wave along the vortex line (Thomson, 1880). Kelvin-waves were first observed by making torsional oscillations in uniformly rotating superfluid ^{4}He (Hall, 1958, 1960). The approximate dispersion relation for a rectilinear vortex is given by

$$\omega_k = \frac{\kappa k^2}{4\pi}\left[\ln\left(\frac{1}{ka_0}\right) + c\right], \tag{35}$$

with a constant $c \sim 1$. It should be noted that this k is the wavenumber of an excited Kelvin-wave and is different from the wavenumber used for the energy spectrum in the last section. At a finite temperature where there is a significant fraction of normal fluid, Kelvin-waves should be damped by mutual friction. At very low temperatures in which the normal fluid component becomes negligible, however, mutual friction does not occur, and the only possible mechanism of dissipation is radiation of phonons (Vinen, 2001). Phonon radiation becomes effective only when the frequency becomes very high, typically the order of GHz ($k \sim 10^{-1}$ nm^{-1}), so a mechanism is required to transfer the energy to such high wavenumbers for Kelvin-waves to damp. An early numerical simulation based on the vortex filament model showed that Kelvin-waves are unstable to the buildup of side bands (Samuels and Donnelly, 1990). This indicates the possibility that nonlinear interactions between different Kelvin-wave numbers can transfer energy from small to large wavenumbers, namely the Kelvin-wave cascade. This idea was first suggested by Svistunov (1995) and later developed by Vinen et al. (2003) and Kozik and Svistunov (2004, 2005a,b). This section reviews this issue.

A vortex tangle undergoes frequent reconnections of vortices. The process of each reconnection is studied numerically in detail by the vortex filament model (Schwarz, 1985). When two vortices get close, they twist themselves so that they can become antiparallel at the closest point, growing small cusps or kinks at that point. The kinks lead to reconnection and the subsequent moving apart of the resulting vortices. Svistunov (1995) suggested that the relaxation of the sharp kinks causes the emission of Kelvin-waves, and this process plays an important role in the decay of a tangle. This process was confirmed numerically by Kivotides et al. (2001) by means of the vortex filament model at zero temperature. The dynamics starting with four vortex rings excites Kelvin-waves whenever the vortices collide and reconnect, while the system does not reach a steady state.

As described in the previous section, a statistically steady state is useful for studying the cascade process. In order to obtain a steady state due to Kelvin-wave cascade and a characteristic spectrum, Vinen et al. (2003) performed a numerical simulation of the vortex filament model under the full Biot–Savart law at zero temperature. They considered a model system in which the helium is contained in a space between two parallel plates separated by a distance $\ell_B = 1$ cm, with a single, initially rectilinear (along the z axis), quantised vortex extending between the plates. The allowed wavenumbers of the Kelvin-waves excited on the vortex would then be $k = 2\pi n/\ell_B$ with a positive integer n. Kelvin-waves in a small wavenumber mode n_0 are excited by applying a superflow field $v_{s,a} = V \sin(k_0 z - \omega_0 t)$, where $k_0 = 2\pi n_0/\ell_B$ and ω_0 is the related frequency of Equation (35).

The effective dissipation at high wavenumbers is modeled by a periodic smoothing process at a numerical spatial resolution of $1/60$ cm.

A typical result with $V = 2.5 \times 10^{-5}$ cm/s and $k_0 = 10\pi$ cm^{-1} is shown in Figure 10. The total length of the vortex line increases after drive flow $\mathbf{v}_{s,a}$ is turned on to reach a steady state of about 1.4 cm. The root mean square amplitude $\bar{\zeta}_k(t) = \langle \zeta_k^* \zeta_k \rangle^{1/2}$ of the Fourier components of the displacement of the vortex shows characteristic behaviour. Initially, only the mode that resonates with the drive is excited. However, as time passes, nonlinear interactions lead to the excitation of all the other modes. Eventually the spectrum reaches a steady state, shown by the solid line. In this steady state, energy is injected at a certain rate at the wavenumber k_0, transferred from small to large wavenumbers and eventually dissipated at the same rate at the highest wavenumber. The simulation confirms the energy-cascade behaviour via Kelvin-waves along a single vortex. For large values of k, where the modes practically form a continuum, the steady state seems to have, to a good approximation, a spectrum of the simple form

$$\bar{\zeta}_k^2 = A\ell_B^{-1}k^{-3} \tag{36}$$

with a dimensionless parameter A of order unity. Even if the drive amplitude V increases by a factor of ten or changes the drive wavenumber k_0, the steady state does not change, within the error of the simulations, at least at higher wavenumbers. Thus, the steady state is found to be robust approximately independently of the drive and the dissipation. No vortex
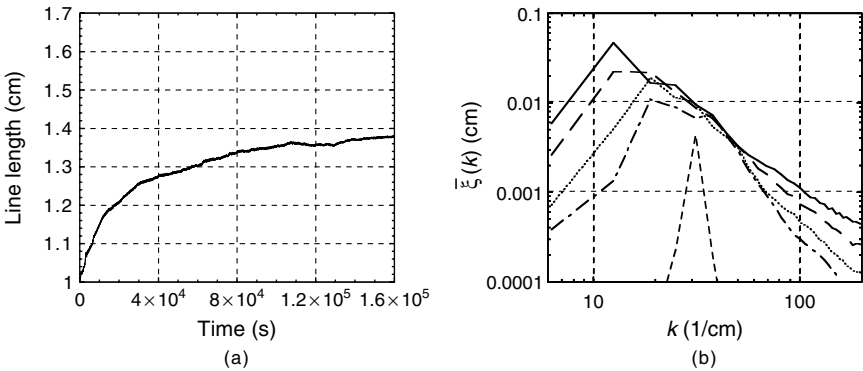
FIGURE 10   Numerical result showing how the steady state of Kelvin-wave cascade is formed. (a) Time development of the total length of the vortex line. (b) Time development of $\bar{\zeta}_k(t)$. The short-dashed line, the dash-dot line, the dotted line, the long-dashed line and the full line refer, respectively, to averages over 0–800 s, 10,000–10,800 s, 20,000–20,800 s, 40,000–40,800 s and 140,000–140,800 s. The full line relates to the steady state (Vinen et al., 2003, reproduced with permission. Copyright (2003) by the American Physical Society).

reconnections occur during the dynamics. In order to see how sensitive the steady state is to the drive or the dissipation, another method was adopted. The Fourier component ζ_k was increased at some k_{ex}, with all $k > k_{dis}$ removed, then returned to the real-space configuration of the vortex by the inverse Fourier transformation and continuing the vortex dynamics. This method yielded the same spectrum as that of the steady state. The mean energy per unit length of vortex in a mode k is related to $\bar{\zeta}_k$ by

$$E_k = \epsilon_K k^2 \bar{\zeta}_k^2 \tag{37}$$

where ϵ_K is an effective energy per unit length of vortex, given by

$$\epsilon_K = \frac{\rho \kappa^2}{4\pi} \left[\ln\left(\frac{1}{ka_0}\right) + c_1 \right]. \tag{38}$$

It follows from Equations (36) and (37) that

$$E_k = A\epsilon_K (k\ell_B)^{-1}. \tag{39}$$

Kozik and Svistunov (2004) analysed the Kelvin-wave cascade using weak-turbulence theory. Their treatment was based on a Hamiltonian describing the vortex line motion (Svistunov, 1995). They assumed that a Kelvin-wave is excited around the z axis, represented by the parametric form $x = x(z)$ and $y = y(z)$. When the amplitude or distortion of the Kelvin-wave is small, x and y are single-valued functions of z. Then, in terms of the complex canonical variable $w(z, t) = x(z, t) + iy(z, t)$, the Biot–Savart dynamics is transformed to the Hamiltonian form $i\, dw/dt = \delta H[w]/\delta w^*$ with

$$H = \frac{\kappa}{4\pi} \int dz_1 dz_2 \frac{1 + \mathrm{Re}[w'^*(z_1)w'(z_2)]}{\sqrt{(z_1 - z_2)^2 + |w(z_1) - w(z_2)|^2}}, \tag{40}$$

where the prime denotes the derivative with respect to z. The Hamiltonian can be expanded under the assumption that the amplitude of the Kelvin-wave is much smaller than its wavelength. When the lowest order Hamiltonian is diagonalised by a Fourier transformation of z, the amplitude means each mode of the Kelvin-wave, called a Kelvon, and the higher-order Hamiltonians describe the interaction or scattering between these Kelvons. Supposing that the leading process should be three-Kelvon scattering, the kinetic equation of the Kelvon occupation number n_k is reduced to

$$\dot{n}_1 \propto \sum_{\mathbf{k}_2, \cdots, \mathbf{k}_6} \left| V_{1,2,3}^{4,5,6} \right|^2 \delta(\Delta\omega)\delta(\Delta\mathbf{k}) \left(f_{4,5,6}^{1,2,3} - f_{1,2,3}^{4,5,6} \right). \tag{41}$$

Here, $V_{1,2,3}^{4,5,6}$ is the vertex for scattering from $(\mathbf{k}_1, \mathbf{k}_2, \mathbf{k}_3)$ to $(\mathbf{k}_4, \mathbf{k}_5, \mathbf{k}_6)$:

$$f_{1,2,3}^{4,5,6} = n_1 n_2 n_3 (n_4 n_5 + n_4 n_6 + n_5 n_6),$$
$$\Delta \mathbf{k} = \mathbf{k}_1 + \mathbf{k}_2 + \mathbf{k}_3 - \mathbf{k}_4 - \mathbf{k}_5 - \mathbf{k}_6,$$
$$\Delta \omega = \omega_1 + \omega_2 + \omega_3 - \omega_4 - \omega_5 - \omega_6.$$

The kinetic equation (Equation (41)) is found to support the energy cascade of Kelvons if two conditions are satisfied. The first is that the characteristic time decreases as the relevant wavenumbers increase, which is apparent from the dimensional estimate and has also been confirmed numerically (Kozik and Svistunov, 2005a). The second is that the collision term is local in wavenumber space, which can also be confirmed numerically. The kinetic equation (Equation (41)) yields $\dot{n}_k \sim k^5 |V|^2 \omega_k^{-1} k^{-1} n_k^5$. Since the relevant wavenumbers are of the same order of k, we have $|V| \sim k^6$ and

$$\dot{n}_k \sim \omega_k^{-1} n_k^5 k^{16}. \tag{42}$$

If we assume only a direct cascade from small to large wavenumbers, the energy flux (per unit vortex length) θ_k for wavenumber k is written as

$$\theta_k = L^{-1} \sum_{k' < k} \omega_{k'} \dot{n}_{k'}, \tag{43}$$

with the system size L. This gives $\theta_k \sim k \dot{n}_k \omega_k$. Combining this with Equation (42) yields $\theta_k \sim n_k^5 k^{17}$. The requirement that θ_k should be independent of k in the cascade process gives $n_k \sim k^{-17/5}$, which does not appear to contradict the numerical results of Vinen et al. (2003).

In order to determine the exponent more clearly, Kozik and Svistunov (2005a) developed a scale-separation numerical scheme effective for studying the Kelvin-wave cascade. The problem in this case is how to calculate the dynamics under the full Biot–Savart law of Equation (11) over a wide scale range. The basic idea is as follows. Interactions at a distance r are significant when the wavelength λ of Kelvin-waves exceeds r because the velocity fields from short wavelengths are cancelled. The characteristic time of a harmonic of wavelength λ scales as λ^2 so that the configuration of these harmonics does not change much for a time interval much shorter than λ^2. These considerations allow a rough time resolution for calculating the Biot–Savart contribution from distant regions, which improves the efficiency of the numerical simulation. Namely the Biot–Savart integral of Equation (11) at a point $\mathbf{s}$ is represented by a series of the integral from

different distances in the form

$$\dot{\mathbf{s}} = \sum_{n=1} \mathbf{Q}_n, \quad \mathbf{Q}_n = \frac{\kappa}{4\pi} \int\limits_{2^{n-1}a_0 < |\mathbf{s}_1 - \mathbf{s}| < 2^n a_0} \frac{(\mathbf{s}_1 - \mathbf{s}) \times d\mathbf{s}_1}{|\mathbf{s}_1 - \mathbf{s}|^3}. \quad (44)$$

The time-step for calculating $\mathbf{Q}_n$ is chosen to be proportional to the square of $\lambda_n = 2^n a_0$. Starting with the Kelvon distribution $n_k \propto k^{-3}$, Kozik and Svistunov (2004) numerically followed the dynamics of Kelvin-waves along a single vortex line. They found that the distribution changes to $n_k \propto k^{-\beta}$ with $\beta = 17/5$ with an absolute error less than 0.1. This result is consistent with that obtained previously by the same authors (Kozik and Svistunov, 2004).

Kinematic theory based on a weak-turbulence approach has been developed into a differential equation model by Nazarenko (2005). A differential equation preserving the essential scaling and solutions of the direct cascade of $n_k \propto k^{-17/5}$ is written as

$$\dot{n} = \frac{C}{\kappa^{10}} \omega^{1/2} \frac{\partial^2}{\partial \omega^2} \left(n^6 \omega^{21/2} \frac{\partial^2}{\partial \omega^2} \frac{1}{n} \right). \quad (45)$$

Here, C is a dimensionless constant, and $n(\omega)$ is related to n_k through the dispersion relation $\omega \simeq \kappa k^2/4\pi$ of the Kelvin-waves. This differential equation preserves the energy E and the wave action N (both per unit length of the vortex):

$$E = \frac{1}{2\sqrt{\kappa}} \int \omega^{1/2} n d\omega, \quad N = \frac{1}{2\sqrt{\kappa}} \int \omega^{-1/2} n d\omega. \quad (46)$$

As a result, Equation (45) has stationary solutions corresponding to the direct cascade of $n \sim k^{-17/5}$ and the inverse cascade of $n \sim k^{-3}$. It also has a family of thermodynamic Rayleigh–Jeans steady solutions $n = T/(\omega + \mu)$, where T and μ are constants representing temperature and chemical potential, respectively. This model is developed to include the effects of mutual friction or acoustic emission (L'vov et al., 2006).

It is now necessary to make experimental studies to observe the Kelvin-wave cascade. However, such studies are not easy for a vortex tangle. The easiest approach is to consider rotation. In a rotating vessel, quantised vortices form a vortex lattice parallel to the rotational axis (Donnelly, 1991). By oscillating the vortices, Kelvin-waves can be excited. This approach was used in the pioneering experiments by Hall (1958, 1960). The challenge is detecting the Kelvin-wave cascade when it occurs. There are two possible methods. The first is the direct visualisation of vortices. Recently, remarkable progress has been made on visualising superflow and quantised vortices (Bewley et al., 2006; Zhang and Van Sciver, 2005).

Bewley et al. (2006) visualised quantised vortices by trapping micron-sized solid hydrogen particles. They also observed a vortex array under rotation. The direct observation of vortex dynamics could reveal important information about the Kelvin-wave cascade. However, it would be necessary to determine whether such small particles are trapped by vortices even at very low temperatures and how they affect the vortex motion. This is discussed in the chapter by Van Sciver and Barenghi in this volume. The second method is to observe acoustic emission resulting from a Kelvin-wave cascade. Since the frequency of emitted phonons is estimated to be of GHz order, this observation may be not easy and it presents a challenging experimental problem.

7. CLASSICAL–QUANTUM CROSSOVER

As discussed in the previous sections, at scales larger than the mean vortex spacing ℓ, the Richardson cascade is effective for transferring energy from large to small scales, and the energy spectrum obeys the Kolmogorov law. This region may be considered classical. On the other hand, when the scale is smaller than ℓ, the Kelvin-wave cascade becomes dominant along each quantised vortex. This case may be considered quantum. This raises an important question: what is the nature of the transition between the classical and quantum regions? Several theoretical considerations on this topic have been made (Kozik and Svistunov, 2008; L'vov et al., 2007), though there are few numerical or experimental works. The problem is still controversial. This section briefly reviews the present status of this issue. In this section, $\Lambda = \ln(\ell/a_0)$ appears as an important parameter. Λ is about 15 in ^{4}He experiments.

L'vov et al. (2007) discussed theoretically a bottleneck crossover between the two regions. Their consideration was based on the idea that a vortex tangle obeying the Kolmogorov spectrum is polarised to some degree, viewed as a set of vortex bundles. This should be the case for a vortex tangle created by a towed grid (Stalp et al., 1999) or by rotation (Finne et al., 2003), but not by a counterflow. The energy spectrum in the classical region is the Kolmogorov form:

$$E_{cl}(k) \simeq \epsilon^{2/3} k^{-5/3}. \tag{47}$$

In the quantum region subject to the Kelvin-wave cascade, the Kelvon occupation number is $n_k \simeq (\ell^2 \epsilon)^{1/5} \kappa^{2/5} k^{-17/5}$ from the analysis by Kozik and Svistunov (2004). The kinetic energy per unit mass for Kelvin-waves is

$$E = \frac{L}{2\pi} \int \omega_k n_k \mathrm{d}k = \frac{1}{2\pi} \int E_{qu}(k) \mathrm{d}k \tag{48}$$

with the line length density $L \simeq \ell^{-2}$ and the frequency ω_k of the Kelvin-wave of Equation (35). The energy spectrum $E_{qu}(k)$ is

$$E_{qu}(k) \simeq \Lambda \left(\frac{\kappa^7 \epsilon}{\ell^8}\right)^{1/5} k^{-7/5}. \tag{49}$$

At the crossover of $k \simeq 1/\ell$, their ratio is

$$E_{qu}(1/\ell)/E_{cl}(1/\ell) \simeq \Lambda^{10/3} >> 1. \tag{50}$$

Thus, a serious mismatch occurs at the crossover scale between the classical and quantum spectra. This mismatch prevents the energy flux from propagating fully through the crossover region; this is called the bottleneck effect. In order to raise E_{cl} to the level of E_{qu} in this region, L'vov et al. (2007) used the so-called warm cascade solutions (Cannaughton and Nazarenko, 2004) and proposed a thermal-equilibrium type spectrum $E_{cross}(k) = Tk^2/\pi\rho$ between the classical and quantum spectra. Here, ρ is the fluid density, and T is a parameter representing the effective temperature, which is determined so that the energy spectra may match at the crossover region.

The analysis of L'vov et al. was based on the assumption that the coarse-grained macroscopic picture of quantised vortices remains valid down to the scale of ℓ. Not holding this assumption, Kozik and Svistunov (2008) investigated theoretically the detail of the structure of the vortex bundle in the crossover region. Depending on the types of the vortex reconnections, the crossover range near ℓ is furthermore divided into three subranges. First, the classical cascade surges into the region between $\Lambda^{1/2}\ell$ and $\Lambda^{1/4}\ell$ where polarised vortices form bundles. These vortex bundles reconnect with each other, giving $n_k \propto k^{-2}$. In the next region between $\Lambda^{1/4}\ell$ and ℓ, reconnections between neighbours in a bundle become dominant, and $n_k \propto k^{-1/2}$. The third range between ℓ and $\Lambda^{-1/2}\ell$ is dominated by self-reconnections of single vortices emitting vortex rings, giving $n_k \propto k^{-1}$. This eventually continues to the quantum region, namely the Kelvin-wave cascade region, with no vortex reconnections, thus allowing the bottleneck to be effectively bypassed. Each scenario looks reasonable while the width of the crossover range is $\Lambda^{1/2}\ell/\Lambda^{-1/2}\ell = \Lambda$, about only an order of magnitude in the case of ^{4}He. The analysis is based on the LIA of the vortex filament model. An intervortex interaction is indispensable for the polarisation of vortices. Hence, it is not obvious that these subranges are clearly distinguishable or observable in real helium systems.

Both theoretical works by L'vov et al. (2007) and Kozik and Svistunov (2008) are based on the idea that quantised vortices are locally polarised in a tangle. However, it is not certain how polarised they actually are. In order to resolve this important problem, a quantitative theory is required

together with a numerical simulation with sufficient resolution in the crossover region. For example, the reconnection rate per unit volume and time depends strongly on the polarisation of the tangle. A numerical or experimental observation could help resolve the problem.

Recently, there are a few experimental works on the topics, showing the reduction of the dissipation at low temperatures. The Helsinki group studied a vortex front propagation into a region of vortex-free flow in rotating superfluid ^{3}He-B by NMR measurements (Eltsov et al., 2007). The observed front velocity as a function of temperature shows the transition from laminar through quasi-classical turbulent to quantum turbulent. The front velocity is related with the effective dissipation, which exhibits the peculiar reduction at very low temperatures below about $0.25T_c$ with the critical temperature T_c. The authors claim that this is attributable to the bottleneck effect. The detail is discussed in the chapter of Eltsov et al. in this volume too. The Manchester group made another observation of the effective viscosity of turbulence in superfluid ^{4}He (Walmsley et al., 2007). Turbulence was produced by an impulsive spin down from an angular velocity to rest of a cube-shaped container, and the line length density was measured by scattering negative ions. The observed effective kinematic viscosity ν' in Equation (5) showed the striking reduction at low temperatures below about 0.8 K. In their case, the bottleneck effect is not so significant. The authors think of another mechanism, that is, the difficulty in transferring energy through wavenumbers from the three-dimensional Richardson cascade to the one-dimensional Kelvin-wave cascade.

8. SUMMARY AND DISCUSSIONS

In this chapter, we have reviewed the present understanding of the energy spectrum of QT. This section summarises the results and presents some additional problems.

A topic of recent interest is the similarities and differences between QT and CT. This interest has likely arisen from pioneering experiments of counter-rotating disks (Maurer and Tabeling, 1998) and towed grids (Stalp et al., 1999) and from theoretical considerations of the low-temperature limit (Svistunov, 1995). These two experiments, made at relatively high temperatures, supported the Kolmogorov spectrum at large scales. The energy spectrum is certainly the most important statistical quantity of turbulence. The observation of the Kolmogorov spectra was interpreted as indicating that the normal fluid and the superfluid components were coupled at scales larger than the mean vortex spacing ℓ by mutual friction (Vinen, 2000). However, the presence of the normal fluid complicates the system, as described below.

Several numerical studies have been made on the energy spectra of QT at zero temperature. Early studies using the GP model could not properly obtain the Kolmogorov spectrum (Nore et al., 1997a,b), while the later works confirmed it using the vortex filament model (Araki et al., 2002) with the GP model (Kobayashi and Tsubota, 2005a,b). The inertial range was found to be sustained by a Richardson cascade of quantised vortices, which is very different from the case of CT in which the cascade is only schematic (Frisch, 1995). Each numerical simulation has a narrow inertial range of only one order, not having sufficient resolution for studying the physics smaller than the mean vortex spacing ℓ.

The energy at scales smaller than ℓ is transferred by a Kelvin-wave cascade, which has been shown to be correct by theoretical and numerical studies (Kozik and Svistunov, 2004, 2005a; Svistunov, 1995; Vinen et al., 2003). However, experimental proof is required. The crossover between the classical (Richardson) and quantum (Kelvin-wave) cascade regions is still controversial.

The rest of this section will be devoted to a few topics not discussed in the text. The first is the effect on QT by the normal fluid at finite temperatures. Recently, the Helsinki group observed a strong dependence of QT on temperature in superfluid ^{3}He-B (Finne et al., 2003, 2006). The normal fluid in ^{3}He-B is so viscous that it is stationary in typical experiments, which is different from superfluid ^{4}He with a small normal-fluid viscosity. Considering ^{3}He-B, Vinen (2005) used a k-space diffusion equation approach and investigated theoretically how the energy spectra are modified by the normal fluid. Volovik (2003, 2004) and his collaborators studied the same problem by the coarse-grained hydrodynamic equation (L'vov et al., 2004). Their turbulent energy spectrum (L'vov et al., 2004) was similar to that obtained by Vinen in spite of the different formulation.

Another interesting topic is the vortex size distribution in QT. Vortices in CT are vague, and hence the distribution does not make sense. However, the case is different for QT comprised of definite quantised vortices. A power-law distribution has been reported in numerical (Araki et al., 2002) and theoretical studies (Mitani and Tsubota, 2006; Nemirovskii, 2006). Such a power-law of the vortex size distribution should indicate a self-similar structure in real space. It would be meaningful to ask how the self-similarity in real space is connected with the self-similarity in wavenumber space, namely the Kolmogorov spectrum. Studies along this direction are only possible for QT.

APPENDIX A

Energy Flux in Wavenumber Space by the GP Model

This appendix describes the derivation of the energy flux Π in Section 5.2.2. We start with the modified GP equation:

$$[i - \gamma(\mathbf{x}, t)]\frac{\partial}{\partial t}\Phi(\mathbf{x}, t) = [-\nabla^2 - \mu(t) + g|\Phi(\mathbf{x}, t)|^2 + V(\mathbf{x}, t)]\Phi(\mathbf{x}, t)$$
(A.1)

with the effective dissipation $\gamma(\mathbf{x}, t)$ and a moving random potential $V(\mathbf{x}, t)$. By using the Madelung transformation $\Phi(\mathbf{x}, t) = f(\mathbf{x}, t)\exp[i\phi(\mathbf{x}, t)]$, we obtain

$$f(\mathbf{x}, t)\frac{\partial}{\partial t}\phi(\mathbf{x}, t) = \gamma(\mathbf{x}, t)[2\nabla f(\mathbf{x}, t) \cdot \nabla\phi(\mathbf{x}, t) + f(\mathbf{x}, t)\nabla^2\phi(\mathbf{x}, t)]$$
$$+ \nabla^2 f(\mathbf{x}, t) - f(\mathbf{x}, t)[\nabla\phi(\mathbf{x}, t)]^2$$
$$- [gf(\mathbf{x}, t)^2 - \mu(t) + V(\mathbf{x}, t)]f(\mathbf{x}, t),$$
(A.2)

neglecting the terms $\nabla f(\mathbf{x}, t)$ and $\partial f(\mathbf{x}, t)/\partial t$ because they are not effective at scales larger than ξ. Defining a new variable $\mathbf{p}(\mathbf{x}, t) = f(\mathbf{x}, t)\nabla\phi(\mathbf{x}, t)$, this equation reduces to

$$\frac{\partial}{\partial t}\mathbf{p}(\mathbf{x}, t) + \mathbf{p}(\mathbf{x}, t) \cdot \nabla\mathbf{v}(\mathbf{x}, t) = \gamma(\mathbf{x}, t)\nabla[\nabla \cdot \mathbf{p}(\mathbf{x}, t)] + \mathbf{F}(\mathbf{x}, t), \quad \text{(A.3)}$$

where $\mathbf{F}(\mathbf{x}, t) = -\nabla[gf(\mathbf{x}, t)^2 - \mu(t) + V(\mathbf{x}, t)]f(\mathbf{x}, t)$. Then, for any function $A(\mathbf{x})$, we introduce the low-pass and high-pass filtered functions $A_k^<(\mathbf{x}) = \sum_{q \leq k} \tilde{A}(\mathbf{q})\exp[i\mathbf{q} \cdot \mathbf{x}]$ and $A_k^>(\mathbf{x}) = \sum_{q > k} \tilde{A}(\mathbf{q})\exp[i\mathbf{q} \cdot \mathbf{x}]$, respectively, and the operator of the low-pass filter $L_k : A(\mathbf{x}) \to A_k^<(\mathbf{x})$. Applying L_k and taking the scalar product with $\mathbf{p}_k^<(\mathbf{x}, t)$ to Equation (A.3), we obtain

$$\frac{1}{2}\frac{\partial}{\partial t}[\mathbf{p}_k^<(\mathbf{x}, t)]^2 + \mathbf{p}_k^<(\mathbf{x}, t) \cdot L_k[\mathbf{p}(\mathbf{x}, t) \cdot \nabla\mathbf{v}(\mathbf{x}, t)]$$
$$= \gamma(\mathbf{x}, t)\mathbf{p}_k^<(\mathbf{x}, t) \cdot \nabla[\nabla \cdot \mathbf{p}_k^<(\mathbf{x}, t)] + \mathbf{p}_k^<(\mathbf{x}, t) \cdot \mathbf{F}_k^<(\mathbf{x}, t). \quad \text{(A.4)}$$

Extracting the incompressible part of Equation (A.4) and integrating it over space yields the scale-by-scale incompressible kinetic energy budget equation:

$$\frac{\partial}{\partial t}\mathcal{E}(k, t) + \Pi(k, t) = -\Omega(k, t) + \mathcal{F}(k, t). \quad \text{(A.5)}$$

Here, we introduce the cumulative incompressible kinetic energy $\mathcal{E}(k,t)$ between 0 and k:

$$\mathcal{E}(k,t) = \frac{1}{N} \int d\mathbf{x}\, [\{\mathbf{p}_k^<(\mathbf{x},t)\}^i]^2, \tag{A.6}$$

the cumulative energy dissipation $\Omega(k,t)$:

$$\Omega(k,t) = -\frac{2}{N} \int d\mathbf{x}\, \gamma(\mathbf{x},t)\{\mathbf{p}_k^<(\mathbf{x},t)\}^i \cdot \{\nabla[\nabla \cdot \mathbf{p}_k^<(\mathbf{x},t)]\}^i, \tag{A.7}$$

the cumulative energy injection $\mathcal{F}(k,t)$:

$$\mathcal{F}(k,t) = \frac{2}{N} \int d\mathbf{x}\, \{\mathbf{p}_k^<(\mathbf{x},t)\}^i \cdot \{\mathbf{F}_k^<(\mathbf{x},t)\}^i \tag{A.8}$$

and the energy flux through k of the incompressible kinetic energy:

$$\Pi(k,t) = \frac{2}{N} \int d\mathbf{x} \left[\{\mathbf{p}_k^<(\mathbf{x},t)\}^i \cdot \{L_k[\mathbf{p}(\mathbf{x},t) \cdot \nabla \mathbf{v}(\mathbf{x},t)]\}^i \right]. \tag{A.9}$$

Equation (A.5) can be interpreted as follows: at a given scale k, the rate of change of the incompressible kinetic energy is equal to the energy injected by the force $\mathcal{F}(k,t)$ minus the energy dissipation $\Omega(k,t)$ minus the energy flux $\Pi(k,t)$ to smaller scales.

ACKNOWLEDGEMENTS

REFERENCES

Allen, J. F. and Misener, A. D. (1938). *Nature*, 141, 75.
Araki, T., Tsubota, M. and Nemirovskii, S. K. (2002). *Physical Review Letters*, 89, 145301.
Batchelor, G. K. (1953). *The Theory of Homogeneous Turbulence*. Cambridge University Press, Cambridge.
Bewley, G. P., Lathrop, D. P. and Sreenivasan, K. R. (2006). *Nature*, 441, 588.
Boratav, O. N., Pelz, R. B. and Zabusky, N. J. (1992). *The Physics of Fluids A*, 4, 581.
Bradley, D. I., Clubb, D. O., Fisher, S. N., Guenault, A. M., Halay, R. P., Matthews, C. J., Pickett, G. R., Tsepelin, V. and Zaki, K. (2006). *Physical Review Letters*, 96, 035301.

Cannaughtoni, C. and Nazarenko, S. V. (2004). *Physical Review Letters*, 92, 044501.

Donnelly, R. J. (1991). *Quantized Vortices in Helium II*. Cambridge University Press, Cambridge.

Eltsov, V. B., Golov, A. I., de Graaf, R., Hänninen, R., Krusius, M., L'vov, V. S. and Solntsev, R. E. (2007). *Physical Review Letters*, 99, 265301.

Eltsov, V. B., de Graaf, R., Hänninen, R., Krusius, M., Solntsev, R. E., L'vov, V. S., Golov, A. I. and Walmsley, P. M. (2008). *Progress in Low Temperature Physics: Quantum Turbulence*. 45–144, 16, 4.

Feynman, R. P. (1955). in edited by Gorter, C. J. (ed.), *Progress of the Low Temperature Physics*, vol. I, p. 17, North-Holland Publications, Amsterdam.

Finne, A. P., Araki, T., Blaauwgeers, R., Eltsov, V. B., Kopnin, N. B., Krusius, M., Skrbek, L., Tsubota, M. and Volovik, G. E. (2003). *Nature*, 424, 1022.

Finne, A. P., Eltsov, V. B., Hänninen, R., Kopnin, N. B., Kopu, K., Krusius, M., Tsubota, M. and Volovik, G. E. (2006). *Reports on Progress in Physics*, 69, 3157.

Fisher, S. N. and Pickett, G. R. (2008). *Progress in Low Temperature Physics: Quantum Turbulence*. 145–192, 16, 4.

Frisch, U. (1995). *Turbulence*. Cambridge University Press, Cambridge.

Gorter, C. J. and Mellink, J. H. (1949). *Physica*, 15, 285.

Hall, H. E. (1958). *Proceedings of the Royal Society of London Series A*, 245, 546.

Hall, H. E. (1960). *Philosophical Magazine Supplement*, 9, 89.

Hinze, J. O. (1975). *Turbulence*, 2nd ed. McGraw Hill, New York.

Kapitza, P. (1938). *Nature*, 141, 74.

Kivotides, D., Vassilicos, J. C., Samuels, D. C. and Barenghi, C. F. (2001). *Physical Review Letters*, 86, 3080.

Kivotides, D. (2007). *Physical Review B*, 76, 054503.

Kobayashi, M. and Tsubota, M. (2005a). *Physical Review Letters*, 94, 065302.

Kobayashi, M. and Tsubota, M. (2005b). *Journal of the Physical Society of Japan*, 74, 3248.

Kobayashi, M. and Tsubota, M. (2006a). *Physical Review Letters*, 97, 145301.

Kobayashi, M. and Tsubota, M. (2006b). *Journal of Low Temperature Physics*, 145, 209.

Kobayashi, M. and Tsubota, M. (2007). *Physical Review A*, 76, 045603.

Kolmogorov, A. N. (1941a). Doklady Akademaike Nauk SSSR, 30, 301 (reprinted in 1991, *Proceedings of the Royal Society A*, 434, 9).

Kolmogorov, A. N. (1941b). *Doklady Akademaike Nauk SSSR*, 31, 538 (reprinted in 1991, *Proceedings of the Royal Society A*, 434, 15).

Koplik, J. and Levine, H. (1993). *Physical Review Letters*, 71, 1375.

Kozik, E. and Svistunov, B. V. (2004). *Physical Review Letters*, 92, 035301.

Kozik, E. and Svistunov, B. V. (2005a). *Physical Review Letters*, 94, 025301.

Kozik, E. and Svistunov, B. V. (2005b). *Physical Review B*, 72, 172505.

Kozik, E. and Svistunov, B. V. (2008). *Physical Review B*, 77, 060502.

Leadbeater, M., Winiecki, T., Samuels, D. C., Barenghi, C. F. and Adams, C. S. (2001). *Physical Review Letters*, 86, 1410.

L'vov, V. S., Nazarenko, S. V. and Volovik, G. E. (2004). *JETP Letter*, 80, 479.

L'vov, V. S., Nazarenko, S. V. and Skrbek, L. (2006). *Journal of Low Temperature Physics*, 145, 125.

L'vov, V. S., Nazarenko, S. V. and Rudenko, O. (2007). *Physical Review B*, 76, 024520.

Maurer, J. and Tabeling, P. (1998). *Europhysics Letters*, 43, 29.

Mitani, A. and Tsubota, M. (2006). *Physical Review B*, 74, 024526.

Nazarenko, S. V. (2005). *JETP Letter*, 83, 198.

Nemirovskii, S. K. (1997). *Physical Review B*, 57, 5792.

Nemirovskii, S. K., Tsubota, M. and Araki, T. (2002). *Journal of Low Temperature Physics*, 126, 1535.

Nemirovskii, S. K. (2006). *Physical Review Letters*, 96, 015301.

Nore, C., Abid, M. and Brachet, M. E. (1997a). *Physical Review Letters*, 78, 3296.

Nore, C., Abid, M. and Brachet, M. E. (1997b). *The Physics of Fluids*, 9, 2644.

Ogawa, S., Tsubota, M. and Hattori, Y. (2002). *Journal of the Physical Society of Japan*, 71, 813.

Pethick, C. J. and Smith, H. (2002). *Bose-Einstein Condensation in Dilute Gases*. Cambridge University Press, Cambridge.

Saffman, P. G. (1992). *Vortex Dynamics*. Cambridge University Press, Cambridge.

Samuels, D. C. and Donnelly, R. J. (1990). *Physical Review Letters*, 64, 1385.

Schwarz, K. W. (1985). *Physical Review B*, 31, 5782.

Schwarz, K. W. (1988). *Physical Review B*, 38, 2398.

Smith, M. R., Donnelly, R. J., Goldenfeld, N. and Vinen, W. F. (1993). *Physical Review Letters*, 71, 2583.

Stalp, S. R., Skrbek, L. and Donnelly, R. J. (1999). *Physical Review Letters*, 82, 4831.

Stalp, S. R., Niemela, J. J., Vinen, W. F. and Donnelly, R. J. (2002). *The Physics of Fluids*, 14, 1377.

Skrbek, L., Niemela, J. J. and Donnelly, R. J. (2000). *Physical Review Letters*, 85, 2973.

Skrbek, L. and Stalp, S. R. (2000). *The Physics of Fluids*, 12, 2000.

Skrbek, L. and Vinen, W. F. (2008). *Progress in Low Temperature Physics: Quantum Turbulence*. 193–244, 16, 4.

Svistunov, B. V. (1995). *Physical Review B*, 52, 3647.

Thomson, J. (1880). *Philosophical Magazine*, 10, 155.

Tilley, D. R. and Tilley, J. (1990). *Superfluidity and Superconductivity*, 3rd ed. Institute of Physics Publishing, Bristol and Philadelphia.

Tough, J. T. (1982). in edited by Gorter, C. J. (ed.), *Progress in Low Temperature Physics*, vol. VIII, North-Holland Publications, Ameterdam [133 and references therein].

Tsubota, M., Araki, T. and Nemirovskii, S. K. (2000). *Physical Review B*, 62, 11751.

Tsubota, M., Araki, T. and Barenghi, C. F. (2003a). *Physical Review Letters*, 90, 205301.

Tsubota, M., Araki, T. and Vinen, W. F. (2003b). *Physica B*, 329-333, 224.

Vinen, W. F. (1957a). *Proceedings of the Royal Society A*, 240, 114.

Vinen, W. F. (1957b). *Proceedings of the Royal Society A*, 240, 128.

Vinen, W. F. (1957c). *Proceedings of the Royal Society A*, 242, 493.

Vinen, W. F. (2000). *Physical Review B*, 61, 1410.

Vinen, W. F. (2001). *Physical Review B*, 64, 134520.

Vinen, W. F. (2005). *Physical Review B*, 71, 024513.

Vinen, W. F. (2006). *Journal of Low Temperature Physics*, 145, 7.

Vinen, W. F. and Niemela, J. J. (2002). *Journal of Low Temperature Physics*, 128, 167.

Vinen, W. F., Tsubota, M. and Mitani, M. (2003). *Physical Review Letters*, 91, 135301.

Volovik, G. E. (2003). *JETP Letter*, 78, 533.

Volovik, G. E. (2004). *Journal of Low Temperature Physics*, 136, 309.

Walmsley, P. M., Golov, A. I., Hall, H. E., Levchenko, A. A. and Vinen, W. F. (2007). *Physical Review Letters*, 99, 265302.

Zhang, T. and Van Sciver, S. W. (2005). *Nature Physics*, 1, 36.

This page intentionally left blank

Turbulent Dynamics in Rotating Helium Superfluids

V. B. Eltsov[*]**, R. de Graaf**[*]**, R. Hänninen**[*]**,**
M. Krusius[*]**, R. E. Solntsev**[*]**, V. S. L'vov**[†]**,**
A. I. Golov[‡] and **P. M. Walmsley**[‡]

Contents

[*] Low Temperature Laboratory, Helsinki University of Technology, P.O.Box 5100, FI-02015-TKK, Finland
[†] Department of Chemical Physics, The Weizmann Institute of Science, Rehovot 76100, Israel
[‡] School of Physics and Astronomy, The University of Manchester, Manchester M13 9PL, UK

Abstract   New techniques, both for generating and detecting turbulence in the helium superfluids ^{3}He-B and ^{4}He, have recently given insight in how turbulence is started, what the dissipation mechanisms are, and how turbulence decays when it appears as a transient state or when externally applied turbulent pumping is switched off. Important simplifications are obtained by using ^{3}He-B as working fluid, where the highly viscous normal component is practically always in a state of laminar flow, or by cooling ^{4}He to low temperatures where the normal fraction becomes vanishingly small. We describe recent studies from the low temperature regime, where mutual friction becomes small or practically vanishes. This allows us to elucidate the mechanisms at work in quantum turbulence on approaching the zero temperature limit.

1. INTRODUCTION

The transition to turbulence is the most well known example of all hydrodynamic transitions. It has been marveled for centuries since dramatic demonstrations can be seen everywhere where a sudden change in the flow occurs, owing to a constriction in the flow geometry, for instance. For 50 years, it has been known that turbulence also exists in superfluids (Vinen and Donnelly, 2007), although by its very nature a superfluid should be a dissipation-free system. In many situations, it is found on the macroscopic level that superfluid vortex dynamics mimics the responses of viscous hydrodynamics. This is one of the reasons why it has been thought that superfluid turbulence might provide a shortcut to better understanding of turbulence in general. From the developments over the past 50 years we see that this has not become the case, superfluid turbulence is a complex phenomenon where experiments have often been clouded by other issues, especially by vortex formation and vortex pinning. Nevertheless, the topic is fascinating in its own right: when the flow velocity is increased, the inherently dissipation-free superfluid is observed to become dissipative and eventually turbulent. This is particularly intriguing in the zero temperature limit where the density of thermal excitations approaches zero and vortex motion becomes undamped down to very short wave lengths (of the order of the vortex core diameter).

There are two isotropic helium superfluids in which turbulence has been studied, namely the B phase of superfluid ^{3}He (^{3}He-B) and superfluid ^{4}He (^{4}He II). In the anisotropic A phase of superfluid ^{3}He (^{3}He-A), dissipation is so large that conventional superfluid turbulence is not expected at the now accessible temperatures above $0.1\,T_c$ (Finne et al., 2003). Instead rapid dynamics and large flow velocities promote in ^{3}He-A a transition in the topology and structure of the axially anisotropic

superfluid order parameter field, a transition from linear line-like vortices to planar sheet-like vortices (Eltsov et al., 2002). Turbulence has also been studied in laser-cooled Bose-Einstein condensed cold atom clouds although so far only theoretically (Kobayashi and Tsubota, 2008; Parker and Adams, 2005), but it is expected that experiments will soon follow. Here, we are reviewing recent work on turbulence in rotating flow in both ^{3}He-B and ^{4}He II, emphasising similarities in their macroscopic dynamics.

A number of developments have shed new light on superfluid turbulence. Much of this progress has been techniques driven in the sense that novel methods have been required, to make further advances in a field as complex as turbulence, where the available techniques both for generating and detecting the phenomenon are not ideal. Three developments will be discussed in this review, namely (i) the use of superfluid ^{3}He for studies in turbulence, which has made it possible to examine the influence of a different set of superfluid properties in addition to those of superfluid ^{4}He, (ii) the study of superfluid ^{4}He in the zero temperature limit where the often present turbulence of the normal component does not complicate the analysis and (iii) the use of better numerical calculations for illustration and analysis.

From the physics point of view, three major advances can be listed to emerge: in superfluid ^{3}He, one can study the transition to turbulence as a function of the dissipation in vortex motion (Eltsov et al., 2006a), known as mutual friction. The dissipation arises from the interaction of thermal excitations with the superfluid vortex when the vortex moves with respect to the normal component. In classical viscous flow, such a transition to turbulence would conceptually correspond to one as a function of viscosity. This is a new aspect, for which we have to thank the ^{3}He-B Fermi superfluid where the easily accessible range of variation in mutual friction dissipation is much wider than in the more conventional ^{4}He II Bose superfluid. We are going to make use of this feature in Section 2 where we examine the onset of superfluid turbulence as a function of mutual friction dissipation (Finne et al., 2006a).

Second, in Section 3, we characterise the total turbulent dissipation in superfluid ^{3}He as a function of temperature, extracted from measurements of the propagation velocity of a turbulent vortex front (Eltsov et al., 2007). A particular simplification in this context is the high value of viscosity of the ^{3}He normal component, which means that in practice the normal fraction always remains in a state of laminar flow.

Finally, our third main topic in Section 4 are the results from recent ion transmission measurements in superfluid ^{4}He (Walmsley et al., 2007a; Walmsley and Golov, 2008a), where the decay of turbulence is recorded from 1.6 K to 0.08 K. Here turbulent dissipation can be examined in the true zero temperature limit with no normal component. As a result we now

know that turbulence and dissipation continue to exist at the very lowest temperatures. Although the dissipation mechanisms of ^{4}He or ^{3}He-B in the $T \to 0$ limit are not yet firmly established (Kozik and Svistunov, 2005b; Vinen, 2000, 2001), it is anticipated that these questions will be resolved in the near future (Kozik and Svistunov, 2008b; Vinen, 2006).

Phrased differently, our three studies address the questions (i) how turbulence starts from a seed vortex which is placed in applied vortex-free flow in the turbulent temperature regime (Section 2), (ii) how vortices expand into a region of vortex-free flow (Section 3) and (iii) how the vorticity decays when the external pumping is switched off (Section 4). The common feature of these three studies is the use of uniformly rotating flow for creating turbulence and for calibrating the detection of vorticity. Turbulence can be created in a superfluid in many different ways, but a steady state of constant rotation does generally not support turbulence. Nevertheless, at present rotation is the most practical means of applying flow in a controlled manner in the millikelvin temperature range. In this review, we describe a few ways to study turbulence in a rotating refrigerator. Superfluid hydrodynamics supports different kinds of flow even in the zero temperature limit so that turbulent losses can vary greatly both in form and in magnitude, but generally speaking, the relative importance of turbulent losses tends to increase with decreasing temperature. Two opposite extremes will be examined: highly polarised flow of superfluid ^{3}He-B when a vortex front propagates along a rotating cylinder of circular cross-section (Section 3), and the decay of a nearly homogeneous isotropic vortex tangle in superfluid ^{4}He (Section 4), created by suddenly stopping the rotation of a container with square cross-section.

Turbulent flow in superfluid ^{3}He-B and ^{4}He is generally described by the same two-fluid hydrodynamics of an inviscid superfluid component with singly-quantised vortex lines and a viscous normal component. The two components interact via mutual friction. There are generic properties of turbulence that are expected to be common for both superfluids. However, there are also interesting differences which extend the range of the different dynamic phenomena which can be studied in the He superfluids:

- In typical experiments with ^{3}He-B, unlike with ^{4}He, the mutual friction parameter α can be both greater and smaller than unity (Figure 1) – this allows the study of the critical limit for the onset of turbulence at $\alpha \sim 1$ (Section 2).
- The viscosity of the normal component in ^{3}He-B is four orders of magnitude higher than in ^{4}He; hence the normal component in ^{3}He-B is rarely turbulent, which amounts to a major simplification at finite temperatures (but not in the $T = 0$ limit with a vanishing normal component).
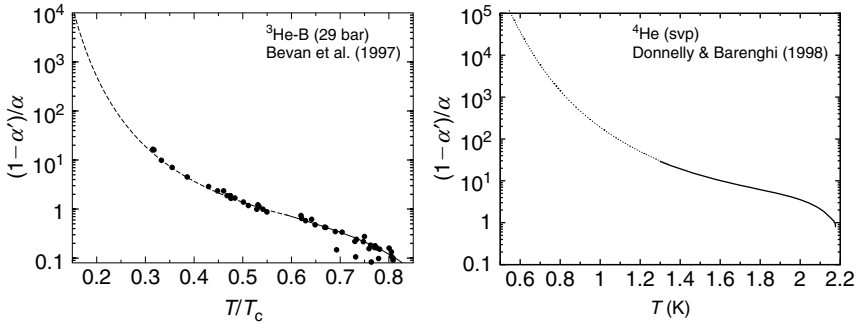
FIGURE 1 Mutual friction parameter $\zeta = (1 - \alpha')/\alpha$ as a function of temperature. In superfluid dynamics, this parameter, composed of the dissipative mutual friction $\alpha(T)$ and the reactive mutual friction $\alpha'(T)$, corresponds to the Reynolds number Re of viscous hydrodynamics. Typically, when $Re > 1$, turbulence becomes possible in the bulk volume between interacting evolving vortices. This transition to turbulence as a function of temperature can readily be observed in ^{3}He-B (at $0.59\,T_c$), while in ^{4}He II, it would be within $\sim 0.01\,$K from the lambda temperature and has not been identified yet.

- While the critical velocity v_c for vortex nucleation is much smaller in ^{3}He-B, pinning on wall roughness is also weaker; this makes it possible to create vortex-free samples which are instrumental in the transitional processes studied in Sections 2 and 3; on the other hand, the ever-present remanent vortices in superfluid ^{4}He are expected to ease the production of new vortices, which becomes important in such experiments as spin-up from rest.
- The vortex core diameter in both liquids is small (which allows us to use the model of one-dimensional line filaments), but in ^{3}He-B, it is up to three orders of magnitude larger than in ^{4}He; hence the dissipation mechanisms in the $T \to 0$ regime, which ultimately rely on the emission of excitations, are expected to work in ^{3}He-B at larger length scales and to lead to more significant energy loss in vortex reconnections.

A comparison of the turbulent dynamics in these two superfluids allows one to identify generic properties that are common for both superfluids, and also to pinpoint specific reasons when there are differences. The main quantity controlling dissipation is the mutual friction dissipation $\alpha(T)$, which dominates the temperature dependence of the dynamic mutual friction parameter $\zeta = (1 - \alpha')/\alpha$, shown in Figure 1. Experimental values are plotted with filled symbols for ^{3}He-B (Bevan et al., 1997) and with a solid line for ^{4}He (Donnelly and Barenghi, 1998). At low temperatures, the following extrapolations are used (shown as dashed lines): for ^{3}He-B at a pressure $P = 29$ bar, we use $\alpha = 37.21 \exp(-1.968T_c/T)$, where

the value for the superfluid gap $\Delta = 1.968 T_c$ is a linear interpolation as a function of density ρ between the weak coupling value at zero pressure and that measured by Todoshchenko et al. (2002) at melting pressure. For ^{4}He at saturated vapour pressure (svp), we follow Kozik and Svistunov (2008b) and use $\alpha = 25.3 \exp(-8.5/T)T^{-1/2} + 5.78 \cdot 10^{-5}T^5$, where T is in K.

2. DYNAMIC INSTABILITY—PRECURSOR TO TURBULENCE

2.1 Introduction

In practice, superfluid flow remains dissipation-free only as long as there are no quantised vortices (or the existing vortices do not move, which is more difficult to arrange). The classic question in superfluid hydrodynamics is therefore: how is the quantised vortex formed (Feynman, 1955; Vinen, 1963)? In flow measurements with bulk liquid, the understanding about the origin of the first vortex has been improving in recent times. Whether it is created in an intrinsic nucleation process (Ruutu et al., 1997) or from remanent vortices (Solntsev et al., 2007), which were created earlier in the presence of flow or while cooling the sample to the superfluid state (Hashimoto et al., 2007), these questions we are not going to address here. Instead we assume that the first vortex is already there, for instance as a remanent vortex. We then ask the question: how is turbulence started when the flow velocity is suddenly increased by external means? After all a turbulent vortex tangle is created through the interaction of many vortices: so how can turbulence start from a single seed vortex?

In rotating ^{3}He-B, one can create reliably a metastable state of vortex-free flow. It is then possible to inject a single vortex ring into the flow with neutron irradiation. When a slow thermal neutron undergoes a capture reaction in liquid ^{3}He with a ^{3}He nucleus, a vortex ring may escape from the overheated reaction bubble into the flow if the flow velocity is above a critical value (Eltsov et al., 2005). Making use of this phenomenon, one can inject a single vortex ring in vortex-free flow at different temperatures. At low temperatures, it is observed that a turbulent vortex tangle is spontaneously formed from the injected ring (Finne et al., 2004a), while at high temperatures, only a single vortex line results (Ruutu et al., 1998a). What is the explanation?

This demonstration in ^{3}He-B shows that in addition to the applied flow velocity also mutual friction matters importantly in the formation of new vortices, in their expansion, and in the onset of turbulence. In ^{3}He-B, mutual friction dissipation $\alpha(T)$ is strongly temperature-dependent (Figure 1), and it so happens that $\alpha(T)$ drops to sufficiently low value for the onset of turbulence in the middle of the accessible temperature range. The principle of seed vortex injection experiments is summarised in
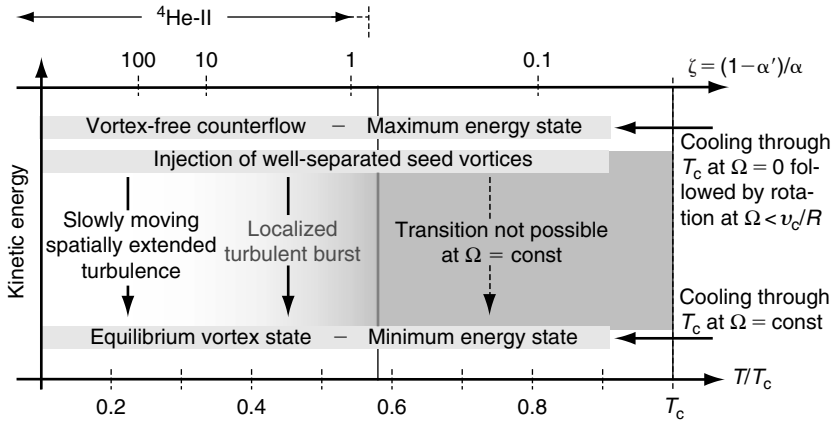
FIGURE 2 Principle of measurements on seed vortex injection at constant rotation Ω and temperature T. Well-separated isolated seed vortices are introduced in rotating vortex-free counterflow. The initial high-energy state may then relax to the equilibrium vortex state via vortex generation processes which become possible at temperatures below the hydrodynamic transition at $0.59\, T_c$. The Kelvin-wave instability of a single evolving seed vortex is the first step in this process. It is then followed by a turbulent burst which is started if the density of newly created vortices grows sufficiently. The combined process depends on the dynamic mutual friction parameter $\zeta = (1 - \alpha')/\alpha$ which is shown on the top. On the very top, the range of variation for this parameter in ^{4}He-II is indicated, that is, the temperature regime of conventional ^{4}He-II measurements.

Figure 2. In these measurements, the number and configuration of the injected vortex loops can be varied. It turns out that the highest transition temperature is observed when turbulence starts in bulk volume from many small vortex loops in close proximity of each other. This transition has been found to be at $T_{\mathrm{on}}^{\mathrm{bulk}} \sim 0.6\, T_c$ (Finne et al., 2004b) and to be independent of flow velocity over a range of velocities ($3 - 6\,\mathrm{mm/s}$). In viscous hydrodynamics, the Reynolds number is defined as $Re = UD/\nu_{\mathrm{cl}}$, where U is the characteristic flow velocity, D the relevant length scale of the flow geometry, and $\nu_{\mathrm{cl}} = \eta/\rho$ the kinematic viscosity. In an isotropic superfluid, the equivalent of the Reynolds number proves to be $\zeta = (1 - \alpha')/\alpha$. It defines the boundary between laminar and turbulent flow as a function of dissipation and is independent of flow velocity or geometry (Finne et al., 2006b).

However, if we inject instead of several closely packed vortex loops only one single seed loop in vortex-free flow (or several loops but so far apart that they do not immediately interact), then the transition to turbulence is found to be at a lower temperature and to depend on the flow velocity. Thus the onset of turbulence must also have a velocity dependent boundary.

To explain all these observations, one has to assume that an independent precursor mechanism exists, which creates more vortices from a seed vortex evolving in externally applied flow. The characterisation of this instability is the topic of this section. It turns out that this can be done in ^{3}He-B in the temperature regime close to the onset T_{on}^{bulk} of turbulence in the bulk volume. Here the precursor often progresses sufficiently slowly so that it can be captured with present measuring techniques, while at lower temperatures turbulence starts too rapidly. This latter case is exactly what happens in ^{4}He II: mutual friction dissipation is always so low in the usual experimental temperature range that the instability has not been explicitly identified.

The central question is the reduced stability of the evolving seed vortex loop when mutual friction dissipation is decreasing on cooling to lower temperature. At sufficiently low $\alpha(T)$, an evolving vortex becomes unstable with respect to loop formation, so that one or more new vortex loops are split off, before the seed vortex has managed to reach its stable state as a rectilinear line parallel to the rotation axis. The evolution during this entire process, from injection to the final state, is depicted in Figure 3 in a rotating cylindrical sample. The final state is the equilibrium vortex state, with an array of rectilinear vortex lines, where their areal density n_v in the transverse plane is given by the rotation velocity Ω: $n_v = 2\Omega/\kappa$. Here, $\kappa = 2\pi\hbar/2m_3 = 0.066 \, \text{mm}^2/\text{s}$ is the superfluid circulation quantum of the condensate with Cooper-pairs of mass $2m_3$. In this equilibrium state at constant rotation, the superfluid component is locked to solid-body
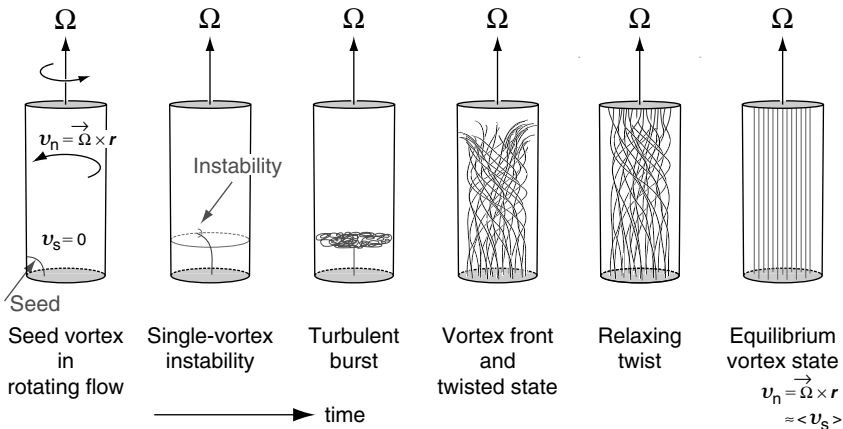
FIGURE 3 Vortex instability and turbulence in a rotating column of ^{3}He-B in the turbulent temperature regime, $T < T_{on}^{bulk}$. A seed vortex loop is injected in applied vortex-free flow and the subsequent evolution is depicted. Different transient states are traversed until the stable rotating equilibrium vortex state is reached.

rotation with the normal component when averaged over lengths exceeding the inter-vortex distance $\ell \sim 1/\sqrt{n_v}$. In the ideal case, all vortices are here rectilinear, while in the transient states in Figure 3, vortices can exist in many different configurations.

In Figure 4, a rough classification is provided of the stability of vortices as a function of temperature (or more exactly mutual friction) in different configurations and rotating situations. The lowest temperatures below $0.3\,T_c$ are in the focus of current research and have by now been probed with a few different types of measurements. The most extensive work has been performed by the Lancaster group. They create with various vibrating oscillators in a quiescent ^{3}He-B bath a vortex tangle and then monitor the decay of the tangle with a vibrating wire resonator (Bradley et al., 2006). The total turbulent dissipation in a vortex front propagating along a rotating column (see Figure 3) has recently been measured (Eltsov et al., 2007) and will be discussed in Section 3. Also the response of the
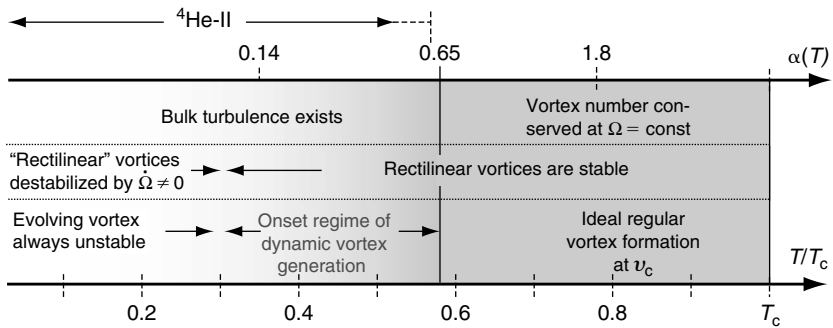
FIGURE 4   Summary of vortex stability in rotating counterflow of ^{3}He-B, as a function of temperature. Top row: the hydrodynamic transition at $T_{on}^{bulk} \approx 0.59\,T_c$ (at $P = 29$ bar pressure) separates regular and turbulent vortex dynamics. Above the transition, vortices are stable in all situations which have been studied, while below the transition, turbulence becomes possible. Middle row: in rotation at constant Ω, rectilinear vortices are stable. In time-dependent rotation ($|\dot{\Omega}| \neq 0$), the "rectilinear" vortex turns out to be an idealisation, presumably because of the experimentally inevitable slight misalignment between the rotation and the sample cylinder axes and because of surface interactions. In practice, the "rectilinear" vortices are found to be stable above $\sim 0.3\,T_c$ in time-dependent rotation, while at lower temperatures, they tend to transform to increasingly turbulent configurations with increasing $|\dot{\Omega}|$. Bottom row: dynamically evolving vortices are stable above the transition, but at lower temperatures, an evolving vortex may become unstable, generate a new vortex and eventually bulk turbulence. The conditions at seed vortex injection determine the onset temperature T_{on} below which turbulence follows. The onset temperatures have been found to concentrate in the regime $0.35\,T_c < T_{on} < 0.59\,T_c$. The very low temperatures below $0.3\,T_c$ display consistently turbulent response.

superfluid component has been studied to rapid step-like changes in rotation when Ω is changed from one constant value to another. This type of measurement is commonly known as spin-up or spin-down of the superfluid fraction and will be extensively described for spin-down in the case of superfluid ^{4}He later in this review.

2.2 Seed Vortex Evolution in Rotating Column

The motion of a seed vortex follows a distinctive pattern while it expands in a rotating cylinder. Numerically calculated illustrations are shown in Figures 5 and 6 which depict the evolution of the seeds to stable rectilinear lines. In Figure 5, an example with remanent vortices is examined, while in Figure 6, the initial configuration is an equilibrium vortex state in the usual situation that the rotation and cylinder axes are inclined by some small

$t = 0$
$N = 22$ vortices
$\Omega = 0.1$ rad/s

$t = 600$ s
$N = 12$
$\Omega_i = 0$

$t = 700$ s
$N = 12$
$\Omega_f = 0.5$ rad/s

$t = 800$ s
$N = 12$
$\Omega_f = 0.5$ rad/s
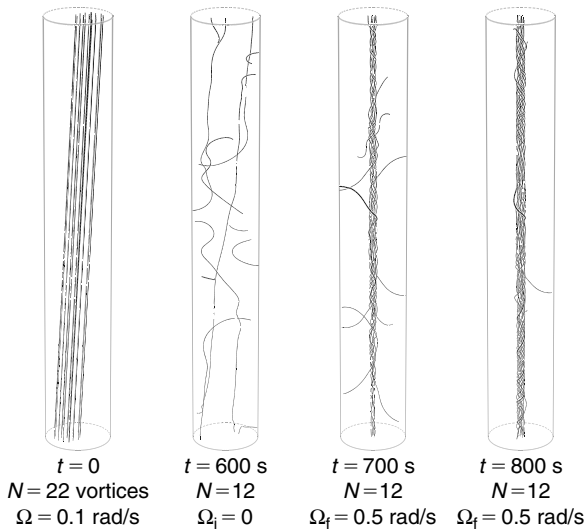
FIGURE 5 Numerical calculation of the evolution of remanent vortices in rotating flow (de Graaf et al., 2007). $t \leq 0$: initial state with 22 vortices at 0.1 rad/s rotation. The vortices have been artificially tilted by 1.4°, by displacing their end points uniformly by 1 mm at both end plates of the cylinder, to break cylindrical symmetry. $t = 0$: rotation is abruptly reduced to zero to allow vortices to annihilate. $t = 600$ s: after a waiting period $\Delta t = 600$ s at zero rotation, 12 remanent vortices remain in dynamic state. Rotation is then suddenly increased to $\Omega_f = 0.5$ rad/s. $t \geq 600$ s: the 12 remnants start evolving towards rectilinear lines. This requires that the vortex ends on the cylindrical wall travel in spiral motion to the respective end plates. The parameters are radius $R = 3$ mm and length $h = 80$ mm of cylinder, $T = 0.4\,T_c$, $P = 29.0$ bar, $\alpha = 0.18$ and $\alpha' = 0.16$ (Bevan et al., 1997). In the figure, the radial lengths have been expanded by two compared to axial distances.
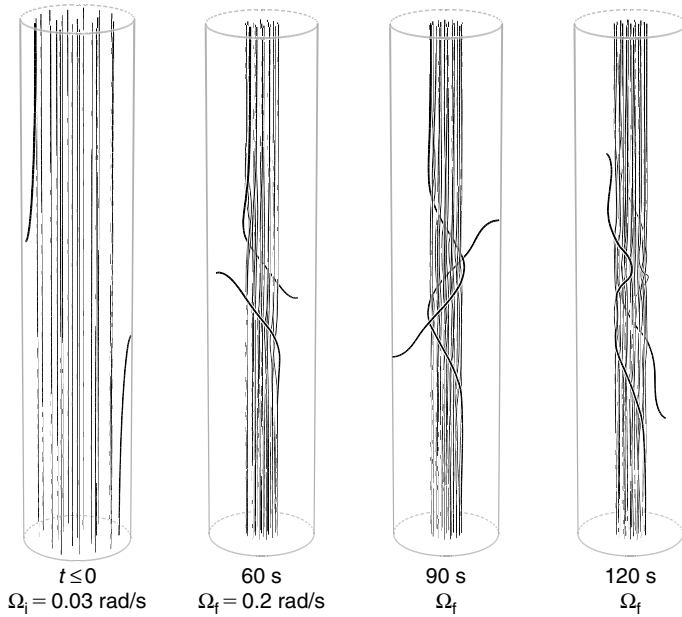
FIGURE 6 Numerical calculation of the evolution of two curved peripheral vortices in an inclined rotating cylinder, when rotation is suddenly increased at $t = 0$ from the equilibrium vortex state at $\Omega_i \approx 0.03$ rad/s to $\Omega_f = 0.2$ rad/s (Hänninen et al., 2007a). There are 22 vortices in this sample, of which two in the outermost ring (lying opposite to each other) have been initially bent to the cylindrical wall, to mimic an inclined cylinder. In the later snapshots at Ω_f, the two short vortices expand towards the top and bottom end plates of the cylinder, to reach their final stable state as rectilinear lines. Parameters: $R = 3$ mm, $h = 30$ mm, $P = 29.0$ bar and $T = 0.4\,T_c$ (which corresponds to $\alpha = 0.18$ and $\alpha' = 0.16$).

residual angle $\sim 1°$. These calculations (in a rotating circular cylinder with radius R and length h) describe the situation at intermediate temperatures when the vortex instability does not yet occur. The purpose is to focus on the motion of the expanding vortices and the transient configurations which thereby evolve. The characteristic property is the spiral trajectory of a vortex end along the cylindrical wall and the strong polarisation on an average along the rotation axis. The calculations have been performed using the numerical techniques described in Section 2.5 (de Graaf et al., 2007).

In Figure 5, the remnants are obtained from an equilibrium vortex state rotating at 0.1 rad/s, by reducing rotation to zero in a sudden step-like deceleration. The vortices are then allowed to annihilate at zero rotation for a period Δt. Some leftover remnants, which have not yet managed to annihilate, still remain after this annihilation time. Ideally smooth walls

are assumed without pinning. By suddenly increasing rotation from zero to a steady value $\Omega_f = 0.5\,\mathrm{rad/s}$, the remaining remnants are forced to expand. The configuration 100 s later shows how the spiral vortex motion has created a twisted vortex cluster in the centre, with a few vortex ends still traveling in circular motion around the cluster. This motion thus winds the evolving vortex around the straighter vortices in the centre. On the far right 200 s after the start of the expansion, the cluster is almost completed. Nevertheless, this state is still evolving since ultimately also the helical twist relaxes to rectilinear lines, while the vortex ends slide along the end plates of the container.

In Figure 6, a calculation is presented with 20 rectilinear vortex lines and two short vortices which connect at one end to the cylindrical wall. This configuration mimics the equilibrium vortex state in a real rotating experiment where there exists some residual misalignment between the rotation and sample cylinder axes. Depending on the angle of misalignment and the angular velocity of rotation Ω_i, some of the peripheral vortices may then end on the cylindrical sidewall in the equilibrium vortex state, as shown on the far left. At $t = 0$, rotation is increased in step-like manner from Ω_i to a higher value Ω_f. Two types of vortex motion are started by the rotation increase. First, the $N = 20$ rectilinear vortices are compressed to a central cluster with an areal density $n_v = 2\Omega_f/\kappa$ by the surrounding azimuthally flowing counterflow. Outside the vortex cluster, the counterflow has the velocity

$$v(\Omega_f, r, N) = v_n - v_s = \Omega_f r - \kappa N/(2\pi r). \tag{1}$$

The normal excitations are in solid-body rotation and thus $v_n = \Omega_f r$, while the superflow velocity around a cluster of κN circulation quanta is decaying as $v_s = \kappa N/(2\pi r)$, where $r \geq R_v$ and the cluster radius $R_v \approx R\sqrt{\Omega_i/\Omega_f}$. Experimentally it is convenient to define the number of vortices N via the initial equilibrium vortex state: $N = N_{eq}(\Omega_i)$, where the externally adjusted rotation velocity $\Omega_i \sim \kappa N_{eq}/(2\pi R^2)$ uniquely defines N_{eq} in a given experimental setup. It is customary to denote this specially prepared calibration value with $\Omega_v = \Omega_i$. The maximum counterflow velocity at Ω_f at the cylinder wall is then given by $v \approx (\Omega_f - \Omega_v)R$. This definition has been used in Figure 7 to characterise the number of vortices in the central cluster.

The second type of vortex motion, which is enforced by the increased rotation in Figure 6, is the spiral motion of the two short vortices as they become mobile and start expanding towards the top and bottom end plates, respectively. Let us now examine this motion in more detail.

A vortex moving with respect to the superfluid component is subject to the influence from the Magnus lift force. This force can be written as
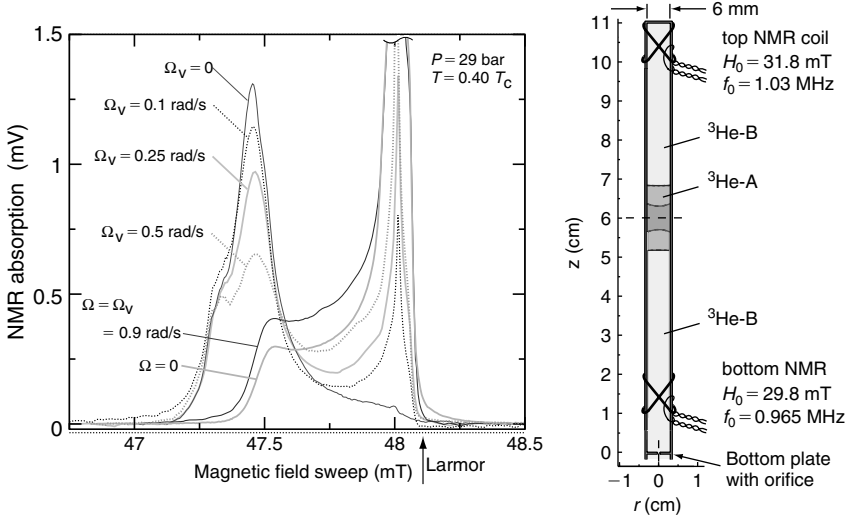
FIGURE 7 On the left, the NMR absorption spectra constitute an image of the 'flare-out' order parameter texture in the long rotating cylinder (Kopu et al., 2000). The Larmor field, around which the NMR absorption is centred in the normal phase, is here at 48.1 mT. In the B phase, the Larmor value becomes a sharp edge beyond which at higher fields the absorption vanishes, while most of the absorption is shifted to lower fields. The dominant absorption maximum on the left is the counterflow peak. Its height depends on the number of vortices N in the central cluster. N can be defined in terms of the rotation velocity Ω_v at which the vortices form the equilibrium state: $N = N_{eq}(\Omega_v)$. Here all counterflow peaks have been recorded at the counterflow velocity $\Omega - \Omega_v = 0.8$ rad/s. The conversion from peak height to N in given conditions (T, Ω, P) can be obtained experimentally or from a numerical calculation of the order parameter texture and the corresponding line shape (Kopu, 2006). The two line shapes without a counterflow peak, but with a large truncated maximum bordering to the Larmor edge, are for the nonrotating sample ($\Omega = 0$) and for the equilibrium vortex state ($N = N_{eq}$) at $\Omega_v = 0.9$ rad/s. For both of them, the absorption at the site of the counterflow peak is close to zero. On the right, a NMR setup is shown which was used to study the onset temperature of turbulence (cf. also Figure 13). Two different contours of the AB interface are shown when the A-phase barrier layer is present at $0.6\,T_c$. The contours correspond to a current of 4 A (narrow A-phase sliver with curved concave interfaces) and 8 A (wider A-phase layer with flat interfaces) in the superconducting A-phase stabilisation solenoid (Finne et al., 2004b).

(Donnelly, 1991) (ρ_s is the density of the superfluid fraction)

$$\mathbf{f}_M = \rho_s \kappa \, \hat{\mathbf{s}} \times (\mathbf{v}_L - \mathbf{v}_s), \tag{2}$$

which acts on a vortex element $\mathbf{s}(\xi, t)$ with a tangent unit vector $\hat{\mathbf{s}} = d\mathbf{s}/d\xi$ moving with velocity $\mathbf{v}_L = d\mathbf{s}/dt$ with respect to the superfluid

component, which locally has the velocity $\mathbf{v}_s$. The motion from the Magnus force is damped by mutual friction which arises when the vortex moves with respect to the surrounding cloud of normal excitations:

$$\mathbf{f}_{mf} = -\gamma_0 \rho_s \kappa \, \hat{\mathbf{s}} \times [\hat{\mathbf{s}} \times (\mathbf{v}_n - \mathbf{v}_L)] + \gamma_0' \rho_s \kappa \, \hat{\mathbf{s}} \times (\mathbf{v}_n - \mathbf{v}_L). \qquad (3)$$

The mutual friction force has dissipative and reactive components, which here are expressed in terms of the two parameters γ_0 and γ_0'. Balancing the two hydrodynamic forces, $\mathbf{f}_M + \mathbf{f}_{mf} = 0$, one gets the equation of motion for the vortex line element, which when expressed in terms of the superfluid counterflow velocity $\mathbf{v} = \mathbf{v}_n - \mathbf{v}_s$ has the form

$$\mathbf{v}_L = \mathbf{v}_s + \alpha \hat{\mathbf{s}} \times (\mathbf{v}_n - \mathbf{v}_s) - \alpha' \hat{\mathbf{s}} \times [\hat{\mathbf{s}} \times (\mathbf{v}_n - \mathbf{v}_s)]. \qquad (4)$$

Here the dissipative and reactive mutual friction coefficients α and α' appear. Conversion formulae between different sets of friction parameters are listed by Donnelly (1991). Evidently solutions of the equation of motion can be classified according to the ratio of the two components. The important parameter proves to be $\zeta = (1 - \alpha')/\alpha$ (Figure 1), which is the equivalent of the Reynolds number of viscous fluid flow (Finne et al., 2003).

Two elementary examples are useful to consider. A single rectilinear vortex in rotating counterflow at $v = \Omega r$ moves such that its velocity components in the transverse plane consist of the radially oriented dissipative part $\alpha \Omega r$ and the azimuthally oriented reactive part $-(1 - \alpha') \Omega r$, when expressed in the rotating coordinate frame. The former is responsible for the contraction of the rectilinear vortices to a central cluster in Figures 5 and 6. The latter causes the rectilinear vortex to rotate with the azimuthal flow with respect to the cylindrical wall.

The second simple consideration concerns the end point motion of an evolving vortex along the cylindrical wall. Since the vortex end is perpendicular to the cylindrical wall, it has from Equation (4) a longitudinal velocity $v_{Lz} = \alpha v(\Omega_f, R, N)$ and an azimuthal component $v_{L\phi} = -(1 - \alpha')v(\Omega_f, R, N)$. Evidently other parts of the vortex also contribute to its motion, in particular its curvature where it connects to the cylindrical wall. However, it turns out that the end point velocity is an approximate guide for the expansion of a single vortex in vortex-free rotation. For comparison, the calculated velocities of the two vortex ends in Figure 6 are $v_{Lz} \approx 0.84\,\alpha \Omega R \approx 0.96\,\alpha v(R)$ and $v_{L\phi} \approx 0.73(1 - \alpha')\Omega R \approx 0.83(1 - \alpha')v(R)$. The wave length of the spiral trajectory is $\lambda = 2\pi R\,v_{Lz}/v_{L\phi} \approx 5\,\text{mm}$ and the period $p = 2\pi R/v_{L\phi} \approx 50\,\text{s}$. Thus the end point motion can be used to construct a simplified model of the motion of the two short vortices in Figure 6.

As seen in Figure 6, the spiral motion of the vortex end point along the cylindrical wall winds the rest of the evolving vortex around the central vortex cluster with a wave vector Q such that $QR = v_{L\phi}/v_{Lz} = \zeta$. The other almost straight end of the evolving vortex is fixed to a flat end plate of the cylinder and resides there at the edge of the vortex cluster, where the counterflow velocity is close to zero. Therefore, the helical twist is removed only by a slow sliding of the vortex end along the end plate. As seen in Figure 6, occasional reconnections between the twisted evolving vortex and a straight outer vortex in the cluster or with a second oppositely twisted vortex can help to reduce the twist. Finally, we see in Figure 6 that while the evolving vortex is wound tightly around the cluster, this induces Kelvin-wave oscillations which propagate vertically along the vortices in the cluster (Hänninen et al., 2007a).

2.3 Onset Temperature of Turbulence

When the dynamics calculated in Figures 5 and 6 is probed with measurements, the final state proves to depend crucially on temperature. At temperatures above the transition to turbulence, $T > T_{\text{on}}^{\text{bulk}}$, the calculations are confirmed and the number of vortices remains constant. At low temperatures, in contrast, evolving vortices may become unstable in applied counterflow and trigger a turbulent burst. The evolution after the burst continues as illustrated in Figure 3. The final state is then consistently close to the equilibrium vortex state. Interestingly, it turns out that for each initial configuration, such as those in Figures 5 or 6, there exists a specific temperature T_{on}, which characterises the onset of turbulence: well above T_{on} no turbulent burst occurs, while well below T_{on} a burst always occurs.

In these onset measurements, only two different types of final states are observed: sufficiently far above T_{on} the number of vortices is conserved, while well below T_{on} close to the equilibrium number of vortices is formed. The changeover takes place within a narrow temperature interval around T_{on}, typically within $\pm 0.02\, T_c$. Within this interval, either of the two final states can emerge. The reason for the narrow width is the strong, nearly exponential temperature dependence of the mutual friction parameter $\zeta = (1 - \alpha')/\alpha$, which controls the dynamic instability of seed vortices evolving in the applied counterflow (Figure 1). As sketched in Figure 3, two sequential processes are needed to start the low-temperature evolution: first, the single-vortex instability (Finne et al., 2006a), the precursory process which becomes possible only at temperatures below $T_{\text{on}}^{\text{bulk}}$ and which is responsible for generating a bunch of new evolving vortices. Second, the turbulent burst has to be triggered as a collective process in which several evolving vortices interact and generate a sudden localised event of turbulence, which expands across the entire cross-section of the rotating column but only over a short section of its length (of order $\sim R$).

The experimental confirmation of this scenario is obtained by examining the final state as a function of temperature. By recording the line shape of the NMR absorption profile, when the magnitude of the magnetic polarisation field is swept across the resonance region, the number of vortices in the final state can be determined. The line shapes of the two types of final states differ drastically, as seen in Figure 7, where all the spectra have been recorded at the same temperature of $0.40\,T_c$ and where thus the integrated area under each line shape is the same. The characteristic features are the large NMR shifts. These are controlled by the temperature and pressure dependent spin-orbit coupling. If the central vortex cluster is surrounded by applied counterflow at some sizeable velocity, a large sharp peak is formed, which is shifted downfield from the Larmor value. The number of vortices in the central cluster can be determined from the height of this so-called counterflow peak. At small vortex numbers ($N \ll N_{eq}$), the reduction in the counterflow peak height is directly proportional to the number of rectilinear vortices N in the cluster. At larger N, the dependence becomes nonlinear and ultimately the peak height drops to zero well before N_{eq} is reached, in practice around $v(R) \lesssim 1\,\text{mm/s}$ (Kopu, 2006). Accordingly, in the equilibrium vortex state the line shape is radically different and easily distinguished from a state with sizeable counterflow.

A measurement of T_{on} for any particular initial setup, such as in Figure 5 for remanent vortices, requires repeating the measurement at different temperatures and recording the line shape in the final state. Surprisingly, it turns out that in the final state the vortex number is either preserved or it has increased close to that in the equilibrium vortex state. Practically no intermediate cases are observed. As a result, in practice, a measurement of T_{on} requires simply a visual check of the measured line shape in the final state. This feature about the turbulent burst is similar to recent observations from measurements with a closely spaced pair of vibrating wires in superfluid ^{4}He (Goto et al., 2008). One of the wires is driven at high oscillation amplitude as generator while the second is operated at low amplitude as detector. Once turbulence has been switched on by running the generator at high drive, the generator can be switched off and turbulent flow will still be maintained around the detector. Only if the detector drive is reduced to sufficiently low level, turbulence ceases and the flow around the detector returns to the laminar state. This shows that once turbulence has been switched on it can be sustained at much lower flow velocities. Similarly, once the turbulent burst is started in the rotating column, turbulent vortex formation will continue until the counterflow velocity has dropped close to zero in a section of the column of height $\sim R$.

The situation at temperatures above T_{on} is illustrated by the measurements on vortex remanence in Figure 8 (Solntsev et al., 2007). These measurements have been performed at two different temperatures above onset, where no increase in the number of vortices is expected. This is
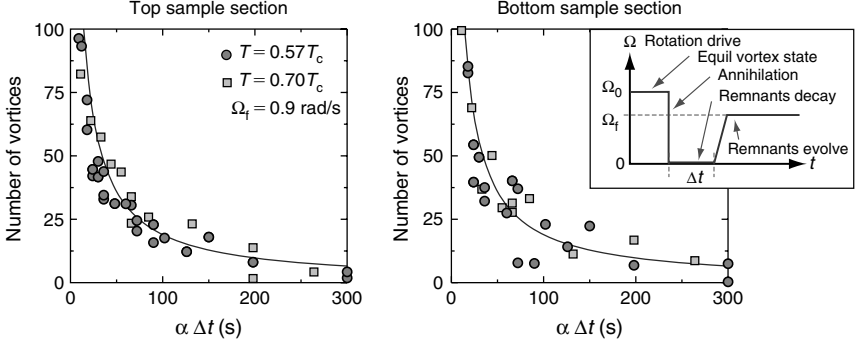
FIGURE 8 Number of remanent vortices $\mathcal{N}(\Delta t)$ for A-phase separated top and bottom sample sections, measured as a function of the annihilation time Δt in the temperature regime of laminar vortex motion. The results of these two independent measurements can be fitted in both cases with the solid curve $\mathcal{N}(\Delta t) \approx 2 \cdot 10^3/(\alpha \Delta t + b)$ (Δt in seconds, $b \approx 7$ s). Inset: in the upper right corner, the sequence of rotations $\Omega(t)$ is shown which was used to perform the measurement. The data are for 0.57 T_c with $\alpha = 0.60$ and 0.7 T_c with $\alpha = 1.1$. Parameters: $\Omega_f = 0.9$ rad/s, $R = 3$ mm, length of top sample section $h_t = 44$ mm (41 mm) and $h_b = 54$ mm (51 mm) for the bottom section at 0.57 T_c (0.70 T_c).

confirmed by extracting from the counterflow peak height the number of vortex lines in the final state. The measurement proceeds as sketched in the inset on the top right of Figure 8. An equilibrium vortex state is decelerated to zero, and the vortices are allowed to annihilate for a time interval Δt before rotation is turned back on. The measurement is repeated many times by varying the annihilation time Δt at zero rotation. The annihilation time is found to govern the number of rectilinear vortex lines in the final state and thus the number of remnants at the end of the annihilation period: $N(\Delta t) \propto (1 + \Delta t/\tau_{mf})^{-1}$, where the mutual-friction-controlled time constant is $\tau_{mf} = [2\alpha\Omega_0]^{-1}$ and $\Omega_0 = \Omega(t < 0)$. This is exactly as expected for the mutual-friction damped motion of vortices in the radial direction, when straight vortices move outward to annihilate on the cylindrical wall at zero rotation. For this to apply, the vortices have to be polarised along the cylindrical symmetry axis (Krusius et al., 1993). As seen in Figure 5 (second from left, at $t \leq 600$ s) this is the case: the polarisation remains at high level even in the remnant state at zero rotation. Consequently, the measurements in Figure 8 confirm that at constant temperature above T_{on}, the number of vortices in this experiment is controlled by the annihilation period Δt and no uncontrolled increase occurs.

It is useful to note some additional features about vortex remanence in the measurements of Figure 8. Let us denote the number of remnants after the annihilation period with $\mathcal{N}(\Delta t)$ and the number of rectilinear lines in

the final state with N. Although the annihilation time Δt controls the number of remnants $\mathcal{N}(\Delta t)$, the result $N = \mathcal{N}$ is independent of Δt. It is also to a large extent independent of how the measurement is performed, that is, what the rotation velocity Ω_f in the final state is or what acceleration $\dot{\Omega}$ is employed to reach Ω_f (as long as $\mathcal{N}(\Delta t) < N_{eq}(\Omega_f)$ or the critical velocity for vortex formation, $\Omega_f - \Omega_v < v_c/R$, is not exceeded). Furthermore, the result $N = \mathcal{N}$ is established separately both for the top and bottom sections of the cylinder, when these are separated by a magnetic-field-stabilised A-phase barrier layer (cf. Figure 7), and for the entire cylinder without A-phase barrier. The A-phase barrier layer prevents vortices from traversing across the AB interfaces at low counterflow velocity (Blaauwgeers et al., 2002). In this way, the number of remanent vortices $\mathcal{N}(\Delta t)$ has been found to be proportional to the length h of the cylinder (as long as $h \gg R$). All these properties are consistent with the conclusions that when $T > T_{on}$, the vortex number is conserved in dynamical processes, the annihilation decay of remnants is a laminar process regulated by mutual friction damping, and that pinning is weak. For simplicity, we neglect vortex pinning altogether and assume ideal wall properties throughout this review.

The situation at temperatures around T_{on} is illustrated by the measurements in Figure 9 which determine T_{on} for this particular choice of initial state (de Graaf et al., 2007; Solntsev et al., 2007). The probability of the turbulent burst is plotted as a function of temperature, when the annihilation time $\Delta t = 20\,\text{min}$ (on the left) and $\Delta t = 2\,\text{min}$ (on the right). The striking feature is the abrupt changeover from the laminar behaviour, where the vortex number is conserved, to turbulence, where the vortex number surges close to N_{eq} and the system relaxes to its minimum energy state. The centre of the narrow transition defines the onset temperature of turbulence T_{on}, which proves to be different for the two cases studied in Figure 9.

As seen in Figure 9, T_{on} depends on the annihilation time Δt and thus on the initial number and configuration of evolving remnants $\mathcal{N}(\Delta t)$ at the moment when the step increase in rotation from zero to Ω_f is applied. Calculating from the results in Figure 8, one finds that the number of remnants at the start of acceleration is $\mathcal{N}_i \approx 40$, when $\Delta t = 2\,\text{min}$ and $T \approx T_{on} = 0.44\,T_c$, and $\mathcal{N}_i \approx 10$, when $\Delta t = 20\,\text{min}$ and $T = 0.39\,T_c$. Thus, at a higher temperature, a larger number of remnants is needed to achieve the turbulent burst. Both panels in Figure 9 refer to the top sample half where, with no orifice, there is no preferred site for the remnants to accumulate, and the turbulent burst occurs randomly at any height z in the column (de Graaf et al., 2007). Similar measurements at different values of Δt and final rotation velocity Ω_f show that the onset temperature depends weakly on both the initial number of remnants $\mathcal{N}_i$ and the applied flow velocity.
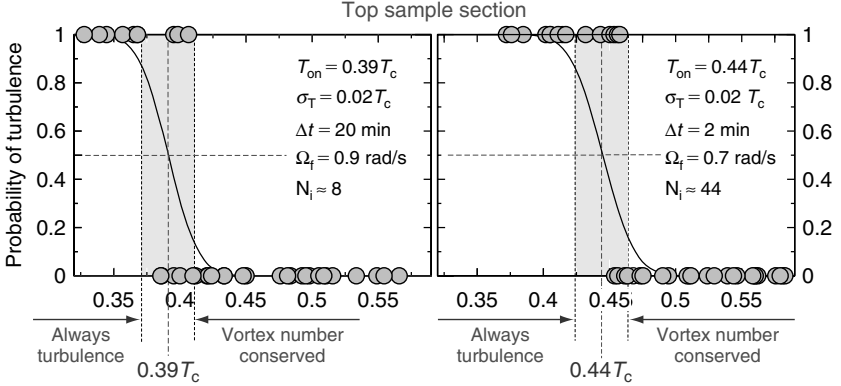
FIGURE 9 Measurements on the onset temperature T_{on} of the transition to turbulence. The measurements are performed similar to those in Figure 8 and start from an initial state which is obtained by decelerating an equilibrium vortex state at 1.7 rad/s to zero at a rate 0.01 rad/s^2. The remaining vortices are left to annihilate for a period Δt at $\Omega = 0$. Rotation is then increased to Ω_f at a rate 0.02 rad/s^2. When all transients have decayed, the number of vortices is measured in the final steady state at Ω_f. The result is plotted as a function of temperature with 30–40 data points per panel. The solid curve is a gaussian fit which represents the probability for turbulence with a half width $\sigma_T = 0.02\,T_c$, centred around T_{on}. Comparing results in the two panels for $\Delta t = 20$ min and 2 min, we see that T_{on} decreases with increasing Δt since the number, average size and density of remnants are reduced as Δt increases. Both panels have been measured for the upper sample section which is separated from the bottom half with an A-phase barrier layer. Parameters: $R = 3$ mm, $h = 45$ mm and $P = 29.0$ bar.

These dependences can be summarised in the form

$$\zeta(T_{on})^{-1} \propto \mathcal{N}_i^{0.3}\Omega_f^{1.3}. \tag{5}$$

Thus the onset temperature T_{on} depends primarily on the mutual friction parameter $\zeta(T)$, but also weakly on other factors which influence the likelihood of achieving locally somewhere in the maximum available counterflow velocity a density of evolving vortices which allows to trigger the turbulent burst. Among these additional factors, most important are (i) the applied counterflow velocity $v = v_n - v_s$, (ii) the number and configuration of the injected seed vortices and (iii) the sample geometry. In Figures 8 and 9, we examined the response of remanent vortices to a step-like increase in rotation. The same measurements can also be performed by starting from the equilibrium vortex state at finite rotation, as discussed in the context of Figure 6. In fact, the most extensive study of the scaling law in Equation (5) was performed using this approach.

Finally we note that in the rotating container, all measured onset temperatures, which depend on the presence of the precursor, are found to be below the transition to turbulence in the bulk: $T_{on} < T_{on}^{bulk}$. Furthermore, since the onset also depends on the applied counterflow velocity in Equation (5), the instability is expected to occur first close to the cylinder wall, where the applied velocity $v = \Omega r$ reaches its maximum value at $r = R$. Thus the reconnection of the expanding loop will most likely occur with the wall. Surprisingly, it is also found that once the instability is triggered, the turbulent burst essentially always follows next, since little if no increase in the vortex number is detected at $T \sim T_{on}$ in such cases where the turbulent burst does not switch on (cf. Figure 9). To provide more understanding on the role of the single-vortex instability as the precursor mechanism to turbulence, we next examine it in the onset temperature regime, $T \sim T_{on}$, where the instability proceeds sufficiently slowly in time so that it can be monitored with continuous-wave NMR measurement.

2.4 Single-Vortex Instability in Applied Flow

Since the time when it was first understood that superfluid turbulence is made up of tangled quantised vortices (Hall and Vinen, 1956; Vinen, 1961), the most basic question has been its onset as a function of applied counterflow velocity: how is turbulence started and what defines its critical velocity? An important clue was provided by the rotating experiments of Cheng et al. (1973) and Swanson et al. (1983), who found that rectilinear vortex lines in rotation are broken up in a turbulent tangle if a heat current is applied parallel to the rotation axis. The thermal current is transported as a counterflow of the normal and superfluid components along the rotation axis. Rectilinear vortices become unstable in this parallel flow and above a low critical velocity transform to a tangle which tends to be aligned in the plane transverse to the heat current.

This phenomenon was explained by Glaberson et al. (1974) who showed that an array of rectilinear vortices becomes unstable in longitudinal counterflow above the critical velocity $v = 2(2\Omega\kappa_e)^{1/2}$, where $\kappa_e \approx \kappa$ is an effective circulation quantum (supplemented with the logarithmic cut-off term $\kappa_e = (\kappa/4\pi) \ln (\ell/a_0)$, where the average inter-vortex distance is $\ell \sim (\kappa/2\Omega)^{1/2}$ and the vortex core radius a_0). The instability appears when a Kelvin-wave mode with wave vector $k = (2\Omega/\kappa_e)^{1/2}$ starts to build up, whose amplitude then grows exponentially in time. The Glaberson instability has also been examined in numerical calculations which qualitatively confirm the instability and the vortex tangle in the transverse plane which starts to form above a first critical velocity (Tsubota et al., 2003).

In general, the dispersion relation of a helical Kelvin-wave disturbance $\propto \exp[-i(\omega_k t - kz)]$ can be written as (Donnelly, 1991; Finne et al., 2006b)

$$\omega_k(k) = \kappa_e k^2 - \alpha'(\kappa_e k^2 - kv) - i\alpha(\kappa_e k^2 - kv). \tag{6}$$

In the absence of flow ($v = 0$), these Kelvin modes are always damped, at high temperatures they are actually overdamped, but at low temperatures ($\alpha < 1 - \alpha'$) this is not the case. In applied flow ($v > 0$), the long wave length modes with $0 < k < v/\kappa_e$ become exponentially unstable. If an evolving vortex accumulates enough length $L_\parallel$ parallel to the applied flow, then a disturbance with wave length $\lambda_{min} \sim L_\parallel \sim \kappa_e/v \sim 1/k_{max}$ may start to grow. The expanding loop may reconnect, either with the wall of the container, with itself, or with another vortex. This leads to a growing number and density of evolving vortices, which ultimately start interacting and trigger the onset of turbulence in the bulk.

No rigorous analytical calculation has been presented of the single-vortex instability in the rotating container, but a simple scaling model illustrates the problem. Consider a vortex ring in vortex-free counterflow, which is initially perpendicular to the plane of the ring in a rotating cylinder of radius R. If the ring is large enough, then it expands until it reaches the container size R. The time needed for this expansion is of order $\delta t \sim R/\alpha v$, where v is the average normal velocity through the ring. The ring also has a self-induced velocity component $v_r \sim \kappa_e/R$, which arises from its own curvature and is directed along the normal of the plane of the ring. Because of this velocity component, the plane of the ring is rotated away from being perpendicular to the azimuthal flow in the cylinder while it drifts in the flow. During the time δt, the vortex length parallel to the flow becomes of order $(1 - \alpha')v_r \delta t$. Equating this to $L_\parallel$, it is seen that the instability condition $L_\parallel \gtrsim \lambda_{min}$ leads to the requirement $\zeta = (1 - \alpha')/\alpha \gtrsim 1$. This condition is virtually independent of velocity; the only restriction is imposed by the finite container radius, $L_\parallel < R$, which defines a critical velocity $v_c \sim \kappa_e/R$. Typically, the time spent by a vortex in radial motion before reaching the sample boundary is of order $R/(\alpha\Omega R) = (\alpha\Omega)^{-1}$. At $0.45\,T_c$ and $\Omega = 0.6\,\mathrm{rad/s}$, the inverse of this quantity equals $0.20\,\mathrm{s}^{-1}$, which fits with the measured vortex generation rate of $\mathrm{d}N/\mathrm{d}t = \dot{N} = 0.23\,\mathrm{s}^{-1}$ in Figure 10. However, numerical calculations confirm that the presence of surfaces is required to demonstrate the single-vortex instability in usual experimentally relevant flow conditions (Finne et al., 2006a). Also the calculations demonstrate that the instability is not characterized by a unique critical velocity, since it depends on the relative orientation of the flow with respect to the vortex, while the vortex expands in helical motion in the rotating cylinder. Thus the above model is incomplete.

Let us now examine direct observations of the single-vortex instability in rotating flow. In the onset temperature regime, $T \sim T_{on}$, in about half of the measured cases, which lead to a turbulent burst, a slow increase in the number of vortex lines $N(t)$ can be observed to precede the turbulent burst. If present, the increase is invariably followed by a turbulent burst. Thus it appears reasonable to associate the slow increase with the single-vortex instability. In Figure 10, the number of vortex lines $N(t)$ is
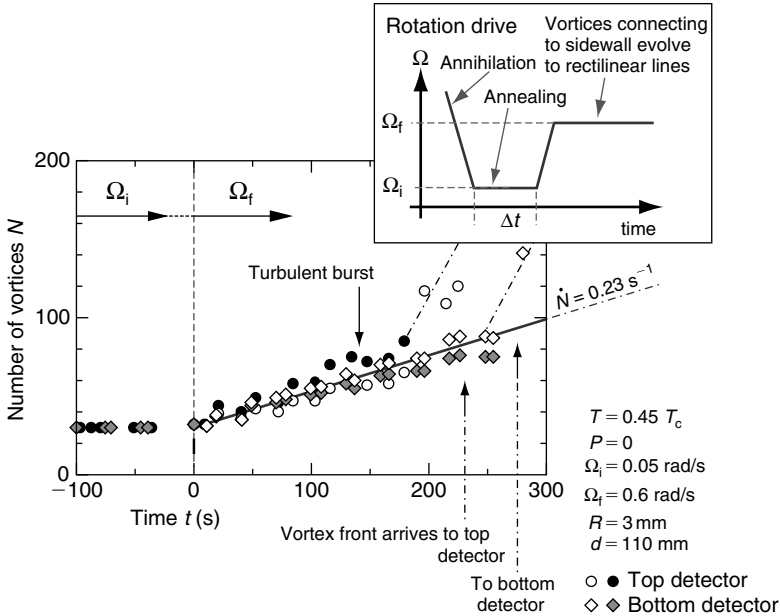
FIGURE 10 Experimental illustration of single-vortex instability as precursor of bulk turbulence. The number of vortices $N(t)$ is recorded with NMR coils at the top and bottom ends of the sample. As seen in the inset, initially the sample is in the equilibrium vortex state at $\Omega_i = 0.05$ rad/s with $N \approx 30$ vortices, of which close to one half connect to the cylindrical sidewall. Rotation is then increased to a new stable value $\Omega_f = 0.6$ rad/s, which is reached at $t = 0$. During the ramp to Ω_f, the counterflow builds up, compresses the rectilinear sections of all vortices to a central cluster, and starts the spiral motion of the vortex ends connecting to the sidewall. Eventually in the increased applied flow at Ω_f, the instability starts to generate new vortices which contribute to the average slow rate $\dot{N}$ of vortex formation, shown by the solid straight line. After about 140 s, the turbulent burst occurs 63 mm above the bottom end plate. Vortex fronts traveling up and down along the column then approach the two detector coils and reach their closer ends as indicated by vertical arrows (at 230 s and 275 s). The filled data symbols are derived from experimentally calibrated counterflow peak heights and the open symbols from order parameter texture calculations fitted to the NMR signal in the non-rotating state.

plotted as a function of time while the precursor generates new vortices at slow rate. In this example, the increase in $N(t)$ is almost linear (solid line) until the turbulent burst sets in and starts the vortex front motion along the rotating column both upwards and downwards from the site of turbulence. At $\Omega_f = 0.6$ rad/s, the slow, increase lasts in this example for about 140 s, generating approximately one vortex every five seconds, until some 30 new vortices have been created and the turbulent burst manages to switch on. The time interval from $t = 0$ to the turbulent burst

is called the burst time which here is $t_b = 140$ s. At larger Ω_f, the burst time is shorter in duration; for example, in a repetition of the measurements in Figure 10 at $\Omega_f = 1$ rad/s, the turbulent burst was found to start in less than 30 s.

Two further observations about the precursor can be made from Figure 10. First, vortex formation proceeds independently in different parts of the sample. At $\Omega_f = 0.6$ rad/s, it takes more than 300 s for a vortex created at one end of the sample to reach the other end. Still, vortex formation at the top and bottom ends is observed to proceed at roughly the same rate. Thus, vortex generation by the single-vortex instability is not localised, in contrast to the turbulent burst. The random occurrence of the single-vortex instability agrees with the notion of ideal walls (or at least weak pinning), as opposed to a vortex mill localised at a surface defect on the cylinder wall.

Secondly, in Figure 10 the equilibrium vortex state at low initial rotation $\Omega_i = 0.05$ rad/s has been used to introduce evolving vortices in the applied flow. This approach provides a more reproducible initial vortex configuration than remanent vortices since the number of those vortices, which connect to the cylindrical sidewall, is primarily determined by the misalignment between the cylinder and rotation axes (Figure 6). In a given experiment, the residual angle between the two axes is generally a constant.

To appreciate the influence of the vortices curving to the sidewall, the experiment was repeated differently. A cluster with only rectilinear vortices ($N < N_{eq}$) was prepared at higher temperatures and was then cooled below $0.5\,T_c$. As long as this cluster is separated by a sufficiently wide vortex-free counterflow annulus from the cylindrical boundary, Ω can be increased or decreased without change in N at any temperature down to $0.35\,T_c$ (which is the lower limit of the so far measured onset temperatures T_{on}). If Ω is reduced too much, the cluster makes contact with the cylindrical sidewall, some outermost vortices become curved, and during a subsequent increase of Ω, while $T < 0.5\,T_c$, the behaviour in Figure 10 is reproduced. Therefore, we are led to assume that, to observe the vortex instability, at least one curved vortex connecting to the cylindrical sidewall needs to be present. At temperatures below $0.35\,T_c$, this may not be the case, since in rapid changes of rotation even rectilinear vortices seem to be destabilised (Figure 4).

More statistics on the properties of the precursor have been collected from measurements similar to that in Figure 10 by de Graaf et al. (2007). Important characteristics are the initial rate of vortex generation $\dot{N}(t = 0)$ and the burst time t_b. These can be examined for events with sufficiently long burst times $t_b \gtrsim 20$ s, so that the rate of the counterflow peak height decrease with time can be adequately resolved. In general, it is found that $\dot{N}$ increases and t_b decreases rapidly with decreasing temperature below T_{on}.

To find events with well-resolved preturbulent vortex generation and long burst time, one has to scan for data (i) in the onset temperature regime, $T \approx T_{on}$, (ii) with a low initial formation rate $\dot{N} \lesssim 1\,\text{vortex/s}$, (iii) by starting from a state with a small number of seed vortices and (iv) at low applied flow velocity.

These measurements demonstrate that the precursor generates new independent vortex loops which start to evolve along spiral trajectories towards the final state of a rectilinear vortex line. When the density of evolving vortices rises sufficiently, so that interactions between them in the bulk volume become possible, then the process is terminated in a turbulent burst. The burst is a localised event which from one measurement to the next happens randomly at different heights z of the sample (Figure 7). The measured properties of the precursor are consistent with those expected for a single-vortex instability based on the excitation of Kelvin-wave modes of sufficiently long wavelength. Overall, measurements in the onset regime reveal the precursor mechanism, owing to the strongly temperature dependent mutual friction of ^{3}He-B, which makes the precursor observable within a narrow temperature interval around the onset temperature. At lower temperatures, the turbulent burst develops so rapidly that the measuring techniques, which have been employed so far, are not fast enough to capture the details. The latter case is the typical situation in superfluid ^{4}He experiments.

2.5 Numerical Calculation of Dynamic Vortex Generation

Numerical calculations on vortex dynamics are carried out with the vortex filament model introduced by Schwarz (1988). With today's computing power, one uses Biot-Savart integration along all vortex lines so that the superfluid velocity field from vortices is obtained from (Hänninen et al., 2005)

$$\mathbf{v}_{s,\omega}(\mathbf{r}, t) = \frac{\kappa}{4\pi} \int \frac{(\mathbf{s} - \mathbf{r}) \times d\mathbf{s}}{|\mathbf{s} - \mathbf{r}|^3} \; . \tag{7}$$

The line integral is taken along all vortices in the system, $\mathbf{s}(\xi, t)$ denotes the location of the vortex core at time t and ξ is measured along the arc length of the vortex core. In the presence of solid boundaries, the total superfluid velocity field, $\mathbf{v}_s = \mathbf{v}_{s,\omega} + \mathbf{v}_b$, is modified by the boundary-induced velocity $\mathbf{v}_b$. At a plane boundary, one can use image vortices to satisfy the requirement of zero flow through the boundary, $\hat{n} \cdot \mathbf{v}_s = 0$, where $\hat{n}$ is the unit vector along the surface normal. More generally, we obtain $\mathbf{v}_b = \nabla \Phi$ by solving the Laplace equation $\nabla^2 \Phi = 0$ combined with the requirement that at the boundary $\hat{n} \cdot \nabla \Phi = -\hat{n} \cdot \mathbf{v}_{s,\omega}$.

No surface pinning or even surface friction is generally included, the boundaries are assumed ideal, as indicated so far by measurements on ^{3}He-B in smooth-walled simple cylindrical containers. Mutual friction in the bulk superfluid is included using the equation of motion (Equation (4)) for the vortex element at $\mathbf{s}(\xi, t)$, which moves with the velocity $\mathbf{v}_L = \mathrm{d}\mathbf{s}/\mathrm{d}t$. For the mutual friction parameters $\alpha(T, P)$ and $\alpha'(T, P)$, one uses the ^{3}He-B data measured by Bevan et al. (1997) at 10 and 29 bar pressures. A reconnection between two vortex segments is enforced if they have drifted within a distance from each other, which is less than the minimum spatial resolution of the calculation (usually $\sim$0.05 mm). The configuration after reconnection should correspond to shorter overall vortex length than the initial state. In practice, the computing time limits severely what can be calculated and what becomes too time consuming. Therefore, the practical implementation becomes of great importance, how the Biot-Savart integration and the proper solution for the boundary conditions are worked out. For details, we refer to de Graaf et al. (2007).

In Figure 11, two snapshots are shown from calculations on vortex formation and the configurations which evolve in a rotating cylinder (de Graaf et al., 2007). Recently formed younger vortices are here in helical configurations on the outer circumference closer to the cylindrical wall. There in the outer regions, one can see loops of Kelvin-waves, small separated loops with both ends of the vortex on the cylindrical wall, and even closed vortex rings (lower right corner at $t = 50$ s). Since it is primarily surface reconnections at the cylindrical wall, which contribute to the formation of new vortices in the early stages of the calculation (at $t < 100$ s), the many newly formed short loops are still close to the sidewall.

$t = 50.5$ s $t = 77.5$ s
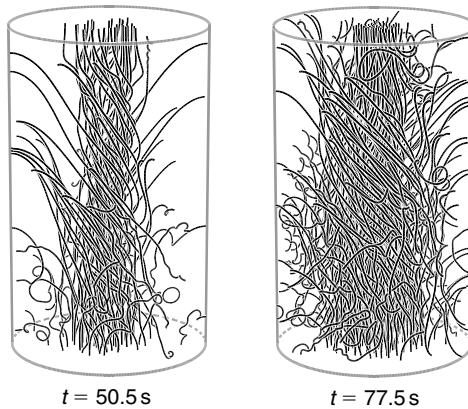
FIGURE 11   Two snapshots from a calculation of vortex generation in a rotating cylinder. The summary of these calculations with results accumulated over more than 100 s is shown in Figure 12.

Further inside the cluster, one can see older and straighter vortices which congregate within the central parts.

The general observation from these calculations is that evolving vortices in a rotating sample are more stable in the numerical experiment than in measurements. For instance, in Figure 11 vortex formation has to be started from an artificial initial configuration (Finne et al., 2006a). This consists from an initial single vortex ring which is placed in the plane perpendicular to the rotation axis at height $0.2\,h$ slightly off centre, to break cylindrical symmetry (de Graaf et al., 2007). This is an unstable configuration where Kelvin-waves of large amplitude immediately form and then reconnect at the cylindrical wall. The end result is the sudden formation of roughly 30 vortices which have one end on the bottom end plate and the other moving in spiral trajectory along the cylindrical wall. After the initial burst, the later evolution is followed as a function of time t, the number of vortices $N(t)$ is listed and the reconnections of different type are classified. The results are shown in Figure 12.

In Figure 12, one keeps account of all reconnection processes which occur in the rotating sample as a function of time while it is evolving towards its final stable state with an array of rectilinear vortices and $N \rightarrow N_{\text{eq}}$. After the initial burst of the first $\sim$30 vortices, N increases first gradually, but after about $50\,\text{s}$, the rate $\dot{N}$ picks up. During the first $50\,\text{s}$, reconnections in the bulk do not contribute to the generation of new vortices, but later such processes also start to appear. However, even during the later phase, a reconnection of a single vortex at the cylindrical wall, while Kelvin-waves expand along this vortex, remains the dominant mechanism of vortex generation. This is seen from the fact that the curve for N follows closely that of the successful surface reconnections (dashed curve marked as '$\Delta N = +1$'). The most frequent reconnections after the first $40\,\text{s}$ are denoted by the solid '$\Delta N = 0$' curve and occur in the bulk between two different vortices. These inter-vortex reconnections do not lead to changes in N and are primarily associated with processes occurring between the twisted vortices in the bundle further away from the wall.

The inset in Figure 12 compares the rates of vortex generation from reconnections at the wall and in the bulk. The reconnection of a single vortex at the cylindrical wall is clearly the most important mechanism for the generation of new independent vortex loops in the early stages of the calculation. The dominant role of such wall reconnections is compelling. A second important consideration is correspondence with measurement. The obvious difference is the higher stability of evolving vortices in the calculation as compared to experiment. In Figure 12, the rate of vortex generation remains modest, no clearly identifiable turbulent burst can be distinguished, and the vortex number approaches the equilibrium value from below. After $115\,\text{s}$ of evolution, the vortex number has progressed to $N \approx 400$, where the increase is almost stopped, well below the saturation
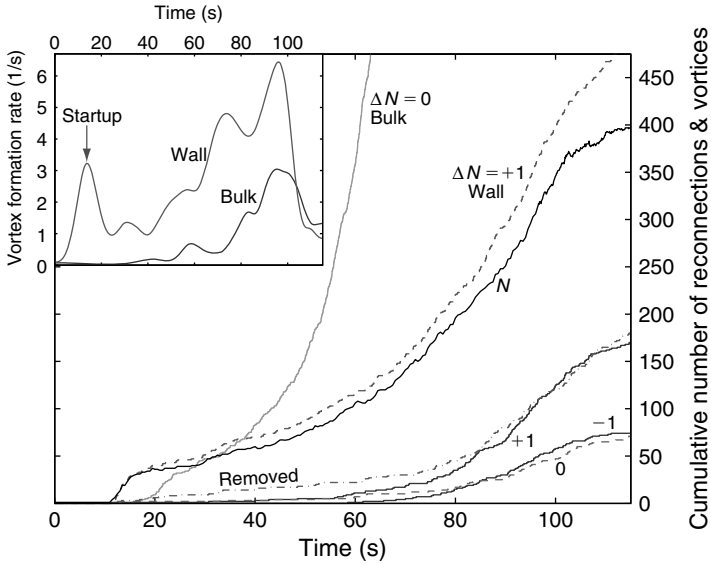
FIGURE 12 Calculation of the cumulative number of reconnections and vortices in a rotating cylinder. The different curves denote: ($\Delta N = 0$, solid curve) reconnections in the bulk which do not change N; (+1, dashed) reconnections with the cylindrical wall which add one new vortex loop; (N, solid) total number of vortices; (removed, dash-dotted) small loops which form in reconnections mainly close to the cylindrical wall, but which are contracting and are therefore removed; (+1, solid) reconnections in the bulk which add one vortex and (−1, solid) which remove one vortex; (0, dashed) reconnections at the cylindrical wall which do not change N. Inset: averaged rate of increase in N owing to reconnections on the cylindrical wall and in the bulk. The large initial peak in the boundary rate represents the starting burst, which is used to start vortex formation. Parameters: $R = 3$ mm, $h = 10$ mm, $\Omega = 0.9$ rad/s and $T = 0.35\,T_c$ (where $\alpha = 0.095$ and $\alpha' = 0.082$).

value of $N_{eq} \approx 780$ (de Graaf et al., 2007). This is the general experience from calculations on an ideal rotating cylinder, with smooth surfaces and no surface friction or pinning. The calculations become more and more time consuming with decreasing temperature, which limits the possibilities to obtain a more comprehensive understanding of their predictions and of the origin of the differences with measurement. The low probability of the single-vortex instability in the calculations appears to be a particular property of rotating flow in a circular cylinder since linear pipe flow, for instance, displays a steady rate of vortex generation (de Graaf et al., 2007).

Clearly numerical calculations provide important illustrations and guidance in situations where measurements answer only specific limited questions. The calculations take full account of interactions between vortices and between a vortex and the ideal container wall. Nevertheless,

the correspondence between calculation and measurement is not satisfactory at present, when we speak about the single-vortex instability and the onset of turbulence in a rotating cylinder. It appears that some mechanism, which makes vortices more unstable and adds to the vortex generation rate, is missing from the calculations. The difficulty is likely to reside on the cylindrical wall, where the assumption of ideal conditions should be examined closer. Attempts in this direction have so far not produced more clarification. However, these uncertainties about the mechanisms behind the single-vortex instability in rotating flow do not change the fact that, at low vortex density Kelvin-wave formation on a single vortex, followed by a reconnection at the surface, is the only efficient mechanism for generating new vortices.

2.6 Summary: Onset of Turbulence

Since the advent of ^{3}He-B, new possibilities have appeared to study turbulence. First, it has become possible to distinguish and characterise, in measurements with large samples, vortex formation at a stable reproducible critical velocity, vortex remanence and turbulent proliferation of vortices. Second, the mutual friction dissipation $\alpha(T)$ with strong temperature dependence around $\alpha \sim 1$ has made it possible to evaluate the role of mutual friction in the onset of turbulence. The important dynamic parameter proves to be $\zeta = (1 - \alpha')/\alpha$. It controls the onset of the single-vortex instability, where an evolving vortex becomes unstable and generates, during a reconnection at the wall, a new vortex loop. After several such events, the density of evolving vortices is sufficient to produce a turbulent burst. The necessary condition is $\zeta \gtrsim 1$ to start the cascade of the single-vortex instability followed by the turbulent burst.

The single-vortex instability becomes possible only at temperatures below the turbulent transition in the bulk volume and thus $T_{on} \le T_{on}^{bulk}$. The onset temperature T_{on} of these two series-coupled processes has been found to obey a power-law dependence which relates the mutual friction parameter ζ to the magnitude of the 'flow perturbations' in Equation (5). Well above T_{on}, no new vortices are detected (with a resolution < 10 new vortices), while well below T_{on} all final states are found to be equilibrium vortex states with close to the equilibrium number of vortices, $N \lesssim N_{eq}$. In the onset regime itself, $T \sim T_{on}$, one finds events with and without turbulent burst but surprisingly practically no incomplete transitions with $N_i < N \ll N_{eq}$.

In the intermediate temperature regime $0.3\,T_c < T < 0.6\,T_c$, the equilibrium vortex state is reached after a single turbulent burst. In fact, in the measurements with the sample setup of Figure 7, no case of two or more almost simultaneous bursts was identified above $0.35\,T_c$. Apparently the probability of the single vortex instability to start a turbulent burst is still

low at these temperatures. Second, after the burst, the vortex front moves rapidly and removes the vortex-free flow. At these intermediate temperatures, the burst is both spatially and temporally a localised event in a short section (of length $\sim R$) of the column. From one measurement to the next, it occurs randomly at different heights of the column. Below $0.3\,T_c$, the longitudinal propagation velocity of vortices becomes slow and evolving vortices go rapidly unstable everywhere. As a result turbulence tends to be both spatially and temporally more extended, filling larger sections of the column. The later events, the evolution after the turbulent burst, are the subject of the next section.

3. PROPAGATING VORTEX FRONT IN ROTATING FLOW

3.1 Introduction

In rotation at constant angular velocity, the steady state superfluid response is generally not turbulent. Nevertheless, transient states of turbulence can be formed by rapidly changing the rotation velocity, especially if the sample container does not have circular cross-section or its symmetry axis is inclined by a larger angle from the rotation axis. The decay of turbulence and the approach to equilibrium can then be monitored at constant Ω. The normal component relaxes back to solid body rotation by means of viscous interactions, while the superfluid component adjusts much slower, coupled only by mutual friction dissipation from vortex motion with respect to the normal component and (if any) by the deviations of the container walls from being axially symmetric around the rotation axis. Such measurements on transient turbulence are generally known as spin-up or spin-down of the superfluid component. This used to be an important topic in superfluid ^{4}He work in the fifties and sixties (Andronikashvili and Mamaladze, 1967) but was replaced (with few exceptions (Adams et al., 1985)) by other methods which were expected to lead to more straightforward interpretation.

The turbulent burst, which suddenly starts the motion of $N \approx N_{eq}$ vortices along the rotating column at temperatures $T \lesssim T_{on}$, as discussed in Section 2 (cf. Figure 3), provides a novel technique to investigate transient turbulence in rotation. Originally it was assumed that this motion would take place as a tangle of vortices, which spreads longitudinally along the rotating column. It was soon realised from NMR measurements (Eltsov et al., 2006b) that this could not be the case; rather the propagating vortices were highly polarised and had to be coiled in a helical configuration owing to their spirally winding motion. This recognition presented a new problem: is there any room at all for turbulence in this kind of motion and if there is, how is it expressed? Or perhaps the nature of the motion changes

on approaching the zero temperature limit, when mutual friction dissipation vanishes $\alpha \propto \exp(-\Delta/T)$? These questions provided the incentive to examine the propagation more closely and to measure its velocity as a function of temperature. The results demonstrate that turbulent losses depend crucially on the type of flow, flow geometry, external conditions, the physical properties of the superfluid itself, etc.

A measurement of the front propagation in the laminar and turbulent temperature regimes allows one to determine the rate of kinetic energy dissipation. The measurement proceeds as follows: the initial starting state is the rotating vortex-free state, the so-called Landau state, which is metastable with much larger free energy than the stable equilibrium vortex state. The latter consists of rigidly co-rotating normal and superfluid components, owing to the presence of a regular array of rectilinear vortices, while in the vortex-free state the superfluid component is not rotating at all: it is at rest in the laboratory frame of reference. When the turbulent burst is triggered in the Landau state, a rapid evolution towards the equilibrium vortex state is started, where a boundary between the vortex-free and the vortex states propagates along the rotating column and displaces the metastable vortex-free counterflow. Particularly at temperatures below $0.4\,T_c$, the boundary has the form of a sharp thin vortex front which travels at a steady velocity V_f. The dissipation rate of the total kinetic energy, $\mathcal{E}(t)$, is related to V_f as

$$\mathrm{d}\mathcal{E}\big/\mathrm{d}t = -\pi\rho_s V_f \Omega^2 R^4/4\,. \tag{8}$$

By measuring V_f, one determines directly the energy dissipation $\mathrm{d}\mathcal{E}/\mathrm{d}t$ as a function of temperature.

At high temperatures, the motion is laminar and the front velocity is determined by mutual friction dissipation between the normal and superfluid components, $V_f(T) \approx \alpha(T)\,\Omega R$. Below $0.4\,T_c$, $V_f(T)$ deviates more and more above the laminar extrapolation (Eltsov et al., 2007), in other words, the dissipation becomes larger than expected from mutual friction in a laminar flow. At the very lowest temperatures, a striking anomaly becomes apparent: $\mathrm{d}\mathcal{E}(t)\big/\mathrm{d}t$ does not go to zero, but the measured velocity $V_f(T)$ appears to level off at a constant value which corresponds to an effective friction $\alpha_{\mathrm{eff}} \sim 0.1$, even though $\alpha(T) \to 0$, when $T \to 0$. Evidence for a similar conclusion has been offered by the Lancaster group (Bradley et al., 2006), who measured the density of the vortex tangle created by an oscillating grid and found that this kind of turbulence decays at a temperature-independent finite rate below $0.2\,T_c$.

When mutual friction decreases and turbulent motions in the vortex front cascade downward to progressively smaller length scales, eventually individual quantised vortex lines must become important. This is the quantum regime of superfluid hydrodynamics. The energy cascade

on length scales smaller than the inter-vortex distance and the nature of dissipation on these scales are currently central questions in superfluid turbulence (Vinen and Niemela, 2002). Theoretical predictions exist on the role of nonlinear interactions of Kelvin-waves and the resulting Kelvin-wave cascade, which is ultimately terminated in quasi-particle emission (Kozik and Svistunov, 2004, 2005a, 2008a; Vinen, 2000; Vinen et al., 2003), or on the importance of reconnections which could rapidly redistribute energy over a range of scales and also lead to dissipation (Svistunov, 1995). From their front propagation measurements, Eltsov et al. (2007) conclude that the Kelvin-wave cascade accounts for an important part in the increased dissipation below $0.3\,T_c$. The different sources of dissipation in this analysis are discussed in Sections 3.4 and 3.5.

It is worth noting that a propagating turbulent vortex front has many interesting analogues in physics (van Saarloos 2003). For instance, it is similar to the propagation of a flame front in premixed fuel. Flame front propagation can also proceed in laminar or in turbulent regimes. In the latter case, the effective area of the front increases and its propagation speed becomes higher than in the laminar regime. This property finds its practical use in combustion engines but has also been used by Blinnikov et al. (2006) to describe intensity curves of type Ia supernovae. In all such cases, a metastable state of matter is converted to stable state in the front and V_f is determined by the rate of dissipation of the released energy.

3.2 Measurement of Vortex Front Propagation

The velocity of the vortex front was measured by Eltsov et al. (2007) with the setup in Figure 13. The initial vortex-free state was prepared by warming the sample above $0.7\,T_c$, where remanent vortices annihilate rapidly, and by then cooling it in the vortex-free state at constant rotation to the target temperature. Two different procedures were used to trigger the turbulent burst at the target temperature. These are sketched in Figure 13. In both cases, the front velocity is determined by dividing the flight distance by the flight time, assuming that the front propagates in steady-state configuration. Although this is not exactly true, for instance owing to initial equilibration processes which follow injection, it is assumed for now that this simplification is justified. Especially, since the two injection techniques for different propagation lengths give the same result.

The first injection technique (depicted on the left, Figure 13) makes use of remanent vortices (Solntsev et al., 2007). By trial and error it was found that one or more remnants can be freed with a small step increase in rotation from the region around the orifice on the bottom of the sample cylinder. This was done by increasing Ω in small steps, until at some point usually above $1\,\mathrm{rad/s}$ a remnant starts expanding which below $0.35\,T_c$ immediately gives rise to a turbulent burst. The ensuing vortex front then
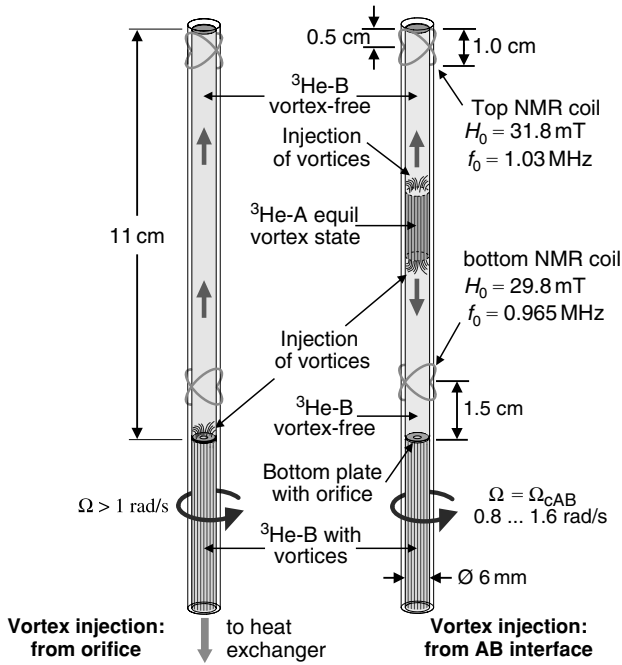
FIGURE 13 Experimental setup for measuring the propagation velocity of the vortex front in the rotating column. Two methods are shown for measuring the front motion across different flight lengths in one single experimental setup. On the left, the seed vortices are tiny remnants at the orifice. In increasing rotation at $\Omega \gtrsim 1\,\text{rad/s}$, they produce a turbulent burst in the volume around the orifice below the bottom detector coil. A single vortex front is then observed to pass first through the bottom coil and later through the top coil. The time difference separating the signals from the passing front over the flight path of 90 mm defines the front velocity V_f. On the right, the seed vortices are injected via the Kelvin-Helmholtz shear flow instability of the two AB interfaces. The injection event is followed instantaneously by a turbulent burst close to the AB interface on the B-phase side. A vortex front is then observed to propagate independently both up and down along the cylinder. The lengths of the flight paths are equal for the upper and lower halves. In Figure 14, it is explained how the flight time is determined in this case.

propagates upwards along the entire column through both pick-up coils in succession.

The second injection method (depicted on the right, Figure 13) relies on the superfluid Kelvin-Helmholtz (KH) instability of the interface between the A and B phases of superfluid ^{3}He (Blaauwgeers et al., 2002). Two stable AB interfaces are formed by applying a specially configured magnetic field which stabilises a narrow A-phase barrier layer over the midsection of the sample cylinder. The shear flow instability of these two AB interfaces is

controlled by rotation velocity, temperature and the stabilisation field. At the target temperature, the instability can be triggered with a step increase of the rotation velocity or of the stabilisation field (Finne et al., 2004b). The instability causes vortices from the A phase to escape across the AB interface into the vortex-free B-phase flow in the form of a bunch of small closely packed loops. Once in the B phase, at temperatures below $0.59\,T_c$, the loops immediately interact and generate a turbulent burst. Two vortex fronts then propagate independently up and down from the AB interfaces, arriving to the top and bottom pick-up coils practically simultaneously (since the setup is symmetric with respect to the midplane of the stabilisation field). An example of the NMR readout as a function of time is shown in Figure 14. The KH shear flow instability and the associated vortex leak across the AB interface have been extensively described in the review by Finne et al. (2006b).

In Figure 14 one of the signal traces records the absorption at the counterflow peak (cf. Figure 7). It is at maximum in the initial vortex-free flow at $v = v_{n\phi} - v_{s\phi}$ (where $v_{n\phi} = \Omega r$ and $v_{s\phi} = 0$ in the laboratory frame). To trigger the KH instability, Ω is increased by a small increment across the critical rotation velocity Ω_{cAB}, which is instantaneously registered as a small increase in absorption level, owing to the increased counterflow velocity. Following the instability and the turbulent burst, the vortices subsequently propagate along the column, but a response in the counterflow peak height is not observed until they reach the closer end of the NMR coil. From thereon, the absorption in the peak rapidly decreases and drops to zero. Keeping in mind that the peak height measures the azimuthally circulating flow in the transverse plane (cf. Equation (1)), its sudden removal requires that the passage of the vortices through the coil must occur as an organised sharp front, followed by a highly polarised state behind the front. The passage is characterised by the time τ_{CF}, which is defined in Figure 14. The propagation velocity V_f of the front is determined from its flight time, measured from the AB interface instability (when $\Omega(t) = \Omega_{cAB}$) to the arrival of the front at the closer edge of the pick-up coil, that is, where the rapid drop in the counterflow peak height starts. Compared to the flight time, the AB interface instability and the turbulent burst can be considered as instantaneous.

The second signal trace in Figure 14 records the absorption in the Larmor peak. It is near zero in the initial vortex-free state, displays a sharp maximum after the collapse of the counterflow peak, and then decays to a small but finite value, which is a characteristic of the final equilibrium vortex state. The transient maximum is the new feature, which arises from flow in the axial direction, created by a helically twisted vortex bundle (Eltsov et al., 2006b). With increasing wave vector Q of the helix, the axial flow at a velocity v_{sz} and the absorption in the Larmor peak increase monotonically (Kopu, 2006). Thus the maximum Larmor peak height h_{tw} in Figure 14 is
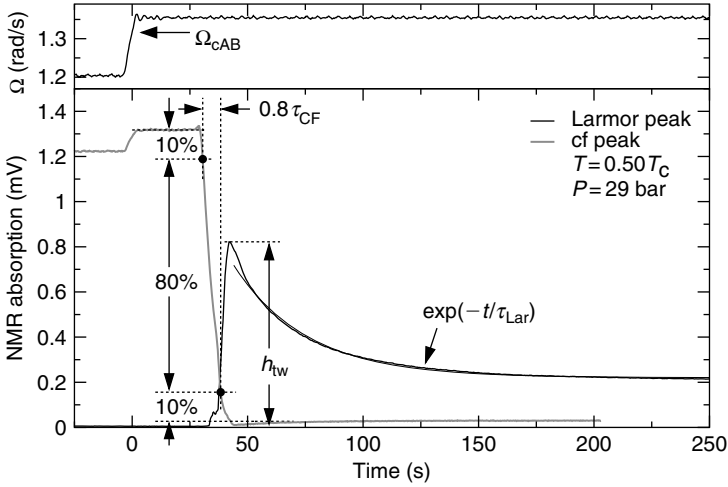
FIGURE 14   NMR signal responses of the propagating vortex front and the twisted vortex state behind it. Here the turbulent burst is started with the Kelvin-Helmholtz instability of the AB interface. Top panel: it is triggered by increasing Ω by a small amount $\Delta\Omega$ across the critical value Ω_{cAB} at 1.3 rad/s. Main panel: two absorption responses are shown, which have been recorded with the bottom detector coil at constant but different values of magnetic field. The responses are from two consecutive identical measurements to allow direct comparison of signal amplitudes. The counterflow peak height (thick grey line) shows the KH trigger $\Delta\Omega$ and a rapid collapse when the front moves through the coil. The time interval from $t = 0$ (when $\Omega(t) = \Omega_{cAB}$) to the start of the collapse measures the flight time of the front from the AB interface to the closer end of the detector. The moment when the peak height reaches zero corresponds to the point when the front has passed through the rear end of the coil. The time required for the collapse, $\sim\tau_{CF}$, measures the width of the vortex front. The second signal (thin black line) is recorded close to the Larmor edge and is sensitive to the longitudinal velocity v_{sz} which is generated by the twisted vortex state (Figure 21). Its sudden steep rise at $t \approx 30$ s is caused by the passage of the first helical sections of the twisted state through the coil. Its later exponential decay reflects the unwinding of the twist, which starts when the front has reached the end plate of the cylinder and the vortex ends begin to slip along the flat surface.

reached when v_{sz} reaches its largest value inside the detector coil. This happens when the most tightly spiralled section of the twisted cluster (which is just behind the front, as seen in Figure 21) passes through the middle of the detector coil. When the front arrives at the bottom end plate of the cylinder, the twist starts to relax since the vortices have to obey the boundary condition on the flat end plate, where they slip to reduce their length and winding. The unwinding produces the exponentially relaxing absorption

with time constant τ_{Lar}. The signal decay continues down to the absorption level characteristic of the equilibrium vortex state, with an array of rectilinear vortex lines. At their other end, the vortices, after crossing the AB interface, have a continuation as doubly quantised A-phase vortices (Hänninen et al., 2003).

To interpret measurements on the front velocity, it is of importance that the structure of the twisted state and the front itself are known. Information on these characteristics can be obtained by measuring quantitatively the various features denoted in Figure 14 as a function of temperature.

3.3 Velocity of vortex front

A striking consequence from the twisted state is the appearance of superflow directed along the helically spiralling vortex cores. This situation is reminiscent of a "force-free" vortex configuration, where all the flow is directed along the vortex core. Such a structure is expected to be stable up to some instability limit, similar to the Glaberson limit of a rectilinear vortex array in parallel flow (Section 2.4). In the twisted state, which is uniform in the axial and azimuthal directions, the superflow has both an azimuthal component at the velocity $v_{s\phi}$ and an axial component at v_{sz}, which depend on the radial coordinate r and are described by the expressions (Eltsov et al., 2006b):

$$v_{s\phi}(r) = \frac{(\Omega + Qv_0)r}{1 + Q^2 r^2}, \quad v_{sz}(r) = \frac{v_0 - Q\Omega r^2}{1 + Q^2 r^2} . \tag{9}$$

Since the net flow through the cross-section of the cylindrical container should vanish, from this condition for v_{sz} one finds that $v_0 = (\Omega/Q)[Q^2 R^2/\ln(1 + Q^2 R^2) - 1]$. The axial flow is directed along the vortex expansion direction close to the cylindrical wall and in the opposite direction closer to the centre. In practice, there has to exist also a radial velocity v_{sr} since any laboratory example of the twisted state is nonuniform. In the case of a propagating vortex front, the wave vector Q has its maximum value close to the rear end of the front and decreases to zero at the bottom and top end plates of the sample. As seen in Figure 14, the twisted state prominently changes the line shape of the NMR spectrum and it is the axial superflow which here has the strongest influence.

As discussed in Section 2.2, in vortex-free counterflow, the end point of a single vortex moves on the cylindrical sidewall roughly with the longitudinal velocity $v_{Lz} \approx \alpha\Omega R$ while its azimuthal velocity is $v_{L\phi} \approx -(1 - \alpha')\Omega R$ (in the rotating frame). Thus the wave vector of the spiral trajectory is $Q = |v_{L\phi}/(Rv_{Lz})| \approx (1 - \alpha')/(R\alpha) = \zeta/R$. If this value is used as an estimate

for the wave vector of the twisted state, it follows that the helical winding of the vortex bundle becomes tighter with decreasing temperature. The tighter twist increases the flow velocities in Equation (9), that is, flow parallel to the vortex cores is enhanced, which will ultimately destabilise the 'force-free' twisted-cluster configuration. Nevertheless, twisted-cluster propagation appears to persist even below $0.2\,T_c$. The twist is removed by the slip of the vortex ends along the flat end plates of the cylinder, which generates the exponentially relaxing absorption in Figure 14 with the time constant τ_{Lar}.

In Figure 15, left panel, the measured temperature dependence of the magnitude of the twist is plotted in terms of the maximum height of the Larmor peak h_{tw}, normalised to the height of the Larmor peak at $\Omega = 0$ at the same temperature (left vertical axis). Two experimental setups with slightly different specifications were used in these measurements. The line shape of the NMR absorption spectrum in the Larmor region depends both on the magnitude and homogeneity of the magnetic polarisation field. In the two setups, the homogeneities varied by a factor of two, which is believed to explain the differences in the absolute values between the two
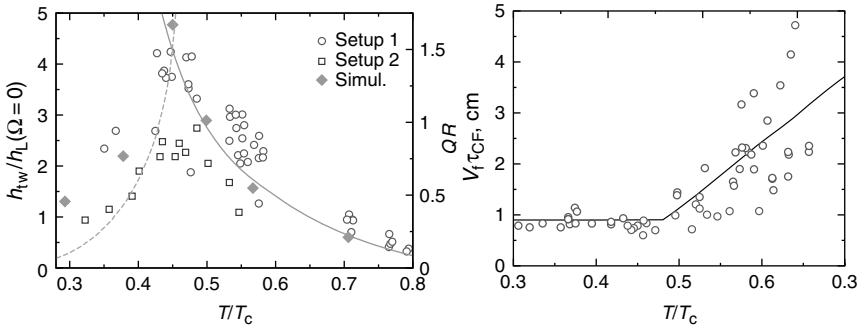
FIGURE 15 Left: magnitude of the twist as a function of temperature. The measurements are performed using the bottom spectrometer. Setups 1 and 2 refer to measurements with the detector coils positioned in two different sets of positions along the sample cylinder; in Figure 13 setup 2 is depicted. ($\circ$, $\square$): the measured ratio of the maximum amplitude h_{tw} of the Larmor peak in the twisted state to the amplitude $h_L(\Omega = 0)$ of the Larmor peak in the nonrotating sample is plotted on the left axis. ($\blacklozenge$): the maximum value of the twist wave vector Q, obtained from simulation calculations, is plotted on the right axis. The solid curve shows the fit $QR = 0.7(1 - \alpha')/\alpha$. The dashed curve shows the minimum Q at which the vortex front still propagates in a thin steady-state configuration. Right: apparent thickness of the vortex front $\tau_{CF}V_f$ as a function of temperature, as determined from measurements triggered with the Kelvin-Helmholtz instability (Figure 13). The solid line is the prediction of the model in Equation (11).

data sets (for details, we refer to Eltsov et al. (2008)). Nevertheless, it is seen here that the twist increases towards low temperatures as expected, but only until a maximum at $0.45T_c$, whereas below $0.45\,T_c$ it abruptly starts to decrease.

The nonmonotonic temperature dependence of the twist is confirmed in numerical calculations: the value of the twist wave vector behind the front, as determined from a fit of the calculated velocity profiles to Equation (9) (Eltsov et al., 2008) and plotted in Figure 15 (left panel, right vertical axis), also peaks at $0.45T_c$. Two reasons can be suggested for the change in temperature dependence at $0.45\,T_c$. First, the twist can relax via reconnections between vortices in the bundle, which become more frequent with decreasing temperature below $0.4\,T_c$ (cf. Figure 25). Second, the source of the twist is at the vortex front, while the sink is at the end plate of the cylinder where the twist vanishes because of the boundary conditions. From there the relaxation of the twist advances in a diffusive manner along the twisted bundle. The effective diffusion coefficient increases as the temperature decreases (Eltsov et al., 2006b), and thus the faster diffusion limits the maximum twist in a finite-size sample at low temperatures. However, overall the stability of twisted-cluster propagation appears to be a complicated question at temperatures below $0.3\,T_c$, where it controls the average number of vortices threading through each cross section of the column behind the front.

The properties of the twist in Figure 15 roughly agree with the estimate that the front velocity can be approximated with the longitudinal velocity of a single vortex expanding in vortex-free rotation, $v_{Lz} \approx \alpha\Omega R$. However, this simplification suffers from the following difficulty: ahead of the front, the vortex-free superfluid component is at rest and the effective counterflow velocity might really be approximated with $v = \Omega r$, but behind the front, the density of vortices is close to equilibrium and $v_{s\phi} \approx v_{n\phi}$. In this case, a vortex, which has fallen behind in the motion, feels a much reduced counterflow and continues to fall more behind. Therefore the thickness of the front should increase with time. The explanation to this dilemma is that behind the front the superflow induced by the twisted vortex bundle has to be taken into account. The longitudinal expansion velocity should now be modified to $v_{Lz} = \alpha\left[v_{n\phi}(R) - v_{s\phi}(R)\right] + (1 - \alpha')v_{sz}(R)$. Since here $v_{sz}(R)$ is oriented in the direction of the front propagation and $v_{s\phi}(R) < v_{n\phi}(R)$ in the twisted state, the longitudinal expansion velocity V_t of the vortices in the tail of the front is enhanced. This velocity can be estimated taking $v_{sz}(R)$ and $v_{s\phi}(R)$ from Equation (9):

$$V_t = \alpha\Omega R\left[1 + \frac{1 - \alpha'}{\alpha}\frac{1}{QR}\right]\left[1 - \frac{Q^2R^2}{(1 + Q^2R^2)\,\log(1 + Q^2R^2)}\right]. \quad (10)$$

Equation (10) has a maximum as a function of the Q vector. If $(1 - \alpha')/\alpha <$ 1.9 (which corresponds to $T > 0.46\,T_c$ according to the measurements of Bevan et al. (1997)), the maximum value of V_t is less than the velocity of the foremost vortices $V_f \approx \alpha\Omega R$. In these conditions, the thickness of the front increases while it propagates. When $T < 0.46\,T_c$, a wide range of Q values exists for which formally $V_t \geqslant V_f$. The minimum possible value of Q is shown in Figure 15 (left panel) as the dashed curve. In these conditions, the front propagates in a steady state 'thin' configuration.

Experimentally, the decay time of the counterflow peak τ_{CF} in Figure 14 can be used to extract the front thickness. The decay starts when the head of the front arrives at the closer edge of the detector coil and it is over when that part of the front leaves the far edge of the detector coil where the counterflow is not sufficient to generate a nonzero absorption response. The product $\tau_{CF}V_f$ has the dimension of length and can be called the apparent thickness of the front. At higher temperatures, the actual thickness of the front grows with time. Here the apparent thickness depends on the distance of the observation point from the site of the turbulent burst and on the rate at which the thickness increases and vortices fall behind. With decreasing temperature, the front starts to propagate as a thin steady-state structure and ultimately its apparent thickness decreases to equal the height of the pick-up coil ($h_c = 9\,\text{mm}$, Figure 7) and remains thereafter approximately constant.

Measurements of the apparent thickness of the front are presented in the right panel of Figure 15. At $T > 0.45T_c$, $\tau_{CF}V_f > h_c$ and the apparent thickness increases with increasing temperature. At $0.45\,T_c$, the apparent front thickness becomes comparable with the height of the detector coil and thereafter at lower temperatures remains at that value. Assuming that initially at the turbulent burst the front is infinitely thin, we can write

$$\tau_{CF} = \frac{h_b + h_c}{V_t^*} - \frac{h_b}{V_f}, \tag{11}$$

where h_b is the distance from the site of the turbulent burst to the nearest edge of the pick-up coil, and V_t^* is the expansion velocity at the position in the front where the NMR signal from the counterflow vanishes. Given that the latter condition roughly corresponds to $v_{s\phi} \sim (1/2)v_{n\phi}$, we take $V_t^* = (V_t + V_f)/2$ if $V_t < V_f$ and simply $V_t^* = V_f$ otherwise. Using V_t from Equation (10) and the simple estimates $QR = (1 - \alpha')/\alpha$ and $V_f = \alpha\Omega R$, we get from Equation (11) the solid line in Figure 15 (right panel), which is in reasonable agreement with experiment.

The rapid change in the counterflow peak height during the passage of the vortex front through the detector coil provides a convenient signal for measuring the propagation velocity V_f. Examples of these signals
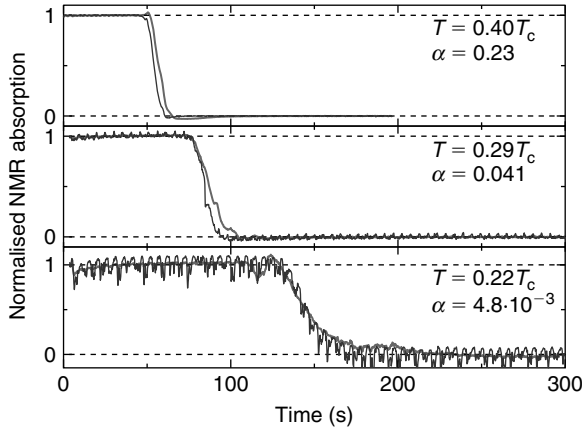
FIGURE 16 Measurement of vortex front propagation. The NMR absorption in the counterflow peak is monitored as a function of time, after triggering the Kelvin-Helmholtz instability at $t = 0$ (cf. Figure 14). The instability is started in constant conditions in the vortex-free state at 1.2 rad/s by increasing Ω in one small step above the critical value Ω_{cAB}, when a magnetic field stabilised A-phase layer is present (topmost panel), or by increasing the magnetic field stepwise above H_{AB} at constant Ω (two lower panels). The two signal traces denote the top (thin noisy line) and the bottom (thick line) detector. Since the flight paths for the upper and lower sample sections are almost equal, the two traces display almost identical flight times.

are shown in Figure 16. They have been measured at different temperatures to illustrate how the temperature dependence of V_f is expressed in the practical measurement. All three examples have been measured using the externally triggered KH instability to start the turbulent burst. In Figure 16, the vortex fronts have traveled a distance of ~4 cm, before they pass through the detector coil, and thus have already acquired their steady-state thin-front configuration.

Measurements on the front velocity V_f are shown in Figure 17. As a function of temperature, two different regimes of front propagation can be distinguished, the laminar and turbulent regimes. The crossover between them is gradual and smooth. This is in sharp contrast to the sudden onset of bulk turbulence (as a function of temperature around $\zeta \sim 1$) in injection measurements in the same circular column, when a bundle of closely spaced seed vortex loops escapes across the AB interface in a Kelvin-Helmholts instability event (Figure 4). A sharp transition with a clearly defined critical velocity is the usual case, for instance in all measurements with mechanical vibrating objects (in the regime $\zeta > 1$) as a function of drive and flow velocity (Vinen and Skrbek, 2008). The smooth crossover here in front
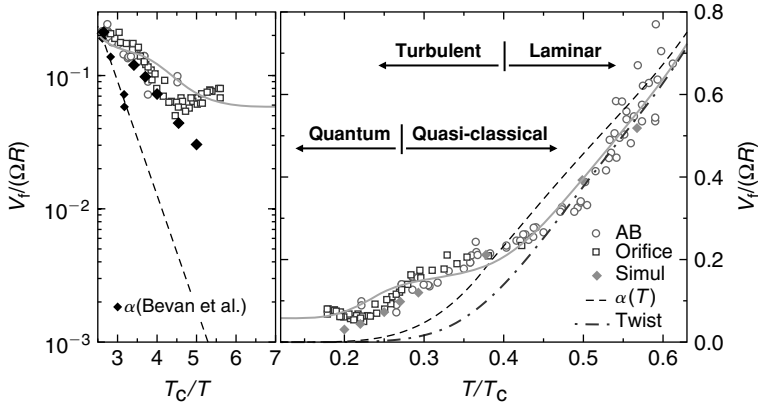
FIGURE 17 Normalised velocity $V_f/\Omega R$ of vortex front propagation in a rotating column. All externally controlled variables are kept constant during this measurement where the initial state is vortex-free rotation and the final state an equilibrium array of rectilinear vortices. Main panel: the assignments of different hydrodynamic regimes refer to the dynamics in the front motion. The open circles denote measurements in which the turbulent burst is started from the AB interfaces in the middle of the column. The squares refer to the case where the front is started at the orifice and then moves upward through the entire column. The large filled diamonds mark results from numerical calculations. The dashed line represents the mutual friction dissipation $\alpha(T)$ measured by Bevan et al. (1997) and extrapolated below $0.35\,T_c$ with $\exp(-\Delta/T)$ (Todoshchenko et al., 2002). The dash-dotted curve takes into account the twisted vortex state behind the propagating front (Equation (12)). The solid curve displays the theoretical model from Section 3.5 which includes corrections from the twisted vortex state, turbulent energy transfer and quantum bottleneck. Left panel: this semilog plot shows that the analytically calculated model provides a reasonable fit to the low temperature data.

propagation may be a special property of the circular column where vortex polarization along the rotation axis is always $\gtrsim 90\,\%$. Nevertheless, smooth crossovers have been observed before, for instance from linear to turbulent wave acoustics in second sound propagation in a circular cylinder as a function of driving amplitude (Kolmakov et al., 2006).

Above $0.4T_c$ in the laminar regime, the results in Figure 17 are consistent with the earlier measurements of Finne et al. (2004c). Here the single-vortex dynamics apply when inter-vortex interactions can be neglected and $V_f \approx \alpha \Omega R$ (Section 2.2). At closer inspection, it is noticed that the data for the normalised front velocity $v_f = V_f/\Omega R$ lie on average below $\alpha(T)$ (dashed curve). The reason is that behind the front the vortices are in the twisted state and not as rectilinear vortex lines in an equilibrium array. If we integrate the kinetic energy stored in the twist-induced flow

(Equation (9)) over the sample cross-section, the result is found to be

$$v_{f,lam} = 2[1/\log(1 + \zeta^2) - \zeta^2]\,\alpha\,. \tag{12}$$

After including this reduction from the twisted state, the agreement is improved (dash-dotted curve). In the turbulent regime below $0.4T_c$, the data deviate with decreasing temperature more and more above the extrapolations from the laminar regime. Eventually at the lowest temperatures, the measurements become temperature independent, with a peculiar transition from one plateau to another at around $0.25\,T_c$. These features are attributed to turbulent dynamics and are analysed in the next sections in more detail.

The measured properties of the propagating vortex front are confirmed qualitatively in numerical calculations. They show that in the laminar regime the thickness of the front grows with time, but with decreasing temperature the twist increases (Figure 15) and finally at about $0.45\,T_c$ the thin steady-state front configuration is established, with a time-independent thickness roughly equal to the radius of the sample. Below $0.45\,T_c$, the twist decreases with decreasing temperature but remains within the limits where the twist-induced superflow is sufficient to maintain a thin time-invariant front configuration. The calculated front velocity in Figure 17 approximately agrees with the measurements down to about $0.22\,T_c$. It is therefore instructive to analyse the calculations to identify where and by what mechanisms turbulent losses occur in the rotating column. This will be discussed in the next section.

3.4 Numerical Calculation of Turbulence in Vortex Front Propagation

The promising agreement of the calculated vortex front velocity v_f with the measurements in Figure 17 suggests that numerical calculations could provide useful guidance for the interpretation of the measurements in Section 3.3 and for constructing the analytic theory in Section 3.5. Our main question is the following: why are the numerical results on v_f deviating with decreasing temperature more and more above the mutual-friction-controlled extrapolation from the laminar regime? For simplicity, we split the discussion of vortex motions to three different length scales: (i) large scales of order $\sim R$, where turbulent fluctuations become visible as variations in the number and distribution of vortices, (ii) the inter-vortex scale $\sim\ell$, where the presence of Kelvin-waves on individual vortex lines can be seen to grow and (iii) small scales, where reconnections between neighbouring vortices might occur and excite turbulent fluctuations on

individual vortex lines. In contrast to the more usual studies of turbulent tangles, which generally monitor their free decay as a function of time when the external pumping is switched off, we are here dealing with highly polarised steady-state motion along the rotating column. This motion appears to remain intact down to the lowest temperatures but becomes dressed with turbulent fluctuations in growing amounts towards decreasing temperatures.

Two examples are shown in Figure 18, which illustrate the development with decreasing temperature. These configurations at $0.4\,T_c$ and $0.3\,T_c$ in an ideal column of radius $R = 1.5\,\text{mm}$ rotating at $\Omega = 1\,\text{rad/s}$ have been calculated using the techniques described in Section 2.5. Similar results at

28 mm

$t = 140\text{s}$
$T = 0.3T_c$

$t = 80\text{s}$
$T = 0.4T_c$
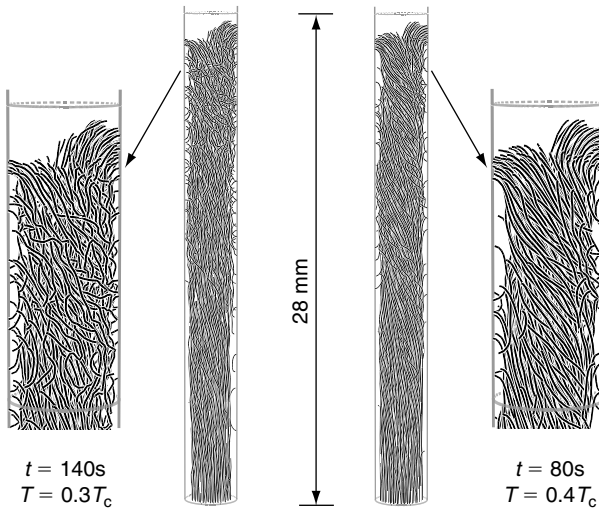
FIGURE 18 Calculated vortex propagation at $0.3\,T_c$ and $0.4\,T_c$. The motion is started from the bottom end of the cylinder by placing the equilibrium number of vortices in the form of quarter loops between the bottom end plate and the cylindrical sidewall. On the right at $0.4\,T_c$, the front has traveled for 80 s to a height $z \approx 28\,\text{mm}$ above the bottom end plate in a cylinder of 3 mm diameter rotating at 1 rad/s. The zoom on the far right shows the vortices in the front and immediately below in more detail. On the left at $0.3\,T_c$, the same distance is covered in 140 s. Here the vortices appear more wrinkled, owing to short-wavelength Kelvin-wave excitations. The vortices are tightly twisted below the front but become straighter and smoother on approaching the bottom end plate. Many vortices can be seen to connect to the cylindrical sidewall also below the front. Their average length is shorter than the distance from the front to the bottom end plate, although the number of vortices $N(z)$ threading through each cross-section of the cylinder below the front is roughly constant and comparable to that in the equilibrium vortex state: $N(z) \lesssim N_{eq}$. The average polarisation along the vertical axis is high, $\sim 90\,\%$.

$0.4\,T_c$ and higher have been reported in the review by Finne et al. (2006b). The calculations are started from an initial configuration with roughly the equilibrium number of vortices placed as quarter loops between the bottom end plate and the sidewall of the cylinder. During the subsequent evolution, the propagating vortex front is formed and the twisted cluster starts to acquire its shape (Hänninen, 2006).

Above $0.45\,T_c$, the motion is laminar with relatively smooth vortices, which only twist at large length scales. Below $0.45\,T_c$, the thickness of the front (in the axial direction) settles at $\Delta(r) \simeq r\,d$, where the parameter $d \sim 1$. The large-scale characteristics as a function of temperature from 0.3 to $0.6\,T_c$ are displayed in Figure 19 for the setup of Figure 18. The counterflow energy $\mathcal{E}(z)$ is obtained by integrating the momentary distribution of counterflow $\mathbf{v}(r, \phi, z, t)$ over each cross section z of the column, while the polarization $p_z(z)$ is similarly derived by integrating over the vortices threading through this cross section. With decreasing temperature, the front acquires more and more turbulent features which become visible as increasing small-scale structure: Kelvin-waves, kinks and inter-vortex

$$\varepsilon(z) = \int v_{ns}^2 d^2 r / \int (\Omega r)^2 d^2 r \qquad p_z^2 = \int (\hat{\mathbf{s}} \cdot \hat{\mathbf{z}})^2 d\xi / \int d\xi$$
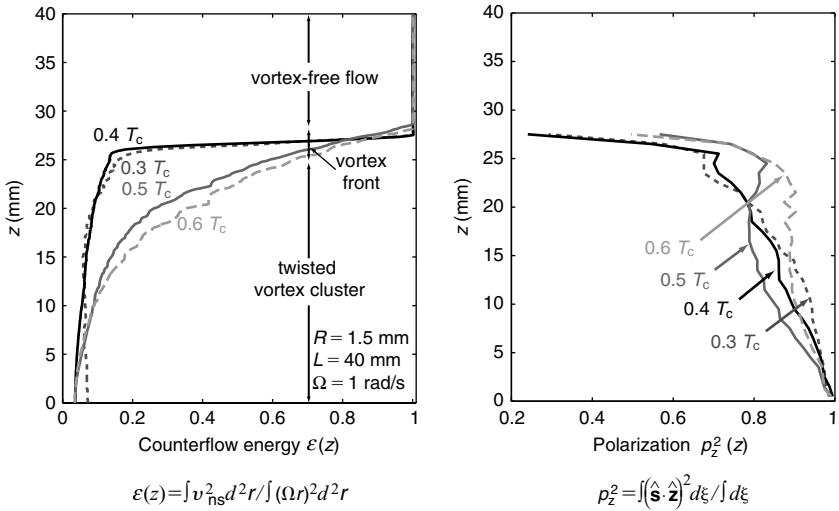
FIGURE 19   Axial distributions of counterflow energy $\mathcal{E}(z)$ (see Eq. (8)) and polarization $p_z(z)$ (both in normalized units), calculated for the vortex propagation in Figure 18. On the left $\mathcal{E}(z)$ is seen to drop steeply within the narrow vortex front at the temperatures 0.4 and $0.3\,T_c$. Here the front is in steady-state time-invariant motion and its velocity provides a direct measure of dissipation. Above $0.45\,T_c$ some vortices tend to fall more and more behind during the motion and the shape of the front becomes more extended with time. As seen in Figure 18, small-scale structure from Kelvin waves accumulates increasingly on the vortices below $0.45\,T_c$, but as shown in the panel on the right, the polarization $p_z(z)$ remains always high behind the front.

reconnections. These small-scale fluctuations exist on top of a strongly polarised vortex orientation, which is preserved even at $0.2\,T_c$. The high polarisation along the rotation axis and the organised configuration of the twisted cluster is expected to reduce loop formation and self-reconnection on individual vortex lines, but it also suppresses reconnections between neighbouring vortices from what one would find in turbulent tangles. The amount of twist, in turn, is reduced by the unwinding from the slip of the vortices along the flat bottom end plate of the column.

The comparison of the two examples in Figure 18 is continued in Table 1. As a rule, we expect that with decreasing mutual-friction-damping turbulent disturbances are expected to cascade down to ever smaller length scales. In Table 1, this is examined by defining the quantity δ which measures on an average the distance over which the vortex front moves during the time interval between two inter-vortex reconnections. Since the axial motion of the front slows down and the reconnection rate increases with decreasing temperature, δ decreases rapidly below $0.4\,T_c$. Thus, δ provides a measure between mutual friction and reconnections. The bottom line in Table 1 uses the dimensionless ratio δ/ℓ to characterise the relative importance of mutual friction dissipation to reconnection losses. When $\delta/\ell > 1$, the energy loss from reconnections, which presumably excite Kelvin-waves, is not important in the total energy balance of the propagation. At $0.4\,T_c$, where $\delta/\ell \sim 2$, this is what one expects. If $\delta/\ell < 1$, as is the case below $0.3\,T_c$, then it becomes possible that inter-vortex reconnections might play a role in the total energy balance. Table 1 thus hints that

TABLE 1 Comparison of vortex front propagation at $0.3\,T_c$ and $0.4\,T_c$. The bottom line of the table shows that below $0.4\,T_c$ front propagation is rapidly moving into the quantum regime. The calculations are for a cylinder of radius $R = 1.5\,mm$ and length $h = 40\,mm$, which is filled with ^{3}He-B at a liquid pressure of $P = 29\,bar$ and rotates at an angular velocity $\Omega = 1\,rad/s$. The number of vortex lines is the average through each cross-section of the cylinder over the length of the twisted cluster. The maximum resolution of the calculations is $0.05\,mm$.

T/T_c	0.3	0.4
Mutual friction parameter α	0.040	0.18
Mutual friction parameter α'	0.030	0.16
Front velocity V_f	$0.12\,\Omega R$	$0.22\,\Omega R$
Front velocity V_f (mm/s)	0.18	0.33
Total Reconnection rate (event/s)	300	130
Number of vortex lines/cross-section	125	150
Reconnection rate per line $1/\tau$ [events/(line s)]	2.4	0.87
Front shift δ during τ (mm)	0.075	0.38
Interline separation ℓ (mm)	0.20	0.19
Ratio δ/ℓ	0.36	2.0

new phenomena are expected to emerge on length scales approaching the inter-vortex distance ℓ.

The characteristics of the propagating vortex front and the trailing twisted cluster are further illustrated in Figures 20–22. In Figure 20 it is the modulus of the total velocity of the superfluid component, $|v_s(r, \phi, z, t)|$, whose $[r, z]$ profiles are displayed. The top panel shows the velocity $\langle v_s \rangle_{t,\phi}$ in the laboratory coordinate frame, averaged over time t and azimuthal angle ϕ, while the bottom panel displays its mean fluctuation amplitude $[\langle (v_s - \langle v_s \rangle_{t,\phi})^2 \rangle_{t,\phi}]^{\frac{1}{2}}$. In Figure 21, it is the axial component v_{sz} and in Figure 22 it is the radial component v_{sr}, which are analysed in the same fashion. The largest component $v_{s\phi}$ is omitted since its profiles are so similar to those of $|v_s|$. In fact, at large radii $r \gtrsim R/5$, the profiles of the two velocities as a function of $[r, z]$ are almost indistinguishable, while at small radii $r \lesssim R/5$ the axial velocity v_{sz} in Figure 21 is the main contributor to $|v_s|$.

The vortex front becomes clearly defined in Figures 20–22. For instance, in Figure 20, the steep almost linear rise in $|v_s|$ in the interval $-1 < z/R < 0$ signifies the transition from the nonrotating state $v_{s\phi} = 0$ at $z > 0$ to almost equilibrium rotation at $v_{s\phi} \approx \Omega r$ at $z < -R$. This is the vortex front with its narrow thickness $\sim R$ and strong shear flow, created by the vortices terminating within the front on the cylindrical sidewall perpendicular to the axis of rotation. Below the front, the number of vortices threading through any cross-section of the cylinder remains roughly constant. This is seen from the fact that at $0.3\, T_c$ the maximum value of v_s, $\langle v_{s\phi} \rangle_{\max} \approx 0.6\, \Omega R$, remains stable over the entire length of the twisted cluster, starting from $z/R < -1$ immediately behind the front. At higher temperatures some vortices tend to fall behind the front and thus at $0.4\, T_c$ one finds that v_s slowly increases to $\langle v_{s\phi} \rangle_{\max} \approx 0.75\, \Omega R$ at $z/R < -5$. Note also that radially the azimuthal flow $v_{s\phi}$ increases monotonously behind the front up to the edge of the cluster at $\sim 0.9\, R$ and then slightly decreases towards the cylindrical wall.

The fluctuations of $|v_s|$ around its mean value, as shown in the bottom panel of Figure 20, are substantial of order $30\,\%$ in the sharp peak created by the vortex front. The same applies to other velocity components; their fluctuations also tend to be largest in the front region $-1 < z/R < 0$ and typically only half as large over the length of the twisted cluster. In Figures 20–22, the fluctuations are sampled at a relatively slow rate of $2\,\mathrm{Hz}$. As seen in Figure 18, in the front, the vortices are not perfectly distributed: it is this disorder in the structure of the front, and the variations in its number of vortices which gives rise to the fluctuation peak. In Figure 23, the radial distribution of the fluctuations in $|v_s|$ in the front region $-1 < z/R < 0$ is analysed. As expected, they grow rapidly towards large radii. In Section 3.5, we make use of this radial distribution.

However, not only large-scale disorder contributes to velocity fluctuations but also Kelvin-waves start to expand on individual vortices at
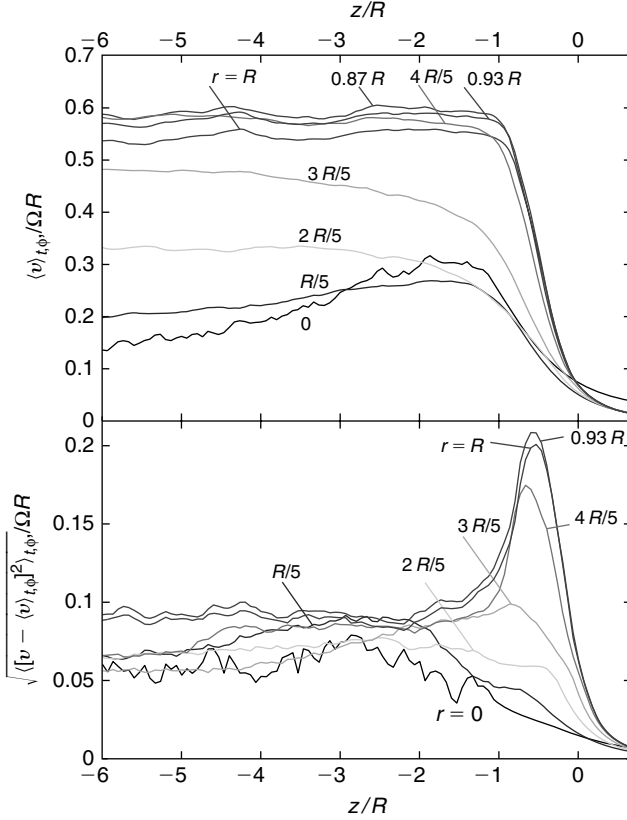
FIGURE 20 Axial and radial distributions of the velocity $|v_s(r, \phi, z, t)|$ and its fluctuations in vortex front propagation. Both quantities are normalised with respect to ΩR and are expressed in the laboratory frame in terms of their averages, $\langle v_s \rangle_{t,\phi}$ (top panel) and $[\langle (v_s - \langle v_s \rangle_{t,\phi})^2 \rangle_{t,\phi}]^{\frac{1}{2}}$ (bottom panel), by integrating over the azimuthal coordinate ϕ and time t. The different contours are plotted as a function of z at fixed radial value, $r = 0, R/5, 2R/5, \ldots$. They are calculated, for example, at $0.3\,T_c$ in Figure 18, over the time interval from 60 to 80 s after starting the front motion. At $t = 80$ s, the front has climbed to a height $z(80\,s) \approx 16$ mm (here placed at $z/R = 0$). Both plots are generated from vortex configurations, which are saved every 0.5 s. The steep change in the top panel in the interval $-1 < z/R < 0$ signifies the front with its narrow thickness $\Delta z \sim R$. Similarly in the bottom panel the amplitude of fluctuations (sampled at 2 Hz) reaches a sharp maximum in the front region $-1 < z/R < 0$ at large radii $r \gtrsim 3R/5$. This peak is twice larger than the flat values from behind the front in the region of the twisted cluster. At $0.4\,T_c$ (the case of Figure 18, right), the fluctuation peak from the front is 14% lower.
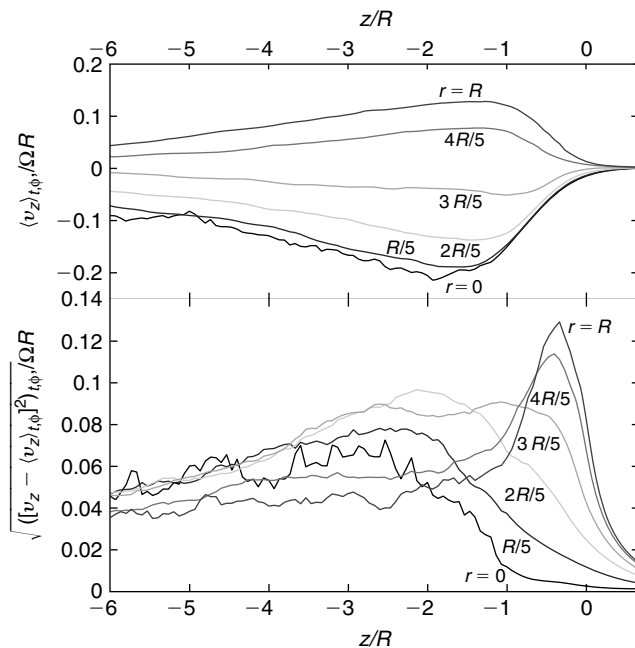
FIGURE 21 Axial and radial distributions of the axial velocity component $v_{sz}(r, \phi, z, t)$ and its fluctuations. The profiles have been generated in the same calculations at $0.3\,T_c$ as Figure 20. This component is generated by the helically wound sections in the twisted cluster. The slowly unwinding twist at the bottom end plate (on the left of the figure) causes the characteristic linear increase in $|v_{sz}|$ towards the right where new twist is continuously formed by the spirally winding motion of the vortex front. Note that v_{sz} changes sign since it is directed antiparallel to the propagation direction of the front in the central parts $r \lesssim 2R/3$ and parallel at larger radii. Its maximum magnitude is in the centre just behind the front where it is the dominant component in $|v_s|$. Its largest fluctuations are at large radii within the front region.

temperatures $\lesssim 0.3\,T_c$, as seen in Figure 18 (Hänninen, 2006). In Figure 24, a momentary vortex configuration (when the front has reached the height $z \approx 28\,\text{mm}$ in Figure 18) is broken down in curvature radii $\mathcal{R}_c$ and the average curvature $\langle \mathcal{R}_c^{-1} \rangle$ is plotted as a function of z. At $T \geq 0.4\,T_c$, the sharp peak at the front is caused by the vortices curving to the cylindrical sidewall with $\mathcal{R}_c \approx R$. However, at $0.3\,T_c$, the Kelvin-wave contribution at shorter length scales becomes dominant and the average radius of curvature drops to $\langle \mathcal{R}_c \rangle \approx 0.4\,\text{mm}$. The characteristic Kelvin-wave frequency $\omega_k \sim \kappa k^2$ corresponds at this length scale to $0.4\,\text{Hz}$ (which is less than the sampling frequency of $2\,\text{Hz}$). Thus the dominant Kelvin-waves are included in the velocity fluctuations in Figures 20–22. Nevertheless, in
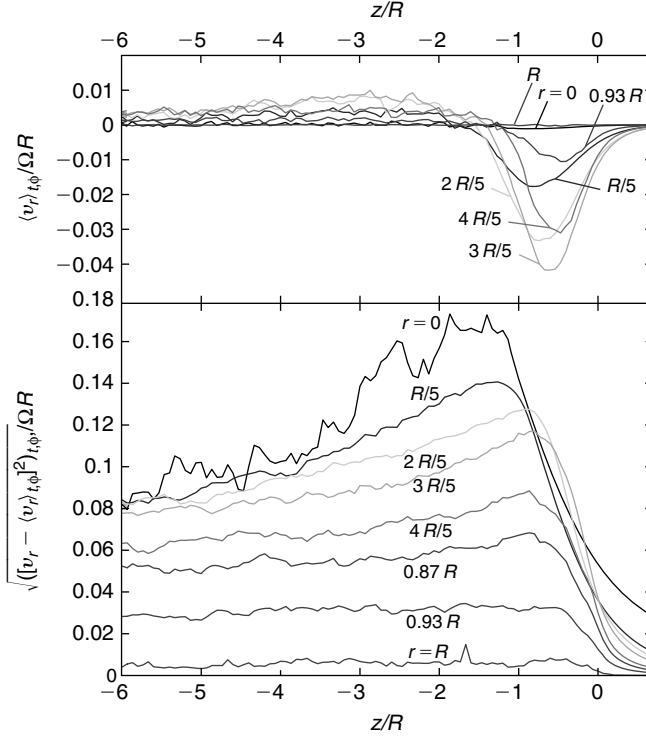
FIGURE 22 Axial and radial distributions of the radial velocity component $v_{sr}(r, \phi, z, t)$ and its fluctuations in vortex front propagation at $0.3\,T_c$ in Figure 18. This component provides the return currents to the axial component v_{sz}. It is an order of magnitude smaller than either the azimuthal $v_{s\phi}$ or the axial v_{sz} component. It is directed inward towards the central axis in the narrow front region, while the outward flowing radial return currents are distributed more evenly along the length of the twisted cluster. The fluctuations in v_{sr} are largest close to the cylinder axis and steadily decrease as a function of r. As a function of z, the maximum fluctuations are just behind the front where v_{sr} changes sign.

these figures, Kelvin-waves represent only a small part of the total fluctuations $\langle (v_s - \langle v_s \rangle_{t,\phi})^2 \rangle_{t,\phi}$ in the sharp peak created by the front. This is seen from the fact that the peak is localised in the z direction within the vortex front at $-1 < z/R < 0$, while the Kelvin-wave excitations in Figure 24 extend half way down the twisted cluster to $z/R \sim -10$, as can also be directly seen from Figure 18.

Figure 25 shows that also reconnections between neighbouring vortices become rapidly more frequent at temperatures $\lesssim 0.3\,T_c$ (see also Hänninen, (2006)). The reconnections peak in the region around $z/R \lesssim -1$, where the front ends and the twisted cluster starts. The increasing
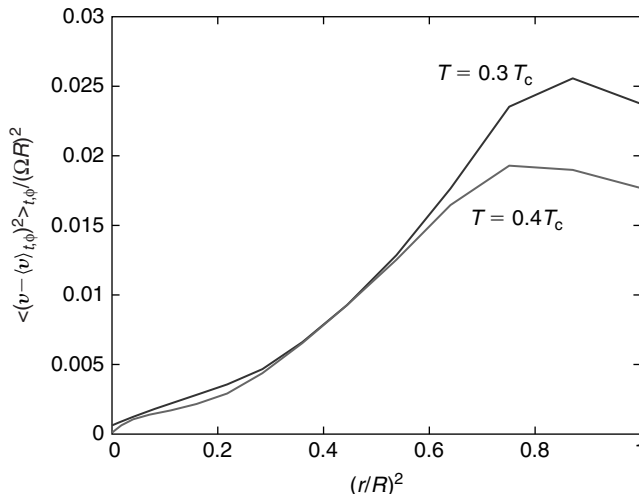
FIGURE 23 Radial distribution of velocity fluctuations within the propagating vortex front from Figure 20. The normalised square of the velocity deviation from the average is plotted on the vertical scale, $\langle (v_s - \langle v_s \rangle_{t,\phi})^2 \rangle_{t,\phi}/(\Omega R)^2$, versus the square of the normalised radial position, $(r/R)^2$. The averages in the angled brackets, besides having been integrated over time t and azimuthal coordinate ϕ (or front motion), represent an average over the interval $-1 < z/R < 0$. The fluctuations are seen to increase rapidly towards large radii, up to where the vortex-free annulus starts at $R_v \approx 0.87\,R$.

reconnection rate with decreasing temperature is one factor which helps to reduce the helical twist behind the front and might be one reason why the measured twist appears to be reduced towards low temperatures below $0.45\,T_c$ (Figure 15).

A further characteristic of front propagation in the rotating column is that fluctuations in vortex length are small since these are mainly restricted to the transverse plane. The total vortex length $L(t)$ in the moving front and in the twisted cluster behind it increases linearly in time and thus the fluctuations can be expressed with respect to a linearly increasing fitted average $L_{fit}(t)$. The average deviation from the mean $\langle \Delta L \rangle = [\langle (L - L_{fit})^2 \rangle]^{\frac{1}{2}}$ turns out to be small. In the conditions of Figure 18 at $0.3\,T_c$, one obtains $\Delta L/L \sim 10^{-3}$. This is as expected since fluctuations in length are energetically expensive in polarised vortex motion.

Finally, we point out two features which are seen in the calculations, which both grow in prominence with decreasing temperature below $0.3\,T_c$ but which have not yet been searched for in measurements. The calculations are started with the number of seed vortices equal to or larger than
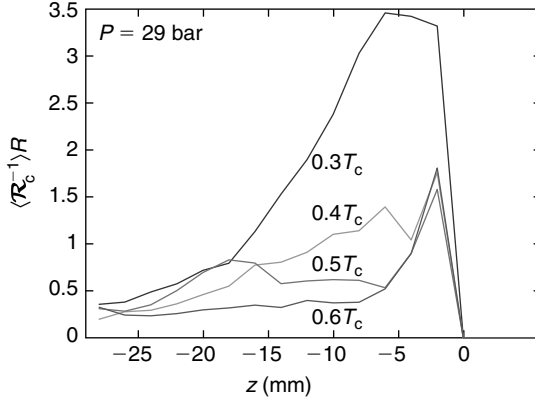
FIGURE 24 Distribution of curvature radii along vortices during front propagation, calculated for the setup in Figure 18. The curvature is defined as the inverse of the local vortical curvature radius $\mathcal{R}_c$, that is $\mathcal{R}_c^{-1} = |d^2 s(\xi, t)/d\xi^2|$, where ξ is the coordinate along the vortex core. The curvature is calculated on an equidistant linear grid along each line vortex. On the vertical axis, the average curvature $\langle \mathcal{R}_c^{-1} \rangle$ is plotted as a dimensionless quantity $\langle \mathcal{R}_c^{-1} \rangle R$ as a function of z at different temperatures. The averages are taken over the cross-section of the cylinder and over an interval $\Delta z = 2$ mm in length centred at z. The sharp peak at the very front ($z \approx -2$ mm) at temperatures $T \geq 0.4\, T_c$ represents the vortices curving to the cylindrical sidewall with $\mathcal{R}_c \approx R$. In contrast, at $0.3\, T_c$, small-scale curvature dominates, the average radius of curvature has dropped to $\mathcal{R}_c \approx 0.4$ mm and extends from the front well inside the twisted cluster.

N_{eq}, but nevertheless, the number of vortex lines does not remain stable at N_{eq} during steady-state propagation.[1]

The first feature concerns the number of vortices which in free steady-state propagation thread through any cross-section of the column behind the front. This number is roughly constant but less than in equilibrium (for instance in Figure 18 at $0.3\,T_c$, there are about 130 vortices per cross-section while $N_{eq} \approx 160$ vortices). In the simplest model of the twist in Equation (9), the number of vortices in the twisted state is smaller than in the equilibrium vortex state by the factor $\approx (QR)^2 / \big([1 + (QR)^2]\, \ln[1 + (QR)^2]\big)$. This reduction is of correct order of magnitude compared to that seen in the calculations at $\gtrsim 0.3\,T_c$. In addition to improving the stability of the twisted state, the reduction in the number of twisted vortices decreases the axial flow velocity v_{sz} (Figure 21), which has the effect of reducing the longitudinal front velocity v_f and counteracts

[1] In the equilibrium vortex state $N_{eq} \approx \pi(R - d_{eq})^2\, n_v$, where the width of the vortex-free annulus around the central cluster is $d_{eq} \approx n_v^{-1/2}$ (Ruutu et al., 1998b).
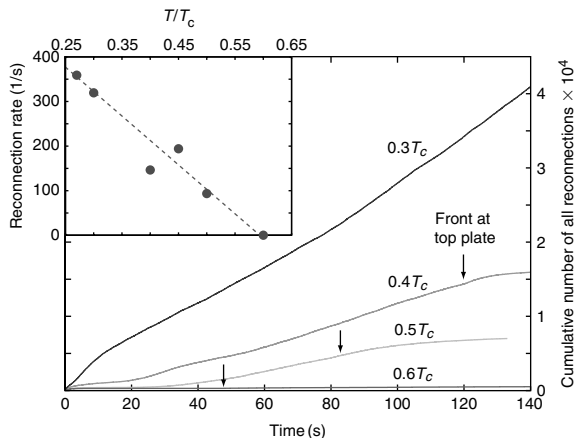
FIGURE 25   Main panel: cumulative number of all vortex reconnection events during vortex front propagation in the setup of Figure 18, as a function of time. The reconnections occur between two different vortices and mainly in the twisted cluster where they reach a maximum close behind the front. This process does not change the number of vortices. The vertical arrows indicate the moment when the front reaches the top end plate (at height $h = 40$ mm). The reconnections are here seen to increase rapidly at low temperatures, reaching a rate of $300\,\mathrm{s}^{-1}$ or ~ 1 reconnection/(vortex s) at $0.3\,T_c$. Inset: the roughly constant reconnection rate from the main panel (when the front is in steady-state propagation before the end plate is reached) plotted as a function of temperature.

its increase above the laminar extrapolation in Figure 17. While the number of vortices per cross section of the twisted cluster decreases with decreasing temperature below $0.3\,T_c$, the density of vortices, nevertheless, remains constant over the cross section (but less than the equilibrium value: $n_v \lesssim n_{v,eq} = 2\Omega/\kappa$). When the front finally reaches the upper end plate in Figure 18 and the twist starts to relax, simultaneously N gradually recovers and approaches N_{eq} from below.

The second feature of the calculations is that in steady state propagation the average length of the vortices is less than that of the twisted cluster (which means that the total number of individual vortices in the column may be well above N_{eq}). For instance at $0.3\,T_c$ in Figure 18, the average length is ~ 15 mm and only ~ 6 mm for those vortices with both ends on the cylindrical sidewall. Nevertheless, the polarisation of all vortices along $\hat{z}$ is high, $\sim 90\,\%$. After the front has reached the upper end plate in Figure 18 and the twist starts relaxing, the short vortices provide an ample storage from which to add more vortices so that N_{eq} is reached.

To summarise the calculations, we return to our starting point, namely the increasing deviation of the calculated front velocity above the laminar extrapolation below $0.4\,T_c$ (Figure 17). The analysis of the calculated vortex

configurations shows increasing turbulent disorder at large length scale $\sim R$, growing Kelvin-wave amplitudes on individual vortices on scales $\sim \ell$ and the presence of inter-vortex reconnections. Combined these changes from the increasing turbulent influence with decreasing temperature make up for the difference, in the presence of a still finite mutual friction dissipation. An additional sink of energy is the cascading of Kelvin-wave excitations below the resolution limit of the numerical calculations (usually ~ 0.05 mm), which are lost from the energy balance. The calculations are in reasonable agreement with measurements down to $0.3\,T_{\mathrm{c}}$, but at lower temperatures changes in the twisted cluster propagation appear to occur, to maintain stability and polarization. These have not been adequately studied and may lead to revisions of the current model at the very lowest temperatures.

3.5 Analytical model of turbulent front

The measured front velocity in Figure 17 displays below $0.4\,T_{\mathrm{c}}$ two plateaus which are separated by a transition centred at $0.25\,T_{\mathrm{c}}$. The numerical analysis in Section 3.4 places this transition in the temperature region where the Kelvin-wave cascade acquires growing importance, that is, in the regime where subinter-vortex scales start to influence energy transfer. The peculiar shape of the measured $v_{\mathrm{f}}(T)$ curve prompted L'vov et al. (2007a) to examine energy transfer from the quasi-classical length scales (where bundles of vortices form eddies of varying size with a Kolmogorov spectrum) to the quantum regime (where Kelvin-waves expand on individual vortex lines). The result is a bottleneck model (L'vov et al., 2008) which matches energy transfer across the crossover region from superinter-vortex length scales to subinter-vortex scales. It can be fitted with reasonable parameters to the measured $v_{\mathrm{f}}(T)$ curve (Eltsov et al., 2007).

3.5.1 Two-Fluid Coarse-Grained Equations

To describe the superfluid motions on length scales exceeding the inter-vortex distance ℓ, we make use of the coarse-grained hydrodynamic equation for the superfluid component. This equation is obtained from the Euler equation for the superfluid velocity $\mathbf{U} \equiv \mathbf{U}_{\mathrm{s}}$, after averaging over the vortex lines which are assumed to be locally approximately aligned, forming vortex bundles which mimic the eddies in viscous flow (see the review by Sonin, 1987),

$$\frac{\partial U}{\partial t} + (U \cdot \nabla)U + \nabla \mu = f_{\mathrm{mf}}. \tag{13}$$

Here, μ is the chemical potential and f_{mf} the mutual friction force (Equation (3)), which can be rewritten as follows:

$$f_{mf} = -\alpha'(\mathbf{U} - \mathbf{U}_n) \times \omega + \alpha\,\hat{\omega} \times [\omega \times (\mathbf{U} - \mathbf{U}_n)]. \tag{14}$$

We use $\omega = \nabla \times \mathbf{U}$ for the superfluid vorticity; $\hat{\omega} \equiv \omega/\omega$ is the unit vector in the direction of the mean vorticity; $\mathbf{U}_n$ is the velocity of the normal component (which is fixed). In flow with locally roughly aligned vortices, the mutual friction parameters define the reactive ($\propto \alpha'$) and dissipative ($\propto \alpha$) forces acting on a bunch of vortex lines as it moves with respect to the normal component in a field of slowly varying vortex orientation.

We shall work in the rotating reference frame where $U_n = 0$. In this frame, the reactive first term in Equation (14) renormalizes the inertial term $U \times \omega$ on the left-hand side (LHS) of Equation (13), introducing the factor $1 - \alpha'$ (Finne et al., 2003). The relative magnitude of the two nonlinear terms, the ratio of the inertial term and of the friction term (the latter is the second term on the right-hand side RHS of Equation (14)), is the Reynolds number in this hydrodynamics. It proves to be the flow velocity independent ratio of the dimensionless mutual friction parameters: $\zeta = (1 - \alpha')/\alpha$ (which was introduced by Finne et al., 2003 in the form $q = 1/\zeta$). To arrive at a qualitative description of the front, we follow L'vov et al. (2004) and simplify the vectorial structure of the dissipation term and average Equation (14) over the directions of the vorticity ω (at fixed direction of the applied counterflow velocity v). With the same level of accuracy, omitting a factor 2/3 in the result, we get

$$f_{mf} \Rightarrow \langle f_{mf} \rangle_{\omega/|\omega|} = -\frac{2}{3}\alpha\,\omega_{eff}\,v \Rightarrow -\alpha\,\omega_{eff}\,v\,, \tag{15}$$

$$\omega_{eff} \equiv \sqrt{\langle |\omega|^2 \rangle}.$$

Here and henceforth, $\langle \ldots \rangle$ denotes 'ensemble averaging' in the proper theoretical meaning. From the experimental point of view, $\langle \ldots \rangle$ can be considered as time averaging in a frame which moves with the front (over a time interval, during which the front propagates a distance equal to its width). The resulting mean values, to be discussed in Equations (16) and (19), can be considered as functions of (slow) time and space. We follow L'vov et al. (2004) and neglect the fluctuating turbulent part of ω_{eff} in Equation (15). We thus replace $|\omega|$ by its mean value, the vorticity from rotation. In this approximation, Equation (15) takes the simple form:

$$f_{mf} = -\Gamma U\,, \quad \Gamma \equiv \alpha\,\omega_{eff}. \tag{16}$$

3.5.2 Flow Geometry, Boundary Conditions and Reynolds Decomposition

Axial flow geometry and flat idealisation. As a simplified model of the rotating cylinder, we consider first the flat geometry with $\hat{x}$ as the streamwise, $\hat{y}$ as the cross-stream and $\hat{z}$ as the front-normal directions. A more realistic axial symmetry will be discussed later. We denote the position of the front with $\mathcal{Z}(t)$ and look for a stationary state of front propagation at constant velocity $-V_f$:

$$\mathcal{Z}(t) = -V_f t. \tag{17}$$

The normal velocity is zero everywhere, $U_n(r, t) = 0$, which corresponds to co-rotation with the rotating cylinder. The vortex front propagates in the region $z < \mathcal{Z}(t)$, where the superfluid velocity is $-V_\infty$, while far away behind the front at $z > \mathcal{Z}(t)$, the superfluid velocity U tends to zero (i.e., towards the same value as the normal fluid velocity).

Reynolds decomposition and definitions of the model. Following the customary tradition (see, Pope, 2000), we decompose the total velocity field U into its mean part V and the turbulent fluctuations v with zero mean:

$$U = V + v, \quad V = \langle U \rangle, \quad \langle v \rangle = 0. \tag{18a}$$

In our model,

$$V = \hat{x} V, \quad V \approx \Omega\, r. \tag{18b}$$

The following mean values are needed: the mean velocity shear $S(r, t)$, the turbulent kinetic energy density (per unit mass) $K(r, t)$ and the Reynolds stress $W(r, t)$. Their definitions are as follows:

$$S(r, t) \equiv \frac{\partial V}{\partial z}, \; K(r, t) \equiv \frac{1}{2} \left\langle |v|^2 \right\rangle, \; W(r, t) \equiv - \langle v_x v_z \rangle. \tag{19a}$$

Also we will be using the kinetic energy density of the mean flow

$$K_V(r, t) \equiv \frac{1}{2} \left[V(r, t) \right]^2 \tag{19b}$$

and the total density of the kinetic energy

$$\mathcal{K}(r, t) \equiv K_V(r, t) + K(r, t) \tag{19c}$$

Clearly, the total kinetic energy in the system, $\mathcal{E}(t)$, is:

$$\mathcal{E}(t) = \int \mathcal{K}(r, t) \, dr. \tag{20}$$

3.5.3 Balance of Mechanical Momentum and Kinetic Energy

Balance of mechanical momentum.   Averaging Equation (13), with the dissipation term in the form of Equation (16), one gets for the planar geometry:

$$\frac{\partial V}{\partial t} - \frac{\partial W}{\partial z} + \alpha \, \omega_{\text{eff}} \, V = 0. \tag{21}$$

Mean-flow kinetic energy balance.   Multiplying Equation (21) with V, one gets the balance for the kinetic energy of the mean flow, K_V, defined in Equation (19b):

$$\frac{\partial K_V}{\partial t} - \frac{\partial}{\partial z}[VW] + S \, W + \alpha \, \omega_{\text{eff}} \, K_V = 0. \tag{22}$$

The second term on the LHS of this equation describes the spatial energy flux and does not contribute to the global energy balance of the entire rotating cylinder. The next term, $S \, W$, is responsible for the energy transfer from the mean flow to the turbulent subsystem; this energy finally dissipates into heat. The last term, $\alpha \, \omega_{\text{eff}} \, K_V$, represents direct dissipation of the mean flow kinetic energy into heat via mutual friction.

Turbulent kinetic energy balance.   Let us take Equation (13) for the velocity fluctuations, with the dissipation term in the form Equation (16), and we get an equation for the energy balance which involves triple correlation functions. It describes the energy flux in (physical) space. In the theory of wall bounded turbulence (Pope, (2000)), these triple correlations are traditionally approximated with second-order correlation functions. For more details about the closure procedures we refer to L'vov et al. (2006a, 2007b) and references cited therein.

To be brief, notice that the total rate of kinetic energy dissipation in the vortex front has two contributions in well-developed turbulence,

$$\varepsilon_{\text{diss}} = \varepsilon_{\text{diss},1} + \varepsilon_{\text{diss},2}. \tag{23a}$$

The first term, $\varepsilon_{\text{diss},1}$, arises from mutual friction which acts on the global scale. It can be estimated from Equation (13) as

$$\varepsilon_{\text{diss},1} \simeq \alpha\omega_{\text{eff}}K(z,r), \tag{23b}$$

where $K(z,r)$ is the turbulent kinetic energy from Equation (19a). The second contribution, $\varepsilon_{\text{diss},2}$, originates from the energy cascade towards small scales, where the actual dissipation occurs. In well-developed turbulence of viscous normal fluids, this dissipation is caused by viscosity. It dominates at the smallest length scales known as the Kolmogorov microscope. In superfluid turbulence, the viscous contribution is absent. Instead, at moderate temperatures, it is replaced by mutual friction. When mutual friction becomes negligibly small at the lowest temperatures, the turbulent energy, while cascading down to smaller length scales, is accumulated into Kelvin-waves at some crossover scale. Ultimately the energy then cascades further down where it can dissipate, for example, by the emission of excitations (phonos in ^{4}He II and quasiparticles in ^{3}He-B). In any case, the energy has to be delivered to small length scale motions owing to the nonlinearity of Equation (13). Clearly in steady state conditions, the rate of energy dissipation at small scales, $\varepsilon_{\text{diss},2}$, is equal to the energy flux, $\varepsilon_{\text{flux}}$, from the largest scales, where the energy is pumped into the system (from the mean flow via the shear S, as follows from Equation (22)). The nonlinearity of Equation (13) is of standard hydrodynamic form, and the associated energy flux can be estimated by dimensional reasoning, as suggested by Kolmogorov in 1941 (see Pope, 2000):

$$\varepsilon_{\text{diss},2} = \varepsilon_{\text{flux}} \simeq b\,K^{3/2}(r)/\mathcal{L}(r). \tag{23c}$$

Here b is a dimensionless parameter, which in the case of classical (viscous) wall-bounded turbulence can be estimated as $b_{\text{cl}} \simeq 0.27$ (see L'vov et al., 2006a). In Equation (23c), $\mathcal{L}(r)$ is the outer scale of turbulence (which defines the length scale of the largest eddies containing the main part of the turbulent kinetic energy). Clearly near the centreline of the cylinder, $\mathcal{L}(r)$ is determined by the thickness $\Delta(r)$ of the turbulent front at given radius r: $\mathcal{L}(r) \simeq \Delta(r)$. Near the wall of the cylinder, the size of the largest eddies is limited by the distance to the wall, $R - r$. Therefore in this region, $\mathcal{L} \simeq R - r$. In the whole cylinder, $\mathcal{L}$ should be the smaller of these two scales so that one can use an interpolation formula

$$\mathcal{L}^{-1}(z) = \Delta(r)^{-1} + (R-r)^{-1}. \tag{23d}$$

The resulting energy balance equation, which accounts for the energy dissipation in Equations (23a–23d), can be written (in cylindrical coordinates r, z and φ) as follows:

$$\frac{\partial K}{\partial t} + \alpha\,\omega_{\text{eff}}\,K + \frac{b\,K^{3/2}}{\mathcal{L}}$$

$$-g\left[\frac{\partial}{\partial z}\,\mathcal{L}\sqrt{K}\frac{\partial}{\partial z}K + \frac{1}{r}\frac{\partial}{\partial r}\,r\,\mathcal{L}\sqrt{K}\frac{\partial}{\partial r}K\right] = S\,W.$$

(24)

Here K, W and S are defined in Equation (19a). Generally speaking, they are functions of r, z and time t. The outer scale of turbulence $\mathcal{L}$ depends on r and t in our approximation (Equation (23d)).

The RHS of Equation (24) represents the energy flux (per unit mass) from the mean flow to the turbulent subsystem. This expression rigorously follows from Equation (13) and is exact. The two terms on the LHS of Equation (24) (proportional to α and b) describe the energy dissipation (Equation (23)). The last two terms on the RHS of Equation (24) are proportional to the phenomenological dimensionless parameter $g \approx 0.25$, which was estimated by L'vov et al. (2007b). These terms model turbulent diffusion processes (in the differential approximation) with the effective turbulent diffusion parameter $\mathcal{L}\,g\,\sqrt{K}$, now expressed in cylindrical coordinates. The first term in parenthesis describes turbulent diffusion in the direction normal to the front, which is the main reason for the propagation of the turbulent front. The second term, which vanishes in the flat geometry, describes the turbulent energy flux in the radial direction towards the centreline of the sample cylinder. This term plays an important role in the propagation of the front as a whole. The reason is that the central part of the front, where the direct conversion of the mean flow energy to turbulence is small, does not contain enough energy to exist without the radial flux of energy.

Total kinetic energy balance.   Adding $\partial K_{\text{V}}/\partial t$ from Equation (22) and $\partial K/\partial t$ from Equation (24), one can see that the term $S\,W$, responsible for the transfer of energy from the mean flow to the turbulent flow, cancels and we arrive at a balance equation for $\mathcal{K} \equiv K_{\text{V}} + K$:

$$\frac{\partial\mathcal{K}}{\partial t} + \alpha\,\omega_{\text{eff}}\,\mathcal{K} + \frac{b\,K^{3/2}}{\mathcal{L}} - \frac{\partial}{\partial z}[VW]$$

$$-g\left[\frac{\partial}{\partial z}\,\mathcal{L}\sqrt{K}\frac{\partial}{\partial z}K + \frac{1}{r}\frac{\partial}{\partial r}\,r\,\mathcal{L}\sqrt{K}\frac{\partial}{\partial r}K\right] = 0.$$

(25a)

Integrating this relation over the cylinder, we see that the energy diffusion terms do not contribute to the total energy balance:

$$\mathcal{E}(t) \equiv \int \mathcal{K}(r,t)\mathrm{d}r, \tag{25b}$$

$$\frac{\mathrm{d}\mathcal{E}}{\mathrm{d}t} = -\int \mathrm{d}r\left[\alpha\,\omega_{\mathrm{eff}}\,\mathcal{K} + \frac{b\,K^{3/2}}{\mathcal{L}}\right]. \tag{25c}$$

To summarise this section, we note that Equations (21) and (24) allow us, at least in principle, (i) to describe the propagating turbulent front in a rotating superfluid, (ii) to find the front velocity V_f and (iii) to describe the structure of the front: its effective width $\Delta(r)$, the profiles for the mean shear $S(r,z)$ the Reynolds stress $W(r,z)$ and the kinetic energy $K(r,z)$. Here we present only some preliminary steps in this direction, based on a qualitative analysis in Section 3.5.4 of the global energy balance (Equation (25a)), and discuss the role of the radial turbulent diffusion of energy in Section 3.5.5. In Section 3.5.6, we finally specify the model, accounting explicitly for the bottleneck at the classical-quantum crossover, as described by L'vov et al. (2007a), and explain how it is influenced by the temperature-dependent mutual friction.

3.5.4 Qualitative Analysis of Global Energy Balance

The total kinetic energy $\mathcal{E}$ is dissipated by the propagation of the turbulent front at constant velocity V_f, as expressed in Equation (8). This means that during time t the length of the cylinder with unperturbed mean flow $V = \Omega r$ decreases by $V_f t$. Using Equation (8), we can write the overall energy budget (Equation (25c)) as:

$$V_f = \frac{4}{\pi\,\Omega^2 R^4} \int \mathrm{d}r\left[\alpha\,\omega_{\mathrm{eff}}\,\mathcal{K}(z,r) + \frac{b\,K^{3/2}(z,r)}{\mathcal{L}(r)}\right]. \tag{26a}$$

This equation requires some corrections, because in its derivation we were a bit sloppy. First of all, approximation (Equation (16)) for the mutual friction force f_{mf} cannot be applied for the analysis of laminar flow, where the actual orientations of vorticity and velocity are important. To fix this, we present the RHS of Equation (26a) as a sum of two contributions,

$$V_f = V_{f,\mathrm{lam}} + V_{f,\mathrm{turb}}, \tag{26b}$$

and for $V_{f,\mathrm{lam}}$, we use Equation (12). To get the corrected equation for $V_{f,\mathrm{turb}}$, we replace in Equation (26a) $\mathcal{K}$ with its turbulent part K and replace b with $\widetilde{b} \equiv b(1 - \alpha')$ in order to account for the correction to the

nonlinear term in Equation (13) from the reactive part of the mutual friction (Equation (14)) (proportional to α'). Integrating the result over the azimuthal angle φ and making use of the axial symmetry of the problem, we get

$$V_{\text{f,turb}} = \frac{8}{\Omega^2 R^4} \int_0^{R-\ell} r\,dr\,dz \left[\alpha\,\omega_{\text{eff}}\,K(z,r) + \frac{\widetilde{b}\,K^{3/2}(z,r)}{\mathcal{L}(r)}\right]. \quad (26c)$$

The hydrodynamic equation (Equation (13)) is not applicable near the wall, where $R - r$ is less than the mean inter-vortex distance ℓ. Therefore, this region is excluded from the integration (Equation (26c)).

In the limit of a fully-developed turbulent boundary layer (TBL), the turbulent kinetic energy and Reynolds stress are independent of the distance in the z direction to the boundary of turbulence. Here we consider the turbulence in the front to be bounded in the z direction, that is, we assume that the front thickness $\Delta(r) < R$ and ignore the influence of the cylindrical container wall. Therefore, it is reasonable in the qualitative analysis of Equation (26c) to ignore the z dependence of $K(z,r)$ and $W(z,r)$, replacing these objects with their mean values across the TBL:

$$K(r,z) \Rightarrow \overline{K}(r), \quad W(r,z) \Rightarrow \overline{W}(r), \quad \omega_{\text{eff}}(r,z) \Rightarrow \overline{\omega}_{\text{eff}}(r). \quad (26d)$$

As seen from Equation (26d), we use the same approximation also for ω_{eff}. Now we can trivially integrate Equation (26c) with respect to z:

$$V_{\text{f,turb}} = \frac{8}{\Omega^2 R^4} \int_0^{R-\ell} \left[\alpha\,\overline{\omega}_{\text{eff}}(r)\,\overline{K}(r) + \frac{\widetilde{b}\,\overline{K}^{3/2}(r)}{\mathcal{L}(r)}\right]\Delta(r)r\,dr. \quad (26e)$$

Here $\Delta(r)$ is the characteristic width of the TBL at the distance r from the central axial. To perform the next integration over r, one needs to know the r-dependence of Δ, $\overline{\omega}_{\text{eff}}$ and K. Notice first that $\Delta(r)\overline{\omega}_{\text{eff}}(r)$ has the dimension of velocity. Therefore, one expects that in the self-similar regime of a fully-developed TBL, $\Delta(r)\overline{\omega}_{\text{eff}}(r)$ has to be proportional to the characteristic velocity, which is Ωr. In other words, we expect that $\Delta(r)\overline{\omega}_{\text{eff}}(r) \propto r$. As we will see below in Section 3.5.5, $\Delta(r) \propto r$ while $\overline{\omega}_{\text{eff}}$ is r-independent. With the same kind of reasoning, we can conclude that K and W have to be proportional to r^2 since they have the dimensionality of velocity squared:

$$\Delta(r)\overline{\omega}_{\text{eff}} = a\,\Omega r, \quad \overline{K}(r) = \frac{c}{2}(\Omega r)^2, \quad \overline{W}(r) = \widetilde{c}\,(\Omega r)^2. \quad (27)$$

Now integrating (Equation (26e)), one gets

$$v_f \equiv \frac{V_f}{\Omega R} \simeq (2\,c)^{3/2} b\,(1-\alpha')A(R/\ell) + \frac{4\,c\,\alpha}{5\,a}, \tag{28a}$$

$$A(R/\ell) = 0.2 + d[\ln(R/\ell) - 137/60 + 5\ell/R + \dots], \tag{28b}$$

where we used $d = \Delta(r)/r$. At $\Omega = 1\,\mathrm{rad/s}$, the ratio $R/\ell \approx 17$. This gives $A(R/\ell) \approx A(17) \approx 1.8$. We take $b = b_{cl}$ and choose the parameters $a = 0.2$, $c = 0.25$ and $d = 2$ to fit the measurement in the region $(0.3 - 0.4)\,T_c$. With these parameters, Equation (28) gives $v_f \approx 0.16$ in the limit $T \to 0$ (when $\alpha = \alpha' = 0$) and a very weak temperature dependence up to $T \simeq 0.45\,T_c$.

3.5.5 Role of the Radial Turbulent Diffusion of Energy

According to experimental observations, in steady state, the front propagates as a whole with the velocity v_f, independent of the radial position r. To make this possible, the turbulent energy has to flow from the near-wall region, where the azimuthal mean velocity and consequently the energy influx into the turbulent subsystem are large, towards the centre, where the influx goes to zero.

To clarify the role of the radial energy flux, consider Equation (24) averaged in the z direction:

$$\alpha\,\overline{\omega}_{\text{eff}}\,\overline{K}(r) + \frac{\widetilde{b}\,[\overline{K}(r)]^{3/2}}{\mathcal{L}(r)} - \frac{g}{r}\frac{\partial}{\partial r}\,r\,\mathcal{L}(r)\sqrt{\overline{K}(r)}\,\frac{\partial}{\partial r}\,\overline{K}(r) = \frac{\Omega\,r}{\Delta(r)}\,\overline{W}(r). \tag{29}$$

On the RHS of this equation we replaced $\overline{S}(r)$ with its natural estimate $\Omega\,r/\Delta(r)$. According to Equation (23d), close to the cylinder axis, $\mathcal{L}(r) \approx \Delta(r)$. In this region, Equation (29) has a self-similar scaling solution (Equation (27)), in which ω_{eff} is indeed r-independent, $\Delta(r) \propto r$, and for the Reynolds-stress constant $\widetilde{c}$ in Equation (27) one finds the relationship

$$\frac{\widetilde{c}}{c} = \alpha\,\frac{\omega_{\text{eff}}}{\Omega}\,\frac{\Delta(R)}{R} + \frac{\widetilde{b}}{2}\sqrt{\frac{c}{2}} + 2\,d\,\sqrt{2\,c}\left[\frac{\Delta(R)}{R}\right]^2. \tag{30a}$$

In the vicinity of the wall, where $R - r \ll R$, the outer scale of turbulence is $\mathcal{L} \approx R - r$ and goes to zero when $r \to R$. To account for the influence of the cylindrical wall in this region, we assume that, similar to a classical TBL, the two pair velocity correlations $W(r)$ and $K(r)$ have the same dependence on distance from the wall. Therefore, their ratio is approximately constant:

$W(r)/K(r) \approx$ const. If so, the energy balance Equation (24) dictates

$$W(r) \sim K(r) \sim (R - r)^2, \tag{30b}$$

with some relation between constants, similar to Equation (30a). Actually, when $R - r$ becomes smaller than the inter-vortex distance ℓ, the whole hydrodynamic approach (Equation (13)) together with Equation (29) fails. Therefore, we cannot expect that $W(r)$ and $K(r)$ really go to zero when $r \to R$. Rather they should approach some constant values dominated by the vortex dynamics at distances $R - r \simeq \ell$.

To summarise, we should say that Equation (29) and its solution (Equation (30)) cannot be taken literally as a rigorous result. They give a qualitative description of the kinetic energy profiles. Indeed, the predicted profiles are in qualitative agreement with numerical simulation calculations, as seen in Figure 23: here $K(r)$ goes to zero when $r \to 0$, increases at small r approximately as r^2, as concluded in Equations (27) and (30a), reaches a maximum at $r/R \lesssim 1$ and then decreases in qualitative agreement with Equation (30b). Similar comparison with other numerical results in Section 3.4 makes it believable that the analysis of the global energy balance in Section 3.5.4 and the predicted plateau for v_{f} in the $T \to 0$ limit are reasonable.

Nevertheless, both in the region of lower and higher temperatures, the experiment shows deviation from this 'plateau' (Figure 26). The reason for this deviation at $T > 0.35\,T_{\mathrm{c}}$ is that turbulence is not well developed near the cylinder axis where the shear of the mean velocity, responsible for the turbulent excitation, decreases. Therefore, in the intermediate temperature region only part of the front volume is turbulent. When the temperature decreases, the turbulence expands towards the axis. We should therefore account also for the laminar contribution to the front velocity (Equation (12)) near the axis. Notice furthermore that the simple sum of laminar and turbulent contributions to V_{f} in Equation (26b) oversimplifies the situation, by not accounting for the turbulent motions in Equation (26c). We will not discuss this issue but just suggest an interpolating formula between the laminar and turbulent regimes, which has a shorter intermediate region than Equation (26b):

$$v_{\mathrm{f}} = \sqrt{v_{\mathrm{f,\,lam}}^2 + v_{\mathrm{f,\,turb}}^2}, \tag{31}$$

where $v_{\mathrm{f,\,lam}}$ and $v_{\mathrm{f,\,turb}}$ are given by Equations (12) and (28). This interpolation is shown in Figure 26 as a thin line for $T < 0.3\,T_{\mathrm{c}}$ and as a thick line for $T > 0.3\,T_{\mathrm{c}}$. The agreement with measurements above $0.3\,T_{\mathrm{c}}$ is good, but there is a clear deviation below $0.25\,T_{\mathrm{c}}$, where $\alpha \lesssim 10^{-2}$. Below an
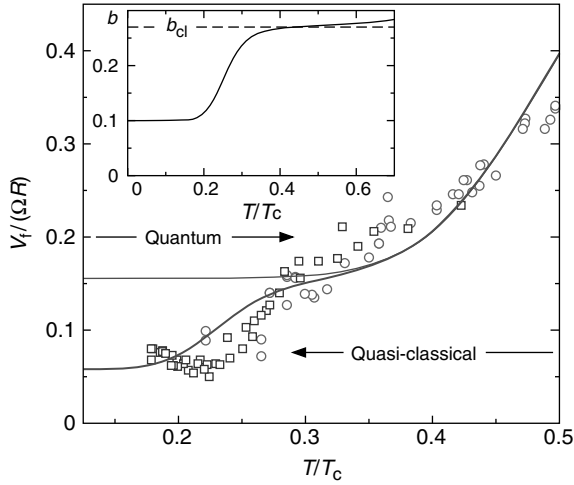
FIGURE 26 Scaled front velocity versus temperature, similar to Figure 17 but emphasising the comparison of measurements in Section 3.3 to analytical results in Section 3.5 in the turbulent regime at low temperatures. The thin and thick solid lines show consecutive model approximations which sequentially account for dissipation in turbulent energy transfer Equation (28b) and bottleneck effect in Section 3.5.6. Insert: value of parameter $b(T)$ in Equation (28), which was used for the thick solid line in the main panel.

explanation is outlined which takes into account the quantum character of turbulence, since as shown by Volovik (2003), individual vortex lines become important below $0.3\,T_c$ in the region where the transition to the lower plateau occurs in Figure 26.

To appreciate the last aspect, note that the mean free path of ^{3}He quasi-particles at the conditions of the measurements at 29 bar pressure and $T \simeq 0.3\,T_c$ is close to ℓ, while at $0.2\,T_c$ it exceeds R. This change from the hydrodynamic to the ballistic regime in the normal component may influence the mutual friction force acting on individual vortices. However, what is important for the interpretation of the measurements is that the effect of the normal component on the superfluid component becomes negligibly small. Therefore, it actually does not matter what the physical mechanism of this interaction is: ballistic propagation of thermal excitation with scattering on the wall or mutual friction that can only be described in the continuous-media approximation, as given by Equation (14). For simplicity, we use the hydrodynamic approximation (Equation (14)) in Section 3.5.6 to describe the turbulent kinetic energy dissipation at low temperatures.

3.5.6 Mutual Friction and Bottleneck Crossover from Classical to Quantum Cascade

Bottleneck at zero temperature.   At low temperatures, when mutual friction becomes sufficiently small, the energy flux towards small length scales (or large wave vectors k), ε_k, propagates down to the quantum scale ℓ, and vortex discreteness and quantisation effects become most important. Even though some part of the energy is lost in intermittent vortex reconnections, the dominant part proceeds to cascade below the scale ℓ by means of nonlinearly interacting Kelvin-waves (see Kozik and Svistunov (2008a,b); Vinen et al. (2003) and references there). The Kelvin-waves are generated by both slow vortex filament motions and fast vortex reconnection events. As shown by L'vov et al. (2007a), the important point for the rate of energy dissipation (and consequently for the turbulent front velocity) is that Kelvin-waves are much less efficient in the downscale energy transfer than classical hydrodynamic turbulence: in order to provide the same energy flux as in the hydrodynamic regime, the energy density of Kelvin-waves at the crossover scale ℓ has to be $\Lambda^{10/3}$ times larger than that of hydrodynamic motions. For ^{3}He-B, $\Lambda \equiv \ln(\ell/a_0) \simeq 10$, where a_0 is the vortex-core radius. Assuming that the energy spectrum is continuous at the crossover scale ℓ and that no other mechanisms intervene between the classical and Kelvin-wave cascades, then to maintain the same value of energy flux, there must be a bottleneck pile-up of the classical spectrum near this scale by the factor $\Lambda^{10/3}$. To account for this phenomenon of energy pileup, we construct the 'warm cascade' solution which will be described in what follows.

For a qualitative description, we first define the hydrodynamic kinetic energy density (in the 1D k-space), $\mathcal{E}_k$, related to the total kinetic energy $\mathcal{E}$ as follows:

$$\mathcal{E} \equiv \int \mathcal{E}_k \, dk. \tag{32a}$$

The Kolmogorov-1941 cascade of hydrodynamic turbulence (with k-independent energy flux, $\varepsilon_k \Rightarrow \varepsilon$=const) is described with the spectrum:

$$\mathcal{E}_k^{K41} \simeq \varepsilon^{2/3} |k|^{-5/3}. \tag{32b}$$

The energy flux carried by the classical hydrodynamic turbulence with the K41 spectrum (32b) cannot adequately propagate across the crossover region at ℓ. Therefore, hydrodynamic motions on larger length scales (smaller wave-vectors) will have increased energy content up to the level $\mathcal{E}_{1/\ell}$, as required when the same energy flux has to be maintained by

means of Kelvin-waves. As a result, for $k \leq 1/\ell$, the spectrum of hydro-dynamic turbulence $\mathcal{E}_k^{\mathrm{HD}}$ will not have the K41 scale-invariant form $\mathcal{E}_k^{\mathrm{K41}}$ given by Equation (32b). To get a qualitative understanding of the result-ing bottleneck effect, we use the so-called warm cascade solutions found by Connaughton and Nazarenko (2004). These solutions follow from the Leith (1967) differential model for the energy flux of hydrodynamical turbulence,

$$\varepsilon_k = -\frac{1}{8} \sqrt{|k|^{13} F_k} \frac{\mathrm{d} F_k}{\mathrm{d} k}, \quad F_k \equiv \frac{\mathcal{E}_k^{\mathrm{HD}}}{k^2}, \tag{33}$$

where F_k is the 3-dimensional (3D) spectrum of turbulence. The generic spectrum with a constant energy flux can be found as the solution to the equation $\varepsilon_k = \varepsilon$:

$$F_k = \left[\frac{24\varepsilon}{11|k|^{11/2}} + \left(\frac{T}{\pi \rho} \right)^{3/2} \right]^{2/3}. \tag{34}$$

Here the range of large k values belongs to the thermalised part of the spectrum, with equipartition of energy characterised by an effec-tive temperature T, namely $T/2$ of energy per degree of freedom, thus, $F_k = T/\pi\rho$ and $\mathcal{E}_k = Tk^2/\pi\rho$. At low k, Equation (34) coincides with the K41 spectrum (Equation (32b)).

This 'warm cascade' solution describes reflection of the K41 cascade and stagnation of the spectrum near the bottleneck scale which, in our case, corresponds to the classical-quantum crossover scale. To obtain the spectrum in the classical range of scales, it remains to find T by matching Equation (34) with the value of the Kelvin-wave spectrum at the crossover scale $\mathcal{E}_k \sim \kappa^2/\ell$. This gives $T/\rho \sim \kappa^2 \ell \sim (\kappa^{11}/\Lambda^5 \varepsilon)^{1/4}$.

Obviously, the transition between the classical and quantum regimes is not sharp, and in reality we should expect a gradual increase of the role of the self-induced wave-like motions of individual vortex lines with respect to the collective classical eddy type of motions of vortex bundles. Thus, the high-wave number part of the thermalised range is likely to be wave rather than eddy dominated. However, the energy spectrum for this part should still be of the same k^2 form which corresponds to equipartition of thermal energy. This picture, as explained below, relies on the assumption that the self-induced wave motions have small amplitudes and, therefore, do not lead to reconnections.

The resulting spectrum, including its classical, quantum and crossover parts, is shown in Figure 27 as a log-log plot. It is important to note that in the quantum range $k > 1/\ell$, in addition to the cascading energy associated with Kelvin-waves, there is also energy associated with the tangle of vortex
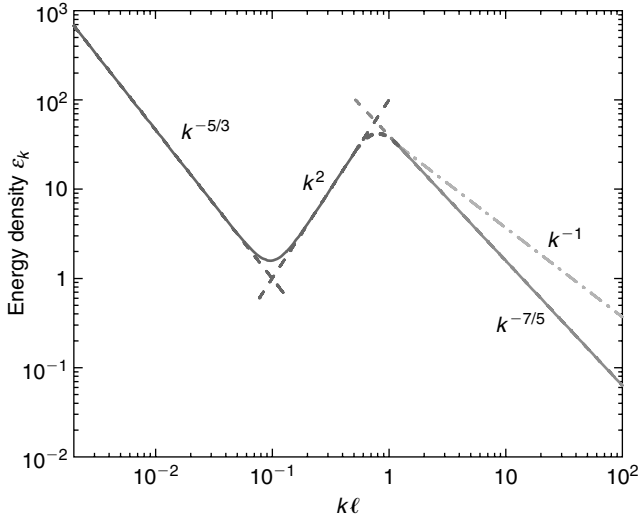
FIGURE 27 Energy spectra $\mathcal{E}_k$ in the classical, $k < 1/\ell$, and quantum, $k > 1/\ell$, ranges of scales. The two straight lines in the classical range indicate the pure K41 scaling $\mathcal{E}_k^{K41} \propto k^{-5/3}$ of Equation (32b) and the pure thermodynamic scaling $\mathcal{E}_k \propto k^2$. In the quantum range, the solid line indicates the Kelvin-wave cascade spectrum $\propto k^{-7/5}$, whereas the dash-dotted line marks the spectrum corresponding to the non-cascading part of the vortex tangle energy $\propto k^{-1}$.

filaments (shown in Figure 27 with the dash-dotted line). The energy spectrum of this part is $\sim |k|^{-1}$, which is simply the spectrum associated with a singular distribution of vorticity along 1D curves in 3D space (Araki et al., 2002). It does not support a downscale cascade of energy. The cascading and noncascading parts have similar energies at the crossover scale, that is, the wave period and the amplitude are of the order of the characteristic time and size of evolving background filaments. In other words, the scales of the waves and of the vortex 'skeleton' are not separated enough to treat them as independent components. This justifies matching the classical spectrum at the crossover scale with the Kelvin-wave part alone, ignoring the vortex skeleton. This is valid up to an order-one factor and justifies the way of connecting the skeleton spacing ℓ to the cascade rate ε.

Effect of mutual friction on the bottleneck crossover. Returning back to the propagating turbulent vortex front, recall that in the measurements of Section 3.3 the inertial interval R/ℓ is about one decade. Therefore, the distortion of the energy spectrum owing to the bottleneck reaches the outer scale of turbulence. This leads to an essential suppression of the energy flux at any given turbulent energy or, in other words, to a decrease in the

effective parameter b, which relates ε and K in the estimate (Equation (23c)). The effect is more pronounced at low temperatures when mutual friction is small; thus $b(T)$ should decrease with temperature. We analyse this effect with the help of the stationary energy balance equation for the energy spectrum $\mathcal{E}_k$ in k-space:

$$\frac{d\varepsilon_k}{dk} = -\Gamma(T)\,\mathcal{E}_k\,,\ \ \varepsilon_k \equiv -(1-\alpha')\sqrt{k^{11}\mathcal{E}_k}\,\frac{d(\mathcal{E}_k/k^2)}{8\,dk}, \tag{35}$$

where $\Gamma(T)$ is the temperature-dependent damping in Equation (16), and the energy flux over scales $\varepsilon(k)$ is taken in the Leith (1967) differential approximation. In addition to Equation (33), we included in Equation (35) the mutual friction correction factor $(1-\alpha')$ and substituted $F_k = \mathcal{E}_k/k^2$.

Figure 28 displays the set of solutions for Equation (35). We use $\mathcal{L}/\ell = 12$ as the ratio of the outer and crossover scales and characterise the bottleneck with the boundary condition $\mathcal{E}_k/[k^3 d(\mathcal{E}_k/k^2)/dk] = -4 \cdot 10^5$ at the crossover scale. One goal of these calculations is to find the slope of the function F_k at the beginning of the inertial interval $k = k_+ \equiv 2\pi/\mathcal{L}$ which, according to Equation (35), characterises the rate of energy input into the system at fixed value of the total energy $\mathcal{E}$, that is, the phenomenological parameter b in the estimate (Equation (23c)). The dashed line in the right panel shows the Kolmogorov value of this slope, $-11/3$, which is associated with the classical value of $b = b_{cl} \approx 0.27$. Thus the ratio $3b_{cl}|F'|/11$ can be interpreted as the effective value of b for a given value of damping Γ. To relate Γ with the temperature-dependent value
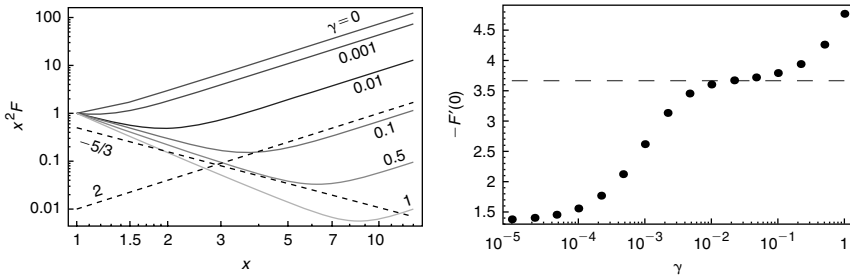

FIGURE 28 On the left, the solutions of the differential Equation (35) for different values of the dimensionless mutual friction parameter $\gamma \equiv \Gamma/\sqrt{k_+^3\,\mathcal{E}_{k_+}}$ have been plotted. The smallest wave vector k_+ corresponds to the outer scale of turbulence: $\mathcal{L} \approx 2\pi/k_+$. The wave vectors are normalised with respect to k_+: $x \equiv k/k_+$ and $F(x) \equiv F_{xk_+}/F_{k_+}$. The dashed lines denote slopes of $\mathcal{E}_k$ with K41 scaling $\mathcal{E}_k \propto k^{-5/3}$ and thermodynamic scaling $\mathcal{E}_k \propto k^2$. On the right, the slope $F' \equiv dF(x)/dx$ is shown at $x = 1$ for different values of mutual friction γ. The horizontal dashed line marks the K41 value of slope, 11/3.

$\alpha(T)$, we substitute the r independent ω_{eff} from Equation (27) to Equation (16). This gives $\Gamma = \alpha\,(a/d)\,\Omega$. The resulting function $b(T)$, shown in the inset of Figure 26 (for $\Omega = 1\,\mathrm{rad/s}$), decreases from its classical value $b_{\mathrm{cl}} \approx 0.27$ to $\simeq 0.1$ at $T < 0.2\,T_{\mathrm{c}}$. Now, after accounting for the temperature dependence of $b(T)$ in Equation (28), we get the temperature dependence for the propagation velocity v_{f} of the quantum-turbulent front shown in Figure 26 by the bold solid line below $0.3\,T_{\mathrm{c}}$. This fit is in good agreement with the measured data. We thus have to conclude that in this particular measurement the rapid drop in the dissipation rate on entering the quantum regime can be explained as a consequence of the relatively close proximity of the outer and quantum crossover scales in this measuring setup.

3.6 Summary: Turbulent Vortex Front Propagation

In ^{3}He-B, strong turbulence is restricted to the lowest temperatures below $0.4\,T_{\mathrm{c}}$. Depending on the type of flow, turbulence varies in form and losses. The usual reference point is an isotropic and homogeneous turbulent vortex tangle. Here we have discussed an opposite extreme, the conversion of metastable rotating vortex-free counterflow to the stable equilibrium vortex state. The task is to explain how increasing turbulence with decreasing temperature influences this type of polarized vortex motion in steady state propagation. The deterministic part of this motion takes place in the form of a spiraling vortex front followed by a helically twisted vortex cluster. When mutual friction decreases, turbulent losses start to contribute to dissipation, concentrating in the propagating front and immediately behind it.

Experimentally, the conversion of a metastable vortex-free state to an equilibrium array of rectilinear vortex lines can be arranged to occur at constant externally adjusted conditions. This is done with different types of injection techniques, which trigger the formation of a propagating vortex front and the trailing twisted cluster behind it. In a long rotating column, the propagation can be studied in steady state conditions. At temperatures above $0.4\,T_{\mathrm{c}}$, the propagation is laminar, but below $0.4\,T_{\mathrm{c}}$ a growing influence from turbulence appears. This is concluded from the measured propagation velocity which provides a measure of the dissipation in vortex motion. In addition to the increasing turbulent dissipation below $0.4\,T_{\mathrm{c}}$, the measurement shows a peculiar transition at $\sim 0.25\,T_{\mathrm{c}}$ between two plateaus, and a temperature-independent finite value of dissipation on approaching the $T \to 0$ limit.

So far measurements on vortex propagation exist only for a column with circular cross section. This is an exceptional case of high stability (if the cylindrical symmetry axis and the rotation axis are sufficiently well aligned). Here the crossover from the laminar to the turbulent regime is

smooth as a function of mutual friction dissipation. The same smooth behavior is also seen in the response to spin down, after a step-like stop of rotation. This is in stark contrast to the spin down of a column with rectangular or square cross section, as we will see in Section 4. Similar differences seem to apply in viscous hydrodynamics where flow in a circular pipe is believed to be asymptotically linearly stable for all Reynolds numbers, in contrast to a pipe with square cross section (Peixinho and Mullin, 2006). In these measurements the formation and decay of turbulent plugs is monitored. Vortex plugs and fronts have also been observed in pipe flow of superfluid ^{4}He through long circular capillaries (Marees et al., 1987).

Numerical vortex dynamics calculations have been used to examine the turbulent contributions to dissipation in vortex front propagation. This analysis demonstrates the increasing role of turbulent excitations on subinter-vortex scales with decreasing temperature. Analytical arguments have been developed which explain that the transition to the lower plateau in the measured overall dissipation is caused by the difficulty to bridge the energy cascade from the quasi-classical to the quantum regime as a function of decreasing mutual friction dissipation. This bottleneck scenario of L'vov et al. (2007a) in energy transfer was thus directly inspired by the experimental result. It is expected to apply foremost to polarised vortex motion in the rotating column where vortex reconnections are suppressed. This situation differs from the case of an ideal homogeneous vortex tangle, where Kozik and Svistunov (2008a,b) suggest that a bottleneck is avoided owing to the high reconnection rate.

As for the second leveling off at the lowest temperatures, at present time three different types of measurements (Bradley et al., 2006; Eltsov et al., 2007; Walmsley et al., 2007a) conclude that dissipation in vortex motion remains finite at the lowest temperatures. This applies for both the fermion superfluid ^{3}He-B and the boson case of ^{4}He. Although the mechanisms for dissipation in the $T \rightarrow 0$ limit in these two superfluids are different and still under discussion, the results suggest that coherent quantum systems can be inherently lossy even in the $T = 0$ state.

4. DECAY OF HOMOGENEOUS TURBULENCE IN SUPERFLUID ^{4}HE

4.1 Introduction and Experimental Details

4.1.1 Quasiclassical and Ultraquantum Types of Superfluid Turbulence

In this section, we switch to nearly homogeneous and isotropic superfluid turbulence with an emphasis on the recent experiments in Manchester. A truly homogeneous turbulence is of course impossible to achieve in real

experiments because the tangle is always confined by the container walls and can have other inhomogeneities specific to the particular process of its generation.

The modern paradigm of homogeneous isotropic turbulence at high Reynolds numbers Re in classical liquids is that there is a broad range of wave numbers k within which the energy, pumped at large scales, gets continuously redistributed without loss towards smaller length scales, thus arranging a steady-state distribution in k-space of the Kolmogorov type (Batchelor, 1953; Frisch, 1995; Kolmogorov, 1941a,b) (Equation (32b)):

$$\mathcal{E}_k^{\text{K41}} = C\varepsilon^{2/3}|k|^{-5/3}, \tag{36}$$

where the Kolmogorov constant was found to be $C \approx 1.5$ (Sreenivasan, 1995). In the steady state, the energy flux ϵ is equal to the dissipation of the kinetic energy through the shear strain in the flow at short length scales; its rate integrates to

$$\dot{\mathcal{E}} = -\nu_{\text{cl}}\omega_{\text{cl}}^2, \tag{37}$$

where ν_{cl} is the kinematic viscosity and ω_{cl} is the r.m.s. vorticity. In realistic systems, the distribution Equation 36 is truncated at small $k = k_1$ by either the length scale of forcing or the container size h, and at large $k = k_2$ by the Kolmogorov dissipation scale $\lambda_{\text{cl}}(Re) \sim k_2^{-1}$ which decreases with increasing $Re = (k_2/k_1)^{4/3}$. In superfluids, the inertial cascade is expected to operate if the mutual friction parameter α is sufficiently small (Vinen, 2000). At large length scales $> \ell$, the cascade is *classical*. However, at short length scales $< \ell$, the cascade becomes *quantum* as the discreteness of the vorticity in superfluids adds new behaviour. At sufficiently low temperatures, when the energy reaches very small scales $\ll \ell$ without dissipation, it is expected that the quantum cascade takes the form of a nonlinear cascade of Kelvin-waves (Kozik and Svistunov, 2004; Svistunov, 1995), eventually being truncated at some quantum dissipation scale $\lambda_{\text{q}}(\alpha)$. While the theory of this regime at very high k is now established, no direct observations exist so far. The most complicated is, of course, the transitional region between these two clear-cut limits, the Kolmogorov and Kelvin-wave cascades. The question being currently debated is whether the energy stagnates at $k < \ell^{-1}$ due to the poor matching in the kinetic times of the two cascades (L'vov et al., 2007a), or gets efficiently converted from 3D classical eddies to 1D waves along quantised vortex lines with the help of various reconnection processes (Kozik and Svistunov, 2008a).

When comparing the two superfluid isotopes from the experimental point of view, the $T = 0$ limit in superfluid ^{4}He is achievable at some $T < 0.5\,\text{K}$ (Vinen, 2000; Walmsley et al., 2007a) while for ^{3}He-B much lower

temperatures $T < 0.5$ mK are required. Owing to the two or three orders of magnitude smaller core size in ^{4}He, $a_0 \sim 0.1$ nm, the Kelvin-wave-cascade is expected to extend over a broader range of length scales, down to ~ 3 nm (Kozik and Svistunov, 2008b; Vinen, 2001). It has been suggested (Vinen and Niemela, 2002; Vinen, 2002) that in ^{3}He-B Kelvin-waves should become overdamped at frequencies ~ 10 kHz (corresponding to wavelengths ~ 2 μm) due to the resonant scattering on core-bound quasiparticles (Kopnin and Salomaa, 1991)).

Flow on a scale greater than the inter-vortex distance ℓ, which is initially typically between ~ 10 and 100 μm in experiments, can be obtained by mechanical stirring of the liquid. So far the following methods have been used: counter-rotating agitators with blades (Maurer and Tabeling, 1998), pipe flow (Roche et al., 2007; Smith et al., 1999), flow through an orifice (Guenin and Hess, 1978), towed grids (Niemela et al., 2005; Smith et al., 1993; Stalp et al., 1999), vibrating grids (Bradley et al., 2006; Davis et al., 2000; Fisher and Pickett, 2008; Hänninen et al., 2007a; Vinen and Skrbek, 2008), as well as wires (Bradley, 2000; Nichol et al., 2004.) and microspheres (Schoepe, 2004), plus most recently impulsive spin-down to rest (Walmsley et al., 2007a) of a rotating container. It is also possible to initiate large-scale flow in superfluid ^{4}He without any moving parts or rotation of the cryostat: by either running thermal counterflow in wide channels at $T > 1$ K (Barenghi and Skrbek, 2007; Chagovets et al., 2007) or a jet of injected current (Walmsley and Golov, 2008a).

Actually, the turbulence can take two very different forms depending on whether the forcing is at scales above or below ℓ. So far we were discussing the flow on classical scales $> \ell$, where the energy cascades towards shorter length scales like in the Richardson cascade in classical turbulence; the large quasiclassical eddies being the result of correlations in polarisation of vortex lines. On the other hand, when forced on quantum scales $< \ell$, the resulting uncorrelated tangle has no classical analogs and should have completely different dynamics first described by Vinen (1957a,b,c, 1958) and later investigated numerically by Schwarz (1988). In both cases, the dissipation of flow energy is through the motion of vortex lines; its rate per unit mass can be assumed to be (Stalp et al., 1999, 2002; Vinen, 2000)

$$\dot{\mathcal{E}} = -\nu(\kappa L)^2, \tag{38}$$

where $\kappa^2 L^2$ is an effective total mean square vorticity and the parameter ν is believed according to various models to be approximately constant for a given temperature and type of flow. This formula is the quantum analog of the classical expression Equation (37). As we will show below, the efficiency of the vortices in dissipating energy in the $T = 0$ limit, expressed through the 'effective kinematic viscosity' ν, is different for these two regimes of turbulence.

To measure the values of ν, one can monitor the free decay of homogeneous tangles of both types. In any tangle, the *quantum* energy associated with the quantised flow on length scales $r < \ell$ is $\mathcal{E}_q = \gamma L / \rho_s$ (per unit mass), where the energy of vortex line per unit length is $\gamma = B \rho_s \kappa^2$ and $B \approx \ln(\ell/a_0)/4\pi$ is approximately constant. This is the same energy that is shown in the quantum range $k > 1/\ell$ (including both noncascading vortex skeleton and Kelvin-waves) in Figure 27. If the total energy is mainly determined by $\mathcal{E}_q$, from Equation (38), we arrive at the late-time free decay

$$L = B\nu^{-1}t^{-1}. \tag{39}$$

This type of turbulence, without any motion on classical scales, will be called *ultraquantum* (in the literature one can find, e.g., 'Vinen turbulence' (Volovik, 2003, 2004) and 'random' or 'unstructured' vortex tangle). For ^{4}He, $\kappa_4 = 2\pi\hbar/m_4$, $a_0 \sim 0.1$ nm and $B \approx 1.2$, while for ^{3}He-B, $\kappa_3 = 2\pi\hbar/(2m_3)$, $a_0 \sim 13-65$ nm and $B \approx 0.7$.

Now suppose that the tangle is not random but structured due to the presence of flow on classical length scales $r > \ell$, and the additional energy of this classical flow $\mathcal{E}_c$ is much greater than $\mathcal{E}_q$. This type of turbulence will be called quasiclassical (e.g., 'Kolmogorov turbulence' and 'structured' or 'polarised' vortex tangle). For the Kolmogorov spectrum between wavenumbers k_1 and k_2 ($k_1 \ll k_2$), while the size of the energy-containing eddy stays equal to the size of container h (that is, $k_1 \approx 2\pi/h$), the late-time free decay follows (Stalp et al., 1999)

$$L = (3C)^{3/2}\kappa^{-1}k_1^{-1}\nu^{-1/2}t^{-3/2}. \tag{40}$$

Eventually, when the energy flux from the decay of classical energy $\mathcal{E}_c$ will become smaller than that from the quantum energy $\mathcal{E}_q$ (which should typically happen when only a couple of vortex lines are left in the container, that is, $L \sim h^{-2}$), the quasiclassical regime will cross over to the ultraquantum one, so $L \propto t^{-3/2}$ decay will be replaced by $L \propto t^{-1}$. Deviations from the described scenario are also possible if some fraction of the classical energy is stored in non-cascading 'thermal spectrum' (L'vov et al., 2007a).

In this Section, we first review the relevant experimental techniques of detecting and generating turbulence. Next we describe the more recent developments at the very lowest temperatures. The results of these measurements will be discussed in detail in the last part of this section, where we conclude with a general discussion of the significance of the observed temperature dependence of ν.

4.1.2 Techniques of Measuring the Vortex Line Density *L*

The attenuation of second sound in superfluid ^{4}He, which is proportional to the total length of vortex lines, has been the prefered technique of measuring L in the temperature range 1–2 K (Barenghi and Skrbek, 2007; Niemela et al., 2005; Stalp et al., 1999; Vinen, 1957a) since Hall and Vinen (1956); however, it cannot be extended below 1 K. Very recently, scattering of negative ions off vortex lines has been succesfully utilised at temperatures 80 mK–1.6 K (Walmsley et al., 2007a), showing good agreement with previous measurements of ν at overlapping temperatures (Stalp et al., 2002). Actually, the first use of ions for the observations of a vortex tangle was reported almost 50 years ago (Careri et al., 1960), and numerous further experiments revealed their potential for investigating turbulence in superfluid ^{4}He (see the reviews by Tough (1982) and Donnelly (1991) for more references on early studies).

It is worth mentioning possible alternative techniques of detecting turbulence in ^{4}He in the $T = 0$ limit that are currently being developed, such as calorimetric (Ihas et al., 2008) and others (Vinen, 2006). The design of towed grid for turbulence generation, suitable for experiments at $T <$ 0.5 K in ^{4}He, is presently being attempted by McClintock at Lancaster and Ihas at Gainsville. Optical vizualisation of individual vortex lines in the turbulent tangle (Bewley et al., 2006, 2008; Rellergert et al., 2008; Sergeev et al., 2006; Zhang et al., 2005) (see the contribution by Van Sciver and Barenghi, 2008, in this volume) is another promising development, although the prospects of extending this technique down to at least $T = 0.5$ K seem distant. As we mentioned in Sections 2 and 3, computer simulations have contributed a great deal to our understanding of certain processes in the dynamics of tangles and of the Kelvin-wave cascade at $T = 0$ in particular (Hänninen et al., 2007a; Kivotides et al., 2001; Schwarz, 1988; Tsubota et al., 2000; Vinen et al., 2003) (see also the contribution by Tsubota and Kobayashi, 2008 in this volume); however the proper modelling of the inertial cascade pumped at large (quasiclassical) length scales and dissipated at short (quantum) scales requires a considerable range of length scales and hence remains a challenge.

4.1.3 General Properties of Injected Ions in Liquid Helium

Injected ions (see reviews (Borghesani, 2007; Donnelly, 1991; Fetter, 1976; Schwarz, 1975)) are convenient tools to study elementary excitations and quantised vortices in superfluid helium. They were used to detect vortex arrays in rotating helium (Careri et al., 1962; Yarmchuk et al., 1979), quantised vortex rings (Rayfield and Reif, 1964) and vortex tangles (Careri et al., 1960) in ^{4}He. To create a *negative ion*, an excess electron is injected into liquid helium, where it self-localises in a spherical cavity ('electron bubble') of radius ∼2 nm at zero pressure. To create a *positive ion*, an electron

is removed from one atom, which results in a positively-charged cluster ion ('snowball') of radius ~ 0.7 nm. These objects are attracted to the core of a quantised vortex, resulting in trapping with negligible escape rate provided the temperature is low enough ($T < 1.7$ K for negatives and $T < 0.4$ K for positives in ^{4}He at zero pressure). Because of this interaction, both species have been used a great deal to study quantised vortices although negative ions are often more convenient, especially if one wants to cover a wider range of temperatures. The binding energy of a negative ion trapped by a vortex is about 50 K (Donnelly, 1991). In superfluid ^{3}He, thanks to much larger diameters of vortex cores, this binding is much weaker; hence there were no observations of ion trapping on vortex cores yet. Still, the anisotropy of ions motion in ^{3}He-A made it possible to use negative ions to detect textural changes around vortex cores (Simola et al., 1986).

In this section, we focus on negative ions in superfluid ^{4}He. Their mobility is limited by scattering thermal excitations and is hence rapidly increasing with cooling. Below some 0.8 K, it is so high that they quickly reach the critical velocity for creation of (depending on pressure and concentration of ^{3}He impurities) either rotons (and then move with the terminal Landau velocity ~ 60 m/s, shedding off rotons continuously) or quantised vortex rings (and then get trapped by such a ring and move with it as a new entity, a charged vortex ring) (Berloff and Roberts, 2000a,b; Hendry et al., 1988, 1990; Winiecki and Adams, 2000). Above 1 K, the trapping diameter σ of an ion by a vortex line is inversely proportional to the electric field, $\sigma \propto E^{-1}$. In a field $E = 33$ V/cm, it is decreasing with temperature from $\sigma = 100$ nm at $T = 1.6$ K to $\sigma = 4$ nm at $T = 0.8$ K (Ostermeier and Glaberson, 1974).

Rayfield and Reif (1964) produced singly-charged, singly-quantised vortex rings in ^{4}He at $T = 0.4$ K and, by measuring the dependence of their self-induced velocity $v \propto \kappa^3 K^{-1}$, Equations (41) and (42), on their energy K, confirmed the value of the circulation quantum $\kappa = 1.00 \times 10^{-3}$ cm^{2}s^{-1}. Schwarz and Donnelly (1966) investigated the trapping of charged vortex rings by rectilinear vortices in a rotating cryostat and found the trapping diameter to be of order of the ring radius, meaning that the interaction is basically geometrical. They wrote: "quantised vortex rings are very sensitive "vortex-line detectors," making them suitable probes for a number of problems in quantum hydrodynamics". Guenin and Hess (1978) used charged vortex rings to detect turbulent vortex tangles in ^{4}He at $T = 0.4$ K, created by forcing a jet of superfluid through an orifice at supercritical velocities.

While charged vortex rings are more convenient than free ions because of their much greater trapping diameter, their dynamics is more peculiar (Figure 29; all figures in Sections 4.1–4.3 represent the Manchester experiments (Walmsley et al., 2007a; Walmsley and Golov, 2008a)). The energy
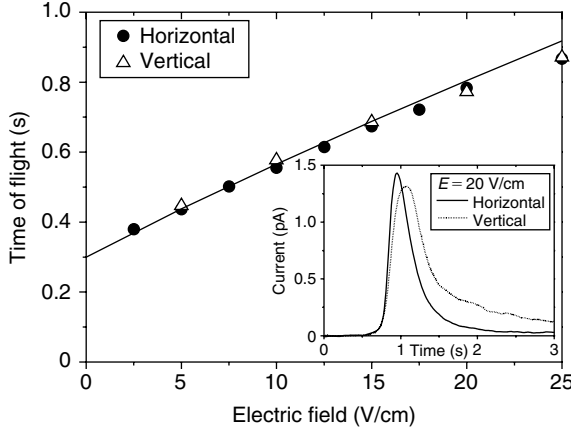
FIGURE 29 Time of flight (corresponding to the leading edge of the pulse of collector current shown in inset) of charged vortex rings as a function of electric field at $T = 0.15$ K in both the horizontal and vertical direction. The solid line shows the times of flight for rings with initial (as injected into the drift volume) radii and energies of 0.53 μm and 21 eV, calculated using Equations (41), (42) and (43).

K, velocity v and impulse P of a quantised vortex ring of radius $\mathcal{R}$ with a hollow core of radius a_0 and no potential energy in the core are (Donnelly, 1991; Glaberson and Donnelly, 1986)

$$K = \frac{1}{2}\rho_s\kappa^2\mathcal{R}\left(\ln\frac{8\mathcal{R}}{a_0} - 2\right),\tag{41}$$

$$v = \frac{\kappa}{4\pi\mathcal{R}}\left(\ln\frac{8\mathcal{R}}{a_0} - 1\right)\quad\text{and}\tag{42}$$

$$P = \pi\rho_s\kappa\mathcal{R}^2.\tag{43}$$

By integrating these equations, one can calculate the trajectories of the charged vortex rings subject to a particular electric field (Walmsley et al., 2007b).

4.1.4 Measuring the Vortex Line Density *L* by Ion Scattering

In the absence of vortex lines, the ions would propagate either freely (these dominate at $T > 0.8$ K) or riding on small vortex rings (dominate at $T < 0.6$ K). Without other vortex lines in their way, the time of flight of
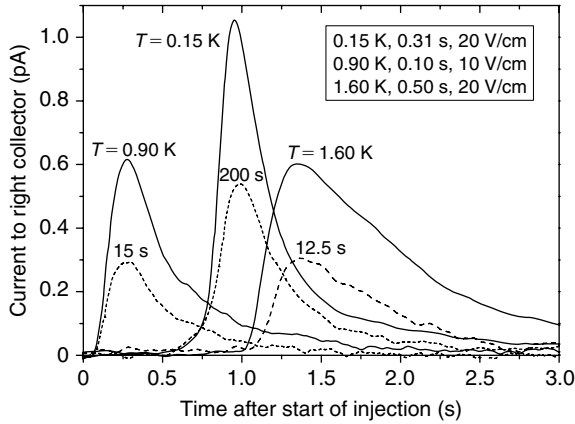
FIGURE 30 Examples of current transients produced by short pulses for three different temperatures (the temperatures, pulse durations and mean driving fields are indicated in the legend). The solid lines show the transients without a vortex tangle in the ions' path, while the dashed ones represent the transients suppressed by the vortex tangle which has been decaying a specified time (indicated near curves) after stopping generation. The charge carriers are either free ions ($T = 1.60$ K and $T = 0.90$ K) or charged vortex rings ($T = 0.15$ K). The electronics time constant is 0.15 s; hence the time of arrival of the fastest peak ($T = 0.90$ K) cannot be resolved.

both species over a particular distance is a well-defined function of temperature, electric field and initial radius of the attached vortex ring (if any). Hence, after injecting a short pulse of such ions, a sharp pulse of current arrives at the collector as shown in Figure 30. The interaction with other existing vortices, that happened to be in the way of the propagating ions, is characterised by a 'trapping diameter' σ (Ostermeier and Glaberson, 1974; Schwarz and Donnelly, 1966) and leads to the depletion of the pulses of the collector current. This is used to measure the average density of vortex lines L between the injector and collector through

$$L(t) = (\sigma h)^{-1} \ln(I(\infty)/I(t)). \tag{44}$$

To calibrate the value of σ for either free negative ions or ions trapped on a vortex ring at different temperature and electric field, one can measure the attenuation of the pulses of the collector current when the cryostat is at continuous rotation at angular velocity Ω (thus having an equilibrium density of rectilinear vortex lines $L = 2\Omega/\kappa$) as in Figure 31. This is best done in the direction perpendicular to the rotation axis.

At low temperatures in quantum cascade Kelvin-waves of a broad range of wavelengths are excited; however the main contribution to the total length L converges quickly at scales just below ℓ (Kozik and Svistunov,
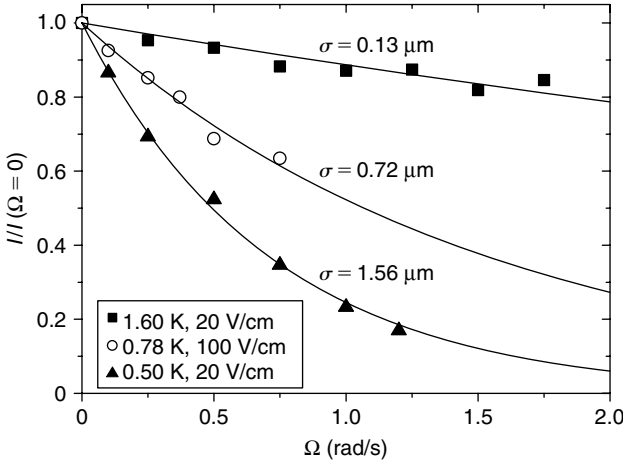
FIGURE 31 Dependence of pulse amplitude on the angular velocity of rotation, Ω, in examples of calibration measurements. The temperatures, driving fields and trapping diameters σ are indicated. The charge carriers are either free ions ($T = 1.60$ K) or charged vortex rings ($T = 0.78$ K and $T = 0.50$ K).

2008b). Hence, a probe ion with the trapping diameter $\sigma \ll \ell$, moving at a speed ($v \sim 10$ cm/s) much greater than the characteristic velocities of vortex segments ($\sim \kappa/\ell < 10^{-1}$ cm/s), should sample the full length L. Experimental measurements with different $\sigma = 0.4$–1.7 µm (using charged vortex rings in a range of driving electric fields) indeed produce consistent values of L.

There are evidences that small concentrations of trapped space charge (when the ratio of trapped space charge density n to the vortex line length L does not exceed $n/L \sim 10^5$ cm^{-1}) do not affect the tangle dynamics (Walmsley and Golov, 2008b). For example, experiments generating quasiclassical tangles at $T \geq 0.7$ K by a jet of ions (and hence resulting in a substantial trapped space charge) revealed that the late-time decay is identical to that for the tangles generated by an impulsive spin-down to rest without injecting any ions. Still, one might worry that the very presence of trapped charge, as it interacts with the beam of probe ions, might affect the result of measuring L. Hence, in order not to introduce extra turbulence and not to contaminate the tangle with any ions, the measurement was performed by probing each realisation of turbulence only once, after a particular waiting time t during its free decay. Then the contaminated tangle was discarded and a fresh tangle generated.

4.1.5 Design of Ion Experiment

The cell used in the Manchester experiments had cubic geometry with sides of length $h = 4.5$ cm. A schematic drawing of the cell is shown in
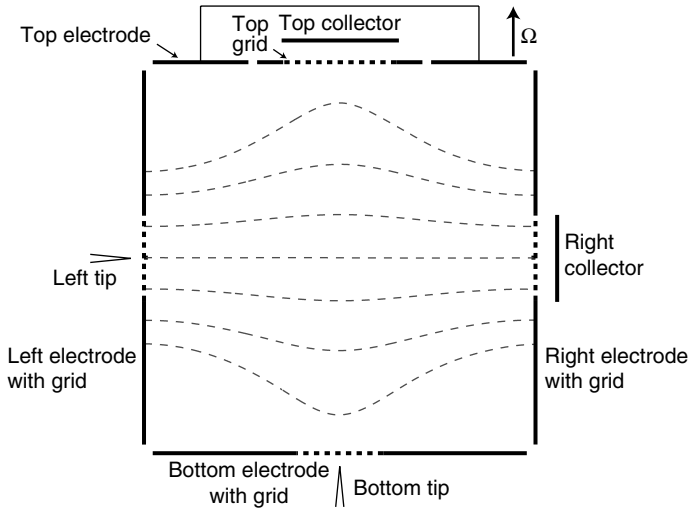
FIGURE 32 A side cross-section of the Manchester cell. The distance between opposite electrode plates is 4.5 cm. An example of the driving electric field is shown by dashed lines. Such a configuration was used in all the Manchester experiments described in this section. It was calculated for the following potentials relative to the right electrode: left electrode at −90 V, side, top and bottom electrodes at −45 V, and the right electrode and collector at 0 producing a 20 V/cm average driving field in the horizontal direction. To inject ions, the left tip was usually kept at between −500 to −350 V relative to the left grid. When ions traveling vertically across the cell (injected from bottom tip and detected at the top collector) were required, the potentials on the electrodes were rearranged as appropriate.

Figure 32. The relatively large size of the cell was important to enhance the efficiency of ion trapping and the time resolution of vortex dynamics, and was really instrumental to ensure that the continuum limit $\ell \ll h$ holds even when the vortex line density drops to as low as just $L \sim 10\,\text{cm}^{-2}$. This also helped ensure that the presence of the walls, which might accelerate the decay of turbulence within some distance $\sim\ell$, does not affect the dynamics of the turbulent tangle in the bulk of the cell. In order to probe the vortex densities along the axial and transverse directions, there were two independent pairs of injectors and collectors of electrons. Both injectors and collectors were protected by electrostatic grids, enabling injecting and detecting pulses of electrons. The injectors were field emission tips made of 0.1 mm diameter tungsten wire (Golov and Ishimoto, 1998). The threshold for ion emission was initially $\simeq -100\,\text{V}$ and $-210\,\text{V}$ for the bottom and left injectors, respectively; however, after over two years of almost daily operation, they changed to some $-270\,\text{V}$ and $-520\,\text{V}$. The fact that the two injectors had very different threshold voltages helped

investigate the dependence (or rather lack of it) of the radius of initial charged vortex rings on the injector voltage. The six side plates (electrodes) that make up the cube can be labelled 'top', 'bottom', 'left', 'right', and two 'side' electrodes. The top, bottom, left and right electrodes had circular grids in their centres. All grids were made of square tungsten mesh with period 0.5 mm and wire diameter 0.020 mm, giving a geometrical transparency of 92%. The grids in the bottom, left and right plates had a diameter 10 mm and were electrically connected to those plates. The grid in the top plate had diameter of 13 mm and was isolated from the top plate. The injector tips were positioned about 1.5–2 mm behind their grids. The two collector plates were placed 2.5 mm behind their grids and were typically biased at +10 to +25 V relative to the grids. Further details can be found in Walmsley et al. (2007b).

4.1.6 Tangles Generated by an Impulsive Spin-down

This novel technique of generating quasiclassical turbulence, suitable for any temperatures down to at least 80 mK, relied on rapidly bringing a rotating cubic-shaped container of superfluid ^{4}He to rest (Walmsley et al., 2007a). The range of angular velocities of initial rotation Ω was 0.05–1.5 rad/s. In classical liquids at high Re, spin-down to rest is always unstable, especially at high deceleration and in axially asymmetric geometries. It is known that, within a few radians of initial rotation upon an impulsive spin-down to rest, a nearly homogeneous turbulence develops with the energy-containing eddies of the size of the container. In a cylindrical container, centrifugal and Taylor-Görtler instabilities usually break up at the perimeter, thus facilitating slowing down of the outer region of the initially rotating liquid. Simultaneously, because of the Ekman pumping of nonrotating liquid into the central axis via the top and bottom walls, the central core of the initial giant vortex slows down too (Donnelly, 1991). In a cubic container, the turbulence becomes homogeneous much faster. Some residual rotation of the central region in the original direction might still survive for a while but, as we show below, the generated turbulence is in general pretty homogeneous.

   This behaviour is well-documented for classical liquids (van Heijst, 1989), and one expects similar processes to occur in a superfluid liquid providing the process of initial multiplication of vortices does not affect the dynamics. As spin-down experiments always begin from already existing dense rectilinear vortex arrays of equilibrium density $L = 2\Omega/\kappa$, and rapid randomisation and multiplication of these vortices is expected due to the lack of axial symmetry of the container, as well as surface pinning (friction) in the boundary region, these seem to be sufficient for the superfluid to mimic the large classical turbulent eddies. In Figure 33, we show the four different stages of the evolution from a vortex array to a decaying
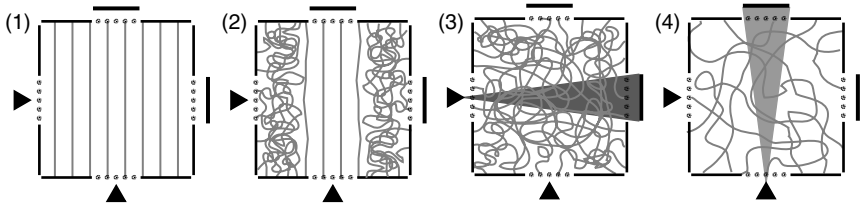
FIGURE 33 Cartoon of the vortex configurations produced by spin-down in the experimental cell (side view) at different stages. (1) Regular array of vortex lines during rotation at constant Ω before deceleration. (2) Immediately after stopping rotation ($0 < \Omega t < 10$), turbulence appears at the outer edges but not on the axis of rotation. (3) After about 30 rad of initial rotation ($\Omega t \sim 30$), 3D homogeneous turbulence is everywhere. (4) Then ($\Omega t \sim 10^3$) the 3D turbulence decays with time. Shaded areas indicate the paths of probe ions when sampling the vortex density in the transverse (L_t, 3) and axial (L_a, 4) directions.

homogeneous tangle upon an impulsive spin-down to rest, which are in agreement with the observations outlined below.

Before making each measurement, the cryostat was kept at steady rotation at the required Ω for at least 300 s before decelerating to full stop, then waiting a time interval t and taking the data point. Then the probed tangle was discarded and a new one generated. Hence, different data points represent different realisations of the turbulence. The deceleration was linear in time taking 2.5 s for $\Omega = 1.5\,\text{rad/s}$ and 0.1 s for $\Omega = 0.05\,\text{rad/s}$. The origin $t = 0$ was chosen at the start of deceleration.

4.1.7 Current-Generated Tangles

An alternative technique of generating turbulence, by a jet of injected ions that does not require any moving parts in the cryostat, has been developed (Walmsley and Golov, 2008a) (Figure 34). In early experiments with injected ions at low temperatures (Bruschi et al., 1966, Bowley et al., 1982) it was observed that a pulse of negative ions through superfluid ^{4}He leaves behind a tangle of vortices. Walmsley et al. (2008a) found that the properties of these tangles can be quite different. As we explain below, the tangles generated after long injection at high temperatures possess the properties of developed quasiclassical turbulence while those produced after short injection at low temperatures have signatures of random tangles with little large-scale flow.

At high temperatures $T > 0.7\,\text{K}$, while moving relative to the normal component, the ions experience viscous drag through scattering of excitations – this means that the ions entrain the normal component along. They can also get trapped by an existing vortex line (provided $T < 1.8\,\text{K}$), after which the vortex line will be pulled along with the current of such ions.
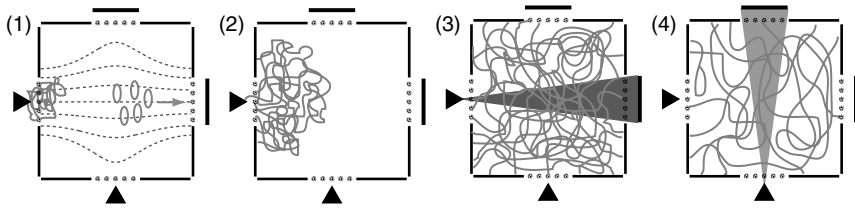
FIGURE 34   Cartoon of the vortex configurations produced by a pulse of injected ions at $T < 0.5\,$K in the experimental cell (side view) at different stages. (1) $< 1\,$s: a pulse of charged vortex rings is injected from the left injector. While most make it to the collector as a sharp pulse, some got entangled near the injector. (2) $\sim$5 s: the tangle spreads into the middle of the cell. (3) $\sim$20 s: the tangle has occupied all volume; from now on, it is nearly homogeneous (as probed in two directions). (4) Up to 1000 s: the homogeneous tangle is decaying further. The shaded areas indicate the trajectories of ions used to probe the tangle along two orthogonal directions.

The existing vortices and hence the superfluid component, through the action of mutual friction, will be pulled by the already entrained normal component too, and vice versa. Then one can expect the injected current to produce a large-scale jet-like flow of liquid helium, which is an efficient way of driving quasiclassical turbulence at large scales. This is similar to jet flow through an orifice – one of the traditional means of generating turbulence in classical liquids (Chanal et al., 2000). On the other hand, at low temperatures the ions always bring small vortex rings along, and hence, upon formating a tangle, can directly pump up the vortex length L without introducing substantial large-scale flow – at least for not too long injections.

4.2 Experimental Results

4.2.1 Quasiclassical Turbulence Generated by a Spin-Down to Rest

At $1\,$K $< T < 2\,$K, the $L \propto t^{-3/2}$ free decay was monitored by second sound for towed grid turbulence in Oregon (Stalp et al., 1999). The recent spin-down experiments at Manchester are in good agreement with them at overlapping temperatures. At $T < 1\,$K, only scattering of ions off vortex lines has been used to measure L so far.

In Figure 35, the measured densities of vortex lines along the horizontal axis (transverse, L_t) are shown for four different initial angular velocities Ω. During the transient, which lasts some $\sim$100Ω^{-1}, $L_t(t)$ goes through the maximum after which it decays eventually reaching the universal late-time form of $L \propto t^{-3/2}$. For $\Omega \geq 0.5\,$rad/s, the values of L at maximum were too high to be detected. The initial vortex densities at steady rotation, $L = 2\Omega/\kappa$, are shown by horizontal lines. Similarly, the densities of vortex lines measured along the vertical axis (axial, L_a) are shown in Figure 36.
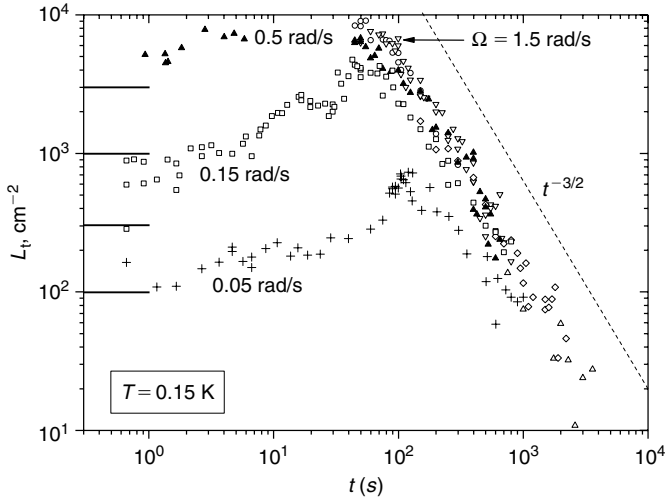
FIGURE 35 $L_t(t)$ at $T = 0.15$ K for four values of Ω. The average driving fields used for $\Omega = 1.5$ rad/s: 5 V/cm ($\circ$), 10 V/cm ($\triangledown$), 20 V/cm ($\diamond$), 25 V/cm ($\triangle$). At other values of Ω, the electric fields used were either 20 V/cm (0.05 rad/s) or 10 V/cm (0.5 and 0.15 rad/s). The dashed line shows the dependence $t^{-3/2}$. The horizontal bars indicate the initial vortex densities at steady rotation, $L = 2\Omega/\kappa$, at $\Omega = 1.5$ rad/s, 0.5 rad/s, 0.15 rad/s and 0.05 rad/s (from top to bottom).
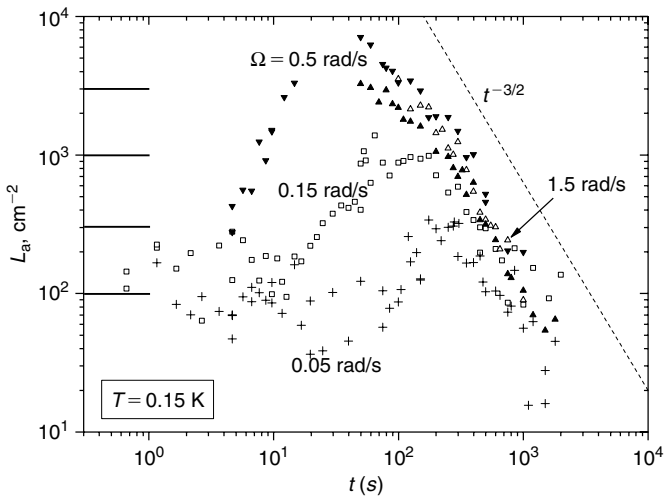

FIGURE 36 $L_a(t)$ at $T = 0.15$ K for four values of Ω. The average driving field used was 20 V/cm in all cases except at 0.5 rad/s where both 10 V/cm ($\triangledown$) and 20 V/cm ($\triangle$) were used. The dashed line shows the dependence $t^{-3/2}$. The horizontal bars indicate the initial vortex densities at steady rotation, $L = 2\Omega/\kappa$, at $\Omega = 1.5$ rad/s, 0.5 rad/s, 0.15 rad/s and 0.05 rad/s (from top to bottom).
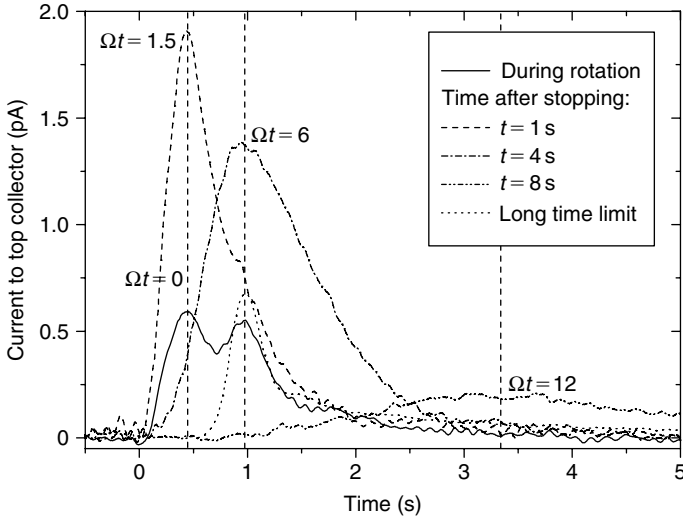
FIGURE 37 Records of the current to the top collector, injected from the bottom injector as a 0.1 s-long pulse at the time t after an impulsive spin-down from $\Omega = 1.5$ rad/s to rest. $T = 0.15$ K, $E = 20$ V/cm.

To illustrate what is happening near the vertical axis of the container at different stages of the transient after a spin-down, in Figure 37 we show five records of the current to the top collector arriving after a short (0.1 s) pulse of probed ions was fired from the bottom injector. Each is characteristic of a particular configuration of vortex lines near the rotational vertical axis of the container during the transformation from an array of parallel lines to a homogeneous decaying vortex tangle. One can see three different characteristic times (vertical dashed lines in Figure 37) of arrival of ions via different means. The first peak at ≈ 0.4 s (determined by the time constant of the current preamplifier, 0.15 s) corresponds to the ions trapped on the rectilinear vortex lines which can slide along those lines very quickly, provided those lines are continuous from the injector to collector as during steady rotation. The second peak at ≈ 1 s corresponds to the coherent arrival of the ballistic charged vortex rings from the bottom to the top. The third broad peak at times ~ 3 s (but with a long tail detectable until ~ 40 s) corresponds to the charge trapped on the vortex tangle and drifting with the tangle. Hence, we have the following regimes (and curves in Figure 37) labelled by the time t after the spin-down:

1. $\Omega t \leq 0$, steady rotation. The nearly equal first and second peaks tell that there exist a vortex array without disorder (otherwise the second peak would get suppressed and the third would appear).

2. $\Omega t = 1.5$. The first peak gets enhanced three-fold while the second one is still there (and no third peak) – meaning more trapped ions can reach the collector along the rectilinear vortex lines while there is not much turbulence in this region yet.

3. $\Omega t = 6$. The first peak has disappeared in favour of the second one which has got broadened – at this stage, the rectilinear vortices should have become scrambled in the Ekman layers near the top and bottom walls/grids while the ballistic charged vortex rings are still the dominant transport of charge.

4. $\Omega t = 12$. Now both fast peaks have disappeared completely while the third broad peak has emerged – this means that a turbulent tangle has finally reached the axial region.

5. $\Omega t \to \infty$. The sharp second peak has recovered but all others vanished – after the turbulence has decayed only ballistic charged vortex rings carry the charge, neither the rectilinear array nor turbulent tangle contributes to the transport any more.

In Figure 38, the measured densities of vortex lines along the horizontal, L_t, and vertical, L_a, axes are shown by solid and open symbols, respectively. To stress the scaling of the characteristic times with the initial turnover time Ω^{-1} and the universal late-time decay $\propto t^{-3/2}$, the data for different Ω are rescaled accordingly. We can see that at all Ω the
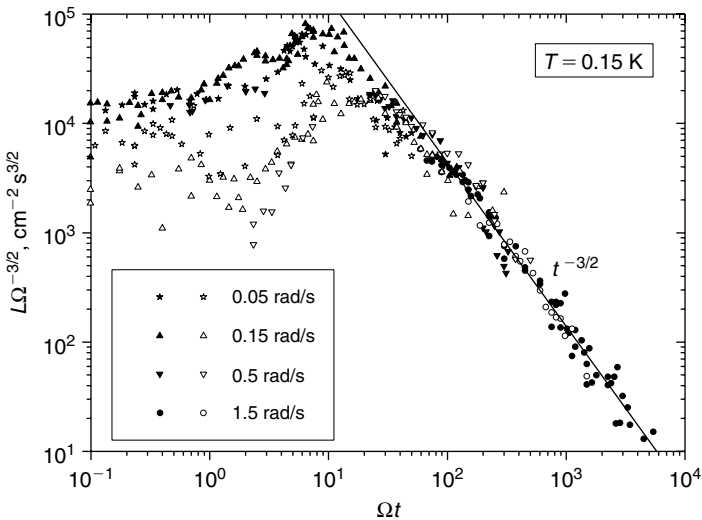

FIGURE 38 $\Omega^{-3/2}L_t(t)$ (filled symbols) and $\Omega^{-3/2}L_a(t)$ (open symbols) versus Ωt for four values of Ω at $T = 0.15$ K. The straight line $\propto t^{-3/2}$ guides the eye through the late-time decay.

transients are basically universal. Immediately after deceleration, L_t jumps to $\approx 10^4 \Omega^{3/2}$ cm^{-2}s$^{3/2}$, indicating the appearance of the TBL at the perimeter, while L_a is stable at $L_i \approx 2\Omega/\kappa$. Only at $\Omega t \approx 3$, the latter starts to grow, signalling the destruction of the rotating core with vertical rectilinear vortices. After passing through a maximum at $\Omega t = 8$ and $\Omega t = 15$, L_t and L_a merge at $\Omega t \sim 30$ and then become indistinguishable. This implies that from now on the tangle density is distributed nearly homogeneously. The scaling of the transient times with the turnover time Ω^{-1} indicates that transient flows are similar at different initial velocities Ω, which is expected for flow instabilities in classical inviscid liquids. Eventually, after $\Omega t \sim 100$, the decay takes its late-time form $L \propto t^{-3/2}$ expected for quasiclassical isotropic turbulence, whose energy is mainly concentrated in the largest eddies bound by the container size h but homogeneous on smaller length scales. We hence assume that the turbulence in ^{4}He at this stage is nearly homogeneous and isotropic, and can apply Equation (40) to extract the effective kinematic viscosity ν. The crossover to the $L \propto t^{-1}$ regime at late time has never been observed, probably because the measured values of L never dropped below $10\,\text{cm}^{-2} \gg h^{-2} \sim 0.05\,\text{cm}^{-2}$.

At $0.08 < T < 0.5$ K, the measured $L(t)$ were independent of temperature. In Figure 39, we compare the transients $L_t(t)$ at low ($T = 0.15$ K) and high ($T = 1.6$ K) temperatures. The prefactor in the late-time dependence $L \propto t^{-3/2}$ at $T = 0.15$ K is almost an order of magnitude larger than that for $T = 1.6$ K. This implies that at low temperatures, the steady state inertial cascade with a saturated energy-containing length and constant energy flux down the range of length scales requires a much greater total vortex line density. This means that in the $T = 0$ limit the effective kinematic viscosity ν is approximately 70 times smaller than at $T = 1.6$ K (provided $C \approx 1.5$ and $k_1 \approx 2\pi/h$ are independent of temperature).

At all temperatures, the transients $L_t(t)$ after a spin-down are, in first approximation, universal, that is, the timing of the maximum is the same, $\Omega t \approx 8$, and the amplitudes of the maximum are comparable. This supports our approach to turbulent superfluid helium at large length scales as to an inviscid classical liquid, agitated at large scale and carrying an inertial cascade down the length scales, independent of temperature. On the other hand, as the temperature increases and interaction with the viscous normal component becomes stronger, changes in the shape of transients might be expected. Indeed, one can see that the slope of $L(t)$ after the maximum but before reaching the ultimate late-time decay $L \propto t^{-3/2}$ (that is, for $10 < \Omega t < 100$) is changing gradually with increasing temperature from being less steep than $t^{-3/2}$ at $T = 0.15$ K to more steep than $t^{-3/2}$ at $T = 1.6$ K (Figure 39). At temperatures around $T = 0.85$ K (Figure 41), it nearly matches $t^{-3/2}$, thus making an erroneous determination of ν possible by taking this part of the transient for the late-time decay $L \propto t^{-3/2}$. Indeed, in the first publication (Walmsley et al., 2007a), parts of some
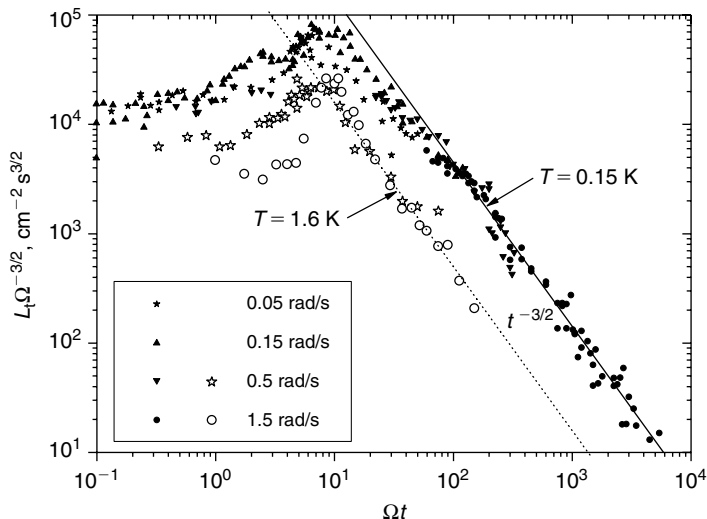
FIGURE 39 $\Omega^{-3/2}L_t(t)$ versus Ωt for $T = 0.15$ K (filled symbols) and $T = 1.6$ K (open symbols). Dashed and solid lines $\propto t^{-3/2}$ guide the eye through the late-time decay at $T = 1.6$ K and 0.15 K, respectively.

transient at $T = 0.8-1.0$ K for as early as $\Omega t > 15$ were occasionally used to be fitted by $L \propto t^{-3/2}$ that often resulted in overestimation of the value for ν. To rectify this, we have refitted the data sets used in the original publication as well as subsequent measurements with $L \propto t^{-3/2}$ for spin-downs using the following rules: for $T \leq 0.5$ K, only points for $\Omega t > 300$ were used, between 0.5 K and 1.0 K only points for $\Omega t > 150$ were used and at $T > 1.0$ K, only $\Omega t > 75$ were used. This resulted in slight systematic reduction of the extracted values of $\nu(T)$ at temperatures 0.8–1.2 K from those published in Walmsley et al. (2007a); what looked as a rather steep drop in $\nu(T)$ at 0.7–0.8 K, now occurs at 0.85–0.90 K and is somewhat reduced in magnitude.

4.2.2 Quasiclassical Turbulence Generated by an Ion Jet

As mentioned above, ion jets can produce quasiclassical tangles decaying as $L \propto t^{-3/2}$ (Walmsley and Golov, 2008a). Examples of the decay of such tangles alongside with those obtained by a spin-down at $T = 1.6$ K and $T = 0.8$ K are shown in Figures 40 and 41, demonstrating good quantitative agreement between the late-time decays. At temperatures 0.7–1.6 K, the late-time decays of quasiclassical turbulences generated by these two different techniques were identical within the experimental errors.
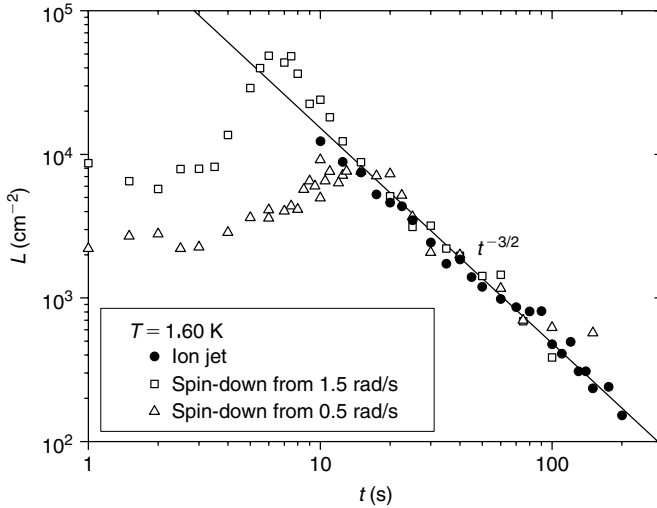
FIGURE 40 Free decay of a tangle produced by a jet of free ions from the bottom injector (•) (Walmsley and Golov, 2008a), as well as by an impulsive spin-down to rest (□) (Walmsley et al., 2007a) from 1.5 rad/s and 0.5 rad/s, at $T = 1.60$ K. All tangles were probed by pulses of free ions in the horizontal direction. The line $L \propto t^{-3/2}$ corresponds to Equation (40) with $\nu = 0.2\,\kappa$.
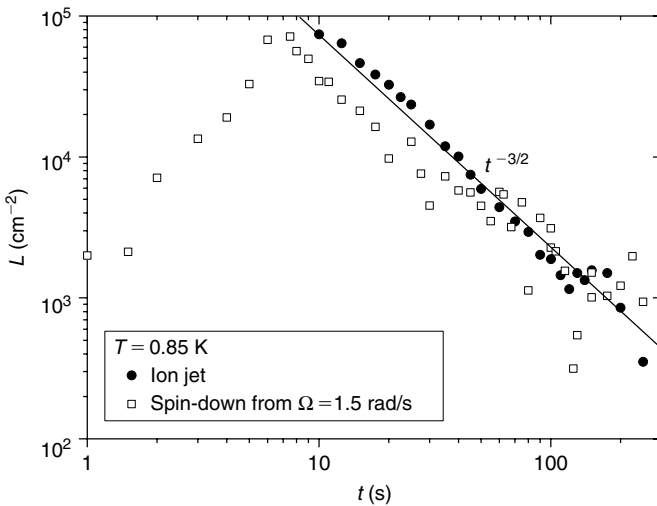

FIGURE 41 Free decay of a tangle produced by a jet of free ions from the bottom injector (•) (Walmsley and Golov, 2008a), as well as by an impulsive spin-down to rest (Walmsley et al., 2007a) from 1.5 rad/s, at $T = 0.85$ K. All tangles were probed by pulses of free ions in the horizontal direction. The ion jet data are the average of nine measurements at each particular time, but the spin-down data show individual measurements.

4.2.3 Ultraquantum Turbulence Generated by a Jet of Charged Vortex Rings

In the temperature range $0 < T < 0.5\,\text{K}$, all tangles produced by a pulse of injected current of duration 0.1–1 s, intensity 10^{-12}–10^{-10} A and in the driving field $0 - 20\,\text{V/cm}$ revealed the late-time decay $L \propto t^{-1}$, all with the same prefactor (Figure 42) (Walmsley and Golov, 2008a). This universality of the prefactor for all initial vortex densities is a strong argument in favour of the random character of the tangles whose decay is described by Equation (39) (ultraquantum turbulence). During the injection, the tangle originates near the injector, presumably as the result of colliding many charged vortex rings all of the same radius $R \approx 0.5\,\mu\text{m}$, and then spreads into the centre of the cell in 3–5 s, eventually filling all container and becoming nearly homogeneous after $\sim$20 s. This can be seen at the transient in Figure 42 ($*$) where the tangle was initiated at the bottom injector but then sampled along the horizontal axis of the container. The dynamics of the tangle spreading was found to be independent of the driving field 0–20 V/cm.

The tangles produced by the bottom and left injectors had very nearly identical late-time decays $L \propto t^{-1}$ (Figure 42). The corresponding values of ν/κ, inferred using Equation (39), are 0.120 ± 0.013 and 0.083 ± 0.004. As the scattering diameters σ of charged vortex rings produced only by the
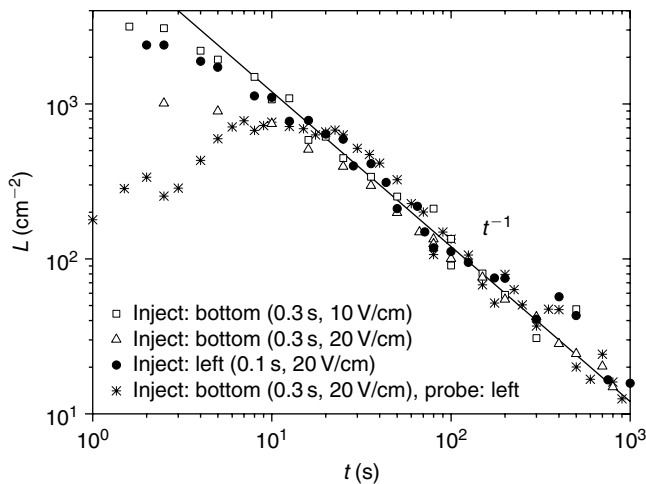

FIGURE 42 Free decay of a tangle produced by beams of charged vortex rings of different durations and densities, $T = 0.15$ K. The injection direction and duration and driving field are indicated. Probing with pulses of charged vortex rings, of duration 0.1–0.3 s were done in the same direction as the initial injection, except in one case ($*$). The line $L \propto t^{-1}$ corresponds to Equation (39) with $\nu = 0.1\kappa$.

left injectors could be calibrated directly in situ on the arrays of rectilinear vortex lines at steady rotation, the absolute value of $\nu = 0.08\kappa$ for these tangles probed along the horizontal axis is treated as more reliable.

4.3 Discussion: Dissipation in Different Types of Turbulence

4.3.1 Dissipation in ^{4}He at Different Temperatures

Let us now summarise what is known about the dissipation of various types of turbulence in superfluid ^{4}He at different temperatures. As the relevant parameter, we plot in Figure 43 the effective kinematic viscosity ν (as defined in Equation (38)) which is a function of the mutual friction parameter $\alpha(T)$ but can be different for different types of flow. One can see that at high temperatures, $T > 1\,\mathrm{K}$, all experimental points group around $\sim 0.1\,\kappa$, give or take a factor of two. The fact that different types of experiments seem to produce slightly different absolute values and temperature dependences might have various reasons. First, experimental techniques rely on the means of calibrating the sensitivity to the absolute value of L and on the knowledge of other parameters in the model. The calibration is normally performed on an array of rectilinear vortex lines in the direction perpendicular to the lines but not on tangles of vortex lines. For example, recent refined calculations (Chagovets et al., 2007) suggested to correct all previous second sound measurements of L on isotropic tangles by a factor of $3\pi/8 \approx 1.2$, which we apply here. Second, the exact values and dependence on temperature of the effective parameters relating $L(t)$ to ν (such as $B \approx 1.2$ in Equation (39) and $C \approx 1.5$ and $k_1/h \approx 2\pi$ in Equation (40)) are not known, thus complicating precise comparison of ν for different temperatures and types of flow. Third, at $T > 1\,\mathrm{K}$, the normal component can also become turbulent (Barenghi et al., 2002; L'vov et al., 2006b; Schwarz and Rozen, 1991; Vinen, 2000), hence its velocity field might vary for different means of generating turbulence.

Theoretically, one can consider two limiting cases: either completely locked ($\mathbf{v}_n = \mathbf{v}_s$) turbulent flow of both components or an absolutely laminar normal component ($\mathbf{v}_n = 0$ in a local reference frame) that slows down the segments of quantised vortices moving past it. The former is favourable at high mutual friction $\alpha(T)$ and low viscosity of the normal component $\eta_n(T)$ (that is, at the high-temperature end) and is expected to be described by the kinematic viscosity η_n/ρ (dotted line in Figure 43), where $\rho = \rho_n + \rho_s$, while the latter is favourable at low α and high η_n (that is, at the low-temperature end) and is expected to follow the predictions of mutual-friction-controlled models which assume a laminar normal component (e.g., line-connected stars and asterisks for random tangles in Figure 43). The experimental situation is obviously somewhere in between (and the measured ν should probably tend to the smaller value
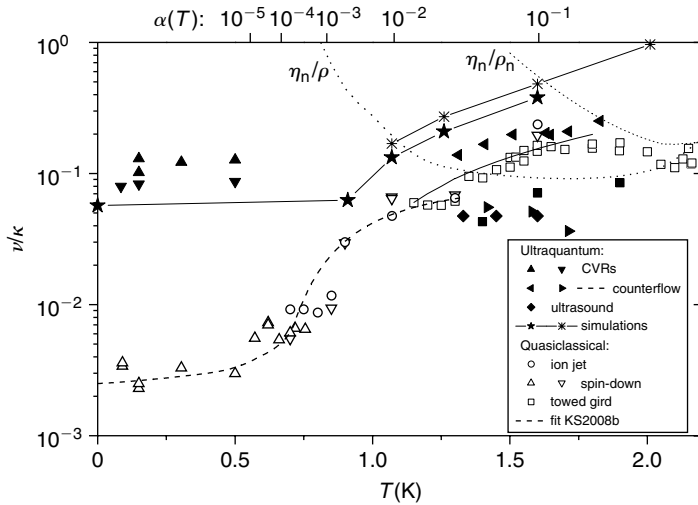
FIGURE 43   The effective kinematic viscosity $\nu(T)$ for various types of turbulence in
^{4}He. (i) Quasiclassical turbulence: $\nu(T)$ inferred from the $L \propto t^{-3/2}$ dependent free
decay of tangles using Equation (40) and produced by impulsive spin-down (open
triangles Walmsley et al. (2007a)); an ion jet (open circles Walmsley and Golov,
2008a); towed grids of two different designs (open squares Niemela et al., 2005; Stalp
et al., 2002). The solid curve is theory (Eq. 45) by Vinen and Niemela, 2002, and the
dashed curve is a fit to the Walmsley et al. (2007a) data (open triangles and circles) by
Kozik and Svistunov (2008b). (ii) Ultraquantum turbulence: $\nu(T)$ inferred using
Equation (39) from $L \propto t^{-1}$ dependent free decay of tangles produced by colliding
charged vortex rings (filled up and down triangles, Walmsley and Golov, 2008a);
counterflow (filled right-pointing triangles, Vinen, 1957b and filled squares, Schwarz
and Rozen, 1991); ultrasound (filled diamonds, Milliken et al., 1982); computer
simulations (line-connected stars, Tsubota et al., 2000); as well as from the analysis of
the measured tangle density in applied counterflow (filled left-pointing triangles,
Vinen, 1957b); and computer simulations (line-connected asterisks, Schwarz, 1988).
Note that in simulations ($\star$ and $*$), the normal component was artificially clamped to
laminar flow, while in most experiments at $T > 1\,K$ it is involved in turbulent motions
to different extent. The values of the kinematic viscosities, η_n/ρ_n of the normal
component and $\eta_n/(\rho_n + \rho_s)$ of the 'coupled normal and superfluid components' are
shown by dotted lines (Donnelly and Barenghi, 1998).

of those predicted by the two limits), although the particular means of
driving might tip the balance towards either of the limits. This might be
one reason why different techniques show systematic disagreement in the
temperature range above 1 K.

   One can speculate that quasiclassical turbulent flow generated by
mechanical stirring is less prone to such uncertainties since both the super-
fluid and normal large-scale flows are generated simultaneously and are

probably locked. On the other hand, the generation of quasi-random tangles was attempted by a variety of techniques: those continuously pumped by counterflow in narrow channels might have the normal component more laminar, while those with freely decaying turbulence in wide channels were shown to evolve towards coupled superfluid and normal turbulence at high temperatures (Barenghi and Skrbek, 2007), especially so if created with ultrasound which equally pumps turbulence in both components. In any case, on approaching $T = 1\,$K from above, when the normal component progressively becomes more viscous and less dense, all experimental and numerical values of $\nu(T)$ for quasi-random tangles seem to converge, which supports these reasonings.

At temperatures below 1 K, the values of $\nu(T)$ appear to split rapidly: those for ultraquantum turbulence apparently stay at nearly the same level, $\sim 0.1\,\kappa$, as at high temperatures, while those for quasiclassical turbulence keep decreasing until the zero-temperature limit of $\sim 0.003\,\kappa$. The mean free path of excitations in ^{4}He rapidly increases with decreasing temperature and becomes comparable with $\ell \sim 100\,\mu$m at 0.7 K and with the container size $h = 4.5\,$cm at 0.5 K. At these temperatures, the normal component is too viscous to follow the turbulent superfluid component and hence the convenient model of a laminar normal component becomes adequate here (in this respect, this regime of ^{4}He is similar to that in superfluid ^{3}He-B below $0.4\,T_c$, discussed in previous sections). It is indeed comforting that numerical simulations of tangles initiated at short scales (without large-scale turbulence (Tsubota et al., 2000)) are in good agreement with experiments for random tangles at these temperatures (Walmsley and Golov, 2008a). As yet, there are no satisfactory computer simulations of homogeneous quasiclassical turbulence in the limit of zero temperature.

Between 1.1 K and 1.6 K, the values of $\nu(T)$ for quasiclassical turbulence generated with towed grids of different designs (Niemela et al., 2005; Stalp et al., 1999), impulsive spin-down to rest and an ion jet are reasonably consistent between each other and show an increase from $\nu = 0.05\,\kappa$ to $0.2\,\kappa$. There was an early attempt (Stalp et al., 1999) to relate these values with the kinematic viscosity $\eta_n/\rho = 10^{-4}\,$cm^2/s $\approx 0.1\,\kappa$, assuming locked turbulence of the superfluid and normal components. However, it was soon realised (Stalp et al., 2002) that the contribution of quantised vortex lines to dissipation controlled by mutual friction and reconnections is also important. This certainly dominates below 1.2 K, where η_n/ρ begins to increase with cooling (hence, making the normal component effectively decoupled from vortices on short length scales) while the measured $\nu(T)$ decreases with cooling.

In the mutual-friction-dominated regime and provided the normal component is only locked to the superfluid velocity at scales $> \ell$, the actual dissipation is through the self-induced motion of vortex lines

relative to the normal component, whatever the kinetics of the quantum cascade. In this regime, a segment of a vortex line bent at radius $\mathcal{R}$ and hence moving at self-induced velocity $v \sim B\kappa\mathcal{R}^{-1}$ dissipates energy at the rate $\sim \rho_s \alpha B^2 \kappa^3 \mathcal{R}^{-2}$ per unit length, where $B \approx 1.2$ is introduced in Equation (39). This approach leads to the formula (Vinen, 2000; Vinen and Niemela, 2002)

$$\nu = sB^2 c_2^2 \alpha\kappa \,. \tag{45}$$

The multiplier s is meant to account for the degree of correlation between the motion of individual segments of vortex lines and the surrounding superfluid in a structured quasiclassical tangle ($s \approx 0.6$), compared to a random tangle of the same density L ($s = 1$). In the simulations of counterflow-maintained tangles in the local induction approximation by Schwarz (1988), the measure of the relative abundance of small-scale kinks on vortex lines, $c_2^2 = L^{-1} \langle \mathcal{R}^{-2} \rangle$, was found to increase from 2 to 12 as α decreased from 0.3 to 10^{-2} with decreasing temperature from 2 to 1 K. This formula nicely agrees with the simulations by Tsubota et al. (2000). It also captures the trend and magnitude of $\nu(T)$ for all experimental quasiclassical tangles as well as for the random tangle maintained by counterflow (Vinen, 1957a) (where the normal component is expected to be nearly laminar); although to fit it to the data of quasiclassical tangles in Figure 43 (solid line), we used $s = 0.2$, apparently owing to partial locking between the flows in the normal and superfluid components.

As vortex segments with smaller radii of curvature $\mathcal{R}$ lose their energy faster, for a given energy flux down the length scales, there exists a dissipative scale λ_q below which the cascade essentially cuts off (Kozik and Svistunov, 2008b; L'vov et al., 2006b; Svistunov, 1995; Vinen, 2000). For a developed nonlinear Kelvin-wave cascade ($\lambda_q \ll \ell$), with the amplitude spectrum $b_k \propto k^{-6/5}$ (Kozik and Svistunov, 2004), this implies that $\langle \mathcal{R}^{-2} \rangle \sim \ell^{-2/5} \lambda_q^{-8/5}$. In this sense, the Schwarz's parameter $c_2^2 \sim (\ell/\lambda_q)^{8/5}$ quantifies the range of wavelengths involved in the quantum cascade and becomes another quantum analog of the classical Reynolds number: $Re = (h/\lambda_{cl})^{4/3}$. With decreasing α, the value of λ_q progressively decreases until, at $T < 0.5$ K (Kozik and Svistunov, 2008b; L'vov et al., 2006b; Vinen, 2001), it reaches the wavelength $\lambda_{ph} \sim 3$ nm at which phonons can be effectively emitted. Below this temperature, as the dissipation of Kelvin-waves due to mutual friction becomes negligible compared to the emission of phonons, $\nu(T)$ is independent of temperature. However, in the presence of the quantum cascade at larger wavelengths, it is the cascade's kinetics that controls the energy flux, and it might happen that the vortex length L already saturates at higher values of α, thus signalling the onset of the regime with $\nu(T) = \text{const}$ as $T \to 0$, Equation (38).

Let us now discuss the specific models for the low-temperature behaviour of $\nu(T)$. For the dissipative mechanisms that involve individual quantised vortices, such as those maintained by vortex reconnections, simple considerations (Vinen and Niemela, 2002) usually predict ν to be of order κ. However, more involved models, such as that of a 'bottleneck' for quasiclassical turbulence, might suggest smaller values (L'vov et al., 2007a). If certain configurations of vortices are inefficient in transferring energy down to short wavelengths (e.g., either there exists a noncascading part of the spectrum or reconnections are less efficient in polarised tangles), the resulting accumulation of an extra contribution to L leads to a reduction of the parameter ν. This is what is observed for quasiclassical tangles in ^{4}He on approaching the $T = 0$ limit.

An important question remains: how is the energy of classical eddies passed over to the shorter quantum length scales? Two main mechanisms are currently discussed: (i) the excitation of Kelvin-waves through purely nonlinear interactions in classical eddies or (ii) vortex reconnections (each leaving a sharp kink on both vortex lines, hence effectively redistributing the energy to smaller length scales). Both predict an increase in $L(T)$ at constant energy flux down the cascade (i.e., the decrease of $\nu(T)$) with decreasing temperature. The former considers the accumulation of extra noncascading quasiclassical vorticity at length scales above ℓ due to the difficulty in transferring energy through wave numbers around ℓ^{-1} if reconnections do not ease the process (referred to as the bottleneck model in Section 3) (L'vov et al., 2007a). The latter mainly associates the excess vortex length L with the contributions from the new self-similar structures produced by vortex reconnections on length scales shorter than ℓ when vortex motion becomes progressively less damped at low temperatures (Kozik and Svistunov, 2008b). This model relies on four types of processes: reconnections of vortex bundles, reconnections of neighbouring vortices, self-reconnections of a vortex, and nonlinear interactions of Kelvin-waves, which bridge the energy cascade from the Kolmogorov to the Kelvin-wave regimes. It can be successfully fitted to the experimental $\nu(T)$, as seen in Figure 43. In short, both models predict an enhancement of vortex densities but on different sides of the crossover scale ℓ.

Finally, we may ask why is $\nu(T{=}0)$ larger for ultraquantum (random) tangles than for quasiclassical tangles in the $T = 0$ limit? Whatever the model, this means that, for the same total density of vortex lines L, the rate of energy dissipation in random tangles is larger. Within the bottleneck model (L'vov et al., 2007a), this seems straightforward as these tangles have no energy on classical scales at all. Within the reconnections/fractalisation scenario (Kozik and Svistunov, 2008b), this is explained by the fact that reconnections in partially polarised tangles are less frequent and less efficient. In the framework of this latter model, to explain why there is apparently no temperature dependence of $\nu(T)$ for ultraquantum tangles

below $T = 1\,\mathrm{K}$ (although no experimental data exist for the range 0.5–1.3 K), one should assume that for this type of tangle all significant increase in the total line length L caused by the fractalisation with decreasing temperature has already occurred above 1 K.

4.3.2 Comparing Turbulent Dynamics in ^{3}He-B and ^{4}He

It would be instructive to provide a comparison of turbulent dissipation in superfluid ^{4}He and ^{3}He-B. Unfortunately at present, with only few measurements on varying types of flow, this remains a task for the future. The Lancaster measurements on the decay of an inhomogeneous tangle generated with a vibrating grid by Bradley et al. (2006) revealed a $L \propto t^{-3/2}$ late-time decay (Fisher and Pickett, 2008). Assuming that the origin of the $t^{-3/2}$ dependence is the same as in quasiclassical turbulence with a saturated energy-containing length, and that this length is equal to the spread of the turbulent tangle over a distance of 1.5 mm, using Eq. (40) they extract the temperature-independent value of $\nu \approx 0.2\,\kappa$ at $0.156 < T/T_c < 0.2$. However, it is questionable whether the condition for the applicability of Eq. (40), that the classical energy $\mathcal{E}_c$ dominates over the quantum energy $\mathcal{E}_q$, is met for this turbulence. From their recent measurements of the initial velocity of mean large-scale flow, $u \sim 0.5\,\mathrm{mm/s}$ (Bradley et al., 2008), and vortex density, $L \sim 10^4\,\mathrm{cm}^{-2}$, we estimate $\mathcal{E}_c \sim u^2/2 \sim 10^{-3}\,\mathrm{cm}^2/\mathrm{s}$ while $\mathcal{E}_q \sim 0.7\kappa^2 L \sim 10^{-2}\,\mathrm{cm}^2/\mathrm{s}$; i.e. $\mathcal{E}_c \ll \mathcal{E}_q$ even at the early stage of decay. Hence, it is possible that the dynamics of the decay of their localized tangles is that of an ultraquantum turbulence but accelerated due to the diffusion or emission of vortex rings into space; thus the decay $L(t)$ is steeper than $\propto t^{-1}$. More experiments with grid turbulence in ^{3}He-B are desirable, which could shed light on the temperature dependence of turbulent dynamics, for example, if there is a similar decrease in $\nu(T)$ below $\alpha \sim 10^{-3}$ as measured for ^{4}He or to provide an independent characterisation of the energy-containing length scale. It would also be important to reproduce the results for ^{4}He in the $T = 0$ limit with another method of generating turbulence (for example, by means of towed or vibrating grids).

The Helsinki experiments on the propagating vortex front (Section 3) provide a measure of dissipation via the front velocity V_f. The observed relative enhancement of the rate of decay below $0.4\,T_c$ ($\alpha < 1$) proves the efficiency of the turbulent cascade in dissipating the energy of large-scale flow. The leveling off of this rate below $0.28\,T_c$ ($\alpha < 10^{-2}$) is qualitatively similar to that observed in ^{4}He at $T < 0.5\,\mathrm{K}$ ($\alpha < 10^{-5}$), and might hint at the $T = 0$ limit in the inertial cascade. However, the respective values of α, at which the leveling-off occurs, differ substantially. Various reasons can be given to explain this difference, for example that different types of flow have their own specific $\nu(\alpha)$ dependence (evidence for this is the

difference in the $\nu(T)$ values of quasiclassical and random tangles). For instance, to test the interpretation of the temperature dependence of $V_f(T)$ on approaching the $T \to 0$ limit, given in Section 3.5.6 in terms of the proximity of the outer and quantum crossover scales, it would be instructive to conduct similar measurements in containers of different radii.

In front propagation, the energy dissipation rate is proportional to $V_f(T)$, while in experiments described in this section the rate is proportional to $\nu(T)$. Thus, it is interesting to compare the temperature dependences of $V_f(T)$ and $\nu(T)$ in the two superfluids. We plot in Figure 44 the effective kinematic viscosity ν/κ and the normalised velocity of the propagating front $v_f = V_f/\Omega R$ as a function of mutual friction dissipation α. Note that the role of turbulence comes into play in a very different manner in these two types of flow: as nearly homogeneous and isotropic turbulence in ^{4}He in the Manchester experiments and, roughly speaking, via the deviation from laminar vortex front propagation, owing to turbulent excitations in ^{3}He-B in the Helsinki experiments.

It is striking that for $\alpha < 0.1$ (i.e., the regime where developed turbulence becomes possible) and before leveling off at $T \to 0$, the data for all experiments and numerical simulations discussed here approach a similar slope of $\sim \alpha^{0.5}$. For $\nu(\alpha)$ in the spirit of Equation (45), this implies that the parameter c_2^2 is roughly proportional to $\alpha^{-0.5}$ – even well below the values of α of the calculations by Schwarz (1988). On a finer scale, particular models of matching the classical and quantum cascades, as discussed in the previous subsection, might produce specific dependences of $c_2(\alpha)$, which perhaps can be tested in future experiments in more detail, provided that the quality of data is improved.

We do not attempt to compare the absolute values of ν/κ and v_f in Figure 44. Instead, we concentrate on the α-dependences, especially on the values of α at which the dissipation rates level off as $T \to 0$. The fact that the measured ^{3}He-B data level off at higher values of α might suggest that the quantum cascade in ^{3}He-B is not as developed as in ^{4}He and that the ultimate dissipative mechanism, independent of α in the $\alpha \to 0$ limit, is stronger and takes over at larger length scales in ^{3}He-B. Indeed, the numerically calculated velocity of front propagation $v_f(\alpha)$, which does not explicitly incorporate any excess dissipation beyond mutual friction dissipation and hence is equally suitable for ^{3}He-B and ^{4}He, is steadily decreasing with decreasing α, following the same trend as the experimental and numerical $\nu(T)$ for ^{4}He. In contrast, the measured $v_f(\alpha)$ levels off below $\alpha \sim 1 \cdot 10^{-2}$, which seems to imply that the $T = 0$ regime prevails at $\alpha < 1 \cdot 10^{-2}$ in ^{3}He-B, while this happens only below $\alpha < 1 \cdot 10^{-5}$ in ^{4}He. The fermionic nature, the large vortex core diameter, and the much lower absolute temperatures lead to different inherent dissipation mechanisms in ^{3}He-B. For example, the energy loss during each reconnection event can be substantial in ^{3}He-B but not in ^{4}He. This is supported by the fact that the
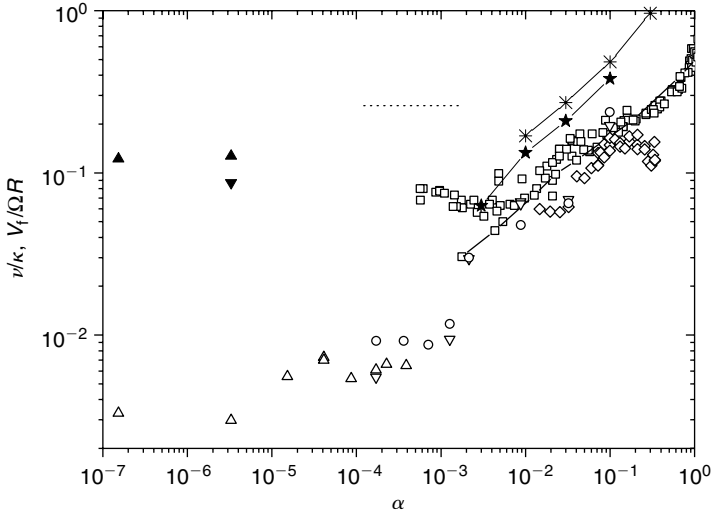
**FIGURE 44** Normalised measures of dissipation rate, the effective kinematic viscosity ν and the normalised velocity of the propagating vortex front $v_f = V_f / \Omega R$, as a function of mutual friction dissipation α in ^{4}He and ^{3}He-B: (i) $\nu(T)$ for quasiclassical turbulence in ^{4}He: spin-down, open triangles (Walmsley et al., 2007a); ion jet, open circles (Walmsley and Golov, 2008a); towed grid, open diamonds (Niemela et al., 2005; Stalp et al., 2002); (ii) $\nu(T)$ for ultraquantum turbulence in ^{4}He: colliding charged vortex rings, filled triangles (Walmsley and Golov, 2008a); numerical simulations, line-connected stars (Tsubota et al., 2000), and asterisks (Schwarz, 1988). (iii) $\nu(T)$ estimates for ultraquantum turbulence in ^{3}He-B: dashed line (Bradley et al., 2006). (iv) v_f in ^{3}He-B: experiment, open squares (Eltsov et al., 2007); and numerical simulations, line-connected squares (Section 3).

values of ν measured in Lancaster for ^{3}He-B with $a_0 \sim 30$ nm (at $P = 12$ bar) level off (i.e., branch away from the common trend of $\nu(\alpha)$ marked by the numerically calculated dependences) at larger values of $\alpha \sim 3 \cdot 10^{-2}$ than the measured front velocity v_f for $a_0 \sim 16$ nm (at $P = 29$ bar) at $\alpha \sim 1 \cdot 10^{-2}$. We conclude by noting that further work on turbulence in different types of flow in both ^{4}He and ^{3}He-B is highly desired.

4.4 Summary: Decay of Turbulence on Quasiclassical and Ultraquantum Scales

The newly developed technique of measuring the density L of a vortex tangle by the scattering of charged vortex rings of convenient radius $\sim 1\,\mu$m has made it possible to monitor the evolution of tangles in superfluid ^{4}He down to below 0.5 K, that is, deep into the zero-temperature limit. The dynamics of two very different types of tangles can be studied.

Quasiclassical tangles, mimicking the flow of classical liquids on large length scales, were generated by an impulsive spin-down from angular velocity Ω to rest of a rotating cubical container with helium. After a transient of duration $\sim 100/\Omega$, the turbulence becomes nearly isotropic and homogeneous and decays as $L \propto t^{-3/2}$, as expected for turbulence posessing a Kolmogorov cascade of energy from the energy-containing eddies of constant size, set by the container size h. This was studied in isotopically pure ^{4}He in a broad range of temperatures of 80 mK–1.6 K, corresponding to the range of mutual friction α from $\sim 10^{-10}$ to 10^{-1}. Identical results were obtained for the free decay of quasiclassical tangles generated by a central jet of ions although only at temperatures above 0.7 K so far.

Alternatively, nonstructured (ultraquantum) tangles of quantised vortices, that have little flow at scales above the inter-vortex distance and hence no classical analog, can be obtained by colliding many small quantised vortex rings of radius $R \ll \ell$ at temperatures below 0.5 K, that is in the zero-temperature limit. These tangles took about 10 s to spread from an injector into all experimental volume of size $h = 4.5$ cm, followed by free decay with the universal dynamics $L \propto t^{-1}$, independent of the initial conditions. The relatively fast rate of spreading is indeed surprising and might be due to the small polarisation (mean velocity) of the tangle.

Quantitative measurements of the free decay for both types of tangles allow the extraction of the 'effective kinematic viscosities' ν – the flow-specific parameter linking the rate of energy dissipation with the total density of vortices L. It turned out that at high temperatures $T > 1$ K, where the quantum cascade is not well developed, the values of ν for both types of turbulence are comparable. However, in the zero-temperature limit, where the dissipation can only take place at very short length scales $\ll \ell$, to which the energy can only be delivered by a cascade of nonlinear Kelvin-waves on individual vortex lines, the saturated value of ν for quasiclassical turbulence seems to be smaller than that for ultraquantum turbulence. On the microscopic level, this is most probably related to the fact that in the presence of quasiclassical eddies the partial mutual alignment of vortex lines in 'bundles' slows down the process of exciting Kelvin-waves for a given vortex density L. For instance, this mutual alignment is expected to reduce the frequency and efficiency of vortex reconnections, which are believed to be the defining process of the dynamics of nonstructured (ultraquantum) tangles as they fuel the Kelvin-wave cascade. At present, two microscopic models are developed to describe the energy transfer from classical to quantum scales (cascades) in quasiclassical tangles: one relying on reconnections and the other assuming that additional noncascading vortex density helps maintain the continuity of the energy flux down to the dissipative length scale.

We have also compared the rates of dissipation as a function of mutual friction in superfluid ^{4}He and ^{3}He-B. Both similarities and differences

in the behaviour are spotted and discussed. However, a final quantitative verdict on the role of specific mechanisms cannot be delivered at this stage, pending further development of theoretical models and of experiments on different types of turbulent flow in both superfluids.

5. SUMMARY

In the last five years, we have witnessed important advances in the understanding of the appearance, growth and decay of different types of superfluid turbulence, especially in the fundamentally important limit of zero temperature where the intrinsic processes within the superfluid component set the dynamics of the tangle of quantised vortices. As these are absolutely undamped on a broad range of length scales down to wavelengths of order $10\,\mathrm{nm}$–$1\,\mu\mathrm{m}$, depending on the type of superfluid, a principally new microscopic dynamics emerges – set by the instabilities of individual vortices, their reconnections and 1-dimensional cascades of energy from nonlinear Kelvin-waves (wave turbulence) along individual vortex lines. Amazingly, even in this limit, various turbulent flows behave classically on large length scales, and often the observed rate of decay is no different from that at high temperatures – owing to the fact that the energy-containing and dissipative lengths and times are well separated.

However, the discrete nature of quantised superfluid vorticity also becomes important in such processes as the growth of an initial seed vortex tangle out of a single-vortex instability, the efficiency of dissipating the energy of large-scale eddies through short-wavelength Kelvin-waves on individual vortex lines, or the dynamics of nonstructured tangles possessing no large-scale flow. In the helium superfluids these underlying processes are separately observable and are ultimately expected to become the corner stones of a detailed theoretical framework. This should make it possible to develop a consistent picture of turbulence in helium superfluids, which describes the nonlinear turbulent dynamics of discrete line vortices in a macroscopically coherent quantum liquid of zero viscosity.

ACKNOWLEDGEMENTS

REFERENCES

Adams, P. W., Cieplak, M. and Glaberson, W. I. (1985). *Physical Review B*, 32, 171.

Andronikashvili, E. L. and Mamaladze, Yu. G. (1967). Rotation of He II, in edited by Gorter, C. J. (ed.), *Progress Low Temperature Physics*, vol. V, p. 79, North-Holland Publications, Amsterdam.

Araki, T., Tsubota, M. and Nemirovskii, S. K. (2002). *Physical Review Letters*, 89, 145301.

Barenghi, C. F., Hulton, S. and Samuels, D. C. (2002). *Physical Review Letters*, 89, 275301.

Barenghi, C. F. and Skrbek, L. (2007). *Journal of Low Temperature Physics*, 146, 5.

Batchelor, G. K. (1953). *The Theory of Homogeneous Turbulence*. Cambridge University Press, Cambridge.

Berloff, N. G. and Roberts, P. H. (2000). *Journal of Physics A: Mathematical and General*, 33, 4025.

Berloff, N. G. and Roberts, P. H. (2000). *Physics Letters A*, 274, 69.

Bevan, T. D. C., Manninen, A. J., Cook, J. B., Armstrong, A. J., Hook, J. R. and Hall, H. E. (1997). *Journal of Low Temperature Physics*, 109, 423; (1995). *Physical Review Letters*, 74, 750.

Bewley, G. P., Lathrop, D. P. and Sreenivasan, K. R. (2006). *Nature*, 441, 588.

Bewley, G. P., Paoletti, M. S., Sreenivasan, K. R. and Lathrop, D. P. arXiv:0801.2872v1 [cond-mat.other].

Blaauwgeers, R., Eltsov, V. B., Eska, G., Finne, A. P., Haley, R. P., Krusius, M., Ruohio, J. J., Skrbek, L. and Volovik, G. E. (2002). *Physical Review Letters*, 89, 155301.

Blinnikov, S. I., Röpke, F. K., Sorokina, E. I., Gieseler, M., Reinecke, M., Travaglio, C., Hillebrandt, W. and Stritzinger. M. (2006). *Astronomy and Astrophysics*, 453, 229.

Borghesani, A. F. *Ions and Electrons in Liquid Helium*. Oxford Science Publications, Oxford.

Bowley, R. M., McClintock, P. V. E., Moss, F. E., Nancolas, G. G. and Stamp, P. C. E. (1982). *Philosophical Transactions of the Royal Society of London Series A*, 307, 201.

Bradley, D. I. (2000). *Physical Review Letters*, 84, 1252.

Bradley, D. I., Clubb, D. O., Fisher, S. N., Gu'enault, A. M., Haley, R. P., Matthews, C. J., Pickett, G. R., Tsepelin, V. and Zaki, K. (2006). *Physical Review Letters*, 96, 35301.

Bradley, D. I., Fisher, S. N., Guénault, A. M., Haley, R. P., O'Sullivan, S., Pickett, G. R. and Tsepelin, V. (2008). *Physical Review Letters*, 101, 065302.

Bruschi, L., Maraviglia, B., Mazzoldi, P. (1966). *Physical Review*, 84, 143.

Careri, G., Scaramuzzi, F. and Thomson, J. O. (1960). *Nuovo Cimento*, 18, 957.

Careri, G., McCormic, W. D. and Scaramuzzi, F. (1962). *Physics Letters*, 1, 61.

Chagovets, T. V., Gordeev, A. V. and Skrbek, L. (2007). *Physical Review E*, 76, 027301.

Chanal, O., Chabaud, B., Castaing, B. and Hebral, B. (2000). *European Physical Journal B*, 17, 309.

Cheng, D. K., Cromar, M. W. and Donnelly, R. J. (1973). *Physical Review Letters*, 33, 1197.

Connaughton, C. and Nazarenko, S. V. (2004). *Physical Review Letters*, 92, 044501.

Davis, S. I., Hendry, P. C. and McClintock, P. V. E. (2000). *Physica B*, 280, 43.

Donnelly, R. J. *Quantized Vortices in Helium II*. Cambridge University Press, Cambridge.

Donnelly, R. J. and Barenghi, C. F. (1998). *The Journal of Physical Chemistry Reference Data*, 27, 1217; http://www.uoregon.edu/~rjd/vapor1.htm.

Eltsov, V. B., Blaauwgeers, R., Kopnin, N. B., Krusius, M., Ruohio, J. J., Schanen, R. and Thuneberg, E. V. (2002). *Physical Review Letters*, 88, 065301.

Eltsov, V. B., Krusius, M. and Volovik, G. E. (2005). Vortex Formation and Dynamics in Super-fluid ^{3}He and Analogies in Quantum Field Theory, in edited by Halperin, W. P. (ed.), *Progress Low Temperature Physics*, vol. XV, p. 1, Elsevier B. V., Amsterdam.

Eltsov, V. B., Krusius, M. and Volovik, G. E. (2006a). *Journal of Low Temperature Physics*, 145, 89.

Eltsov, V. B., Finne, A. P., Hänninen, R., Kopu, J., Krusius, M., Tsubota, M. and Thuneberg, E. V. (2006b). *Physical Review Letters*, 96, 215302.

Eltsov, V. B., Golov, A., de Graaf, R., Hänninen, R., Krusius, M., L'vov, V. and Solntsev, R. E. (2007). *Physical Review Letters*, 99, 265301.

Eltsov, V. B., de Graaf, R., Hänninen, R., Krusius, M. and Solntsev, R. E. (2008). *Journal of Low Temperature Physics*, 150, 373.

Fetter, A. L. (1976). in edited by Bennemann, K. H. and Ketterson, J. B. (eds.), *The Physics of Liquid and Solid Helium*, Wiley, New York.

Feynman, R. P. (1955). Application of Quantum Mechanics to Liquid Helium, in edited by Gorter, C. J. (ed.), *Progress Low Temperature Physics*, vol. I, p. 17, North-Holland Publication, Amsterdam.

Finne, A. P., Araki, T., Blaauwgeers, R., Eltsov, V. B., Kopnin, N. B., Krusius, M., Skrbek, L., Tsubota, M. and Volovik, G. E. (2003). *Nature*, 424, 1022.

Finne, A. P., Boldarev, S., Eltsov, V. B. and Krusius, M. (2004a). *Journal of Low Temperature Physics*, 135, 479.

Finne, A. P., Boldarev, S., Eltsov, V. B. and Krusius, M. (2004b). *Journal of Low Temperature Physics*, 136, 249.

Finne, A. P., Eltsov, V. B., Blaauwgeers, R., Krusius, M., Janu, Z. and Skrbek, L. (2004c). *Journal of Low Temperature Physics*, 134, 375.

Finne, A. P., Eltsov, V. B., Eska, G., Hänninen, R., Kopu, J., Krusius, M., Thuneberg, E. V. and Tsubota, M. (2006a). *Physical Review Letters*, 96, 85301.

Finne, A. P., Eltsov, V. B., Hänninen, R., Kopnin, N. B., Kopu, J., Krusius, M., Tsubota, M. and Volovik, G. E. (2006b). *Reports on Progress in Physics*, 69, 3157.

Fisher, S. N. and Pickett, G. R. (2008). this volume.

Frisch, U. (1995). *Turbulence*. Cambridge University Press, Cambridge.

Glaberson, W. I., Johnson, W. W. and Ostermeier, R. M. (1974). *Physical Review Letters*, 33, 1197; Ostermeier, R. M. and Glaberson, W. I. (1975). *Journal of Low Temperature Physics*, 21, 191.

Glaberson, W. I. and Donnelly, R. J. (1986). Structure, Distributions and Dynamics of Vortices in Helium II, in edited by Brewer, D. F. (ed.), *Progress in Low Temperature Physics*, vol. IX, North-Holland Publications, Amsterdam.

Golov, A. and Ishimoto, H. (1998). *Journal of Low Temperature Physics*, 113, 957.

Goto, R., Fujiyama, S., Yano, H., Nago, Y., Hashimoto, N., Obara, K., Ishikawa, O., Tsubota, M. and Hata, T. (2008). *Physical Review Letters*, 100, 045301.

de Graaf, R., Solntsev, R. E., Chagovets, T. V., Eltsov, V. B., Hänninen, R. and Krusius, M. (2007). *Journal of Low Temperature Physics*, in print (2008); Preprint arXiv:0708.3003v1 [cond-mat].

Guenin, B. M. and Hess, G. B. (1978). *Journal of Low Temperature Physics*, 33, 243.

Guo, W. and Maris, H. (2007). *Journal of Low Temperature Physics*, 148, 199.

Hall, H. E. and Vinen, W. F. (1956). *Proceedings of the Royal Society (London, Ser. A)*, 238, 204; Vinen, W. F. (1957). ibid. 240, 114; (1957). 240, 128; (1957). 242, 489.

Hänninen, R., Blaauwgeers, R., Eltsov, V. B., Finne, A. P., Krusius, M., Thuneberg, E. V. and Volovik, G. E. (2003). *Physical Review Letters*, 90, 225301.

Hänninen, R., Mitani, A. and Tsubota, M. (2005). *Journal of Low Temperature Physics*, 138, 589.

Hänninen, R. (2006). Movies on Calculated Vortex Front Propagation, can be viewed at the site http://www.ltl.tkk.fi/~rhannine/front.

Hänninen, R., Eltsov, V. B., Finne, A. P., de Graaf, R., Kopu, J., Krusius, M. and Solntsev, R. E. (2007a). Submitted to Physical Review B, Preprint arXiv:condmat/0701647v2.

Hänninen, R., Tsubota, M. and Vinen, W. F. (2007b). *Physical Review B*, 75, 064502.

Hashimoto, N., Goto, R., Yano, H., Obara, K., Ishikawa, O. and Hata, T. (2007). *Physical Review B*, 76, 020504.

van Heijst, G. J. F. (1989). *Journal of Fluid Mechanics*, 206, 171.

Hendry, P. C., Lawson, N. S., McClintock, P. V. E. and Williams, C. D. H. (1988). *Physical Review Letters*, 60, 604.

Hendry, P. C., Lawson, N. S., McClintock, P. V. E., Williams, C. D. H. and Bowley, R. M. (1990). *Philosophical Transactions*, 332, 387.

Ihas, G. G., Labbe, G., Liu, S. C. and Thompson, K. J. (2008). *Journal of Low Temperature Physics*, 150, 384.

Kasamatsu, K., Machida, M., Sasa, N. and Tsubota, M. (2005). *Physical review A*, 71, 063616.

Kivotides, D., Vassilicos, J. C., Samuels, D. C. and Barenghi, C. F. (2001). *Physical Review Letters*, 86, 3080.

Kobayashi, M. and Tsubota, M. (2005). *Physical Review Letters*, 94, 065302.

Kobayashi, M. and Tsubota, M. (2008). Journal of Low Temperature Physics, 150, 402; *Journal of Low Temperature Physics*, 150, 587.

Kolmakov, G. V., Efimov, V. B., Ganshin, A. N., McClintock, P. V. E. and Mezhov-Deglin, L. P. (2006). *Physical Review Letters*, 97, 155301.

Kolmogorov, A. N. (1941a). Doklady Akademii Nauk SSSR, 30, 301 (reprinted in 1991, *Proceedings of the Royal Society Series A*, 434, 9).

Kolmogorov, A. N. (1941b). Doklady Akademii Nauk SSSR, 31, 538 (reprinted in 1991, *Proceedings of the Royal Society Series A*, 434, 15).

Kopnin, N. B. and Salomaa, M. M. (1991). *Physical Review B*, 44, 9667.

Kopnin, N. B. (2001). *Theory of Nonequilibrium Superconductivity*. Clarendon Press, Oxford.

Kopnin, N. B. (2004). *Physical Review Letters*, 92, 135301.

Kopu, J., Schanen, R., Blaauwgeers, R., Eltsov, V. B., Krusius, M., Ruohio, J. J. and Thuneberg, E. V. (2000). *Journal of Low Temperature Physics*, 120, 213.

Kopu, J. (2006). *Journal of Low Temperature Physics*, 146, 47.

Kozik, E. V. and Svistunov, B. V. (2004). *Physical Review Letters*, 92, 035301.

Kozik, E. V. and Svistunov, B. V. (2005a). *Physical Review Letters*, 94, 025301.

Kozik, E. V. and Svistunov, B. V. (2005b). *Physical Review B*, 72, 172505.

Kozik, E. V. and Svistunov, B. V. (2008a). *Physical Review B*, 77, 060502.

Kozik, E. V. and Svistunov, B. V. (2008b). *Physical Review Letters*, 100, 195302.

Kovasznay, L. J. (1947). *Aeronautical Science*, 15, 745.

Krusius, M., Kondo, Y., Korhonen, J. and Sonin, E. B. (1993). *Physical Review B*, 47, 15113.

Leith, C. (1967). *The Physics of Fluids*, 10, 1409; (1968). *The Physics of Fluids*, 11, 1612.

L'vov, V. S., Nazarenko, S. V. and Volovik, G. E. (2004). *JETP Letters*, 80, 535.

L'vov, V. S., Procaccia, I. and Rudenko, O. (2006a). *JETP Letters*, 84, 67.

L'vov, V. S., Nazarenko, S. V. and Skrbek, L. (2006b). *Journal of Low Temperature Physics*, 145, 125.

L'vov, V. S., Nazarenko, S. V. and Rudenko, O. (2007a). *Physical Review B*, 76, 024520.

L'vov, V. S., Pomyalov, A., Ferrante, A. and Elghobashi, S. (2007b). *JETP Letters*, 86, 102.

L'vov, V. S., Nazarenko, S. V. and Rudenko, O. (2008). *Journal of Low Temperature Physics*, in print (2008); preprint arXiv:0807.1258v1 [physics.flu-dyn].

Marees, G., Mudde, R. F. and van Beelen, H. (1987). *Physica* 144B, 292; Slegtenhorst, R. P., Marees, G. and van Beelen, H. (1982), *ibid.* 113B, 367; van Beelen, H., van Joolingen, W. and Yamada, K. (1988), *ibid.* 153B, 248.

Maurer, J. and Tabeling, P. (1998). *Europhysics Letters*, 43, 29.

Milliken, F. P., Schwarz, K. W. and Smith, C. W. (1982). *Physical Review Letters*, 48, 1204.

Nichol, H. A., Skrbek, L., Hendry, P. C. and McClintock, P. V. E. (2004). *Physical Review Letters*, 92, 244501.

Niemela, J. J., Sreenivasan, K. R. and Donnelly, R. J. (2005). *Journal of Low Temperature Physics*, 138, 537.

Ostermeier, R. M. and Glaberson, W. I. (1974). *Physics Letters*, 49A, 223.

Parker, N. G. and Adams, C. S. (2005). *Physical Review Letters*, 95, 145301.

Peixinho, J. and Mullin, T. (2006). *Physical Review Letters*, 96, 094501; *Journal of Low Temperature Physics*, 145, 75.

Pope, S. B. (2000). *Turbulent Flows*. Cambridge University Press, Cambridge.

Rayfield, G. W. and Reif, F. (1964). *Physical Review*, 136, A1194.

Rellergert, W. G., Cahn, S. B., Garvan, A., Hanson, J. C., Lippincott, W. H., Nikkel, J. A. and McKinsey, D. N. (2008). *Physical Review Letters*, 100, 025301.

Roche, P.-E., Diribarne, P., Didelot, T., Francais, O., Rousseau, L. and Willaime, H. (2007). *Europhysics Letters*, 77, 66002.

Ruutu, V. M. H., Parts, Ü., Koivuniemi, J. H., Kopnin, N. B. and Krusius, M. (1997). *Journal of Low Temperature Physics*, 107, 93; see also Parts, Ü., Ruutu, V. M. H., Koivuniemi, J. H., Bunkov, Yu. M., Dmitriev, V. V., Fogelström, M., Huebner, M., Kondo, Y., Kopnin, N. B., Korhonen, J. S., Krusius, M., Lounasmaa, O. V., Soininen, P. I. and Volovik, G. E. (1995). *Europhysics Letters*, 31, 449.

Ruutu, V. M. H., Eltsov, V. B., Krusius, M., Makhlin, Yu. G., Plaçais, B. and Volovik, G. E. (1998a). Physical Review Letters, 80, 1465.

Ruutu, V. M., Ruohio, J. J., Krusius, M., Plaçais, B. and Sonin, E. B. (1998b). *Physica B*, 225, 27.

van Saarloos, W. (2003). *Physics Reports*, 386, 29.

Schoepe, W. (2004). *Physical Review Letters*, 92, 095301.

Schwarz, K. W. and Donnelly, R. J. (1966). *Physical Review Letters*, 17, 1088.

Schwarz, K. W. (1975). In edited by Prigogine, I. and Rice, S. A. (eds.), *Advances in Chemical Physics*, vol. 33, p. 3, Wiley, New York.

Schwarz, K. W. (1985). *Physical Review B*, 31, 5782.

Schwarz, K. W. (1988). *Physical Review B*, 38, 2398.

Schwarz, K. W. and Rozen, J. R. (1991). *Physical Review B*, 44, 7563.

Van Sciver, S. W. and Barenghi, C. F. (2008). this volume.

Sergeev, Y. A., Barenghi, C. F. and Kivotides, D. (2006). *Physical Review B*, 74, 184506.

Simola, J. T., Nummila, K. K., Hirai, A., Korhonen, J. S., Schoepe, W. and Skrbek, L. (1986). *Physical Review Letters*, 57, 1923.

Skrbek, L. (2004). *JETP Letters*, 80, 474.

Smith, M. R., Donnelly, R. J., Goldenfeld, N. and Vinen, W. F. (1993). *Physical Review Letters*, 71, 2583.

Smith, M. R., Hilton, D. K. and Van Sciver, S. W. (1999). *The Physics of Fluids*, 11, 751.

Solntsev, R. E., de Graaf, R., Eltsov, V. B., Hänninen, R. and Krusius, M. (2007). *Journal of Low Temperature Physics*, 148, 311.

Sonin, E. B. (1987). *Reviews of Modern Physics*, 59, 87.

Sreenivasan, K. R. (1995). *The Physics of Fluids*, 7, 2778.

Stalp, S. R., Skrbek, L. and Donnelly, R. J. (1999). *Physical Review Letters*, 82, 4831.

Stalp, S. R., Niemela, J. J., Vinen, W. F. and Donnelly, R. J. (2002). *The Physics of Fluids*, 14, 1377.

Svistunov, B. V. (1995). *Physical Review B*, 52, 3647.

Swanson, C. E., Barenghi, C. F. and Donnelly, R. J. (1983). *Physical Review Letters*, 50, 190.

Todoshchenko, I. A., Alles, H., Babkin, A., Ya Parshin, A. and Tsepelin, V. (2002). *Journal of Low Temperature Physics*, 126, 1449.

Tough, J. T. (1982). Superfluid Turbulence, in edited by Brewer, D. F. (ed.), *Progress Low Temperature Physics*, vol. VIII, p. 133, North-Holland Publications, Amsterdam.

Tsubota, M., Araki, T. and Nemirovskii, S. K. (2000). *Physical Review B*, 62, 11751.

Tsubota, M., Araki, T. and Barenghi, C. F. (2003). *Physical Review Letters*, 90, 205301.

Tsubota, M. and Kobayashi, M. (2008). this volume.

Vinen, W. F. (1957a). *Proceedings of the Royal Society of London Series A*, 240, 114.

Vinen, W. F. (1957b). *Proceedings of the Royal Society of London Series A*, 240, 128.

Vinen, W. F. (1957c). *Proceedings of the Royal Society of London Series A*, 242, 493.

Vinen, W. F. (1958). *Proceedings of the Royal Society of London Series A*, 243, 400.

Vinen, W. F. (1961). Vortex Lines in Liquid Helium II, in edited by Gorter, C. J. (ed.), *Progress Low Temperature Physics*, vol. III, p. 1–57, Elsevier Publications, Amsterdam.

Vinen, W. F. (1963). in edited by Careri, G. (ed.), *Liquid Helium*, p. 336, Academic Press, New York.

Vinen, W. F. (2000). *Physical Review B*, 61, 1410.

Vinen, W. F. (2001). *Physical Review B*, 64, 134520.

Vinen, W. F. and Niemela, J. (2002). *Journal of Low Temperature Physics*, 128, 167.

Vinen, W. F. (2002). *Journal of Low Temperature Physics*, 126, 333.

Vinen, W. F., Tsubota, M. and Mitani, A. (2003). *Physical Review Letters*, 91, 135301.

Vinen, W. F. (2005). *Physical Review B*, 71, 024513.

Vinen, W. F. (2006). *Journal of Low Temperature Physics*, 145, 7.

Vinen, W. F. and Donnelly, R. J. (2007). *Physics Today*, 43.

Vinen, W. F. and Skrbek, L. (2008). this volume.

Volovik, G. E. (2003). Pisma ZhETF, 78, 1021; (2003). *JETP Letters*, 78, 533.

Volovik, G. E. (2004). *Journal of Low Temperature Physics*, 136, 309.

Walmsley, P. M., Golov, A. I., Hall, H. E., Levchenko, A. A. and Vinen, W. F. (2007a). *Physical Review Letters*, 99, 265302.

Walmsley, P. M., Levchenko, A. A., May, S. E. and Golov, A. I. (2007b). *Journal of Low Temperature Physics*, 146, 511.

Walmsley, P. M. and Golov, A. I. (2008a). *Physical Review Letters*, 100, 245301.

Walmsley, P. M. and Golov, A. I. (2008b). unpublished.

Winiecki, T. and Adams, C. S. (2000). *Europhysics Letters*, 52, 257.

Yarmchuk, E. J., Gordon, M. J. V. and Packard, R. E. (1979). *Physical Review Letters*, 43, 214.

Zhang, T. and Van Sciver, S. W. (2005). *Journal of Low Temperature Physics*, 138, 865.

Quantum Turbulence in Superfluid ^{3}He at Very Low Temperatures

S. N. Fisher* and **G. R. Pickett***

Contents			

* Department of Physics, Lancaster University, Lancaster, LA1 4YB, United Kingdom

Abstract   Turbulence is a very complex motion of a fluid which occurs at sufficiently high flow rates in a wide range of physical systems and has far-reaching technological implications. Although the underlying equations of fluid dynamics are well known, a comprehensive theoretical description of turbulence is a major unresolved problem of classical physics. A better understanding of turbulence might be gained by investigating systems which offer simplifications. Quantum turbulence is represented by the seemingly complex dynamics of a tangle of quantised vortex lines in a superfluid. At very low temperatures, there is no normal fluid component and therefore no associated viscosity. These are very simple conditions, both from conceptual and mathematical view points. We have recently developed techniques for detecting quantum turbulence in superfluid ^{3}He-B in the low temperature limit. We use quasiparticle excitations to directly probe the superfluid flow field. We describe various experiments investigating the production, evolution and decay of quantum turbulence. The results obtained give the first empirical steps towards addressing a number of interesting questions, such as how closely does quantum turbulence resemble classical turbulence and how does quantum turbulence decay in the absence of the viscous dissipation.

1. QUANTUM TURBULENCE

Quantum turbulence, as we use the term in this chapter, refers to the complex rotational behaviour of a pure superfluid condensate. This is a fascinating subject in its own right since rotation manifests itself as an array or tangle (depending on circumstances) of similar quantised vortices. In the absence of a viscous normal fluid component, the coherent nature of a condensate such as in ^{4}He or ^{3}He-B obeys Euler's equation, with constraints $\nabla \cdot v = 0$ and $\nabla \times v = 0$, rather than the Navier-Stokes equations for a classical fluid. As the constraint does not allow rotational motion, rotation can only be introduced by the introduction of vortices where the condensate is distorted/suppressed in the central core region. In this chapter, we first discuss how a random tangle of such vortices can be detected at low temperatures. Armed with these tools, we look at some properties and 'applications' of vortex tangles, and finally we discuss the interesting problem of how such a vortex tangle can decay in the absence of any 'conventional' viscous dissipation processes. Lurking behind this interest is our knowledge that despite the fact that turbulent behaviour is seen on all length scales from the cosmological to the subnuclear and impacts on all aspects of human endeavour, we still lack a satisfactory 'theory' of turbulence. The behaviour of a viscid fluid is still too complex to admit a full analytical solution of the detailed

motion. Classical turbulence with its wide range of eddy sizes and eddy amplitudes is a very hard problem to grapple with, both from mathematical and conceptual view points. In the quantum turbulence case, we feel we have, in our identical building blocks of quantised vortices, the making of an 'atomic theory' of turbulence which we hope may shed some light and insight on the more intractable scenario of classical turbulence.

Quantum turbulence can in principle exist in the superfluid states of the two isotopes of helium ^{4}He and ^{3}He, and in Bose-Einstein condensates. In this chapter, we focus our attention on the B-phase of superfluid ^{3}He where we have so far acquired the majority of our empirical knowledge of quantum turbulence in the low temperature regime.

2. DETECTION OF QUANTUM VORTICITY BY THE QUASIPARTICLE GAS

2.1 Andreev Scattering of a Quasiparticle Beam by a Vortex Line

Superfluid ^{3}He-B is ideal for studies of quantum turbulence since its mechanical properties are quite simple, similar to superfluid ^{4}He, and its vortices are quite easy to detect even at very low temperatures. We are very fortunate that the Andreev scattering (Andreev, 1964; Enrico et al., 1993) of quasiparticles by the flow field around a vortex is so strong that we can easily observe vortices via the reflected quasiparticles. This mechanism provides a very powerful tool for studying vortices and turbulence in the low temperature regime.

Let us begin by considering the dispersion curve of the ^{3}He quasiparticle excitations, shown in the upper part of Figure 1. This dispersion curve is tied to the reference frame of the superfluid condensate, which implies that in a frame moving with respect to the condensate (or equivalently, in a frame in which the condensate moves with velocity v) the curve becomes tilted since in the moving frame the excitation energies undergo a Galilean transformation,

$$E(\mathbf{p}) \rightarrow E(\mathbf{p}) + \mathbf{p} \cdot \mathbf{v},\tag{1}$$

as shown in the lower part of Figure 1.

In consequence, the effective potential seen by the quasiparticle excitations (i.e., the appropriate minimum in the dispersion curve) varies with the local liquid velocity as

$$E_{min} = \Delta + \mathbf{p} \cdot \mathbf{v}(\mathbf{r}).\tag{2}$$
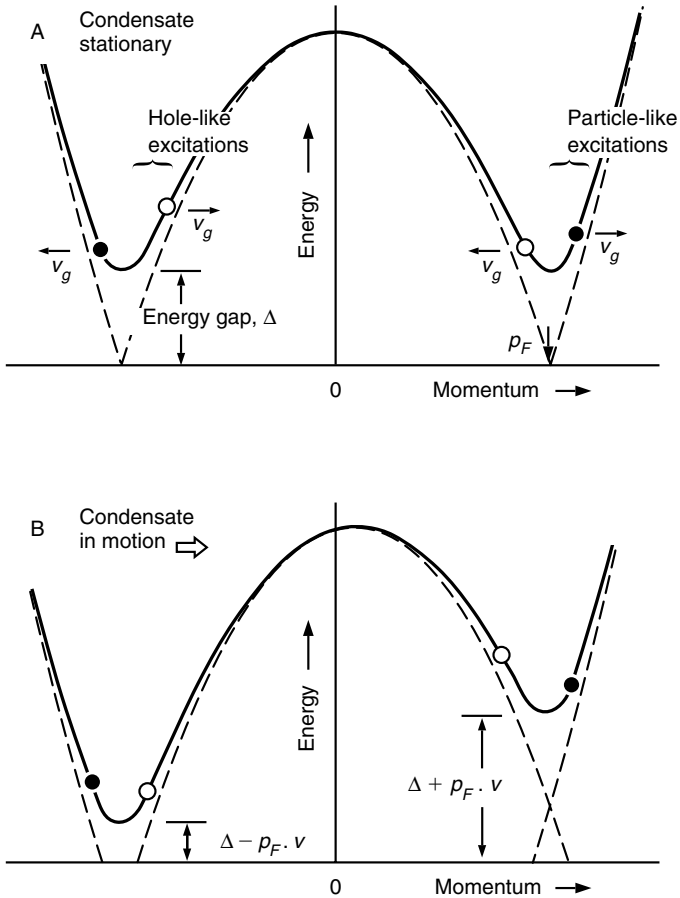
FIGURE 1   The dispersion curves for the quasiparticle excitations. A: for stationary condensate. There are two classes of excitations; quasiparticles (filled circles) with the group velocity parallel to the momentum and quasiholes (open circles) with group velocity antiparallel to the momentum. B: when the condensate is moving relative to the observer, the dispersion curve is tipped by the Galilean transformation.

The flow field around a vortex thus presents a local barrier to excitations with the appropriate momentum direction. If an incoming excitation has a lower energy than the barrier height, then it must be Andreev reflected. It is this effect which allows us to detect vortices.

The situation in the presence of a vortex is shown in Figure 2. First we consider excitations incident on the upper side of the vortex from the left. The appropriate dispersion curves (top of Figure 2) are given for the
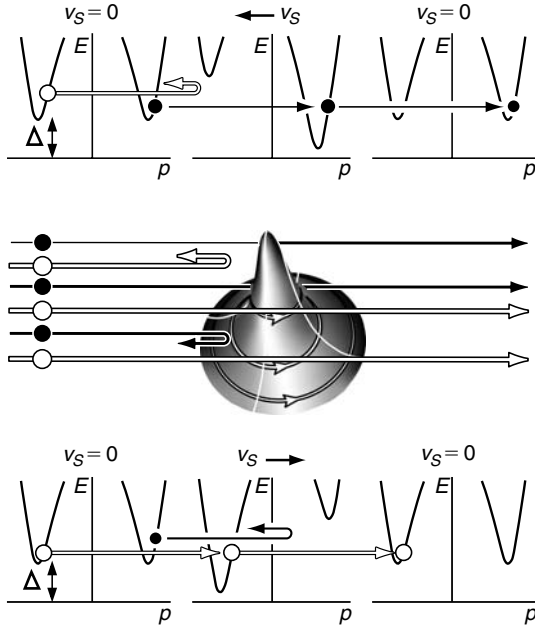
FIGURE 2 Top and bottom, the dispersion curves in the vicinity of the vortex line, on left and right the un-tilted bulk dispersion curves and in the centre the curves tilted by the vortex flow field. Centre: above the vortex, quasiparticles pass unimpeded but a fraction of quasiholes are Andreev reflected; below the vortex, quasiholes pass while a fraction of quasiparticles are reflected, creating an excitation shadow.

stationary superfluid (far to the left and right of the vortex) and for the moving superfluid close to the vortex (top centre). Consider excitations approaching from the left. The excitations move with constant energy in the laboratory reference frame. Since the tipping of the dispersion curve is downwards for quasiparticles moving to the right, these excitations pass through the flow unimpeded. (The group velocity actually increases as the quasiparticle energy in the condensate rest frame increases in the flow field.) Therefore, the full flux of quasiparticles incident on the top side of the vortex line is transmitted (here we neglect the core region of the vortex and the very small probability of 'over-barrier' reflection). However, for quasiholes on the upper side approaching from the left, their branch of the dispersion curve is tipped to higher energies. In this case, the flow presents an effective energy barrier. The quasihole will not have enough energy to pass if it passes too close to the core (where the flow velocity is higher). As the quasihole approaches, its energy in the superfluid reference frame decreases towards the energy minimum (the energy gap), and its group

velocity decreases. If it has insufficient energy, then its energy in the condensate frame will become equal to the energy gap at some point; here it is at the bottom of the dispersion curve and its group velocity is zero. The excitation is effectively pushed around the bottom of the dispersion curve by the flow gradient, and so it emerges as a quasiparticle with a group velocity in the opposite direction. The momentum transfer is extremely small (negligible) but the excitation trajectory is reversed. This, almost perfect retro-reflection, is called Andreev reflection (or Andreev scattering). The overall effect is that quasiholes passing close to the top side of the vortex are almost perfectly retroreflected, thus casting a quasihole shadow behind the vortex.

Referring to the lower half of Figure 2, on the lower side of the vortex, the flow direction is reversed, tipping the dispersion curve in the opposite direction, with the result that all the incident quasiholes are transmitted but quasiparticles which pass too close to the vortex are Andreev reflected, producing a particle shadow.

Overall, the vortex casts a symmetric shadow (a quasihole shadow on the top side, mirrored by a quasiparticle shadow on the bottom side). If we can measure the excitation flux (which we effectively do with vibrating wire techniques), then we can detect the vortex line. This is the essence of the technique. The important point to note (as we show below) is that the width of this shadow is very large, making quasiparticles very sensitive vortex line 'detectors'. We can calculate the width of the shadow as follows.

Consider a beam of thermal excitations incident from the left of the vortex line, as depicted in Figure 2. We can write the flux of incident excitations (number passing unit area per unit time) as

$$
\begin{aligned}
\langle nv_g \rangle_i &= \int_{\Delta}^{\infty} v_g(E)G(E)f(E)\mathrm{d}E \\
&= G(p_F) \int_{\Delta}^{\infty} \exp(-E/k_BT)\mathrm{d}E \\
&= G(p_F)k_BT\exp(-\Delta/k_BT) ,
\end{aligned}
\tag{3}
$$

where $v_g(E)$ is the group velocity of an excitation with energy E, $G(E)$ is the density of states function, $f(E)$ is the Fermi distribution function which approximates to the Boltzmann distribution at low temperatures, and $G(p_F)$ is the density of momentum states at the Fermi surface.

Consider a quasihole trajectory incident on the top side of the vortex with a distance of closest approach r (the impact parameter). The maximum tilt of the dispersion curve corresponding to the flow $\mathbf{v}(r)$ at this point is simply $\mathbf{p}_F \cdot \mathbf{v}(\mathbf{r}) = p_F\hbar/(2m_3r)$. Incident quasiholes will only be

transmitted if they have an energy greater than $\Delta + \mathbf{p}_F \cdot \mathbf{v(r)}$, so the flux transmitted is

$$
\begin{aligned}
\langle nv_g \rangle_t &= \int_{\Delta + p_F \hbar / 2m_3 r}^{\infty} v_g(E) G(E) f(E) \mathrm{d}E \\
&= G(p_F) \int_{\Delta + p_F \hbar / 2m_3 r}^{\infty} \exp(-E/k_B T) \mathrm{d}E \\
&= G(p_F) k_B T \exp[-(\Delta + p_F \hbar / 2m_3 r)/k_B T].
\end{aligned}
\tag{4}
$$

The fraction of the quasihole flux transmitted on the top side of the vortex is thus

$$
\begin{aligned}
f_t &= \langle nv_g \rangle_t / \langle nv_g \rangle_i \\
&= \exp(-p_F \hbar / 2m_3 r k_B T).
\end{aligned}
\tag{5}
$$

Similarly, this is also the fraction of quasiparticles transmitted on the bottom side of the vortex. (Note that all quasiparticles are transmitted on the top side of the vortex and all quasiholes are transmitted on the bottom side of the vortex.) The half width of the combined shadow $d = 2r$ is then obtained by setting $f_t = 1/2$ giving

$$
d = \frac{p_F \hbar}{m_3 k_B T \ln(2)}.
\tag{6}
$$

Or in terms of the circulation quantum $\kappa = h/2m_3$,

$$
d = \frac{p_F \kappa}{\pi k_B T \ln(2)}.
\tag{7}
$$

This equates to around $20\,\mu\mathrm{m}$ at $T = 100\,\mu\mathrm{K}$, which is of order a thousand times larger than the vortex core size. So vortices have an enormous cross-section for Andreev scattering quasiparticle excitations, which makes them relatively simple to observe using quasiparticle detection techniques (vibrating wire resonators).

2.2 Detecting a Cloud of Vorticity around a Vibrating Wire Resonator

The arguments of the previous section show how the vortex throws a shadow in an incident beam of excitations. In this section, we extend these ideas to the general problem of detecting a vortex tangle by a vibrating wire resonator (Guénault et al., 1986).

Vibrating wire techniques have been developed for many years in Lancaster specifically to probe the very dilute excitation gas in superfluid ^{3}He at the lowest achievable temperatures. The active part of the resonator is typically a ~3 mm loop of a fine (~5 μm) NbTi superconducting filament as shown in Figure 3. An alternating current is passed through the loop in a vertical magnetic field, which sets the loop oscillating. It resonates at a frequency, typically ~1 kHz, determined by the stiffness of the wire. As the wire moves through the field, it generates a Faraday voltage proportional to its velocity, which is measured with a lock-in amplifier. The quantity usually measured with a vibrating wire is its damping (damping force per unit velocity) which determines the frequency width Δf_2 of the resonance line.

The vortices may be detected by their effect on the vibrating wire damping. In the B-phase at low temperatures, the thermal damping arises from the normal scattering of ballistic excitations at the wire surface (Fisher et al., 1989). Counter-intuitively, the thermal damping is enhanced by orders of magnitude by the Andreev reflection of excitations by the superfluid backflow around the wire (Fisher et al., 1989), but we do not need to discuss the details here. The important point to note is that the damping is a sensitive measure of the flux of excitations incident on the wire. Since this flux varies rapidly with temperature, dominated by the Boltzmann factor $\exp(-\Delta/k_B T)$, the wires are often used as very sensitive thermometers at low temperatures (Bäuerle et al., 1998).

Figure 4 shows a simplified one-dimensional scenario representing the interaction of quasiparticles with a vibrating wire resonator in the presence of vortex lines. The scene is set in the top section, A. On the right, we show the vibrating wire surface moving slowly to the left taking the liquid near the surface with it and thus giving a slightly tilted dispersion curve near the wire. Some distance from the wire we have another region of rightward flow (generated by a nearby vortex) giving a tilted dispersion curve, and in between we have bulk undisturbed liquid with no dispersion curve
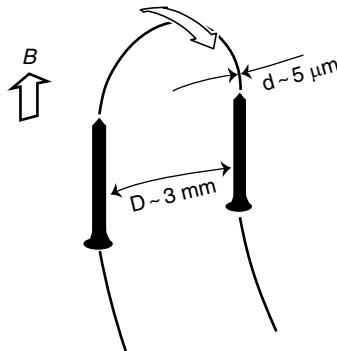
FIGURE 3   A typical vibrating wire resonator used for turbulence measurements.
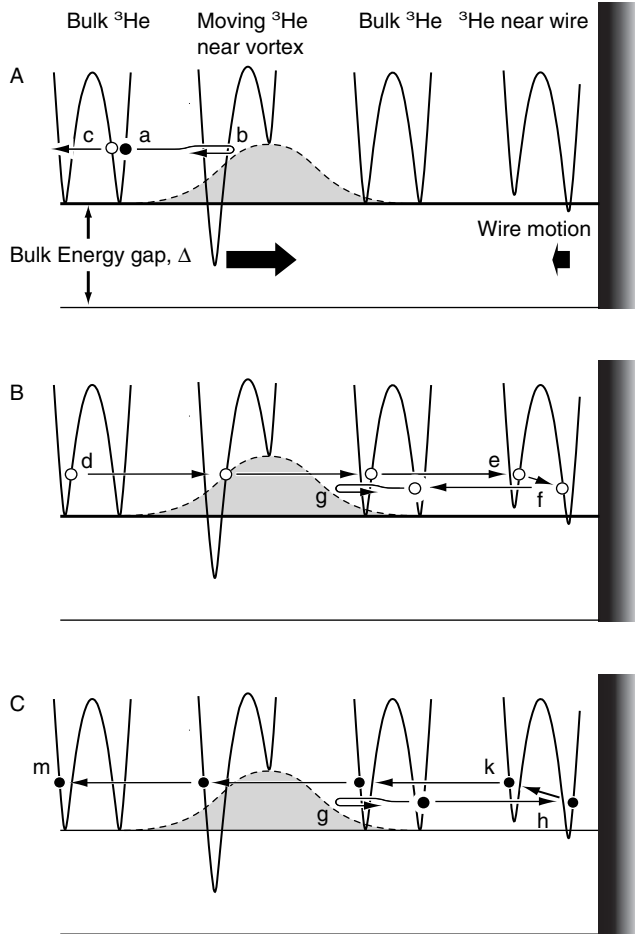
FIGURE 4 The trajectories (in one dimension) of excitations approaching a moving wire in the vicinity of a flow field which tips the dispersion curve locally. A: an incoming quasiparticle (a) cannot proceed through the flow region at (b) (see text) and is Andreev reflected to emerge (c) as a quasihole. B: an incoming quasihole (d) can pass through the flow region and reach the superfluid near the wire (e) where it is normally reflected (f) but now cannot penetrate the flow region and is Andreev reflected (g). C: it returns to the wire in as a quasiparticle (h), is normally reflected (k) and can now pass the flow region and emerges as a quasiparticle (m). In neither of these processes is significant momentum exchanged with the wire.

tilt. The region of flow near the vortex provides an effective barrier which is shaded. Since it is the right-hand side of the dispersion curve which rises, this barrier acts on rightward-traveling quasiparticles and leftward-traveling quasiholes. Furthermore, since this is a one-dimensional picture

and the wire surface is on the right, all incoming excitations are incident from the left.

There are two classes of incoming excitations: quasiparticles with momenta in the rightward direction and quasiholes with momenta in the reverse direction. Let us consider first incoming quasiparticles as shown in the top A section of the figure. An incoming quasiparticle at position 'a' comes into the flow field from the vortex and finds an increasing barrier which it cannot surmount. At 'b', it is Andreev reflected and retraces its path as a quasihole, 'c'. Thus all low-energy incoming quasiparticles are Andreev reflected and never reach the wire surface to exchange momentum with the wire. We should also note here that the condensate has a very limited capacity for absorbing the excitation momentum and the incoming quasiparticle and the outgoing quasihole have virtually the same momenta, only the group velocity is reversed (the dispersion curves are not drawn to scale).

Referring now to the central B section of the figure, there is an incident quasihole at 'd' which being on the other side of the dispersion curve does not experience a potential barrier. This quasihole travels all the way to the wire surface where it is normally scattered 'e' to 'f', exchanging $-2p_F$ of momentum with the wire (a quasihole exchanges negative momentum, pulling rather than pushing the wire). The small jump in energy on scattering at the wire surface is simply a reflection of the fact that the wire is moving in our laboratory frame, and it is in the wire frame that the scattering process is elastic. The quasihole retraces its path but now it does see the potential barrier and is Andreev reflected back to the wire at 'g'. Its subsequent trajectory continues in the lower panel C. At 'g' it returns to the wire as a quasiparticle, is normally scattered 'h' to 'k', now exchanging $2p_F$ of momentum with the wire, it no longer sees the potential barrier and emerges at 'm' still as a quasiparticle. The net result of this trajectory is that the excitation emerges with virtually the same momentum that it had initially, and the two normal scattering processes at the wire surface cancel out. Thus again no net momentum is exchanged with the wire for all low-energy incident quasiholes. It is clear that if the flow field were in the opposite direction, the same arguments would hold with the particle flavours exchanged, and also for particles incident on the wire from the rear rather than the front. Adding multiple flow regions does not change the result. Whatever the configuration of flow regions both flavours of low-energy excitations will emerge with virtually the same momentum as they had on entry and so will not damp the wire motion.

The vortex flow field acts like a momentum-space Maxwell demon ensuring that no momentum is exchanged with the wire by sufficiently low-energy excitations coming from infinity. When we first aired these ideas, there was much disquiet that in some way the laws of thermodynamics were being flouted. However, we should emphasise that apart

from the minuscule changes in energy of the excitations when normally scattered by the wire, the distribution of the excitation gas is unchanged. Note that summing over all three panels of the figure there are two incoming and two outgoing excitations in both of the two regions on the two sides of the barrier, and particle-hole symmetry is maintained as the net momentum of all trajectories in the two regions is zero. The flow field of surrounding vortices only influences how momentum is exchanged between the wire and thermal quasiparticle excitations. The removal of momentum exchange by low-energy excitations results in a proportionate reduction in the damping of the wire motion.

These very simple arguments can be extended to three dimensions; however, further considerations come into play. First, there is the geometrical effect that the vortex flow fields are localised and thus a large fraction of incoming excitations might reach the wire without experiencing any significant energy barrier and thus can damp the moving wire as normal. Furthermore, the above one-dimensional arguments assume that the Andreev reflection leads to a perfect retracing of the excitation trajectory ensuring the 'ideal' sequence of normal scatterings and Andreev reflection to give full momentum cancellation. Referring again to Figure 3 in the second and third panels, if the incoming quasihole which crosses unscathed the barrier is reflected in a slightly different direction and thus misses it after its first reflection, then it will not be reflected back to the wire and there will be no cancellation.

The precise details of the vibrating wire damping in the presence of surrounding vortex lines are quite complex. Indeed, the details of thermal quasiparticle damping even in the absence of vortex lines is a complex problem particularly for diffuse scattering at the wire surface (Enrico et al., 1995; Fisher et al., 1991). However, intuitively we know that the damping on a vibrating wire resonator is proportional to the overall net flux of excitations which are able to directly transverse the flow field to reach the wire surface, where they are normally scattered, effectively exchanging momentum between the wire and the walls of the cell where the excitations are thermalised. So the fractional reduction in damping caused by surrounding vortices represents the fraction of excitations (with some appropriate angular and spatial average) which are Andreev reflected by the intervening vortex flow field.

3. EARLY VIBRATING WIRE MEASUREMENTS

It had long been thought that turbulence could not be sustained in superfluid ³He since the normal fluid component is so viscous. It was by accident that turbulence in superfluid ³He-B (Fisher et al., 2000, 2001) was first discovered at very low temperatures with the experimental configuration

Heater
(Source) wire

Thermometer
(Detector) wire
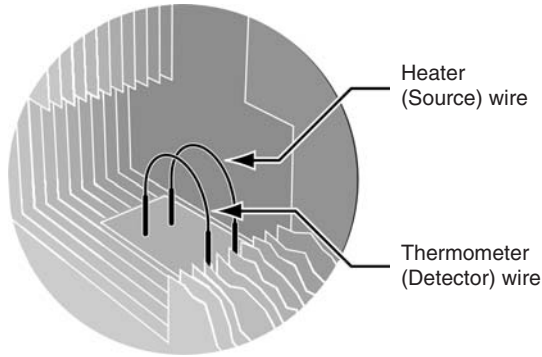
FIGURE 5   The experimental arrangement used for the first observation of turbulence in superfluid ^{3}He at low temperatures (see text).

shown in Figure 5. In this setup, there are two vibrating wire resonators, spaced 1 mm apart, intended for use as a heater and thermometer for an NMR experiment located in a different part of the cell. For the current purposes, we will refer to these as the detector and source wire. The wires are located in a cavity deep within the stack of copper plus silver sinter refrigerant plates.

The first observation was initially very puzzling. We would normally expect that when heat is injected into the cell on driving the heater (source) wire above its pair-breaking critical velocity (Fisher et al., 1992), the thermometer should show an increase in damping corresponding to the rise in quasiparticle density/temperature. This was indeed found to be the case at the lowest temperatures where the background quasiparticle density (before driving the source wire) was immeasurably small. However, at somewhat higher temperatures, in the presence of a significant background of thermal excitations, despite the production of nearby quasiparticles the detector wire damping actually decreased, as shown in Figure 6 (top). This was a counterintuitive result as it was very well known that the wire damping arises from quasiparticles, and an increased density of quasiparticles should lead to an increase in damping. If the detector wire damping fell while the source wire was being driven hard, then the only possible conclusion is that something is screening the detector wire from the thermal background quasiparticles. The only objects which could do this in the B-phase are vortices. Therefore, the source wire, as well as producing excess quasiparticles by pair-breaking, must also be generating vortices. The damping was also observed to be quite 'noisy' in the presence of the generated vorticity, implying that the source wire was generating an erratic vortex tangle, that is to say quantum turbulence.
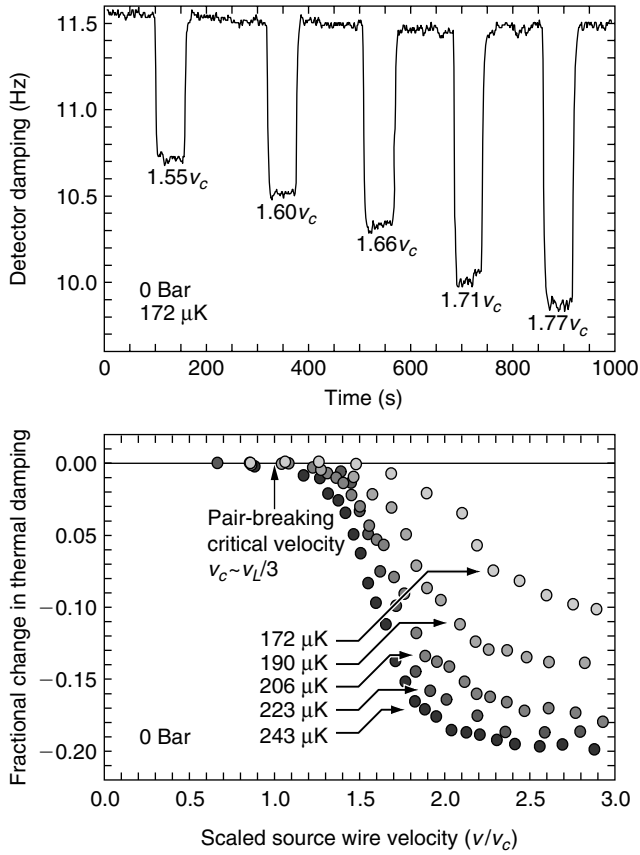
FIGURE 6 The first observations of turbulence in superfluid ³He-B. Top: the damping on the detector wire as the source wire is driven to various velocities (given in terms of the pair-breaking critical velocity). Bottom: the fractional reduction in the thermal damping of the detector wire (due to turbulence) as a function of the source wire velocity.

As argued in the previous section, the fractional change in the thermal damping of the detector wire measures the fraction of incident thermal quasiparticles which are Andreev reflected by the turbulent flow field. This may also be considered as a measure of the surrounding line density (to be discussed in more detail below). The fractional change in the detector wire thermal damping is shown in the lower half of Figure 6 as a function of the source wire velocity at various temperatures.

The data clearly show that turbulence from a vibrating wire is only produced above the pair-breaking critical velocity (equal to one-third of the Landau critical velocity, ~10mm/s at low pressures). This is an interesting

result, especially when compared with corresponding critical velocities in
^{4}He. The critical velocity for a similar vibrating wire to produce turbu-
lence in ^{4}He is of order a few tens of mm/s (Bradley et al., 2005a), roughly
a thousand times smaller than the Landau critical velocity in ^{4}He. The
very different behaviours can be explained by the size of the coherence
length and surface roughness. In superfluid ^{4}He the coherence length is
on the atomic scale (0.1 nm) making the superfluid sensitive to atomic
roughness. Any macroscopic object is in practice very rough on this scale
and able to hold remnant loops of vortices pinned to surface excrescences.
In relatively slow flows, these remnant vortices may grow, and recon-
nect producing turbulence. In consequence, potential vortices are always
lurking in surface imperfections and capable of growing at velocities way
below any theoretical nucleation velocity, in which case the Landau critical
velocity is irrelevant. In the case of superfluid ^{3}He, on the other hand, the
coherence length is much larger (~60 nm at low pressures). The superfluid
flow is not sensitive to roughness on any smaller scale, and the vibrating
wire surfaces appear smooth on this larger scale and so are unlikely to trap
vortices. Thus, for turbulence to be generated in superfluid ^{3}He, entirely
new vortices must be nucleated, and this requires a velocity close to that
of the pair-breaking critical velocity.

It is also clear from the data in Figure 6 that the fractional screening of
quasiparticles is smaller at higher temperatures. This is partly due to the
fact that the average energy of quasiparticles is higher at higher tempera-
tures, so they are more likely to be able to cross the energy barriers created
by the flow field.

To be more quantitative, the turbulent flow field can be considered as
creating a random terrain of peaks and troughs through which the quasi-
particles move. This is shown in Figure 7. Only peaks are drawn since the
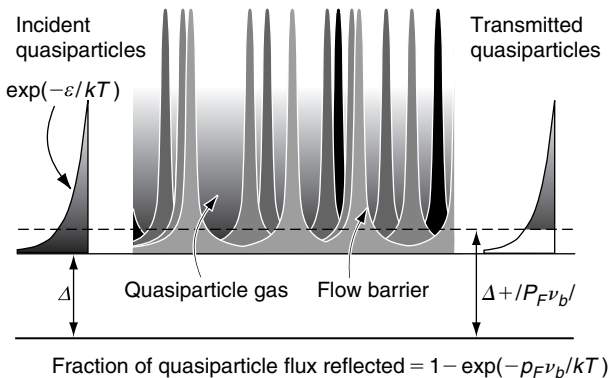
FIGURE 7 The effective flow barrier experienced by thermal excitations incident on
quantum turbulence.

troughs do not impede the excitation's motion, and we should remember that a flow providing a potential peak for a quasiparticle (quasihole) acts as a trough for a quasihole (quasiparticle) moving in the same direction. The peaks mark the regions of high flow velocity around the vortex cores. Excitations are incident with a thermal energy distribution as shown at the left. Low-energy excitations are Andreev reflected, and only higher energy excitations are transmitted. The effect of the flow can then be modeled as an effective flow barrier $p_F v_b$, corresponding to an angular-averaged maximum flow v_b along quasiparticle trajectories incident on the detector. The fractional screening (reduction in thermal damping) can then be written as

$$f = 1 - \exp(-p_F v_b / k_B T). \tag{8}$$

The inferred flow barrier as a function of source wire velocity is shown in Figure 8.

    As shown in the figure, the maximum flow barriers observed are of order 1 mm/s or less. To put this in perspective, this is the flow that would be observed at a distance of order 10 to 100 μm from a vortex core, so this sets a lower limit to the vortex line spacing in the turbulent tangle. It was not possible to obtain a precise number for the line density for this experiment since the fractional screening also depends on the size of the turbulent tangle, which was only measured later (see below).

    Note also that the effective flow barrier is measured to become independent of temperature below about $0.22 T_c$. This suggests that the low temperature regime has been reached where the dissipation of the vortex tangle (which must limit its size/density) becomes temperature
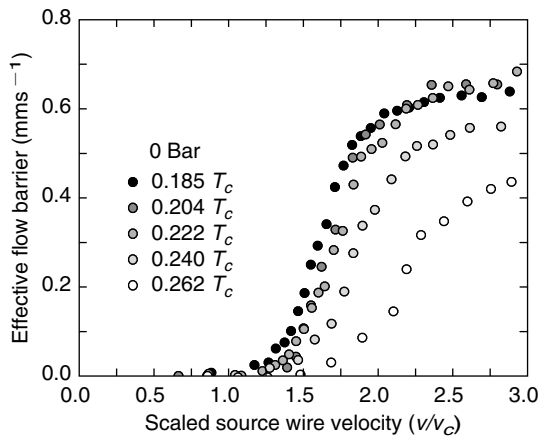
FIGURE 8   The effective flow barrier measurements for turbulence produced by a vibrating wire resonator.

independent, no longer governed by thermal excitations (normal fluid component). In the low temperature regime where the thermal excitation density is virtually zero, some other dissipation mechanism must operate, dependent on the quantum nature of vortex lines.

4. SPATIAL DISTRIBUTION OF TURBULENCE PRODUCED FROM A VIBRATING WIRE RESONATOR IN ^{3}HE-B

After the first observations of turbulence, we began to investigate its properties in a more systematic way. In the first purpose-built experiment, we set out to measure the spatial extent of the turbulence produced by a vibrating wire resonator (Bradley et al., 2003). The experimental arrangement used for this is shown in Figure 9.

Six vibrating wire resonators are positioned in a row, with ~1 mm separation. One wire is chosen as the source wire. The source is driven hard to produce turbulence while we monitor the damping on the other (detector) wires continuously. Vortices are detected via the associated Andreev scattering of excitations, which causes a proportionate decrease in the thermal damping of the detector wires as discussed above. The fractional reduction in damping gives a measure of the surrounding vortex line density. Figure 9 also illustrates the fact that the vibrating wire produces both turbulence and a beam of ballistic quasiparticles when driven above its critical velocity. From other experiments (Fisher et al., 1992), we know that the quasiparticle beam is quite narrowly focussed along the axis of motion.

The fractional reduction in damping as a function of distance from the source wire (corresponding to different detector wires) is shown in Figure 10, plotted on a log-linear scale. We see that the spatial decay of the
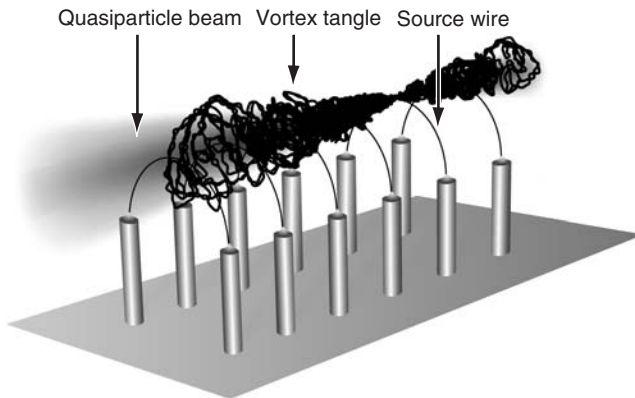
FIGURE 9   Schematic diagram showing the experimental arrangement for measuring the spatial extent of turbulence produced by a vibrating wire resonator.
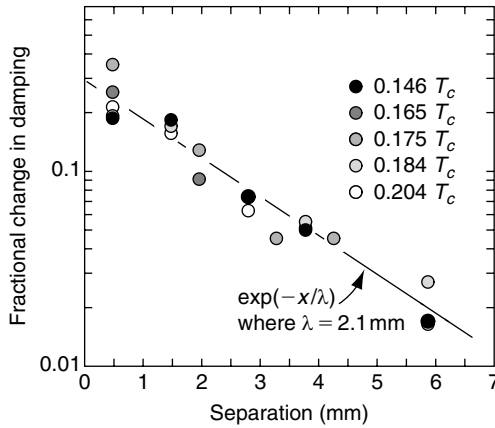
FIGURE 10   Measurements of the spatial extent of turbulence produced by a vibrating wire resonator. Data show the fractional reduction in damping (fraction of Andreev screening by vortices) as a function of distance from the source wire at various temperatures.

vortex tangle is consistent with an exponential decay (solid line) with a decay length of ~2 mm. We should note that this is enormous compared to the diameter of the vibrating wires (~5 μm). We also see that the decay is temperature independent at these low temperatures.

This experiment also shows that the turbulence produced is focussed along the axis of motion of the source wire (as is the quasiparticle beam). Not shown in Figure 9 is an additional vibrating wire resonator located just to the side of the line of wires shown. This 'side' wire shows very little vortex signal. One possible explanation for this is that the excitation beam produced by the source wire is pushing the turbulence outwards along the beam axis. There are however alternative explanations.

Now that we know the spatial extent of the turbulence, we should be able to infer the density of vortex lines in the turbulence observed. Before doing this, we describe below another experiment which was designed to observe the Andreev reflection directly. Here, a beam of quasiparticles is fired at the vortex tangle while the reflected component of the beam is measured. This is done using a quasiparticle black-body radiator described below.

5. QUASIPARTICLE BEAM EXPERIMENTS USING A BLACK-BODY RADIATOR

In order to produce and observe a ballistic beam of quasiparticle excitations in the B-phase, two criteria must be met. First, the temperature must be low enough for the beam to propagate without significant loss from scattering

with existing equilibrium quasiparticles, that is, the quasiparticle mean free path must be sufficiently large. Second, the intensity of the beam must be comparable, at least, to that of the background quasiparticles, otherwise the beam cannot be resolved.

The quasiparticle mean free path becomes comparable to a typical length of the experimental region ($\sim$1 cm) at $T \sim T_c/4$ and rises to several hundred metres for $T < T_c/10$. Most of the experiments which we have performed with ballistic quasiparticle beams were operated at $T < T_c/6$. Thus, any loss from scattering with existing quasiparticles is entirely negligible. The second criterion for observing a quasiparticle beam is met by the design of the Lancaster style nuclear cooling stages (Cousins, 1999; Pickett and Fisher, 2003), giving excellent thermal contact to the nearby refrigerant.

A quasiparticle black-body radiator (Fisher et al., 1992) is shown in Figure 11, alongside an external vibrating wire resonator which will be used to generate turbulence (described later). The radiator is simply a box with a small hole (the radiator orifice) in one face. The box contains two vibrating wire resonators, one to act as a heater and the other as a thermometer. Quasiparticles created inside the radiator volume by the heater wire bounce ballistically from wall to wall, which allows them to thermalise before eventually leaving the radiator volume through the orifice as a quasiparticle beam. The time constant of the radiator is governed by the hole size and is typically less than 1 s. Therefore, steady state is rapidly established inside the radiator. We can analyse the energy flow by noting
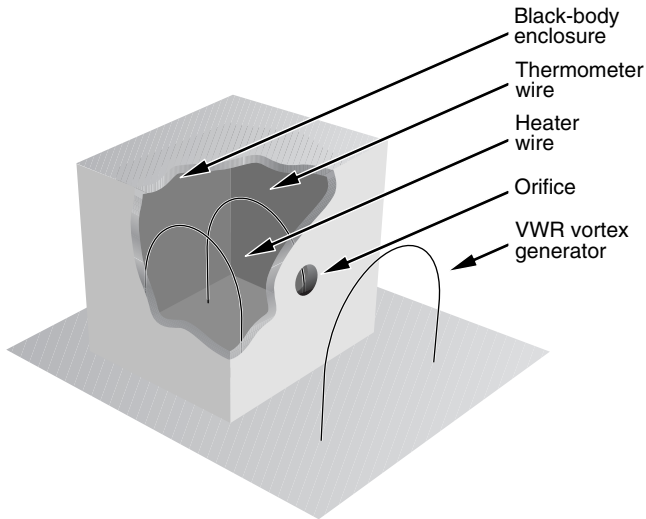
FIGURE 11   The quasiparticle black-body radiator used for ballistic quasiparticle beam experiments.

that the total power Q_T introduced into the liquid in the radiator must be balanced by the power leaving in the beam emitted from the orifice (the beam power).

When in thermal equilibrium, the power Q_T emitted from the hole is given by (Fisher et al., 1992)

$$Q_T = 2\frac{\langle nv_g \rangle}{4}\tilde{E}_T A_h, \tag{9}$$

where the factor of 2 accounts for both quasiparticle and quasihole contributions, the factor of 1/4 arises from averaging the thermal flux along outgoing direction, A_h is the area of the hole and $\tilde{E}_T$ is the average thermal quasiparticle energy (averaged over the quasiparticle flux), found to be simply $\tilde{E}_T = \Delta + k_B T$.

The quasiparticle flux may be rewritten in terms of the thermal damping (or frequency width, Δf_2) measured by the vibrating wire thermometer:

$$\Delta f_2 T \tilde{E}_T = \gamma' \frac{2d}{\pi m A_h} \frac{p_F^2}{k_B} Q_T, \tag{10}$$

where d is the diameter of the thermometer wire and m is its mass per unit length. The quantity γ' is an unknown wire-geometry dependent factor, of order unity, which is to be determined by the 'radiator calibration' discussed below.

The quasiparticle beam power must balance the total power entering the radiator. This has three contributions:

$$Q_T = Q_{wall} + Q_{ex} + Q_{ap}. \tag{11}$$

The first term, Q_{wall}, represents the heat leak into the liquid in the radiator from the walls. Q_{ex} represents the power entering the radiator from outside, through the orifice. This component arises from the background excitation gas outside of the radiator, determined by the outside temperature. Finally, Q_{ap} represents the power applied to the liquid in the box using the heater wire.

The power entering from outside the radiator, Q_{ex}, can be estimated from the damping of an outside thermometer wire. It is usually found to be negligible and for the purposes of the following discussion we will set it to zero. The heat leak into the box, Q_{wall}, determines the frequency width of the thermometer wire inside the radiator when there is no applied power. The wires also have a small intrinsic or vacuum damping which we can neglect here.

Consider first the state before the heater is switched on, that is, setting Q_{ap} to zero. Equation 10 then reduces to

$$\Delta f_2^0 T^0 \tilde{E}_T^0 = \gamma' \frac{2d}{\pi m A_h} \frac{p_F^2}{k_B} Q_{wall}. \tag{12}$$

The superscripts '0' refer to the measured values when there is no applied heat. When we apply heat to the radiator, the quantity on the left-hand side of the equation increases proportionately. We call this quantity the 'width parameter,' W. That is:

$$W = \Delta f_2 T \tilde{E}_T - \Delta f_2^0 T^0 \tilde{E}_T^0. \tag{13}$$

The width parameter is determined only by the measured frequency width (damping) of the thermometer wire inside the radiator (T and $\tilde{E}_T$ are both determined directly from the width).

In terms of the width parameter, Equation (10), which determines the steady state operation of the radiator, becomes:

$$W = \gamma' \frac{2d}{\pi m A_h} \frac{p_F^2}{k_B} Q_{ap}. \tag{14}$$

So the width parameter of the radiator is simply proportional to the applied heat. The constant of proportionality, the 'radiator calibration constant' can be easily measured by applying heat Q_{ap} with the heater wire and measuring the resulting thermometer wire damping to obtain the width parameter W. An example of such a calibration is shown in Figure 12.
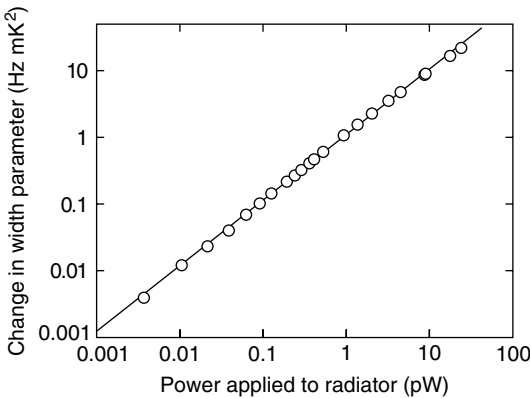
FIGURE 12   Calibration of a black-body radiator. Note the linearity over many orders of magnitude of the applied power and the very high sensitivity to low power inputs.

The radiator response (width parameter) is found to be linear in the applied power over several decades. For the width parameter, T and $\tilde{E}_T$ are expressed in units of mK, using the temperature scale of Greywall (1985). The values used for the Fermi momentum p_F are those given by Wheatley (1975). Note that the large dynamic range provides an extremely good test of the model. The value for γ' is found to be around 0.3 for typical thermometer wires used for such measurements (Bäuerle et al., 1998).

Once calibrated, the black-body radiator is able to detect power entering the radiator volume from any source (provided that the power is dissipated in the form of quasiparticle excitations). This simple bolometric behaviour, with high sensitivity (powers of order 10^{-3}pW are relatively easy to detect), has enabled us to perform a very wide variety of applications, including measurements of the excitation 'wind' emitted by a vibrating wire when exceeding the pair-breaking velocity (Fisher et al., 1992), direct observations of Andreev reflection (Cousins et al., 1996; Enrico et al., 1993), measurements of thermodynamic properties (Bartkowiak et al., 1999), phase nucleation (Bartkowiak et al., 2000) and interfacial energies (Bartkowiak et al., 2004). It has also been used for particle and vortex detection as described below.

6. PARTICLE ABSORPTION, DETECTION AND VORTEX CREATION IN A BLACK-BODY RADIATOR

A small energy deposition E into a black-body radiator produces a (near) instantaneous temperature rise given by

$$\Delta T = E/C(T), \tag{15}$$

where $C(T)$ is the heat capacity of the superfluid ^{3}He-B contained within the radiator, dominated by the bath of thermal quasiparticle excitations. The heat capacity is roughly proportional to the quasiparticle density which falls very rapidly at low temperatures from the effect of the gap Boltzmann factor $\exp(-\Delta/k_BT)$. In consequence, a small energy deposition can produce a relatively large temperature rise at low temperatures. This combined with the very high sensitivity of a vibrating wire thermometer makes for a very sensitive energy detector/bolometer. The mechanism in this context is reminiscent of that of a scintillation counter, but in the black-body radiator case the excitations produced are quasiparticle excitations which quickly thermalise with an energy of $\sim 10^{-7}$ eV as opposed to visible light scintillation photons with energies of a few eV.

Figure 13 shows an example of how the radiator can be used for particle detection. The upper plot in the figure shows the raw measurement of
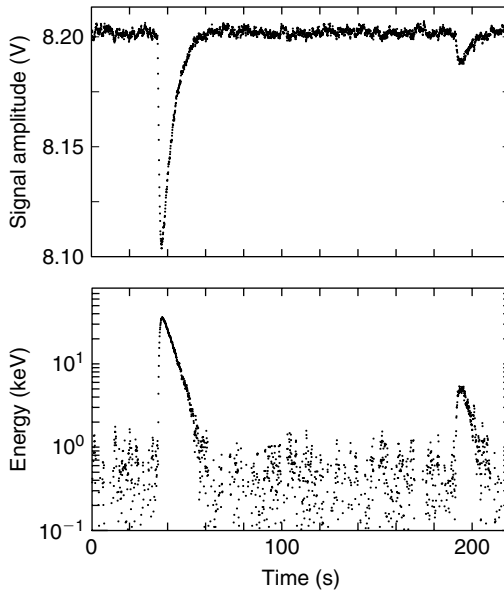
FIGURE 13   Particle detection using a black-body radiator. The upper plot shows the raw measurement of the signal height of the thermometer wire inside a radiator as a function of time. Occasional events are observed from background activity arising from cosmic rays and surrounding remnant radioactivity. The lower plot shows the same data converted to energy deposition. Note the good energy resolution, in this case of order 1 keV.

the resonant signal height of the thermometer wire inside a radiator as a function of time, where the signal has been amplified by a SQUID (super-conducting quantum interference device) to improve the signal-to-noise ratio. When a particle interaction occurs in the superfluid in the radiator, the energy released is converted into a pulse of quasiparticle excitations which increase the damping on the thermometer wire, thus depressing the signal. Two clear events can be seen in the trace, in this case arising from background cosmic activity or remnant radioactivity in the materials of the refrigerator and surrounding laboratory. The events correspond to a high energy particle (e.g., a cosmic ray muon) colliding with one or more of the ^{3}He atoms and thereby depositing energy. The sudden dip in the signal marks the rapid conversion of the energy into quasiparticle excitations. The slower recovery corresponds to the flow of the excess excitations out through the radiator hole (in the form of a ballistic excitation beam). The recovery time is set by the volume of the radiator and the size of the radiator hole, so can be optimised for the particular application. In the lower plot, the signal reduction has been converted into energy deposition. The energy is plotted on a logarithmic scale to show the exponential form of

the return to equilibrium. The energy deposition can be obtained in several ways. It can be obtained from Equation (15), or the energy deposited may be found by integrating the excess power ΔQ leaving the radiator,

$$E = \int \Delta Q \mathrm{d}t, \tag{16}$$

where the extra power is obtained from the increase in width parameter using the radiator calibration as given by Equation (14). Alternatively, the radiator can be calibrated directly for energy pulses by applying pulses to the heater wire. The various methods essentially give the same result.

Note the very good energy resolution, in this case of order 1 keV. This is comparable to the sensitivities provided by other state-of-the-art cryogenic particle detectors, and superfluid ^{3}He has been proposed as a potential dark matter WIMP (weakly interacting massive particle) detector (Bradley et al., 1995). Indeed, such an application is currently underway in the form of the ULTIMA project at the CNRS in Grenoble.

7. NONMECHANICAL GENERATION OF VORTICITY BY THE KIBBLE-ZUREK MECHANISM DURING A RAPID PHASE TRANSITION

Superfluid ^{3}He has many analogies with cosmology. In particular, various predicted defects in space-time have direct analogies with known defects in the superfluid ^{3}He condensate (with various types of monopoles, vortices and domain walls). The similarity becomes more apparent when we note that the symmetries broken by the Universe during the Grand Unification transitions are $SU(3) \times SU(2) \times U(1)$ when the strong, weak and electromagnetic forces became differentiated. In the most general form of the superfluid order parameter, the Cooper pair spin and orbital moments must choose a direction, thus each breaking $SO(3)$ symmetry in spin and orbital spaces. Also, the wavefunction has to choose a phase, breaking $U(1)$. Thus the symmetries broken by the superfluid are $SO(3) \times SO(3) \times U(1)$. These symmetries are broken during the transition to the superfluid phase. The broken symmetries in superfluid and Grand Unification transitions are clearly not identical, but the similarities are quite significant (Volovik, 1992). Associated with the different broken symmetries are various types of defects in the order phases. For example, in the context of this chapter, quantum vortices in the superfluid and their analogues, cosmic strings in space-time. The accepted theory for the formation mechanism of defects in cosmology is known as the Kibble mechanism (Kibble, 1976).

The Kibble mechanism describes defect formation during rapid symmetry-breaking phase transitions. During such a rapid transition, fluctuations ensure that the transition occurs independently in different regions. This leads to the formation of an order parameter 'glass' after the transition. Most of this disorder can relax but inevitably defects are left in the structure which are topologically stable and therefore long lived. The defects might be zero-, one- or two-dimensional, for example, monopoles, strings and branes. These ideas have been extended in more recent years by Zurek (Zurek, 1985) to be more widely applicable, in particular to condensed matter systems, in which context it is thus commonly known as the Kibble-Zurek Mechanism.

In the case of superfluid ^{3}He, we can produce a very rapid phase transition by irradiating the fluid with low-energy neutrons (from a source placed outside of the cryostat). Since the ^{3}He nucleus is an α-particle minus one neutron, ^{3}He has an extremely large cross-section for thermal neutron capture. However, any virtual α-particle does not survive and the capture process is exothermic leaving a tritium nucleus and a proton:

$$^3\text{He} + \text{n} \rightarrow {}^3\text{H} + \text{p} + 764\,\text{keV}.$$

The proton and triton fly apart carrying the combined kinetic energy of 764 keV. This energy is quickly transferred to the surrounding atoms forming a very localised intense hot-spot of normal fluid which then subsequently cools very quickly as the quasiparticles disperse into the surrounding cold superfluid. This produces a very rapid phase transition as the hot spot cools through the superfluid transition.

On cooling through a phase transition, the type of defects that are possible in the final ordered phase depends on the details of the symmetries which are broken. For instance, a discrete symmetry (e.g., up/down for spins in a ferromagnet) leads to domain walls as the order parameter changes from one value (e.g., up) to another (e.g., down). If the order parameter has a phase, then line defects (vortices/strings) are possible in which the phase changes by 2π around the core. The core of the defect usually has a heavily distorted or broken order parameter, so the ordering is at least partially destroyed. The core material thus often resembles the higher temperature disordered phase (vortex cores can often be considered to contain normal fluid, and cosmic strings may have enormously heavy cores corresponding to the enormous energy of the high temperature phase).

The Kibble-Zurek mechanism is depicted in Figure 14 for the case of our superfluid ^{3}He experiment (although the extension to other systems is self-evident). Part 'A' of the figure shows the initial energy deposition following the neutron capture. This produces a localised hot spot of normal fluid (B), analogous to early moment of the Big Bang when all forces were unified. As the system rapidly cools (the Universe expands), the rapid
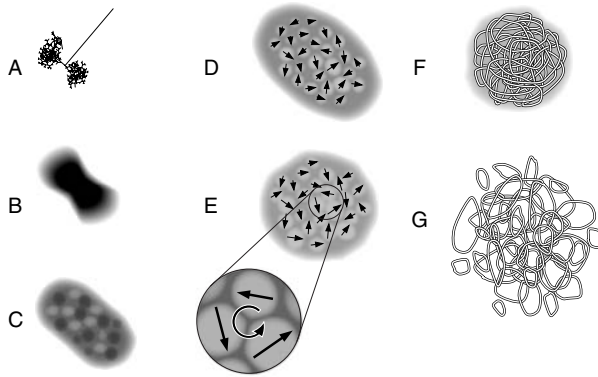
FIGURE 14 Schematic of the Kibble-Zurek mechanism, applied in this case to vortex creation via a rapid neutron-induced phase transition in ^{3}He-B (see text).

phase transition(s) occurs. During the transition, various protodomains form in the system (C). Since there is no time for the ordering information to be transmitted from one protodomain to the next, the regions are causally disconnected, so they must choose the order parameter independently (D). As the system cools further, the protodomains grow and coalesce leaving a phase 'glass' (E). The gradients in the order parameter then relax. However, relaxation to a uniform state may not be possible. For instance, when the order parameter is described by a phase factor, regions may form in which the phase evolves by 2π around some central core (E expanded). This corresponds to the formation of a line defect (vortex/string). Many such defects may form in random locations producing a tangle (F), which then subsequently evolves/decays on much longer time scales (G). The density of the defects generated depends directly on the size of the protodomains, which in turn depends on the rate of the transition (the faster the transition, the smaller the regions which are casually disconnected, hence the higher the density of vortex lines).

Measurements of the neutron events observed in a black-body radiator are shown in Figure 15. Further details can be found in Bäuerle et al. (1996). The arrows indicate the events observed, most of which arise from background radiation and gamma rays which are also emitted from the source. The neutron absorption events produce the largest signals and are easily resolved.

The energy of each of the observed events can be measured and then plotted as a histogram of event count number versus energy. The resultant spectrum is dominated by a clear peak associated with the neutron capture processes with the vast majority of background events occurring at much lower energies. A series of spectra taken in this way is shown in Figure 16 for three different fluid pressures (the pressure changes the superfluid
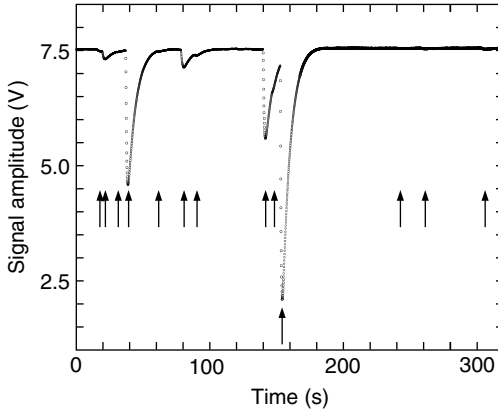
FIGURE 15 Measurements of events in a black-body radiator in the presence of a neutron source. The arrows mark the times of events.
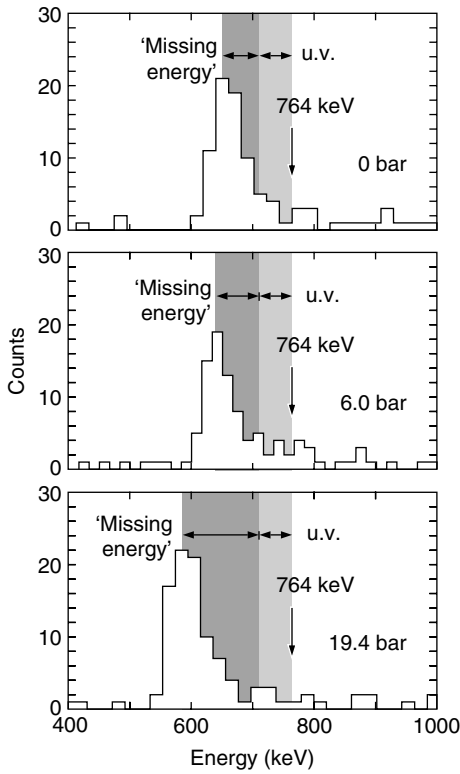
FIGURE 16 The measured neutron absorption peak for three different fluid pressures, clearly revealing a 'missing energy,' as expected for vortex production via the Kibble-Zurek mechanism.

coherence length which in turn determines the number of defects predicted by the Kibble-Zurek mechanism).

Significantly, while we know that the neutron capture process is exothermic and associated with an energy release of 764 keV, we see in the figure that the neutron capture peak occurs at a significantly lower energy. Part of the discrepancy can be attributed to the emission of UV scintillation photons (i.e., some of the energy is converted to UV). However, we know the value of these losses from other experiments. The remaining energy deficit is pressure dependent and is in excellent quantitative agreement with the amount of energy which is stored in the tangle of vortices predicted by the Kibble-Zurek mechanism (Bäuerle et al., 1996). These vortices decay on such long timescales that the energy they release on decay is not observed in these measurements. It is very seldom that a cosmological theory can be tested so rigorously in the laboratory; thus these experiments, and similar experiments in Helsinki (Ruutu et al., 1996), received a great deal of interest leading to much further research and the formation of a European network dedicated to developing analogies between various areas of cosmology and condensed-matter systems.

8. DIRECT MEASUREMENTS OF ANDREEV REFLECTION FROM VORTICES

Extremely precise and direct measurements of the Andreev reflection of quasiparticles from a vortex tangle can be made with black-body radiator techniques. The first black-body radiator measurements of turbulence Bradley et al. (2004a) were made with arrangement shown in Figure 11, which consists of a black-body radiator and a vibrating wire outside facing the radiator orifice.

The radiator is first heated, with the internal heater vibrating wire, to produce a quasiparticle beam directed at the external wire, as shown in Figure 17. The beam contains a thermal energy distribution of quasiparticles corresponding to the temperature of the radiator. The external wire is then driven to some, relatively high, velocity to produce a vortex tangle (quantum turbulence). The flow field around the vortex Andreev reflects low-energy quasiparticles in the beam. The beauty of Andreev reflection is that the quasiparticles are almost perfectly retroreflected. Thus, regardless of the angle of incidence, a reflected excitation will accurately retrace its path back through the orifice and into the radiator. Therefore, the reflection by the tangle restricts the probability of excitations escaping the radiator. This means that since the beam flux (power) is fixed by the heat applied to the radiator, the Andreev reflection leads to an increase in the quasiparticle density (width parameter) within the radiator.
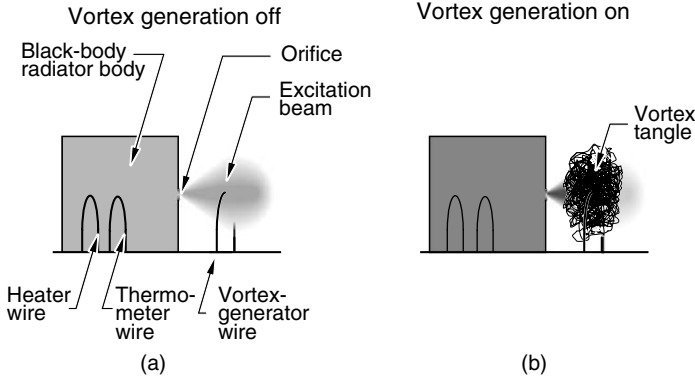
FIGURE 17   Direct measurements of the Andreev reflection of a quasiparticle beam incident on a vortex tangle, see text.

To be a more quantitative, in the absence of the tangle (when the external wire is not driven, $v = 0$), the measured width parameter in the box is

$$W(0) = CQ, \tag{17}$$

where C is the box calibration constant described above, and Q is the applied power which may be taken as the beam power since the heat leak into the radiator may be neglected. To simplify the discussion, we will also assume that the intrinsic damping of the resonators can be neglected and that the density of excitations outside the resonator is negligible, see reference (Bradley et al., 2004a) for a more detailed analysis. In the presence of vortices, some fraction f of the beam power incident on the tangle Q_i is reflected back into the box, thereby increasing the box temperature and width parameter $W(v)$. The beam power which is transmitted through the tangle must balance the power supplied, so

$$Q = Q_i(1 - f) = W(0)/C. \tag{18}$$

However, the power emerging from the radiator Q_i is simply determined by the radiator width parameter, $W(v) = CQ_i$. Substituting this in Equation (18) and then rearranging gives the fraction of the beam which is Andreev reflected:

$$f = 1 - W(0)/W(v). \tag{19}$$

Note that if the fraction reflected were unity, then the radiator would effectively be closed, and the width parameter would rise to infinity.
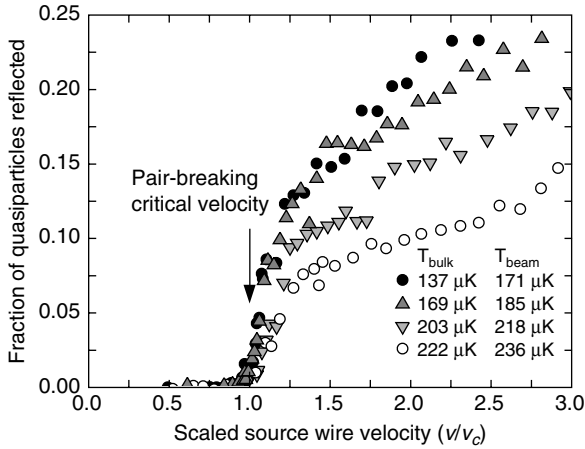
FIGURE 18   The fraction of excitations Andreev reflected in a quasiparticle beam incident on a vortex tangle as a function of the source wire velocity scaled by the pair-breaking critical velocity.

Equation 19 now allows the fraction of the beam Andreev reflected by the turbulence to be obtained from the measured width parameters. The result is shown in Figure 18. The data are very similar to that obtained by measuring the fractional reduction in damping of a wire inside a vortex tangle (compare Figure 18 with Figure 6). In particular, the largest measured fraction of excitations which are Andreev reflected by the vortex tangle is of order 20% in both cases, and the critical velocity for the production of the tangle (turbulence) is clearly very close to the pair-breaking critical velocity.

9. MEASUREMENT OF THE VORTEX LINE DENSITY

Now that we know the fraction of excitations Andreev reflected from a vortex tangle and the spatial extent of the tangle, we can infer the vortex line density. An exact calculation would require detailed knowledge of the spatial and angular distribution of the vortices, which we cannot obtain from the current experiments. However, we can estimate the average line density in the tangle using a simple model (Bradley et al., 2004a) as follows.

Consider a thin slab of unit cross-section and thickness Δx containing a homogeneous vortex tangle of line density (length of line per unit volume) L, as depicted in Figure 19. The total length of line in the slab is $L\Delta x$. Taking the vortex as a tube of radius r and projecting its area onto the face of the slab gives an area of order $2rL\Delta x$, which gives the probability that
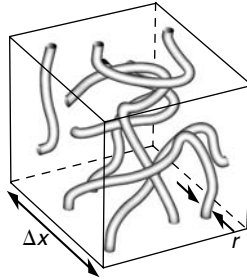
FIGURE 19   Simple model for estimating the vortex line density from the Andreev reflection measurements, see text.

a quasiparticle normally incident on the slab may pass within a distance r of the vortex core. Following the arguments made in Section 2.1, excitations with a mean energy of energy $E = \Delta + k_B T$ (and momentum in the appropriate direction) will be retroreflected if they approach to within a distance $p_F \hbar / 2m_3 k_B T$ of a vortex core (assuming that the vortices are well enough separated that their flow fields do not overlap significantly). Thus the fraction of excitations reflected is of order $p_F \hbar L \Delta x / 2m_3 k_B T$. Integrating, we find that the fraction of excitations Andreev reflected by a tangle of thickness D is

$$f \sim 1 - \exp(-D/\lambda), \tag{20}$$

where

$$\lambda \sim \frac{2m_3 k_B T}{p_F \hbar L}, \tag{21}$$

That is, the flux of quasiparticles transmitted through homogeneous turbulence decays exponentially with distance with a decay length given by Equation (21). Using these equations and setting $D \simeq 2\,\text{mm}$ as inferred from the data shown in Figure 10, we can convert the fractional Andreev reflection data of Figure 18 into a vortex line density. The results are shown in Figure 20.

The arguments given above allow us to estimate the line densities, based on a simplified picture of what is, in reality, quite a complex problem. To solve the problem precisely requires a detailed knowledge of the turbulent flow field including its spatial and angular variation. One should also take into account the fact that the vortex lines are moving and may have collective motion producing large scale flows (although this does not qualitatively change the physics of the Andreev reflection process). Given our lack of detailed knowledge concerning the tangle geometry, we
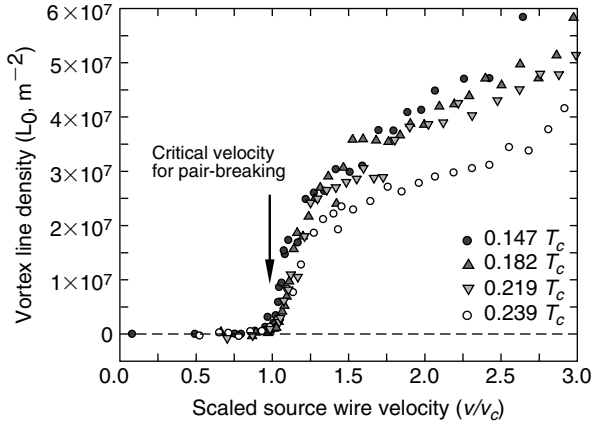
FIGURE 20   The inferred vortex line density of turbulence produced by a vibrating wire as a function of the wire velocity. See text.

cannot make a precise determination of the line densities, and the simple model given above should be sufficient for our purposes. We expect that the inferred line densities should be correct to within a factor of order 2 (and the values should be considered as spatial and angular averages).

   The tangle density shown in Figure 20 is seen to become temperature independent below around $0.2\,T_C$, suggesting a temperature-independent decay mechanism operates. It is not too surprising that the thermal decay mechanism (mutual friction) becomes redundant at such low temperatures since the density of thermal excitations is so small that they should have very little effect on the tangle dynamics. The maximum observed line densities are of order $10^7\,\mathrm{m}^{-2}$ to $10^8\,\mathrm{m}^{-2}$ corresponding to a minimum vortex line spacing $l = L^{-2} \sim 200\,\mu\mathrm{m}$. Also note that we can resolve line densities of the order of $10^6\,\mathrm{m}^{-2}$ which corresponds to vortex spacings of order 1 mm (approaching the size of the tangle), showing that these techniques are very sensitive and can resolve relatively small amounts of vortex line.

10. VIBRATING GRID EXPERIMENTS

While we can readily produce turbulence with a vibrating wire resonator, the resulting tangle is very localised and also appears to be somewhat polarised in the direction of the wire motion. In order to produce more homogeneous turbulence with a greater intensity (line density), we turned to using a vibrating grid resonator. Grids are commonly used in studies of classical turbulence, where the turbulence is usually generated by passing

a steady flow through the grid and observing the turbulence downstream. This is not practical for a low-temperature superfluid experiment. However, a similar arrangement has been realised in superfluid ^{4}He at relatively high temperatures by towing a grid through the superfluid (Skrbek et al., 2000; Stalp et al., 1999). At the temperatures required for superfluid ^{3}He experiments, a towed grid configuration would be very difficult to achieve without producing excessive heating. However, we can easily vibrate a grid backwards and forwards through the superfluid even at the lowest achievable temperatures.

The experimental arrangement for the first vibrating grid experiments (Bradley et al., 2004b) in ^{3}He-B at low temperatures is shown in Figure 21. The grid is made from a 5.1 × 2.8 mm mesh of fine copper wires. The wires have an approximately 11 µm square cross-section and are spaced 50 µm apart, leaving 40 µm square holes. A 125 µm diameter Ta wire is bent into a 5 mm square frame and glued through the epoxy-impregnated paper which forms the inner cell wall of a Lancaster style nuclear cooling stage (Pickett and Fisher, 2003). The mesh is glued to the Ta wire over thin strips of cigarette paper for electrical insulation.

Facing the grid are two vibrating wire resonators made from 2.5 mm diameter loops of 4.5 µm NbTi wire. The 'near' and 'far' wires are positioned 1 mm and 2 mm from the grid, respectively. An additional wire resonator is used as a background thermometer. This wire, not shown in the figure, is located about 4 mm to the side of the grid and is itself enclosed in a mesh cage to ensure that its response is not influenced by any stray turbulence.
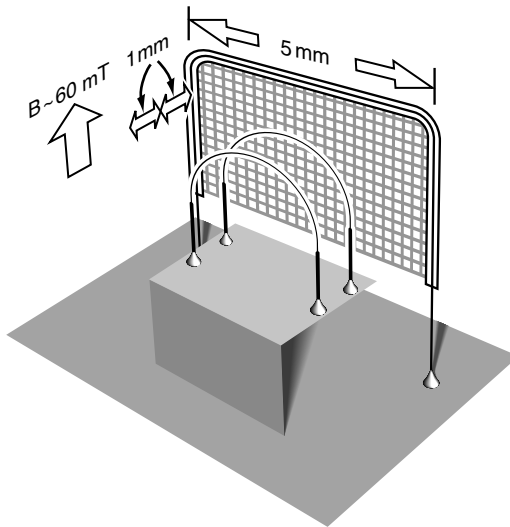
FIGURE 21   The arrangement of the grid and associated vorticity detector wires.

The grid is operated in a similar way to a wire resonator. It is exposed to a vertical applied magnetic field and driven by the Lorentz force generated by passing an AC current through the Ta wire. As the grid moves, the Ta wire develops a Faraday voltage proportional to its velocity. The particular grid used for the following experiments resonates at a frequency of ~1300 Hz, determined by the stiffness of the Ta wire legs and the effective mass of the grid assembly.

The frequency width (damping) of the grid resonance (at low velocities) was measured as a function of the thermometer resonant width as the cell warmed throughout the experiments (Bradley et al., 2004b). The frequency width is proportional to the damping force per unit velocity, $(\mathrm{d}F/\mathrm{d}v)_{v=0}$. After subtracting the intrinsic damping (0.22 Hz for the grid and 0.05 Hz for the thermometer), we obtain the thermal damping at low velocities for the two wires, which is plotted in Figure 22.

The thermal damping of the grid and the thermometer vibrating wire are seen to be proportional to each other over the range of the measurements (more than 3 orders of magnitude in the damping). This clearly indicates that the thermal damping on the grid at low velocities arises from the same mechanism as that of a vibrating wire (this conclusion is also confirmed by the magnitude of the damping).

Measurements of the resonant peak velocity v of the grid as a function of the peak driving force F are shown in Figure 23. The measurements (Bradley et al., 2004b) were taken as the cell was slowly warming under its external heat leak. Also, significant warming occurred at the highest velocities due to the power required to drive the grid. The temperatures indicated in the figure cover the range of cell temperatures as measured by the thermometer wire over the given set of data. At low velocities, the
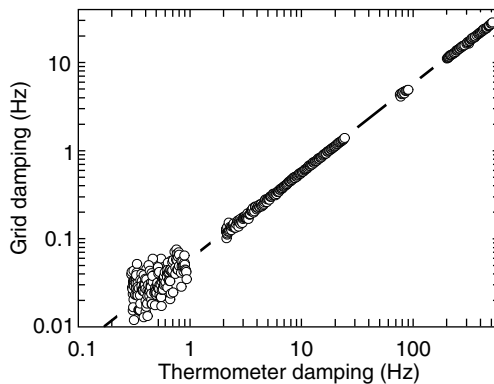
FIGURE 22 The inferred thermal damping of the grid resonator as a function of the thermal damping of a conventional wire resonator. A linear relationship is found as expected for thermal quasiparticle damping.
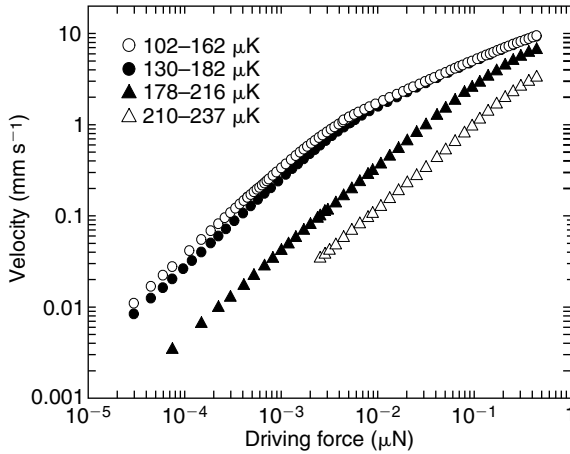
FIGURE 23   The grid velocity as a function of driving force for various temperatures.

grid response is quite linear and is due to a combination of the intrinsic (vacuum) damping of the resonator and the thermal quasiparticle damping. At higher velocities, the grid response becomes nonlinear.

Note that the grid response, shown in Figure 23, does not have any well-defined critical velocity, but rather a gradual changeover from a near-linear regime at low velocities to a nonlinear response at higher velocities. As the size of near-linear damping increases (as the temperature increases), the crossover velocity increases. This is simply a result of adding an extra thermal damping to a temperature-independent turbulent damping as verified below.

To obtain the grid response curve without the complicating effects of the thermal excitation damping, we can subtract the thermal contribution as follows. We can use the damping data in Figure 22 to infer directly the thermal damping force on the grid at low velocities. The thermal damping force at higher velocities becomes nonlinear. However, the non-linearity for the vibrating wires is known to be proportional to $1 - \exp(-\lambda p_F v_0/kT)$, where the constant λ is found to be 0.85. Assuming that the thermal damping on the grid has this same form, then the thermal contribution to the damping force can be found with no free parameters.

The thermal damping force for the grid is thus inferred and can then be removed from the data of Figure 23 to leave the inferred zero temperature response curve shown in Figure 24. The corrected data collapse to a single curve, verifying the assumptions made.

Referring to Figure 24, the zero temperature response of the grid shows linear behaviour below about 0.5 mm/s. This corresponds to the intrinsic damping of the resonator. At higher velocities, the response tends to a power law behaviour, approximately proportional to the square root of
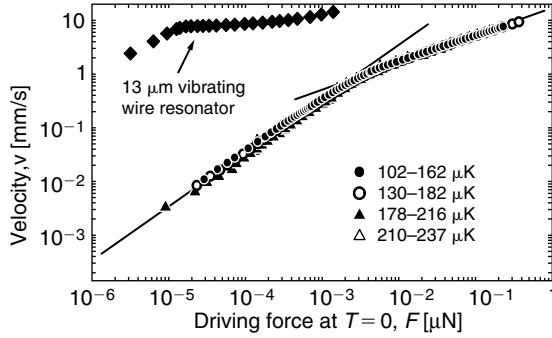
FIGURE 24   The inferred $T = 0$ grid response and the response of a conventional wire resonator. Lines show linear and $v \propto \sqrt{F}$ behaviour.

the force. This is the expected variation for turbulent-dominated damping in classical fluids (Landau and Lifshitz, 1966). The corresponding behaviour for conventional vibrating wire resonators, also shown in the figure, is very different. These show a pair-breaking critical velocity of around 8 mm/s at 0 bar above which the response is seen to be very flat. This indicates that the pair-breaking contribution to the damping on the grid is much smaller and may well be negligible. This makes the grid very advantageous for studying turbulence in ^{3}He-B since the pair-breaking beam not only causes massive heating but may also have a significant effect on the vortices generated by conventional wires as discussed above.

11. THE DETECTION OF GRID TURBULENCE

Vortices generated by the grid are detected by the two facing vibrating wire resonators via the screening effect on the thermal damping as discussed above. Briefly, with the grid stationary, the two resonators and the thermometer resonator are driven on resonance at relatively low velocity. The resulting induced voltages across the wires are continuously monitored, allowing us to deduce the quasiparticle damping $\Delta f_2(T)$ for all three wires. The grid is then driven to some velocity v generating vortex lines. This vorticity causes the Andreev reflection of some fraction f of those quasiparticles approaching a vibrating wire, giving rise to a reduced damping

$$\Delta f_2(v, T) = (1 - f)\Delta f_2^0(T), \tag{22}$$

where $\Delta f_2^0(T)$ is the damping in the absence of turbulence.
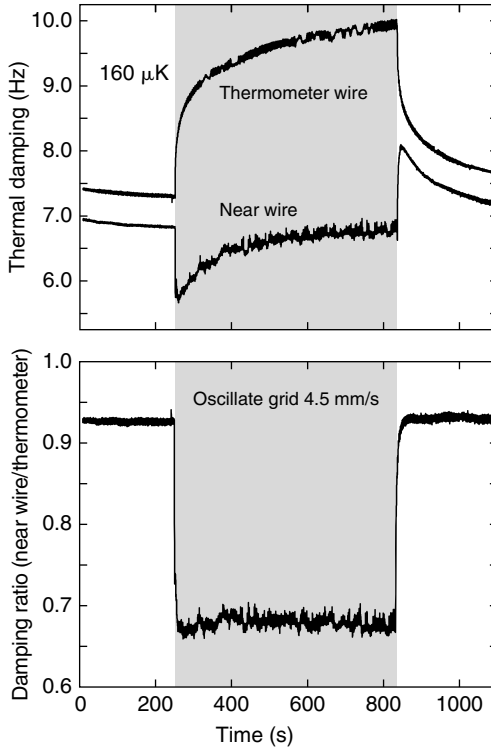
FIGURE 25 Upper figure: the thermal damping on the thermometer wire and the nearest detector wire as a function of time. The grid is driven, producing vorticity, during the shaded interval. Lower figure: the ratio of the two above responses providing the temperature-corrected vorticity signal.

In practice, significant power is required to drive the grid, resulting in an overall warming of the cell, as measured by the thermometer wire damping shown in the upper plot of Figure 25. The detector wires show this same overall warming effect, but in addition show a reduction in damping due to vortices produced by the grid, also shown in the upper plot. The damping in the absence of turbulence $\Delta f_2^0(T)$ is simply proportional to the thermometer wire damping. (Ideally, they should be equal, but in practice small scale factors, typically less than 10%, are needed to account for the slight differences in the two wire geometries.) Therefore, the factor $1 - f$ in Equation (22) is simply given by the scaled ratio of the detector and thermometer wire dampings. The damping ratio corresponding to the two curves in the upper plot of Figure 25 is shown in the lower part of the figure. The ratio is scaled to equal unity when the grid is undriven, which is now equivalent to $(1 - f)$ in Equation (22). The
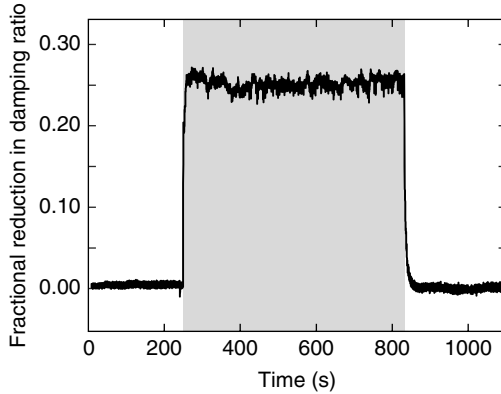
FIGURE 26 The fractional screening of quasiparticles from the nearest detector wire, due to vorticity produced by the grid, inferred from the data of Figure 25.

corresponding inferred fractional screening f due to the vortices emitted by the grid is shown in Figure 26.

The steady state average values of the fractional screening f are found to increase roughly as v^2. The far wire, 2 mm from the grid, has roughly a factor of two less screening than the near wire, 1 mm from the grid, over the entire velocity range. If the variation with distance followed an exponential decay, as found previously for turbulence generated by vibrating wires (Bradley et al., 2003) (see above), then this would correspond to a spatial decay length of $D \sim 1.5$ mm. This allows the approximate vortex line density to be inferred from these measurements using the arguments given above (Equations (20) and (21)).

12. VORTEX RING PRODUCTION

We can gain a great deal of information from the transient behaviour of the line density as the grid is switched on and off. The transient behaviour after the drive to the grid is turned off is shown in Figure 27 for the wire nearest to the grid. Data are shown for various initial grid velocities. At high grid velocities (corresponding to high vortex production rates) the line density decays over several seconds, while at lower grid velocities (lower vorticity production) the line density falls to zero essentially instantaneously. Significantly there is a very abrupt transition between these two behaviours at grid velocities of around 3.5 mm/s (depending a little on pressure). This is very clearly shown in Figure 28 where we plot the initial decay time constants as a function of the initial grid velocity.
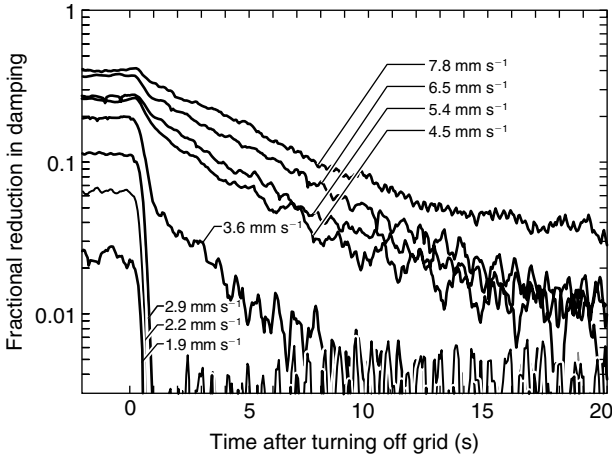
FIGURE 27 The fractional screening of quasiparticles from the nearest detector wire as a function of time after switching off the grid for various initial grid velocities.
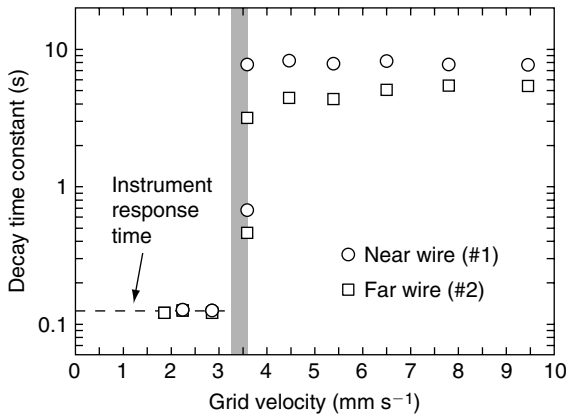
FIGURE 28 The initial decay time constant as a function of initial grid velocity for the data shown in Figure 27.

As shown in Figure 28, there is a very sharp transition in the initial decay time constant of the observed vorticity (Bradley et al., 2005b). Note that there are two points for the 3.6 mm/s data corresponding to the short, fast decay followed by the longer slow tail of the data of Figure 27. At low grid velocities, the decay time is limited by the response time of the measuring equipment and of the grid resonator, so the observed decay time of ~0.1 s provides an upper limit for the decay time of the observed vorticity. At higher initial grid velocities, the decay is much slower, on the scale of 10 s.

The slow decay corresponds to the decay of a vortex tangle (quantum turbulence) as discussed further below, but what could give rise to the very rapid decay seen at lower grid velocities? To produce such a rapid response (~0.1 s) at a distance of 1 mm, the vorticity must disperse from the grid with a velocity in excess of 10 mm/s. The only possible explanation for such fast vortex dynamics is that the vorticity is being produced in the form of small individual vortex rings. An isolated vortex ring self-propagates. Crudely speaking, the vortex core on one side is moving with the flow field generated by the other side, and thus the smaller the ring, the larger this flow field and the faster the ring moves. A ring of radius R travels at a self-induced velocity given by (Donnelly, 1991):

$$v(R) \simeq \frac{\kappa}{4\pi R}(\ln(8R/\xi) - 0.5), \qquad (23)$$

where ξ is the core size, which is approximately equal to the coherence length. The ring velocity exceeds 10 mm/s only for ring diameters less than 5 μm. We, therefore, must conclude that at low grid velocities the emitted vorticity takes the form of a gas of vortex rings with diameters no larger than ~5 μm.

It is interesting to note that, under some circumstances, vibrating wire resonators have also been found to emit vortex rings (Bradley, 2000). Here, the ring production is not very reproducible and is thought to be due to a vortex line trapped and pinned to some defect ('dirt') on the wire surface. The measurements suggest that, above some critical velocity, the vortex line extracts energy from the AC flow, stretching and eventually pinching off a vortex ring. The process is found to be quite periodic, with a time period which shortens as the driving force on the wire increases.

Hänninen et al. (2006) have made computer simulations of ring production by a vortex line pinned at its ends and exposed to a perpendicular AC superflow. They find that, provided that the AC flow exceeds some critical velocity amplitude, large amplitude oscillations of the vortex lines are excited, leading eventually to reconnections and the emission of vortex rings. A range of ring diameters is produced but diameters are typically of order the initial line length. The critical velocity becomes very small when the flow frequency matches the frequency of the first Kelvin-wave resonance of the vortex line. Kelvin-waves are helical excitations which propagate along a vortex line (Donnelly, 1991) and, as in this case, may form standing wave resonances. At the operating grid frequency (~1250 Hz), the first Kelvin-wave resonance will be excited on vortices with initial line lengths of around 5 μm, consistent with our upper limit for the vortex ring diameters.

Since the grid is very rough on the μm scale, there will be a wide range of trapped vortex semiloops. The upper limit of their size will be given

approximately by the grid mesh size. On oscillating the grid, Kelvin waves are preferentially excited on the vortex lines which are initially around 5 μm long, leading to the production of ~5 μm vortex rings. Such rings would propagate quickly away from the grid, consistent with the rapid response observed. Although this scenario for vortex ring production provides a natural mechanism for producing rings with diameters of a few μm, which is consistent with the experiments discussed in the next section, we cannot rule out the possibility of intrinsic nucleation, as suggested in more recent work (Hänninen et al., 2007).

13. THERMAL DECAY OF VORTEX RINGS

We can confirm the interpretation of the data discussed above by measuring the temperature dependence of the vortex ring signals. Vortex motion in a superfluid is damped by the normal scattering of thermal quasiparticle excitations with the vortex cores, which effectively couples the superfluid and normal fluid components at higher temperatures, a phenomenon known as 'mutual friction'. Since the very small mutual friction remaining at these low temperatures will extract energy from the moving rings, the rings gradually shrink and eventually dissipate. At some sufficiently high temperatures, the mutual friction will be large enough that the rings dissipate too rapidly to reach the nearby vibrating wire detectors. We can observe this in experiments. Since the cross-section for Andreev scattering by a straight vortex line is inversely proportional to the temperature T (Equation (7)), the quantity of vortex line/rings surrounding the two detector wires should be proportional to the quantity fT, which we designate the 'vorticity signal'. The steady state value of the vortex signal while the grid is driven at 2.5 mm/s is plotted in Figure 29 as a function of the thermal damping on the thermometer wire (and the corresponding temperature).

The range of a vortex ring, at low temperatures, with initial radius R_0 can be estimated as (Donnelly, 1991)

$$x \simeq R_0/q, \tag{24}$$

where q is a mutual friction parameter which measures the size of the damping force from the thermal excitations and is roughly proportional to the thermal damping on a vibrating wire at low temperatures. Mutual friction has been measured down to temperatures of around $0.35\,T_c$ by Bevan et al. (1997). Using their fitting formula for q extrapolated to the lower temperatures, we find that a 5 μm diameter vortex ring should have a range of 1 mm and 2 mm at temperatures of $0.178\,T_c$ and $0.194\,T_c$, respectively.
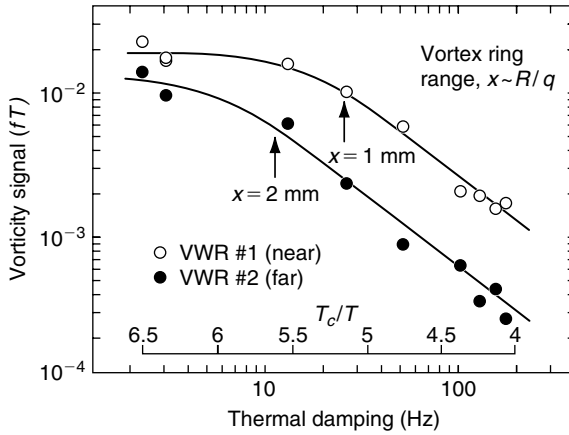
FIGURE 29   The vortex signal as a function of temperature for the two vibrating wire detectors. The arrows indicate the temperature at which the range of 5μm diameter rings is expected to correspond to the distance to the detector wires.

As indicated by the arrows in the figure, these temperatures are consistent with the temperatures at which the vortex signals for the two wires begin to fall with increasing temperature. Measurements have also been made at different cell pressures (Bradley et al., 2007) and these are also consistent with our picture that the grid predominantly emits 5 μm vortex rings. Note that, at the lowest temperatures, the range of the rings should exceed the size of the cell and the vorticity signal becomes temperature independent. Presumably in this case, the rings are effectively absorbed (and dissipate) on collision with the cell walls.

14. THE TRANSITION TO TURBULENCE

As revealed by the observations discussed above, at low grid velocities, small vortex rings are emitted which travel ballistically away from the grid region and with increasing grid velocity, the emitted ring density increases. Eventually, the emitted ring density will become so high that the rings can no longer remain independent. When two rings collide, a larger loop may form, and being larger, it will move at a lower velocity and thus will be more likely to collide with further rings. This will lead to a cascade process in which collisions and reconnections suddenly generate a vortex tangle which can only disperse on much longer timescales. This scenario explains the sudden transition observed in the decay data of Figures 27 and 28. This picture is confirmed by recent computer simulations by Mitani and Tsubota (Tsubota, 2008) in collaboration with Lancaster.
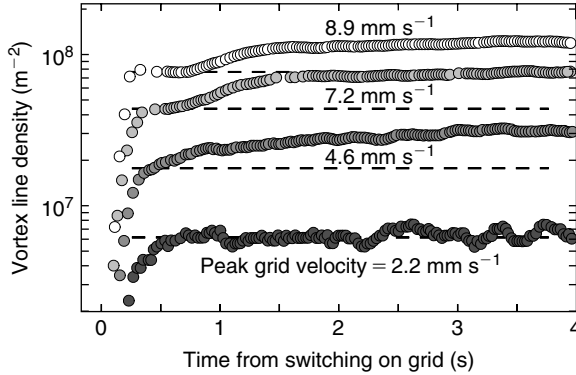
FIGURE 30   The vortex line density, as inferred from the nearest detector wire, as a function of time after switching on the grid to various velocities.

15. EVOLUTION OF QUANTUM TURBULENCE

The vortex line density can be inferred from the measured fractional screening f and the estimated vortex tangle size D, as discussed above. In Figure 30, we show the inferred line density surrounding the wire nearest to the grid as a function of time after switching on the grid to various velocities as indicated. The initial fast rise time is limited by that of the measurement equipment and the response time of the grid itself (which is velocity dependent). We can interpret this initial rise as reflecting the flow of ballistic independent vortex rings away from the grid, as discussed above. At higher grid velocities, the upper three curves in the figure, we see a slower further increase in the line density at later times, which reflects the buildup of ring collisions and the formation of a vortex tangle. The equilibrium line density is ultimately given by the balance between the ring injection rate and the rate of dissipation (see below). It is interesting to note that the timescale for the development of the turbulent tangle is comparable to the timescale of the motion of the largest vortex rings. The largest possible ring sizes are limited by the size of the overall turbulent region D. The transit time of such a ring across the active region gives an upper timescale, $\tau \sim D/v(D)$, which is of order a few seconds, consistent with the measurements shown in the figure.

16. DECAY OF ^{3}HE QUANTUM TURBULENCE AT LOW TEMPERATURES

We return now to the decay behaviour observed at higher grid velocities (Bradley et al., 2006), corresponding to the decay of a vortex tangle
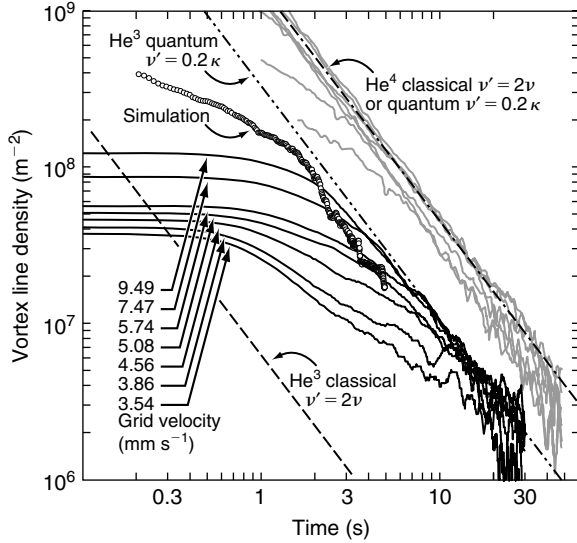
FIGURE 31 The vortex line density as inferred from the nearest detector wire as a function of time, after switching the grid off from various velocities (solid lines). Grey lines show results from the towed grid experiments in superfluid ⁴He at relatively high temperatures. Circles show the results of a computer simulation and dashed lines correspond to a Richardson cascade model with classical and quantum expressions for the effective kinematic viscosity. See text.

(quantum turbulence). The inferred vortex line density as a function of time after switching off the grid is shown in Figure 31. Note the log-log scale. Also shown in the figure is data obtained from a towed grid in superfluid ⁴He at relatively high temperatures using second sound techniques (Skrbek et al., 2000; Stalp et al., 1999).

In the case of superfluid ⁴He at high temperatures, the superfluid and normal fluid components are thought to be effectively clamped together by mutual friction and both flow fields are locked together. In this case, we have combined superfluid and normal fluid turbulence. This led the authors of this work to consider the application of the ideas of classical turbulence to their measurements (Skrbek et al., 2000; Stalp et al., 1999). Classically, turbulence decays via a Richardson cascade in which energy flows from the largest eddies to smaller and smaller eddies, eventually being dissipated by viscosity. Energy is only dissipated at the smallest length scales. Simple dimensional arguments lead to the well-known Kolmogorov spectrum for the energy content of the turbulent flow as a function of the length scale, or wave number k,

$$E(k) = C\xi^{2/3}k^{-5/3}, \tag{25}$$

where C is the dimensionless Kolmogorov constant, close to unity, and ξ is the energy dissipation rate, which for a classical fluid is given by $\nu\omega^2$. In the early work on superfluid grid turbulence (Stalp et al., 1999), it was argued that in the case of a superfluid, the effective kinematic viscosity ν' could be approximated by the kinematic viscosity of the coupled fluids, ν, defined as the normal fluid viscosity divided by the total fluid density, that is, $\nu' \simeq \nu = \eta/\rho$. It was also argued that the vorticity ω can be simply related to the average vortex line density L by $\omega = \kappa L$. It was further assumed that the maximum eddy size (the large-scale cutoff of the Kolmogorov spectrum) should be given by the size of the turbulent region or the size of the experimental cell d. The details will not be given here, but the model leads to the prediction that the line density at late times should evolve with time as

$$L = (d/2\pi\kappa)\sqrt{(27C^3/\nu')}\, t^{-3/2}. \tag{26}$$

This equation reproduces with the measured decay at late times, shown in Figure 31, with an effective kinematic viscosity which is within a factor of two of the actual kinematic viscosity. This represents very good agreement given the simplicity of the model and of the assumptions made. However, it was later realised that quantum effects are important even at relatively high temperatures (Stalp et al., 2002).

If we take this classical expression for the late-time line density and apply it to the superfluid ^{3}He case, then we obtain the lower line in Figure 31 labelled '^{3}He classical'. The classical decay line lies very much lower than that for ^{4}He, partly since the dimension d is smaller ($d = 1.5$ mm in our case against $d = 10$ mm for the ^{4}He experiments) but mainly because the normal fluid viscosity is orders of magnitude larger for ^{3}He (Carless et al., 1983). Clearly our results cannot be explained by the classical decay mechanism. However, this is not at all surprising. The ^{3}He measurements were made in the low temperature limit where the normal fluid fraction is negligible. In this regime, there can be no significant mutual friction and viscosity cannot play a role. In fact, the entire concept of a normal fluid component in the spirit of the two-fluid model breaks down in this temperature regime since the quasiparticle excitations behave independently, and we cannot define a local normal fluid velocity.

In classical turbulence, the Kolmogorov energy spectrum is a consequence of the fact that dissipation is negligible on large length scales. It seems reasonable to expect, as suggested by Vinen (Vinen and Niemela, 2002), that superfluid turbulence as generated by grids may display a similar spectrum owing to the similar absence of large length scale dissipation mechanisms. This expectation is supported by numerical simulations (Araki et al., 2002) which show evidence of a Kolmogorov-like spectrum in

pure superfluid turbulence in the absence of any normal fluid component. At high temperatures, mutual friction will strongly couple superfluid turbulence to the normal fluid component. In this case, turbulence is actually found to be completely suppressed (Finne et al., 2003), owing to the very high ^{3}He normal fluid viscosity which rigidly clamps the normal fluid stationary with respect to the cell walls (normal fluid turbulence is not possible in low temperature ^{3}He under typical experimental conditions). At intermediate temperatures, the behaviour is more complicated and a different energy spectrum arises since, with a stationary normal fluid component, mutual friction acts over all length scales (Vinen, 2005; Volovik, 2004a,b).

Our measurements in superfluid ^{3}He at low temperatures show the same power-law behaviour observed in the ^{4}He towed grid experiments and can, therefore, also be explained by a Richardson type cascade with energy dissipated at the smallest length scales. However, in the absence of viscosity, what determines the decay rate? As argued by Vinen (Vinen and Niemela, 2002) on purely dimensional grounds, any dissipation process associated with pure superfluid turbulence is likely to give a dissipation of order $\kappa(\kappa L)^2$. The effective kinematic viscosity in the decay equation should therefore be replaced by a term $\zeta\kappa$, where ζ is a dimensionless constant. The line density associated with the turbulent decay at late times should thus be described by

$$L = (d/2\pi\kappa)\sqrt{(27C^3/\zeta\kappa)}\, t^{-3/2}. \tag{27}$$

By chance, in superfluid ^{4}He, the kinematic viscosity and circulation quantum are numerically similar, $\nu \approx 0.1\kappa$, so the ^{4}He data are also consistent with this scenario with $\zeta \approx 0.2$. If we apply this same equation to our data, with $d = 1.5\,\text{mm}$ and $\zeta = 0.2$, then we obtain the line labeled '^{3}He quantum' in the figure. (This is equivalent to scaling the late-time He-II data by d and κ). The excellent agreement between the ^{4}He and ^{3}He data is very remarkable, given that not only is the superfluidity in the two systems based on completely different mechanisms, but the data were also taken in opposing temperature regimes. We should note, however, that the similarity may be somewhat coincidental. Recent measurements using ion trapping techniques to observe the turbulent decay of vorticity after stopping the rotation of a sample of superfluid ^{4}He indicate a transition at lower temperatures in which the effective kinematic viscosity decreases by an order of magnitude or two (Walmsley et al., 2007). The transition may be due to a 'bottleneck' in the flow of energy to smaller length scales, which is predicted to occur when Kelvin-waves become the dominant source of dissipation in superfluid ^{4}He (Kozik and Svistunov, 2008; L'vov et al., 2007). There has also been some recent work which suggests that

there might be interesting features in the temperature dependance of the dissipation in superfluid ^{3}He (Eltsov et al., 2007).

Finally, we comment on the data labeled simulation in Figure 31. These represent the results of a recent computer simulation of the vibrating grid experiments by Mitani and Tsubota (Tsubota, 2008). The turbulence is produced by vortex rings injected randomly from a plane (representing the grid). The injected ring density is sufficiently high that they collide and produce a vortex tangle (quantum turbulence). The vortex line density is then measured as a function of time after stopping the ring injection, and plotted with the experimental data in Figure 31. Although the simulation volume is somewhat smaller than the turbulent region in the experiments, the simulation results show a comparable late time behaviour. This is remarkable for two reasons. First, the simulations were based on the local induction approximation in which inter-vortex coupling is neglected. Second, the simulation is done for zero temperature and has no physical dissipation mechanism. In practice, the simulation does have a loss mechanism associated with its finite space resolution in that energy transferred to smaller length scales is effectively lost, resulting in the observed decay. While the similarity of the simulation results to the experimental decay data is intriguing, further work is required to make a more meaningful comparison. However, this early work highlights the powerful potential of computer simulations as an aid to better understand and interpret experiments on quantum turbulence.

17. SUMMARY

During the past few years, we have made some very significant findings concerning the behaviour of quantum turbulence in the low temperature limit. The work is only made possible by the very large quasiparticle Andreev scattering cross-sections of vortices in ^{3}He-B. This allows us to effective shine quasiparticles on to the vortices and observe their behaviour using vibrating wire techniques. The system, being relatively simple, is particularly accessible to computer simulations, and we can learn a great deal by comparing these with experiments. Although we have already learnt much about the vortex production, tangle generation and decay processes, there is still much more to be learnt. For instance, we would like to understand quantitatively what controls the vortex production rate, the entanglement process, the spatial extent and the dynamics of the quantum turbulence. We are currently investigating the fluctuations and spatial correlations in the vortex signals which we hope could reveal much more information concerning the tangle dynamics. Other important questions still to be answered concern the microscopic decay mechanisms in the zero temperature limit and how we might investigate them experimentally.

The remarkable similarities between turbulent decay behaviour observed in the ^{3}He experiments at low temperatures, the ^{4}He experiments at high temperatures, the simplified zero temperature simulations and the simple model based on the classical Richardson cascade strongly suggest that, despite the high complexity of turbulence, some of its underlying properties can be understood on rather simple principles common to very different systems, whether quantum or classical. The particular simplicity of quantum turbulence in the low temperature limit therefore provides a valuable tool which may eventually lead to a better understanding of turbulence in general.

REFERENCES

Araki, T., Tsubota, M. and Nemirovskii, S. K. (2002). *Physical Review Letters*, 89, 145301.

Andreev, A. F. (1964). *Soviet Physics JETP*, 19, 1228.

Bartkowiak, M., Daley, S. W. J., Fisher, S. N., Guénault, A. M., Plenderleith, G. N., Haley, R. P., Pickett, G. R. and Skyba, P. (1999). *Physical Review Letters*, 83, 3462.

Bartkowiak, M., Fisher, S. N., Guénault, A. M., Haley, R. P., Pickett, G. R., Plenderleith, G. N. and Skyba, P. (2000). *Physical Review Letters*, 85, 4321.

Bartkowiak, M., Fisher, S. N., Gunault, A. M., Haley, R. P., Pickett, G. R. and Skyba, P. (2004). *Physical Review Letters*, 93, 045301.

Bäuerle, C., Bunkov, Y. M., Fisher, S. N., Godfrin, H. and Pickett, G. R. (1996). *Nature*, 382, 332.

Bäuerle, C., Bunkov, Y. M., Fisher, S. N. and Godfrin, H. (1998). *Physical Review B*, 57, 14381.

Bevan, T. D. C., Manninen, A. J., Hook, J. B. and Hall, H. E. (1997). *Journal of Low Temperature Physics*, 109, 423.

Bradley, D. I., Bunkov, Yu. M., Cousins, D. J., Enrico, M. P., Fisher, S. N., Follows, M. R., Guénault, A. M., Hayes, W. M., Pickett, G. R. and Sloan, T. (1995). *Physical Review Letters*, 75, 1887.

Bradley, D. I. (2000). *Physical Review Letters*, 84, 1252.

Bradley, D. I., Fisher, S. N., Guénault, A. M., Lowe, M. R., Pickett, G. R. and Rahm, A. (2003). *Physica B*, 329, 104.

Bradley, D. I., Fisher, S. N., Guénault, A. M., Lowe, M. R., Pickett, G. R., Rahm, A. and Whitehead, R. C. V. (2004a). *Physical Review Letters*, 93, 235302.

Bradley, D. I., Clubb, D. O., Fisher, S. N., Guénault, A. M., Matthews, C. J. and Pickett, G. R. (2004b). *Journal of Low Temperature Physics*, 134, 381.

Bradley, D. I., Clubb, D. O., Fisher, S. N., Guénault, A. M., Haley, R. P., Matthews, C. J., Pickett, G. R. and Zaki, K. L. (2005a). *Journal of Low Temperature Physics*, 138, 493.

Bradley, D. I., Clubb, D. O., Fisher, S. N., Guénault, A. M., Haley, R. P., Matthews, C. J., Pickett, G. R., Tseplin, V. and Zaki, K. (2005b). *Physical Review Letters*, 95, 305302.

Bradley, D. I., Clubb, D. O., Fisher, S. N., Guénault, A. M., Haley, R. P., Matthews, C. J., Pickett, G. R., Tsepelin, V. and Zaki, K. (2006). *Physical Review Letters*, 96, 035301.

Bradley, D. I., Fisher, S. N., Guénault, A. M., Haley, R. P., Matthews, C. J., Pickett, G. R., Roberts, J., O'Sullivan, S. and Tseplin, V. (2007). *Journal of Low Temperature Physics*, 148, 235.

Carless, D. C., Hall, H. E. and Hook, J. R. (1983). *Journal of Low Temperature Physics*, 50, 605.

Cousins, D. J., Enrico, M. P., Fisher, S. N., Phillipson, S. L., Pickett, G. R., Shaw, N. S. and Thibault, P. J. Y. (1996). *Physical Review Letters*, 77, 5245.

Cousins, D. J., Fisher, S. N., Guńault, A. M., Haley, R. P., Miller, I. E., Pickett, G. R., Plenderleith, G. N., Skyba, P., Thibault, P. Y. A. and Ward, M. B. (1999). *Journal of Low Temperature Physics*, 114, 547.

Donnelly, R. J. (1991). *Quantized Vortices in Helium II*. Cambridge University Press, Cambridge.

Eltsov, V. B., Golov, A. I., de Graaf, R., Häninen, R., Krusius, M., L'vov, V. S. and Solntsev, R. E. (2007). *Physical Review Letters*, 99, 265301.

Enrico, M. P., Fisher, S. N., Guénault, A. M., Pickett, G. R. and Torizuka, K. (1993). *Physical Review Letters*, 70, 1846.

Enrico, M. P., Fisher, S. N. and Watts-Tobin, R. J. (1995). *Journal of Low Temperature Physics*, 98, 81.

Finne, A. P., Araki, T., Blaauwgeers, R., Eltsov, V. B., Kopnin, N. B., Krusius, M., Skrbek, L., Tsubota, M. and Volovik, G. E. (2003). *Nature*, 424, 1022.

Fisher, S. N., Guénault, A. M., Kennedy, C. J. and Pickett, G. R. (1989). *Physical Review Letters*, 63, 2566.

Fisher, S. N., Pickett, G. R. and Watts-Tobin, R. J. (1991). *Journal of Low Temperature Physics*, 83, 225.

Fisher, S. N., Guénault, A. M., Kennedy, C. J. and Pickett, G. R. (1992). *Physical Review Letters*, 69, 1073.

Fisher, S. N., Guénault, A. M., Hale, A. J. and Pickett, G. R. (2000). *Journal of Low Temperature Physics*, 121, 393.

Fisher, S. N., Hale, A. J., Guénault, A. M. and Pickett, G. R. (2001). *Physical Review Letters*, 86, 244.

Greywall, D. S. (1985). *Physical Review B*, 33, 7520.

Guénault, A. M., Keith, V., Kennedy, C. J., Mussett, S. G. and Pickett, G. R. (1986). *Journal of Low Temperature Physics*, 62, 511.

Hänninen, R., Mitani, A. and Tsubota, M. (2006). *AIP Conference Proceedings*, 850, 217.

Hänninen, R., Tsubota, M. and Vinen, W. F. (2007). *Physical Review B*, 75, 064502.

Kibble, T. W. B. (1976). *Journal of Physics A*, 9, 1387.

Kozik, E. V. and Svistunov, B. V. (2008). *Physical Review B*, (in press).

Landau, L. D. and Lifshitz, E. M. (1966). *Fluid Mechanics*. Pergamon Press, London.

L'vov, V. S., Nazarenko, S. V. and Rudenko, O. (2007). *Physical Review B*, 76, 024520.

Pickett, G. R. and Fisher, S. N. (2003). *Physica B*, 329, 75.

Ruutu, V. M. H., Eltsov, V. B., Gill, A. J., Kibble, T. W. B., Krusius, M., Makhlin, Y. G., Placais, B., Volovik, G. E. and Xu, W. (1996). *Nature*, 382, 334.

Skrbek, L., Niemela, J. J. and Donnelly, R. J. (2000). *Physical Review Letters*, 85, 2973.

Stalp, S. R., Skrbek, L. and Donnelly, R. J. (1999). *Physical Review Letters*, 82, 4831.

Stalp, S. R., Niemela, J. J., Vinen, W. F. and Donnelly, R. J. (2002). *The Physics of Fluids*, 14, 1377.

Tsubota, A, private communication.

Walmsley, P. M., Golov, A. I., Hall, H. E., Levchenko, A. A. and Vinen, W. F. (2007). *Physical Review Letters*, 99, 265302.

Wheatley, J. C. (1975). *Reviews of Modern Physics*, 47, 415.

Vinen, W. F. and Niemela, J. J. (2002). *Journal of Low Temperature Physics*, 128, 167.

Vinen, W. F. (2005). *Physical Review B*, 71, 024513.

Volovik, G. E. (1992). *Exotic Properties of Superfluid 3He*. World Scientific, Singapore.

Volovik, G. E. (2004a). *Journal of Low Temperature Physics*, 136, 309.

Volovik, G. E. (2004b). *JETP Letters*, 80, 479.

Zurek, W. H. (1985). *Nature*, 317, 505.

CHAPTER **4**

The Use of Vibrating Structures in the Study of Quantum Turbulence

L. Skrbek* and **W. F. Vinen**[†]

* Faculty of Mathematics and Physics, Charles University, V Holešovičkách 2, 18000 Prague, Czech Republic
[†] School of Physics and Astronomy, University of Birmingham, Birmingham B15 2TT, UK

Abstract   Vibrating structures such as discs, spheres, grids and wires have been widely used in research on quantum fluids and are playing a valuable role in the investigation of quantum turbulence. Quantum turbulence, a form of turbulence observed in superfluids, differs from that in classical fluids for three reasons: except at the lowest temperatures, superfluids exhibit two-fluid behaviour; the superfluid component can flow without dissipation; and superflow is subject to severe quantum restrictions, so that rotational motion can exist only through the presence of quantised vortex lines. In spite of these differences, there is evidence that quantum turbulence can exhibit features similar to those observed in its classical counterpart, especially on large length scales. Therefore, we first describe and try to understand how the simplest form of laminar flow breaks down around various oscillating structures in a classical fluid, leading at high enough Reynolds number to fully turbulent flow. Then we address analogous questions in the quantum cases so that our study combines the challenges met in the study of classical turbulence with those associated with quantum phenomena in condensed matter systems. We emphasise that, in spite of undoubted similarities between the quantum and classical cases, there must be an important difference relating to the initial transition from the simplest laminar flow: in the classical case, this simplest flow is of a viscous laminar type with no slip at a solid boundary, whereas in the quantum case the simplest flow is irrotational with complete slip. We discuss evidence that the transition to quantum turbulence can take place in two steps: the first occurs in the superfluid component and leads to the generation of a random tangle of vortex lines; the second involves the generation of large-scale rotational motion in both the superfluid and, if appropriate, the normal fluid, the motion mimicking the behaviour observed in a classical fluid.

1. INTRODUCTION

Turbulence in the superfluid component of ^{4}He was first mentioned as a theoretical possibility by Feynman (1955), who suggested that it takes the form of a random tangle of quantised vortex lines. At about the same time, it was shown experimentally that counterflow of the two fluids, associated with a heat current, exhibits the characteristics of turbulent flow, and it was suggested that this turbulence is homogeneous and maintained in the superfluid component by the relative motion of the two fluids (Vinen, 1961). There followed much study of counterflow quantum turbulence, both experimentally (Tough, 1982) and theoretically, and an understanding of at least some of its principal characteristics owed much to the pioneering simulations of Schwarz (1988). Steady-state counterflow turbulence has no

classical analogue, and it was not until the 1990s that there was serious study of forms of quantum turbulence that do have classical counterparts.

A particularly simple but important form of classical turbulence is produced by steady flow through a grid. At a significant distance downstream from the grid, the turbulence is at least approximately homogeneous and isotropic, and the development of an understanding of this simple form of turbulence has been important in contributing to our general understanding of turbulent flow (Batchelor, 1953; Frisch, 1995). The quantum analogue was first studied by Stalp et al. (1999); Skrbek et al. (2000); Skrbek and Stalp (2000), although a very important experiment by Maurer and Tabeling (1998) on turbulence generated by counter-rotating blades pointed the way towards an understanding of the experimental results. Although these experiments were concerned with superfluid ^{4}He at temperatures above 1K, the helium carried no heat current, so that at least on average the two fluids could flow without relative motion, in contrast to the situation in counterflow turbulence. Indeed, as has now become widely accepted (Vinen, 2000), the two fluids have velocity fields that are closely similar, except on length scales comparable with or less than the spacing between vortex lines. The statistical properties of this single velocity field prove to be very similar to those in classical grid flow, and to involve a Richardson cascade in which there is a flow of energy from large-scale to small-scale motion; the energy flow is due to the nonlinear terms in the Navier-Stokes equation. Correspondingly, in the *inertial range* of wave numbers, the energy spectrum has, to a good approximation, the Kolmogorov (K41) form

$$E(k) = C\epsilon^{2/3}k^{-5/3}; \tag{1}$$

$E(k)\mathrm{d}k$ is the turbulent energy per unit mass associated with wave numbers in the range k to $k + \mathrm{d}k$ in a spatial Fourier analysis of the velocity field; ϵ is the rate of flow of energy per unit mass down the cascade, equal to the rate of dissipation of the total energy; and C (the *Kolmogorov constant*) is of order unity. By the inertial range, we mean the range of wave numbers in which there is negligible dissipation; dissipation must of course exist at higher wave numbers to provide a sink into which the energy flux ϵ can ultimately flow. In classical turbulence, there are small deviations from Kolmogorov scaling associated with, for example, intermittency, and even these have been observed in the quantum case (Maurer and Tabeling, 1998). The physical picture we have of classical grid turbulence is therefore as follows. Steady flow through the grid produces eddy motion on a (large) scale, comparable with that of the confining boundaries (the mesh of the grid or the size of the channel in which flow takes place); nonlinear coupling transfers energy in a cascade to smaller and smaller scales until the scale is so small that dissipation occurs. In a classical fluid, dissipation

is associated with viscosity and it sets in at wave numbers greater than the reciprocal of the *Kolmogorov dissipation length*, which is equal to $(\nu^3/\epsilon)^{1/4}$, where ν is the kinematic viscosity of the fluid. In superfluid ^{4}He above 1K, the dissipation occurs on a scale comparable with the vortex spacing and is due to a combination of normal fluid viscosity and mutual friction (Vinen and Niemela, 2002), mutual friction being the force that acts between a vortex line and the normal fluid when there is appropriate relative motion (Donnelly, 1991).

We see then that quantum grid turbulence can be very similar in its structure to its classical counterpart. The reasons have been discussed extensively in the literature (Vinen and Niemela, 2002). The turbulent superfluid component contains a more or less random array of quantised vortex lines. The flow of such a component, isolated from any normal fluid, is believed to be governed by principles very similar to those operating in an inertial range for a classical fluid, provided that the scale of the motion is large compared with the spacing, ℓ, between the vortex lines (Figure 1). A Richardson cascade can develop, characterised by a Kolmogorov energy spectrum. Flow of the superfluid on a scale larger than ℓ is achieved by some local polarisation of the vortex tangle so that the tangle ceases to be strictly random. If both fluids are present, each can support a classical Richardson cascade independently of the other, and mutual friction will serve to ensure that the two velocity fields are essentially identical. This picture can apply only if, as is the case for ^{4}He, the normal fluid has a sufficiently small viscosity so that there is a wide inertial range in the normal fluid. Indeed, in the case of ^{4}He above 1K, there is typically dissipation in the normal fluid only at wave numbers greater than ℓ^{-1}. The situation in superfluid ^{3}He-B is very different, because in this case the normal fluid
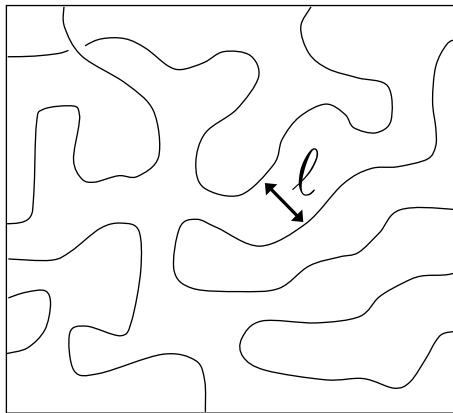
FIGURE 1   Illustrating the average spacing between vortex lines in a tangle.

has such a high viscosity that normal fluid turbulence is hardly possible on any laboratory scale (Finne et al., 2006).

The type of quantum turbulence that we have just described, in which the superfluid system is behaving like a single classical fluid, will be called *quasiclassical*. We emphasise that such quasiclassical behaviour can occur only on length scales larger than ℓ. On length scales less than ℓ, the discrete structure associated with the quantised vortices rules out behaviour that is similar to that of a classical fluid.

The observations of quantum turbulence that we have been describing lead to a number of interesting questions. The observation of quasiclassical behaviour has been confined for the most part to superfluid ^{4}He at temperatures above about 1.1 K. Although the normal fluid fraction at these lowest temperatures is less than 2%, there exists the possibility that the classical normal fluid is somehow forcing quasiclassical behaviour on the superfluid component. This possibility, albeit remote, requires that we attempt to observe quasiclassical grid turbulence in the superfluid component, in both ^{4}He or ^{3}He-B, at temperatures so low that the fraction of normal fluid is negligible.

A second, and very interesting, question relates to the mechanism by which homogeneous quantum turbulence can be dissipated in the absence of the normal fluid: the mechanisms operating in ^{4}He above 1 K, which depend on the viscosity of the normal fluid and on the force of mutual friction between the vortices and the normal fluid, disappear at temperatures well below 1 K. The continuing existence of a Richardson cascade depends of course on the continuing existence of dissipation at a large wave number.

A third group of questions relate to the extent to which other types of flow can exhibit quasiclassical characteristics. A type of classical turbulent flow that is commonly studied is that occurring at high Reynolds number past some obstacle: a sphere, a cylinder or a plate (Figure 2). For example, can superflow past a sphere involve the shedding of quasiclassical vortices, similar to those seen in classical fluids, and if so, at what critical velocity, analogous to the critical Reynolds number, does the flow cease to be laminar (or potential)? Flow in the immediate neighbourhood of a grid is also interesting, before the flow settles into the homogeneous isotropic type of turbulence that we find well downstream of the grid. These questions are perhaps especially interesting and perhaps easier to answer at the lowest temperatures, where the processes cannot be influenced by any normal fluid.

It is with studies relating to this last group of questions that this chapter is primarily concerned although, as we shall see, there is significant overlap between the three groups of questions. The plan of the chapter is as follows. It turns out, as we shall discuss in Section 2, that the study of quantum turbulence at the lowest temperatures is severely influenced by

(a)   (b)

(c)   (d)   (e)
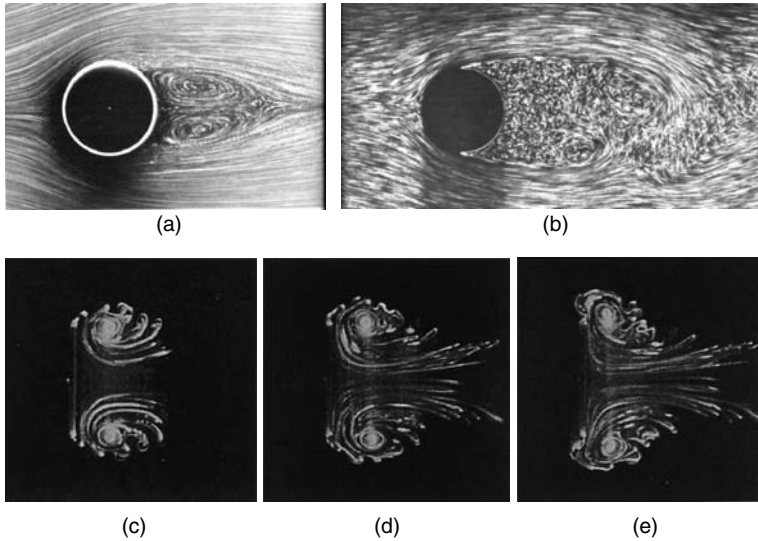
FIGURE 2 Upper photographs (due to S. Taneda): steady flow of a classical fluid past a circular cylinder for Reynolds number Re of (a) 26 and (b) 2000. Lower photographs: the evolution of the vortex structure behind flat disc of diameter d set moving at dimensionless time $T = U_0 t/d = 0$ with velocity U_0 normal to the disc; (c) $T = 2.4$; (d) $T = 3.4$; (e) $T = 3.7$ (Higuchi and Balligant, 1996).

experimental difficulties. Consideration of these difficulties has led to the extensive experimental study of oscillating structures (spheres, cylinders or grids) in a superfluid at the lowest temperatures, in spite of associated difficulties in interpretation. Such experimental techniques as are available will be described. In Section 3, we summarise briefly what we know about the steady flow of a classical fluid past various forms of obstacle. As we shall see in Section 4, the behaviour in an oscillating classical flow, or the behaviour of a structure undergoing oscillatory movement in a classical fluid, can be quite complicated; more complicated, and probably less well understood, than is the case for steady flow. We shall attempt to give the reader some flavour of these complications, too much detail being at this stage unnecessary and undesirable. Nevertheless we devote significant space to the discussion of the various classical cases, because we believe that some understanding of these cases is important in developing an understanding of the corresponding quantum cases. In Section 5, we summarise the experimental results that have been obtained with oscillating structures in superfluids, focussing our attention significantly but not exclusively on the lowest temperatures. An important message in this Section is that the experimental results are often incomplete so that dependence on important parameters, such as the frequency of oscillation and

the size of the structure, cannot be elucidated with any confidence. In Section 6, we shall attempt to understand the experimental results using classical analogies, simple physical arguments and the results of computer simulations. Overall, we shall be left with many unanswered questions, and we hope that this chapter will serve to stimulate more work.

2. EXPERIMENTAL TECHNIQUES

Much of our real and detailed knowledge of classical turbulence depends on an ability to visualise the flow. Seeding the flow with appropriate small particles allows the naked eye to form a picture of the flow, and the more sophisticated technique of particle image velocimetry allows one to obtain detailed information about the turbulent velocity field. Attempts to visualise the flow of a superfluid face serious difficulties, and although some intriguing experimental results are starting to appear, they can as yet throw little light on the problems discussed in this chapter (Bewley et al., 2006; Zhang et al., 2004). There are two fundamental difficulties (Poole et al., 2005). First, as in normal liquid helium, it is hard to find suitable seeding particles, which must be small enough to allow observation of the motion on a very small scale that is often characteristic of quantum turbulence, and which must be at least approximately neutrally buoyant in the low-density helium. Second, a turbulent superfluid has associated with it in general a number of different velocity fields: that of the normal fluid, that of the superfluid and that of the quantised vortex lines. The hope is that different sizes of particle will respond to these fields in different ways and so allow pictures of the fields to be built up, but we remain a long way from the realisation of this hope.

Various forms of velocimeter are available for the study of classical fluid flow, especially hot wire anemometers and laser-Doppler anemometers. Again there is the question of what velocity field is being measured. The work of Maurer and Tabeling (1998) was based on the use of a small pressure sensor that allowed the observation of pressure fluctuations from which velocity fluctuations can be deduced; the development of this promising technique has received very little attention, probably because the study of small-scale turbulence would require the construction of pressure sensors that are smaller than are at present commercially available.

Much early work on quantum turbulence in ^{4}He thermal counter-flow depended on the use of second sound as a probe of the turbulent velocity field. Second sound is attenuated by the mutual friction that accompanies the presence of vortex lines, and a measurement of this attenuation provides valuable data on the density of vortex line within the volume of the second-sound field. Recent attempts to use a very small

second-sound cell as a localised probe are proving hard to interpret (Roche et al., 2007). Unfortunately, second sound does not propagate in either ^{4}He at low temperatures or ^{3}He-B at any temperature. Measurements of pressure and temperature gradients in superflows through tubes provide the analogues of similar measurements in classical systems as do measurements of the force on an obstacle in the flow. We shall find that measurements of this type of force provide us with practically all we often know about turbulent superflow past an obstacle.

Ions are trapped by vortex lines at low temperatures; measurement of such trapping can in principle yield vortex densities although trapping cross-sections for bare ions are probably rather too small. The idea of using small charged vortex rings as a probe of turbulence in ^{4}He at low temperatures is being explored by Golov and his colleagues with very interesting results on turbulence generated by stopping the rotation of a vessel containing superfluid ^{4}He at a very low temperature (Walmsley et al., 2007). These ion-based techniques are unlikely to yield the localised probes that are required for the study of flow past an obstacle. A promising technique based on the use of neutral He$_2$ excimer molecules as tracers, combined with localised detection based on very sensitive spectroscopic techniques, has been suggested recently (McKinsey et al., 2005), and we look forward to the development of this approach. The possibility that a small vibrating structure might respond in a well-defined way to turbulence localised in its neighbourhood is being explored and could lead to a useful localised detector for use in ^{4}He at very low temperatures.

Special techniques based on nuclear magnetic resonance and Andreev reflection processes are available for the study of turbulence in superfluid ^{3}He-B, and these are described in other chapters in this volume. They are potentially very interesting, although they do not as yet provide the detailed information that is available through visualisation techniques to the student of classical turbulence. We shall wish to refer later to the use of Andreev scattering of thermal quasiparticles to provide an image of a localised region of turbulence in ^{3}He at a very low temperature, especially in connection with turbulence produced by a vibrating grid.

We have focussed on difficulties in finding suitable detectors of quantum turbulence. But at very low temperatures, there are also problems associated with the production of simple and well-characterised forms of quantum turbulence. Ideally, it would be desirable to study steady flows, either through a grid or past an obstacle. The generation of such a steady flow, without this flow being itself turbulent, seems practically impossible. The existing experiments on quantum grid turbulence at temperatures above 1 K by Stalp et al. (1999) were based on a grid moving steadily through a stationary fluid, but attempts to build such a towed grid system in ^{4}He at low temperatures are proving difficult: the

helium has a very small heat capacity so that even a minute amount of dissipation arising from the towing mechanism can raise the temperature of the helium by an unacceptable amount. Indeed the decay of the quantum turbulence itself can raise the temperature significantly, and this has been proposed as the basis of a technique for the study of this important decay process.

The fact that quantum turbulence involving steady flow seems so difficult to achieve has led to the use of oscillating structures in practically all existing experiments at very low temperatures, in spite of the fact that interpretation of the results is difficult. It is to the results obtained with such structures, and to their interpretation, that we now turn. We begin by reminding the reader about patterns of *steady* classical flow past an obstacle before going on to the case of *oscillating* flow.

3. STEADY CLASSICAL FLOW PAST VARIOUS STRUCTURES

As is well known, the character of the incompressible steady flow of a classical fluid past an obstacle is determined by a single dimensionless parameter: the Reynolds number defined by the relation

$$\text{Re} = \frac{UR}{\nu}, \tag{2}$$

where U is the velocity of flow past the obstacle (measured at a distant point), R is the characteristic dimension of the obstacle (for example, the radius of a sphere), and ν is the kinematic viscosity of the fluid. In Figure 3, we show a sequence of diagrams depicting the evolution of the flow past a circular cylinder as the Reynolds number is increased. For Re $\ll$ 1, the flow is laminar. At Re $\sim$ 10 a pair of eddies appears behind the cylinder, and at Re $\sim$ 100 these eddies start to be cast off from the cylinder and a so-called *Karman vortex street* is formed. Further increase in the Reynolds number leads gradually to a region of fully-developed turbulence in the wake of the cylinder.

These patterns of flow can be understood physically as follows. Consider the forces acting on the fluid immediately behind the cylinder in the laminar regime. There are two contributions: a viscous force, in the direction towards the stagnation point at the rear of the cylinder, and a Bernoulli pressure force acting in the opposite direction. The viscous force per unit volume has a magnitude of order $\eta U/R^2$; the Bernoulli force per unit volume has a magnitude of order $\rho U^2/R$ (η is the dynamic viscosity of the fluid, and ρ is its density). As long as the Bernoulli force is much less than the viscous force, its effect is negligible, but as soon as it exceeds the viscous force, the flow near the rear surface of the cylinder tends to be
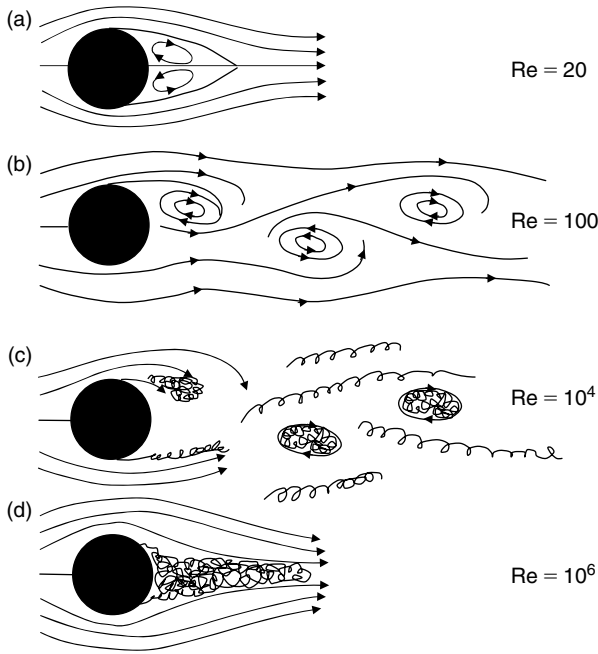
FIGURE 3   Patterns of flow in the wake of a cylinder moving with constant velocity in a classical fluid.

reversed with the consequent formation of an eddy. This change in regime occurs when the two forces become roughly equal, which is easily seen to correspond to Re ∼ 2, which is not far wrong.

The flow at high Reynolds number can be divided into two regions, separated by a *surface of separation*. Inside the region at the rear of the cylinder bounded by the surface of separation, there is fully-developed turbulence; outside it the flow is approximately that of an ideal fluid (irrotational) except in a thin boundary layer close to the surface of the cylinder (see Figures 2 and 3).

The net drag force, F, on the cylinder is of particular interest, and its value is often expressed in terms of a drag coefficient, C_D, defined by the equation

$$F = \frac{1}{2} C_D \rho A U^2, \tag{3}$$

where A is the projected area of the structure on a plane normal to the bulk flow. For laminar viscous flow, the drag is approximately proportional to U so that $C_D \sim U^{-1}$; the multiplicative constant is proportional to the dynamic viscosity of the fluid. In the opposite limit of high Re, the total

force on the cylinder is due mainly to Bernoulli pressure forces. We first recall that in the case of laminar (potential) flow of an ideal fluid past a cylinder the flow is symmetrical about a plane through the centre of the cylinder and perpendicular to the flow. The net Bernoulli force then vanishes (the d'Alembert paradox). In the case of flow at high Reynolds number, as we have noted, flow outside the wake is similar to that for ideal flow with an appropriate contribution to the net Bernoulli force. But within the wake, the flow velocities are much smaller, and the net Bernoulli force is very small. The cancellation leading to the d'Alembert paradox no longer holds, and, as is easily seen, there must be a net drag force given by a drag coefficient of order unity. Similar considerations apply to forms of obstacle other than a cylinder.

The observed behaviour of the drag coefficient for obstacles of different shape is shown in Figure 4. We see that in general terms it accords with the discussion that we have just presented. The exact value of C_D at high Reynolds number depends on the position of the surface of separation. In the case of a disc placed normal to the flow, the surface of separation coincides closely (to within a boundary layer thickness) with the edge of the disc, and C_D is very close to unity. In the case of a sphere, the surface of separation tends to be further to the rear of the obstacle, leading to a
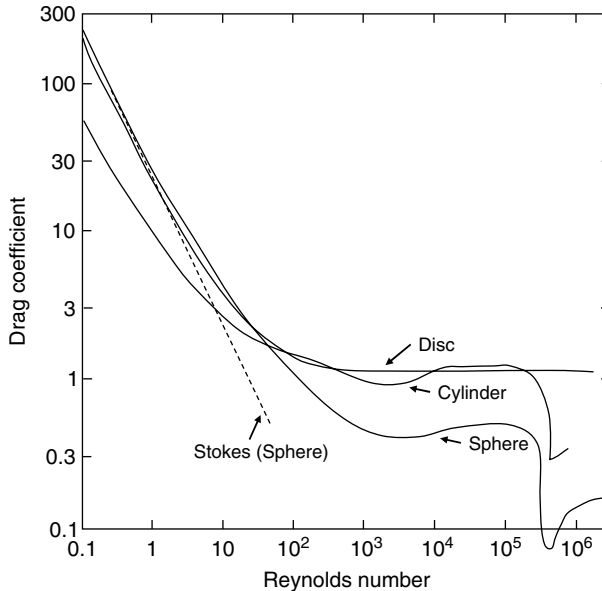
FIGURE 4   Plots of drag coefficient against Reynolds number for steady flow past various forms of obstacle. Stokes law for a sphere (Batchelor, 1967), valid at low Re, is represented by the broken line.

smaller value of C_D. The sudden fall in the value of C_D for a cylinder or sphere at a Reynolds number of about 3×10^5 (the so-called *drag crisis*) is associated with a transition from laminar to turbulent flow within the very thin boundary layer, a transition that results in a sudden shift in the surface of separation towards the rear of the sphere. We note the interesting fact that this is the only Reynolds number at which there is an abrupt change in the drag coefficient. This suggests that the formation of large-scale vortices behind a cylinder at Re ~ 10 occurs to some extent gradually, although strictly speaking there may be a velocity below which no vortices are present.

A photograph showing steady flow of a classical fluid through a grid formed by drilling small holes in a thin solid sheet is shown in Figure 5. We see that a jet is formed at each hole, and that each opaque region of the grid acts like an individual disc, with separation occurring at the edge of the disc. Downstream the vortex sheets formed at the surfaces of separation become unstable, and the flow gradually breaks up into fully-developed turbulence. We can expect the drag on the grid Equation (3) to correspond to a drag coefficient close to unity if A is taken to be the area of the opaque regions.

Although this chapter is primarily concerned with turbulence generated by structures vibrating in superfluids, we believe that it is useful to mention here one experiment on steady-state flow of superfluid helium past a sphere, performed by Van Sciver's Group in Tallahassee, Florida (Smith et al., 1999). A sphere was placed in a steady flow of the helium achieved by squeezing bellows. The pressure distribution around the sphere was measured, from which the total drag could be calculated. Although the scatter in the data is rather large, the dependence of drag
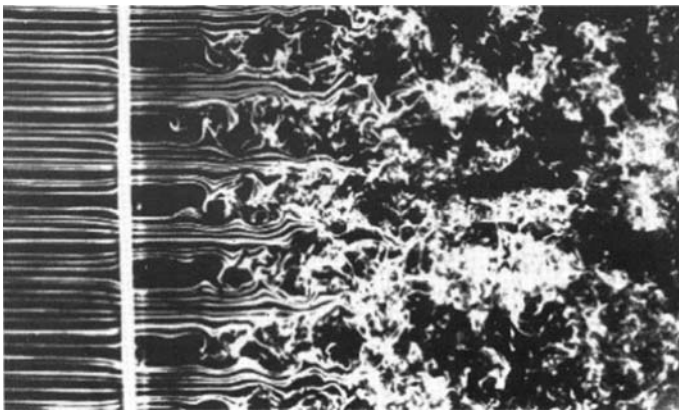
FIGURE 5   Steady flow (from the left to the right) of a classical fluid through a grid. Photograph by T. Corke and H. Nagib.

coefficient on velocity was found to be very similar to that in a classical flow, including the dip associated with the drag crisis. In this experiment, flow of both the normal fluid and the superfluid component was turbulent, and the two velocity fields were locked together by mutual friction; the coupled fluids then behaved like a single classical fluid. Later, we shall encounter similar situations in oscillatory flow.

4. OSCILLATORY FLOW OF A CLASSICAL FLUID PAST VARIOUS STRUCTURES

We turn now to the case when the steady flow past the structure is replaced by a flow that oscillates at angular frequency ω. The case in which we are really interested is that in which a structure oscillates within an otherwise stationary fluid, and we shall assume that the two are equivalent. Throughout our discussion, we shall ignore the phenomenon of steady streaming (Batchelor, 1967; Schlichting and Gersten, 2000).

The oscillatory case is more complicated than that of steady flow because a second length scale appears in addition to the linear size of the obstacle. This new length scale is the viscous penetration depth given by

$$\delta = \sqrt{\frac{2\nu}{\omega}}. \tag{4}$$

The character of the flow is therefore determined by two dimensionless parameters instead of one. These two parameters can be chosen in different ways. We shall follow much of the classical literature and take them to be the *Keulegan-Carpenter number*, defined by

$$K_C = \frac{2\pi a}{d}, \tag{5}$$

and the *Stokes number*, defined by

$$\beta = \frac{\omega d^2}{2\pi\nu}, \tag{6}$$

where d is the characteristic linear size of the obstacle and a is the amplitude of oscillation. We see that apart from a numerical factor the Stokes number is the ratio of the square of the linear dimension, d, to the square of the viscous penetration depth, δ, at the frequency ω. The Reynolds number is formed from the product of K_C and β. Sometimes the Keulegan-Carpenter number is called the Strouhal number (Landau and Lifshitz, 1987), although sometimes, confusingly, the Strouhal number is taken as the reciprocal of the Keulegan-Carpenter number (Batchelor, 1967).

4.1 Oscillatory Flow Past a Circular Cylinder

We shall start by considering the case of a cylinder of circular cross-section, for which we can take d as the diameter.

Owing, in part, to the importance of this topic in marine engineering, a considerable number of experimental studies have been published on the oscillatory flow of a classical fluid past a cylinder. As examples, we quote the work of Williamson (1985), Sarpkaya (1986), Obasaju et al. (1988) and Tatsuno and Bearman (1990). Most of these chapters include both visual representations of the flow and values of the drag coefficient. At a finite frequency, the drag coefficient has an imaginary part, which is related to the effective mass of the cylinder, although here we shall focus on the real (dissipative) part.

Most of this published work relates to values of β that are large compared with unity; that is, the viscous penetration depth is much less than the diameter of the cylinder. For cases of this type, the drag in the laminar regime (Re $<< 1$) is given generally by the formula

$$F_{\text{lam}} = \alpha S \, (\omega \eta \rho)^{1/2} \, U \,, \tag{7}$$

where S is the surface area of the structure, and α is a numerical coefficient, of order unity, that depends on the shape of the structure (Batchelor, 1967). For a cylinder of circular cross-section, $\alpha = 3\pi/4\sqrt{2}$. It follows from Equation (7) that the drag coefficient is given by

$$C_D = 2\alpha \frac{S}{A} \sqrt{\omega v} \, \frac{1}{U} = 2\sqrt{2} \, \pi \alpha \frac{S}{A} \frac{1}{K_C} (\pi \beta)^{-1/2} \,, \tag{8}$$

where, as before, A is the projected area of the structure.

At a large enough amplitude of oscillation, this laminar flow becomes unstable, and, as in the case of steady flow, the drag coefficient tends to a value of order unity. However, this tendency is accompanied by complicated oscillations in C_D within the range 0.5 to 2.0, suggesting that the details of the transition to turbulence are more complicated than is the case for steady flow. Visual observations confirm that this is indeed the case. Vortices are formed in the wake of the moving cylinder, but they can perform leapfrog motions over the surface of the cylinder as the velocity of the cylinder reverses, and they can be cast off in various transverse directions, the precise behaviour depending on the values of K_C and β. We refer the reader to the original papers for details.

It is interesting to consider the form of the initial instability and to ask for the corresponding critical values of K_C and β. It is tempting to suppose that the process involves a form of separation similar to that occurring in the case of steady flow. Such an argument leads to a critical value of K_C

equal to a constant of order unity, independently of β. It turns out that this is an overestimate, and that, at least for large values of β, the instability seems actually to be analogous to that occurring in the boundary layer of a rotating cylinder. In this case, it is due to a centrifugal effect analogous to the production of Taylor vortices in Couette flow, with the separation between the two rotating cylinders being replaced by the viscous penetration depth (Park et al., 1980); in other words, the instability is associated with the convex curvature of the boundary layer. This idea was first proposed by Honji (1981). A detailed theoretical analysis by Hall (1984) shows that for large values of β the critical value of the Keulegan-Carpenter number should be given by

$$K_C^{(\text{crit})} = 5.778\,\beta^{-1/4} \qquad (\beta \to \infty), \tag{9}$$

a relationship that was verified experimentally (Sarpkaya, 1986). The initial instability does not lead to what is strictly speaking turbulent flow; fully-developed turbulence is observed to appear at a value of K_C that is larger by a factor of about two than that given by Equation (9), and the drag coefficient is then close to unity.

In the limit of small β and large K_C, the behaviour of an oscillating cylinder ought to become similar to that of a steadily moving cylinder. In this latter case, the transition to turbulence takes place when the Reynolds number exceeds about 10. This means that

$$K_C^{(\text{crit})} = 10\,\beta^{-1} \qquad (\beta \to 0). \tag{10}$$

A single formula that interpolates sensibly between these two limits is

$$K_C^{(\text{crit})} = 10\,\beta^{-1} + 5.778\,\beta^{-1/4}. \tag{11}$$

Some evidence in support of this equation comes from the work of Tatsuno and Bearman (1990), where it is shown that for values of β in the range 5 to 50 the exponent in β is closer to $-1/2$ than to $-1/4$. We shall make use of formula (Equation (11)) in our later discussion.

4.2 Oscillatory Flow Past a Sphere

As far as we have been able to determine, very little work has been published on oscillatory flow past a sphere. Very recently, Donnelly (1991, private communication) has made preliminary observations of the flow generated by an oscillating sphere in water, and a typical pattern at $K_C = 3.0$ and $\beta = 430$ is shown in Figure 6. A single vortex ring, similar to that seen in Figure 6, is generated and flies away during each half
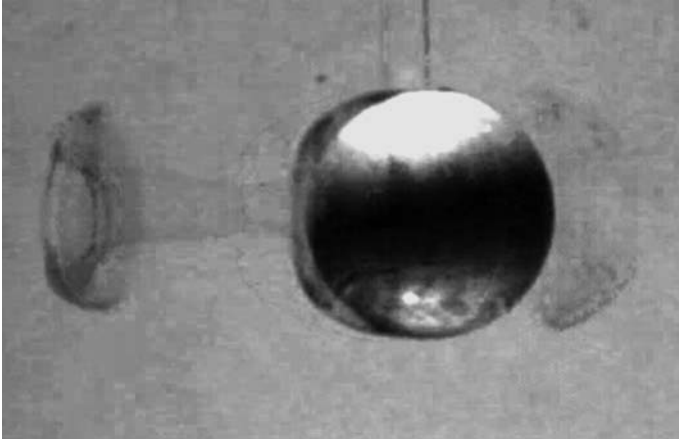
FIGURE 6   An oscillating sphere in water.

cycle of the oscillation. This is much simpler than is seen typically with an oscillating cylinder so that there is at least a hint that the behaviour of an oscillating sphere might generally be simpler than that of an oscillating cylinder. Although our own preliminary vizualisation experiment with a stainless steel sphere suspended as a pendulum in water qualitatively confirms this observation, there has been so far no systematic experimental study of the critical value of K_C, and there has been no measurement of the drag coefficient. It seems very likely that the situation depicted in Figure 6 will lead to a drag coefficient close to, or a little less than, unity, as we can see as follows. Let a be the amplitude of oscillation at angular frequency ω, and let Γ be the circulation in each vortex ring. Let the ring have radius R when it has moved from the sphere by a large distance, R being closely similar to the radius of the sphere. The impulse of the ring is equal to $\rho \pi R^2 \Gamma$. Given that one ring is produced during each half cycle, we see that the force on the sphere must have amplitude given by

$$F = \rho \pi R^2 \Gamma \frac{2\,\omega}{2\pi} = \rho R^2 \Gamma \omega.$$
(12)

If simple separation of the flow were to occur in each half cycle of the oscillation, a slug of fluid, at rest with respect to the sphere, would form in the wake of the sphere, this slug having length $\sim a$ and a discontinuity $\sim a\omega$ in the fluid velocity at its surface. In practice, this slug breaks up into a vortex ring, with circulation $\Gamma \sim a^2\omega$. It follows that the drag coefficient is of order unity. Since the ring at large distances from the sphere is observed to have a radius that is a little less than the radius of the sphere, we guess that the drag coefficient is a little less than unity.

There has been some consideration of the relevant theory by Otto (1992). He considered the linear stability of the flow around an oscillating sphere (for the cases of both transverse and torsional oscillations). He has shown that the flow, interacting with rigid boundaries of convex curvature, may become unstable to Taylor–Görtler vortices. This mechanism for the breakdown of the simplest form of laminar flow (basic flow) is similar to that described in the preceding section for the case of a transversally oscillating cylinder, and indeed Otto (1992) derives a formula for a sphere at high β that is similar to Equation (9) for a cylinder. In our later discussion, we shall therefore make the reasonable assumption that the initial instability in the case of a sphere is due to the centrifugal effect, as in the case of a cylinder, and that a formula similar to Equation (11) is applicable for all β.

4.3 Oscillatory Flow Past a Thin Flat Plate or Past a Cylinder of Rectangular Cross-section

The steady flow of a classical fluid past a thin flat disc is observed to be rather simple. As we have already mentioned, laminar flow at low velocities gives way at a critical velocity to a flow with separation occurring close to the edge of the disc. The fluid immediately behind the disc is initially at rest, although with increasing flow velocity this fluid becomes turbulent. The corresponding drag coefficient is obviously very close to unity (Figure 4).

We expect similar behaviour in the oscillating case. As far as we know, this precise case has not been investigated experimentally. However, recently some of us have investigated the damping in various fluids of a quartz tuning fork in which each prong is rectangular in shape with sharp corners (Figure 7). These small quartz tuning forks, manufactured to provide frequency standards in digital watches, provide interesting high-Q oscillating structures that can be used in cryogenic conditions. We might expect that the sharp corners on their prongs will lead to behaviour similar to that of a thin flat disc. The observation that the supercritical drag coefficient is close to unity tends to confirm the validity of this view.
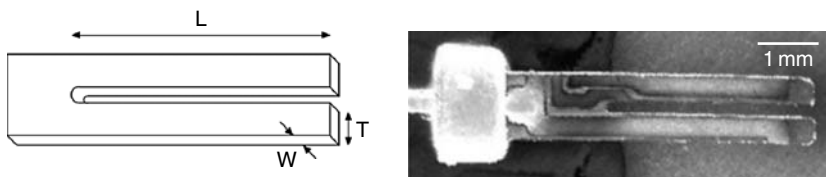
FIGURE 7 Schematic diagram and photograph of a typical commercially available quartz tuning fork.

We must now describe in more detail how the drag coefficient is observed to vary with velocity for these forks. In the laminar regime, the drag coefficient is given by an expression of the form in Equation (8) (Blaauwgeers et al., 2007), as is the case for a cylinder with circular cross-section, and, as we have just mentioned, the drag coefficient tends to a constant value, γ, close to unity, for large velocities (Blažková et al., 2007a). The transition from one regime to the other appears to be very smooth, suggesting a rather gradual transition from laminar to turbulent flow, and it is quite well represented by the equation

$$C_D = 2\alpha \frac{S}{A} (\omega v)^{1/2} \frac{1}{U} + \gamma. \tag{13}$$

The uppermost set of points in the plot of C_D against velocity in Figure 20 relates to liquid ${}^4\text{He}$ in the normal phase and has this form. The critical velocity, from which a critical Keulegan-Carpenter number can be calculated, is therefore somewhat ill defined, but we shall take it as given by the velocity at which the two terms on the right hand side of Equation (13) are equal, that is, by the equation

$$U_c = \frac{2\alpha}{\gamma} \frac{S}{A} (\omega v)^{1/2}. \tag{14}$$

It proves interesting and instructive to display the results obtained with these tuning forks in the form of a plot of the critical Keulegan-Carpenter number against the Stokes number, taking the parameter d as the width W of a prong of the fork. The result is shown in Figure 8, where we have included for comparison a solid line showing the relationship (Equation (11)) and the result of a visual observation (using the Baker pH technique) made recently by the present authors on a rod of square cross-section oscillating in water. The visual observation revealed a clear transition to turbulence close to the rod, although it has so far proved too difficult to elucidate the precise nature of this transition. We see from Figure 8 that oscillating rods of rectangular cross-section do not obey Equation (11). Instead they are consistent for large values of β with the relation

$$K_C^{(\text{crit})} = 17 \beta^{-1/2}, \tag{15}$$

which implies that the critical velocity is independent of the dimensions of the rod and proportional to $(\omega v)^{1/2}$, in contrast to a proportionality to $\omega^{3/4} d^{1/2} v^{1/4}$ characteristic of an oscillating cylinder of circular cross-section at high Stokes number. In view of the fact that the instability in this latter case is believed to be centrifugal in character and dependent therefore on
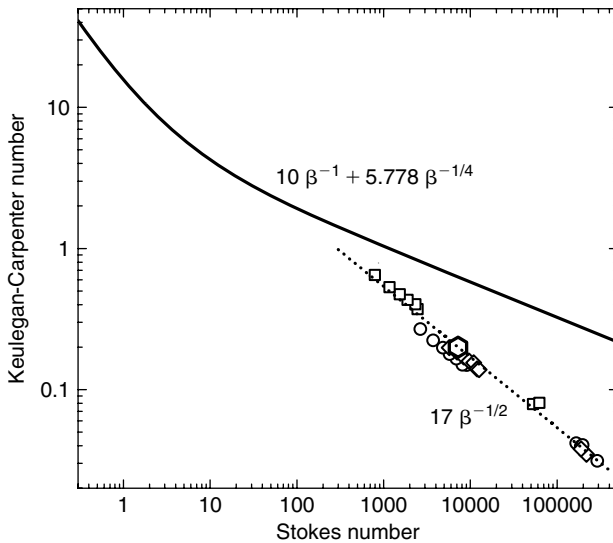
FIGURE 8 The logarithmic plot of the critical Keulegan-Carpenter number versus Stokes number, β, measured in normal liquid and gaseous helium with three quartz forks of different sizes: two of them oscillating at 32 kHz (○, ○) and one at 8.4 kHz (□); the large hexagon represents the visualisation result with a square cylinder oscillating at 8 Hz in water. The dotted line is a power law that represents the observed behaviour. The curved solid line is a plot of Equation (11) for a round cylinder.

the radius of curvature of the surface of the cylinder, this difference is not surprising. If a centrifugal instability is still involved in the case of a rod of square cross-section, the relevant radius of curvature must be associated with the sharp corners. In the case of an ideally sharp corner, it seems likely that the minimum effective radius of curvature must be approximately equal to the viscous penetration depth, and if this were indeed the case, then the physical dimensions of the rod become irrelevant and the proportionality of critical velocity to $(\omega\nu)^{1/2}$ follows straightforwardly. But other processes may be at work in the case of a rod of rectangular cross-section, and a convincing understanding must await the results of further work.

4.4 Oscillatory Flow Through a Grid

The grid is assumed to oscillate in a direction normal to its plane. At small amplitudes of oscillation, the flow through the grid is presumably laminar, and at a critical velocity, this laminar flow must give way to turbulent flow. We have found no reports of the details of this transition for a classical fluid. However, there has been much study of the fully-developed turbulent regime. The results of three types of experiment have been

reported: those in which the grid starts to oscillate at time $t = 0$, and a study is made of the way in which turbulence propagates away from the grid (e.g., Voropayev and Fernando, 1996); those in which a study is made of the steady state obtained at large times; and those in which the decay of this steady state is studied following removal of the grid drive (e.g., De Silva and Fernando 1994). In our later discussion, we shall wish to refer to the results obtained in the second of these types of experiment, and we shall therefore summarise them here. But we remark that a developing programme of experimental work on vibrating grids in superfluids will almost certainly call in due course for comparison with the other two types of classical study, the existence of which should therefore be borne in mind.

For the regimes of fully-developed turbulent flow, each mesh length of the grid generates localised rotational flow, and these regions of localised rotational flow merge to produce something like homogeneous turbulence within a few mesh lengths of the grid. We do not know what happens at velocities close to critical; whether, for example, with an appropriate design of grid, the laminar flow gives way first to a regime in which vortex rings propagate away from the grid, in a way similar to that occurring with an oscillating sphere.

The results of experiments on the fully-turbulent steady state can be summarised as follows. The rms fluid velocity at a distance z from the grid with mesh M is given by

$$u_0 = C_1 s^{3/2} M^{1/2} \frac{\omega}{2\pi} z^{-1}, \tag{16}$$

where C_1 is a numerical factor that depends on the details of grid structure, but is typically about 0.3, s is the stroke of the grid, and ω is the angular frequency with which the grid oscillates. Strictly speaking, the turbulence is not quite isotropic so that the rms value of the component of the velocity perpendicular to the grid is not quite the same as that parallel to the grid. The distance z is measured from a virtual origin that is displaced a little from the grid (by a distance of order M). The integral length scale at the distance z is given by

$$l_0 = C_3 z, \tag{17}$$

where C_3 is another numerical factor that is typically equal to 0.12. The integral length scale is closely related to the size of the largest eddies which contain most of the turbulent energy (the *energy-containing eddies*); the precise numerical relationship can be obtained from formulae given by Batchelor (1953)(Chapter 6). We guess that in the immediate neighbourhood of the grid the turbulence is on a length scale of order M and a velocity scale proportional to, but somewhat less than, U. The forms of

Equations (16) and (17) then arise from a combination of three processes: the diffusion of turbulent energy in real space, the diffusion of turbulent energy in wave number space in the directions greater than and less than M^{-1}, and the decay of turbulence through viscous dissipation. We guess that at any particular value of z the spectrum of the turbulent energy is roughly of the Kolmogorov form, ranging in wave numbers from $k \sim l_0^{-1}$ down to the inverse of the Kolmogorov dissipation length.

Assuming that the individual elements of a grid are like flat plates normal to the flow, we expect the high-velocity drag coefficient (calculated with an area equal to the opaque part of the grid) to be close to unity. Furthermore, we expect the critical Keulegan-Carpenter number to be given by Equation (15).

We emphasise finally that no hysteresis seems to be associated with any of the classical transitions to turbulent flow that we have been describing.

5. EXPERIMENTS ON OSCILLATING STRUCTURES IN SUPERFLUIDS

5.1 Oscillating Spheres

Although some experiments on large spheres oscillating torsionally in superfluid ^{4}He were reported many years ago (e.g., Benson and Hallett, 1956), we shall focus here on more recent work on transversally oscillating spheres. We shall describe some interesting work by Luzuriaga (1997) and then go on to the systematic and pioneering work of Schoepe and his colleagues (Jäger et al., 1995; Niemetz et al., 2002; Niemetz and Schoepe, 2004).

The 7 mm solid (BeCu) sphere used by Luzuriaga was attached to one end of a flexible BeCu strip, the other end of which was fixed, as shown in the inset of Figure 9. Oscillation of the sphere at a frequency of about 320 Hz and Q value of about 3000 was driven and detected capacitively. The main result is shown in Figure 9, which plots the amplitude of resonant response against the drive voltage. The solid lines through the data points are fits to a dependence of drag force F_D on velocity v of the forms

$$F_D = \gamma(T)(v^2 - v_0^2) \text{ (high velocities)} \quad \text{and}$$
$$F_D = \lambda(T)\, v \text{ (low velocities)}, \tag{18}$$

with a continuous transition between the two forms. For an excitation less than about 1 V_{rms}, the resonant frequency at fixed temperature is observed within the experimental accuracy to be constant, and on exceeding this
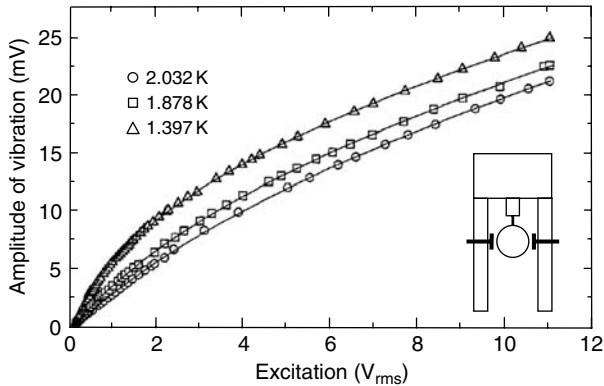
FIGURE 9 The experiment by Luzuriaga (1997) on flow due to an oscillating sphere in superfluid ^{4}He: plots of the relative amplitude of vibration of the sphere versus the excitation voltage, and a schematic view of the apparatus.
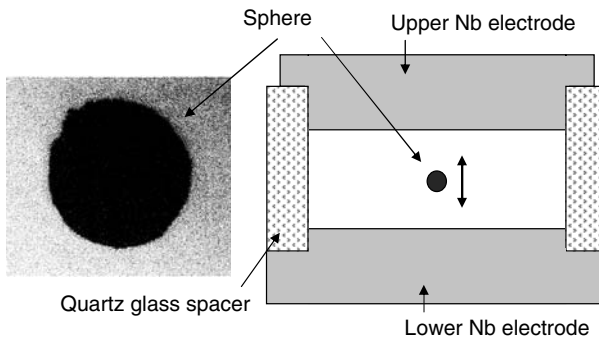
FIGURE 10 Micrograph of one of magnetic spheres and a schematic diagram of the cell used by Schoepe's group for experiments on flow due to an oscillating sphere in superfluid ^{4}He.

value it starts to decrease. The behaviour described by Equation (18) points to a transition from a 'laminar' to a turbulent drag regime. Unfortunately, no quantitative analysis in terms of a drag coefficient is possible because the author does not provide any calibration. An important feature, however, is that at the relatively high temperatures studied in this experiment the transition between laminar and turbulent flow was accompanied by no appreciable hysteresis.

The sphere and the experimental cell used by Schoepe's group is shown schematically in Figure 10. The sphere has a radius of about 100 μm, it is made from a strongly ferromagnetic material (SmCo5), and its surface is very rough. It is placed between two horizontal niobium electrodes, about 1 mm apart, so that it becomes magnetically levitated

when the niobium is superconducting; the natural frequency of vertical oscillation of the sphere is in the range 100 Hz to 500 Hz. It is arranged that the sphere carries an electric charge of about 1.5 pC. Vertical resonant oscillations of the sphere can then be driven by applying an alternating voltage of the appropriate frequency between the niobium plates, and these oscillations can be detected through the induced charge on one plate. Experiments were carried out in ^{4}He in the temperature range from 2.2 K to 0.35 K.

Typical results showing the dependence of oscillation amplitude on driving force are shown in Figure 11, and equivalent plots of drag coefficient against velocity amplitude are shown in Figure 12. We see that there is a region at low drives where the response is proportional to drive, indicating some form of 'laminar' flow, but that at higher drives this linear response is replaced by one in which the drive is proportional to the square of the velocity, indicating turbulent flow; as in the work of Luzuriaga (1994), the data can be accurately fitted by Equation (18). At the lower temperatures (lower than those studied by Luzuriaga (1994)), the transition from laminar to turbulent response is accompanied by significant hysteresis; at the lowest temperature, this region of hysteresis is replaced by a region in which neither the laminar state nor the turbulent state appears to be stable, the response switching periodically between the two states.
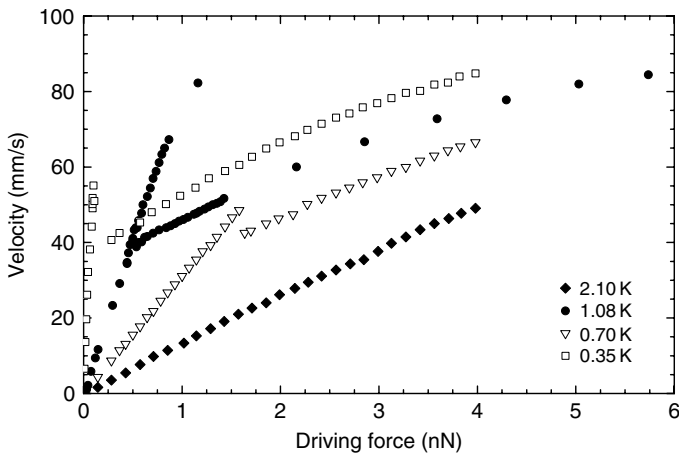
FIGURE 11 Typical results showing the dependence of velocity amplitude on driving force for the oscillating sphere in the experiments of Schoepe's group at four temperatures. Note that the laminar drag coefficient at 0.7 K is higher than that at 1.08 K. This reflects the fact that the laminar drag force displays a maximum in the temperature range below 1 K associated with a crossover from the hydrodynamic to the ballistic drag regime.
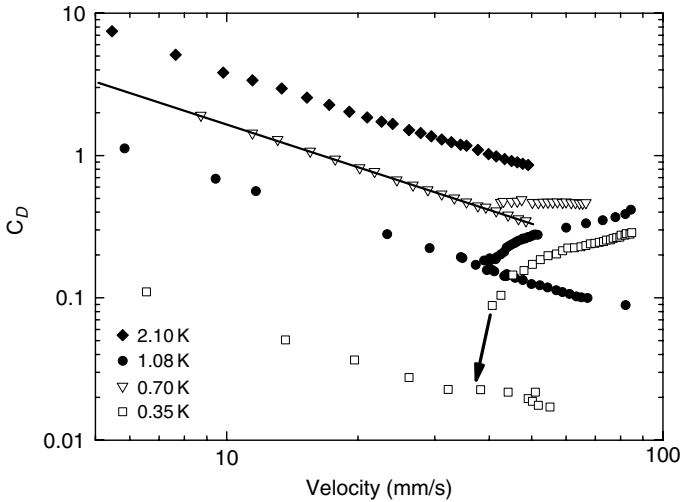
FIGURE 12   The results displayed in Figure 11 plotted as the drag coefficient against the velocity amplitude. For details on hysteresis and intermittent switching, see the text. The solid line is a linear fit in the laminar regime at $T = 0.7$ K.

The drag in the 'laminar' regime can be understood in terms of a viscous drag arising from the normal fluid at high temperatures and in terms of a drag arising from the ballistic scattering of normal fluid quasiparticles from the sphere at low temperatures; the transition from one regime to the other occurs when the mean free path of the quasiparticles becomes equal to roughly the diameter of the sphere. The drag in the turbulent regime will be discussed later in this chapter; we note here only that the drag coefficient, C_D, tends at high velocities to be of order unity, as in the classical case, the precise value of C_D tending to 0.36 at the lowest temperature. But the existence of either hysteresis or switching indicates behaviour different from classical, as we discuss in more detail later.

We note that Schoepe's group have carried out no studies in which he has changed significantly either the diameter of his sphere or its frequency of oscillation.

It is interesting to ask whether the results with a sphere oscillating in superfluid ^{4}He are reproducible. They seem not to be. Thus the critical velocity reported by Jäger et al. (1995) at 350 mK is in the range 37 to 55 mms^{-1}, whereas that reported by Niemetz and Schoepe (2004) at the closely similar temperature of 300 mK is in the range 18 to 26 mms^{-1}. The two spheres may be different, but they have closely similar radii.

No experiments have been reported on oscillating spheres in superfluid ^{3}He-B.

5.2 Vibrating Wires

The oscillating cylinders in recent experiments on superfluid helium have actually taken the form of vibrating wires, the wire being in the form of a loop as shown in Figure 13. A loop is chosen to avoid degenerate or closely spaced resonant modes that are associated with a straight wire. A magnetic field is applied in the plane of the loop; resonant vibrations can then be excited by passing an alternating current of appropriate frequency through the wire, and they can be detected and measured by observing the induced voltage across the ends of the wire. The wire is superconducting (typically NbTi) to avoid resistive electrical dissipation.

Experiments with a vibrating wire in ^{4}He have been reported by the Osaka City University Group (Hashimoto et al., 2007; Yano et al., 2005a,b, 2006, 2007) and by the Lancaster University Group (Bradley et al., 2005a). Most of the Osaka work was carried out with fairly smooth wires of diameter 2.5 μm at two temperatures: 1.4 K and 30 mK. The Lancaster experiments used rather rough wires of diameter 4.5 μm and 9 μm, and were carried out at about 7 mK. In all the experiments, the wires were subjected to steadily increasing or decreasing drives; the amplitude of the response of the wires, at resonance, was observed together with the resonant frequency.

It was observed in the Osaka work that the behaviour of the wire at 1.4 K was quite complicated and depended on the previous history of the surrounding helium. We describe the results obtained with one particular wire at a frequency of 610 Hz. If the wire was surrounded initially by helium in the normal phase, and if the helium is then pumped through the λ-transition and cooled rapidly to 1.4 K, the initial response of the wire indicated very strong damping, even at low drives, with very strong hysteretic effects (Figure 14a); however, repeated scanning of the drive, up and down, leads eventually to the steady and reproducible response shown in Figure 14b. We see that this response exhibits a transition from what is taken as a laminar regime to a turbulent regime at a velocity of about 29 mms^{-1} with very little, if any, hysteresis. The corresponding drag coefficient is shown in Figure 14c. Alternatively, the wire can be immersed
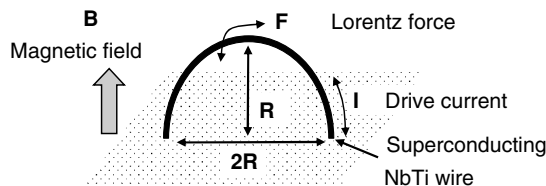
FIGURE 13 Schematic diagram of a wire loop used in studies of vibrating wires in superfluid helium.
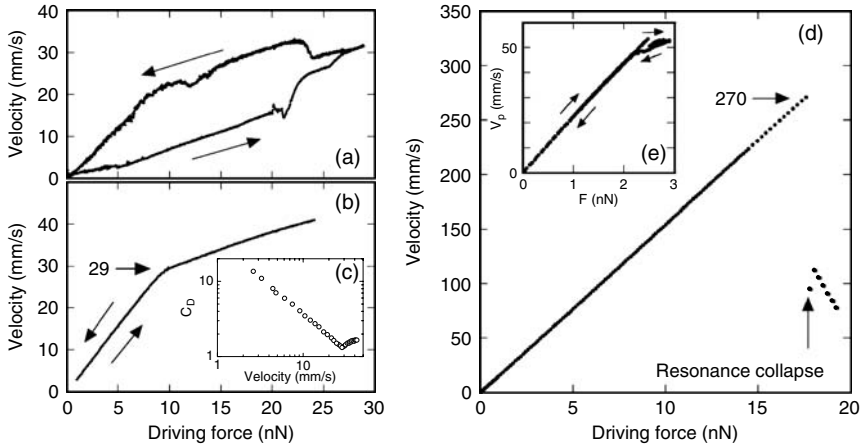
FIGURE 14   Typical experimental results (Yano et al., 2005b) showing the dependence of amplitude of oscillation on driving force for a wire of diameter 2.5 μm oscillating at 610 Hz in ^{4}He at 1.4 K. Left panel: after fast cooling through the λ-transition (a) followed by repeated scanning of the drive (b); an inset (c) to this latter diagram shows the behaviour of the drag coefficient. Right panel: after careful immersion of the wire directly into the superfluid phase (d) followed by repeated scanning of the drive (e).

slowly and carefully into the superfluid phase directly. In this case, the critical velocity is significantly higher; indeed with care it can sometimes be seen to exceed several hundred mms^{-1} (Figure 14d). However, such a high critical velocity is not stable, and repeated scanning of the drive will lead to a reduction to about 50 mms^{-1}, again with no significant hysteresis, as shown in Figure 14e. As we shall discuss later, these different types of behaviour must be associated with different configurations of the remanent vortex that allow extrinsic nucleation of the quantum turbulence.

Experiments with different wires of different natural frequencies suggest that the critical velocity increases with increasing frequency, especially above about 2 kHz, although the possibility cannot perhaps be ruled out that the increased critical velocities are due to a different configurations of remanent vortex. The earlier papers from the Osaka group do not report the temperature dependence of the critical velocity, although a graph appearing in their latest publication (Yano et al., 2007), dealing primarily with other matters to which we refer later, shows a critical velocity that increases with increasing temperature above 1 K, apparently at a frequency of 700 Hz (see Figure 25). However, this critical velocity at 1.4 K, is larger than that reported earlier at 610 Hz; although this difference might be due to different configurations of remanent vortex. The publication of more complete and systematic studies would be valuable.
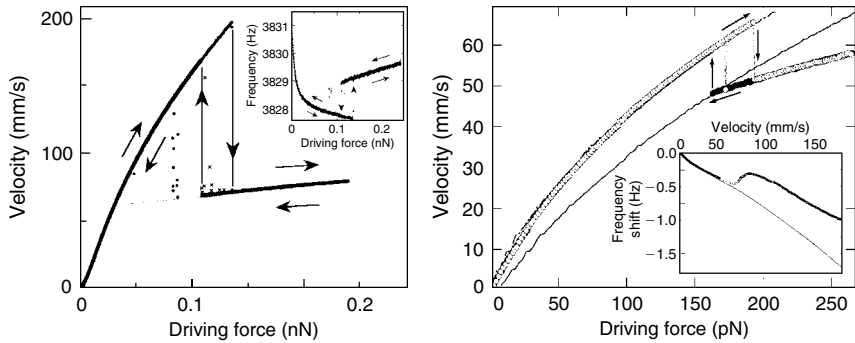
FIGURE 15 Typical experimental results showing the behaviour of vibrating wires in superfluid helium at low temperatures. Left panel: peak velocity of oscillation against driving force measured at 30 mK for wire of diameter 2.5 μm oscillating at 3.8 kHz (Yano et al., 2006). The inset shows the resonant frequency as a function of the driving force. Right panel: peak velocity of oscillation against driving force measured at 7 mK for a wire of diameter 4.5 μm (Bradley et al., 2005a). The inset shows the shift in resonant frequency as a function of the velocity. The corresponding vacuum data are represented by the solid lines.

We note that the transition to turbulence is accompanied by an increase in the resonant frequency of the wire, which can display some hysteresis.

The behaviour of a wire at much lower temperatures has been studied by both the Lancaster group and the Osaka group. Typical results are displayed in Figure 15. Again there is a transition that is identified as from a laminar regime to a turbulent regime, but now with considerable hysteresis. We note that in the region identified as involving laminar flow the response is not proportional to the drive. This is associated with the fact that a substantial part of the damping in this region is due to a nonlinear internal friction in the wire.

Sometimes there is switching between the turbulent and laminar regimes in the region of hysteresis, similar to that observed by Schoepe (2004). Recent experiments by the Osaka group with a 2.5 μm wire oscillating at 700 Hz (Yano et al., 2007) suggest that switching becomes more frequent as the resonant frequency is reduced.

The critical velocities observed by the Osaka group are larger than those observed by the Lancaster group, and the extent of the hysteresis is larger, but it is not clear whether this is associated with a different size of wire. Judging from the observations on the two Osaka wires (3.8 kHz and 700 Hz), we find that neither the critical velocities nor the extent of the hysteresis depends significantly on frequency at low temperatures. However, the available experimental data are scarce. There is an urgent need for more systematic work on vibrating wires at low temperatures,

in which the dependence on frequency and wire size is carefully and systematically studied. The existing data do not provide a clear view of these dependences.

Very recently, the Osaka group have repeated their measurements at 35 mK, taking greater care in filling the region round the wire with helium (Hashimoto et al., 2007). They placed the wire inside a small cell, which was then filled very carefully and slowly through a small (0.1 mm) pinhole at a very low temperature. They found in this case that the response remains laminar up to the largest velocity that can be imposed, which was greater than $1\,\mathrm{ms}^{-1}$. As we shall emphasise later, this observation confirms in a striking way that transitions to turbulence in ^{4}He depend on the extrinsic nucleation of vortex line.

Both the Lancaster group and the Osaka group compared the resonant frequency of their wire in vacuo with that in the laminar flow regime at their lowest temperatures. The Lancaster reported that the difference (reduction) in frequency could be understood entirely from an expected increase in effective mass due to potential flow past the wire (Milne-Thomson, 1955). The Osaka group has reported that with their smaller wires, the difference can be much larger, indicating, apparently, that there can be some source of effective mass in addition to that due to potential flow (Yano et al., 2007). However, the effect does not seem to follow a rational pattern: for example, for a $2.5\,\mu$m wire oscillating at 3.9 kHz, the excess effective mass is equivalent to a layer of helium of thickness $1.1\,\mu$m, whereas for a $2.5\,\mu$m wire oscillating at 0.7 kHz, the excess effective mass is equivalent to a layer of helium of thickness of only $0.08\,\mu$m. More systematic investigation will be required to establish the characteristics of this effect, and indeed to establish whether the effect is real. It has been suggested that it may have its origin in a dense layer of vortex loops attached to the surface of the wire (Vinen et al., 2004), but there seems no good reason to suppose that such loops can persist in metastable equilibrium. Even the wire that exhibited a critical velocity in excess of $1\,\mathrm{ms}^{-1}$ showed an enhanced effective mass (Hashimoto et al., 2007), indicating that the effect is probably not associated with remanent vortex lines.

There has been some study of a vibrating wire in superfluid ^{3}He-B. In this case, the normal fluid has a very large viscosity, so that at a temperature where there is a significant fraction of normal fluid a vibrating wire would suffer very large damping. At the lowest temperatures, this damping disappears, and studies similar to those we have just described for the case of ^{4}He become possible. However, it turns out that they are difficult to interpret for the following reason. For a vibrating wire in ^{3}He, the critical velocity for generation of turbulence is closely similar to that for pair breaking, and the two effects cannot be easily disentangled (Fisher et al., 2001).

5.3 Vibrating Grids in ^{4}He

Experiments on vibrating grids in superfluid ^{4}He have been reported by McClintock and his colleagues (Charalambous et al., 2006; Nichol et al., 2004a,b; Vinen et al., 2004).

The grid (Figure 16) is circular, 8 cm in diameter, clamped at its edge, and it is placed between two electrodes, each separated from the grid by 1 mm. The grid carries a large fixed voltage, and the two electrodes are held at zero average voltage. The fundamental mode of vibration of the grid is excited by applying an alternating voltage to one of the electrodes, and the response is detected by the voltage induced in the other electrode. The surface of the grid is rough on a scale of about 1 μm.

The experimental results show a well-defined critical velocity, which is taken to mark the onset of turbulence. In the earlier reports (Nichol et al., 2004a,b; Vinen et al., 2004), a strange but reproducible shift in the resonant frequency was observed as the drive was increased through the laminar regime, and a speculative interpretation of this effect was proposed (Vinen et al., 2004). However, when a new grid, apparently identical with the old one, was fitted, the effect disappeared. The effect might therefore be spurious, and we shall not discuss it further.

The experimentally observed response of the grid is summarised in Figure 17, where we have plotted the drag coefficient against peak grid velocity (measured at the centre of the grid) for a range of temperatures. (In calculating the drag coefficient, we have taken the area of the grid to be that of the opaque part, and we have allowed by suitable averaging for the fact that the spatial dependence of the displacement is a zero-order Bessel function.) We see a clear transition from what we interpret as a laminar regime to a turbulent regime, and we see that the drag coefficient
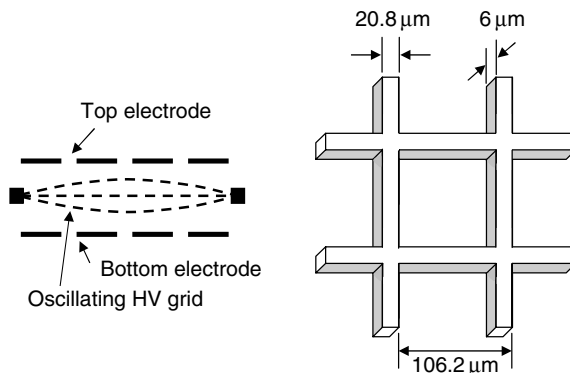
FIGURE 16   Schematic diagram of an electrostatically driven oscillating grid in superfluid ^{4}He.
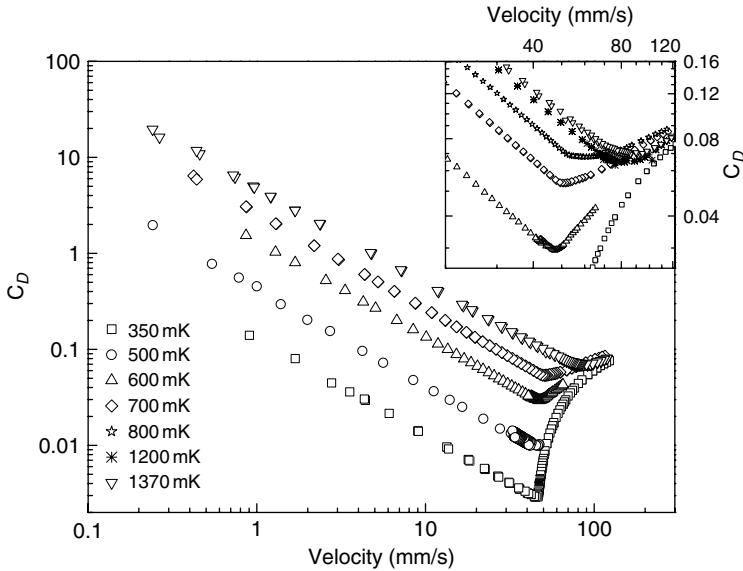
FIGURE 17 The drag coefficient observed for a vibrating grid in superfluid ^{4}He plotted against velocity amplitude for various temperatures. The insert shows a more detailed view at higher temperatures.

probably tends to a constant value, somewhat less than unity, at high velocities. Very little, if any, hysteresis is observed around the transition (for details, see Charalambous et al., 2006). The observed critical velocity is plotted as a function of temperature together with those observed with other oscillating objects in Figure 25 in the Discussion section. There is some experimental evidence that at low velocities and low temperatures the effective mass of the grid is perhaps enhanced to a greater extent than one would expect from simple potential flow (Charalambous et al., 2006), but this evidence is as yet not persuasive.

It would be of great interest to determine the spatial extent of the turbulence generated by the grid, especially at the lowest temperatures, to compare with the classical behaviour summarised in Section 4.4. To observe this spatial extent, we need a localised detector of turbulence in the ^{4}He. It seems likely that a vibrating wire, or a vibrating tuning fork, might serve this purpose, but confirmation must await the completion of experiments that are in progress at the present time.

5.4 Vibrating Grids in ^{3}He-B

Very interesting observations of the behaviour of a vibrating grid in ^{3}He-B at very low temperatures have been reported by Bradley et al. (2004,
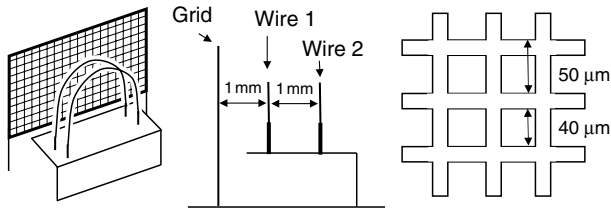
FIGURE 18   Schematic diagram showing the form of the vibrating grid and geometry of the experiment (including the two detector wires) used by Bradley et al. (2004, 2005b, 2006) in superfluid ^{3}He-B at very low temperatures.

2005b, 2006). A detailed account of this work is contained in a separate chapter in this volume, so we need to provide only a brief summary.

The material of the grid is similar to that used in the ^{4}He experiments, but the grid itself has a different shape and vibrates in a quite different way, as shown in Figure 18. We note especially that, in contrast to the grid used in ^{4}He, this grid is not held round its edge with a clamping ring so that it oscillates (nearly) perpendicular to its plane in the free liquid. The measurements were taken as the experiment was slowly warming under its external heat leak, and significant warming occurred at the highest velocities due to the power required to drive the grid. The observed velocity versus drive and drag coefficient versus velocity are plotted in Figure 19. We see that there is a fairly well-defined critical velocity, which is, however, much smaller than that observed for a grid in ^{4}He, and that well above this velocity the drag coefficient tends to a value that is significantly larger than unity and may increase with increasing temperature. The possible significance of these differences was discussed by Hänninen et al. (2007), and we shall return to them later in this chapter. The fact that the grid in ^{3}He is in the free liquid and is not enclosed by a clamping ring means that flow round the edge of the grid cannot be ignored. It seems possible that when flow through the grid exceeds the critical velocity some fraction of the flow is diverted round the edge so that flow velocities within the grid may be smaller than they seem. Such a diverted flow might increase the effective mass of the grid.

These experiments on ^{3}He were especially interesting because they incorporated the 'Andreev scattering technique' (Section 2) to visualise the extent and density of the turbulence. Bradley et al. were able to show that; (i) at grid velocities close to, but just above, critical, vortex line is produced by the grid in the form of what seem to be weakly interacting vortex rings with diameter of about 5 µm, these rings propagating rapidly away from the grid; (ii) at slightly higher velocities, the rings are formed at a higher density and then coalesce to form a turbulent tangle extending few mm from the grid; and (c) when the drive on the grid is removed, the density of vortex line in the vortex tangle decays in time in a way that
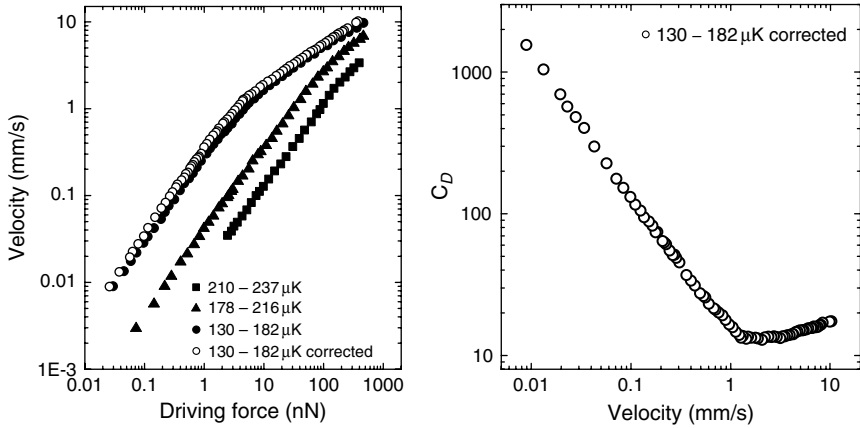
FIGURE 19   Plots of the peak velocity versus the driving force indicating a transition from laminar to turbulent flow as detected by a grid oscillating at 1250 Hz in superfluid ^{3}He-B at very low temperatures and at zero pressure (left). Some of the damping is due to scattering of thermal excitations (thermal damping), and the effect of subtracting this contribution is shown for the lowest temperature; similar corrections applied to the data for higher temperatures lead to a collapse of all the data onto a single line. The drag coefficient corresponding to this single line plotted against velocity amplitude is shown on the right. At the highest grid velocities, considerable heating was observed (Bradley et al., 2004), and this may be the reason for the increase in C_D.

resembles that occurring in homogeneous quantum turbulence confined to a channel of width 1.5 mm. We shall comment on this picture later.

5.5 Vibrating Tuning Forks in ^{4}He

As yet, work here on ^{4}He has been confined to temperatures above 1 K (Blažková et al., 2007a), although an extension to lower temperatures will be made very soon. Typical results showing the peak velocity plotted against the driving force indicating a transition from laminar to turbulent flow in both the normal and superfluid phases are shown in Figure 20.[1] At low drive level (in the laminar regime), the measured velocity is proportional to the applied drive; around a critical value, a crossover to a turbulent regime occurs, characterised by a quadratic dependence of driving force on velocity. There is a distinct difference between the behaviour of the fork when in the normal phase as compared with that in the superfluid phase. This difference is best illustrated by plotting the drag coefficient

---

[1] The data shown for the liquid at 4.2 K have been measured at an elevated pressure because otherwise the fork vibrating at a velocity greater than about 50 cms^{-1} causes cavitation (Skrbek et al., 2007) In the superfluid phase at the saturated vapour pressure, cavitation occurs only at a much higher velocity, of order 2 ms^{-1}.
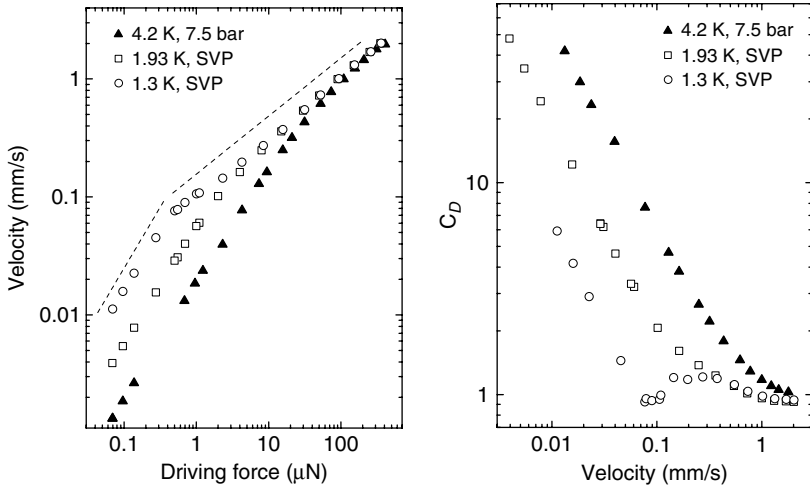
FIGURE 20   Plots of the peak velocity versus the driving force indicating a transition from laminar to turbulent flow as detected by a quartz fork vibrating at 32 kHz in the normal and superfluid phases of ^{4}He (left), and corresponding plots of the drag coefficient (right).

versus the peak velocity of the fork. In the normal phase (a classical viscous fluid), it displays a gradual change towards its constant value in the turbulent regime well above the transition, as described by Equation (13). In the superfluid phase, however, its shape seems to indicate the existence of what may be two transitions: one at the position of the cusp and another smooth transition similar to that seen in the classical fluid and occurring at a higher velocity. We note, however, that in both phases the drag coefficient tends to a constant value close unity at high velocities. We shall discuss these and other results in the following sections.

6. DISCUSSION: SUPERFLUID ^{4}HE

In this section, we shall focus on superfluid ^{4}He, and we shall first concentrate on very low temperatures where there is only the superfluid component. We shall base our discussion in part on the observation that even at these low temperatures there are similarities to the behaviour of classical fluids, in part on the results of simulations, which we shall describe, and in part on our understanding of homogeneous turbulence in ^{4}He at very low temperatures. In view of its importance, we shall summarise in Section 6.1 our understanding of this type of homogeneous turbulence. We shall be concerned to define the nature of the problem

presented to us in the observed behaviour of oscillating structures in the pure superfluid component. We shall offer a tentative solution to this problem, suggesting that the transition to turbulence[2] is a two-stage process, but we shall wish to emphasise that much remains to be done on both the experimental side and the theoretical interpretation. We shall then go on to discuss the behaviour of oscillating structures at temperatures where there is a significant fraction of normal fluid, focussing particularly on the observed behaviour of small tuning forks; in this case, we see even clearer evidence for the existence of two-stage transitions.

6.1 Homogeneous Turbulence in ^{4}He at a Very Low Temperature

As we mentioned in our Introduction, homogeneous turbulence can be produced in both classical fluids and superfluid ^{4}He above 1K by steady flow through a grid. Behaviour very close to the grid is likely to be complicated in a way that is similar to that near an oscillating structure, which we discuss in the next Section, but there is little doubt that well downstream of the grid the turbulence settles down to a slowly decaying homogeneous and isotropic form. As we have explained, grid turbulence observed in superfluid ^{4}He above 1K seems very similar in its structure to that observed in a classical fluid; there is an inertial range of scales greater than the vortex spacing, in which the two fluids have the same quasiclassical velocity fields, and there is dissipation due to a combination of normal fluid viscosity and mutual friction on the scale of the vortex-line spacing. The dissipation per unit mass can be expressed in the form

$$\epsilon = \nu'(\kappa^2 L^2),\tag{19}$$

where ν' is an effective kinematic viscosity and L is the length of vortex line per unit volume in the turbulent helium; the quantity $\kappa^2 L^2$ can be shown to be a measure of the effective mean square vorticity in the superfluid component (Vinen, 2000) so that Equation (19) has a form similar to that appropriate to a classical fluid.

At very low temperatures, the normal fluid disappears, and the two sources of dissipation that lead to Equation (19) also disappear. For some years now, our understanding of the likely form of homogeneous isotropic turbulence in ^{4}He at a very low temperature has been as follows (Vinen and Niemela, 2002). We suppose there are large eddies, in which most of the energy resides, and that these decay, as in the classical counterpart, through

---

[2] We use the term 'transition to turbulence' to include transitions to states involving trailing vortices that are not strictly fully turbulent.

an inertial–range Richardson cascade in which energy is conserved, and in which the energy spectrum has the Kolmogorov form (Equation (1)). This Richardson cascade, in which there is quasiclassical behaviour, exists over length scales that are larger than the spacing, ℓ, between vortex lines, and the large scale quasiclassical motion is due to a partial polarisation of the underlying tangle of vortex lines. However, in the absence of normal fluid, there is no mechanism by which the energy flux, ϵ, can be absorbed and dissipated on the length scale ℓ. Nonlinear coupling, aided by vortex reconnections, leads to a second cascade operating on length scales less than ℓ. The details of this second cascade have been controversial, but it has seemed likely that it is composed, at least in part, of a Kelvin-wave cascade (a form of wave turbulence), in which energy flows into Kelvin-waves of shorter and shorter wavelength. This second cascade is cut off at a high wavenumber, where the Kelvin-wave energy can be dissipated by phonon radiation. In general, some energy is dissipated during reconnections, but in ^{4}He, this source of dissipation can probably be neglected. An equation of the form of Equation (19) is expected still to hold, and if the Richardson cascade joins the Kelvin-wave cascade smoothly and continuously, then, as is easily shown, the value of ν' must be of order κ (Vinen and Niemela, 2002).

During the past year or so, it has become clear that this assumption (the smooth joining of the Richardson and Kelvin-wave cascades) is unlikely to be correct. No experiments on (steady flow) grid turbulence at very low temperatures have yet been reported, but Walmsley et al. (2007) have studied the decay of vortex density in ^{4}He at a very low temperature when a steadily rotating containing vessel is suddenly brought to rest, and they have shown that the results are consistent with a value of ν' equal to only about $3 \times 10^{-3}\kappa$. It can be shown that this small value implies that there is a range of wave numbers, around presumably the value ℓ^{-1}, in which the turbulence has the form of neither a Richardson cascade nor a Kelvin-wave cascade. The character of this transition regime is presently the subject of discussion. It might arise because, as suggested by L'vov et al. (2007), energy cannot be transferred from the Richardson cascade to the Kelvin-wave cascade at the rate required to match the energy flux in the Richardson cascade. Indeed L'vov et al. (2007) suggested that as a result there is a bottleneck, which results in an accumulation of an excess turbulent intensity at wave numbers less than that at which the Kelvin-wave cascade takes over. Kozik and Svistunov (2007) have suggested a somewhat different scenario in which there is a more complicated form of transition regime extending over almost a decade in wave number on either side of ℓ^{-1}. The L'vov et al. scenario implies that ν' should be even smaller than is observed, although the Kozik-Svistunov scenario does seems to suggest values of ν' that are in agreement with experiment.

We believe it important to recognise that there can be different effective kinematic viscosities depending on the context in which they are used. We have just discussed one such effective viscosity defined by Equation (19). However, there are others relating, for example, to effective eddy viscosities[3] in quantum turbulence. Later in our presentation, we shall introduce one particular eddy viscosity, relating to a random tangle of vortex lines, by which we mean a tangle that gives rise to relatively little large-scale motion. A random tangle has associated with it a characteristic length scale equal to the line spacing, ℓ, and a characteristic velocity given in order of magnitude by $u_\ell = \kappa/\ell$. A more precise value of this characteristic velocity raises questions about the precise form of the random tangle: the velocity generated by a rectilinear vortex at a distance ℓ is actually $\kappa/2\pi\ell$, while the velocity with which a vortex with local radius of curvature ℓ moves under the influence of its self-field (local induction) is $(\kappa/4\pi\ell)\ln(\ell/\xi_0)$ (ξ_0 is the vortex core parameter), which is close in practice to about κ/ℓ. The associated eddy viscosity, relevant to flows with length scales much larger than ℓ, can probably be taken as $\nu'' = (1/3)u_\ell\,\ell$, and we shall therefore take it that

$$\nu'' = \zeta\kappa, \tag{20}$$

where ζ is a numerical factor lying probably in the range 0.05 to 0.3. Thus a random tangle of vortex line might behave in appropriate circumstances like a viscous fluid with a kinematic viscosity given by Equation (20).

6.2 Oscillating Structures in ^{4}He at Very Low Temperatures

We turn now to the behaviour of an oscillating structure in ^{4}He at a temperature so low that there is a negligible fraction of normal fluid. Experiment tells us that at low velocities, there is then no drag; that the drag sets in at a critical velocity U_{cS} in the manner shown in Figure (12) or (17); and that the drag coefficient tends to a value of order unity (or a little less than unity) at high velocities.

This last feature suggests strongly that at velocities significantly larger than U_{cS}, the flow round the structure mimics that found with a classical fluid, which has been described in Section 4. However, this comparison with an analogous classical flow must be made with two important reservations. First, in the classical case, the transition to turbulence starts with a laminar viscous flow round the obstacle, a flow in which $\mathrm{curl}\mathbf{v} \neq 0$, whereas in the quantum case it starts from a flow that is largely irrotational

---

[3] In the study of classical turbulence in fluids, a common practical strategy is to ignore the smallest eddies in the motion and to calculate the large-scale motion with an eddy viscosity that characterises the transport of energy in the smaller scale flow; the method is called large eddy simulation.

in character. Secondly, the transition in the quantum case is often strongly hysteretic in character, in contrast to the corresponding classical transitions which exhibit no hysteresis.[4] We say that the initial state in the quantum case is largely irrotational for the following reason. At the relevant flow velocities, intrinsic nucleation of quantised vortices is virtually impossible; nucleation must be extrinsic and depend on the growth of remanent vortices. Striking evidence for the importance of these remanent vortices comes from the history-dependent critical velocities observed by, especially, the Osaka Group (Section 5.2). The number of such vortices is likely to be small, but, nevertheless, they do involve some localised rotational motion in the superfluid.

It seems reasonable to assume that the need for appropriate remanent vortices is responsible for the observed hysteresis. The growth of a remanent vortex may well not occur until the flow velocity exceeds some large critical value, but the quantum turbulence once fully established can probably be maintained at lower velocities.

The transition to a quasiclassical flow that mimics the transition in a classical fluid, in which large rotational eddies form in the neighbourhood of the structure, raises a serious difficulty. The formation of such eddies in the superfluid can occur only if there is already a high density of vortex line, the partial polarisation of which leads to the large-scale rotational flow, as explained in Section 6.1. In some sense, therefore, the formation of this high density of vortex tangle must precede the establishment of the quasiclassical flow structure.

As we explained in Section 6.1, ^{4}He containing such a high density of vortex tangle is likely to behave like a classical fluid with kinematic viscosity given by Equation (20) on scales greater than the vortex separation ℓ. The flow of the superfluid can therefore mimic to some degree a state of laminar viscous flow, provided that vortices are not completely random but polarised in such a way as to produce this quasi-laminar flow. We shall refer to this type of flow as *quasiclassical laminar flow*. This laminar flow can then give way to turbulent flow (or to flow with trailing vortices), in much the same way as occurs in a classical fluid. We shall refer to this last state as *quasiclassical turbulent flow*. We conclude that the breakdown of superflow at U_{cS} is likely to involve a sequence of two processes: the formation of the high density of vortex tangle, allowing the superflow to mimic laminar viscous flow, and a transition to a flow that mimics a classical turbulent flow (or, more accurately, flow with trailing eddies or, at high velocities, flow that is fully turbulent). It is not immediately obvious whether these two processes can be regarded as separate, a point to which we shall return. (Strictly speaking, the limiting value of the drag coefficient at high velocities seems to be a slightly smaller than that expected

---

[4] Some classical transitions, such as those in pipe flow, do exhibit hysteresis.
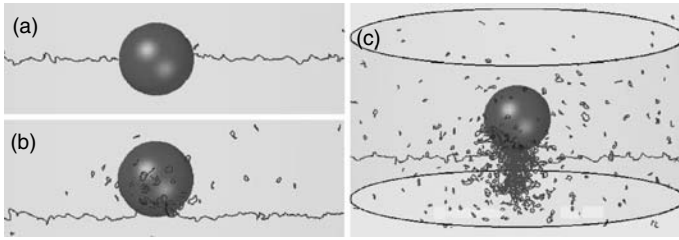
FIGURE 21   The evolution of vortex line near a sphere of radius 100 μm in an oscillating superflow of 150 mm^{-1} at 200 Hz (from the simulations of Hänninen et al., 2007).

classically, especially in the case of small structures. This may be associated with a vortex spacing in the quasiclassical flow that is not sufficiently small compared with the size of the structure.)

To proceed further, we shall call on the results of simulations reported by Hänninen et al. (2007). The simulations relate to a smooth sphere of diameter 200 μm, enclosed in a vertical cylinder as shown in Figure 21c, and flow past the sphere oscillates vertically with a frequency of 200 Hz. The sphere has a diameter close to that used in the experiments of Schoepe et al. although the surface of their sphere was quite rough. The required remanent vortex is taken to have the form shown in Figure 21a. At low velocities (Figure 21a), Kelvin-waves are excited on the remanent vortex. At slightly higher velocities (Figure 21b), the amplitude of these Kelvin-waves has increased to the point where self-reconnections can lead to the generation of small vortex rings, with size of order the wavelength of the Kelvin-waves. The resulting drag on the sphere would be too small to detect. Then at a critical velocity of about 120 mms^{-1}, there is a sudden growth in the density of vortex line around the sphere, and especially in a wake behind the sphere (Figure 21c). The total length of vortex line in the neighbourhood of the sphere is observed to grow as shown in Figure 22. Unfortunately, it has not been possible to follow this growth for times greater than those shown in Figure 22; the computing time becomes excessive, and the high vortex density requires too high a spatial resolution. Thus the growth in vortex density cannot be followed to the point where it must presumably level off. But a crucial observation is that up to the largest values of vortex density shown in Figure 22 the vortex lines in the wake of the sphere appear to be randomly arranged, in the sense that they produce no observable flow on scales larger than the vortex-line spacing; in other words, there is no sign of the appearance of any quasiclassical eddies. This suggests that the two processes that we have tentatively identified are indeed separate; that the formation of a random tangle of vortex line precedes the quasiclassical transition to a flow structure that mimics a classical turbulent flow. It is unfortunate that at present it is not practicable
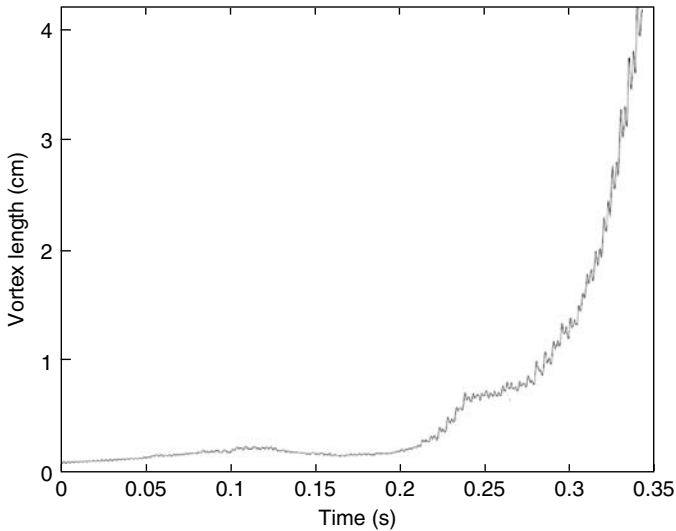
FIGURE 22 Growth with time of the total length of vortex line near the sphere in the simulations of Hänninen et al. (2007).

to take the simulations to the point where they might confirm the existence and nature of the second stage. It is unfortunate also that the simulations are unrealistic in the sense that the surface of the sphere is smooth. This shortcoming may be particularly serious in the present context in view of our suggestion that a tangle of vortices allows the superfluid to mimic classical viscous laminar flow; without surface roughness, such viscous flow would involve complete slip at the boundary of the sphere. The development of a technique that would allow surface roughness to be incorporated in the simulations would be most valuable.

An interesting feature of the simulations is that they show no hysteresis: if the velocity is taken above the critical value for formation of the dense random tangle, and then reduced below this value, the vortex density immediately decays to a small value. But we should recognise that the critical velocity observed in the simulations is too large by a factor of about four in comparison with that reported by Schoepe (2004). Perhaps a lower critical velocity, together with hysteresis, is associated with forms of remnent vortex different from that shown in Figure 21, and perhaps also the assumed smooth surface of the sphere is relevant. It should be emphasised that hysteresis need not necessarily accompany the operation of a remanent vortex, as we see from the experimental results of the Osaka group on a vibrating wire above 1 K, or indeed from the observed behaviour of an oscillating grid at very low temperatures.

The tentative picture that is emerging is therefore as follows. At some critical velocity, evolution of one or more remanent vortices leads to the

formation around the structure of a dense tangle of vortex line, which can lead to a flow that mimics, at least to a significant extent, viscous laminar flow (*quasiclassical laminar flow*). Tangles with the density comparable with those shown in Figure 21 give rise to only a small drag on the structure, but this is unlikely to be true for tangles of higher density. Then there is a quasiclassical transition in this tangle with the formation of a large-scale eddy structure similar to that observed in the analogous classical flow (*quasiclassical turbulent flow*), giving rise eventually to a drag coefficient of order unity.

We emphasise that the viscous laminar flow to which we refer is oscillatory and is therefore in the form of a viscous penetration wave. Our suggestion that such a flow can be established in the superfluid component is reasonable only if the viscous penetration depth $(2\nu''/\omega)^{1/2}$ is less than the spatial extent of the tangle generated around the structure. We judge from the simulations that this condition is likely to be satisfied, at least for the larger structures.

In principle this picture implies that there may be two distinct critical velocities: the first associated with a transition to quasiclassical laminar flow; the second with the transition to quasiclassical turbulent flow. The first transition might be hysteretic; the second probably not since the corresponding classical transition is not hysteretic. There is as yet little or no clear evidence for two distinct critical velocities in the experiments at very low temperatures that have so far been reported, although, as we shall see in Section 6.3, there is evidence of two critical velocities for vibrating tuning forks at higher temperatures. Comparison with the behaviour that we see at higher temperatures suggests that the appearance of a sharp cusp in a plot of drag coefficient against velocity at low temperatures signals the onset of quasiclassical laminar flow (see, e.g., Figure 17). Evidence for two critical velocities at high temperatures comes from rather extensive data that encompass velocities much larger than those at which the cusp appears, but comparable data do not yet exist at lower temperatures for any of the systems that we discussed in Section 5. However, comparison with the high-temperature data does suggest that the low-temperature data are at least consistent with the idea that the transition to quasiclassical laminar flow is followed almost immediately by a transition to quasiclassical turbulent flow, but more extensive measurements are needed before we can be sure.

Looking at the low-temperature data, we must allow in many cases for hysteresis. Let us distinguish between observations made as the drive is increased and those made as it is decreased. In the former case, there seems to be a transition from essentially potential flow to quasiclassical turbulent flow, the intermediate regime with quasiclassical laminar flow existing only as a transient. It is clear that the velocity at which this double

transition occurs must be determined by that at which there is onset of quasiclassical laminar flow, and that this velocity must exceed that at which a classical fluid with kinematic viscosity given by Equation (20) would make a transition to quasiclassical turbulent flow. According to our discussion in Section 4, this latter critical velocity, v_{critKC}, is given in terms of the critical Keulegan-Carpenter number by Equation (11), with the Stokes number β being calculated with a kinematic viscosity given by Equation (20). In the latter case, the quasiclassical turbulent flow persists to a lower velocity than was originally required to establish the quasiclassical laminar flow, but eventually there is a transition back directly to the state of potential flow. Tentatively, we suggest that the velocity at which this last transition takes place can be identified as v_{critKC}.

To check whether this tentative conclusion is correct we use the data displayed in Table 1, in which we have taken ζ in Equation (20) to be 0.11, which is a plausible possibility. In the case of the tuning fork, no data yet exist for low temperatures, but a reasonable extrapolation of the existing data to low temperatures suggests that the critical velocity must be less than 60 mm/s.

However, before proceeding to discuss these results we must sound a note of warning. In judging whether a transition to a quasiclassical flow can take place, we need to check that the scale of the quasiclassical flow is large compared with the vortex line spacing (see Section 6.1). It is not easy to estimate this spacing with any certainty in any particular case, but we present the following argument as the best we can do at the present time. Let us make the reasonable assumption that the dense vortex tangle exists over a volume d^3, where d is the characteristic linear size of the structure, and we denote by L the line density in this volume. As explained in Section 6.1, we can expect the rate of dissipation of turbulent energy in

TABLE 1 Parameters for various structures vibrating in superfluid ^{4}He.

Structure	d	f	U_c	$K_C^{(\text{crit})}$	β
	μm	kHz	mms^{-1}		
Schoepe sphere	248	0.12	19	0.64	671
Schoepe sphere	200	0.24	38	0.79	873
Lancaster wire	4.5	1.0	48	10.7	1.84
Osaka wire	2.5	3.8	70	7.37	2.16
Osaka wire	2.5	0.7	50	28.6	0.40
Lancaster grid	21	1.0	45	2.14	40.1
Tuning fork	400	32	<60	4.7×10^{-3}	4.6×10^5

this volume to be of order $3 \times 10^{-3}\kappa^3 L^2$ per unit mass,[5] which leads to a total rate of dissipation of energy equal to $3 \times 10^{-3}\rho\kappa^3 L^2 d^3$. At velocities, U, significantly larger than critical, the drag coefficient for the structure is of order unity so that the mechanism that is driving the oscillations must be responsible for an input of power of order $(0.5\,\rho\,U^2 d^2)\,U$. Equating these two powers, we obtain for the vortex line spacing

$$\ell = L^{-1/2} \sim \left(\frac{6 \times 10^{-3}\kappa^3 d}{U^3} \right)^{1/4}. \tag{21}$$

By equating the two powers, we are assuming that energy lost by classical vortices being thrown off the oscillating structure is negligible (likely to be the case near the critical velocity), and therefore our estimate of the vortex line spacing must be a lower limit. For all the cases set out in Table 1, the spacing calculated from Equation (21) is significantly less than the size of the structure. It must also be significantly less than the viscous penetration depth $(2\nu''/\omega)^{1/2}$. This condition fails in the case of the tuning fork. Otherwise, however, the vortex line spacing can be expected to be small enough for a quasiclassical transition to hold, at least qualitatively.

A comparison of the critical values of K_C and β with those expected classically, with the effective kinematic viscosity of $0.11\,\kappa$, is shown in Figure 23. The solid curve in this figure is the relation in Equation (11); this was suggested as correct for a cylinder in a classical fluid, but, as we have indicated, it might be expected to be valid also for a sphere. The broken line shows the relation in Equation (15), which seems to apply to cylinders with rectangular cross-sections. We see that there is a pleasing measure of agreement. The experimental points for the sphere are a little too low and seemingly in better agreement with Equation (15) than with Equation (11). Perhaps this feature is associated with the very rough surface of the sphere (see Figure 10), the turbulence being nucleated at a sharp protuberance on the sphere. The observed value of K_C for the tuning fork appears to be much less than that given by Equation (15), but we have already noted that in this case the vortex line density is probably too small for quasiclassical behaviour. The significant measure of agreement in most cases suggests that our identification of the observed critical velocity at very low temperatures with the classical critical velocity v_{critKC} is correct. This gives us in turn some confidence that our overall picture may be correct.

---

[5] It has been suggested recently that the dissipation in a truly random tangle is rather larger than is given by this formula (Walmsley and Golov, private communication), but it is too early to be sure that this is correct. In practice, such a change does not seriously change our conclusions.
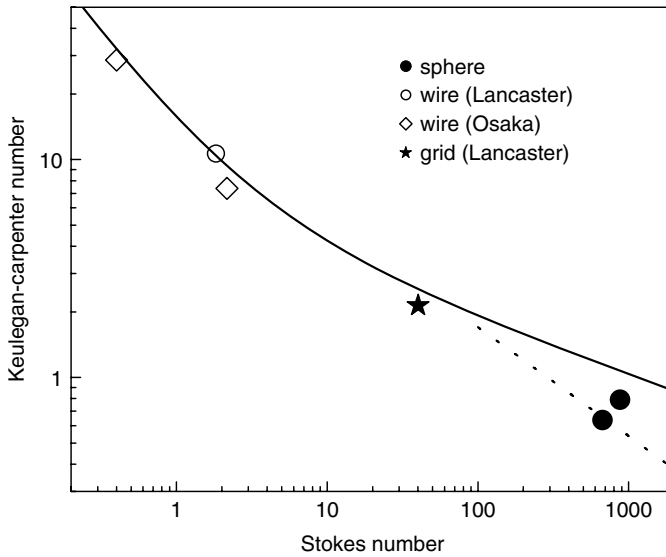
FIGURE 23   A comparison of the observed critical values of K_C and β with those expected classically (Equations (11) and (15)), with an effective kinematic viscosity given by $\zeta = 0.11$.

This tentative conclusion must be accepted with some reservations. The classical analogue carries with it clear predictions about the dependence of critical velocity that we have identified as v_{critKC} on frequency and the characteristic linear size of the oscillating structure. Experimental data for smooth spheres or cylinders at high values of β are clearly required. Furthermore, we are conscious that we have not seen clear evidence for separate critical velocities associated with the transitions to quasiclassical laminar flow and quasiclassical turbulent flow. Although, as we shall see later (Section 6.3), there is evidence for separate critical velocities with vibrating forks at high temperatures, their presence in systems at very low temperatures has only been inferred. We look forward to the extension of the vibrating fork experiments to low temperatures and to efforts to locate both critical velocities in other systems. Different conditions, such as different frequencies, might lead to better separation. Other matters that require further study relate to *switching behaviour*, observed by both Schoepe's group and the Osaka group. Although the statistical properties of this switching have been investigated in some detail by Schoepe (2004), we are not aware of any discussion of the conditions required for it to take place.

We are left then with unanswered questions and the need for more experiments. Systematic studies of the dependence on frequency and size

of structure could be very valuable, as could be experiments on the effect of systematic changes in surface roughness.

6.3 Critical Velocities in the Presence of Two Components

The interpretation of experiments with oscillating structures in ^{4}He at temperatures above 1 K, where there is a significant fraction of normal fluid, could be very complicated. Both fluids can become turbulent, and once the superfluid component becomes turbulent, mutual friction can serve to couple the two motions. Of course this coupling could simplify the problem, as it does in fully-developed homogeneous turbulence, where, as we have noted, the helium behaves as a single fluid on length scales greater than the vortex-line spacing. The most complete set of relevant experimental results relate to vibrating tuning forks: behaviour in a classical fluid was described in Section 4.3, and that in superfluid ^{4}He in Section 5.5. As we have already noted, behaviour in the superfluid above 1K seems to suggest the existence of two transitions: a sharp transition, marked by a sharp dip in the drag coefficient, followed by a broad transition, similar to that occurring in a classical fluid, after which the drag coefficient tends to a constant value close to unity.

At first sight, it might be thought that these two transitions are separate transitions to turbulence in the superfluid and normal components respectively, and indeed we have made this suggestion in a recent review chapter devoted to the cryogenic applications of the tuning forks (Blazkova et al., 2008). The suggestion was backed by some model calculations, based on the assumption of two independent transitions, which gave fair agreement with experiment. However, we are now conscious that the suggestion is not very reasonable: the first transition, in the superfluid component, would lead to the generation of a high density of vortex line and hence to a strong force of mutual friction between the two fluids, and this mutual friction would then have a serious effect on any turbulent transition in the normal fluid. Here we shall put forward a different explanation based to some extent on the ideas developed in Sections 6.1 and 6.2.

In these earlier sections, we developed the idea that at a very low temperature the transition to turbulence in the superfluid component involves two steps: the first leads to the production of a dense vortex tangle in the neighbourhood of the oscillating structure, a tangle that allows the flow of the superfluid component to mimic viscous laminar flow, with a kinematic viscosity ν'' (Equation (20)); the second is a quasiclassical transition in which this quasiclassical laminar flow gives way to quasiclassical turbulent flow.

Applying the same idea at a finite temperature, we are led to suggest the following sequence: the first observed transition leads to a tangle

of vortices in the superfluid component, which leads in turn to strong coupling between the two fluids; these strongly coupled fluids undergo laminar flow with some effective viscosity that involves both the viscosity of the normal fluid and an eddy viscosity ν'' (Equation (20)) of the superfluid component; the second transition is then a quasiclassical transition to a state with large-scale trailing vortices (or actual turbulence) with the coupled fluids acting as a single fluid. The following equations, which are a generalisation of Equation (13), serve to express these ideas in mathematical form.

$$C_D = 2\alpha \frac{S}{A}(\omega x_e v_e)^{1/2} \frac{1}{U} + x_e \gamma, \tag{22}$$

where

$$x_e = x + (1 - x)\Phi(U - U_{cS})\frac{(U - U_{cS})^2}{\varepsilon + (U - U_{cS})^2} \tag{23}$$

and

$$v_e = v_n + (v_c - v_n)\Phi(U - U_{cS})\frac{(U - U_{cS})^2}{\varepsilon + (U - U_{cS})^2}. \tag{24}$$

U is the velocity of a prong of the fork; x is the normal fluid fraction, ρ_n/ρ; $v_n = \eta_n/\rho$ is the kinematic viscosity of the normal fluid, referred to the total fluid density; $\Phi(y)$ is the Heaviside step function; U_{cS} is the critical velocity of the superfluid component; v_c is the effective kinematic viscosity of the fully coupled fluids; and α, γ and ε are constants. We see that, according to these equations, the effective normal fluid fraction, x_e, starts to rise from x to unity when the superfluid velocity exceeds the critical velocity U_{cS}, the change taking place over range of velocity determined by the parameter ε, and that the effective kinematic viscosity changes (increases or decreases) from v_n to v_c in a similar way.

We have fitted this equation to the experimental results, taking α, γ, ε, v_c and U_{cS} as adjustable parameters. The results for one fork are shown in Figure 24. The details will be published shortly. The values of the parameters α, γ and ε required for these fits turn out to be independent of temperature, as we would expect. (The values of α and γ are therefore derived in effect by fitting above the superfluid transition temperature; that is they are taken to have the values required to account for the behaviour of the fork in a classical fluid. This means that as far as the
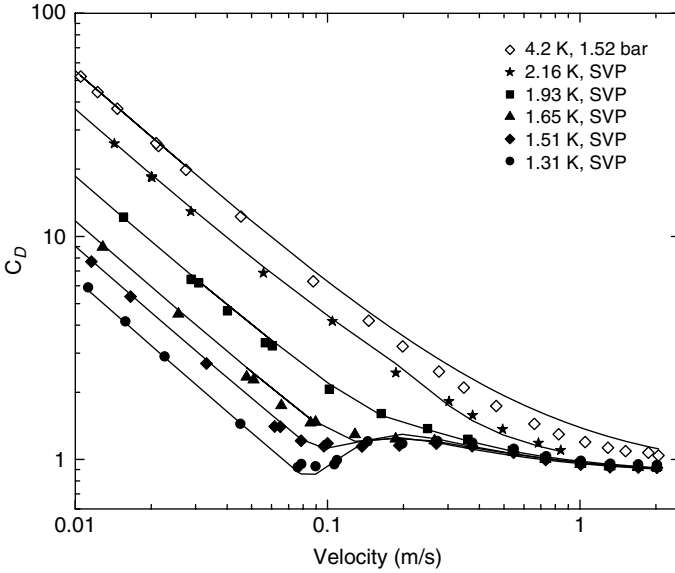
FIGURE 24   Fits of Equation (22) to the observed drag coefficient for a vibrating tuning fork.

behaviour of the superfluid is concerned our fitting procedure is based on only three adjustable parameters, v_c, ε and U_{cS}.) Note also that values of v_c are, as expected, similar in magnitude to both kinematic viscosity of the normal fluid and the eddy viscosity associated with a random vortex tangle. We see that the fit is good (better than is possible with our earlier model with separate normal and superfluid critical velocities), and this provides evidence that our picture of the way in which turbulence develops around a vibrating tuning fork at a temperature where there is a significant fraction of normal fluid is correct. It seems reasonable to suppose that a similar picture should apply to other forms of vibrating structure, although the available experimental evidence is insufficient to allow confirmation.

Values of the superfluid critical velocity, U_{cS}, and the effective kinematic viscosity, v_c, extracted from our fitting procedures are shown as functions of temperature in Figures 25 and 26, respectively. We have included in Figure 25 critical velocities, assumed to be superfluid critical velocities, observed with other vibrating structures, as described in the caption. It is interesting that all these critical velocities, relating to very different shapes of object and to different resonant frequencies, exhibit the same temperature dependence. A theory of the temperature dependence of superfluid critical velocity must account for these results.
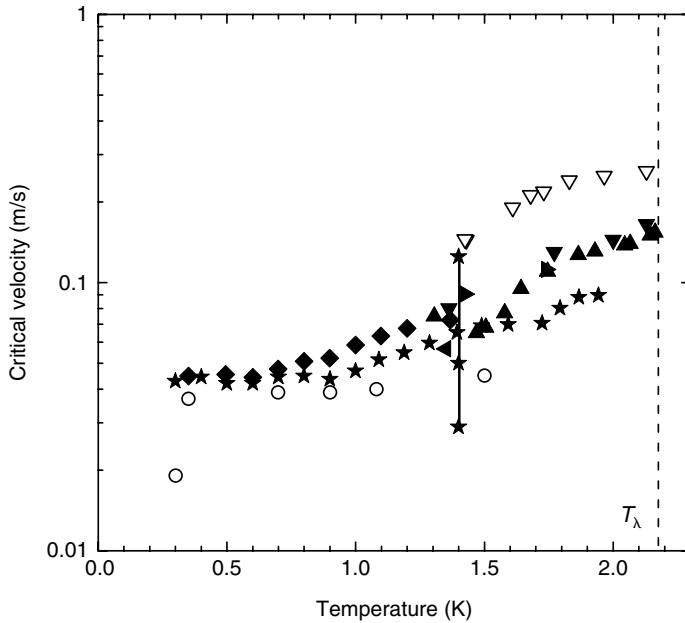
FIGURE 25   Superfluid critical velocities in superfluid ^{4}He plotted against temperature. Various triangles: data obtained by fitting Equations (22), (23) and (24) to results obtained with vibrating forks of various sizes vibrating at frequencies 4 kHz to 32 kHz. Stars: data from the Osaka Group with 2.5 μm NbTi wires vibrating at 710 Hz (Yano et al., 2006, 2007). Stars on a vertical line: data from the Osaka group with a 2.5 μm wire vibrating at various frequencies from 500 Hz to 9 kHz. Diamonds: data from the Lancaster vibrating grid at 1 kHz (Charalambous et al., 2006). Open circles: data from Schoepe's group on oscillating spheres (200 μm in diameter) at 120 Hz (data point at 300 mK) and 235 Hz (other data points) (Jäger et al., 1995; Niemetz et al., 2002).

7. DISCUSSION: SUPERFLUID ^{3}HE

As we have already explained, the only experiments on superfluid ^{3}He-B that we can discuss are those of the Lancaster group with a vibrating grid, carried out at temperatures where the fraction of normal fluid is negligible. The results of these experiments were described very briefly in Section 5.4, and a more detailed account is contained in a separate chapter in this volume.

At first sight, we might expect that the behaviour of the ^{3}He to be similar to that of the ^{4}He. The quantum of circulation and the vortex core parameter are slightly different, but making the necessary changes in the simulations discussed in the last section produces practically no effect. Nevertheless, as we saw in Section 5.4, the observed drag coefficient seems
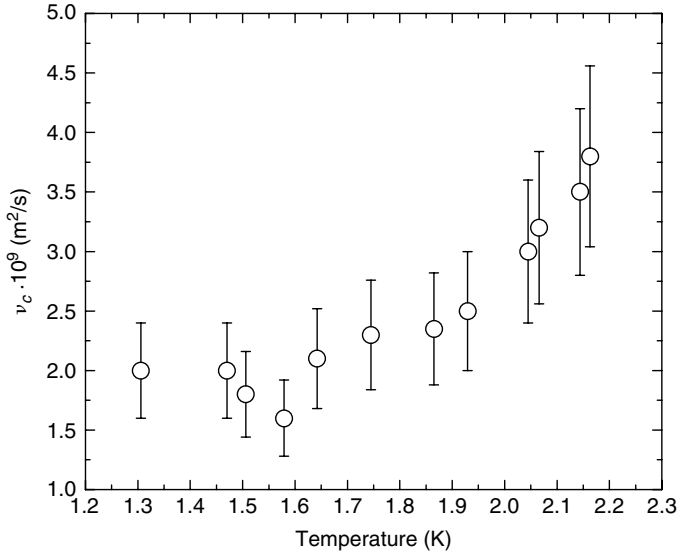
FIGURE 26   The effective kinematic viscosity, ν_c, plotted against temperature, obtained from the fits shown in Figure 24 using the data for the fork vibrating at 32 kHz.

to be larger by a factor of about 20, and the critical velocities are smaller by a similar factor. The large drag coefficient suggests that quasiclassical behaviour does not occur, and this view is confirmed by the fact that the small critical velocities lead to experimental points that are well below the solid line in Figure 23.

A possible reason for this difference was suggested by Hänninen et al. (2007). The critical velocity for intrinsic nucleation of vortex line in superfluid ^{4}He is known to be very large, and therefore our discussion in Section 5 was based on the assumption that vortex nucleation in ^{4}He is extrinsic. The situation in superfluid ^{3}He-B is different. Experiments in Helsinki (Parts et al., 1995; Ruutu et al., 1997) show single-vortex intrinsic nucleation can occur at a surface in rotating ^{3}He-B at quite small velocities, of order 4 mms^{-1}, which decrease with increasing surface roughness.

The surface of the grid used in the Lancaster experiments was much rougher than any studied by the Helsinki Group, and therefore the nucleation of vortex lines in the Lancaster ^{3}He grid experiments is very likely to have been intrinsic. This intrinsic process probably involves the production of vortex loops at the surface of the grid, which then expand and fly away under the influence of the superflow relative to the grid. Neither the rate at which this process occurs nor the associated critical velocity is known for the case of the surface of the grid, but the rate could well be very much greater than for ^{4}He, and the critical velocity very much

smaller. This could well explain the observed small critical velocity. The anomalously large drag may arise for the following reason. Whenever a vortex is attached to the grid, the tension in the vortex will lead to a force on the grid. In our discussion of the case of ^{4}He, we implicitly assumed that the number of attached vortices is small enough that the total tension force is relatively small. But if vortices are produced at a great rate, then the force due to attached vortices could become large and could be significantly greater than that due to quasiclassical effects of the type supposed to act in the case of ^{4}He. We assume that the oscillating component of this force has a substantial component in phase with the oscillating velocity of the grid.

We recall from Section 5.4 that the imaging capability of the Andreev scattering technique allowed the Lancaster group to deduce that, at velocities just above critical, small vortex rings are produced by the oscillating grid in numbers that allow them to fly away without much interaction. If our views are correct, then we can deduce that these rings are probably produced by intrinsic nucleation.

The imaging allowed the Lancaster group to show that, at higher velocities, coalescence of the rings leads to turbulence, and that this turbulence spreads away from the grid by a distance of about 1.5 mm. Furthermore, the group observed the rate of decay of this turbulence following removal of the drive on the grid. By comparing this rate of decay with that observed in experiments on the decay of homogeneous turbulence in ^{4}He (Stalp et al., 1999), and by assuming that the energy-containing eddies have a size of about 1.5 mm, the group were able to show that the effective kinematic viscosity ν' (Equation (19)) for ^{3}He-B at very low temperatures is about $0.2\,\kappa$. It is not clear why this value is so much larger than the value for ^{4}He. One possible reason is that the energy-containing eddies in the ^{3}He experiment are significantly smaller than was assumed. It is tempting to use the classical formula (Equation (17)) to obtain what might be a better value for the size of the energy-containing eddies. However, this approach is sensible only if the classical Equation (16) predicts the correct depth to which the turbulence diffuses from the grid. In fact, this formula predicts that

$$\frac{u_0}{U} = \frac{3.7 \times 10^{-7}}{z}, \tag{25}$$

where U is the velocity amplitude of the grid and z is measured in metres. Application of this formula leads to the conclusion that significant turbulent intensity could not penetrate to a depth as large as 1.5 mm from the Lancaster grid. Thus, we conclude that the classical formulae are inapplicable. This conclusion adds weight to our view that grid turbulence in ^{3}He-B at a low temperature is probably not quasiclassical in its character. More work is required in order to throw light on this interesting situation.

8. SUMMARY AND CONCLUSIONS

In this chapter, we have attempted to survey the experiments that have been reported on the production of quantum turbulence by oscillating structures in both superfluid ^{4}He and ^{3}He-B, and we have tried to compare the observed behaviour with that found in analogous classical systems. We find that for ^{4}He there are similarities, although important differences arise from the fact that any type of rotational motion, even when acting only as a precursor for turbulence, requires the presence of vortex lines in the superfluid component. There are also important differences between the results of preliminary and incomplete simulations and those of experiments on a sphere, which may be the result of a failure to take surface roughness into account. In the case of ^{3}He-B, there are more serious differences, which we attribute tentatively to the ease with which quantised vortex lines can be created in comparison with ^{4}He. An important general conclusion is that much more work is required experimentally and in the development of satisfactory simulations.

When this review was written (in 2007) the ideas proposed in Section 6 were at an early stage in their development. They have since been refined, with the result that some of the conclusions require modification. In particular we have recently concluded that the critical superfluid velocity and the velocity corresponding to the first stage of a quasi-classical transition to turbulence are not distinct; the two seem to be intimately connected, in the sense that the generation of a high density of vortex line depends on the presence of large-scale rotational motion associated with the transition to quasi-classical turbulence. The details of these refinements, together with further experimental data, will be published shortly.

ACKNOWLEDGEMENTS

REFERENCES

Batchelor, G. K. (1953). *The Theory of Homogeneous Turbulence*. Cambridge University Press, Cambridge.
Batchelor, G. K. (1967). *An Introduction to Fluid Mechanics*. Cambridge University Press, Cambridge.
Benson, C. B. and Hallett, A. C. H. (1956). *Canadian Journal of Physics*, 34, 668.
Bewley, G. P., Lathrop, D. P. and Sreenivasan, K. R. (2006). *Nature*, 441, 588.

Blaauwgeers, R., Blažková, M., Člověčko, M., Eltsov, V. B., de Graaf, R., Hosio, J. J., Krusius, M., Schmoranzer, D., Schoepe, W., Skrbek, L., Skyba, P., Solntsev, R. E. and Zmeev, D. E. (2007). *Journal of Low Temperature Physics*, 146, 537.

Blažková, M., Schmoranzer, D. and Skrbek, L. (2007a). *Physical Review E*, 75, 025302.

Blažková, M., Člověčko, M., Eltsov, V. B., Gažo, E., de Graaf, R., Hosio, J. J., Krusius, M., Schmoranzer, D., Schoepe, W., Skrbek, L., Skyba, P., Solntsev, R. E. and Vinen, W. F. (2008). Vibrating Quartz Fork – a Tool for Cryogenic Helium Research. *Journal of Low Temperature Physics*, 150, 525.

Bradley, D. I., Clubb, D. O., Fisher, S. N., Guénault, A. M., Matthews, R. P. and Pickett, G. R. (2004). *Journal of Low Temperature Physics*, 134, 381.

Bradley, D. I., Clubb, D. O., Fisher, S. N., Guénault, A. M., Haley, R. P., Matthews, C. J., Pickett, G. R. and Zaki, K. (2005a). *Journal of Low Temperature Physics*, 138, 493.

Bradley, D. I., Clubb, D. O., Fisher, S. N., Guénault, A. M., Haley, R. P., Matthews, C. J., Pickett, G. R., Tsepelin, V. and Zaki, K. (2005b). *Physical Review Letters*, 95, 035302.

Bradley, D. I., Clubb, D. O., Fisher, S. N., Guénault, A. M., Haley, R. P., Matthews, C. J., Pickett, G. R., Tsepelin, V. and Zaki, K. (2006). *Physical Review Letters*, 96, 035301.

Charalambous, D., Hendry, P. C., McClintock, P. V. E., Skrbek, L. and Vinen, W. F. (2006). *Physical Review E*, 74, 036307.

De Silva, I. P. D. and Fernando, H. J. S. (1994). *The Physics of Fluids*, 6, 2463.

Donnelly, R. J. (1991). *Quantized Vortices in Helium II*. Cambridge University Press, Cambridge.

Feynman, R. P. (1955). in edited by Gorter, C. J. (ed.), *Progress in Low Temperature Physics*, vol. I, p. 17, North-Holland Publications, Amsterdam.

Finne, A. P., Eltsov, V. B., Hanninen, R., Kopnin, N. B., Kopu, J., Krusius, M., Tsubota, M. and Volovik, G. E. (2006). *Reports on Progress in Physics*, 69, 3157.

Fisher, S. N., Hale, A. J., Guénault, A. M. and Pickett, G. R. (2001). *Physical Review Letters*, 86, 244.

Frisch, U. (1995). *Turbulence*. Cambridge University Press, Cambridge.

Hall, P. (1984). *Journal of Fluid Mechanics*, 146, 347.

Hänninen, R., Tsubota, M. and Vinen, W. F. (2007). *Physical Review B*, 75, 064502.

Hashimoto, N., Goto, R., Yano, H., Obara, K., Ishikawa, O. and Hata, T. (2007). *Physical Review B*, 76, 020504.

Higuchi, H. and Balligant, H. (1996). *Journal of Fluids and Structures*, 10, 705.

Honji, H. (1981). *Journal of Fluid Mechanics*, 107, 509.

Jäger, J., Schuderer, B. and Schoepe, W. (1995). *Physical Review Letters*, 74, 566.

Kozik, E. V. and Svistunov, B. V. arXiv:cond-mat/0703047v2.

Landau, L. D. and Lifshitz, E. M. (1987). *Fluid Mechanics*. Pergamon Press.

Luzuriaga, J. (1997). *Journal of Low Temperature Physics*, 138, 267.

L'vov, V. S., Nazarenko, S. V. and Rudenko, O. *Physical Review B*, 76, 024520.

Maurer, J. and Tabeling, P. (1998). *Europhysics Letters*, 43, 29.

McKinsey, D. N., Lippincott, W. H., Nikkel, J. A. and Rellergert, W. G. (2005). *Physical Review Letters*, 95, 111101.

Milne-Thomson, L. M. (1955). *Theoretical Hydrodynamics*. MacMillan, London.

Nichol, H. A., Skrbek, L., Hendry, P. C. and McClintock, P. E. V. (2004a). *Physical Review Letters*, 92, 244501.

Nichol, H. A., Skrbek, L., Hendry, P. C. and McClintock, P. E. V. (2004b). *Physical Review E*, 70, 056307.

Niemetz, M., Kerscher, H. and Schoepe, W. (2002). *Journal of Low Temperature Physics*, 126, 287.

Niemetz, M. and Schoepe, W. (2004). *Journal of Low Temperature Physics*, 135, 447.

Obasaju, E. D., Bearman, P. W. and Graham, J. M. R. (1988). *Journal of Fluid Mechanics*, 196, 467.

Otto, S. R. (1992). *Journal of Fluid Mechanics*, 239, 47.

Park, K., Barenghi, C. F. and Donnelly, R. J. (1980). *Physics Letters*, 78A, 152.

Parts, Ü., Ruutu, V. M. H., Koivuniemi, J. H., Bunkov, Y. M., Dmitriev, V. V., Fogelstrom, M., Huebner, M., Kondo, Y., Kopnin, N. B., Korhonen, J. S., Krusius, M., Lounasmaa, O. V., Soininen, P. I. and Volovik, G. E. (1995). *Europhysics Letters*, 31, 449.

Poole, D. R., Barenghi, C. F., Sergeev, Y. A. and Vinen, W. F. (2005). *Physical Review B*, 71, 064514.

Roche, P. E., Diribarne, P., Didelot, T., Français, O., Rousseau, L. and Williame, H. (2007). *Europhysics Letters*, 77, 66002.

Ruutu, V. M. H., Parts, Ü., Koivuniemi, J. H., Kopnin, N. B. and Krusius, M. (1997). *Journal of Low Temperature Physics*, 107, 93.

Sarpkaya, T. (1986). *Journal of Fluid Mechanics*, 165, 61.

Schlichting, H. and Gersten, K. (2000). *Boundary-Layer Theory*. Springer, Berlin.

Schoepe, W. (2004). *Physical Review Letters*, 92, 095301.

Schwarz, K. W. (1988). *Physical Review B*, 38, 2398.

Skrbek, L., Niemela, J. J. and Donnelly, R. J. (2000). *Physical Review Letters*, 85, 2973.

Skrbek, L. and Stalp, S. R. (2000). *The Physics of Fluids*, 12, 1997.

Skrbek, L., Blažková, M., Chagovets, T. V., Rotter, M. and Schmoranzer, D. (2007). Cavitation in Liquid Helium Observed in a Flow Due to a Vibrating Quartz Fork. *Journal of Low Temperature Physics*, 150, No 3/4, In Print.

Smith, M. R., Hilton, D. K. and VanSciver, S. V. (1999). *The Physics of Fluids*, 11, 751.

Stalp, S. R., Skrbek, L. and Donnelly, R. J. (1999). *Physical Review Letters*, 82, 4831.

Tatsuno, M. and Bearman, P. W. (1990). *The Physics of Fluids*, 211, 157.

Tough, J. T. (1982). in edited by Brewer, D. F. (ed.), *Progress in Low Temperature Physics*, vol. VIII, p. 133, North-Holland Publications, Amsterdam.

Vinen, W. F. (1961). in edited by Gorter, C. J. (ed.), *Progress in Low Temperature Physics*, vol. III, p. 1, North-Holland Publications, Amsterdam.

Vinen, W. F. (2000). *Physical Review B*, 61, 1410.

Vinen, W. F. and Niemela, J. J. (2002). *Journal of Low Temperature Physics*, 128, 167.

Vinen, W. F., Skrbek, L. and Nichol, H. A. (2004). *Journal of Low Temperature Physics*, 135, 423.

Voropayev, S. I. and Fernando, H. J. S. (1996). *The Physics of Fluids*, 8, 2435.

Walmsley, P. M., Golov, A. I., Hall, H. E., Levchenko, A. A. and Vinen, W. F. (2007). *Physical Review Letters*, 99, 265302.

Williamson, C. H. K. (1985). *Journal of Fluid Mechanics*, 155, 141.

Yano, H., Handa, A., Nakagawa, H., Nakagawa, M., Obara, K., Ishikawa, O. and Hata, T. (2005a). *The Journal of Physics and Chemistry of Solids*, 66, 1501.

Yano, H., Handa, A., Nakagawa, H., Obara, K., Ishikawa, O., Hata, T. and Nakagawa, M. (2005b). *Journal of Low Temperature Physics*, 138, 561.

Yano, H., Handa, A., Nakagawa, M., Obara, K., Ishikawa, O. and Hata, T. (2006). *American Institute of Physics, Conference Proceedings No 850*. American Institute of Physics, Melville, New York, 195.

Yano, H., Hashimoto, N., Handa, A., Nakagawa, M., Obara, K., Ishikawa, O. and Hata, T. (2007). *Physical Review B*, 75, 012502.

Zhang, T., Celik, D. and Van Sciver, S. W. (2004). *Journal of Low Temperature Physics*, 134, 985.

Visualisation of Quantum Turbulence

Steven W. Van Sciver* and **Carlo F. Barenghi**[†]

* National High Magnetic Field Laboratory, Mechanical Engineering Department, Florida State University,
  Tallahassee, Florida 32310, USA
[†] School of Mathematics, University of Newcastle, Newcastle upon Tyne, NE1 7RU, UK

Abstract   The application of modern flow visualisation techniques to quantum turbulence studies of helium II is reviewed. Emphasis is on those techniques that employ micron-scale particles as tracers of the flow fields. Different types of tracer particles are evaluated for this application including solid particles and particles made from solidifying hydrogen gas in liquid helium. The physics of small particles in helium II is then reviewed and discussed in the context of recent flow visualisation experiments. An interaction between suspended particles and quantised vortex lines can lead to drag force on the particles, which affects the particle velocity field in counterflow helium II. Recent experiments using the particle visualisation techniques show clear evidence of this interaction. In counterflow helium II, the particles are seen to track the normal fluid velocity field although at a reduced velocity that can be explained based on the particle-superfluid component interaction. Particle trapping by vortex lines has also been observed. On the other hand, in flowing helium II, the particles follow the total velocity field displaying a boundary layer very similar to that of classical fluids. The chapter concludes with suggestions for future experimental and theoretical investigation.

1. INTRODUCTION

1.1 General Goal

If the temperature of liquid helium is cooled below the critical value of $T_\lambda = 2.1768$ K (at saturated vapour pressure), the liquid becomes a quantum fluid called helium II. The most important property of helium II is superfluidity: mass flow without viscous friction. This phenomenon is similar to superconductivity (current flow without electrical resistance); both arise from the same fundamental physics of Bose–Einstein condensation (Pethick and Smith, 2001). As explained in Section 2, following the two–fluid model of Landau and Tisza, helium II can be described as two independent fluid components, the normal fluid and the superfluid. What makes the superfluid particularly interesting is that the rotational motion is constrained by quantum mechanics and occurs only in the form of discrete (quantised) vortex filaments. Quantised vortices and their turbulence are subjects of great experimental and theoretical interest which goes beyond helium II and involves also the rare isotope ^{3}He, atomic Bose–Einstein condensates and neutron stars. However, helium II is still the most studied superfluid; it is also the context where there is more overlap with

classical turbulence, so we hereafter concentrate our attention to helium II only. Given the long history of superfluidity in helium II, it is remarkable that there is so little direct experimental information about actual flow patterns. The comparison between flow visualisation in helium II and in classical fluids (such as water or air) is striking. In classical fluid mechanics, a wide range of visualisation techniques is available (Smits, 2001): ink, smoke, Kalliroscope flakes, hydrogen bubbles, Baker's pH technique, laser Doppler velocimetry (LDV), particle image velocimetry (PIV) and others. The most widely used techniques to monitor the dynamics in helium II (second sound and ion trapping) probe only the vortex-line density averaged over a relatively large volume, typically $\sim 10^3$ mm^3. Measurements of temperature, pressure and chemical potential suffer the same problem of poor spatial resolution. For example, they are unable to probe the fluid boundary layer near the wall of the channel or in the wake of an obstruction in the flow field. Also, all these types of measurements (temperature, pressure or second sound attenuation) are model dependent and thus do not directly measure the dynamics of the flow field (component velocity, vortex line density, boundary layer dimensions, etc.). Turbulent fluctuations, especially on small scales, are relatively unexplored. Thus, it has been of long-term interest to develop methods that can both visualise the flow field and probe the local characteristics of the fluid. Clearly the study of superfluid turbulence has been held back over the years by the lack of good flow visualisation. This problem has been recognised and the situation is rapidly changing.

The present chapter is a review of the recent developments in flow visualisation techniques applied to turbulence studies in helium II. Although this topic has been of interest to scientists for many years, it has not received much attention until fairly recently with the application of modern quantitative fluid dynamics visualisation techniques such as LDV and PIV. Implementation of these techniques has largely been enabled by the development of methods to seed the helium II with particles that can track the flow field without disturbing the dynamics. This latter topic has in turn spawned interest in the physics of small particle interactions with the quantised turbulent states in helium II.

We begin the chapter with a review of the previous attempts at particle seeding and flow visualisation in helium II. For the most part, these efforts have been qualitative in nature although still relevant to current research. We follow this discussion with a summary of the physics of helium II particularly as it affects the dynamics of suspended micron–scale particles. We then introduce for the nonexpert quantitative particle velocimetry techniques with emphasis on PIV as it represents the most versatile approach. The principles of particle seeding and its application to helium II experiments are then reviewed as an enabling technology to particle visualisation. We then provide a summary of results from recent helium II visualisation experiments emphasising the current

state of the field. We conclude with some recommendations for further research and comment on technical developments that can facilitate such work.

1.2 Approaches to Flow Visualisation

In order to visualise dynamic phenomena in helium II, it is necessary to introduce tracer objects within the fluid that follow the flow field and can be detected externally. The type of object to be seeded into helium II depends on the method of detection. One such method is to introduce charged particles into the liquid and track their motion collecting them at various locations along the channel. Positive ions in helium II attract the helium molecules and form very small solid helium particles, while negative ions repel the helium molecules forming microbubbles of diameter a few nm (Careri, 1961). In the case of the ions, the solid particles are assumed to track the normal fluid component dragged along by the viscous interaction. Awschalom et al. (1984) measured the motion of the normal fluid component in counterflow helium II using positive ions demonstrating that they travelled as a velocity very close to the normal fluid velocity $\mathbf{v}_n$. On the other hand, negative ions form very small bubbles within helium II of diameter ~ 2 nm that are attracted to the quantised vortex cores of the superfluid component presumably affected by both normal fluid and superfluid velocities $\mathbf{v}_n$ and $\mathbf{v}_s$, as shown by Gou and Maris (Guo and Humphrey, 2007). Also, recent experiments by McKinsey et al. (2005) have explored the use of laser-induced fluorencence in helium molecules. These elegant experiments tell us much about the motion of the two fluid components in helium II but are complicated to interpret and still lack the ability to visualise the local dynamics of the flow field.

   If one wants to use optical techniques to visualise the flow field, it is necessary to insert objects that will scatter light within the helium II flow field. Traditionally, there are two approaches to this problem. One method which works well for classical thermal convection experiments is to use the temperature-dependent index of refraction of the fluid, or in the extreme case the vapor bubbles in a two-phase mixture. However, such methods are not effective for helium II because the liquid has nearly constant density except very near the λ-point. Seddon et al. (2005) recently suggested that small quantities of ^{3}He injected into helium II should act as suitable tracers for observing thermal counterflow. The mass diffusivity of ^{3}He in ^{4}He is sufficiently slow to maintain the ^{3}He concentrated region for a long enough time to make a measurement. Small droplets of ^{3}He provide local changes in the refractive index that could be traced by optical methods tuned to this effect (e.g., Schlieren, laser holography or shadowgraph).

1.3 Previous Attempts to Visualise Helium II with Solid Particles

To visualise the flow fields in helium II, one can seed the fluid with solid particles that follow the helium II dynamics as long as they do not affect its behaviour and are observable using appropriate optical techniques. For the particles to follow the flow field, they should be small in size and neutrally buoyant. To our knowledge, Chopera and Brown (1957) were the first to employ neutral density particle seeding in helium II. They condensed a mixture of hydrogen and deuterium gas to produce ~1 mm particles with densities close to that of helium II ($145 \, \text{kg/m}^3$) and used this system to observe acoustic streaming. Later Kitchens et al. (1965) used similar methods to produce solid H_2/D_2 particles of 20–100 µm in diameter and employed these particles to the study of Helmholtz flow in rotating helium II. Although this group did not use modern visualisation techniques to record the flow field, they were able to qualitatively observe similar behaviour to that of classical fluids, including flow separation and vortex shedding. Also, Chung and Critchlow (1965) produced solid H_2/D_2 particles of a few hundred microns in diameter and studied their motion with turbulent superflow in helium II. Of particular note in these experiments was the observation that the particles follow the pure superflow, thus demonstrating the existence of an interaction between the turbulent superfluid and the suspended particles. The authors suggested that this interaction may be due to a kind of form drag between the particle and the superfluid component. Finally, qualitative visualisation of helium II in a counterflow jet was also reported by Dimotakis and Smith (Liepmann and Laguna, 1984) although in this case, the quality of the imagery is rather poor.

Other groups have used hollow glass spheres of varying size and density to visualise flow in helium II. Murakami et al. (1986) injected hollow glass spheres of 20 to 100 µm in diameter to observe the flow fields in a counterflow jet. Bielert and Stamm (1993) used hollow glass spheres of 20 to 50 µm in diameter to study Taylor–Couette flow in helium II. In both these cases, the results lacked quantitative evaluation due in part to the size and mass distribution of the particles.

Murakami et al. (1986) was the first to seed helium II with solid H_2/D_2 for LDV studies. These results are particularly significant as they represent the first quantitative flow visualisation study (in this case, LDV) with helium II. LDV is a technique that yields the local average velocity within a flow field by recording the motion of individual particles suspended within the fluid. By this method, Murakami (Murakami et al., 1989a; Murakami and Ichikawa, 1989b) was able to plot the particle velocity profile at the exit of the jet and compare its value to theoretical predictions. Although the velocity profile had the same qualitative shape as that of

classical fluids, the measured particle velocity was below that of the normal fluid component based on the two-fluid model particularly at temperatures well below T_λ. This observation, along with that of Chung and Critchlow (1965), suggests that the particle-helium II interaction may be more complex than previously assumed and that some force between the particle and the superfluid component is necessary to explain the observations.

2. TURBULENT HELIUM II

2.1 Two Fluid Model

Helium II is a quantum fluid, but a convenient semiclassical description is offered by the two-fluid model of Landau and Tisza. According to the two-fluid model, helium II can be described as the intimate mixture of two-fluid components (Landau and Lifschitz, 1987), the normal fluid and the superfluid. The superfluid (of density ρ_s and velocity $\mathbf{v}_s$) is related to the quantum ground state, and, having zero viscosity and zero entropy, is similar to a classical inviscid Euler fluid. We refer to Putterman (1974) and Barenghi (2008) for discussions of the relation between an inviscid Euler fluid and a superfluid and for the nonlinear Schroedinger equation that governs the evolution of the complex order parameter. The normal fluid (of density ρ_n and velocity $\mathbf{v}_n$) consists of thermal excitations, and, carrying nonzero viscosity µ and entropy, is similar to a classical, viscous Navier–Stokes fluid. The total density of helium II, ρ, is the sum of the superfluid and normal fluid densities, $\rho = \rho_s + \rho_n$, and is approximately independent of temperature. However, the relative fractions of normal fluid (ρ_n/ρ) and superfluid (ρ_s/ρ) are strong functions of the temperature T, as shown in Figure 1. Note that in the high temperature limit $T \to T_\lambda$, we have $\rho_s/\rho \to 0$ and $\rho_n/\rho \to 1$, so helium II becomes similar to a viscous Navier–Stokes fluid, whereas in the low temperature limit $T \to 0$, we have $\rho_n/\rho \to 0$ and $\rho_s/\rho \to 1$, so helium II becomes similar to an inviscid Euler fluid. The normal fluid fraction decreases very rapidly with temperature; for example (Donnelly and Barenghi, 1998), at $T = 1$ K we have $\rho_n/\rho = 0.007$ only. Below 1 K, at temperatures which can be accessed experimentally, the normal fluid is negligible and helium II is effectively a pure superfluid.

Because of the existence of two separate fluid components, waves in helium II are different from waves in a classical fluid. We distinguish between first sound, pressure and density oscillations which are similar to ordinary sound, and second sound, which consists of temperature and entropy oscillations. Second sound is particularly relevant to our subject because its amplitude is reduced in the presence of quantised vortices and can be used to detect them.
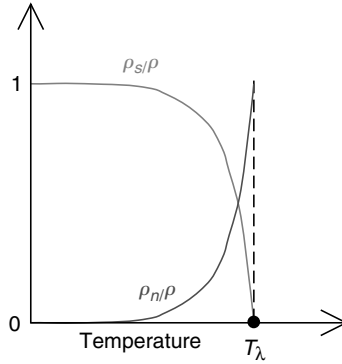
FIGURE 1 Relative proportion of normal fluid and superfluid as a function of temperature.

2.2 Quantum Turbulence

Vortices and eddies in the normal fluid can be of any size and strength. On the contrary, the rotational motion of the superfluid is constrained to very thin, quantised vortex filaments, all with the same strength (Donnelly, 1991). The superfluid velocity field around each filament satisfies the condition

$$\oint_C \mathbf{v}_s \cdot \mathbf{d\ell} = \kappa = 9.97 \times 10^{-8} \ \mathrm{m^2/s}, \tag{1}$$

where $\kappa = h/m$ is the quantum of circulation, h is Planck's constant, m is the mass of one helium atom and C is any path of integration around the vortex core. Using cylindrical coordinates (r, ϕ, z), it follows from Equation (1) that the velocity field around a vortex line set along the z axis is $\mathbf{v}_s = (0, v_{s\phi}, 0)$, where

$$v_{s\phi} = \frac{\kappa}{2\pi r}. \tag{2}$$

From a more fundamental point of view, the superfluid velocity field is proportional to the gradient of the phase of the complex order parameter. Thus, moving about the vortex along the path C, the phase changes from 0 to 2π. The superfluid density (which is related to the amplitude of the order parameter), drops from its bulk value away from the vortex to zero on the axis of the vortex over a characteristic distance of the order of $a_0 \approx 10$ nm. This distance is called the vortex core radius. Vortex lines are thus topological defects of the order parameter. When liquid helium is cooled through the lambda transition and becomes superfluid, it is unavoidable that some defects are left in the form of remanent vortex lines. These metastable vortices have been detected using the ion

trapping technique (Awschalom and Schwarz, 1984) and, more recently, using particle trapping and visualisation techniques (Bewley et al., 2006a).

The simplest way to create vortex lines in helium II is to rotate a vessel of helium at constant angular velocity Ω. A laminar vortex configuration is produced (Donnelly, 1991) in the form of a uniform vortex array. The vortices are aligned along the axis of rotation and their density (number of vortex lines per unit area) is given by Feynman's formula

$$n = \frac{2\Omega}{\kappa}. \tag{3}$$

Particle imaging techniques have been used to verify Equation (3), detecting individual vortex lines (Bewley et al., 2006a). The resulting images confirmed the early ionic pictures obtained by Packard and collaborators (Yarmchuk et al., 1979).

Quantised vortex lines interact with the thermal excitations which make up the normal fluid, thus coupling the superfluid and the normal fluid. The interaction has the form of a simple linear drag acting on each fluid called mutual friction (Barenghi et al., 1982). Mutual friction modifies the propagation of second sound in helium II, attenuating second sound waves which travel across vortex lines. The measurement of the attenuation of second sound is thus one of most common techniques used to detect vortex lines.

Numerical simulations reveal that quantum turbulence consists of a disordered tangle of quantised vortex filaments, see for example Figure 2. The filaments agitate each other and reconnect with each other, but, in the presence of constant forcing, achieve a statistical steady state, in which the vortex line density L (length of vortex line per unit volume) fluctuates around a mean value. Quantum turbulence can be excited in many ways: thermal counterflow (Tough, 1982), isothermal flow through a channel (Holmes and Van Sciver, 1992), flow past a sphere (Smith et al., 1999), towed grid (Smith et al., 1993), oscillating fork (Blazkova et al., 2007), vibrating grid (Charalambous et al., 2006), rotating propellers (Maurer and Tabeling, 1998; Roche et al., 2007), etc. Another way to generate quantum turbulence is to apply a heat flux to a rotating vortex array (Swanson et al., 1983; Tsubota et al., 2003). In this case, quantum turbulence results from the destabilisation of Kelvin-waves on individual vortex lines, which grow in amplitude until the lines reconnect with each other and a tangle is formed.

If the flow's Reynolds number is large, $Re = u_0 \ell_0 / \nu_n \gg 1$ (where u_0 and ℓ_0 are the characteristic velocity and length scales of the flow and $\nu_n = \mu_n / \rho_n$ is the kinematic viscosity based on the normal fluid), then we expect that the normal fluid is turbulent too. In this case, turbulent helium II consists of two coupled turbulent fluids which exchange energy with each other. This coupled turbulence and its remarkable similarities

FIGURE 2   Computed vortex tangle in a box with periodic boundary conditions (Barenghi, 2007).

with classical turbulence has attracted theoretical attention (Barenghi et al., 2002; Vinen and Niemela, 2002). Unfortunately there is little direct experimental information about normal fluid turbulence. In the case of thermal counterflow in a channel of circular cross section, however, it has been shown (Melotte and Barenghi, 1998) that a sufficiently intense vortex line density can destabilise the normal fluid profile and make it turbulent at values of Re which are less than the onset of turbulence in a classical fluid. The predicted critical vortex line density agrees with the observed transition from the T-1 (weak) state to T-2 (strong) state of counterflow turbulence (Tough, 1982).

2.3 Classical Turbulence

For the sake of clarity of the following discussion, here we summarise the basic understanding of classical homogeneous isotropic turbulence (Frisch, 1995). Consider a turbulent flow which is in a statistical steady state. It is convenient to examine the flow of kinetic energy in wave number space k, which is the magnitude of the three-dimensional (3D)

wave number $\mathbf{k}$ used to Fourier–transform the velocity field. Kinetic energy is injected at some large scale $k_0 \sim 1/\ell_0$ and transformed into heat at some small scale $k_1 \sim 1/\ell_1$ (called the Kolmogorov scale) by viscous dissipation. In the inertial range $k_0 \ll k \ll k_1$, kinetic energy is not destroyed but is simply shifted to higher k. The Reynolds number of the flow, defined as $Re = u_0 \ell_0/\nu$, measures the ratio of inertial and viscous forces, so $Re \gg 1$ in turbulent flows. At the Kolmogorov scale ℓ_1, viscous forces become as important as inertial forces, and by definition, $u_1 \ell_1/\nu = 1$, where u_1 is the typical velocity at the scale ℓ_1. The rate of kinetic energy dissipation, ϵ, must be the same at all scales $k_0 \ll k \ll k_1$, otherwise kinetic energy would pile up at some wave number. At the large scale, we can estimate $\epsilon \sim u_0^3/\ell_0$, whereas at the Kolmogorov scale, $\epsilon \sim \nu u_1^2/\ell_1^2$. Knowing the Reynolds number, we can thus infer that the ratios of small scales to large scale and small velocity to large velocity are, respectively, $\ell_1/\ell_0 \sim Re^{-3/4}$ and $u_1/u_0 \sim Re^{-1/4}$. These expressions are relevant to PIV experiments as ℓ_1 must be compared to the size of the tracer particles for example.

3. DYNAMICS OF TRACER PARTICLES

In order to interpret the experimental particle imaging results, it is essential to understand the motion of small tracer particles in helium II. We shall proceed in steps. In this section, we make the simplifying assumption that the tracer particles do not disturb the helium; in particular, that they do not disturb the quantised vortices. This is enough to understand the basic physics involved; for example, we can account for the tendency of particles to be trapped on quantised vortices and even estimate the time scale of the interaction. The motion of particles is thus studied under prescribed helium flow ($\mathbf{v}_n$, $\mathbf{v}_s$ and the quantised vortices), which is assumed to be unaffected by the particles. In Section 3.8, we shall go beyond this approximation and tackle the problem of the interaction of particles and vortices in a 'dynamically self-consistent' way, thus revealing the details of the trapping process.

3.1 Equations of Motion

The motion of small particles advected by incompressible turbulent flows is an important problem of fluid dynamics (Falkovich et al., 2002) and has many applications ranging from atmospheric physics to industrial processes. However, proper understanding of the particles' equation of motion has been achieved only recently. Since some details are subtle, we refer the interested reader to Auton et al. (1988), Maxey and Riley (1983), Mei (1994) and Kim et al. (1998). A recent article by Sergeev (2008) contains the derivation of the various forces acting on particles, distinguishing effects arising from irrotational and rotational inviscid flows and uniform and nonuniform viscous flows. A summary of this

derivation is contained in Poole et al. (2005), who generalised the classical equations of motion of a small particle in a nonuniform flow to Landau's two-fluid model of helium II, in which the normal fluid and the superfluid are represented as a viscous fluid and an inviscid fluid, respectively.

Let the tracer particle be a small sphere of radius a_p, diameter $d_p = 2a_p$, density ρ_p, position $\mathbf{r}_p = \mathbf{r}_p(t)$ and velocity $\mathbf{v}_p = \mathbf{v}_p(t)$, where t is time. Following Poole et al. (2005), we assume that the presence of the particles does not affect the flow, or, if the flow is turbulent, modify this turbulence. We also assume that the particles are much smaller than any macroscopic flow scale of interest in experiments of superfluid turbulence at temperatures above 1 K; assuming (in some cases for the lack of more precise information) that the vortex tangle is random, such small macroscopic scale is the average intervortex spacing $\delta \approx L^{-1/2}$ (Vinen and Niemela, 2002), where L is the vortex line density (smaller microscopic scales, as small as the vortex core a_0, are relevant when studying individual vortex reconnections or superfluid turbulence at very low temperature in the absence of the normal fluid). The smallest flow scale of the normal fluid is the Kolmogorov length ℓ_1, so we assume $a_p \ll \delta$ and $a_p \ll \ell_1$. Another mathematically convenient assumption is that the Reynolds number of the particle relative to the normal fluid is small,

$$Re_p = \frac{d_p|\mathbf{v}_p - \mathbf{v}_n|}{\nu_n} \ll 1, \tag{4}$$

so that the viscous interaction between the particle and the normal fluid can be modelled by a linear Stokes drag force. If $Re_p > 1$, a nonlinear form of the drag must be used.

Under these assumptions, neglecting effects which, in the fluid dynamics literature, are called the Faxen correction, the Basset history force, the Saffman lift force and the Magnus lift force, and which can be shown to be small in typical experimental conditions, Poole et al. (2005) argued that the Lagrangian equations of motion of a particle are:

$$\frac{d\mathbf{r}_p}{dt} = \mathbf{v}_p, \tag{5}$$

where $\mathbf{v}_p$ is evaluated at $\mathbf{r} = \mathbf{r}_p$, and

$$\frac{d\mathbf{v}_p}{dt} = \frac{1}{\tau}(\mathbf{v}_n - \mathbf{v}_p) + \frac{(\rho_p - \rho)}{\rho_o}\mathbf{g} + \frac{3\rho_n}{2\rho_o}\frac{D\mathbf{v}_n}{Dt} + \frac{3\rho_s}{2\rho_o}\frac{D\mathbf{v}_s}{Dt}, \tag{6}$$

where $\mathbf{g}$ is gravity,

$$\rho_o = \rho_p + \frac{1}{2}\rho, \tag{7}$$

the relaxation time is

$$\tau = \frac{2\rho_0 a_p^2}{9\mu} \tag{8}$$

and the convective derivatives are

$$\frac{D\mathbf{v}_n}{Dt} = \frac{\partial \mathbf{v}_n}{\partial t} + (\mathbf{v}_n \cdot \nabla)\mathbf{v}_n, \tag{9}$$

$$\frac{D\mathbf{v}_s}{Dt} = \frac{\partial \mathbf{v}_s}{\partial t} + (\mathbf{v}_s \cdot \nabla)\mathbf{v}_s. \tag{10}$$

Essentially, Equation (6) states that the motion of the particle is governed by viscous forces arising from the normal fluid alone (the first term at the right-hand side), buoyancy arising from the density difference with respect to the helium (the second term); the remaining third and fourth terms arise, respectively, from the streaming of the normal fluid and the superfluid around the small but finite-size particle. Note that the radius of the particle a_p appears only in the viscous drag term.

In the case of neutrally buoyant particles, $\rho_p = \rho$, Equation (6) is simplified and we have instead

$$\frac{d\mathbf{v}_p}{dt} = \frac{1}{\tau}(\mathbf{v}_n - \mathbf{v}_p) + \frac{\rho_n}{\rho}\frac{D\mathbf{v}_n}{Dt} + \frac{\rho_s}{\rho}\frac{D\mathbf{v}_s}{Dt}, \tag{11}$$

where ρ_0 and τ become

$$\rho_0 = \frac{3}{2}\rho \tag{12}$$

and

$$\tau = \frac{a_p^2 \rho}{3\mu_n}. \tag{13}$$

3.2 Sedimentation

If the normal fluid and the superfluid are both stationary ($\mathbf{v}_n = \mathbf{v}_s = 0$), then in the presence of gravity, spherical particles fall with slip (terminal) velocity

$$v_\infty = \frac{2a_p^2 g(\rho_p - \rho)}{9\mu}. \tag{14}$$

Equation (14) can be used to determine the particle radius from measuring u_∞ and knowing ρ_p.

3.3 Time-Dependent Flows with no Spatial Dependence

Equation (6) has simple solutions if the normal fluid and superfluid velocities are uniform in space and vary harmonically with time (Poole et al., 2005). Let $\mathbf{v}_n = \mathbf{V}_n \exp i\omega t$ and $\mathbf{v}_s = \mathbf{V}_s \exp i\omega t$, where ω is the angular frequency. The solution is

$$\mathbf{v}_p = \mathbf{U}_p^{(0)} \exp\left(-\frac{t}{\tau}\right) + \mathbf{U}_p \exp(i\omega t), \tag{15}$$

where $\mathbf{U}_p^{(0)} \exp(-t/\tau)$ is a transient term which depends on the initial condition and becomes negligible for $t \ll \tau$, and

$$\mathbf{U}_p = \frac{1}{(1 + i\omega\tau)}\left[\left(1 + \frac{3i\omega\tau\rho_n}{2\rho_0}\right)\mathbf{V}_n + \left(\frac{3i\omega\tau\rho_s}{2\rho_0}\right)\mathbf{V}_s\right]. \tag{16}$$

This solution has two interesting limits. If $\omega\tau \gg 1$, then $\mathbf{U}_p = \frac{3}{2}\rho^{-1}(\rho_n\mathbf{V}_n + \rho_s\mathbf{V}_s)$, while if $\omega\tau \ll 1$, then $\mathbf{U}_p = \mathbf{V}_n$, that is to say the particles track the normal fluid.

The case of particles that are neutrally buoyant is particularly simple. In the limit $\omega\tau \gg 1$, we have $\mathbf{U}_p = \rho^{-1}(\rho_n\mathbf{V}_n + \rho_s\mathbf{V}_s)$, which means that the particles move with a velocity corresponding to the total current density ($\mathbf{j} = \rho_n\mathbf{v}_n + \rho_s\mathbf{v}_s$), which is equal to zero in, for example, a second sound wave, and is equal to simply $\mathbf{v}_s$ at very low temperatures. In the limit $\omega\tau \ll 1$, we have again $\mathbf{U}_p = \mathbf{V}_n$, so the particles move with the normal component.

3.4 Classical Limit and Comparison with Ideal Lagrangian Tracer

It is instructive to rewrite the particle equation of motion in the classical limit of a single fluid of density ρ_f and velocity $\mathbf{v}_f$. We have

$$\frac{d\mathbf{r}_p}{dt} = \mathbf{v}_p \quad \text{and} \tag{17}$$

$$\frac{d\mathbf{v}_p}{dt} = \frac{1}{\tau}(\mathbf{v}_f - \mathbf{v}_p) + \frac{(\rho_p - \rho_0)}{\rho_0}\mathbf{g} + \frac{3\rho}{2\rho_0}\frac{D\mathbf{v}_f}{Dt}. \tag{18}$$

The motion of the particle must be compared to the motion of an ideal Lagrangian tracer (a parcel of fluid), which is determined by the single equation

$$\frac{d\mathbf{r}_p}{dt} = \mathbf{v}_f, \tag{19}$$

where $\mathbf{v}_f$ is evaluated at $\mathbf{r} = \mathbf{r}_p$. The ideal Lagrangian tracer has thus velocity $\mathbf{v}_p = \mathbf{v}_f$ by definition.

If the particle is neutrally buoyant, Equation (18) becomes

$$\frac{d\mathbf{v}_p}{dt} = \frac{1}{\tau}(\mathbf{v}_f - \mathbf{v}_p) + \frac{D\mathbf{v}_f}{Dt}. \tag{20}$$

If we approximate

$$\frac{D\mathbf{v}_f}{Dt} = \frac{\partial \mathbf{v}_f}{\partial t} + (\mathbf{v}_f \cdot \nabla)\mathbf{v}_f \approx \frac{\partial \mathbf{v}_f}{\partial t} + (\mathbf{u}_p \cdot \nabla)\mathbf{v}_f = \frac{d\mathbf{v}_f}{dt}, \tag{21}$$

then Equation (20) would become

$$\frac{d(\mathbf{u}_p - \mathbf{v}_f)}{dt} = -\frac{1}{\tau}(\mathbf{u}_p - \mathbf{v}_f). \tag{22}$$

The solution would be

$$\mathbf{u}_p - \mathbf{v}_f = [\mathbf{u}_p(0) - \mathbf{v}_f(0)]e^{-t/\tau}, \tag{23}$$

that is $\mathbf{u}_p \rightarrow \mathbf{v}_f$ for $t \gg \tau$. However, this is not necessarily correct because the trajectories of neutrally buoyant particles can be unstable (Babiano et al., 2000), and $\mathbf{v}_p$ and $\mathbf{v}_f$ can diverge. This means that the path of a solid particle which starts with the local fluid velocity becomes different from the path of an ideal fluid tracer (although at a given time the velocity of the solid particle need not be very different from the velocity of the local fluid tracer). Indeed, it has been known for some time that particles which are denser than the surrounding fluid are ejected from regions of high vorticity and tend to preferentially segregate into regions of high rate of strain (Squires and Eaton, 1990). Clearly, solid particles are not ideal Lagrangian tracers, and the PIV technique, popular in classical fluid mechanics, has its own limitations. In practice, however, stability issues are less important, and the more dominant Stokes drag force is compared to inertial effects; for example, Poole et al. (2005) showed that, in a simple ABC model of turbulent eddy, segregation occurs on the time scale of few
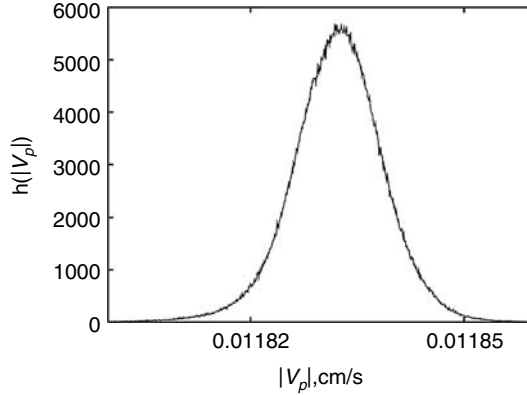
FIGURE 3 Histogram of particle velocities at $T = 2.171$ K, $v_n = 0.1183$ mm/s, $L = 75,000$ m^{-2}, $d_p = 6.25$ μm. In the figure, v_p has units of cm/s.

turnover times; since an eddy's lifetime is of the order of the turnover time, segregation is not necessarily a problem as it has no time to set in.

3.5 Tracer Particles in Counterflow Turbulence

Kivotides et al. (2006a) studied the statistical properties of tracer particles in counterflow turbulence. They applied the approximation that the particles are affected by the vortices but cannot be trapped in them or influence them. They found that, at $T = 1.3$ K and 2.171 K, the particles' average velocity was very close to the imposed normal fluid velocity which generated the vortex tangle. An example is shown in Figure 3. However, almost all particles came in the vicinity of a vortex line during the duration of the calculation, which means that they could have become trapped.

3.6 Tracer Particles at Very Low Temperatures

At temperatures below 1 K, helium II is effectively a pure superfluid, so $\rho \approx \rho_s$ and $\mu_n \approx 0$. In this low temperature limit, the equation of motion of a neutrally buoyant particle becomes

$$\frac{\mathrm{d}\mathbf{v}_p}{\mathrm{d}t} = \frac{D\mathbf{v}_s}{Dt}. \tag{24}$$

Since the superfluid has no viscosity, it can be modelled with Euler's equation:

$$\frac{\partial \mathbf{v}_s}{\partial t} + (\mathbf{v}_s \cdot \nabla)\mathbf{v}_s = -\frac{1}{\rho_s}\nabla p, \tag{25}$$

hence the particle obeys

$$\frac{d\mathbf{v}_p}{dt} = -\frac{1}{\rho_s}\nabla p. \tag{26}$$

The right-hand side is the force per unit mass acting on a parcel of super-fluid; it is also equal to the force on the particle that replaces that superfluid. Therefore, Equation (26) predicts that $\mathbf{v}_p(t) = \mathbf{v}_s(\mathbf{r}_p(t), t)$ and $\mathbf{r}_p(t) = \mathbf{r}_s(t)$, where $\mathbf{r}_s(t)$ is the Lagrangian displacement of a superfluid parcel, that is to say the solution to $d\mathbf{r}_s/dt = \mathbf{v}_s(\mathbf{r}_s(t))$. It would seem that at low temperatures small solid particles are ideal Lagrangian tracers, suitable for studying low temperature turbulence, but this is not the case, because, in the total absence of damping forces, the issue of stability of particle trajectories becomes crucial.

To illustrate the problem, consider the motion of a particle in the super-fluid velocity field due to a single, fixed rectilinear vortex (Sergeev et al., 2006a). Using cylindrical coordinates (r, θ, z) and assuming that the vortex is on the z axis, the velocity field is $\mathbf{v}_s = (v_{sr}, v_{s\theta}, v_{sz}) = (0, \kappa/(2\pi r), 0)$ and Equation (24) reduces to

$$\frac{d\mathbf{v}_p}{dt} = \frac{\kappa^2}{8\pi^2}\nabla\left(\frac{1}{r^2}\right). \tag{27}$$

This is the equation of motion of a particle of unit mass in the two-dimensional (2D) central potential $-\kappa^2/(8\pi^2 r^2)$. Let $\mathbf{r}_p = (r, \theta)$ and $\mathbf{v}_p = (v_r, v_\theta) = (dr/dt, rd\theta/dt)$ be the position and the velocity of the particle. The particle's angular momentum $l = rv_\theta$ is a constant of motion. Conservation of energy requires that $v_\theta^2 + v_r^2 - \kappa^2/(4\pi^2 r^2)$ is also constant.

Suppose that $v_r = 0$ when $r = r_0$. Then the radial equation is

$$\frac{dr}{dt} = \left[\frac{\kappa^2}{4\pi^2} - l^2\right]^{1/2}\left[\frac{1}{r^2} - \frac{1}{r_0^2}\right]^{1/2}. \tag{28}$$

It is useful to distinguish three cases, depending on the relative values of l and $\kappa/2\pi$, and to introduce $x = r/r_0$ so that $x = 1$ at $t = 0$. If $l > \kappa/2\pi$, then

$$x^2 = 1 + \left(l^2 - \frac{\kappa^2}{4\pi^2}\right)\frac{t^2}{r_0^4} \tag{29}$$

and

$$\theta = \left(1 - \frac{\kappa^2}{4\pi^2 l^2}\right)^{-1/2}\tan^{-1}\left[\left(l^2 - \frac{\kappa^2}{4\pi^2}\right)^{1/2}\frac{t}{r_0^2}\right], \tag{30}$$

hence the particle spirals outwards towards $r \to \infty$. Vice versa if $l < \kappa/2\pi$, then

$$x^2 = 1 - \left(\frac{\kappa^2}{4\pi^2} - l^2 \right) \frac{t^2}{r_0^4} \tag{31}$$

and

$$\theta = \left(\frac{\kappa^2}{4\pi^2 l^2} - 1 \right)^{-1/2} \tanh^{-1} \left[\left(\frac{\kappa^2}{4\pi^2} - l^2 \right)^{1/2} \frac{t}{r_0^2} \right], \tag{32}$$

hence the particle spirals inwards towards the vortex. In both cases, the difference $|(r - r_0)|$ between the path of the solid particle and that of a superfluid particle is proportional to t^2 for small t. Only if $l = \kappa/2\pi$, exactly does the particle follow the superfluid for all times; this is the case when initially the velocity of the particle is exactly equal to the velocity of the superfluid. But it can be shown (Sergeev et al., 2006c) that this orbit is unstable. We conclude that the tracer particle cannot even trace the orbit around a single vortex line.

Figure 4 illustrates a similar instability for the more complicated case of the motion of a particle in the presence of three vortices which orbit each other. We conclude that small particles cannot be used to visualise superfluid turbulence at very low temperature.

3.7 Approach of Particle to Vortex Line

Tracer particles have the tendency to become attracted to quantised vortex lines. In some cases, particles can become trapped into vortices. To understand why, notice that when a particle of radius a_p is trapped on a vortex, the energy of the helium is reduced by an amount approximately equal to the kinetic energy of the displaced superfluid (Parks and Donnelly, 1966). To evaluate this energy, first we find the energy per unit length of a vortex line. Consider a straight vortex line aligned along the z direction. The kinetic energy per unit length is

$$E = \int_0^{2\pi} \mathrm{d}\phi \int_0^\infty \mathrm{d}r \, r \frac{1}{2} \rho_s v_{s\phi}^2 \approx \frac{\rho_s \kappa^2}{4\pi} \ln (b/a_0), \tag{33}$$

where $v_{s\phi}$ is given by Equation (2) and we have introduced upper and lower radial cutoffs. If there is only one vortex line in the container, the upper cutoff b is the radius of this container; if there are many vortex lines,
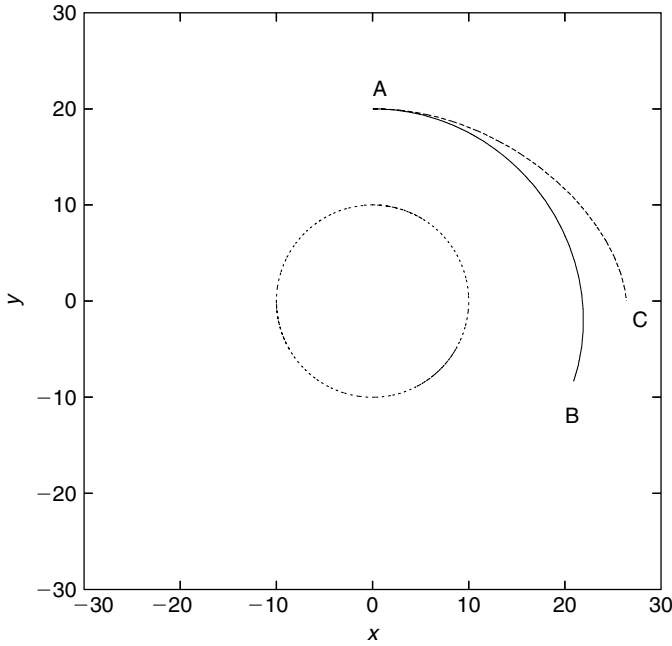
FIGURE 4 Trajectory of a solid particle (dashed line A to C) and superfluid particle (solid line A to B) around three vortices which move along the closed orbit shown (dotted line).

then b is the distance from the vortex to the next vortex. The lower cutoff is the vortex core radius a_0. Therefore, if a sphere of radius a_p is trapped into a vortex, the kinetic energy is reduced by the amount

$$E_{trap} \approx \frac{\rho_s \kappa^2 a_p}{4\pi} \log{(a_p/a_0)}. \tag{34}$$

For typical particle sizes $E_{trap} \gg k_B T$, where k_B is Boltzmann's constant, and we conclude that thermal effects do not inhibit trapping.

From an energetic point of view, it is apparent that the problem of trapping tracer particles (of typical size $a_p \approx 1 \, \mu m$) is rather different from the problem of trapping ions (typical size: $a_p \approx 10$ nm). Ions which have been extensively used in helium II experiments (Allum et al., 1977) have dimension which is bigger but not much bigger than the vortex core radius ($a_0 \approx 0.1$ nm), thus can be untrapped by thermal noise. Nevertheless there are many points of contact between our problem and that of ions in liquid helium, and we refer the reader to Parks and Donnelly (1966).

Let us consider the dynamics of the approach of the particle to the vortex at nonzero temperature. We assume that the particle is neutrally buoyant and is at rest at a distance r_0 from an isolated stationary rectilinear vortex, the normal fluid being also at rest. Following the kinematic approximation, we also assume that the vortex line does not move in response to any movement of the particle. Then the equation of motion of a neutrally buoyant particle is

$$\frac{d\mathbf{v}_p}{dt} = -\frac{1}{\tau}\mathbf{v}_p + \frac{3\rho_s}{2\rho_o}(\mathbf{v}_s \cdot \nabla)\mathbf{v}_s. \tag{35}$$

The equation shows that the motion of the particle in the radial direction is driven by the radial term $(\mathbf{v}_s \cdot \nabla)\mathbf{v}_s$, which has the form of a radial pressure gradient $\nabla(1/r^2)$. Let v_p denote the radial component of $\mathbf{v}_p$. We have

$$\frac{dv_p}{dt} = -\frac{v_p}{\tau} - \frac{2\beta}{r^3}, \tag{36}$$

where

$$\beta = \frac{\rho_s \kappa^2}{8\pi^2 \rho}. \tag{37}$$

We solve this equation and conclude that the particle, which started at distance r_0 from the vortex, arrives at radial distance $r = 2a_p$ from the vortex at time t_a given by

$$t_a = \frac{r_0^4}{8\beta\tau}\left(1 - \frac{(2a_p)^4}{r_0^4}\right). \tag{38}$$

We stress that our estimate assumes that, during the particle's approach, the vortex has remained straight; this would not be a good approximation if we let the particle come closer than the distance $2a_p$ to the vortex where we stopped the calculation. A more precise calculation (Kivotides et al., 2007c) which lets the particle to dynamically affect the vortex yields the result shown in Figure 5: clearly the simple expression given by Equation (38) is a fair approximation.

3.8 Particle-Vortex Collision

In this section, we allow the tracer particle which approaches a quantised vortex to affect it in a dynamically self-consistent way (Kivotides et al., 2006b, 2007a,b) to come close to the vortex and even to connect to it.
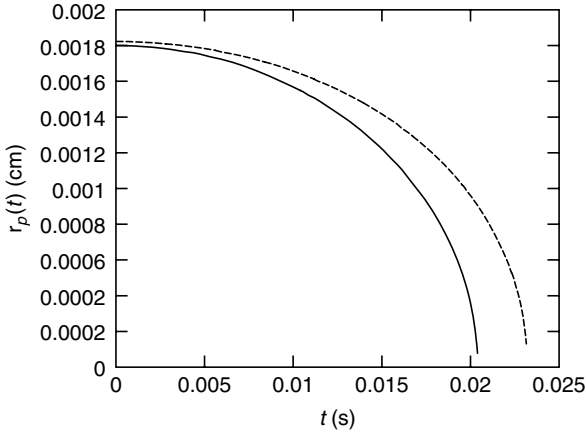
FIGURE 5 Vortex-particle separation. Solid line: kinematic approximation given by Equation (38). Dashed line: dynamic numerical calculation (see next section).

It is important to stress that in the model of Poole et al. (2005) expressed by Equation (6) the particle is essentially point-like; the model takes into account the streaming of the superfluid and the normal fluid around the sphere, but the radius of the sphere, a_p, appears only in the expression for the relaxation time, Equation (8). The model which we use in this section allows the particle and the vortex to become very close to each other and touch. A key step in this approach is a paper of Schwarz (1974) who showed how to efficiently compute the nonuniform pressure distribution around the surface of the particle.

For the sake of simplicity, we assume that the particle is neutrally buoyant and that the normal fluid is at rest. We let the vortex move and change shape as it feels the presence of the approaching particle; as the vortex moves through the normal fluid, it suffers a friction force. In the previous section, the particle was point-like, but here, to determine its motion, we must take into account the nonuniform, time-dependent pressure distribution around its spherical surface.

The particle's equation of motion can be written as

$$\frac{d\mathbf{r}_p}{dt} = \mathbf{v}_p \tag{39}$$

and

$$m_{eff}\frac{d\mathbf{v}_p}{dt} = \mathbf{f} = \mathbf{f}_d + \mathbf{f}_t + \mathbf{f}_b, \tag{40}$$

where $m_{eff} = m + 2\pi\rho a_p^3/3$. The total force $\mathbf{f}$ is decomposed into drag, local and boundary contributions:

$$\mathbf{f}_d = 6\pi a_p \mu(\mathbf{v}_n - \mathbf{v}_p), \tag{41}$$

$$\mathbf{f}_t = 2\pi\rho_s a_p^3 \frac{\partial \mathbf{v}_{si}}{\partial t}, \tag{42}$$

$$\mathbf{f}_b = \frac{\rho_s}{2} \int_S (\mathbf{v}_{si} + \mathbf{v}_b)^2 \widehat{\mathbf{n}} dS, \tag{43}$$

where $\mathbf{v}_n = 0$ in our case, and $\widehat{\mathbf{n}}$ is the unit radial vector pointing out of the surface S of the sphere.

Since the vortex core is many orders of magnitude smaller than the particle, we follow the approach of Schwarz (1988) and represent the vortex line as a space curve $\mathbf{X} = \mathbf{X}(\xi, t)$, where ξ is arc length. The line moves accordingly to

$$\frac{d\mathbf{X}}{dt} = \mathbf{v}_{si} + \mathbf{v}_b + \mathbf{v}_\phi + \mathbf{v}_{mf}. \tag{44}$$

The first term at the right-hand side, $\mathbf{v}_{si}$, is the superfluid velocity which the curved vortex induces upon itself due to its own curvature; it is given by the Biot-Savart integral

$$\mathbf{v}_{si}(\mathbf{X}) = -\frac{\kappa}{4\pi} \int d\xi \frac{\mathbf{X}' \times (\mathbf{X} - \mathbf{x})}{|\mathbf{X} - \mathbf{x}|^3}, \tag{45}$$

where $\mathbf{X}' = d\mathbf{X}/d\xi$ is the unit tangent vector at the point $\mathbf{X}$ in the direction of the circulation. The integral extends on the entire vortex configuration, so this term also describes the advection of a vortex line by another vortex line (which is important as during the particle-vortex interaction, multiple vortex loops can be generated).

The second term, $\mathbf{v}_b$, arises because the effect of the particle on the vortices must be such that the combined flow (that due to the vortex plus that induced by the particle) has zero radial component at the particle's surface. This contribution is obtained by solving a suitable Laplace equation in terms of an expansion in associated Legendre functions. The number of terms in this expansion is variable to keep the same level of approximation throughout the time evolution (Kivotides et al., 2006b, 2007a) and depends on the geometrical configuration (more terms are needed when the particle is close to the vortex).

The third term, $\mathbf{v}_\phi$, is the potential flow field (Drew and Passman, 2004; Kivotides et al., 2007a) induced by the motion of a spherical particle with radius a_p and velocity $\mathbf{v}_p$.

Finally, the fourth term, $\mathbf{v}_{mf}$, describes the friction on the vortex arising from the stationary normal fluid; it is

$$\mathbf{v}_{mf} = h_{\star\star}(\mathbf{v}_{si} + \mathbf{v}_b + \mathbf{v}_\phi) + h_\star \mathbf{X}' \times (\mathbf{v}_n - (\mathbf{v}_{si} + \mathbf{v}_b + \mathbf{v}_\phi)) \quad (46)$$

$$+ h_{\star\star} \mathbf{X}' \times (\mathbf{X}' \times \mathbf{v}_n),$$

where in our case $\mathbf{v}_n = 0$. The dimensionless quantities $h_\star$ and $h_{\star\star}$ depend on the mutual friction coefficient (Kivotides et al., 2007a). The numerical technique to perform the Biot-Savart integral and vortex reconnections is standard (Schwarz, 1988).

The calculation is performed at $T = 1.3\,\mathrm{K}$ so that the system is only slightly damped (the vortex by the mutual friction and the particle by the viscosity). Given the low temperature, we neglect the normal fluid disturbances induced by the particle and by the vortex (Kivotides et al., 2000) in their motion. These disturbances can affect the trajectory of the particle via the Stokes drag force (Sergeev et al., 2007). We find that, if we set the particle initially at rest at a distance $2a_p$ from the vortex, the particle falls into the vortex and becomes trapped, see Figure 6.

More precisely, as the particle approaches the vortex, at first the superflow generated by the particle tends to push away the vortex. As the particle becomes closer, the vortex effectively sees an image vortex with the opposite polarity behind the surface of the particle. Because of the interaction with its image, the vortex moves to the side, hence starts rotating under its self-induced velocity and reconnects with the particle. Initially, when the particle is at rest, the boundary force is the most important force and attracts the particle towards the vortex. It is also instructive to consider the balance of forces on the particle. As the particle accelerates, the main balance is between boundary and drag forces. The local (time-dependent) force is initially negligible because the vortex barely moves, but becomes important when the particle and the vortex are close to the reconnection. After the reconnection, it is the most important force as the particle is shaken by Kelvin-waves.

Figures 7 and 8 show that if the particle has a high initial velocity it can escape from the vortex. It is possible that during the interaction a vortex loop remains attached to the particle (and detaches on not, depending on details of the interaction).
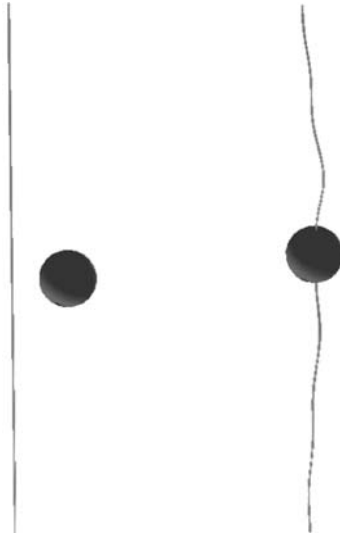
FIGURE 6   The particle approaches the vortex (left) and is trapped (right).
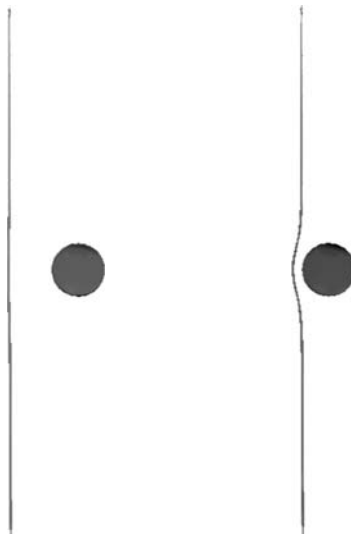
FIGURE 7   The particle approaches the vortex...
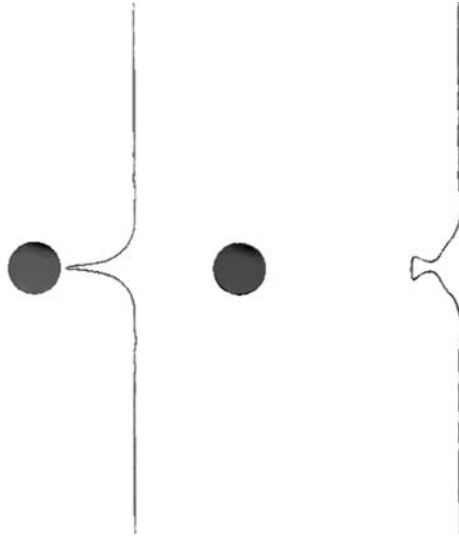
FIGURE 8   . . .reconnects but then escapes.

4. PARTICLE VISUALISATION TECHNIQUES

Particle visualisation techniques are all based on the assumption that the particle motion faithfully follows the flow field of interest. As discussed above, typical visualisation particles have mean diameters in the range of a few micrometers, which for the present discussion should be compared to the relevant length scales in turbulent helium II. With respect to the turbulent superfluid component, the vortex core is of order 1 nm, while (assuming a random tangle with the caveat of Section 3.1) the mean spacing between the vortex lines is $L^{-1/2} \sim 1\,\mu$m. Classical turbulent scales (Kolmogorov, 1941) are also $\sim$1 μm. Thus, typical visualisation particles suspended in helium II are unable to track the detailed structure of these phenomena, although the associated interaction may affect their averaged motion. On the other hand, large-scale turbulent behaviour such as velocity boundary layer development or vortex shedding have scale lengths that are generally larger than the few micrometer particle size so that their behaviour should be readily observable using particle visualisation techniques provided the image resolution defined by the optical system is sufficiently precise.

   The two principal visualisation methods that use suspended particles are LDV also sometimes referred to as laser doppler anemometry and PIV. Here we briefly describe these two methods and their application to helium II experimentation. For details, the reader should consult one of several review articles on the subjects (Adrian, 1991; Cummins, 1967; Grant, 1997).

4.1 LDV

LDV measures the velocity of a suspended particle at a particular point in the flow field defined by the crossing of two laser beams. The two laser beams produce an interference pattern. When a particle moves through this region, the pattern gives off light that is modulated at a frequency that is dependent on the particle velocity. The light is Doppler shifted relative to that which would be emitted if the particle were at rest. This information is converted to a velocity component, and with multiple lasers (of different frequencies) 2D or 3D component measurements can be obtained. The measurements are quantitative but do not produce an image of the flow field. In addition, since the measurement is at a particular point in the flow field, LDV is most suitable for experiments with steady flows where one can sweep the measurement point through the field to obtain a quantitative determination of the velocity field over a finite volume. Since LDV focuses on a specific point in the flow field, it has more relaxed requirements for particle seeding, and the particle concentration is not nearly as crucial a parameter as it is with PIV. Another advantage is that LDV can be used to obtain information about particle size and thus may be useful in conjunction with other flow visualisation techniques such as PIV to produce a range of quantitative information about a flow field. As an example of the application of LDV to helium II dynamics, Murakami et al. (1986) used this technique to obtain a quantitative measure of the particle velocity field at the exit of a counterflow jet.

4.2 PIV

The PIV technique is advantageous for flow visualisation experiments with helium II because it gives an instantaneous measurement of the velocity field over a finite size region, thus acquiring large quantities of data in a short time. The technique utilises a sheet of laser light (typically ~1 mm thick) that illuminates a rectangular region in the seeded flow field. A charge-coupled device (CCD) camera normally oriented at right angles to collect the scattered light and transfers the images to computer for analysis. The light scattered from the suspended particles is recorded at two instants in time determined by the laser pulse sequence. In the data analysis step, the recorded flow field is divided into multiple interrogation regions each containing of order tens of particles. A cross correlation data processing algorithm then provides the average velocity for each of the interrogation regions. A typical flow field might be $20 \times 20 \, \text{mm}^2$ with of order 400 by $1 \, \text{mm}^2$ interrogation regions.

The temporal response to PIV is important to the measurement. Since the measurement requires two images, it is necessarily averaged over the time interval between images. Dual pulse lasers allow images to be acquired on a millisecond time scale, but low velocity flows are in turn

difficult to visualise as the particles must travel a distance much larger than their diameter to produce accurate velocity measurements. These practical considerations are strongly impacted by the selection of seeding particles for the flow field.

5. PARTICLE SEEDING TECHNIQUES FOR HELIUM II

Since PIV measures the entire flow field in an instant, the quality of the particle suspension is critical to this method of measurement; as mentioned above, less so for LDV. Although particle seeding is trivial in classical liquids (Melling, 1997), it requires considerable attention to detail to successfully accomplish in helium II (Zhang et al., 2004a).

5.1 General Requirements for Particle Seeding of Helium II

Generally speaking, the seeding of particles in helium II is critical to the success of a visualisation experiment. Ideally, the particle should be visible to the optical detection system yet nondisruptive to the helium II fluid dynamics. The particles should be small so that they track the flow and occupy a negligible fractional volume. They should be close to neutrally buoyant to stay in suspension for the duration of the experiment. However, they cannot be too small, otherwise they will not scatter enough light to be detected by the optical system. Very small particles are also affected by Brownian motion that can disturb their tracking ability. As we will see below, these general requirements indicate a suitable range of particle diameters between $1\,\mu m$ and $10\,\mu m$ with densities as close to that of helium II as possible.

5.1.1 Particle Settling

It is difficult to obtain and not always necessary to have neutrally buoyant particles for helium II visualisation experiments. Helium II has low density ($145\,kg/m^3$), which is a challenge to reproduce in solid materials that can be made into particles. Thus, in most cases it is necessary to take into consideration the settling of the particle suspension. A spherical particle suspended in static helium II will move under the influence of gravity in a direction based on the net buoyancy force. As discussed in section 3, if the dynamics can be described by Stokes flow ($Re_d = v_\infty d_p/\nu_n < 1$, where v_∞ is the component of $\mathbf{v}_p$ in the direction of gravity), then the particle will move at the slip velocity given by Equation (14) and repeated here for convenience,

$$v_\infty = \frac{2a_p^2 g(\rho_p - \rho)}{9\mu},$$

(47)

where $a_p = d_p/2$ is the particle radius. If the particle density is greater than that of helium II, the slip velocity is negative and the particle will settle out of the fluid. For example, if $\rho_p \sim 1000\,\text{kg/m}^3$ and $d_p \sim 1\,\mu\text{m}$, the predicted settling velocity should be of order a few mm/s. Note that if the particle density is less than that of helium II (e.g., solid H_2 has a density $\sim 89\,\text{kg/m}^3$), then the particles will settle to the top of the liquid. For sH_2 particles of $1\,\mu\text{m}$ diameter, this 'raising' velocity should be $\sim 0.1\,\text{mm/s}$. As discussed above, it is possible to produce truly neutral buoyancy particles by the proper mixture of H_2 and D_2 to form solid particles.

For good experimental measurements in helium II, it is desirable to have v_∞ to be less than a few percent of the velocity to be measured. However, there are subtle practical advantages to having a nonzero slip velocity. Particle agglomeration will occur for most particles that are suitable for visualisation experiments. As a result, it is helpful to be able to periodically sweep the flow field free of old particles to allow an ensemble of new particles to be seeded into the helium II. By selecting particles with nonzero slip velocity, one ensures that the fluid will need to be reseeded periodically during the experiment. Also, having a nonzero slip velocity provides a method for estimating the particle size and distribution (Xu and Van Sciver, 2007; Zhang and Van Sciver, 2004b).

5.1.2 Particle Fidelity

In addition to the requirements on particle size and density based on the settling velocity, one must also consider the fidelity of the particle fluid interaction particularly when attempting experiments that require high-frequency signal detection (e.g., second sound, see Section 7.1.3). For spherical particles the characteristic response time derived from Equation (13) is approximately,

$$\tau = \frac{a_p^2 \rho}{3\mu}. \tag{48}$$

This requirement again drives the particle selection in the direction of small particles as $\tau \sim 10\,\mu\text{s}$ for particles with $\rho_p \sim 1000\,\text{kg/m}^3$ and $d_p \sim 1\,\mu\text{m}$. However, very small size particles are susceptible to Brownian motion, which also affects their tracking ability in helium II. The random particle motion resulting from elastic collisions with helium molecules, known as Brownian motion, leads to a mean square displacement X^2 that for Stokes flow is given by (Russel et al., 1989)

$$X^2 = \frac{k_B T t}{3\pi\mu a_p}. \tag{49}$$

For Brownian motion to have an impact on a visualisation experiment, the mean square displacement needs to be comparable to other important dimensions, in particular the distance travelled by the particle during a measurement, which is typically tens of particle diameters. Equation (49) predicts that a 5 μm particle in helium II will diffuse approximately 1 μm in one second, which is generally negligable compared to particle displacements in the measurement. Furthermore, in PIV the velocity is determined by the ensemble average within an interrogation region so that the individual particle motion caused by collisions with molecules tends to be averaged. Thus, Brownian motion only becomes important for particles of diameter significantly less than one micrometer, which for additional reasons discussed below are not very suitable for PIV.

5.1.3 Light Scattering

The scattering efficiency of small particles is reduced significantly for particle diameters that approach the wavelength λ of the incident light (Melling, 1997). Ideally, the particle diameter should be ∼10 λ although acceptable light scattering occurs to as low as $d \sim 2\lambda$. Since laser light for PIV experiments is typically in the visible to IR range, light scattering efficiency sets a practical lower limit on particle size at about 1 μm. Also, mean exposure averaged over the area of a particle image scales approximately as d_p^n, where $n \sim 3$; the particle image field will be dominated by the larger particles some of which may be too large to accurately track the flow. As a result, there is a clear advantage to using particles with a narrowly peaked size distribution (Adrian, 1991).

5.1.4 Concentration Requirement

Establishing the proper concentration of suspended particles is critical to PIV experimentation. Too high a concentration of particles will impact the dynamics of the fluid and prevent the transmission of light. However on the lower end, the concentration needs to be sufficiently great to meet the requirements for statistical analysis of the data. Generally, this requirement sets a minimum concentration at ∼15 particle image pairs per interrogation region (Melling, 1997). As a typical interrogation region might have a volume ∼1 mm^3, the particle-to-helium volume fraction of the seeded fluid should be in the range of 10^{-6} to 10^{-8}.

5.1.5 Particle Agglomeration

Small particles are attracted to each other due to van der Waals forces that are often strong enough to form particle clusters particularly at low temperatures where the thermal energy of the particles is very small. (Bewley, 2006b) compared the thermal energy and kinetic energy to the

Van der Waals potential for 2 μm polystyrene microspheres and concluded that once two particles come into contact at low temperature, they will remain bonded. Evidence in terms of a higher settling velocity suggesting particle agglomeration in 1.7 μm polystyrene microspheres has been reported by Zhang and Van Sciver (2005a). Hydrogen particles have a similar affinity for each other. At helium temperatures, solid hydrogen particles tend to agglomerate and possibly sinter resulting eventually in very larger particles ($d_p > 1$ mm) that are unsuitable for visualising helium II dynamics.

5.2 Particles Seeding Techniques

Taking into consideration the above issues for particle seeding in helium II, to date there have been two main types of particles that have been successfully used in LDV and PIV experiments: commercial solid particles and particles that are solidified from liquids or gases.

5.2.1 Solid Particles (Hollow Glass Spheres, Polystyrene)

Commercial solid particles are available from a number of vendors in a range of sizes and materials. As discussed above, one common type of visualisation particle is the hollow glass sphere which typically has a diameter in the range from 10 to over 100 μm. These particles can have average densities close to that of helium II ($\rho_p \sim 150$–$200 \, \text{kg/m}^3$) but have rather wide particle size and density distributions which results in a wide range of settling velocities. Also, the large size significantly reduces the fidelity of these particles for time dependent phenomena. Some hollow glass spheres have been made available with a narrower size distribution ($d_p \sim 8$–$12 \, \mu\text{m}$) but in turn a higher average density ($\rho_p \sim 1000 \, \text{kg/m}^3$) (Donnelly et al., 2002), but these particles have enjoyed only limited use in helium II PIV experiments.

Polystyrene microspheres have been successfully used in a number of recent PIV experiments (Zhang and Van Sciver, 2005a,b). Although these particles have a rather high density, $\rho_p \sim 1100 \, \text{kg/m}^3$, relative to that of helium II, they can be obtained in a much smaller size and narrower size distribution than the hollow glass spheres. The small size ensures a low settling velocity and a high frequency response, while the narrow size distribution results in a more uniform settling velocity for the entire particle field that can, in principle, be taken into account as a correction to the measured velocity field.

One of the disadvantages of using solid, dense particles for visualisation experiments is associated with the requirement to use very small particles to ensure fidelity and minimise settling. Smaller particles have a higher tendency to agglomerate, resulting in effectively larger particles

with a higher settling velocity and lower fidelity. Also, the handling of solid particles is more difficult, both in terms of seeding them into the helium II as well as removing them after experiments.

The seeding of particles into helium II is one of the more challenging aspects of flow visualisation experiments. Solid particles such as hollow glass spheres or polystyrene microspheres are normally stored at room temperature either in a gas or liquid suspension. Typical experimental conditions on the other hand are low temperature $(T \sim 2\,\text{K})$ and partial vacuum such that any foreign fluid will solidify possibly bonding the individual particles into clusters. Thus in the case of solid particles, it is extremely important to purge the material with helium gas before introducing into the liquid helium bath.

Zhang et al. (2004a) developed a fluidized bed method for handling commercial particles and seeding them into a helium II bath based on previous work with classical fluid seeding (Melling, 1997). Figure 9 is a schematic of Zhang's device. The particles are placed in a container along with larger $(d \sim 100\,\mu\text{m})$ glass beads above a porous plug. The particle mixture is periodically purged and evacuated with helium gas by intermittently actuating valves 2 and 1 such that the mixture becomes fluidised, thus facilitating the removal of the interstitial gases. After sufficient purging, valve 2 is closed and valve 3 is opened allowing the visualisation particles to be carried into the experimental region.

When performed carefully, Zhang et al. (2004a) was able to seed a helium II bath with a uniform distribution of polystyrene microspheres
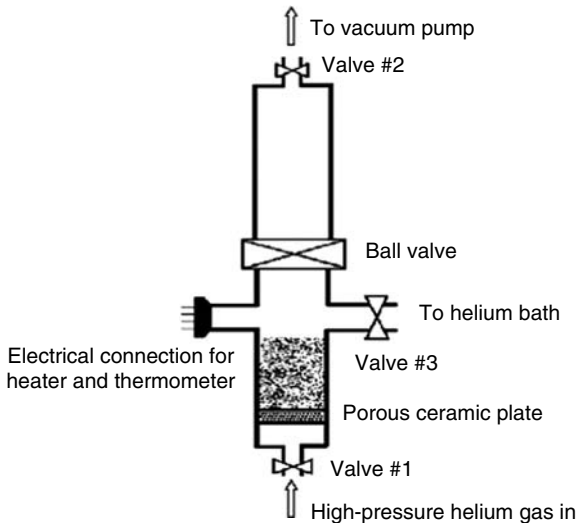
FIGURE 9   Fluidised bed developed to prepare polystyrene particles for insertion into helium II experiments (Zhang et al., 2004a).
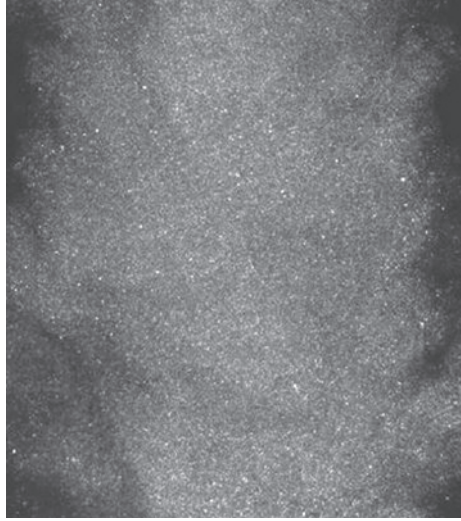
FIGURE 10 1.7 µm polystyrene particles seeded into helium II bath (Zhang et al., 2004a).

as seen in Figure 10. However, some evidence based on higher than expected measured particle settling velocities suggested that these particles may have formed small clusters with effective diameters roughly twice that of the individual particles. None the less, polystyrene particle seeds have been successfully instituted in several counterflow helium II PIV experiments.

5.2.2 Solidified Particles (Solid Hydrogen)

Particles solidified from gases or liquids are an alternative to commercial solid particles for visualisation experiments in helium II. In this case, the particles are most often made from isotopes of hydrogen (H_2 or D_2) because of the near neutral buoyancy. Solid hydrogen particles can be produced by condensation in the helium vapor above the liquid allowing the particles to fall into the helium II (Bolnev et al., 2002; Murakami and Ichikawa, 1989b), by condensing the vapor diluted with helium gas directly into the liquid phase (Bewley, 2006b; Xu and Van Sciver, 2006), or by solidifying a fine spray of liquid hydrogen into helium II (Celik and Van Sciver, 2002).

One clear advantage to solidified hydrogen particles is that one can produce a nearly neutral buoyant seed, particularly if a mixture of H_2 and D_2 is used. Another practical advantage comes with the cleanup after experiments since the particles can easily be removed from the experimental region by raising the temperature to about 30 K and evacuating the apparatus.

The main disadvantages of solidified particles concern their presumed nonuniform size and shape and tendency to agglomerate into larger particles limiting the duration of experiments. A distribution in the size and shape of particles also has the effect of producing a large variation in the brightness of the reflected light and some variation in the fidelity.

Figure 11 is an image of hydrogen particles seeded into helium II using the vapor condensation method. The hydrogen gas is diluted with helium to reduce the intermolecular collision rate between hydrogen molecules, which results in smaller, more uniform particles. The typical hydrogen gas volume fraction for this process is of order 0.01 although a range of concentrations have been successfully used (Xu and Van Sciver, 2006).

It is difficult to determine the size of the particles produced by condensing solid hydrogen into a helium II bath. Bewley et al. (2007) has estimated a range of diameters of order 1 to 4 μm in his experiments based on an average concentration from the known amount of condensing gas. Bolnev et al. (2002) claim to have generated particles of less than 100 nm diameter using neutron diffraction as supporting evidence. Murakami et al. (1989a) generated a broad distribution of solid H_2/D_2 particles, but used a fine mesh screen to preferentially select the small particles although no particle size measurements were reported. Xu and Van Sciver (2008) measured the distribution of settling velocities with solid D_2 and H_2 particles showing that over 90 percent have diameters less than 10 μm with a mean value of 4 μm. Such particles have a settling velocity of less than 1 mm/s and are generally suitable for visualising large-scale turbulent structures
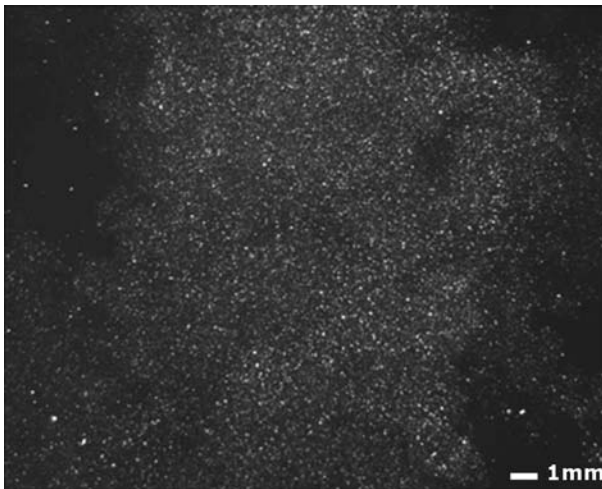
FIGURE 11   Solid hydrogen particles dispersed in helium II bath (Xu and Van Sciver, 2006)

TABLE 1 Tracking characteristics of different tracer particles in liquid helium. The τ and the $v_\infty = v_f - v_p$ are computed using Equations (47) and (48), which are approximate expressions based on simplifying assumptions discussed in the text (Zhang et al., 2004a).

Type of particle	Supplier	density (kg/m³)	d (µm)	He I (4.2 K)		He II (1.8 K)	
				v_∞ (mm/s)	τ (ms)	v_∞ (mm/s)	τ (ms)
Hollow glass	3M	160	30	5.2	2.8	5.4	8.0
spheres		160	120	83.7	44.9	86.4	127.9
	PQ	200	20	5.0	1.2	8.8	3.6
		200	100	124.5	31.2	220	88.8
	TSI	1100	8	10.4	0.20	24.4	0.57
		1100	12	23.3	0.45	55.0	1.3
	TSI	1100	8	10.4	0.20	24.4	0.57
Polymer	Bangs	1100	1.7	0.47	0.0009	1.10	0.026
microspheres	laboratories						
Solid hydrogen		89	10	−1.3	0.31	−2.4	0.89
Solid deuterium		206	10	1.3	0.31	2.4	0.89
Solid neon		1150	10	17.0	0.31	40.2	0.89
Solid H_2/D_2		140	10	−0.25	0.31	−0.20	0.89

as well as quantised vortex lines in helium II. Table 1 lists the properties of various visualisation particles that have been used for LDV or PIV experiments with helium II (Zhang et al., 2004a).

6. RECENT HELIUM II FLOW VISUALISATION EXPERIMENTS

Here we present a review of the most recent visualisation experiments of turbulent flow in helium II. These experiments mostly involve PIV measurements as that technique has provided the most quantitative results.

6.1 Counterflow Helium II

To date, the majority of helium II flow visualisation experiments have concentrated on turbulent thermal counterflow where the net fluid velocity is zero, thus on the average, $\rho_n \mathbf{v}_n = -\rho_s \mathbf{v}_s$. In addition for practical reasons having to do with heat loading on optical cryostats, these experiments have been performed in the temperature range between 1.6 K and T_λ where the density of both fluid components is significant. In this temperature regime, the particles can interact with either of the two fluid component of helium II. The viscous normal fluid provides the shear forces on the

particles, while the turbulent superfluid component contains a tangled mass of quantised vortex lines that can drag or even trap the particles. Evidence for such complex phenomena are seen in the experimental results discussed below.

6.1.1 Counterflow in Channels

Zhang and Van Sciver (2005a) used the PIV technique to quantify the steady counterflow velocity profile of 1.7 μm polystyrene particles ($\rho_p = 1100 \, \text{kg/m}^3$) suspended in a vertically oriented rectangular helium II channel. Their channel had a 19.5 mm × 38.5 mm flow cross-section with visualisation occurring through a 45 mm × 20 mm quartz window. The particle settling velocity was separately measured and subtracted from the measured counterflow velocities to yield a relation between v_p and the applied heat current q. Data were acquired between 1.62 K and 2.0 K for heat fluxes from 1.1 to 13.7 kW/m^2.

Figure 12 shows a typical steady state velocity field acquired using the PIV technique. These results were obtained by averaging five separate sets of velocity vectors under essentially identical conditions. One can see
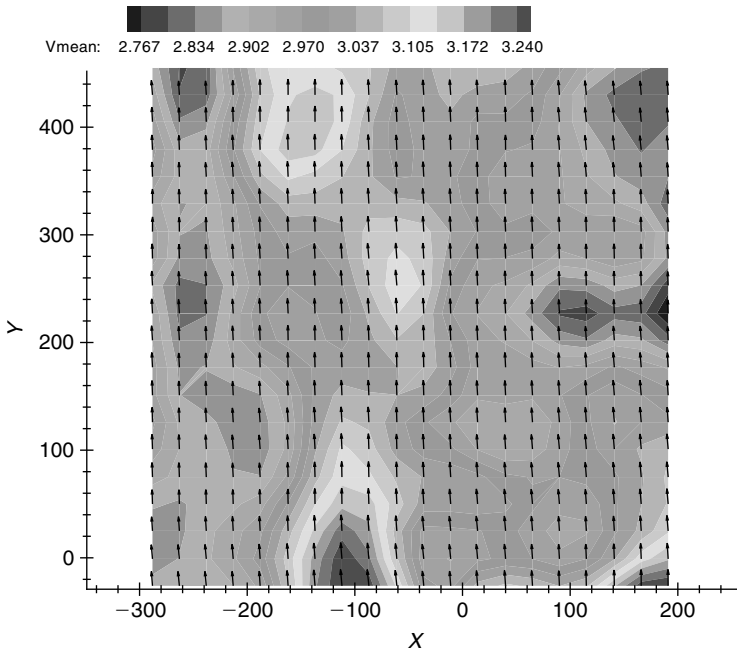
FIGURE 12   Velocity vector field for counterflow helium II at 1.62 K and $q = 7.24 \, \text{kW/m}^2$. Scale at the top is in mm/s. (Zhang and Van Sciver, 2005a).
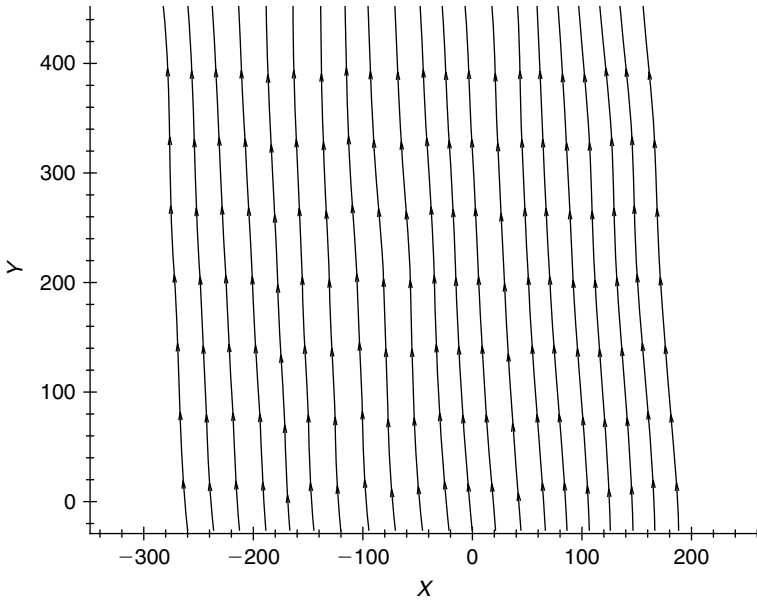
FIGURE 13 Velocity streamline field for counterflow helium II at 1.62 K and $q = 7.24$ kW/m^2 (Zhang and Van Sciver, 2005a).

that the velocity vectors are all parallel to the axis of the channel with approximately constant magnitude, $v_p \sim 40$ mm/s. Also, the computed streamlines in Figure 13 show velocities essentially parallel to the channel walls. There is no evidence of a velocity boundary layer to within the spacial resolution of the measurements ($\sim$1 mm). However, as noted by Zhang, the measured particle velocity is considerably less than the normal fluid velocity, $v_n = q/\rho sT \sim 80$ mm/s, computed for this case.

Figure 14 compares the measured particle velocities versus the applied heat flux at 1.8 K. The channel was configured with v_n both parallel and antiparallel to gravity in order to determine the settling velocity by extrapolation to $q = 0$, which in this case is $\sim$5 mm/s. The significant observation in these data is that the particle velocity is approximately $0.5 v_n$ for all heat currents, a result which appears to be approximately independent of temperature over the range of their investigation. Zhang and Van Sciver (2005a) suggested based on empirical evidence that this reduced particle velocity may be related to a kind of viscous drag force between the particles and the superfluid component. Thus the particle motion should be governed by the combined effect of the normal fluid and superfluid such that $v_p = v_n - v_{add}$, where v_{add} is due to the interaction with the superfluid component. This observation has led to several theoretical studies of particle vortex line interactions, summarised in the next section.
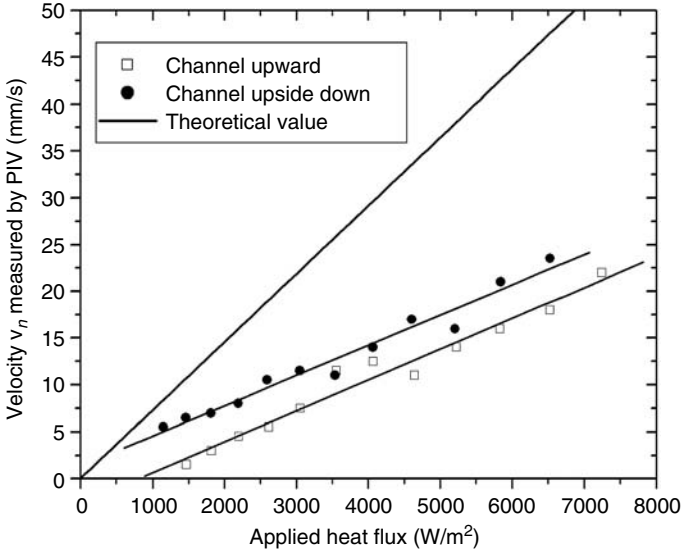
FIGURE 14 Particle velocities versus counterflow heat flux. Open symbol is for the channel facing upward with respect to gravity, solid symbol is for the channel facing downward. The theoretical value is based on the predicted normal fluid velocity (Zhang et al., 2004a).

6.1.2 Modelling Particle-Vortex Interaction

To explain the observation that the adjusted particle velocity is $v_{pa} = v_n - v_{add}$ rather than the expected $v_{pa} = v_n$ resulting from the balance of Stokes drag and gravity, we need to take into account the quantised vortices (Sergeev et al., 2006b,c).

We consider the possibility that, as a particle moves through the counterflow vortex tangle, it traps vortex lines as described in Section 4. We argue that although a vortex line which attaches to the particle may later disconnect from it, on average the particle is likely to have one or more vortex loops attached. It is also reasonable to expect that vortex reconnections with the particle are not very frequent because the radius of the particle is smaller than the typical intervortex spacing δ.

Two forces arise from the presence of a vortex near (or attached to) the particle. The first force (Schwarz, 1974) caused by the nonuniform distribution of pressure around the sphere is

$$\mathbf{F} = \int_S p\hat{\mathbf{n}}dS = \frac{\rho_s}{2}\int_S (\mathbf{v}_\ell + \mathbf{v}_b)^2\hat{\mathbf{n}}dS, \qquad (50)$$

where S is the surface of the particle, $\hat{\mathbf{n}}$ is the radial unit vector point out of S into the fluid, $\mathbf{v}_b$ is a contribution arising from the boundary condition that the normal component of the total superfluid velocity at S vanishes, and $\mathbf{v}_\ell$ is the velocity field around the vortex line. Given an arbitrary vortex configuration, the determination of $\mathbf{v}_b$ requires a numerical calculation; however, if the radius of curvature of the vortex is sufficiently larger than the size of the sphere, then $\mathbf{v}_b$ is negligible because the velocity field $\mathbf{v}_\ell$ at S is approximately tangential to S. By making a simple estimate of the integral, see Sergeev et al. (2006b,c), the first force becomes

$$\mathbf{F} \approx \left(\frac{\rho_s}{2}\right) \int_S (\mathbf{v}_\ell)^2 \hat{\mathbf{n}} \mathrm{d}S \approx \left(\frac{\rho_s}{2}\right) 2\pi \left(\int_{a_0}^{a} \left(\frac{\kappa}{2\pi r}\right)^2 r \mathrm{d}r \right) \hat{\mathbf{n}}_0 \tag{51}$$

$$\approx \frac{\rho_s \kappa^2}{4\pi} \ln\left(a_p/a_0\right) \hat{\mathbf{n}}_0,$$

where we have used a local cartesian approximation to evaluate the surface integral. The quantity $\hat{\mathbf{n}}_0$ is the normal unit vector along one vortex strand pointing out of the plane which represents S. Generalisation to N vortices attached to the sphere, we have

$$\mathbf{F} \approx \frac{\rho_s \kappa^2}{4\pi} \ln\left(a_p/a_0\right) \sum_{i=1}^{N} \hat{\mathbf{n}}_i. \tag{52}$$

Figure 15 illustrates the case of two vortex strands attached to the particle. Clearly, if the configuration of vortices is symmetric, the net force will be zero, as in Figures 16a and 16b. If one or more vortex loops are asymmetrically attached to the sphere, as in Figures 16c and 16d, the contributions from individual vortices will not cancel out, and the pressure distribution cause a net body force which attracts the sphere to the vortices, thus opposing the motion of the sphere.

It is likely that the particle, as it moves through the tangle, carries along one or more vortex lines or even separate loops as the result of previous close encounters with vortices. The simplest scenario is that the particle, after connecting to a vortex line, keeps moving, dragging a vortex loop (two attachments) along for a fraction of the relative distance to the next vortex line of the network with respect to its own size. We thus expect that the force in the direction opposite to the motion of the particle is a body force which has magnitude

$$F \approx \frac{\rho_s \kappa^2}{4\pi} \ln\left(a_p/a_0\right) \left(\frac{2\beta a}{\delta}\right), \tag{53}$$
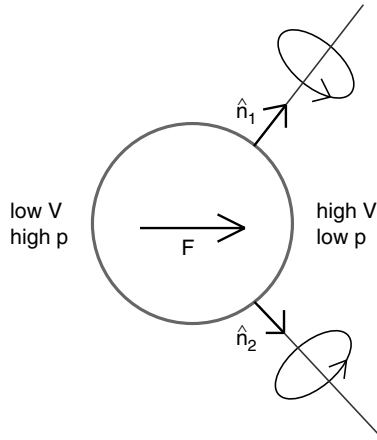
FIGURE 15   Vortex strands attached to particle and the resulting force. Note that both strands have the same circulation as they arise from a vortex which has reconnected to the sphere.
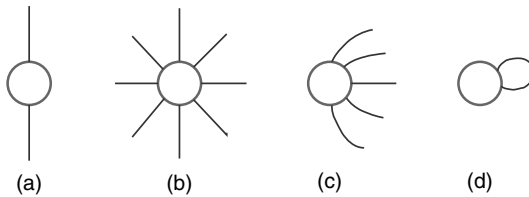
FIGURE 16   Some possible sphere-vortex configurations.

where β is a geometrical factor of the order unity, which depends on the number of pair of vortices attached to the sphere and the relative distance of travel where they remain attached. In the case of a single vortex, we can interpret $2\beta a_p$ as the length of this vortex.

The second force on the sphere arises from the drag of the attached vortex loop with the normal fluid. It is possible that, under the action of this force, the vortex loop slides around the sphere or changes its size, but it is reasonable to expect that, on the average, some vortex length will always be attached to the sphere. The friction force has magnitude approximately equal to $\gamma_0 \ell (v_n - v_\ell)$, where γ_0 is a known temperature-dependence friction coefficient (Barenghi et al., 1982); setting $v_\ell = v_p$ (as vortex and particle move together) and interpreting $\ell = 2\beta a_p$, the friction is thus $2\beta a_p \gamma_0 (v_n - v_p)$.

Taking into account the two forces, the equation of motion of the particle is modified, and we have

$$v_n - v_p = v'_{slip} + v_{add},\tag{54}$$

where $v'_{slip} = v_{slip}/f, f = 1 + \beta\gamma_0/(3\pi\mu)$ and

$$v_{add} = \frac{\beta\kappa^2\gamma\rho}{12\pi^2 f\mu}\ln(a_p/a_0)v_n\tag{55}$$

because $1/\delta \approx L^{1/2} = \gamma v_{ns} = \gamma\rho v_n/\rho_s$. We obtain

$$v_{pa} = \left(\frac{f-1}{f}\right)v_{slip} + \left(1 - \frac{\beta\kappa^2\gamma\rho\ln(a_p/a_0)}{12\pi^2\mu f}\right)v_n.\tag{56}$$

The first term at the right-hand side, $v_{slip}(f-1)/f$, is negligible because in the (q, T) range of interest $0.3 < (f-1)/f < 0.4$ and v_{slip} (of the order of few mm/s) is much smaller than v_n. We conclude that v_{pa} is essentially proportional to v_n. Values of v_{pa} versus v_n for $\beta = 3$ over the independent ranges of T and q used by Zhang and Van Sciver (2005a) are shown in Figure 17. The agreement with the experiment is good. Even without adjusting the value of the undetermined geometrical parameter β, we would have
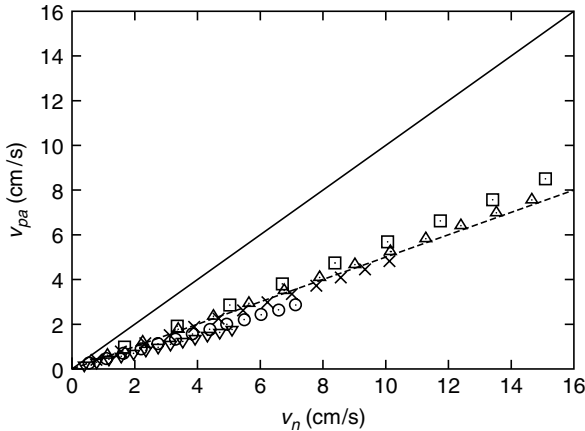
FIGURE 17   Calculated v_{pa} versus v_n with $\beta = 3$. The solid line is $v_{pa} = v_n$ and the dashed line is $v_{pa} = 0.5v_n$. The symbols are Equation (56) for $T = 1.6\,\text{K}$ (squares), $T = 1.7\,\text{K}$ (triangles pointing up), $T = 1.8\,\text{K}$ (crosses), $T = 1.9\,\text{K}$ (circles) and $T = 2.0\,\text{K}$ (triangles pointing down) for heat fluxes in the range from 1100 to 13700 W/m². The results compare well with the experimental data.

order-of-magnitude agreement with the observed result. More importantly, our result has the same linear dependence of v_{pa} on v_n and, in the first approximation, the same temperature independence of the slope v_{pa}/v_n which was observed in the experiment; although some of the terms which appear in Equation (56) depend on temperature, their combination does not. The value of β which best fit the observed slope ($\beta = 3$) suggests that the loops which remain attached to the particles are not big.

6.1.3 Second Sound Shock

Zhang and Van Sciver (2004b) also used the PIV technique to visualise the propagation of a second sound shock front in helium II. Again, 1.7 μm polystyrene particles were injected into the same rectangular counterflow channel equipped with a 45 mm × 20 mm quartz window. In this case, it was particularly important to use small particles in order to have sufficient fidelity to detect the second sound front. Also, a high speed (1 kHz) CCD camera permitted observation of the entire transient velocity profile including the arrival of the second sound shock front followed by the time-dependent development of the mutual friction induced diffusive temperature profile. One clear limitation with these measurements occurs from the fact that a PIV analysis occurs over a time interval (in this case 1 ms). Quantitative results represent averages over this interval that may mask some high-frequency phenomena.

Figure 18 shows the measured particle velocity fields at four different times following a 1 ms rectangular heat pulse of 44.8 kW/m^2 at 1.62 K. In Figure 18b, one can clearly see the arrival of the second sound shock front at a time corresponding to the transit time between the heater and the viewfield, $\delta t = L/c_2 \sim 7.3$ ms, where c_2 is the second sound velocity (~ 20 m/s) and L is the distance from the heater to the measurement location. The second sound front is in the middle of the frame where the particles can be seen to accelerate due to the shock front. For longer times, Figure 18c at 9.1 ms, the particle velocity becomes steady at $v_p \sim 70$ mm/s, which is considerably less than the computed value of v_n for the given heat flux.

It is possible that this larger discrepancy between particle velocity and computed normal fluid velocity comes about as a result of a more intense vortex line density in second sound shock than occurs in steady state thermal counterflow, but further measurements of this kind are needed to verify this hypothesis.

Following the limited duration second sound shock pulse, homogeneous turbulence develops that strongly attenuates the second sound and produces mutual friction between the two fluid components (Shimazaki and Murakami, 1995), (Hilton and Van Sciver, 2005). Figure 18d shows that the particle motion becomes somewhat random following the passage of the front, and that this motion may be able to quantify the level of residual
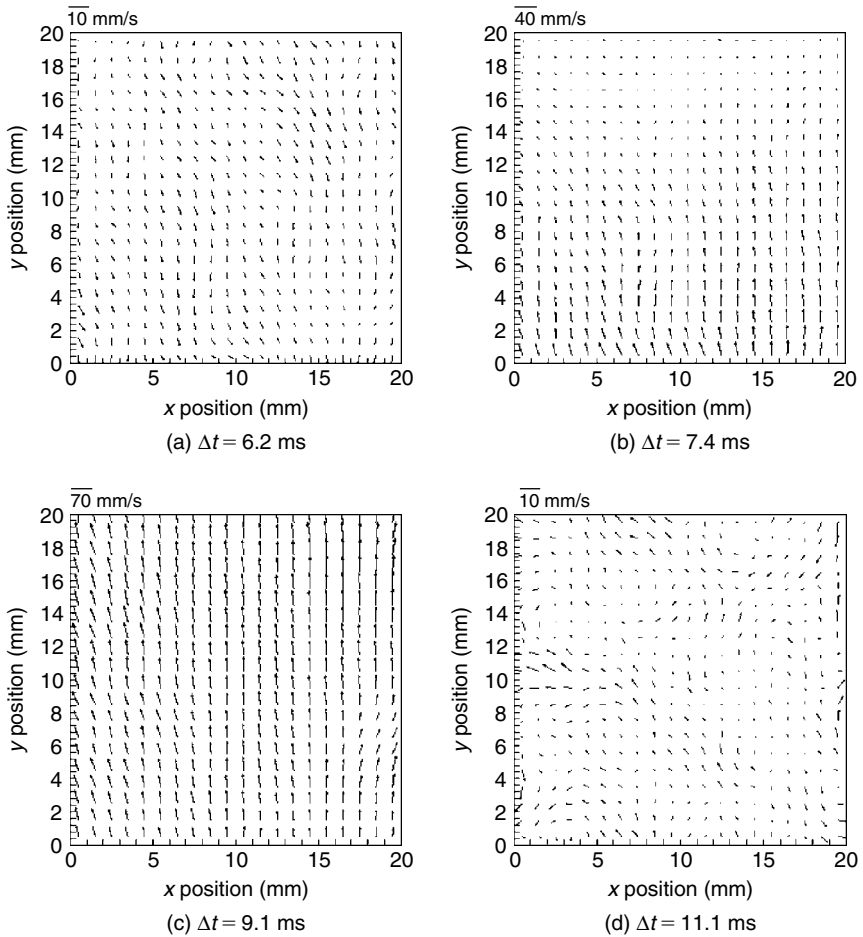
FIGURE 18 Velocity vectors for second sound shock in helium II at 1.61 K. At $t = 0$, a 44.8 kW/m^2 heat pulse of 1 ms duration is initiated along the counterflow channel. Based on the second sound velocity, the pulse should arrive at 7.3 ms as can be seen in image b. (Zhang and Van Sciver, 2004b)

turbulence. However, further work is required to support this assertion (Zhang and Van Sciver, 2004b).

6.1.4 Counterflow Around Cylinders

The PIV technique with polystyrene microspheres seeding has also been used to visualise thermal counterflow around cylinders oriented perpendicularly to the flow field (Fuzier et al., 2006; Zhang and Van Sciver, 2005b). In this case, transparent cylinders of different diameters are placed within

the counterflow channel behind the optical window so that the particle motion in their vicinity can be measured. Using the PIV technique, the particle motion is then converted to velocity vectors or stream lines as discussed above. A typical velocity field near a 6.35 mm cylinder is shown in Figure 19a for 1.6 K and Figure 19b for 2.03 K (Zhang and Van Sciver, 2005a).

Figure 20 is a streamline plot for the same set of conditions. Of particular note is the existence of large-scale turbulent structures both in front of and behind the cylinder relative to the direction of the normal fluid component. In classical fluids, such large-scale turbulent structures are seen downstream of bluff objects such as cylinders, with the structures periodically detaching to form a vortex street (Schlichting, 1979). In the present case of helium II counterflow around the cylinder, the location of the large-scale turbulent structures is relatively stable and they do not detach and move downstream although local fluctuations in the turbulence are evident in time sequence observations. Also, potentially significant is the observation that the turbulent structures in front of the cylinder appear to reside closer to the channel walls than those downstream.

For classical flows, the level of turbulence is usually scaled by the Reynolds number. In the case of thermal counterflow in helium II, the Reynolds number is normally defined as

$$Re_D = \frac{\rho v_n D}{\mu},\tag{57}$$

where D is the cylinder diameter. For the experiments involving flow around a cylinder, the apparent level of turbulence is greater at higher temperatures. Comparing the results in Figure 20a to those in Figure 20b, one can see larger turbulent structures at 2.03 K even though the corresponding Reynolds number (and vortex line density) is lower for that case. At present, there is no precise physical explanation for such a result.

6.1.5 Counterflow Over Back Facing Step

Another geometry of interest to classical fluid dynamics investigations, that has recently been investigated using PIV in counterflow helium II, is flow over a backwards facing step or discontinuous expansion. In classical flows, such a geometry generates turbulent eddies below the step which can detach and be carried downstream by the fluid momentum (Armaly et al., 1983).

To study this geometry in counterflow helium II, Van Sciver et al. (2007) constructed a vertically oriented channel with a discontinuous expansion. The narrow part of the channel was $15 \times 30 \, mm^2$ in cross-section
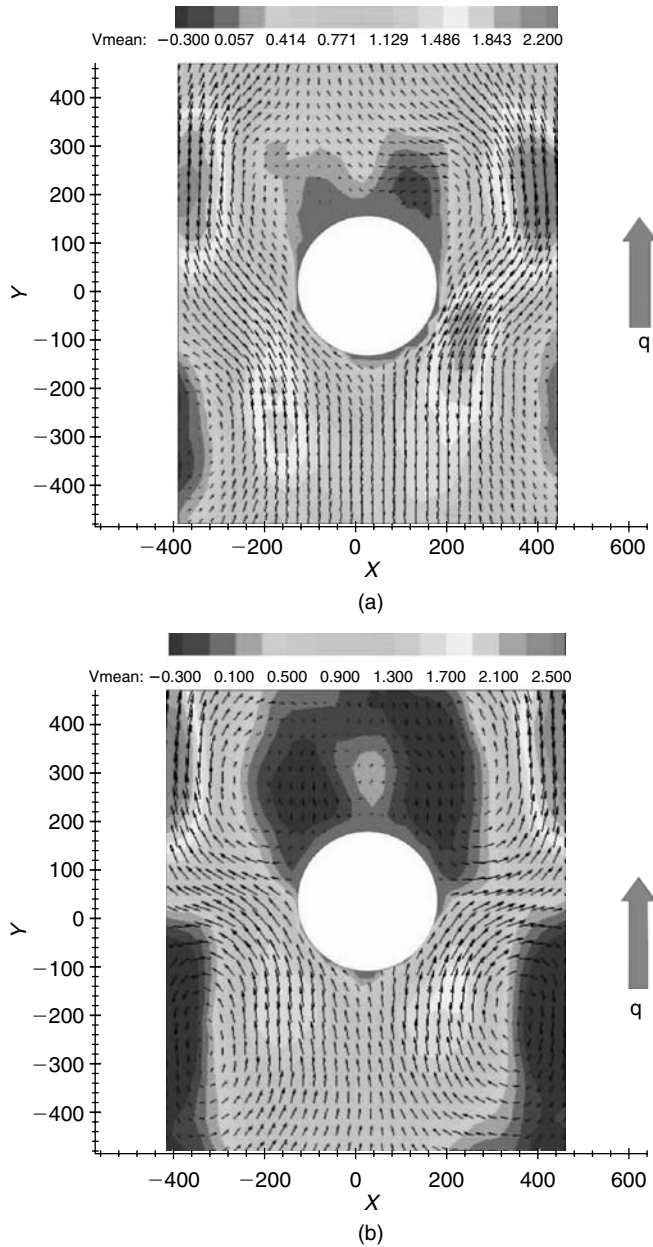
FIGURE 19 Measured particle velocity field around a 6.35 mm cylinder in counterflow helium II. (a) $q = 4 \, \text{kW/m}^2$ at 1.6 K corresponding to $Re_D = 41000$ and (b) $q = 11.2 \, \text{kW/m}^2$ at 2.03 K corresponding to $Re_D = 21000$. The velocity scale at the top is in pixels/ms (1 pixel/ms = 22 mm/s) (Zhang and Van Sciver, 2005b).
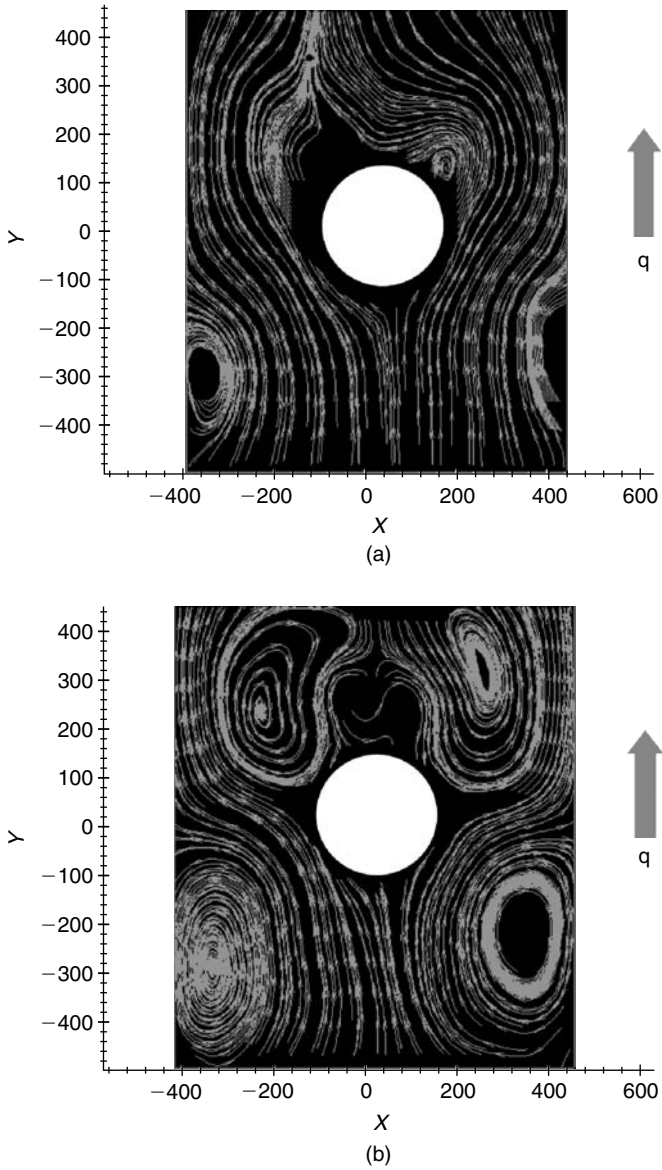
FIGURE 20   Computed streamlines of particle motion for the same conditions as in Figure 19 (Zhang and Van Sciver, 2005b).

expanding to $40 \times 30\,\mathrm{mm}^2$ to form a step. Visualisation occurred through $30 \times 30\,\mathrm{mm}^2$ window in the vicinity of the step. An example of PIV data obtained from these experiments is shown in Figure 21.

As can be seen in the figure, counterflow helium II over a discontinuous expansion produces large-scale turbulent eddies near the channel expansion. However, in a similar fashion to the flow around cylinders, these eddies do not appear to detach and move downstream with the normal fluid rather residing in the vicinity of the step. Also, as with the flow around a cylinder, the observed level of large-scale turbulence is seen to increase with temperature more so than with Reynolds number.

6.1.6 Counterflow Jet

Another geometry of interest to fluid dynamicists is jet or nozzle flow. Dimotakis and Broadwell (1973) were the first to study this configuration for thermal counterflow in helium II by probing the local temperatures in the region of the jet. Subsequently, Murakami and collaborators extensively used the counterflow jet as a platform for flow visualisation studies. Their early work involved making qualitative studies of flow structures by seeding the flow field with hollow glass spheres of order $50\,\mu\mathrm{m}$ diameter and photographing the dynamic phenomena. They also made quantitative velocity field measurements using LDV (Murakami et al., 1986; Murakami and Ichikawa, 1989b). In the latter case, solid H_2–D_2 particles were used as tracers. This work showed that the particles mostly follow the normal fluid component velocity, although the magnitude of the velocity was less than predicted based on the two-fluid model.

More recently, the same group has used to PIV technique and solid H_2–D_2 particles to again study the flow field in at the exit of a counterflow jet (Murakami et al., 2008). In this work, the velocity profile at the exit of the counterflow jet was visualised and quantitatively compared to correlations for classical fluids. Figure 22 shows a typical velocity contour plot in the region of the counterflow jet exit for $v_n = 25.6\,\mathrm{mm/s}$ at $T = 2.00\,\mathrm{K}$. These data represent ensemble averages of 799 measurements and thus mask some of the turbulent structure. The measured particle velocity profile was then compared to predictions based on the two-fluid model and classical flow through a jet as seen in Figure 23. Generally, the shape of the profile is in good agreement with expectations. However, the magnitude of the velocity is seen to be somewhat less than the predicted normal fluid velocity, $v_n = q/\rho sT$. The authors also suggest that the measured centreline velocity may be temperature dependent, a result in contradiction to Zhang's (Zhang and Van Sciver, 2005a) findings for a one-dimensional counterflow channel.
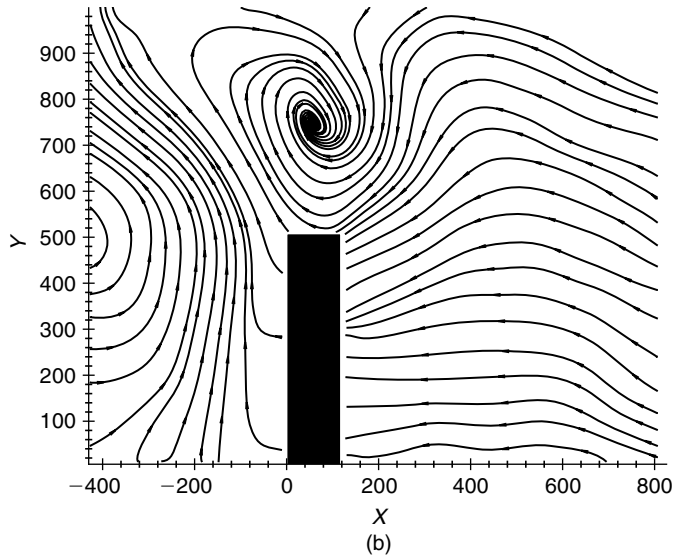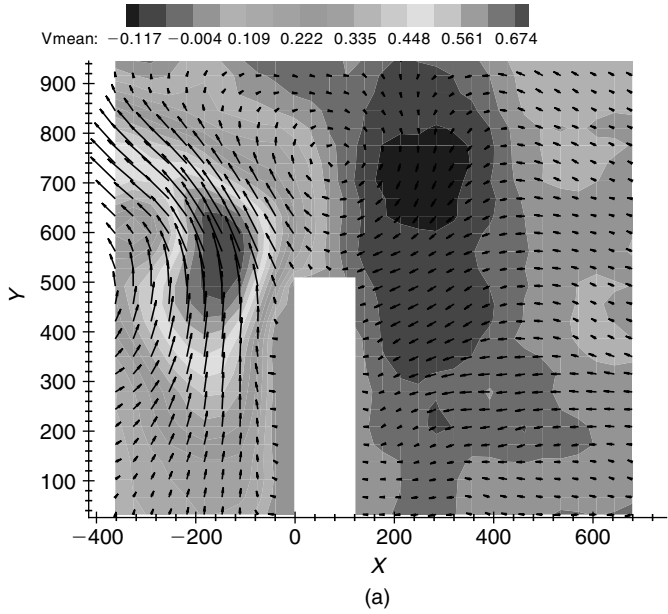
FIGURE 21 Particle motion at the location of a channel expansion at 1.85 K and a heat flux of 6.9 kW/m^2: (a) vectors, (b) streamlines (Van Sciver et al., 2007).
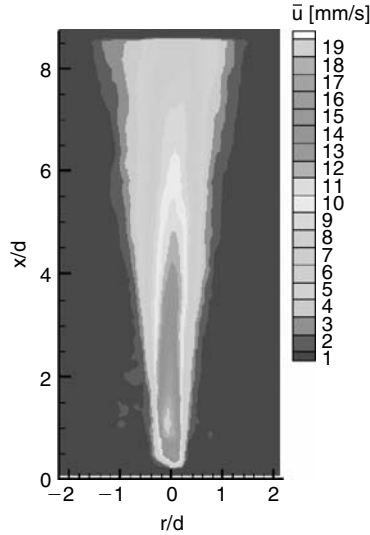
FIGURE 22 Velocity contour plot consisting of an ensemble average of 799 snapshots at $T = 2.00\,\text{K}$ corresponding to $v_n = 25.6\,\text{mm/s}$ (Murakami et al., 2008).
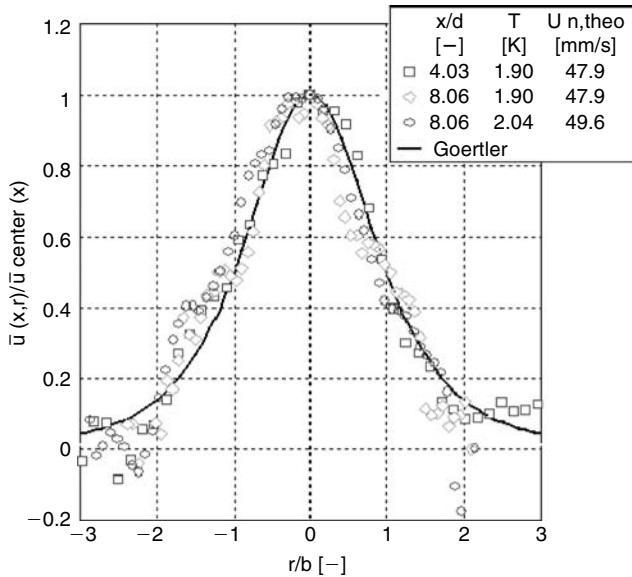
FIGURE 23 Comparison of the velocity profiles of the average axial velocity component at two locations above the exit of the counterflow jet, $x/d = 4.03$ and $x/d = 8.06$ at $T = 1.9\,\text{K}$ and $2.04\,\text{K}$. The smooth curve is a Goertler type profile for fully-developed turbulent jets of viscous fluids (Murakami et al., 2008).

6.2 Visualisation of Vortex Lines

6.2.1 Particle Trapping on Vortex Lines

Bewley et al. (2006a) have used visualisation techniques to observe particle dynamics in helium II near T_λ. In these experiments, the liquid helium was seeded with solid hydrogen particles at a temperature slightly above T_λ after which the fluid was cooled to the helium II regime. In helium I, the particles were seen to form a homogeneous cloud that disperses throughout the fluid. However, on passing through T_λ, the particles collected into a web-like structures as shown in Figure 24. Bewley et al. (2006a) suggest that these structures represent decorated quantised vortex lines in the superfluid component. The exceptional observation in this work is that the vortex lines appear to form connections rather than remaining separated and homogeneously distributed throughout the fluid. The fork like structures may indicate that many vortices are attached to the same particle as expected from computer simulations of vortex pinning (Tsubota, 1994).

Using the same apparatus, Bewley et al., 2006a were able to mark the vortex cores and study their dynamics. In particular, they observed decay
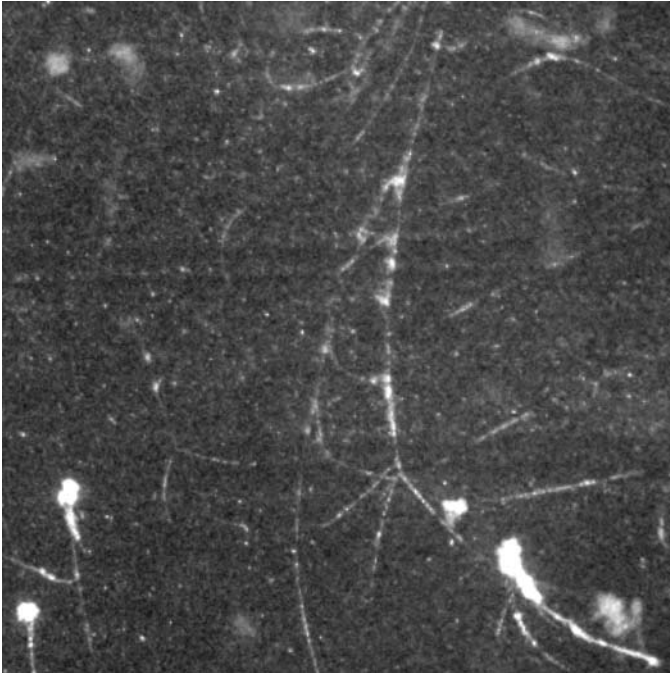
FIGURE 24   Vortex lines helium II decorated with solid hydrogen particles (Bewley et al., 2006a).

of vortex rings and filaments as seen in the sequences in Figure 25a. There was some indication that the trapped particles affect the dynamics as suggested by the slower than expected decay of the vortex rings. Also, the vortex line reconnection as shown in Figure 25b.

6.2.2 Vortex Line Density in Rotating He II

Although counterflow turbulence is the most common form in helium II, other methods exist for generating and studying quantised vortex lines. One such method is to place the helium II in a rotating bucket (Donnelly, 1991). To meet the irrotational requirement of the superfluid component, the rotating fluid generates a uniform triangular array of vortex lines oriented along the axis of rotation. The density of the vortex lines is given by Feynman's formula in Equation (3).

$$n = \frac{2\Omega}{\kappa}. \tag{58}$$

Packard and collaborators (Yarmchuk et al., 1979) were the first to observe the vortex array in rotating helium II by charging the vortex lines with negative ions that were collected as a 2D image onto a photographic plate. In

(a)

1 mm

(b)
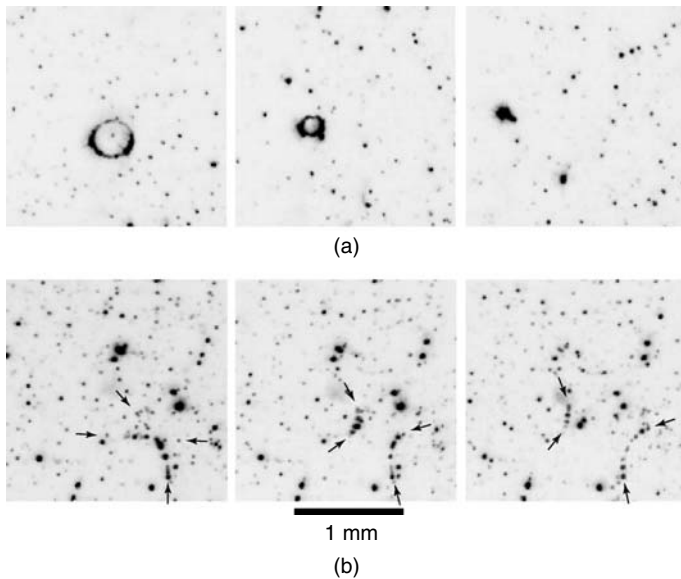
FIGURE 25 Row 'a' is images taken 1.5 s apart of a decaying ring. Row 'b' shows what the authors believe is a reconnection of two vortex lines that have crossed. Frames are taken 0.25 s apart (Bewley et al., 2007).
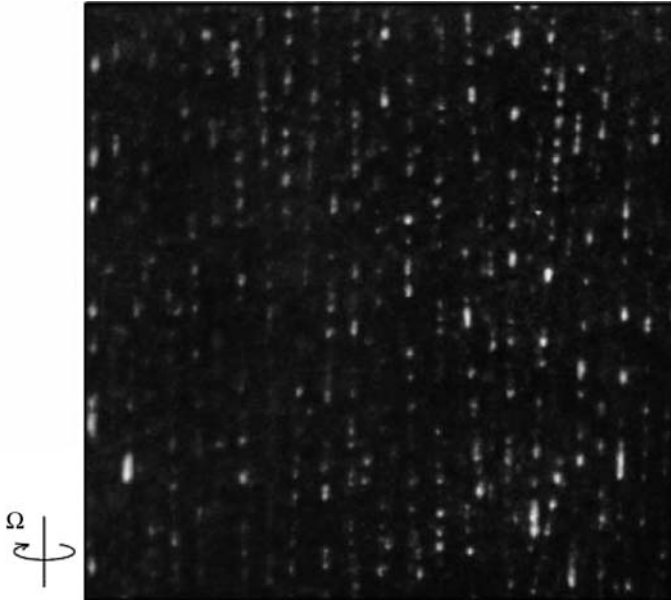
FIGURE 26   Vortex lines in rotating helium II with solid hydrogen particles attached (Bewley et al., 2006a).

this case, the predicted triangular array of the lines was confirmed following Feynman's formula. Very recently, Bewley et al. (2006a) used particle visualisation techniques to observe the vortex line array in rotating helium II in this case by viewing perpendicular to the axis of rotation. An image of solid hydrogen particles in rotating helium II is shown in Figure 26. Overall, the lines are essentially straight, co-axial with the rotation and approximately equally spaced.

By assuming a triangular array, Bewley (2006b) was able to show that the vortex line spacing was consistant with Feynman's formula. A further notable observation is the approximately equal spacing between the solid hydrogen particles that decorate the vortex lines. Since particle agglomeration due to van der Waal's forces is expected in the bulk fluid, it is surprising that the particles remain separated along the vortex lines. Clearly, some additional force must be affecting the trapped solid hydrogen particles on the vortex lines although no mechanism for this force has been suggested to date.

6.3 Forced Flow Helium II

Thus far in the present chapter, we have focused our discussion on visualisation of turbulence in static or rotating helium II. However, there is

a considerable interest in turbulence generated by net fluid motion, and thus, recent experiments have begun to explore the visualisation of helium II forced flow, where $v > 0$.

The simplest case to consider is that of adiabatic flow at high Reynolds number (Re > 1200) such that the fluid is fully turbulent. Helium II forced flow experiments involving pressure drop measurements have shown that helium II follows classical correlations for the friction factor in terms of Reynolds number, defined as $Re_D = \rho v_n D / \mu$ (Fuzier et al., 2002). Xu and Van Sciver (2007) have recently used the PIV technique with solid deuterium particles to study the velocity profile in forced flow helium II in a 20 mm by 20 mm square cross-section channel. These experiments were performed over a range of velocities from 34.5 mm/s to 288 mm/s (corresponding to $5.4 \times 10^4 < Re_D < 6.6 \times 10^5$). Figure 27 shows a contour
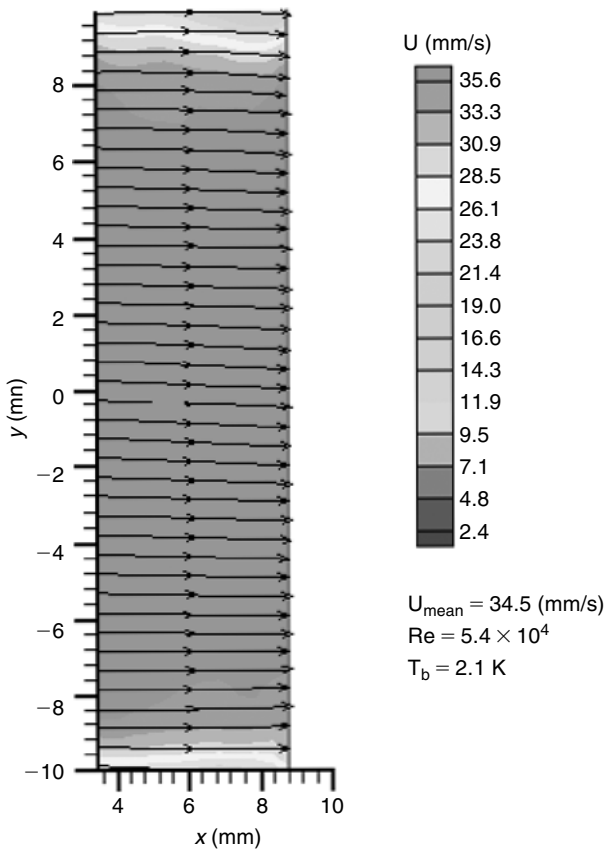
FIGURE 27 Velocity field for solid deuterium particles in forced flow helium II at 2.1 K. The fluid velocity is 35.5 mm/s corresponding to a $Re_D = 5.4 \times 10^4$ (Xu and Van Sciver, 2007).
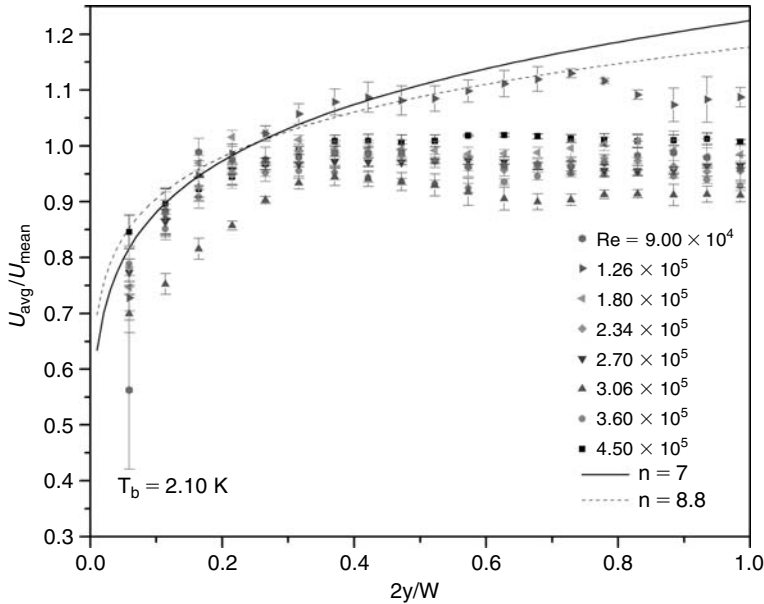
FIGURE 28 Normalised velocity profile at 2.1 K for different Reynolds number. u_{mean} is the average velocity based on the volumetric displacement of the helium II (Xu and Van Sciver, 2007).

plot of the velocity with superimposed computed streamlines for the case where $u_{mean} = 34.5$ mm/s at 2.1 K. The velocity boundary layer is evident at the top and bottom of the viewfield.

From these data, Xu and Van Sciver (2007) were able to compute the local particle velocity as a function of position perpendicular to the flow direction and compare that velocity to u_{mean} based on the total flow rate through the channel. Plotted in Figure 28 is the ratio of the local velocity to the mean velocity for different flow rates (Reynolds numbers) at 2.1 K. These results are plotted versus the nth power velocity distribution function showing reasonable agreement near the wall (Nikuradse, 1932). However, the velocity field in the centre of the channel is flatter than the Nikuradse power law, a result that has yet to be fully understood.

Xu and Van Sciver (2008) also recently reported particle velocity measurements in helium II under conditions of combined forced flow and counterflow. Of interest is to observe the transition from pure counterflow, where other experiments (Zhang et al., 2004a) have shown that the particles track at less than v_n to the adiabatic forced flow case with $v_p \sim v$. Of interest is to determine whether the particles track the sum of the normal fluid velocity and bulk fluid velocity. Plotted in Figure 29 is the measured particle velocity versus normal fluid velocity determined by the
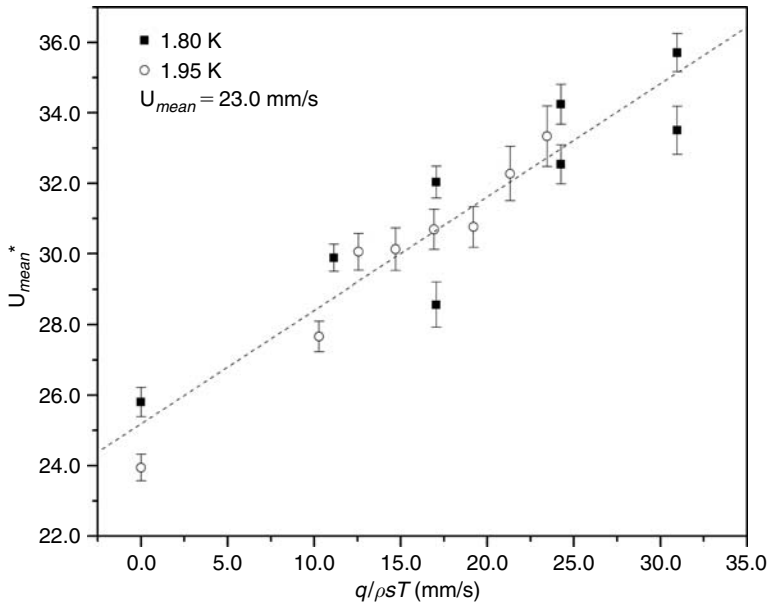
FIGURE 29   Mean particle velocity profile at two temperatures versus v_n, normal fluid velocity based on counterflow heat flux. $u_{mean} = 23$ mm/s is the average velocity based on the volumetric displacement of the helium II (Xu and Van Sciver, 2008).

counterflow heat flux. The line in the figure is a linear fit to the data. Note that although the particles move at a velocity that is greater than v, they are still moving more slowly than predicted based on the two-fluid model. In the present case, the increase in velocity going as 0.38 v_n is somewhat less than observed by Zhang et al. (2005a) for pure counterflow.

7. SUMMARY AND OUTLOOK

From the experimental point of view, the recent use of the PIV technique has shown that it is possible to visualise remnant vortex lines in stationary helium II and vortex arrays in solid body rotating helium (Bewley et al., 2006a). The natural development would be to use the PIV technique to study the destabilisation of vortex arrays by a heat flux which is imposed in the direction parallel to the rotation. Numerical simulations (Tsubota et al., 2003) indicate that the axial flow triggers the growth of Kelvin-waves; when the amplitude of these waves becomes of the order of the intervortex separation, vortex reconnections take place and an anisotropic vortex

tangle is created. This would allow a controlled study of Kelvin-waves and the transition to turbulence. Use of the PIV technique to study second sound has suggested intriguing effects that demand further investigation (Zhang and Van Sciver, 2005a). For example, one could use PIV to study nonlinear second sound (since at low amplitude the particles do not respond to it, as we have shown). However, this has yet to be confirmed by experiment.

Experiments should also explore the transition from pure one-dimensional counterflow behaviour lacking evidence for a normal fluid velocity boundary layer to adiabatic forced flow where the velocity boundary layer is clearly seen (Xu and Van Sciver, 2008). Further experiments that combine counterflow and forced convection should be able to study a range of velocities between these two extremes. Such work can be extended to flow over bluff bodies and through expansions to further compare with classical fluid dynamic behaviour, work which should provide considerable insight into the similarity between classical and quantum fluid dynamics.

From the experimental technique viewpoint, it would be highly desirable to develop methods to seed submicron size particles in helium II and use them for micro-PIV measurements. Such an approach has been successfully applied for experiments near room temperature (Santiago et al., 1998), but has yet to be attempted in liquid helium. To avoid optical limitations, one could use fluorescent particles that are not restricted by the Mie light scattering limit. Seeding techniques that prevent particle agglomeration must also be developed. If successful, micro-PIV measurements could significantly enhance our ability to probe small-scale phenomena in helium II dynamics.

Also of interest would be expand high-speed PIV measurements to explore the time-dependent phenomena in helium II such as vortex motion and second sound. Turbulence decay could also be studied with experiments on towed grids and flow around bluff bodies.

On the theoretical side, the bad news is that particles cannot trace a pure superflow (helium II below 1 K) due to instabilities. The good news is that the detailed mechanism of trapping of a particle onto a vortex line is now better understood (Kivotides et al., 2007b). It has also been possible (Sergeev et al., 2006b) to model the interaction of particles moving through a tangle of vortices. Similar models should allow in the future to interpret other experiments such as counterflow past bluff bodies and steps to determine the superfluid vorticity distributions and the normal fluid profiles.

Although only just getting underway, work on visualising flow in helium II has real potential to provide fundamental understanding of the turbulent states that will in turn feed into a better understanding of this unique fluid system.

ACKNOWLEDGEMENTS

REFERENCES

Adrian, R. J. (1991). *Annual Review of Fluid Mechanics*, 23, 261.

Allum, D. R., McClintock, P. V. E., Phillips, A. and Bowley, R. M. (1977). *Philosophical Transactions of the Royal Society of London A*, 284, 23.

Armaly, B., Durst, F., Pereira, J. and Schoenung, B. (1983). *Journal of Fluid Mechanics*, 127, 473.

Awschalom, D. D., Milliken, F. P. and Schwarz, K. W. (1984). *Physical Review Letters*, 53, 1372.

Awschalom, D. D. and Schwarz, K. W. (1984). *Physical Review Letters*, 52, 49.

Auton, R., Hunt, J. C. R. and Prud'homme, M. *Journal of Fluid Mechanics*, 197, 241.

Babiano, A., Cartwright, J. H. E., Piro, O. and Provenzale, A. (2000). *Physical Review Letters*, 84, 5764.

Barenghi, C. F., Donnelly, R. J. and Vinen, W. F. (1982). *Journal of Low Temperature Physics*, 52, 189.

Barenghi, C. F., Hulton, S. and Samuels, D. C. (2002). *Physical Review Letters*, 89, 275301.

Barenghi, C. F. (2007). Private Communication.

Barenghi, C. F. (2008). *Physica D*, 237, 2195.

Bewley, G. P., Lathrop, D. P. and Sreenivasan, K. R. (2006a). *Nature*, 441, 588.

Bewley, G. P. (2006b). *Using Frozen Hydrogen Particles to Observe Rotating and Quantized Flows in Liquid Helium*. PhD dissertation, Yale University.

Bewley, G. P., Paoletti, M. S., Lathrop, D. P. and Sreenivasan, K. R. (2007). in edited by Kaneda, Y. (ed.), *Proceedings of IUTAM Symposium 2006*, Nagoya, Japan.

Bielert, F. and Stamm, G. (1993). *Cryogenics*, 33, 938.

Blazkova, M., Schmoranzer, D. and Skrbek, L. (2007). *Physical Review E*, 75, 025302.

Bolnev, R. E., Frossati, G., Gordon, E. B., Kkrushinskaya, I. N., Popov, E. A. and Usenko, A. (2002). *Journal of Low Temperature Physics*, 127, 245.

Careri, G. (1961). in edited by Gorter, C. J. (ed.), *Progress in Low Temperature Physics*, vol. III, p. 58, North-Holland Publications, Amsterdam.

Celik, D. and Van Sciver, S. W. (2002). *Experimental Thermal and Fluid Science*, 26, 971.

Charalambous, D., Skrbek, L., Hendry, P. C., McClintock, P. V. E. and Vinen, W. F. (2006). *Physical Review E*, 74, 036307.

Chopera, K. L. and Brown, J. B. (1957). *Physical Review* 108, 157.

Chung, D. Y. and Critchlow, P. R. (1965). *Physical Review Letters*, 14, 892.

Cummins, H. Z. (1967). in edited by Glauber, R. (ed.), *Proceedings of the International School of Physics "Enrico Fermi,"* p. 247, Academic Press, New York.

Dimotakis, P. E. and Broadwell, J. E. (1973). *The Physics of Fluids*, 16, 1787.

Donnelly, R. J. and Barenghi, C. F. (1998). *Journal of Physical and Chemical Reference Data*, 27, 1217.

Donnelly, R. J. (1991). *Quantized Vortices in Helium II*. Cambridge University Press, Cambridge.

Donnelly, R. J., Karpetis, A. N., Niemela, J. J., Sreenivasan, K. R., Vinen, W. F. and White, C. M. (2002). *Journal of Low Temperature Physics*, 126, 327.

Drew, A. D. and Passman, S. L. (2004). *Theory of Multicomponent Fluids*. Springer, Berlin.

Falkovich, G., Fouxon, A. and Stepanov, M. (2002). *Nature (London)*, 419, 151.

Feynman, R. P. in edited by Gorter, C. J. (ed.), *Progress in Low Temperature Physics*, vol. 1, ch. 11, North-Holland Publications, Amsterdam.

Frisch, U. (1995). *Turbulence*. Cambridge University Press, Cambridge.

Fuzier, S., Van Sciver, S. W. and Zhang, T. (2006). *Proceedings LT*, 24.

Fuzier, S., Maier, S. and Van Sciver, S. W. (2002). *Proceedings ICEC 19*, Grenoble, France, 755–758.

Grant, I. (1997). Particle Image Velocimetry: A Review. *Proceedings of the Institution of Mechanical Engineers*, C211, 55.

Guo, W. and Humphrey, H. J. (2007). *Journal of Low Temperature Physics*, 148, 199.

Hilton, D. K. and Van Sciver, S. W. (2005). *Journal of Low Temperature Physics*, 141, 501.

Holmes, D. S. and Van Sciver, S. W. (1992). *Journal of Low Temperature Physics*, 87, 73.

Kim, I., Elghobashi, S. and Sirignano, W. A. (1998). *Journal of Fluid Mechanics*, 367, 221.

Kitchens, T. A., Steyert, W. A., Taylor, R. D. and Craig, P. P. (1965). *Physical Review Letters*, 14, 942.

Kivotides, D., Barenghi, C. F. and Samuels, D. C. (2000). *Science*, 290, 777.

Kivotides, D., Barenghi, C. F. and Sergeev, Y. A. (2006a). *Europhysics Letters*, 73, 733.

Kivotides, D., Barenghi, C. F. and Sergeev, Y. A. (2006b). *Journal of Low Temperature Physics*, 144, 121.

Kivotides, D., Barenghi, C. F. and Sergeev, Y. A. (2007a). *Journal of Low Temperature Physics*, 148, 293.

Kivotides, D., Barenghi, C. F. and Sergeev, Y. A. (2007b). *Physical Review B*, 75, 212502.

Kivotides, D., Barenghi, C. F. and Sergeev, Y. A. (2007c). (Submitted).

Kolmogorov, A. N. (1941a). Dokl. Akad. Nauk SSSR 30, 301 (Reprinted in 1991, *Proceedings of the Royal Society A*, 434, 9).

Landau, L. D. and Lifschitz, E. M. (1987). *Fluid Mechanics*. Pergamon Press.

Liepmann, H. W. and Laguna, G. A. (1984). *Annual Review of Fluid Mechanics*, 16, 139.

Maurer, J. and Tabeling, P. (1998). *Europhysics Letters*, 43, 29.

Maxey, R. R. and Riley, J. J. (1983). *The Physics of Fluids*, 26, 883.

McKinsey, D. N., Lippincott, W. H., Nukkel, J. A. and Rellegert, W. G. (2005). *Physical Review Letters*, 95, 1111.

Mei, R. (1994). *Journal of Fluid Mechanics*, 270, 133.

Melotte, D. J. and Barenghi, C. F. (1998). *Physical Review Letters*, 80, 4181.

Melling, A. (1997). *Measurement Science and Technology*, 8, 1406.

Murakami, M., Nakai, H., Ichikawa, N., Hanada, M. and Yamazaki, T. (1986). *Proceedings of 11th International Cryogenic Engineering Conference (Berlin)*, Butterworth, United Kingdom, 582.

Murakami, M., Yamazaki, T. and Nakai, H. (1989). *Cryogenics*, 29, 1143.

Murakami, M. and Ichikawa, N. (1989). *Cryogenics*, 29, 438.

Murakami, M., Takakoshi, T., Maeda, M. and Nakano, A. (2008). in edited by Weisend II, J. G. (ed.), *Advances in Cryogenic Engineering*, vol. 53, American Institute of Physics.

Nikuradse, J. (1932). *Forschg. Arb. Ing. Wes.*, 356.

Pethick, C. J. and Smith, H. (2001). Bose–Einstein Condensation in Dilute Gases. Cambridge University Press, Cambridge.

Parks, P. E. and Donnelly, R. J. (1966). *Physical Review Letters*, 16, 45.

Poole, D. R., Barenghi, C. F., Sergeev, Y. A. and Vinen, W. F. (2005). *Physical Review B*, 71, 064514.

Putterman, S. J. (1974). Superfluid Hydrodynamics. North-Holland Publications, Amsterdam.

Roche, P. E., Diribarne, P., Didelot, T., Francais, O., Rousseau, L. and Willaime, H. (2007). *Europhysics Letters*, 77, 66002.

Russel, W. B., Saville, D. A. and Schowalter, W. R. (1989). *Colloidal Dispersions*. Cambridge University Press, 65.

Santiago, J. G., Wereley, S. T., Meinhart, C. D., Beebe, D. J. and Adrian, R. J. (1998). *Experiments in Fluids*, 25, 316.

Schlichting (1979). *Boundary Layer Theory*, 7th edition, McGraw-Hill, New York.

Schwarz, K. W. (1988). *Physical Review B*, 38, 2398.

Schwarz, K. W. (1974). *Physical Review A*, 10, 2306.

Seddon, J. R. T., Thurlow, M. S. and Lucas, P. G. J. (2005). *Journal of Low Temperature Physics*, 138, 505.

Sergeev, Y. A. (2008). *Vortices and Turbulence at Very Low Temperatures*, in Barenghi, C. F. and Sergeev, Y. A. (eds.), CISM Courses and Lecture Notes, Springer.

Sergeev, Y. A., Barenghi, C. F., Kivotides, D. and Vinen, W. F. (2006a). *Physical Review B*, 73, 052502.

Sergeev, Y. A., Barenghi, C. F. and Kivotides, D. (2006b). *Physical Review B*, 74, 184506.

Sergeev, Y. A., Barenghi, C. F. and Kivotides, D. (2006c). *Physical Review B*, 75, 019904.

Sergeev, Y. A., Wang, S., Meneguz, E. and Barenghi, C. F. (2007). *Journal of Low Temperature Physics*, 146, 417.

Shimazake, T. and Murakami, M. (1995). *Cryogenics*, 35, 438.

Smith, M. R., Hilton, D. K. and Van Sciver, S. W. (1999). *Physics of Fluids*, 11, 751.

Smith, M. R., Donnelly, R. J., Goldenfeld, N. and Vinen, W. F. (1993). *Physical Review Letters*, 71, 2583.

Smits, A. J. and Lin, T. T. (eds.), (2001). *Flow Visualization: Techniques and Examples*. Imperial College Press, London.

Squires, K. D. and Eaton, J. K. (1990). *The Physics of Fluids A*, 3, 1169.

Sreenivasan, K. R. (2007). Private Communication.

Swanson, C. E., Barenghi, C. F. and Donnelly, R. J. (1983). *Physical Review Letters*, 50, 190.

Takeshi, T., Ryo, T. and Murakami, M. (2006). *Proceedings of the International Cryogenic Engineering Conference*. Prague.

Tough, J. T. (1982). in edited by Brewer, D. F. (ed.), *Progress in Low Temperature Physics*, vol. VIII, p. 133, North-Holland Publications, Amsterdam.

Tsubota, M. (1994). *Physical Review B*, 50, 579.

Tsubota, M., Araki, T. and Barenghi, C. F. (2003). *Physical Review Letters*, 90, 205301.

Van Sciver, S. W., Fuzier, S. and Xu, T. (2007). *Journal of Low Temperature Physics*, 148, 225.

Vinen, W. F. and Niemela, J. J. (2002). *Journal of Low Temperature Physics*, 128, 167.

Vinen, W. F. (1957). *Proceedings of the Royal Society of London A*, 242.

Xu, T. and Van Sciver, S. W. (2006). in edited by Weisend II, J. G. (ed.), *Advances in Cryogenic Engineering*, vol. 51, p. 1685, American Institute of Physics.

Xu, T. and Van Sciver, S. W. (2007). *The Physics of Fluids*, 19, 071703.

Xu, T. and Van Sciver, S. W. (2008a). in edited by Weisend II, J. G. (ed.), *Advances in Cryogenic Engineering*, vol. 53, American Institute of Physics.

Xu, T. and Van Sciver, S. W. (2008). *Teion Kogaku, J. Cryog. Soc. Japan*, 42, 100.

Yarmchuk, E. J., Gordon, M. J. and Packard, R. E. (1979). *Physical Review Letters*, 43, 214.

Zhang, T., Celik, D. and Van Sciver, S. W. (2004a). *Journal of Low Temperature Physics*, 134, 985.

Zhang, T. and Van Sciver, S. W. (2004b). *The Physics of Fluids*, 16, L99.

Zhang, T. and Van Sciver, S. W. (2005a). *Journal of Low Temperature Physics*, 138, 865.

Zhang, T. and Van Sciver, S. W. (2005b). *Nature Physics*, 1, 36.

This page intentionally left blank

CHAPTER **6**

Capillary Turbulence on the Surfaces of Quantum Fluids

German Valentinovich Kolmakov,[*,†]
Maxim Yurievich Brazhnikov,[*]
Alexander Alexeevich Levchenko,[*]
Leonid Victorovich Abdurakhimov,[*]
Peter Vaughan Elsmere McClintock,[†] and
Leonid Pavlovich Mezhov-Deglin[*]

Contents

[*] Institute of Solid State Physics RAS, Chernogolovka, 142432, Russia
[†] Department of Physics, Lancaster University, Lancaster, LA1 4YB, UK

Abstract   We discuss the results of recent studies of weak turbulence in a system of capillary waves on the surface of liquid hydrogen and of helium ^{4}He in normal and superfluid state. It was observed that when the driving amplitude was sufficiently high, a steady state direct Kolmogorov-Zakharov cascade is formed involving a flux of energy towards high frequencies. The wave amplitude distribution follows a power-law over a wide range of frequencies, in agreement with the weak turbulence theory. It was found that the decay of capillary turbulence begins from the high-frequency end of the spectral range, while most of the energy remains localised at low frequencies. We show that this process can be accounted for in terms of a quasiadiabatic decay wherein fast nonlinear wave interactions redistribute energy between frequency scales in the presence of finite damping at all frequencies. Our numerical calculations based on this idea agree well with experimental data.

1. INTRODUCTION

1.1 Wave Turbulence on Liquid Surface

A highly excited state of a system with numerous degrees of freedom, characterised by the presence of an energy flux that is directional in K-space, is referred to as *turbulent*. In its turbulent mode, a system exists far from its thermodynamic equilibrium and it is characterised by significant nonlinear interaction between its degrees of freedom, as well as by the dissipation of energy (Landau and Lifshitz, 1987; Zakharov et al., 1992). The nonlinear interaction brings about an effective redistribution of energy between the degrees of freedom (modes). Turbulence may be observed in systems where the frequencies of excitation (energy pumping) and energy dissipation are widely spaced in frequency.

    Studies of energy propagation in such systems have included capillary waves on the surfaces of liquids, which are of great interest from the standpoint of both fundamental nonlinear physics and practical applications. The theory of weak, or wave, turbulence was developed in the late 1960s (see the monograph by Zakharov et al. (1992) and references therein). However, despite many experimental investigations of the nonlinear dynamics of surface waves, only a few experimental observations of isotropic spectra of capillary waves on the surface of water have been

reported (Brazhnikov et al., 2002c; Henry et al., 2000; Lommer and Levinsen, 2002; Savelsberg and van de Water, 2008; Wright et al., 1992, 1996, 1997), the results of which can be compared with the theoretical predictions. Recently, the surface of mercury was used for studies of gravity-capillary wave turbulence (Falcon et al., 2007a,b).

We review below the results of our recent investigations (Abdurakhimov et al., 2007; Brazhnikov et al., 2001a,b,c, 2002a,b, 2004, 2005a,b; Kolmakov et al., 2004, 2006; Kolmakov, 2006) of nonlinear capillary waves on the surface of liquid hydrogen and helium. Liquid hydrogen and helium are especially suitable objects for such experiments because they are characterised by relatively low values of density ρ and kinematic viscosity ν with respect to water. Also, the coefficient $V \propto (\alpha/\rho^3)^{1/4}$ that describes the nonlinearity of capillary waves (see Table 1) has a high value for liquid hydrogen. This enables us to examine the turbulent mode in liquid hydrogen or helium in a cell with the inner diameter of a few centimetres over a wide frequency range from 10 Hz to 10 kHz. In addition, on account of the low density, the external force required to excite oscillations on the surface of liquid hydrogen and helium is several times less than that in the case of water. This fact proved to be of crucial importance for the excitation of waves on the surface by means of electric forces. Previous experiments had revealed (Levchenko and Mezhov-Deglin, 1996) that one can charge the surface of liquid hydrogen with charges injected initially into the bulk of the liquid, hold the charges in the vicinity of the surface for a long period of time and excite surface waves using AC electric field. An important advantage of this procedure for the observation of capillary turbulence is the possibility of directly affecting the surface of a liquid by an external force, virtually without acting on the bulk of the liquid, as well as the high degree of isotropy of the exciting force enabling one to study the turbulence under well-controlled experimental conditions. Also, the effective gravitation affecting the surface can be reduced greatly, thus allowing one to enlarge the frequency range for studying capillary waves (see below, Section 1.2).

TABLE 1 Comparable properties of liquid hydrogen, ^{4}He in normal state and water.

	Liquid H$_2$, $T = 15$ K	Liquid ^{4}He, $T = 4.2$ K	Water, $T = 293$ K
Density ρ, g/cm^3	0.076	0.125	1.0
Surface tension α, dyn/cm	2.8	0.09	73
Capillary length λ , cm	1.22	0.17	1.71
Nonlinearity coefficient $(\alpha/\rho^3)^{1/4}$, cm$^{9/4}$/g$^{1/2}$s$^{1/2}$	8.9	2.6	2.9
Kinematic viscosity ν, cm^2/s	0.0031	0.00026	0.01
Dielectric permittivity ε	1.25	1.049	81
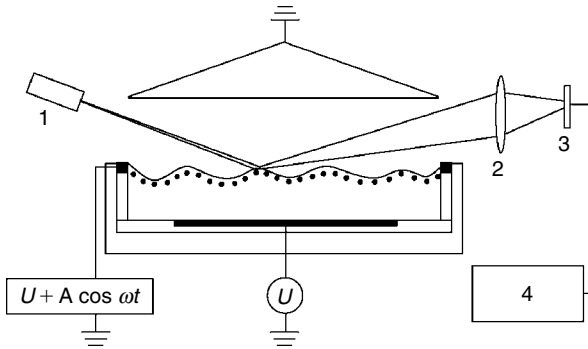
FIGURE 1 Schematic view of the experimental cell: (1) laser, (2) lens,
(3) photodetector, (4) analog-to-digital converter.

Experiments over the last ten years have revealed many interesting nonlinear phenomena (Brazhnikov et al., 2001a,b,c, 2002a,b, 2004, 2005a,b; Kolmakov et al., 2004, 2006; Kolmakov, 2006; Levchenko and Mezhov-Deglin, 1996; Levchenko et al., 1997, 1999, 2000) associated with wave motion on the charged surfaces of liquid hydrogen and helium. In what follows, we present a succinct review of this work, summarising the most important observations and their interpretation, and including a discussion of our most recent experimental and theoretical results. The basis of the experiment is illustrated schematically in Figure 1. A laser beam is reflected from the charged surface of liquid hydrogen. DC and AC electric fields are applied between the charged layer and a conical electrode placed above the liquid. Further details of the experimental arrangement and the procedures used are given in Section 2. We review the theoretical background in Section 1.3. We present and discuss the main experimental and theoretical results in Sections 3 and 4. First, however, we consider the properties to be expected of waves on a charged surface, and we introduce the concept of wave turbulence.

1.2 Waves on the Charged Surface of Liquid Hydrogen

The dispersion law for surface waves on a flat, equipotential, charged layer of liquid between the plates of a horizontal capacitor can in general be written as (Gor'kov and Chernikova, 1976)

$$\omega_k^2 = k \tanh(kh)\left(g + \frac{\alpha k^2}{\rho} - \frac{2kP}{\rho} \coth(kd) \right), \tag{1}$$

where ω_k is the frequency of a wave of wave vector k, h is the thickness of the liquid layer, α is the surface tension, ρ is the density of the liquid, g is the acceleration due to gravity, d is the distance between the surface

and the upper plate of the capacitor, $P = U^2/8\pi d^2$ is the equilibrium pressure of the electric field on the surface and U is the voltage applied to the capacitor (note that the electric force acting on the charged surface is directed upwards, oppositely to the gravitation force, and the surface charges compensate completely the external electric field).

In the case when the distance from the surface to the control (upper) electrode is smaller than the wavelength ($kd \leq 1$), the dispersion law (Equation (1)) for surface waves on a deep liquid simplifies greatly and can be written as

$$\omega_k^2 = k\left(G + \frac{\alpha k^2}{\rho}\right),$$
(2)

where the quantity $G = g - 2P/\rho d$ acts as an effective acceleration due to gravity.

If the applied voltage tends to the critical value $U_{c1} = (4\pi\rho g d^3)^{1/2}$, the effective gravitational acceleration $G \to 0$ and the effective capillary length $\lambda_{eff} = 2\pi(\alpha/\rho G)^{1/2} \to \infty$. In this case, the surface waves can be considered as being purely capillary waves at all values of k, even where the wavelength exceeds the capillary length of a neutral liquid $\lambda = 2\pi(\alpha/\rho g)^{1/2}$. Hence $\omega_k \propto k^{3/2}$ at practically all k, see Figure 2.

From Equation (2) it follows that in high electric fields $U > U_{c1}$, where the effective acceleration due to gravity G becomes negative, a flat charged
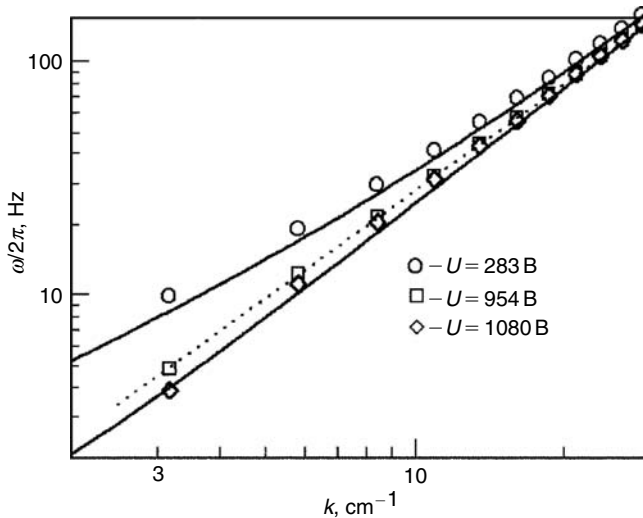
FIGURE 2 Spectrum of oscillations of the charged surface of liquid hydrogen in the cylindrical cell for different values of the DC capacitor voltage U below the first critical voltage U_{c1}. The dashed line corresponds to the dependence $\omega_k \propto k^{3/2}$.

surface should be unstable against a perturbation with $k \leq \sqrt{\rho|G|/\alpha}$. We have observed this instability (reconstruction of the initially flat charged surface of liquid hydrogen) experimentally: at voltages $U > U_{c1}$, a stationary solitary wave (a hump) forms on the surface in a cylindrical cell filled with liquid hydrogen. A similar phenomenon – formation of a stationary dimple – was observed on the negatively charged surface of liquid helium (Levchenko et al., 1997). It should be mentioned that as the voltage increased above a second critical voltage (Levchenko et al., 1999, 2000), $U_{c2} \simeq 1.2\,U_{c1}$, the reconstructed surface of the liquid hydrogen lost stability and a discharge pulse occurred from the top of the hump: it looked like a geyser. After this discharge, the surface relaxed to its original flat state and then the process repeated. Because of this effect, it was in practice impossible to study capillary waves on the reconstructed surface of liquid hydrogen at voltages above $1.2\,U_{c1}$. After a stepwise switching of the voltage U to a value higher than a third critical voltage $U_{c3} > U_{c2}$, the extraction of charges from under the surface of the liquid hydrogen was observed (Levchenko and Mezhov-Deglin, 1996). In this regime, charged clusters (snowballs) penetrate through the liquid-vapor interface under influence of the strong electric force, and a steady state electric current through the surface is established.

Dispersion curves $\omega(k)$ for oscillations of the charged surface are shown in Figure 2. The first critical voltage in these measurements $U_{c1} = 1200$ V, the second critical voltage $U_{c2} = 1440$ V and the temperature was 15 K. As can be seen in the figure, the spectrum is close to $\omega(k) \sim k^{3/2}$ at voltages close to U_{c1}. It was observed also that with increasing voltage, the spectrum was soften and there was no particular changes in fields higher than the first critical value. As pointed out by Levchenko et al. (1997, 1999), the observed reconstruction can be discussed in terms of a second-order phase transition corresponding to a softening of the spectrum of surface waves with increasing external electric field.

1.3 Capillary Turbulence: Theoretical Background

Capillary waves on the surface of a liquid represent an example of a nonlinear interacting system. The theory of homogeneous capillary turbulence was described by Zakharov and Filonenko (1967) who showed that an ensemble of weakly interacting capillary waves may be described within a kinetic equation, similar to the Boltzmann equation of gas dynamics.

The evolution with time t of the occupation numbers $n_{\mathbf{k}} = \langle a_{\mathbf{k}}(t) a_{\mathbf{k}}^{*}(t) \rangle$ for capillary waves, where $a_{\mathbf{k}}(t)$ is the time-dependant canonical amplitude of the wave with the wave vector $\mathbf{k}$, is described by the kinetic equation

$$\frac{\partial n_{\mathbf{k}}}{\partial t} = St(n_{\mathbf{k}}) - 2\gamma_{\mathbf{k}} n_{\mathbf{k}} + F_{\mathbf{k}}(t). \tag{3}$$

The canonical amplitudes of the waves are expressed via the space Fourier components of the liquid surface elevation $\eta_\mathbf{k}(t)$ and of the fluid velocity potential $\Psi_\mathbf{k}(t)$ taken at the liquid surface as follows (Zakharov and Filonenko, 1967; Zakharov, 1968):

$$a_\mathbf{k} = \sqrt{\frac{\alpha k^2}{\omega_k}}\, \eta_\mathbf{k} + i\sqrt{\frac{\rho k}{2\omega_k}}\, \Psi_\mathbf{k}. \tag{4}$$

The collision integral in Equation (3) is equal to

$$St(n_\mathbf{k}) = \int d\mathbf{k}_1 d\mathbf{k}_2 \left(R_{\mathbf{k},\mathbf{k}_1,\mathbf{k}_2} - R_{\mathbf{k}_1,\mathbf{k},\mathbf{k}_2} - R_{\mathbf{k}_1,\mathbf{k}_2,\mathbf{k}} \right).$$

Here,

$$R_{\mathbf{k},\mathbf{k}_1,\mathbf{k}_2} = \pi |V_{\mathbf{k},\mathbf{k}_1,\mathbf{k}_2}|^2 \delta(\mathbf{k} - \mathbf{k}_1 - \mathbf{k}_2)\delta(\omega_\mathbf{k} - \omega_{\mathbf{k}_1} - \omega_{\mathbf{k}_2})$$
$$\times \left[n_{\mathbf{k}_1} n_{\mathbf{k}_2} - n_\mathbf{k} n_{\mathbf{k}_1} - n_\mathbf{k} n_{\mathbf{k}_2} \right],$$

$$V_{\mathbf{k},\mathbf{k}_1,\mathbf{k}_2} = \left(\frac{1}{8\pi}\right)\left(\frac{\alpha}{4\rho^3}\right)^{1/4}\left[(\mathbf{k}_1 \mathbf{k}_2 + k_1 k_2)\left(\frac{k_1 k_2}{k}\right)^{1/4} \right.$$
$$\left. + (\mathbf{k}\mathbf{k}_1 - kk_1)\left(\frac{kk_1}{k_2}\right)^{1/4} + (\mathbf{k}\mathbf{k}_2 - kk_2)\left(\frac{kk_2}{k_1}\right)^{1/4} \right]$$

is the amplitude of the nonlinear interaction between capillary waves, $\gamma_\mathbf{k} = 2\nu k^2$ is the viscous damping coefficient for capillary waves and $F_\mathbf{k}(t)$ is the external driving force.

The main problem in the investigation of wave turbulence is that of finding the energy distribution law in terms of frequency, that is, the stationary spectrum of the turbulent energy E_ω. The energy E per unit surface of liquid may be written in the form

$$E = \int \omega_k n_k d\mathbf{k} = \int E_\omega d\omega, \tag{5}$$

where ω_k is the frequency of a wave with the vector $\mathbf{k}$. The capillary wave dispersion law

$$\omega = (\alpha/\rho)^{1/2} k^{3/2} \tag{6}$$

is of the decay type ($\omega'' > 0$). The main contribution to the wave interaction is therefore made by three-wave processes, such as the decay of a wave

into two waves with conservation of the overall wave vector and overall frequency, as well as the reverse process involving the confluence of two waves into one wave. For a system of capillary waves on the surface of a liquid, there exists a so-called *inertial* frequency range in which the energy distribution E_ω has the power-law-like form

$$E_\omega \sim \omega^s.$$

Here s is an exponent that can be estimated from experimental results.

The inertial range is limited from below by the pumping frequency ω_p and at high frequencies by viscous damping. According to the currently accepted theory (Zakharov and Filonenko, 1967; Zakharov et al., 1992), when the surface of a liquid is excited, at low frequencies within a fairly wide band $\omega_p \pm \Delta\omega$ ('wide-band pumping', $\Delta\omega \approx \omega_p$), there is a constant energy flux Q towards high frequencies, that is, a direct cascade in K-space. The theory of homogeneous capillary turbulence predicts the power-law dependence on frequency for the wave distribution function n_k and the energy distribution E_ω (Kolmogorov-like, or Kolmogorov-Zakharov spectrum (Zakharov et al., 1992)) within the inertial range, which corresponds to

$$n_k = A Q^{1/2} \rho^{3/4} \alpha^{-1/4} k^{-17/4} \tag{7}$$

in terms of k. Here A is a numerical coefficient. The distribution is an exact solution of the kinetic equation (Equation (3)) in the inertial range of frequencies, where direct excitation of waves by driving is absent, $F_{\mathbf{k}} = 0$, and viscous loss is so small that it can be neglected (Zakharov and Filonenko, 1967).

The steady state distribution of the energy of surface waves in the inertial range may also be equivalently described in terms of the pair correlation function in the Fourier representation

$$I_\omega = \langle |\eta_\omega|^2 \rangle \tag{8}$$

of a departure of the surface from the planar state $\eta(r, t)$. From the experimental standpoint, it is most convenient to investigate the correlation function I_ω rather than the energy distribution E_ω because the deviations of the surface from the planar state $\eta(r, t)$ can be measured directly. When surface oscillations are excited over a wide frequency range, the correlation function is predicted by the theory (Zakharov and Filonenko, 1967; Zakharov, 1968; Zakharov et al., 1992) to be

$$I_\omega = \text{const} \times \omega^{-17/6}. \tag{9}$$

Here, the dispersion law (Equation (6)) was used for changing the representation from K-space to ω-space. The theoretical prediction of relation in Equation (7) is supported by the results of numerical calculations of the evolution of nonlinear capillary waves, performed directly from the first principles using the hydrodynamic equations (Pushkarev and Zakharov, 1996, 2000).

In the case of 'narrow-band pumping' ($\Delta\omega < \omega_p$), it was demonstrated by numerical calculations (Falkovich and Shafarenko, 1988) that a system of equidistant spectral peaks is formed on the I_ω curve at multiples of the pumping frequency. The frequency dependence of the peak height is described by a power-law-like function with an exponent of $(-7/2)$,

$$I_\omega = \text{const} \times \omega^{-7/2}. \tag{10}$$

Note that the relations in Equations (9) and (10) were derived for systems of capillary waves with continuous spectra of wave vectors, that is, for an idealised infinite surface of liquid. The limited size of an actual experimental cell means, however, that the $\omega(k)$ spectrum must in reality be discrete. This fact must be taken into account when comparing the real correlation function with theoretical prediction. The effect of discreteness decreases with increasing frequency ω because the resonance width, determined by the quality Q factor and by nonlinear broadening of the resonance, increases faster than the distance between the resonances: the spectrum becomes quasicontinuous. Pushkarev and Zakharov (2000) and Connaughton et al. (2001) used numerical methods to demonstrate that a discrete system of resonances at a fairly high level of excitation can be well approximated as a quasicontinuous one. These results were confirmed recently by analytical calculations (Nazarenko, 2006).

As already mentioned above, the inertial range is limited at high frequencies by a change in the dominant mechanism of energy transfer from nonlinear wave transformation to viscous damping. The high-frequency edge of the inertial range (boundary frequency) can be defined as the frequency ω_b at which the viscous damping time τ_v becomes comparable in order of magnitude with the characteristic time τ_n of nonlinear interaction (the kinetic relaxation time in the turbulent wave system), $\tau_v \sim C\,\tau_n$, where C is some dimensionless constant. The time τ_n is defined by the parameters of the liquid, as well as by the capillary wave distribution function $n(\omega)$, and may be estimated as

$$1/\tau_n \sim |V_k|^2 n_k k^2/\omega_k = |V_\omega|^2 n(\omega), \tag{11}$$

where $V_\omega \sim \alpha^{-1/2}\omega^{3/2}$ is the coefficient of interaction of three capillary waves, whose frequencies are close to each other. The value of τ_n defines

the characteristic timescales for the relaxation of perturbations over the cascade. It is known (Landau and Lifshitz, 1987) that the viscous damping time of capillary waves decreases with increasing frequency as

$$1/\tau_v = 2\nu\omega^{4/3}(\rho/\alpha)^{2/3}. \tag{12}$$

Relations in Equations (11) and (12) enable us to derive the dependence of the wave frequency ω_b on the wave amplitude η_p at the pumping frequency ω_p (narrow pumping):

$$\omega_b \propto \eta_p^{4/3}\omega_p^{23/9}. \tag{13}$$

The values of the exponents in this equation correspond to the frequency dependence of the correlation function (Falkovich and Shafarenko, 1988)

$$I_\omega \propto \eta_p^2(\omega/\omega_p)^{-7/2}. \tag{14}$$

Our investigations have shown (Brazhnikov et al., 2001a) that a power-law dependence on frequency is observed for the correlation function in the frequency range from 100 Hz to 10 kHz when the charged surface of liquid hydrogen is excited by an external periodic electric force at the resonance frequency of the cell. In this case, the exponent in the correlation function was close to (-3.7 ± 0.3) in accordance with Equation (9). When the surface was excited simultaneously at two resonant frequencies, the exponent decreased in magnitude and amounted (Brazhnikov et al., 2001b) close to (-2.8 ± 0.2) in accordance with Equation (10).

The boundary frequency of the upper edge of the inertial range was determined experimentally for the first time by Brazhnikov et al. (2001c). As the wave amplitude η_p at the pumping frequency ω_p increases, the boundary frequency is found to shift towards higher frequencies according to the power-law in (Equation (13)), with an exponent 4/3, as is to be expected when pumping in a narrow band (Brazhnikov et al., 2002b).

Quasiadiabatic decay of capillary turbulence was observed experimentally by Kolmakov et al. (2004) and Brazhnikov et al. (2004), and it was investigated theoretically and numerically by Kolmakov (2006). Comparison of these results with the observations of capillary turbulence formation process (Brazhnikov et al., 2005a) has shown that the formation of turbulence and its decay are both controlled by the same relaxation mechanisms.

For the case of spectrally narrow pumping, it was found (Brazhnikov et al., 2005b) that after an additional low-frequency pumping was switched on, the wave amplitude in the high-frequency part of the turbulent spectrum decreased and that the inertial frequency range consequently became narrower. Conversely, after switching off the additional low-frequency

pumping, the inertial range expands to higher frequencies. The damping is caused by an increase in the number of wave modes (harmonics) involved in the nonlinear energy transfer from the low- to the high-frequency domain and by the redistribution of wave energy among these modes.

2. EXPERIMENTAL PROCEDURE

2.1 Experimental Setup

Experiments were performed in an optical cell located within a helium cryostat (Brazhnikov et al., 2002a). The arrangement is shown schematically in Figure 3. The cell contains a horizontal plane capacitor. A radioactive plate was located on the bottom capacitor plate. Hydrogen or helium was condensed into a cup formed by the bottom capacitor plate and a guard ring. In the preliminary experiments with liquid hydrogen,
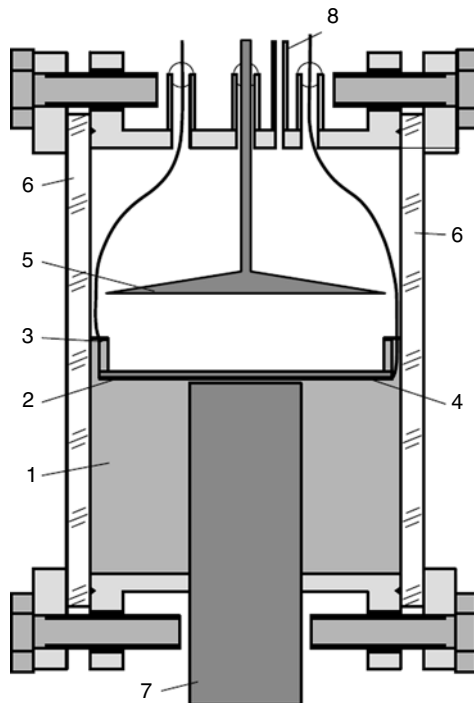
FIGURE 3   Schematic drawing of the experimental cell: (1) textolite bar; (2) bottom plate of the capacitor; (3) guard ring; (4) radioactive target; (5) upper plate of the capacitor; (6) organic glass windows; (7) copper heat sink; and (8) capillary. The dimensions of parts are given in the text.

the cylindrical container was of inner diameter 25 mm, depth 3 mm (the narrow cell). Most of the data presented here were obtained from a wider cell with a container 60 mm in inner diameter and 6 mm in depth. The gap between the fluid surface and the upper capacitor plate was 4 mm in both cells. The temperature of the liquid was held at 15.5 K. In experiments with liquid helium, the container was of 30.5 mm inner diameter, depth 3 mm. The temperature of the liquid was changed from 4.2 K (normal He I) to 1.7 K (superfluid He II).

The free surface of the liquid was charged as the result of β-particle (electron with a mean energy ~5keV and a maximum energy of 18 keV) emission from the radioactive plate located in the bulk of the liquid. These electrons ionised a thin layer of liquid in the vicinity of this plate. A DC voltage U was applied between the capacitor plates. Its polarity determined the sign of the charge that formed a quasi-two-dimensional layer below the surface of the liquid. The lifetime of the positively charged clusters (snowballs) under the liquid hydrogen or helium surface significantly exceeds (by two to three orders of magnitude) the lifetime of the electric bubbles (~10 s). In these experiments, the oscillation of a positively charged surface was studied. The metal guard ring around the radioactive plate prevented escape of charge from under the surface to the container walls. Therefore, it can be assumed that the electric field in the liquid bulk is close to zero, and the charge density in the layer is proportional to the applied voltage.

Oscillations of the liquid surface (standing waves) were excited by application of an AC voltage of amplitude ~100 V to the guard ring, in addition to the DC voltage. Waves were excited due to the nonuniform electric field at the edges of the capacitor. Therefore, surface oscillations were generated at the frequency of an AC voltage but not at the halved frequency as is observed for a parametric resonance. The electric field in such a capacitor is sufficiently isotropic for waves with angular harmonics not to be excited on the liquid surface.

2.2 Measurement and Data Processing Techniques

Surface oscillations were detected through variations of the power of a laser beam reflected from the surface (see Figure 1). The laser beam used in the experiments was ~0.5 mm in diameter and was incident on the surface of the liquid at a grazing angle of about $\alpha = 0.2$ rad. Its plane of incidence was oriented along the cell diameter. The major and minor axes of the elliptical light spot on the surface of the liquid were $a = 2.5$ and $b = 0.5$ mm. The reflected light was focused by a lens onto a photodetector. The voltage across the photodetector was directly proportional to the beam power $P(t)$. It was digitised with the aid of a high-speed 12- or 16-bit analog-to-digital converter and recorded over several seconds duration
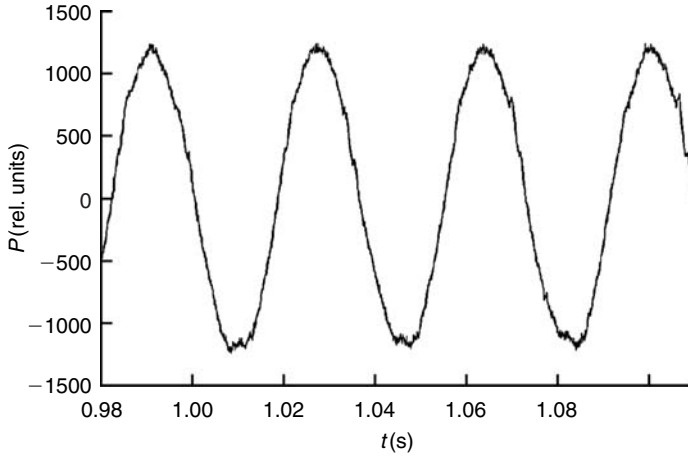
FIGURE 4 Fragment of a digitised time dependence of the variable component of the reflected laser beam power $P(t)$. The driving frequency is 27.5 Hz.

onto the hard disc of a computer. An example of a record of a digitised dependence $P(t)$ is shown in Figure 4.

We analysed the frequency spectrum P_ω of the total power of the reflected laser beam, which was obtained by Fourier transformation in time of the $P(t)$ dependence recorded. The procedures used for processing the experimental data have been described in details by Brazhnikov et al. (2002a) and Abdurakhimov et al. (2007).

When comparing the results of such experiments to a theory, the behaviour of the correlation function of the surface deviation from an equilibrium state in the frequency representation

$$I_\omega = \langle |\eta_\omega|^2 \rangle = k^{-2} \langle |\varphi_\omega|^2 \rangle \propto \omega^{-4/3} \langle |\varphi_\omega|^2 \rangle \tag{15}$$

is usually of interest. Here $\varphi_\omega = k\eta_\omega$ is the angular amplitude of the surface wave. The dependence of the wave vector k on the frequency ω is governed by the dispersion law (Equation (6)).

In order to extract the data on the surface state from the results of measuring the laser beam power $P(t)$, one should apply different processing techniques. The selection of the method depends first on the ratio between the linear size of the spot a formed by the beam on the liquid surface along the cell diameter and the length λ of the capillary wave, and second on the maximum angle of surface deviation from the plane state φ_{max}.

Most of experimental results reported below were obtained in the regime where the spot size is larger than the wave length, $a \gg \lambda$ ($ka \gg \pi$, a wide beam), and $\varphi_{max} \ll \alpha$. In this case, the recorded signal $P(t)$ is defined as an integral characteristic of the surface profile that is proportional to the

reflection coefficient averaged over the spot area:

$$P(t) \propto \int R(\alpha + \varphi(x,t))\, ds$$

$$= C_1 + C_2 \int \varphi(x,t)\, ds + C_3 \int \varphi^2(x,t)\, ds + \cdots, \qquad (16)$$

where $R(\theta)$ is the reflection coefficient, C_1, C_2 and C_3 are some constants. The function $R(\theta)$ was expanded into a Taylor series in the vicinity of α while the condition $\varphi_{max} \ll \alpha$ is satisfied.

When the second-order infinitesimal term in Equation (16) is much smaller than the linear term (small wave amplitudes, linear regime of registration), the variable component of the beam power is proportional to the averaged angular deviation of the liquid surface. In this case, we have the following relation for the Fourier components:

$$|\varphi_\omega|^2 \propto |P_\omega|^2/\Phi(\omega), \qquad (17)$$

where $\Phi(\omega)$ is the instrumental function, with a form dependent on the position of the spot on the surface.

Figure 5 shows an example of the frequency dependence $\Phi(\omega)$ obtained by calculations for an idealised case where the spatial phases of all waves coincide at the centre of the spot. As we see in the region of $ka \gg \pi$ (the wide-beam limit $\omega \gg \omega_{cr}$, where $\omega_{cr} = \omega_{k=\pi/a}$), the instrumental function is nonmonotonic, but its relative maxima decrease following a
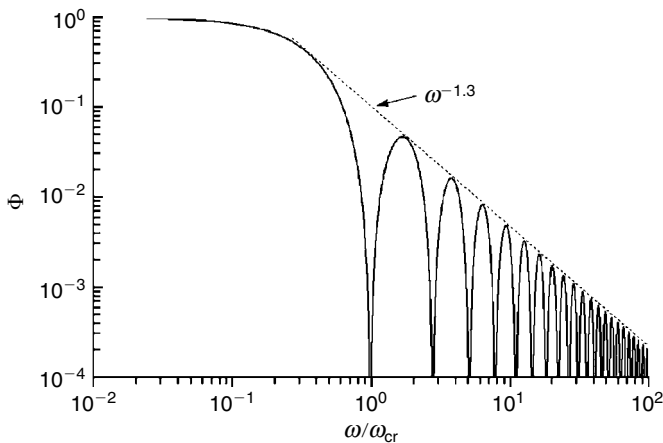
FIGURE 5   Calculated dependence of the instrumental function $\Phi(\omega)$: normalised $|P_\omega|^2/|\varphi_\omega|^2$ ratio. The straight line corresponds to the function $\Phi(\omega) \propto \omega^{-1.3}$.

power-law with an exponent close to (-1.3): $\Phi(\omega) \propto \omega^{-1.3}$. Estimations show that $\omega_{cr} \approx 50\,\text{Hz}$ in experiments with liquid hydrogen surface and $\omega_{cr} \approx 10\,\text{Hz}$ in experiments with liquid helium surface.

Taking into account, the wave phases does not modify qualitatively the instrumental function: peaks are redistributed, but the dependence of their amplitude on frequency remains unchanged.

In principle, this method of detecting surface oscillations allows one to obtain information on the surface state, even if the condition $\varphi \ll \alpha$ is not met (e.g., at $\varphi_{max} \sim \alpha$). It follows from geometrical consideration that the angle φ_{max} must not exceed $\alpha/2$; otherwise, a part of the reflected beam undergoes a repeated reflection from the liquid surface. However, in our experiments on turbulence, the condition $\varphi \ll \alpha$ was always satisfied. Therefore, we obtain the following relation for the correlation function in a wide beam regime:

$$I_\omega \propto \omega^{-4/3}\langle|\varphi_\omega|^2\rangle \propto \omega^{-4/3}|P_\omega|^2/\Phi(\omega) \propto |P_\omega|^2. \qquad (18)$$

The instrumental function $\Phi(\omega)$ in Equation (18) is replaced at $\omega \gg \omega_{cr}$ by a power function $\omega^{-1.3}$, which describes the behaviour of relative maxima of $\Phi(\omega)$ (see Figure 5). Such a replacement does not allow us to identify the spectra of $|P_\omega|^2$ and I_ω but makes it possible, using the experimental spectrum of $|P_\omega|^2$, to determine the parameters of the spectrum I_ω that are of interest for the comparison of the measurement data to the turbulence theory in a system of capillary waves: the exponent in the spectrum I_ω in the inertial interval and the position of the high-frequency viscous edge of the inertial interval.

3. EXPERIMENTAL RESULTS

3.1 Effect of the Type of Pumping on the Frequency Dependence of the Correlation Function

It follows from relations in Equations (9) and (10) that the exponent m in the correlation function $I_\omega \sim \omega^m$ must vary from $m = -21/6$ for the narrow-band pumping to $-17/6$ for the wide-band pumping. The measurement accuracy proved to be sufficient to form a reliable opinion of the variation of the exponent m. The experimental capabilities of the procedure made it possible to obtain and compare the frequency dependences of the correlation functions for three types of excitation of charged surface, namely, at a single resonant frequency of the cylindrical cell, at two resonant frequencies and by noise in a band covering several resonances.

Figure 6 illustrates the frequency dependence of P_ω^2 in the case of excitation of the surface of liquid hydrogen at the resonant frequency of 28 Hz.
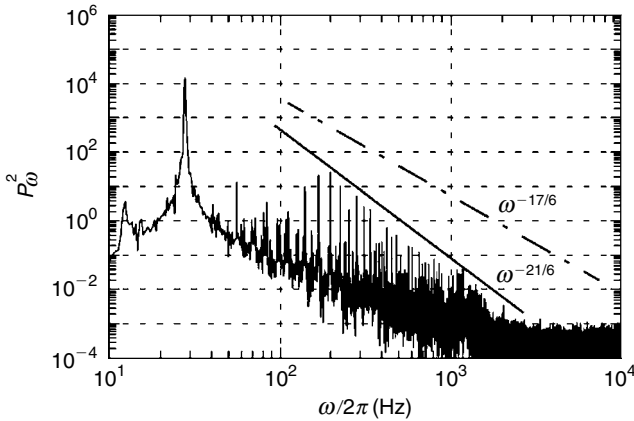
FIGURE 6   Distribution of P_ω^2 in the case of pumping at the frequency of 28 Hz, measured in experiments with liquid hydrogen.

In the frequency range of 0.2 to 2.0 kHz, the dependence P_ω^2 may be well described by a power function. The exponent obtained by averaging over ten measurements is $m = -3.7 \pm 0.3$. For comparison, the solid line in the figure indicates the function $\omega^{-21/6}$, and the dot-dashed line indicates the function $\omega^{-17/6}$. When the surface was excited at two resonant frequencies, the experimentally obtained P_ω^2 dependences could be described by a power function with the exponent $m = -2.8 \pm 0.2$, which was close to the predicted value of $m = -17/6$.

When low-frequency noise was used to excite surface oscillation, the P_ω^2 distribution turned out to be close to the predicted dependence given by Equation (9), as in the case of excitation at two frequencies. Figure 7 gives the P_ω^2 distribution in the case of surface excitation by noise in the frequency band of approximately 1 to 30 Hz. The solid curve indicates the distribution of the square of Fourier harmonics of the noise voltage applied to the guard ring (expressed in arbitrary units). The dot-dashed line corresponds to the function $\omega^{-17/6}$. Figure 7 gives the result obtained by averaging over three files of the distribution. The distribution could be described by a power function of frequency with the exponent $m = -2.8 \pm 0.2$. One can see that the experimentally obtained dependences turn out to be close to $\omega^{-17/6}$.

3.2 Dependence of the Boundary Frequency on the Wave Amplitude at the Pumping Frequency

The P_ω^2 distribution was found to depend both on the type of pumping, its amplitude and the pumping frequency. Figure 8 gives the frequency dependence of the square of the Fourier amplitude P_ω^2 of the $P(t)$ signal measured during excitation of the liquid hydrogen surface at the high
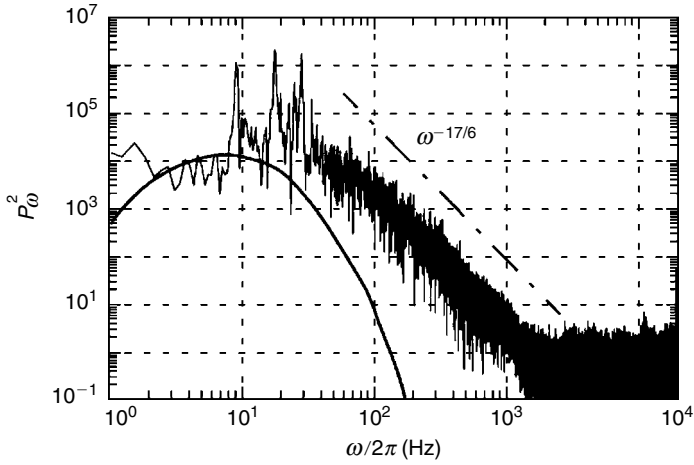
FIGURE 7   Distribution of P_ω^2 in the case of pumping by noise at low frequencies measured in experiments with liquid hydrogen. The full line describes the distribution of the square of Fourier harmonics of the AC voltage applied to the guard ring (in arbitrary units).
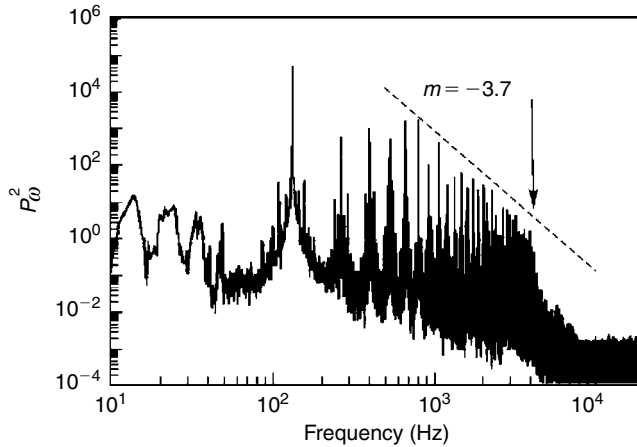
FIGURE 8   Distribution of P_ω^2 for a wave amplitude of 0.016 mm at the pumping frequency of 135 Hz measured in experiments with liquid hydrogen.

frequency $\omega_p/2\pi = 135$ Hz. The wave amplitude η_p at the pumping frequency was 0.016 mm and the wavelength was $\lambda = 2.3$ mm. The arrow indicates the frequency at which an abrupt variation of the dependence P_ω^2 occurs at the edge of the inertial range. For other amplitudes and pumping frequencies η_p and ω_p, similar results are given by Brazhnikov et al. (2001c, 2002b). In Figure 8, the boundary frequency of the edge of the inertial range is $\omega_b/2\pi = 4.0 \pm 0.3$ kHz. We have observed that as the wave

amplitude increases, the boundary frequency of the inertial range shifts towards higher frequencies. When the pumping wave amplitude is not high, a cascade consisting of only a few harmonics of the pumping frequency ω_p is realised in P_ω^2 spectrum. When the pumping wave amplitude increases, the inertial range is expanded, and the P_ω^2 spectrum comes to be made up of tens and even hundreds of harmonics.

Thus, the energy balance in the system of capillary waves is highly non-local: energy is pumped into the system in the low-frequency domain and flows to the high-frequency domain, where it is absorbed by dissipative mechanisms. Our observation confirms the inference that nonlinear interaction between the waves leads to a directed transfer of energy between these two widely separated scales.

Figure 9 gives three dependences of the boundary frequency of the edge of the inertial range ω_b on the wave amplitude η_p at pumping frequencies of 83, 135 and 290 Hz. The ordinates of the points (frequencies) shown in the figure were estimated from experimentally obtained curves similar to those of Figure 8. The pumping wave amplitudes were calculated from the known AC voltages applied to the guard ring. One can see that the experimentally obtained dependences $\omega_b(\eta_p)$ may be described by power-law. The full curves in the figure correspond to the power-law dependences of the boundary frequency of the inertial range ω_b on the amplitude η_p, with the exponent of 4/3, predicted by theoretical considerations, see Equation (13). For better agreement between the experimental data and the theory, we should add the constant term into the fitting function (it is clear that the boundary frequency ω_b cannot be less than the
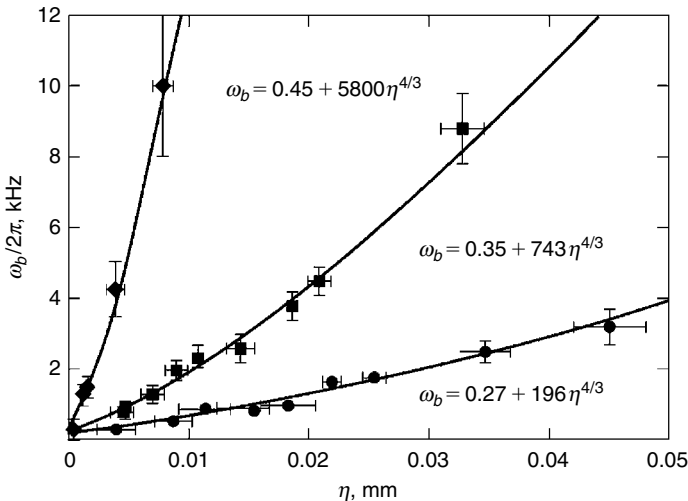
FIGURE 9   Boundary frequency ω_b as a function of the wave amplitude η_p at the pumping frequencies of 83 (circles), 135 (squares) and 290 (diamonds) Hz.

pumping frequency ω_p). The results of fitting are given in Figure 9. The constant term turned out to exceed the pumping frequency ω_p by a factor of 2 to 3.

The amplitude dependence of the boundary frequency ω_b (as given by Equation (13)) implies the existence of scaling with respect to the pumping frequency ω_p. As it was shown by Brazhnikov et al. (2002b), the experimental points for ω_b fit a single straight line in the coordinates $\omega_p/\omega_b^{23/9}$ versus $\eta^{4/3}$, irrespective of the pumping frequency, in agreement with the theoretical estimations with Equation (13), see Figure 10. This supports the validity of our assumption of the determining effect of viscosity when estimating the value of the edge frequency ω_b.

3.3 Free Decay of Capillary Turbulence

In this Section, we describe experiments on the decay of turbulent oscillations of the charged surface of liquid hydrogen after a step-like switching off of the harmonic pumping and the resultant change in the correlation function I_ω.

The surface waves were excited by harmonic pumping at a fixed frequency ω_p for ~10 s, which was sufficient to establish a steady state turbulent distribution in the system of capillary waves. The pumping was then switched off, and the relaxation of free surface oscillations with time was observed. The time of observations was varied from 2 to 10 s. Measurements were carried out for various pump frequencies $\omega_p/2\pi$ in the range from 20 to 400 Hz.
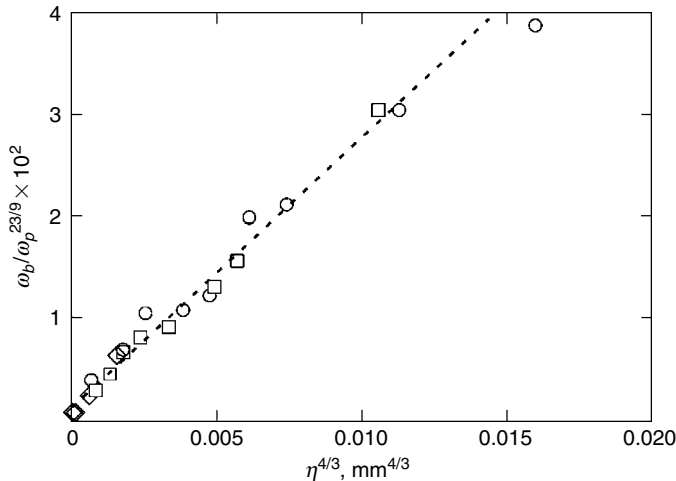
FIGURE 10 The same as Figure 9 but in reduced coordinates with pumping frequencies of 83 (circles), 135 (squares) and 290 (diamonds) Hz.
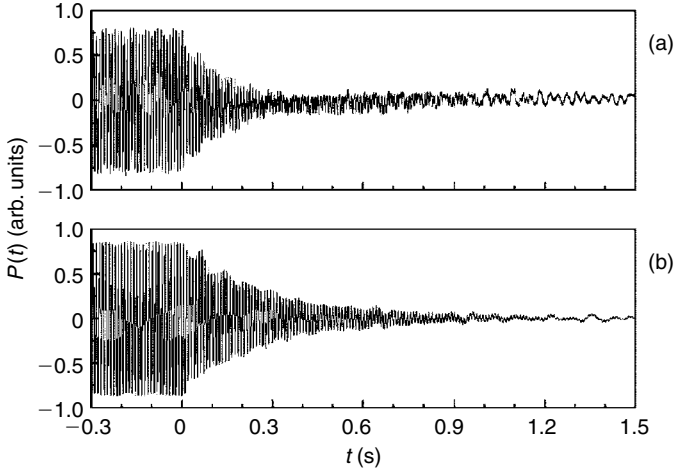
FIGURE 11 Relaxation of the liquid hydrogen surface oscillations after switching off the pumping at frequency $\omega_p/2\pi$ at time $t = 0$: (a) narrow cell with $\omega_p/2\pi = 98$ Hz and (b) wide cell with $\omega_p/2\pi = 97$ Hz.

In Figure 11, sections of the time-dependent photodetector signals $P(t)$ recorded at a pump frequency of (a) $\omega_p/2\pi = 98$ Hz in the narrow cell and (b) 97 Hz in the wide cell are shown. The harmonic pumping is switched off at time $t = 0$, and the oscillation amplitude then starts to decay. The low-frequency modulation of the signals shown in Figure 11 is due to uncontrolled surface oscillations attributable to cryostat vibrations. One can see in Figure 11 that the decay in the narrow cell proceeds appreciably faster than in the wide one. Clearly, the specific energy loss by friction on the container bottom and walls is much stronger than in the wide cell. For this reason, the detailed measurements of the relaxation processes were carried out with the wide cell.

In Figure 12, the time dependences of the signal amplitudes $P(t)$ for pump frequencies of (a) 97 and (b) 173 Hz are obtained by averaging the absolute value of $P(t)$ over a time interval that is a multiple of a half period of the fundamental frequency. It turned out that the decrease in signal amplitude with time after switching off the pumping can be described by an exponential law $P(t) \sim \exp(-t/\tau)$, where the time constant is equal to $\tau = (0.3 \pm 0.03)$ s for the frequency $\omega_p/2\pi = 97$ Hz and is half that value, $\tau = (0.15 \pm 0.02)$ s, for a pump frequency of 173 Hz.

To study the time evolution of the spectrum I_ω of the correlation function, we used the short-time windowed Fourier transform procedure (Mallat, 1999), which is applicable because the experimentally observed signal time decay is much longer than the period of the harmonic force exciting the surface; that is, $\tau \gg 2\pi/\omega_p$. This allows the choice of a time
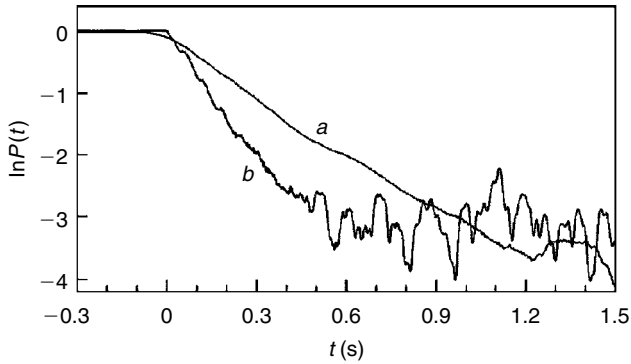
FIGURE 12 Time dependence of the signal amplitude $P(t)$ recorded in the wide cell. The pump frequency $\omega_p/2\pi$ was (a) 97 and (b) 173 Hz.

window with a size smaller than the signal time decay but much larger than the period of the exciting force. By shifting the window position in time, we succeeded in studying the spectral evolution of the turbulent cascade after switching off the pumping. The surface oscillation spectra P_ω^2 for a pump frequency of 97 Hz are shown in Figure 13 at three instants of time after switching off the pumping: after (a) 0.031, (b) 0.49 and (c) 1.07 s.

Immediately after switching off the pumping, the spectrum $I_\omega \sim P_\omega^2$ of the correlation function (Figure 13a) is still close to the steady state distribution of the nonlinear surface oscillations during the narrow-band pumping (Brazhnikov et al., 2002b). The fundamental peak is positioned at the pump frequency of 97 Hz, while the higher harmonics form a cascade whose peak heights are described by a power-law frequency dependence $P_\omega^2 \sim \omega^{-3.5}$. The arrow indicates the position of the high-frequency edge $\omega_b/2\pi \approx 5\,\text{kHz}$ of the inertial range. At time $\Delta t = 0.49\,\text{s}$ after switching off the pumping (Figure 13b), the wave amplitude at frequency $\omega_p/2\pi$ has decreased by approximately a factor of 3, as compared to Figure 13a, while the boundary frequency $\omega_b/2\pi$ has decreased to $\approx 2\,\text{kHz}$. The final decay stage after $\Delta t = 1.07\,\text{s}$, when only a few harmonics are excited, is shown in Figure 13c. It is remarkable that, over a rather longtime interval $\Delta t \leq 0.6\,\text{s}$ after switching off pumping, the high-frequency portion of the spectrum can be described by the distribution $P_\omega \sim \omega^{-3.5}$, which is typical of the steady state cascade; that is, the shape of the spectrum is retained during vibrational relaxation, but the oscillations start to decay on the high-frequency domain of the spectrum.

This observation of a quasistationary spectrum over a rather longtime after switching off the pumping allows one to infer that the nonlinear interaction time of the capillary waves is much shorter than the viscous damping time of a linear wave at the pump frequency ω_p. This must
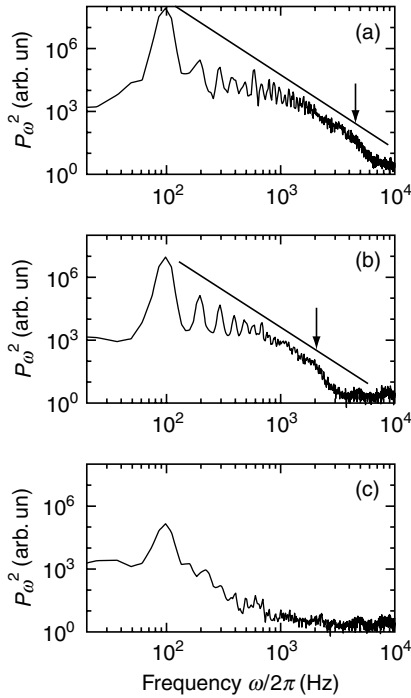
FIGURE 13 Instantaneous spectra of liquid hydrogen surface oscillations in the wide cell at different times after switching off the pumping at frequency $\omega/2\pi = 97$ Hz: after $\Delta t =$ (a) 0.031, (b) 0.49 and (c) 1.07 s. The solid line corresponds to the power-law $P_\omega^2 \sim \omega^{-7/2}$. The arrows in plots (a) and (b) mark the position of the high-frequency edge ω_b of the inertial range.

still be the case even where the surface-oscillation amplitude at pump frequency $\omega_p/2\pi = 97$ Hz has become one order of magnitude smaller than its initial value: it decreases from 0.02 mm 0.03 s after switching off pumping to 0.002 mm after 0.6 s (Figures 13(a) and (b)). As a result, the relatively intense energy exchange between waves with frequencies lying in the inertial range results in a stabilisation of the power-law spectrum in the low-frequency region $\omega < \omega_b$. At the same time, it follows from the experiment (see Figure 13 and Figure 15 below) that the characteristic relaxation time of surface oscillations is determined by the viscous damping of waves at the pump frequency, and decay of the cascade is accompanied by a shift of the high-frequency edge ω_b of the inertial range towards lower frequencies. Hence, when describing the relaxation of nonlinear fluid-surface oscillations within the framework of the kinetic equation (Equation (3)), one should not ignore viscous loss even at the larger surface-oscillation amplitudes.

3.4 Formation of Capillary Turbulence

Figure 14 shows the instantaneous spectra P_ω^2 calculated for times (a) $t = 0\,\text{s}$, (b) $t = 0.58\,\text{s}$ and (c) $t = 1.51\,\text{s}$ after switching on the driving force at a frequency $\omega_p/2\pi = 56\,\text{Hz}$. Figure 14a thus corresponds to the spectrum of liquid hydrogen surface oscillations caused by low-level external noise (mechanical vibration of the cryostat). Figures 14b and 14c demonstrate the formation of the turbulent spectrum at subsequent moments of time.

It can be seen from Figures 13 and 14 that at each moment of time after switching the driving force off and on, the spectra of surface oscillations are similar to the steady state spectra observed in our previous experiments at sufficiently large amplitudes. This implies that both the processes of decay, and the processes of formation, of turbulence are controlled by the same relaxation mechanisms.

It was shown in Section 3.3 that the decreasing signal amplitude following removal of the driving force could be well described by an exponential function $P(t) \sim \exp(-t/\tau)$, where τ is the effective relaxation time. The dependence of τ on frequency $\omega_p/2\pi$ measured in experiments with liquid
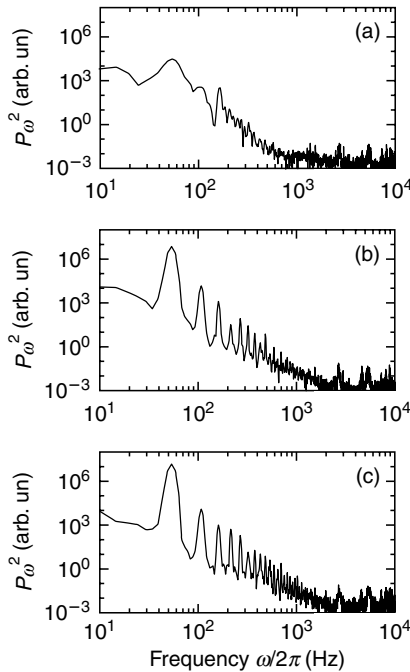
FIGURE 14   Instantaneous spectra of liquid hydrogen surface oscillations calculated for different time intervals after switching on the driving force at frequency $\omega_p/2\pi = 56\,\text{Hz}$: (a) $t = 0\,\text{s}$ (at the moment of time immediately before the switching on the driving force), (b) $t = 0.58\,\text{s}$ and (c) $t = 1.51\,\text{s}$.
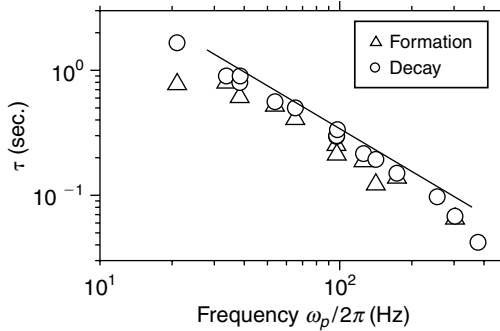
FIGURE 15 Effective relaxation time τ of liquid hydrogen surface oscillations plotted as a function of the driving frequency ω_p after removal of the driving force (open circles) and switching on the driving force (triangles). The solid line corresponds to the viscous damping time for a capillary wave τ_v of frequency $\omega = \omega_p$ calculated from known parameters of liquid hydrogen.

hydrogen is shown by open circles in Figure 15. The straight line shows the dependence of the viscous (linear) damping time for capillary waves τ_v defined by Equation (12), at frequency $\omega = \omega_p$, calculated from the known parameters (Verkin, 1991) of liquid hydrogen at 15.5 K. It is clearly evident from Figure 15 that the measured relaxation time τ for the decay of the turbulent cascade is close to the viscous damping time τ_v of the waves. The triangles in Figure 15 shows the characteristic time of formation of the turbulent cascade after switching on the driving force within the frequency range from 20 to 300 Hz. It is clear from Figure 15 that the time of formation is close to the time of decay and to the time of viscous attenuation of the surface waves at the frequency ω_p.

3.5 Suppression of High-Frequency Turbulent Oscillations of the Fluid Surface by Additional Low-Frequency Pumping

In this Section, we describe investigations of how the spectrum of capillary turbulence on the surface of liquid hydrogen evolves when an additional low-frequency pumping is switched off/on. It was found that when the additional pumping was switched on, turbulence in the high-frequency range was suppressed and the inertial frequency range decreased. When the additional pumping was switched off, the amplitudes of high-frequency turbulent oscillations increased again and the inertial range expanded.

Thus, there were two types of measurement. In the first, waves on the fluid surface were excited by pumping simultaneously at two different resonant frequencies of the cell. After the formation of the steady turbulent distribution, pumping at one of the frequencies (additional frequency)

was stepwise switched off, whereas the intensity of pumping at the other (main) frequency remained unchanged. In measurements of the second type, waves on the fluid surface were first excited at one of the resonant frequencies of the cell and then an additional pumping at another resonant frequency was switched on. In each case, a transient process in the turbulent system of capillary waves was studied after the additional pumping was switched off or on.

Figure 16 shows the steady state spectra of liquid hydrogen surface oscillations before and after the additional pumping is switched off: (a) for simultaneous pumping at two resonant frequencies of the cell: main $\omega_2/2\pi = 274$ Hz and an additional $\omega_1/2\pi = 61$ Hz; and (b) after pumping at the additional frequency ω_1 is switched off. It is worth noting that the wave energy $E_{\omega_1} \propto \omega_1^{4/3}|\eta_{\omega_1}|^2$ at the frequency ω_1 is an order of magnitude lower than the wave energy E_{ω_2} at the frequency ω_2. For this reason, the oscillation spectrum in Figure 16a can be treated as the capillary turbulence spectrum that is generated by the main harmonic pumping at the frequency $\omega_2/2\pi = 274$ Hz and is perturbed by the additional pumping at the frequency $\omega_1/2\pi = 61$ Hz. Correspondingly, near the relatively high
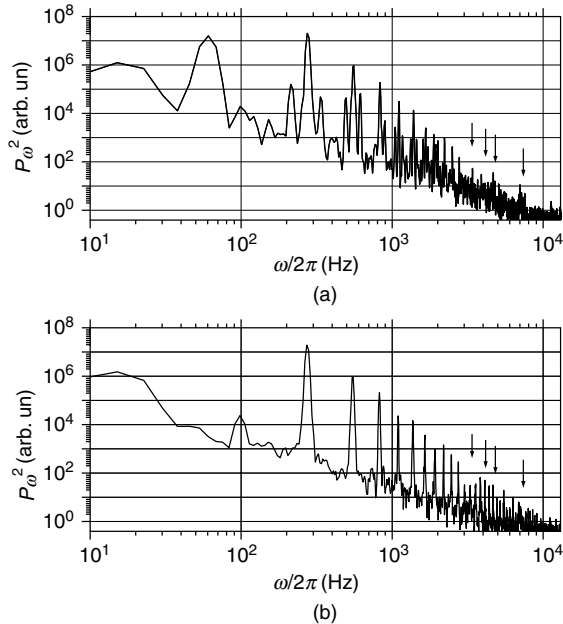
FIGURE 16   Stationary spectrum of the oscillations of the liquid hydrogen surface while pumping (a) simultaneously at two resonant frequencies $\omega_1/2\pi = 61$ Hz and $\omega_2/2\pi = 274$ Hz and (b) only at the main resonant frequency $\omega_2/2\pi = 274$ Hz. The positions of the 13th, 16th, 19th and 29th harmonics of the main frequency $\omega_2/2\pi$ are shown by arrows.

peaks at frequencies that are multiples of ω_2, relatively low peaks at combination frequencies are located on both sides of the harmonics of the main frequency at a distance of the frequency ω_1 from it. The distribution in Figure 16(b) is the stationary spectrum of capillary turbulence generated by the harmonic force at the frequency ω_2: the amplitude of peaks at frequencies that are multiples of the frequency ω_2 decreases in a power-law as the frequency increases. It is seen that the amplitudes of the high-frequency peaks generated by pumping at one frequency (Figure 16b) are noticeably larger than those generated by pumping at two frequencies (Figure 16a).

Figure 17 shows the time dependence of the amplitude squared for waves on the surface of liquid hydrogen at the main (circles) and additional (squares) frequencies: recall that $P_\omega^2 \propto |\eta_\omega|^2$ according to Equations (8) and (18). Pumping at the additional frequency ω_1 is switched off at time $t \approx 0$, whereas the pumping amplitude at the main frequency ω_2 remains unchanged. It is clear from the figure that the amplitude of the wave of frequency ω_1 decreases almost exponentially with time and, in agreement with our previous discussion, the characteristic decay time nearly coinciding with the viscous damping time $\tau_v \sim \gamma_{\omega_1}^{-1}$ of the capillary wave with the frequency ω_1.

Figure 18 shows the time dependence of the amplitude squared for peaks at frequencies that are multiples of the main pumping frequency ω_2 when the additional pumping is switched off at the time $t = 0$. The triangles, closed squares, open squares and circles correspond to the 13th (3.57 kHz), 16th (4.49 kHz), 19th (5.19 kHz) and 29th (7.96 kHz) harmonics of the main frequency ω_2, respectively. The positions of the corresponding harmonics are shown by arrows in Figure 16. As seen in Figure 18, after the additional pumping is switched off, the amplitudes of the high-frequency harmonics increase by a large factor in a time comparable with the damping time for the wave at the frequency ω_1 (Figure 17).

Figure 19 shows an interval of the spectrogram of the surface oscillations for frequencies 3 to 10 kHz in the time interval from -0.8 to 4 s.
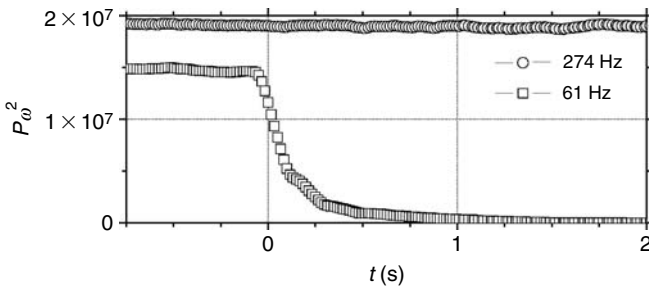
FIGURE 17 Time dependence of the amplitude squared for waves on the surface of liquid hydrogen at the main (circles) and additional (squares) frequencies when the additional pumping is switched off at the time $t = 0$.
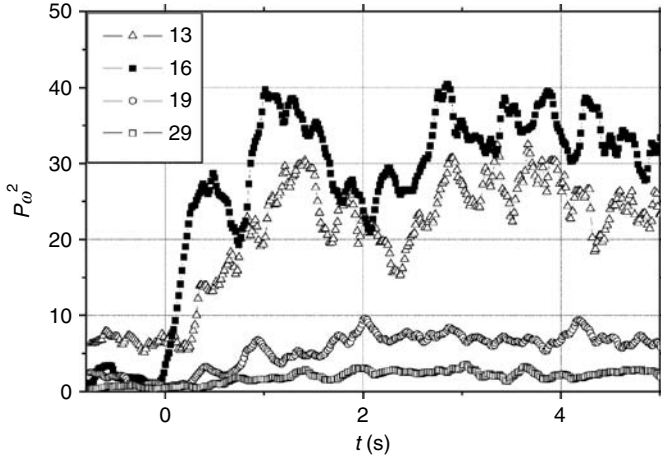
FIGURE 18   Time dependence of the wave amplitude squared for peaks at frequencies that are multiples of the main pumping frequency ω_2 when the additional pumping at the frequency ω_1 is switched off at time $t = 0$. The triangles, closed squares, open squares and circles correspond to the 13th (3.57 kHz), 16th (4.49 kHz), 19th (5.19 kHz) and 29th (7.96 kHz) harmonics of the main frequency $\omega_2/2\pi$, respectively. The positions of the corresponding harmonics are shown by arrows in Figure 16.
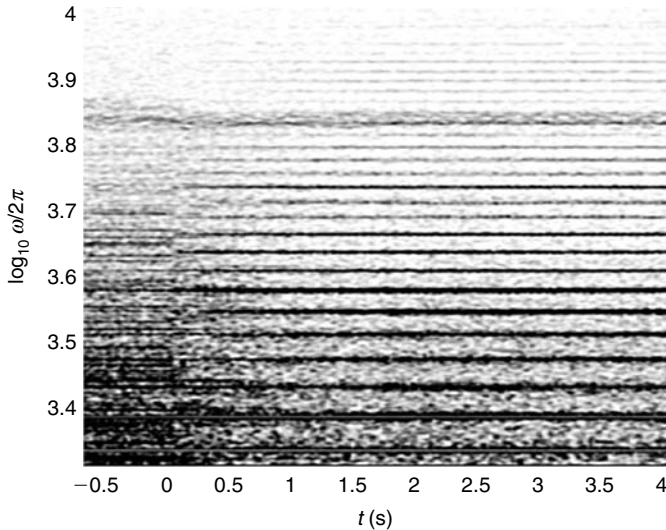
FIGURE 19   Spectrogram of the oscillations of the surface of liquid hydrogen upon simultaneous pumping at frequencies $\omega_1/2\pi = 61$ Hz and $\omega_2/2\pi = 274$ Hz. Darker regions correspond to larger wave amplitudes. The gray colour density is proportional to the amplitude squared for waves with the corresponding frequencies.

The ordinate axis shows the logarithm of the frequency and the abscissa axis presents the time in seconds. The gray colour density is proportional to the amplitude squared for waves with corresponding frequencies. After the additional pumping is switched off ($t > 0$), the spectrogram exhibits the regular density maxima (black horizontal straight lines) at frequencies that are multiples of the main pumping frequency ω_2, which corresponds to an increase in the amplitude of the high-frequency surface oscillations with time.

Analysis of the evolution of the spectrum of the fluid-surface oscillations shows that when the additional pumping is switched on at the time $t = 0$, the amplitudes of the high-frequency oscillations decrease at $t > 0$. Thus, the observed evolution of the turbulent spectrum is completely reversible.

3.6 Turbulence on Normal and Superfluid Helium

High-frequency oscillations on the surface of quantum liquids are traditionally treated using the language of quasiparticles – quantised capillary waves on the surface, or ripplons (Landau et al., 1980). It can easily be estimated that in the experiments reported, the range of frequencies where the surface waves are generated due to nonlinearity is limited by the Kolmogorov cutoff frequency $\omega \leq \omega_b \sim 10^5$ s^{-1}, at which the nonlinear energy transfer mechanism changes to viscous damping. The boundary frequency ω_b is much lower than the frequency of thermal ripplons on the surface of superfluid helium, $\omega_T \sim kT/\hbar \sim 10^{11}$ s^{-1} at $T \sim 1.5$ K. Hence, we are working with a system of essentially subthermal ripplons.

The experimental arrangements were similar to those used in our earlier studies of surface turbulence on the positively charged surface of liquid hydrogen, see Section 2 above. We perform measurements on the surface of liquid helium in its normal state (He I) at temperature $T = 4.2$ K and in its superfluid state (He II) at $T = 1.95$ K; recall that the λ (normal-to-superfluid) transition in liquid ^{4}He occurs at $T_\lambda = 2.17$ K. The cup was 30.5 mm in inner diameter. The liquid helium layer was 4 mm thick. The top capacitor plate was located above the cup at a distance of 3 mm from the liquid surface. The DC voltage applied between the cup and the top capacitor plate was 600 V. The waves on the charged surface were excited by a periodic driving voltage of amplitude 150 V applied between the cup and the top capacitor plate, in addition to the DC voltage.

Figure 20 shows the spectra of waves $|P_\omega|^2$ on the surfaces of He I when driving the surface at a resonant frequency of the cell $\omega_p/2\pi = 18.5$ Hz (plot(a)) and of He II when driving at a resonant frequency $\omega_p/2\pi = 18$ Hz (plot (b)). The resonant frequencies shift slightly due to changes in the surface tension of the liquid with temperature. It can be seen that as in the experiments with liquid hydrogen (cf. Section 3.1), the fundamental
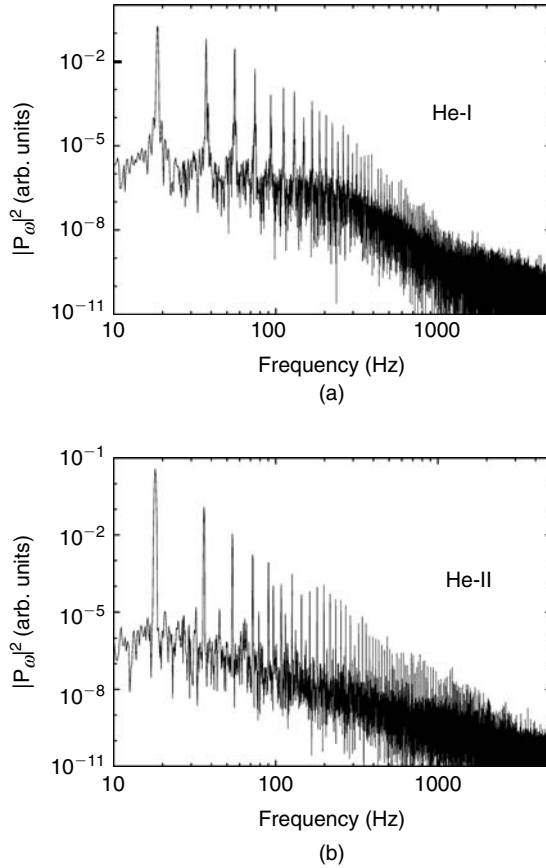
FIGURE 20   Spectrum of standing capillary waves on the surfaces of (a) normal and
(b) superfluid helium.

peak at the spectral curve is positioned at the driving frequency and the
high frequency peaks are positioned at frequencies multiple to the driving
frequency.

   It is evident from Figure 20 that oscillations of the surface are observed
in the frequency range up to the boundary frequency $\omega_b/2\pi \approx 1\,\text{kHz}$ in
experiments with He I and up to $\omega_b/2\pi \approx 5\,\text{kHz}$ in experiments with
He II. Both values of $\omega_b/2\pi$ are much higher than the driving frequency
$\omega_p/2\pi \approx 18\,\text{Hz}$. The relative width of the inertial interval ω_b/ω_p, in which
the turbulent oscillations were observed, is $\sim$50 for normal helium and
$\sim$250 for superfluid helium. For comparison, the relative width of the
inertial interval for waves on the liquid hydrogen surface was $\sim$50 (see
Section 3.2). Thus, measurements made with He II allowed us to expand
the relative frequency range accessible for studies of nonlinear capillary
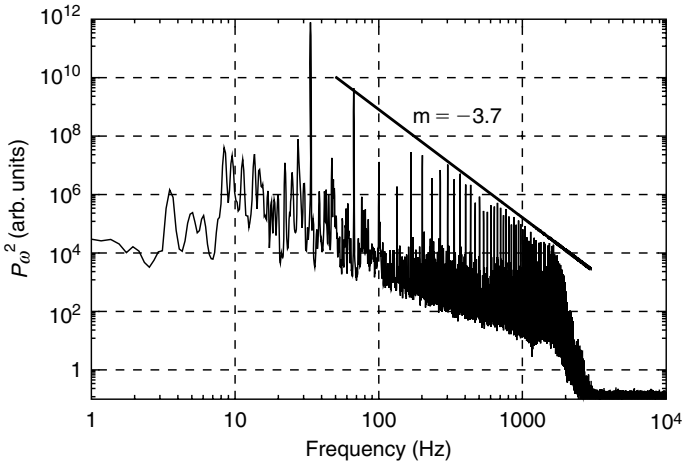
FIGURE 21 Spectrum of capillary waves on the surfaces of superfluid helium measured at $T = 1.65\,K$. The driving frequency was 33.6 Hz. Solid line corresponds to a power-like dependence $|P_\omega|^2 \propto \omega^{-3.7}$.

waves by a factor of about 5, which is of importance for the accurate checking of predictions of the existing theory of steady state and non-stationary capillary turbulence.

A high-frequency edge of the inertial range of capillary turbulence was observed in experiments with superfluid helium, see Figure 21. Inside the inertial range, the dependence of the spectral peak heights on a wave frequency follows a power-like law $|P_\omega|^2 = \text{const} \times \omega^m$ with the exponent m close to -3.7, in agreement with the results obtained in experiments with liquid hydrogen. At frequencies close to the boundary frequency, where viscous damping becomes essential, a sharp decrease of wave amplitudes was observed, as is clearly seen on Figure 21 (cf. the observations in liquid-hydrogen experiments, Figure 8). We plan to study the dependence of the boundary frequency on the driving force amplitude in detail in the near future.

4. THEORETICAL CONSIDERATION OF THE DECAY OF CAPILLARY TURBULENCE

4.1 Self-Similar Decay of Capillary Turbulence

We now present a brief theoretical discussion (Kolmakov, 2006) of the decay of capillary turbulence on the surface of a viscous liquid after the stepwise removal of external pumping. In our subsequent analyses, we suppose that the viscosity of the liquid is sufficiently small and the

boundary frequency ω_b of the inertial range is much higher than the pumping frequency ω_p. In view of experimental observations and numerical calculations (Brazhnikov et al., 2004; Kolmakov et al., 2004), it is natural to assume that the decay of turbulence is self-similar due to the significant difference between the characteristic dissipative and pumping frequency scales.

We search for a nonstationary self-similar solution of the kinetic equation (Equation (3)) describing free decay of the turbulent cascade, in the following form

$$n_{\mathbf{k}} = 4\nu k_b^{\beta}(t)\, g(\xi), \tag{19}$$

where $k_b(t)$ is the time-dependent high-frequency boundary of the inertial range defined in terms of wavenumber, $g(\xi)$ is some function of the self-similar variable $\xi = k/k_b(t)$, and β is an exponent. We assume that the external pumping is stepwise switched off at time $t = 0$; that is, $F_{\mathbf{k}}(t) = 0$ for $t \geq 0$. The numerical factor on the right-hand side of Equation (19) is separated for the convenience of further calculations.

After substitution of the function (Equation (19)) into the kinetic equation (Equation (3)) with $F_{\mathbf{k}} = 0$, the collision integral and dissipative term become $St(n_k) \sim k_b^{2\beta+5}$ and $\gamma_{\mathbf{k}} n_{\mathbf{k}} \sim k_b^{\beta+2}$, respectively. Under the assumption that the evolution of the spectrum is self-similar, we should set $2\beta + 5 = \beta + 2$. From this equality, we obtain

$$\beta = -3 \tag{20}$$

for the exponent in Equation (19).

The substitution of Equation (19) with the exponent β given by Equation (20) into kinetic equation (Equation (3)) yields an equation for the self-similar function $g(\xi)$

$$-(1/4\nu)(3g(\xi) + \xi g'(\xi))k_b(t)^{-3}\dot{k}_b(t) = I(\xi) - \xi^2 g(\xi), \tag{21}$$

where the dot stands for differentiation with respect to time, the prime means differentiation with respect to the variable ξ, and $I(\xi)$ is an integral operator that is quadratic in $g(\xi)$ and is defined by the equality

$$St(n_{\mathbf{k}}(t)) = k_b(t)^{-1} I(\xi).$$

The boundary of the instantaneous inertial range $k_b(t)$ must satisfy the equation

$$k_b^{-3}\dot{k}_b = -C, \tag{22}$$

where C is a certain constant that is positive in accordance with the shift of the edge of the inertial range to lower frequencies with increasing time. From Equation (22), it follows that

$$k_b(t) = \frac{k_b(0)}{\sqrt{1 + t/\tau}}, \tag{23}$$

where $k_b(0)$ is the position of the edge of the inertial range at the time $t = 0$ of removal of the external pumping, and $\tau = 1/2Ck_b(0)$ is the characteristic turbulence decay time. The time dependence of the boundary frequency of the inertial range is described by the expression

$$\omega_b(t) = \frac{\omega_b(0)}{(1 + t/\tau)^{3/4}}, \tag{24}$$

where $\omega_b(0)$ is the initial boundary frequency. For $t \gg \tau$, the boundary frequency of the inertial range depends on time as $\omega_b(t) \sim t^{-3/4}$.

After substitution of solution (Equation (23)) into Equation (21), the constant $C/4\nu$ can be excluded from the latter equation by the following change of variables:

$$\xi \rightarrow (C/4\nu)^{1/2}\xi, \qquad g \rightarrow (C/4\nu)^{-3/2}g. \tag{25}$$

After transformation (Equation (25)), the equation for the self-similar function $g(x)$ acquires the form

$$3g(\xi) + \xi g'(\xi) - I(\xi) + \xi^2 g(\xi) = 0. \tag{26}$$

In what follows, we suppose that the above change of variables has been made.

The boundary conditions for the integro-differential equation (Equation (21)) are of the form

$$Q_k \rightarrow 0 \quad \text{at } k \rightarrow 0, \tag{27}$$
$$g(\xi) \rightarrow 0 \quad \text{at } \xi \rightarrow \infty, \tag{28}$$

where

$$Q_k = -2\pi \int_0^k dk'k'\omega_{k'} St(n_{\mathbf{k}'}) \tag{29}$$

is the energy flux in the K space towards the larger wave number domain (Zakharov et al., 1992). Condition in Equation (27) corresponds to the absence of low-frequency external pumping at $t > 0$. For the case of the

free turbulence decay under consideration, where the wave spectrum is described by Equation (19) with the exponent given by Equation (20), Equation (29) for the energy flux takes the form

$$Q_k = -2\pi \left(\frac{\alpha}{\rho}\right)^{1/2} k_b(t)^{5/2} \int_0^{\xi_k(t)} \mathrm{d}\xi\, \xi^{5/2} I(\xi), \tag{30}$$

where $\xi_k(t) = k/k_b(t)$. For the satisfaction of boundary condition (Equation (27)) at small wave numbers, the self-similar function must satisfy the condition

$$g(\xi) \leq \mathrm{const}\, \xi^{-m} \quad \text{at } \xi \to 0, \tag{31}$$

Here, $m < m_0$, where $m_0 = 17/4$ is the negative of the Kolmogorov exponent in stationary spectrum (Equation (7)).

Below, we analyse the asymptotic expressions for the function $g(\xi)$ in various regions of wave numbers (we assume that $k > k_p$, where k_p is the wave number of the capillary wave whose frequency is on the order of the characteristic pumping frequency ω_p). At $\xi \ll 1$, the nonlinear and dissipative terms can be disregarded in Equation (26). In this case, the self-similar function is given by the expression

$$g(\xi) = \mathrm{const}\, \xi^{-3}. \tag{32}$$

According to Equations (19) and (32), the wave spectrum at small wave number $k \ll k_b$ for the self-similar decay of turbulence takes the form

$$n_{\mathbf{k}} = \mathrm{const}\, k^{-3} \tag{33}$$

and is time independent. We note that wave spectrum (Equation (33)) for small k values differs from stationary spectrum (Equation (7)). According to Equation (33), the frequency distribution of the energy of capillary waves

$$E_\omega = 2\pi k \omega n_{\mathbf{k}} (\mathrm{d}k/\mathrm{d}\omega), \tag{34}$$

(ω is the frequency of the wave with the wave number k) in the low-frequency domain $\omega \ll \omega_b$, acquires the form

$$E_\omega = \mathrm{const}\, \omega^{-2/3}. \tag{35}$$

For $\xi \gg 1$, the nonlinear term $I(x)$ is negligibly small due to the smallness of the function $g(\xi)$ proportional to the occupation number $n_{\mathbf{k}}$. In this case,

from Equation (26), we obtain

$$g(\xi) = \text{const} \, \xi^{-3} \exp(-\xi^2/2). \tag{36}$$

Thus, as the wave number increases, the wave spectrum in the dissipative region $k \gg k_b$, where viscous damping prevails over nonlinear energy transfer, decreases exponentially as

$$n_{\mathbf{k}}(t) = \text{const} \, k^{-3} \exp\left(-\frac{k^2}{2k_b(t)^2}\right). \tag{37}$$

The distribution of energy at high frequencies $\omega \gg \omega_b$ is of form

$$E_\omega(t) = \text{const} \, \omega^{-2/3} \exp\left(-\frac{1}{2}\left(\frac{\omega}{\omega_b(t)}\right)^{4/3}\right). \tag{38}$$

According to Equations (32) and (36), the self-similar function satisfies the necessary boundary conditions (Equations (28) and (31)).

The form of the function $g(\xi)$ for intermediate wavenumbers $k \sim k_b$ depends on the amplitudes of the waves on the surface, that is, on the amplitude of the external pumping before its removal. For small pumping amplitudes, the function $g(\xi)$ is small; that is, $g \ll 1$. In this case, the term nonlinear in $g(\xi)$ can be disregarded in Equation (26) and the wave spectrum is close to the dissipative distribution (Equation (37)). We note that Equation (37) at $\xi \ll 1$ is transformed to Equation (33); therefore, Equation (37), in the case of small pumping amplitudes, describes the spectrum $n_{\mathbf{k}}(t)$ of capillary waves for $t > 0$ over the entire wave number interval $k > k_p$. Formula in Equation (37) becomes inapplicable at very large times $t \sim \tau(k_b(0)/k_p)^2$ at which $k_b(t) \sim k_p$, and the width of the inertial range approaches zero.

At large pumping amplitudes when $g \gg 1$ for $\xi \sim 1$, the nonlinear term $I(\xi)$ dominates in Equation (26) and

$$g(\xi) \sim \xi^{-17/4} \tag{39}$$

because the spectrum (Equation (7)) is the stationary solution of the kinetic equation in the absence of viscosity. This corresponds to the following behaviour at intermediate values $k \sim k_b$:

$$n_{\mathbf{k}}(t) = \text{const} \, k_b(t)^{5/4} k^{-17/4}. \tag{40}$$

According to this expression, the dependence of the wave spectrum $n_{\mathbf{k}}$ on the wave number k for intermediate wave numbers $k \sim k_b$ at large pumping amplitudes coincides with stationary power-law distribution (Equation (7)). The time dependence of the effective energy flux Q_{eff} defined by the relation $n_{\mathbf{k}}(t) = AQ_{\text{eff}}(t)^{1/2}\rho^{3/4}\alpha^{-1/4}k^{-17/4}$ has the form

$$Q_{\text{eff}}(t) = \left(k_b(t)/k_b(0)\right)^{5/2} Q_0,$$

where Q_0 is the flux in the steady state before the removal of external pumping. According to Equation (23), the effective energy flux for large times $t \gg \tau$ approaches zero as $Q_{\text{eff}} = (t/\tau)^{-5/4}Q_0$. Correspondingly, the distribution of the energy of waves for intermediate frequencies $\omega \sim \omega_b$ has the form

$$E_\omega \sim \omega_b(t)^{5/6}\omega^{-3/2}. \tag{41}$$

Thus, in the process of the self-similar decay of turbulence, as time t increases, the frequency distribution of the amplitude of waves in this frequency range decreases uniformly and remains quasi stationary form (Equation (7)). This conclusion agrees qualitatively with the observation results described in Section 4.3.

The total energy of the system of capillary waves given by Equation (34) decreases for $t > 0$ as

$$E = \int d\omega\, E_\omega = 8\pi\nu B(\alpha/\rho)^{1/3}\omega_b(t)^{1/3}, \tag{42}$$

where

$$B = \int_0^\infty d\xi\, \xi^{5/2}g(\xi)$$

and the dependence $\omega_b(t)$ is defined by Equation (24). Most of the energy is concentrated at frequencies $\omega \sim \omega_b$ in contrast to stationary distribution (Equation (7)), where most of the energy is concentrated around ω_p. Therefore, the real wave distribution $n_{\mathbf{k}}$ in the decay of turbulence *asymptotically* approaches distribution (Equation (19)) at large times t. The total energy at $t \gg \tau$ approaches zero as $E \sim (t/\tau)^{-1/4}$. We note that the energy flux P_k given by Equation (30) also has a maximum for wave numbers $k \sim k_b$.

In the experiments on the decay of capillary turbulence on the surface of liquid hydrogen described in Section 3.3, the relative width of the inertial range is equal to $\omega_b/\omega_p \sim 50$ at the time of removal of the

external pumping. As follows from Equations (7) and (11), for the case of the low-frequency noise pumping, the characteristic time of the nonlinear interaction between waves of characteristic frequency ω is $\tau_n \sim \omega^{-1/2}$, whereas the characteristic time for the viscous damping of waves of the same frequency given by Equation (12) is $\tau_v \sim \omega^{-4/3}$. Their ratio is $\tau_v/\tau_n \sim \omega^{-5/6}$. If, according to the results described in Section 3.3, we suppose that this ratio for frequencies ω on the order of the boundary frequency ω_b of the inertial range is $\tau_v/\tau_n \sim 1$, then this ratio for frequencies on the order of the pumping frequency is $\tau_v/\tau_n \sim (\omega_b/\omega_p)^{5/6} \sim 25$ at the cessation pumping and decreases rapidly as the turbulence decays. For the case of pumping at one resonant frequency, the stationary spectrum of capillary turbulence is given by Equation (10). In this case, the characteristic time of the nonlinear interaction is $\tau_n \sim \omega^{1/6}$, and the nonlinear-to-viscous time ratio at the pumping frequency is $\tau_v/\tau_n \sim (\omega_b/\omega_p)^{3/2} \sim 10^2$. Thus, even at the comparatively large ratio τ_v/τ_n, viscosity is of significant importance for the decay of turbulence on the surface of liquid hydrogen. We see also from Equation (40) that inside the inertial range, the distribution of capillary waves is close to the stationary distribution given by (Equation (7)) which is in qualitative agreement with our experimental observations described in Section 3.3.

4.2 Local Model of Capillary Turbulence

Equation (26) for the self-similar function $g(\xi)$ can only be solved numerically. The numerical investigation of the properties of solutions of Equation (26) is a separate problem and will be discussed elsewhere. In what follows, we calculate the self-similar function within the framework of a simplified model. In contrast to the theory (Zakharov et al., 1992) based on application of the kinetic equation, this model suggests that the expression for the energy flux through wave number scales is given by a polynomial in $n_{\mathbf{k}}$ – the so-called 'local' approximation in turbulence theory. The applicability of such an approximation to studies of the decay of capillary turbulence is based on the locality of the turbulence spectrum, which follows from the convergence of the collision integral $St(n_{\mathbf{k}})$ after substitution of the self-similar solution (Equation (19)) with asymptotic expressions (Equations (33), (37), and (40)) (the locality of the weak-turbulence spectra was analysed in detail by Zakharov et al. (1992)). This means that the evolution of the turbulent distribution of capillary waves is primarily determined by the interaction between waves with close frequencies. Similar local models were successfully used previously to study numerically the decay of capillary turbulence on the surface of the liquid (Kolmakov et al., 2004), the turbulence of gravity waves (Connaughton et al., 2003) and optical turbulence (Dyachenko et al., 1992).

In the simplest variant of the local model of capillary turbulence, the energy flux through the frequency scales is of the form

$$Q_\omega = \text{const } \omega^3 E_\omega^2. \tag{43}$$

For more convenient comparison of the results of our calculations with experimental data, we change the wave number k to the circular frequency ω as the independent variable, and express $n_\mathbf{k}$ in terms of the energy E_ω (Equation (34)) of waves of frequency $\omega = \omega(k)$. The relationship between ω and k for capillary waves is given by Equation (6). In this model, an equation similar to the kinetic equation (Equation (3)) in the wave turbulence theory takes the form

$$\frac{\partial E_\omega}{\partial t} + \frac{\partial Q_\omega}{\partial \omega} + v_0 \omega^{4/3} E_\omega = F_\omega(t), \tag{44}$$

where Q_ω is given by Equation (43) and $v_0 = 4v(\rho/\alpha)^{2/3}$. In order to simplify the formulas below, we set const = 1 in Equation (43), which corresponds to an appropriate choice of units for the time t and frequency ω.

In the model specified by Equations (43) and (44), the steady state frequency distribution of the wave energy E_ω for frequencies $\omega > \omega_p$ is described by the equation

$$\frac{\partial}{\partial \omega}(\omega^3 E_\omega^2) + v_0 \omega^{4/3} E_\omega = 0,$$

from which we obtain

$$E_\omega = \omega^{-3/2}\left(Q^{1/2} - \frac{3}{5}v_0\omega^{5/6}\right). \tag{45}$$

Thus, the amplitudes of the waves in the steady state in this model are nonzero only in the finite frequency range $\omega \leq \omega_b$, where the boundary frequency is given by the expression

$$\omega_b = (5/3v_0)^{6/5}Q^{3/5}. \tag{46}$$

For frequencies lower than the boundary frequency ω_b (but higher than the pumping frequency ω_p), Equation (45) acquires the form

$$E_\omega = Q^{1/2}\omega^{-3/2}. \tag{47}$$

The distribution (Equation (47)) corresponds to the power-law solution (Equation (7)) of the kinetic equation (Equation (3)).

The self-similar solution given by Equations (19) and (20), which describes the evolution of the freely decaying turbulent cascade, corresponds to the following solution of Equation (44) of the local model (with external pumping $F_\omega = 0$):

$$E_\omega(t) = v_0\omega_b(t)^{-2/3}f(x), \qquad (48)$$

where $x = \omega/\omega_b(t)$ is the self-similar variable defined in the wave frequency scale. An equation for the self-similar function $f(x)$ that is similar to Equation (26) is of form

$$\frac{2}{3}f(x) + xf'(x) + \frac{\partial}{\partial x}x^3f^2(x) + x^{4/3}f(x) = 0. \qquad (49)$$

The asymptotic solutions of Equation (49) in various frequency ranges have the form (the frequencies are assumed to be larger than the characteristic pumping frequency ω_p)

$$f(x) = \text{const}\, x^{-2/3} \quad \text{for } x \ll 1, \qquad (50)$$

$$f(x) = \text{const}\, x^{-2/3}\exp(-3x^{4/3}/4) \quad \text{for } x \gg 1. \qquad (51)$$

For large pumping amplitudes corresponding to $f(x) \gg 1$ at $\xi \sim 1$, the quasistationary asymptotic expression has the form

$$f(x) = \text{const}\, x^{-3/2}. \qquad (52)$$

Correspondingly, Equations (33), (37) and (40) are obtained for the wave occupation numbers $n_\mathbf{k}$. Thus, the asymptotic expressions for the occupation number are model-independent.

Figure 22 shows the self-similar function $f(x)$ calculated numerically from Equation (49) for four values of $f_1 = f(x)|_{x=1}$ (in effect, the different amplitudes of pumping before its cessation). As is seen in Figure 22, the function $f(x)$ for $x \ll 1$ is approximated by asymptotic expression (Equation (50)). It is also seen that quasistationary asymptotic expression (Equation (52)) is formed in a wide frequency range for $f_1 \geq 10$. The function $f(x)$ at $f_1 = 0.1$ is well approximated by Equation (51) for all x values in agreement with the above discussion.

The decay of capillary turbulence was also simulated numerically using the model specified by Equations (43) and (44). Figure 23 shows the frequency distributions of the energy of capillary waves E_ω that were
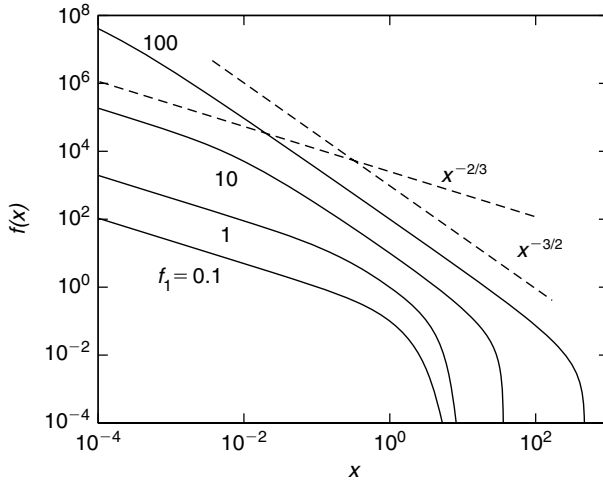
FIGURE 22   Self-similar function $f(x)$ calculated numerically for $f_1 = 100$, 10, 1 and 0.1 and plotted in logarithmic coordinates. The dashed straight lines correspond to power-law dependences (Equations (50) and (52)).
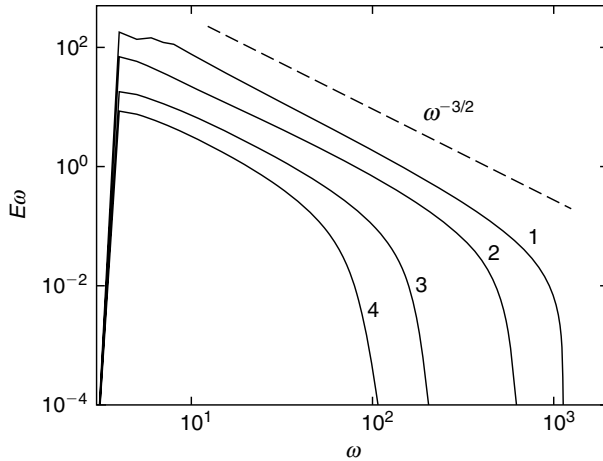
FIGURE 23   Frequency distributions of the energy E_ω of capillary waves at the times $t = 0$ (steady state spectrum, curve 1), 0.5 (curve 2), 2.0 (curve 3) and 4.0 (curve 4). The dashed straight line corresponds to the power-law dependence $E_\omega = const\ \omega^{-3/2}$.

calculated numerically for times $t = 0$ (steady state spectrum), 0.5, 2.0 and 4.0 after the stepwise removal of external broadband pumping. The external pumping is switched off at time $t = 0$. The pumping frequency is close to $\omega_p = 1$. The time t and frequency ω are given in dimensionless
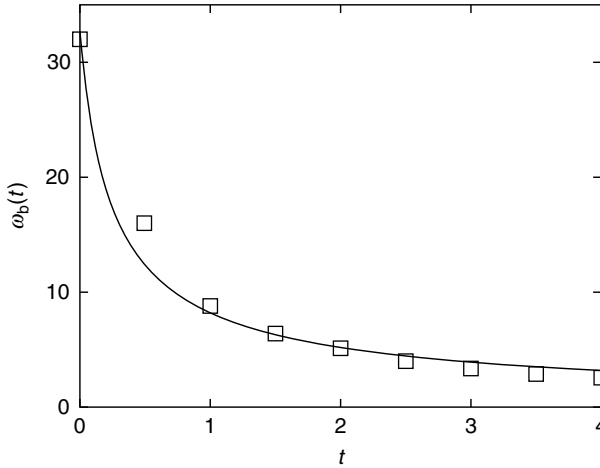
FIGURE 24 Time dependence of the boundary frequency $\omega_b(t)$ of the inertial range as obtained (squares) in numerical calculations and (line) from Equation (24) with $\omega_b(0) = 32.7$ and $\tau = 0.187$.

units. The dashed straight line corresponds to the power-law dependence $E_\omega = \text{const}\,\omega^{-3/2}$, see Equation (47). According to the calculation, the frequency distribution of the energy E_ω in the inertial range is close to the stationary distribution (Equation (47)) for a relatively long time after cessation of pumping. With the passage of time, the boundary frequency of the inertial range shifts towards lower frequencies.

The calculated distribution of energy E_ω at $t > 0$ and $\omega > \omega_p$ was approximated by the distribution (Equation (48)) with the function $f(x)$ calculated for $f_1 = 10$ (see Figure 22). The boundary frequency $\omega_b(t)$ of the inertial range and the common normalisation factor in Equation (48) were taken as fitting parameters. The resulting dependence $\omega_b(t)$ is shown in Figure 24 by squares with sizes corresponding to the calculation errors. The line in Figure 24 is plotted according to Equation (24) with parameters $\omega_b(0) = 32.7$ and $\tau = 0.187$ (dimensionless units). As follows from Figures. 22 to 24, the self-similar description of the decay of capillary turbulence, with inclusion of viscous losses, agrees with the numerical calculations.

4.3 Direct Numerical Study of Capillary Turbulence Decay

We have also modelled directly the free decay of capillary turbulence. The full kinetic equation (Equation (3)) with a dissipative term was solved numerically. The calculations were carried out in two steps. First, the driving force was switched on and we waited for some time until a steady state
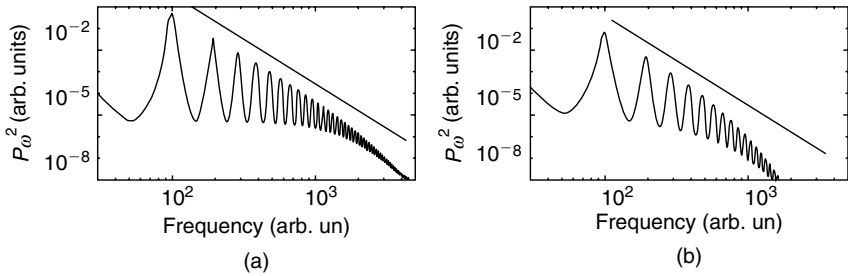
FIGURE 25 Results of numerical calculations of the decay of the turbulent spectrum after removal of the narrow-band driving force, for times corresponding to the experimental observations, shown in plots (a) and (b) of Figure 13.

distribution has been established in the system of waves. The driving force was then removed and we observed the decay of the turbulent spectrum.

The calculation was performed for capillary turbulence created under the actions of both wide-band and narrow-band pumping. The results obtained in the case of wide-band pumping were similar to those described in Section 5.2, where we used the local model of capillary turbulence.

The results following narrow-band driving, for times corresponding to the experimental observations in plots (a) and (b) in Figure 13, are presented in Figure 25. The frequency ω and the correlation function P_ω^2 are given in dimensionless units. The driving frequency was close to $\omega_p \approx 100$. It can be seen in Figure 25 that our calculations are in qualitative agreement with the experimental results (Section 3.3) and theoretical analyses (Section 4.1).

4.4 Numerical Studies of Effect of an Additional Low-Frequency Perturbation on High-Frequency Oscillations

Figure 26 shows the evolution of the steady state spectrum of capillary turbulence after switching on an additional low-frequency driving force. The calculations were performed with kinetic equation (Equation (3)), where the effect of viscous losses on the damping of capillary waves on the surface of liquid hydrogen is taken into account. The solid line in Figure 26 is the dimensionless stationary spectrum of surface oscillations (occupation number n_ω as a function of the wave frequency $\omega/2\pi$) generated by pumping at the two frequencies $\omega_1/2\pi = 10\,\text{Hz}$, and $\omega_2/2\pi = 50\,\text{Hz}$, simultaneously. The dashed line is the stationary spectrum of surface oscillations formed after the application of pumping at a frequency of $10\,\text{Hz}$, leaving the intensity of pumping at $50\,\text{Hz}$ unchanged. It is seen that the amplitude of the fluid-surface oscillations at frequencies $\omega/2\pi > 100\,\text{Hz}$
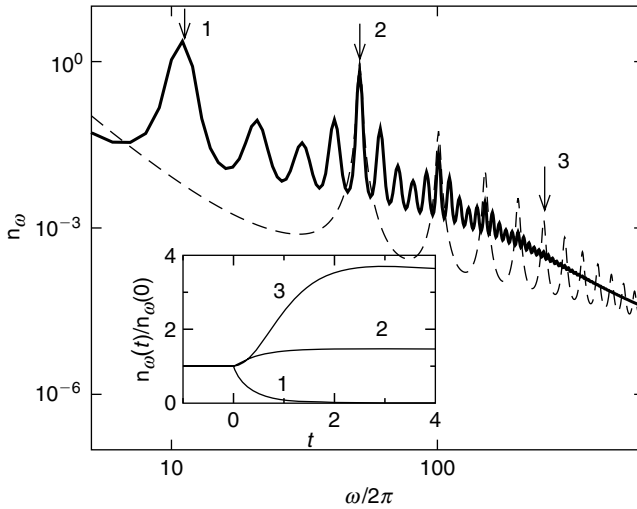
FIGURE 26 Numerically calculated stationary spectra of capillary turbulence generated by pumping at (solid line) two frequencies $\omega_1/2\pi = 10$ Hz and $\omega_1/2\pi = 50$ Hz simultaneously and at (dashed line) one frequency $\omega_2/2\pi$. The inset shows the time dependence of the relative height of the (1) 10-, (2) 50-, and (3) 250-Hz (fifth harmonic of the main pumping) peaks when the additional pumping is switched off at time $t = 0$. The corresponding peaks are marked by the arrows in the main part of the figure.

increases after the additional pumping is switched off. The inset shows the time dependence of the relative height of the (1) 10-, (2) 50- and (3) 250-Hz (fifth harmonic of the main pumping) peaks after pumping at a frequency of 10 Hz is switched off at the time $t = 0$. The corresponding peaks are marked by the arrows in the main part of the figure. The amplitudes $n_\omega(t)$ of the peaks in the inset are normalised to their initial values $n_\omega(0)$. The time in the inset is given in dimensionless units. It is seen that after the low-frequency pumping is switched off, the amplitudes of the high-frequency turbulent oscillations increase by a large factor.

This increase in the amplitudes of the high-frequency turbulent oscillations after the additional low-frequency pumping is switched off can qualitatively be attributed to a decrease in the density of states (number of harmonics excited per unit frequency range) involved in the nonlinear energy transfer from low- to high-frequency oscillations in the inertial frequency range. Indeed, simultaneous pumping at two frequencies excites oscillations at frequencies that are multiples of the pumping frequencies and at combination frequencies. When the additional pumping is switched off, the oscillation amplitudes at this frequency and at multiple harmonics and combination frequencies decrease rapidly. This damping gives rise to

the redistribution of oscillation energy over frequencies, which is manifested in the evolution of the turbulent spectrum and in a noticeable increase in the amplitudes of waves with frequencies that are multiples of the main pumping frequency ω_2.

5. CONCLUSION

Investigations of the evolution in shape of an equipotentially charged liquid surface in an external DC electric field have demonstrated the possibility of observing a reconstruction phenomenon – the formation of a stationary solitary wave on the flat charged surface (a hump in case of the positively charged surface of liquid hydrogen and a dimple in case of the negatively charged surface of superfluid He II). For hydrogen, it occurs at a critical value of the electric field. Assuming total screening of the electric field from the bulk of the liquid by the surface charge, the critical voltage U_{c1} corresponds to the situation where the applied electric force exactly compensates the gravitational force (where the effective acceleration due to gravity tends to zero).

Measurements made with AC electric fields have permitted us to study the propagation and transformation of nonlinear capillary waves on the surface of liquid hydrogen and helium. It has been demonstrated that a weak turbulence state (Kolmogorov-Zakharov spectrum) is formed in a system of capillary waves over wide range of frequencies higher than the driving frequency ω_p. It was found that the turbulent cascade of capillary waves on the surface of He II was formed over a wide frequency range 18 to 5000 Hz. Thus the relative width of the inertial range is expanded by more than 5 times (from ~30–50 to ~250) relative to the cases of liquid hydrogen and He I.

Quasistationary decay of the turbulent cascade of capillary waves has been studied experimentally and theoretically on the liquid hydrogen surface after a stepwise switching off of the low-frequency pumping. It was observed that the decay starts from high frequencies and ends close to the reciprocal viscous damping time of a wave at the pump frequency. The energy-containing part of the spectrum (maximum of the distribution I_ω) is retained at low frequencies during the entire decay process. This indicates that viscous losses at all frequencies are of central importance for the correct interpretation of decay processes in such a system of nonlinearly interacting capillary waves. Observations of the formation of the cascade and the results of analytical studies of self-similar decay of turbulence, as well as of direct numerical modelling, are in satisfactory agreement with those conclusions.

Relaxation of the turbulent oscillations on the surface of liquid hydrogen has been studied for the case where an additional low-frequency

perturbation is switched on/off. For the case of spectrally narrow pumping, it was found that, after the additional pumping was switched off, the wave amplitudes in the high-frequency part of the turbulent spectrum increased, thereby causing the inertial frequency range to expand. The observed evolution of the spectrum is reversible. After the additional perturbation is switched on, the wave amplitudes in the high-frequency part of the turbulent spectrum decrease and the inertial range narrows. It has thus been shown that high-frequency turbulent oscillations on the liquid surface can be suppressed by the addition of an extra low-frequency pump force.

ACKNOWLEDGEMENTS

REFERENCES

Abdurakhimov, L. V., Brazhnikov, M. Yu., Kolmakov, G. V., Levchenko, A. A. and Mezhov-Deglin, L. P. (2007). *Journal of Low Temperature Physics*, 148, 245.

Brazhnikov, M. Yu., Kolmakov, G. V., Levchenko, A. A. and Mezhov-Deglin, L. P. (2001a). *Journal of Experimental and Theoretical Physics Letters*, 73, 398.

Brazhnikov, M. Yu., Kolmakov, G. V., Levchenko, A. A. and Mezhov-Deglin, L. P. (2001b). *Low Temperature Physics*, 27, 876.

Brazhnikov, M. Yu., Kolmakov, G. V., Levchenko, A. A. and Mezhov-Deglin, L. P. (2001c). *Journal of Experimental and Theoretical Physics Letters*, 74, 583.

Brazhnikov, M. Yu., Levchenko, A. A. and Mezhov-Deglin, L. P. (2002a). *Instruments and Experimental Techniques*, 45(6), 758.

Brazhnikov, M. Yu., Kolmakov, G. V. and Levchenko, A. A. (2002b). *Journal of Experimental and Theoretical Physics*, 95, 447.

Brazhnikov, M. Yu., Kolmakov, G. V., Levchenko, A. A. and Mezhov-Deglin, L. P. (2002c). *Europhysics Letters*, 58(4), 510.

Brazhnikov, M. Yu., Kolmakov, G. V., Levchenko, A. A., Mezhov-Deglin, L. P., Silchenko, A. N. and McClintock, P. V. E. (2004). *Journal of Experimental and Theoretical Physics Letters*, 80(2), 90.

Brazhnikov, M. Yu., Kolmakov, G. V., Levchenko, A. A., Mezhov-Deglin, L. P. and McClintock, P. V. E. (2005a). *Journal of Low Temperature Physics*, 139(5/6), 523.

Brazhnikov, M. Yu., Kolmakov, G. V., Levchenko, A. A. and Mezhov-Deglin, L. P. (2005b). *Journal of Experimental and Theoretical Physics Letters*, 82(9), 565.

Connaughton, C., Nazarenko, S. V. and Pushkarev, A. (2001). *Physical Review E*, 63(4), 046306.

Connaughton, C., Newlell, A. C. and Pomeau, Y. (2003). *Physica D (Amsterdam)* 184, 64.

Dyachenko, S., Newell, A. C., Pushkarev, A. and Zakharov, V. E. (1992). *Physica D (Amsterdam)* 57, 96.

Falcon, E., Laroche, C. and Fauve, S. (2007a). *Physical Review Letters*, 98, 094503.

Falcon E., Fauve, S. and Laroche, C. (2007b). *Physical Review Letters*, 98, 154501.

Falkovich, G. E. and Shafarenko, A. B. (1988). *Soviet Physics: Journal of Experimental and Theoretical Physics*, 68, 1393.

Gor'kov, L. P. and Chernikova, D. M. (1976). *Doklady Akademii Nauk SSSR*, 228, 829.

Henry, E., Alstrom, P. and Levinsen, M. T. (2000). *Europhysics Letters*, 52, 27.

Kolmakov, G. V., Levchenko, A. A., Brazhnikov, M. Yu., Mezhov-Deglin, L. P., Silchenko, A. N. and McClintock, P. V. E. (2004). *Physical Review Letters*, 93(7), 074501.

Kolmakov, G. V., Brazhnikov, M. Y., Levchenko, A. A., Silchenko, A. N., McClintock, P. V. E. and Mezhov-Deglin, L. P. (2006). *Journal of Low Temperature Physics*, 145, 311.

Kolmakov, G. V. (2006). *Journal of Experimental and Theoretical Physics Letters*, 83(2), 58.

Landau, L. D. and Lifshitz, E. M. (1987). *Course of Theoretical Physics*, vol. 6: Fluid Mechanics. Pergamon, New York.

Landau, L. D., Lifshits, E. M. and Pitaevskii, L. P. (1980). *Course of Theoretical Physics*, vol. 9: Statistical Physics, pt. 2, Pergamon, New York.

Levchenko, A. A. and Mezhov-Deglin, L. P. (1996). *Journal of Low Temperature Physics*, 22, 162.

Levchenko, A. A., Kolmakov, G. V., Mezhov-Deglin, L. P., Shikin, V. B., Teske, E., Leiderer, P. (1997). *Experimental and Theoretical Physics Letters*, 65, 572.

Levchenko, A. A., Kolmakov, G. V., Mezhov-Deglin, L. P., Mikhailov, M. G. and Trusov, A. B. (1999). *Low Temperature Physics*, 25, 242.

Levchenko, A. A., Kolmakov, G. V., Mezhov-Deglin, L. P., Mikhailov, M. G. and Trusov, A. B. (2000). *Journal of Low Temperature Physics*, 119(3/4), 343.

Lommer, M. and Levinsen, M. T. (2002). *Journal of Fluorescence*, 12, 45.

Mallat, S. (1999). *A Wavelet Tour of Signal Processing*. Academic Press, San Diego.

Nazarenko, S. V. (2006). *Journal of Statistical Mechanics*, L02002.

Pushkarev, A. N. and Zakharov, V. E. (1996). *Physical Review Letters*, 76, 3320.

Pushkarev, A. N. and Zakharov, V. E. (2000). *Physica D (Amsterdam)*, 135, 98.

Savelsberg, R. and van de Water, W. (2008). *Physical Review Letters*, 100, 034501.

Verkin, B. I., Selover, T. B. and Ghojel, J. I. (1991). *Handbook of properties of condensed phases of hydrogen and oxygen.* Hemisphere Pub. Corp., New York.

Wright, W., Hiller, R. and Putterman, S. (1992). *Journal of the Acoustical Society of America*, 92, 2360.

Wright, W. B., Budakian, R. and Putterman, S. J. (1996). *Physical Review Letters*, 76, 4528.

Wright, W. B., Budakian, R., Pine, D. J. and Putterman, S. J. (1997). *Science*, 278(5343), 1609.

Zakharov, V. E. and Filonenko, N. N. (1967). *Zhurnal Prikladnoi Mekhaniki i Tekhnicheskoi Fiziki* [Engl.: Journal of Applied Mechanics and Technical Physics], 5, 62.

Zakharov, V. E. (1968). *Zhurnal Prikladnoi Mekhaniki i Tekhnicheskoi Fiziki* [Engl.: Journal of Applied Mechanics and Technical Physics], 2, 89.

Zakharov, V. E., L'vov, V. and Falkovich, G. (1992). *Kolmogorov Spectra of Turbulence I.* Springer-Verlag, Berlin.

This page intentionally left blank

Quantised Vortices in Atomic Bose–Einsten Condensates

Kenichi Kasamatsu* and **Makoto Tsubota**†

Contents

* Department of Physics, Kinki University, Kowakae 3-4-1, Higashi-Osaka, Japan
† Department of Physics, Osaka City University, Sugimoto 3-3-138, Osaka, Japan

Abstract   In this review, we give an overview of the experimental and theoretical advances in the physics of quantised vortices in dilute atomic gas Bose–Einstein condensates in a trapping potential, especially focusing on experimental research activities and their theoretical interpretations. Making good use of the atom optical technique, the experiments have revealed many novel structural and dynamic properties of quantised vortices by directly visualising vortex cores from an image of the density profiles. These results lead to a deep understanding of superfluid hydrodynamics of such systems. Typically, vortices are stabilised by a rotating potential created by a laser beam, magnetic field and thermal gas. Finite-size effects and inhomogeneity of the system, originating from the confinement by the trapping potential, yield unique vortex dynamics coupled with the collective excitations of the condensate. Measuring the frequencies of the collective modes is an accurate tool for clarifying the character of the vortex state. The topics included in this review are the mechanism of vortex formation, equilibrium properties and dynamics of a single vortex and those of a vortex lattice in a rapidly rotating condensate.

1. INTRODUCTION

The achievement of Bose–Einstein condensation in trapped atomic gases at ultra low temperatures has stimulated intense experimental and theoretical activity in modern physics, as seen by the award of the Nobel Prize in Physics in 2001 (Cornell and Wieman, 2002; Ketterle, 2002). The Bose–Einstein condensate (BEC), a state of matter predicted by Einstein in 1925, is created by the condensation of a macroscopically large number of bosons into one of the eigenstates of the single-particle density matrix below the Bose–Einstein transition temperature. A remarkable consequence of the condensation is an extension of microscopic quantum phenomena into the macroscopic scale. This is an essential origin of superfluidity and superconductivity, in which macroscopically extended phase coherence allows a dissipationless current to flow.

Superfluidity is closely related to the existence of quantised vortices. For weakly interacting BECs, the superfluid velocity $\mathbf{v}$ is given by the gradient of the phase θ of a 'condensate wave function' $\mathbf{v} = (\hbar/m)\nabla\theta$ with the Planck constant $\hbar = h/2\pi$ and particle mass m. Since the wave function remains single-valued, the change in the phase around a closed contour must be an integer multiple of 2π. Thus, the circulation Γ around a closed contour is given by $\Gamma = \oint \mathbf{v} \cdot d\mathbf{l} = (h/m)q$ $(q = 0, 1, 2, \cdots)$, which shows that circulation of a vortex is 'quantised' in units of h/m. Realisation of weakly interacting atomic gas BECs has provided an ideal testing ground to study the physics of quantised vortices; up to now, several experimental

groups have reported many interesting results. This experimental work has been followed by considerable theoretical activity, leading to proposals and new problems to be tackled. (For a review of the early research stages of quantised vortices, see (Fetter, 2001a).

In this chapter, we review the physics of quantised vortices in atomic gas BECs, especially focusing on the progress of the experimental research. We restrict ourselves to arguments on *trapped* condensates with inhomogeneous density profiles. The aim of this review is to stimulate further developments of this field. By reflecting on the history of the current research and on unresolved problems, we hope to encourage researchers in low temperature physics to investigate quantised vortices in this system. While quantised vortices have been extensively studied in the field of superfluid helium (Donnelly, 1991), there has been a resurgence of interest in vortices in atomic BECs because of the following reasons. First, the diluteness of a gas yields a relatively large healing length that characterizes the vortex core size, thus enabling the visualisation of vortex cores by imaging techniques characteristic of this system (see Section 2.3). Because of this observational capability, the ability to manipulate a condensate wave function and the tunability of the rotation over a wide range, these systems provide a unique approach to studying quantised vortices and their dynamics. Second, the finite-size effect due to the trapping potential causes novel properties of vortices. Finally, multicomponent BECs provide new possibilities for studying unconventional vortex states that have been studied in other fields of physics, such as superfluid ^{3}He, anisotropic superconductors and theories in high-energy physics and cosmology (Volovik, 2003).

Since this is the first time that the topic of atomic BECs has appeared in the progress of low temperature physics, we start with a basic introduction to ultracold atomic systems, including how a condensate is formed and how they are manipulated. Although it is desirable to refer to the experimental and theoretical studies of such systems in detail, we will only mention the basic ideas necessary to understand some important issues in experiment and theory because of space restrictions. These issues are described in Section 2. More detailed accounts can be found in the comprehensive text books by Pethick and Smith (2002), Pitaevskii and Stringari (2003) and in the review paper by Leggett (2001). In Section 3, we review the basic theory and experiments on quantised vortices in atomic BECs, addressing how vortices are created in this system and how they are detected. We also show the intrinsic mechanism of vortex nucleation and lattice formation in a trapped BEC. There are two interesting regimes classified by the rotation rate of the system: one at a slow rotation rate close to a critical rotation frequency where there is a single vortex, and another at high rotation rates for which a lattice of a large number of vortices is formed. The details of these two regimes are discussed in

Sections 4 and 5, respectively. Further, interesting topics that cannot be explained sufficiently in this review and remaining future problems are presented in Section 6. We devote Section 7 to conclusions and outlook.

2. INTRODUCTION TO ULTRACOLD ATOMIC GAS BECs

While progress toward the achievement of Bose–Einstein condensation in a dilute atomic gas had proceeded for the past few decades, researchers succeeded in creating a condensate in 1995 (Anderson et al., 1995). This realisation brought great sensation in modern physics and opened a new research field combining condensed matter physics and atomic, molecular, optical (AMO) physics. Here, we briefly summarise the basic introduction about a system of ultra-cold atomic gas BECs, giving background information for understanding the experiments and theories of quantised vortices in the following sections.

2.1 General Information

A typical system considered here is a collection of neutral atoms with particle number $N \sim 10^4$ to 10^7, trapped by a potential created by a magnetic field or an optical laser field. The density of the atomic gas is of the order of $n \simeq 10^{14}\,\mathrm{cm}^{-3}$, which is lower than that of air on the earth ($\sim 10^{19}\,\mathrm{cm}^{-3}$). The transition temperature to Bose–Einstein condensation can be estimated from a dimensional analysis of the relevant physical quantities ($m, n, \hbar$) as $kT_c \simeq \hbar^2 n^{2/3}/m$, which is in a range from $100\,\mathrm{nK}$ to a few $\mu\mathrm{K}$. At such low temperatures, the gas phase cannot be a stable thermodynamic state and could in principle collapse to the solid phase. However, this relaxation is dominated by a three-body recombination process, which is a rare event for dilute and cold gases; the lifetime of the sample is thus long enough (of the order of a few seconds to a few minutes) to carry out experiments.

In typical experiments, there are several steps towards the condensation of atoms. The first is laser cooling, achieved with three pairs of counter-propagating laser beams along three orthogonal axes. Subsequently, the precooled gas is confined in a trapping potential, described typically by a harmonic potential. In this stage, the temperature is of order $100\,\mu\mathrm{K}$, with 10^9 atoms. In the case of a trap created by a magnetic field, the atoms are trapped by the Zeeman interaction of the electron spin with an inhomogeneous magnetic field. Thus, atoms with electron spins parallel to the magnetic field are attracted to the minimum of the magnetic field (weak-field seeking state), while ones with electron spin antiparallel are repelled (strong-field seeking state). Laser cooling alone cannot produce sufficiently high densities and low temperatures for condensation.

The second step, evaporative cooling (a process in some sense similar to blowing on coffee to cool it), allows the removal of more energetic atoms, thus further cooling the cloud. The evaporation is effected by applying a radio frequency magnetic field which flips the electron spin of the most energetic atoms. At the end of the process, the final temperature is about 100 nK and about 10^4 to 10^7 atoms remain.

Experimentally, the atomic gas systems are attractive since they can be manipulated by the use of lasers and magnetic fields. The cold gas is confined in a trap without microscopic roughness, as it is an extremely clean system. In addition, interactions between atoms may be affected either by using different atomic species or by changing the strength of an applied magnetic or electric field for species that exhibit Feshbach resonance. A further advantage is that because of low density, the microscopic length scales are so large that the structure of the condensate wave function may be investigated by optical methods. Finally, the mean collision time $\tau_{coll} \sim (\sigma n v)^{-1} \sim 10^{-3}$ s between atoms (σ is the cross section and v the speed of atom) is comparable to the characteristic time of the collective mode, which prohibits a local equilibrium of the system. Thus, this system is ideal for studying nonequilibrium relaxation dynamics.

2.2 Atomic Species

The characteristics of BECs are mainly determined by atom–atom interactions which depend crucially on the species of the condensed atoms. Most BEC experiments have been performed using alkali atoms because their ground state electronic structure is simple; all electrons except one occupy closed shells and the remaining electron is in an s orbital in a higher shell. This structure is well suited to laser-based manipulation because its optical transitions can be excited by available lasers and the internal energy-level structure is favourable for cooling to very low temperatures. Since the first observation of BEC in atomic gases, BECs have been formed from nine different elements, including the alkali atoms ^{87}Rb (Anderson et al., 1995), ^{23}Na (Davis et al., 1995), ^{7}Li (Bradley et al., 1995), H (Fried et al., 1998), ^{85}Rb (Cornish et al., 2000), ^{41}K (Modugno et al., 2001), ^{133}Cs (Weber, 2003) and ^{39}K (Roati et al., 2007) and the nonalkali atoms metastable He (Dos Santos et al., 2001; Robert et al., 2001), ^{174}Yb (Takasu et al., 2003) and ^{52}Cr (Griesmaier et al., 2005). ^{87}Rb and ^{23}Na atoms are stable and have long lifetimes against inelastic collisional decay and are thus popular atomic species for BEC experiments.

2.3 Detection

Once a BEC has been created in a harmonic trap, it is probed for its properties. This can be achieved either in situ, that is, with the condensate

inside the trap, or using a time-of-flight (TOF) technique. Although in situ diagnostics, such as nondestructive phase-contrast imaging (Andrews et al., 1996), are valuable tools for some applications, the TOF technique is more often used in vortex experiments. The TOF technique involves switching off the trapping field (magnetic or optical) at time $t = 0$ and taking an image of the BEC a few (typically 5 to 25) milliseconds later. Switching off the trap allows the sample to expand before applying the laser beam probe because the probe is difficult to apply at high densities. Images of the sample are most often taken by absorption, that is, shining a resonant laser beam into the atomic cloud and using a Charge-coupled device (CCD) camera to observe the shadow cast by the absorption of photons, from which can be determined the integrated atomic density. This method is inherently destructive since real absorption processes are involved by spontaneous radiation and the accompanying heating.

2.4 Manipulation

2.4.1 Laser Created Potential

Atoms in a laser field experience a force due mainly to the interaction of the laser field with the electric dipole moment induced in the atoms. The force on atoms in a laser field is used in a variety of ways in BEC experiments.

The character of the force is determined by the detuning given by $\Delta \equiv \hbar\omega_{\text{las}} - (E_e - E_g)$, where ω_{las} is the laser frequency and E_g (E_e) the ground (excited) state energy of an atom. The force also depends on the laser beam intensity I_0, given by $I_0 = \epsilon_0 c \Gamma^2 / d^2$, where ϵ_0 is the dielectric constant, c the speed of light, d an appropriately defined dipole matrix element for the transition in question and $\Gamma \equiv \hbar/\tau_e$ with the lifetime of the excited state τ_e. In the limit $\Gamma \ll \Delta$, the change in energy of the atom in the laser field is $\Delta E_{\text{laser}}(\mathbf{r}) = (I(\mathbf{r})/I_0)\Gamma^2/\Delta$. A region of high laser intensity thus provides an attractive potential for $\Delta < 0$ ('red detuning') and a repulsive potential for $\Delta > 0$ ('blue detuning'). A red detuned potential has been used as an optical trap for atoms. A blue detuned potential creates a potential barrier that separates a condensate and an impurity (obstacle) potential. The interference pattern created by counter-propagating laser beams yields a periodic potential for atoms, called an optical lattice.

2.4.2 Hyperfine State

Atomic BECs can have internal degrees of freedom, attributed to the hyperfine spin of atoms. A hyperfine-Zeeman sublevel of an atom with total electronic angular momentum $\mathbf{J}$ and nuclear spin $\mathbf{I}$ may be labelled by the projection m_F of total atomic spin $\mathbf{F} = \mathbf{I} + \mathbf{J}$ on the axis of the field

B and by the value of total F, which can take a value from $|I - J|$ to $|I + J|$. This is because the hyperfine coupling, which is proportional to $\mathbf{I} \cdot \mathbf{J}$, is much larger than the typical temperature of an ultracold atomic system. The hyperfine state is denoted by $|F, m_F\rangle$ with $m_F = -F, -F + 1, \cdots,$ $F - 1, F$. The simultaneous trapping of atoms with different hyperfine sublevels makes it possible to create multicomponent (often called 'spinor') BECs with internal degrees of freedom (Ho, 1998; Ohmi, 1998), characterised by multiple order parameters (Barrett et al., 2001; Chang et al., 2004; Hall, 1998; Kuwamoto et al., 2004; Schmaljohann et al., 2004; Stenger et al., 1998).

An external field can couple the internal sublevels of the atom and cause coherent transition of the population. This coherent transition can be used to control the spatial variation of the condensate wave functions, resulting in an 'imprinting' of a phase pattern onto the condensate. In most schemes, the spatial configuration of the field, the intensity and detuning of the laser fields, and the phase relationship between the different fields need to be carefully controlled to create the right phase pattern that takes full advantage of the complex internal dynamics.

2.4.3 Feshbach Resonance

A salient feature of cold atom systems is that field-induced Feshbach resonance can tune the scattering length between atoms (Inouye et al., 2001), which determines the atom–atom interaction. A Feshbach resonance occurs when a quasibound molecular state in a closed channel has energy equal to that of two colliding atoms in an open channel. Such resonances can greatly effect elastic and inelastic collisions such as dipolar relaxation and three-body recombination.

Scattering near the resonance can be quantified by perturbation theory. To first order in the coupling between open and closed channels, the scattering is unaltered because there are no continuum states in the closed channels. However, two particles in an open channel can scatter to an intermediate state in a closed channel, which subsequently decays to give two particles in an open channel. Considering such second-order processes, we can obtain the contribution to the scattering length as $\sim (E_{\mathrm{op}} - E_{\mathrm{cl}})^{-1}$, where E_{op} is the energy of the particles in the open channel and E_{cl} is the energy of a state in the closed channels. Consequently, there are large effects if the energy E_{op} of the two particles in the entrance channel is close to the energy E_{cl} of a bound state in the closed channels. Therefore, coupling between the channels yields a repulsive interaction if the energy of the scattering particles is greater than that of the bound state and an attractive interaction if it is less. Since the energies of the states depend on external parameters such as the magnetic field, the resonances can be used to control the interaction between atoms.

2.5 Basic Theory of Trapped BECs

2.5.1 The Gross–Pitaevskii Equation

From a theoretical point of view, a major advantage of weakly interacting atomic gas BECs is that almost all the atoms in the system occupy the same quantum state, and the condensate may be described very well in terms of mean-field theory. This is in contrast to liquid ^{4}He, for which a mean-field approach is inapplicable due to the strong correlations induced by the interactions between the atoms. Bogoliubov's treatment of a uniform Bose gas at zero temperature provides a useful mean-field description of a condensate. Subsequently, Gross and Pitaevskii independently considered an inhomogeneous dilute Bose gas, generalising Bogoliubov's approach to include nonuniform states, which includes quantised vortices. Such nonuniform states of a dilute Bose gas can be understood by considering the second-quantised many-body Hamiltonian

$$\hat{H} = \int d\mathbf{r} \hat{\Psi}^\dagger(\mathbf{r}) \left[-\frac{\hbar^2 \nabla^2}{2m} + V_{ex}(\mathbf{r}) \right.$$

$$\left. + \frac{1}{2} \int d\mathbf{r}' \hat{\Psi}^\dagger(\mathbf{r}') V_{int}(\mathbf{r} - \mathbf{r}') \hat{\Psi}(\mathbf{r}') \right] \hat{\Psi}(\mathbf{r}), \qquad (1)$$

expressed in terms of Boson field operators $\hat{\Psi}(\mathbf{r})$ and $\hat{\Psi}^\dagger(\mathbf{r})$ that obey Bose–Einstein commutation relations $[\hat{\Psi}(\mathbf{r}), \hat{\Psi}^\dagger(\mathbf{r}')] = \delta(\mathbf{r} - \mathbf{r}')$, $[\hat{\Psi}(\mathbf{r}), \hat{\Psi}(\mathbf{r}')] = [\hat{\Psi}^\dagger(\mathbf{r}), \hat{\Psi}^\dagger(\mathbf{r}')] = 0$. Here, $V_{ex}(\mathbf{r})$ is a trapping potential. The interparticle potential V_{int} is approximated by a short-range interaction $V_{int} \simeq g\delta(\mathbf{r} - \mathbf{r}')$, where $g = 4\pi\hbar^2 a/m$ is a coupling constant, characterised by the s-wave scattering length a, because only binary collisions at low energy are relevant in a dilute cold gas and these collisions are independent of the details of the two-body potential.

In three dimensions (3D), a remarkable feature of a dilute Bose gas at zero temperature is the existence of a macroscopic wave function Ψ (an 'order parameter'). The macroscopic occupation of condensed particles makes it natural to write the field operator as a sum $\hat{\Psi}(\mathbf{r}, t) = \Psi(\mathbf{r}, t) + \hat{\phi}(\mathbf{r}, t)$ of a classical field $\Psi(\mathbf{r}, t)$ that characterises the condensate and a quantum field $\hat{\phi}(\mathbf{r}, t)$ representing the remaining noncondensed particles. In order to derive the equation of motion for the order parameter, we write the time evolution of the operator $\hat{\Psi}(\mathbf{r}, t) = \exp(i\hat{H}t/\hbar)\hat{\Psi}(\mathbf{r})\exp(-i\hat{H}t/\hbar)$ using the Heisenberg equation with the many-body Hamiltonian:

$$i\hbar \frac{\partial \hat{\Psi}(\mathbf{r}, t)}{\partial t} = [\hat{\Psi}(\mathbf{r}, t), \hat{H}] = \left[-\frac{\hbar^2 \nabla^2}{2m} + V_{ex} + g\hat{\Psi}^\dagger(\mathbf{r}, t)\hat{\Psi}(\mathbf{r}, t) \right] \hat{\Psi}(\mathbf{r}, t).$$

$$(2)$$

To leading order, the Bogoliubov approximation neglects the noncondensed contribution, giving the time-dependent Gross–Pitaevskii (GP) equation

$$i\hbar\frac{\partial\Psi(\mathbf{r},t)}{\partial t} = \left[-\frac{\hbar^2\nabla^2}{2m} + V_{ex} + g|\Psi(\mathbf{r},t)|^2\right]\Psi(\mathbf{r},t) \tag{3}$$

for the condensate wave function $\Psi(\mathbf{r},t)$. The GP equation (Equation (3)) can be used to explore the dynamic behaviour of the system, characterised by variations of the order parameter over distances larger than the mean distance between atoms. This equation is valid when the s-wave scattering length is much smaller than the average distance between atoms and the number of atoms in the condensate is much larger than unity.

The ground state of a trapped BEC can be expressed within the formalism of the GP theory. We can write the condensate wave function as $\Psi(\mathbf{r},t) = \Phi(\mathbf{r})e^{-i\mu t/\hbar}$, where $\Phi(\mathbf{r})$ obeys the time-independent GP equation

$$\left[-\frac{\hbar^2\nabla^2}{2m} + V_{ex} + g|\Phi(\mathbf{r})|^2\right]\Phi(\mathbf{r}) = \mu\Phi(\mathbf{r}); \tag{4}$$

Φ is normalised to the number of condensed particles $\int d\mathbf{r}|\Phi(\mathbf{r})|^2 = N_0$, which determines the chemical potenteial μ. Typically, studies of trapped atomic gases involve the dilute limit (the gas parameter $\bar{n}|a|^3$ is typically less than 10^{-3}, where $\bar{n}$ is the average density of the gas) so that depletion of the condensate is small with $N' = N - N_0 \propto \sqrt{\bar{n}|a|^3}N \ll N$. Hence, most of the particles remain in the condensate such that $N_0 \simeq N$. The time-independent GP equation (Equation (4)) is also derived by minimising the GP energy functional

$$E[\Psi,\Psi^*] = \int d\mathbf{r}\Psi^*\left(-\frac{\hbar^2\nabla^2}{2m} + V_{ex} + \frac{g}{2}|\Psi|^2\right)\Psi \equiv E_{kin} + E_{tr} + E_{int}, \tag{5}$$

subject to the constraint of a fixed particle number N. This constraint is taken into account by the Lagrange multiplier method; we write the minimisation procedure as $\delta(E - \mu N)/\delta\Psi^* = 0$, where the chemical potential μ is the Lagrange multiplier that ensures a fixed N.

Equation (4) provides a starting point for studying the structure of a condensate in a harmonic confining potential $V_{ex} = m(\omega_x^2 x^2 + \omega_y^2 y^2 + \omega_z^2 z^2)/2$. This introduces the length scale $a_{ho} = \sqrt{\hbar/m\omega}$ with $\omega = (\omega_x\omega_y\omega_z)^{1/3}$. Although the exact ground state can be obtained only by solving Equation (4) numerically, an approximate analytic solution can

be gained when the interaction energy E_{int} is much larger than E_{kin} (Baym and Pethick, 1995). To see this argument, let us neglect the anisotropy of the harmonic potential and assume that the cloud occupies a region of radius $\sim R$ so that $n \sim N/R^3$. Then, the scale of the harmonic oscillator energy per particle is $\sim m\omega^2 R^2/2$ while each particle experiences an interaction with the other particles of energy $\sim gN/R^3$. By comparing these energies, the radius is found to be $R \sim a_{ho}(8\pi Na/a_{ho})^{1/5}$. The kinetic energy is of order $\hbar^2/2mR^2$ so that the ratio of the kinetic to interaction (or trap) energies is $\sim (Na/a_{ho})^{-4/5}$. In the limit $Na/a_{ho} \gg 1$, which is relevant to current experiments on trapped BECs, the repulsive interactions significantly expand the condensate so that the kinetic energy associated with the density variation becomes negligible compared to the trap and interaction energies. As a result, the kinetic energy operator can be omitted in Equation (4), giving the Thomas–Fermi (TF) parabolic profile for the ground state density

$$n(\mathbf{r}) \simeq |\Psi_{TF}(\mathbf{r})|^2 = \frac{\mu - V_{ex}(\mathbf{r})}{g} \Theta\left[\mu - V_{ex}(\mathbf{r})\right], \qquad (6)$$

where $\Theta(x)$ denotes the step function. The resulting ellipsoidal density in 3D space is characterised by two types of parameters: the central density $n_0 = \mu/g$ and the three condensate radii $R_j^2 = 2\mu/m\omega_j^2$ $(j = x, y, z)$. The chemical potential μ is determined by the normalisation $\int d\mathbf{r} n(\mathbf{r}) = N$ as $\mu = (\hbar\omega/2)(15Na/a_{ho})^{2/5}$.

2.5.2 The Bogoliubov–de Gennes Equation

The spectrum of elementary excitations of a condensate is an essential ingredient in calculations of the thermodynamic properties. To study the low-lying collective-excitation spectrum of trapped BECs, the Bogoliubov–de Gennes (BdG) equation coupled with the GP equation is a useful formalism.

Let us consider the equation of motion for a small perturbation around the stationary state Φ, which is a solution of Equation (4). The wave function takes the form $\Psi(\mathbf{r}, t) = [\Phi(\mathbf{r}) + u_j(\mathbf{r})e^{-i\omega_j t} - v_j^*(\mathbf{r})e^{i\omega_j t}]e^{-i\mu t}$. By inserting this ansatz into Equation (3) and retaining terms up to first order in u and v, we obtain the BdG equation:

$$\begin{pmatrix} \mathcal{L}(\mathbf{r}) & -g\Phi(\mathbf{r})^2 \\ g\Phi^*(\mathbf{r})^2 & -\mathcal{L}(\mathbf{r}) \end{pmatrix} \begin{pmatrix} u_j(\mathbf{r}) \\ v_j(\mathbf{r}) \end{pmatrix} = \hbar\omega_j \begin{pmatrix} u_j(\mathbf{r}) \\ v_j(\mathbf{r}) \end{pmatrix}, \qquad (7)$$

where $\mathcal{L}(\mathbf{r}) = -\hbar^2\nabla^2/2m + V_{ex} - \mu + 2g|\Phi(\mathbf{r})|^2$, and ω_j are the eigenfrequencies related to the quasiparticle normal mode functions $u_j(\mathbf{r})$ and $v_j(\mathbf{r})$. The mode functions are subject to the orthogonality and symmetry relations $\int d\mathbf{r}[u_i u_j^* - v_i v_j^*] = \delta_{ij}$ and $\int d\mathbf{r}[u_i v_j^* - v_i u_j^*] = 0$.

Since the energy $\hbar\omega_j$ of this quasiparticle is defined with respect to the condensate energy, in Equation (5) with the stationary solution Φ, the presence of quasiparticles with negative frequencies implies an energetic (thermodynamic) instability for the solution Φ. If there is energy dissipation in the system, the excitation of negative-energy modes lowers the total energy of the system and Φ relaxes to a more stable solution. We note that since the matrix element of Equation (7) is nonhermitian, the eigenfrequencies can be complex-valued. When there are complex-valued frequencies, small-amplitude fluctuations of the corresponding eigenmodes grow exponentially during the energy-conserving time development. This is known as dynamical instability and is a main origin of the generation of nonlinear excitations, such as vortices or solitons, in ultracold condensates.

3. VORTEX FORMATION IN ATOMIC BECs

In this section, we describe some basic properties of quantised vortices in trapped BECs and experimental procedures to create them. We also describe the nucleation mechanisms of quantised vortices in trapped BECs, including controlled schemes of phase engineering. Typically, experiments have used a smooth rotating potential, which is created by a laser or magnetic field, with a small transverse anisotropy to rotate the condensate. This potential induces a low-energy collective oscillation or shape deformation of the condensate. Such global motions of the condensate are responsible for the instability of the vortex nucleation, producing interesting nonequilibrium dynamics in the system. This is contrary to superfluid helium systems, where vortex nucleation occurs locally through roughness or impurities in the rotating container.

3.1 Theoretical Background

As a simple example, let us consider the structure of a single vortex in a condensate trapped by an axisymmetric harmonic potential $V_{\text{ex}}(r,z) = m\omega_\perp^2 (r^2 + \lambda^2 z^2)/2$ with aspect ratio $\lambda = \omega_z/\omega_\perp$. The condensate wave function with a quantised vortex line located along the z-axis takes the form $\Phi(\mathbf{r}) = \phi(r,z)e^{iq\theta}$ with winding number q and cylindrical coordinate (r, θ, z). ϕ is a real function related to the condensate density as $n(r,z) = \phi^2$. The velocity field around the vortex line is $\mathbf{v}_s = (q\hbar/mr)\hat{\theta}$. Equation (4) becomes

$$\left[-\frac{\hbar^2}{2m} \left(\frac{\partial^2}{\partial r^2} + \frac{1}{r}\frac{\partial}{\partial r} + \frac{\partial^2}{\partial z^2} \right) + \frac{q^2\hbar^2}{2mr^2} + V_{\text{ex}}(r,z) + gn \right] \phi = \mu\phi. \quad (8)$$

Here, the centrifugal term $q^2\hbar^2/2mr^2$ arises from the azimuthal motion of the condensate. Equation (8), solved numerically, gives the structure of the vortex. In the TF limit $Na/a_{\mathrm{ho}} \gg 1$, we can omit the terms involving derivatives with respect to r and z in Equation (8), and the density can be obtained approximately as

$$n(r,z) = n_0 \left(1 - \frac{r^2}{R_\perp^2} - \frac{z^2}{R_z^2} - q^2\frac{\xi^2}{r^2}\right) \Theta \left(1 - \frac{r^2}{R_\perp^2} - \frac{z^2}{R_z^2} - q^2\frac{\xi^2}{r^2}\right), \quad (9)$$

where $n_0 = \mu/g$ is the density at the centre of the vortex-free TF profile. We define the TF radius $R_\perp^2 = 2\mu/m\omega_\perp^2$ and $R_z^2 = 2\mu/m\omega_z^2$ and the healing length $\xi = (\hbar^2/2mgn_0)^{1/2} = (8\pi a n_0)^{-1/2}$. Equation (9) shows that the condensate density vanishes at the centre, out to a distance of order ξ, due to the centrifugal term ξ^2/r^2 (numerical solution shows that the density grows as r^2 away from the centre), whereas the density in the outer region has the form of an upward-oriented parabola. Hence, the healing length ξ characterises the vortex core size; for typical BEC parameters, $\xi \sim 0.2\,\mu\mathrm{m}$. In the TF limit, the core size is very small because $\xi/R_\perp = \hbar\omega_\perp/2\mu = (15Na/a_{\mathrm{ho}})^{-2/5} \ll 1$. Increasing the winding number q widens the core radius due to the centrifugal effects.

The energy associated with a single vortex line is an important quantity to determine the stability of the vortex state. The dominant contribution to this energy is the kinetic energy of the superfluid flow by a vortex. The energy is estimated as

$$E_1 = \int \frac{1}{2}mnv_s^2 \mathrm{d}\mathbf{r} \simeq \frac{m\bar{n}}{2}R_z \int_\xi^{R_\perp} v_s^2 2\pi r\mathrm{d}r = q^2 R_z \frac{\pi\hbar^2\bar{n}}{m} \ln\left(\frac{R_\perp}{\xi}\right), \quad (10)$$

where we assume the spatially uniform density $\bar{n}$ and the size along the z-axis R_z. Since $E_1 \propto q^2$, vortices with $q > 1$ are energetically unfavourable. For example, the energy cost to create one $q = 2$ vortex is higher than that to create two $q = 1$ vortices. Therefore, a stable quantised vortex usually has $q = 1$, except for that in nonsimply connected geometry, and we will mainly concentrate on the $q = 1$ vortex in the following discussions. In atomic BECs, however, such a multiply quantised vortex can be created experimentally by using topological phase imprinting (Shin et al., 2004) and exhibits interesting disintegration dynamics, as discussed in Section 4.2.3.

It is necessary to ensure the stability of a vortex in a trapped BECs against a nonvortex state to investigate its behaviour. Imposing rotation on the system is a direct way to achieve stabilisation. If the system is under rotation, it is convenient to consider the corresponding rotating frame; for

a rotation frequency $\mathbf{\Omega} = \Omega\hat{z}$, the integrand of the GP energy functional (Equation (5)) acquires an additional term,

$$E' = \int d\mathbf{r}\Psi^* \left(-\frac{\hbar^2\nabla^2}{2m} + V_{ex} + \frac{g}{2}|\Psi|^2 - \Omega L_z \right) \Psi, \qquad (11)$$

where $L_z = -i\hbar(x\partial_y - y\partial_x)$. The corresponding GP equation becomes

$$i\hbar\frac{\partial\Psi(\mathbf{r},t)}{\partial t} = \left[-\frac{\hbar^2\nabla^2}{2m} + V_{ex} + g|\Psi(\mathbf{r},t)|^2 - \Omega L_z \right] \Psi(\mathbf{r},t). \qquad (12)$$

If there is a quantised vortex along the trap axis, $\langle L_z \rangle = N\hbar$, so that the corresponding energy of the system in the rotating frame is $E'_1 = E_1 - N\hbar\Omega$. The difference between E'_1 and the vortex-free energy E'_0 gives the favourable condition for a vortex to enter the condensate. Since E'_0 is equal to the energy E_0 in the laboratory frame, the difference is given by $\Delta E' = E'_1 - E'_0 = E_1 - E_0 - N\hbar\Omega$. Thus, the critical rotation frequency Ω_c for the existence of an energetically stable vortex line is given by $\Omega_c = (E_1 - E_0)/N\hbar$. Above the critical rotation frequency Ω_c, the single vortex state is ensured to be *thermodynamically* stable.

To calculate E_1 more quantitatively, it is necessary to take into account the inhomogeneous effect of the condensate density (Lundh et al., 1997). In the TF limit, for a condensate in a cylindrical trap $\omega_z = 0$ (an effective 2D condensate), the critical frequency is given by $\Omega_c = (2\hbar/mR_\perp^2) \ln(0.888R_\perp/\xi)$. For an axisymmetric trap $V_{ex}(r,z)$, the critical frequency is $\Omega_c = (5\hbar/2mR_\perp^2) \ln(0.671R_\perp/\xi)$. Ω_c for a nonaxisymmetric trap is slightly modified by a small numerical factor and has been discussed analytically (Svidzinsky and Fetter, 2000a) and numerically (Feder, 1999a).

When the rotation frequency is significantly higher than Ω_c, further vortices will appear in the form of a triangular lattice, in analogy to the Abrikosov lattice of magnetic fluxes in type II superconductors. The nature of the equilibrium state changes first to a state with two vortices rotating around each other, then to three vortices in a triangle form and subsequently to arrays of more vortices (Butts and Rokhsar, 1999; Feder, 2001b). The detail of this state will be described in Section 5.

3.2 Vortex Formation in a Stirred Condensate

Rotation effects of atomic BECs were first studied based on the knowledge of deformed atomic-nuclei systems. A slight rotation of a deformed trap excites so-called 'scissors modes', which are closely related to the

irrotationality $\nabla \times \mathbf{v}_s = 0$ of the superfluid hydrodynamics (Guery-Odelin and Stringari, 1999; Marago et al., 2000). Although these experiments demonstrated the superfluidity of atomic BECs, more intuitive evidence can be gained by observing quantised vortices. However, since the first experimental realisation of BECs, there have been technical hurdles to rotating a system. For atomic gases trapped by an impurity-free external potential, it was supposed that rotation of the potential could not transfer a sufficient angular momentum into the condensate. Thus, the first experimental detection of a vortex in an atomic BEC, by (Matthews et al., 1999a), was made by using a complicated phase imprinting technique proposed by Williams and Holland (1999). Subsequently, vortices have been created by stirring a condensate mechanically with an 'optical spoon'; the first success of this 'rotating bucket' experiment was reported by Madison et al., 2000. In the following, we detail the rotating bucket experiments.

3.2.1 Experimental Scheme to Rotate Condensates

Madison et al. (2000) at Ecole Normale Supérieure (ENS) succeeded in observing a vortex and a vortex lattice in an atomic BEC, using a method similar to the observation of superfluid helium in a rotating bucket (Yarmchuk et al., 1979). A schematic illustration of their experimental setup is shown in Figure 1. Since the magnetic trap is axially symmetric, its rotation cannot impart an angular momentum to the condensate. In this scheme, a laser beam is propagated along the z-axis of the condensate. This beam rapidly oscillates around the z-axis with a frequency much larger than the typical trapping frequency, which is effectively regarded to be as if two laser beams are located at an equilibrium position. Thus, the two laser beams break the axisymmetry of the condensate, allowing an angular momentum transfer into the condensate. An optical spoon is then realised by rotating the two beams around the z-axis. Since the beam width is larger than the radial size of the condensate, the condensate is
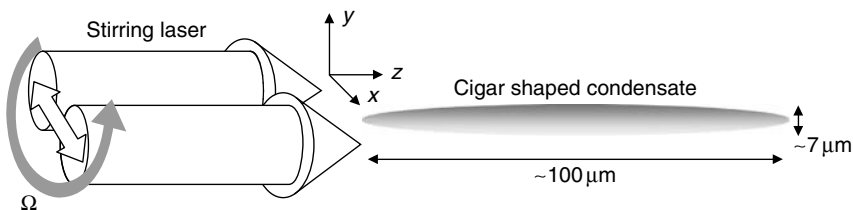
FIGURE 1   Schematic illustration of the experimental setup used by the ENS group. A cigar-shaped condensate is rotated by an effective dipole potential made by the laser beam. The laser beam oscillates rapidly with a very large frequency around the z-axis, with an amplitude $\sim$16 μm. The beam width is about 20 μm. The dipole potential rotates with an angular frequency Ω.

trapped in a trap combining an axisymmetric harmonic potential and a nonaxisymmetric harmonic potential created by a stirring laser beam. In a rotating frame, the combined potential can be written as $(1/2)m\omega_\perp^2[(1 + \epsilon)X^2 + (1 - \epsilon)Y^2] + (1/2)m\omega_z^2 z^2$, where X and Y are the coordinates in the rotating frame, $\epsilon = (\omega_X^2 - \omega_Y^2)/(\omega_X^2 + \omega_Y^2)$ is the anisotropic parameter and $\omega_\perp = \sqrt{(\omega_X^2 + \omega_Y^2)/2}$. By rotating this potential at a frequency Ω, a vortex is formed above a certain critical value of Ω after the equilibration. When Ω is increased further, multiple vortices appear, forming a triangular lattice. The quantised vortices can be directly visualised as 'dips' in the transverse density profile of the TOF image.

Following the experiments of the ENS group, other groups have also observed quantised vortices using slightly different methods under the concept of the rotating bucket. Abo-Shaeer et al. (2001) at Massachusetts Institute of Technology (MIT) observed a vortex lattice consisting of up to 100 vortices in a ^{23}Na condensate, as shown in Figure 2. ^{23}Na condensates can be much larger than ^{87}Rb condensates (Abo-Shaeer et al., 2001). Hodby et al. (2002) created a vortex lattice by rotating the anisotropic magnetic trap directly without using a laser beam, which is similar to the rotating bucket experiment. This method has the advantage that a wider range of the anisotropic parameter ϵ can be selected than for the optical spoon. Rotating an optical spoon made by multiple-spot laser beams or narrow focusing beams has also used for nucleating vortices (Raman et al., 2001).

In the above methods, the condensate was rotated by an external potential. Haljan et al. (2001) at Joint Institute for Laboratory Astrophysics (JILA), in contrast, created a vortex state by cooling an initially rotating thermal gas in a static confining potential. Thermal gas above the transition temperature was rotated by a slightly anisotropic trap. After recovering the anisotropy of the potential, the rotating thermal gas was evaporatively cooled until most of the atoms were condensed. Although the atom number decreased through the evaporative cooling, the condensate continued
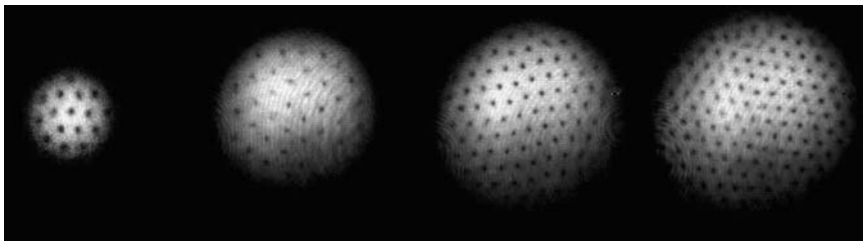
FIGURE 2 Typical density profiles of a rotating condensate taken by TOF measurement. The condensates contain approximately 16, 32, 80 and 130 vortices from left to right.
Source: Abo-Shaeer et al. (2001). Reprinted with permission from AAAS.

to rotate because the angular momentum per atom did not change and thus the vortex lattice was created. This method allows the investigation of the intrinsic mechanism of vortex nucleation, which is independent of the character of the stirring potential. In addition, since atoms can be selectively removed during the evaporation, spinning up of the condensate can be efficiently achieved by removing atoms extending in the axial direction, as opposed to the radial direction, and hence a BEC with a high rotation rate can be obtained.

3.2.2 Theory of Vortex Nucleation and Lattice Formation

Surface Mode Instability   The critical rotation frequency Ω_c indicates the energetic stability of the central vortex state and provides a lower bound for the critical frequency. Vortex nucleation of a nonrotating condensate occurs when the trap is rotated at a higher frequency than Ω_c to overcome the energy barrier that stops the transition from the nonvortex state to the vortex state (Isoshima and Machida, 1999). The threshold of the rotation frequency for instability, leading to vortex nucleation, is related to the excitation of surface modes of the trapped condensate (Anglin, 2001; Dalfovo and Stringari, 2000; Feder, 1999b; Simula, 2002b; Williams et al., 2002). It has been shown that according to the Landau criterion for rotationally invariant systems, the critical frequency is given by $\Omega_v = \min(\omega_\ell/\ell)$, where ω_ℓ is the frequency of a surface mode with multipolarity ℓ. Above Ω_v, negative-energy surface modes appear with high multipolarities in the spectrum of a nonrotating condensate (Dalfovo and Stringari, 2000; Isoshima and Machida, 1999), which may lead to vortex generation. The negative-energy modes can grow only in the presence of dissipation, caused by, for example, thermal atoms (Williams et al., 2002). This mechanism occurred in the experiment of the JILA group (Haljan et al., 2001). In this experiment, vortices were formed by cooling a rotating thermal cloud to below T_c, where the surface modes were excited by the 'wind' of the rotating thermal cloud.

The nucleation frequency Ω_v is insufficient to explain the results of the groups using external stirring potentials (Abo-Shaeer et al., 2001; Hodby et al., 2002; Madison et al., 2000). For example, in the case of the ENS group, the number of nucleated vortices has a peak near $\Omega = 0.7\omega_\perp$, as shown in Figure 3a. These experiments confirm that instability occurs when a particular surface mode is resonantly excited by a deformed rotating potential. The optical spoon of the ENS group mainly excites the surface mode with $\ell = 2$ (quadrupole mode). In a rotating frame with frequency Ω, the frequency of the surface mode is increased by $-\ell\Omega$. This resonance thereby occurs close to the rotation frequency $\Omega = \omega_\ell/\ell$. In the TF limit, the dispersion relation for the surface mode is given by $\omega_\ell = \sqrt{\ell}\omega_\perp$ (Stringari, 1996). Hence, it is expected that the quadrupole mode with
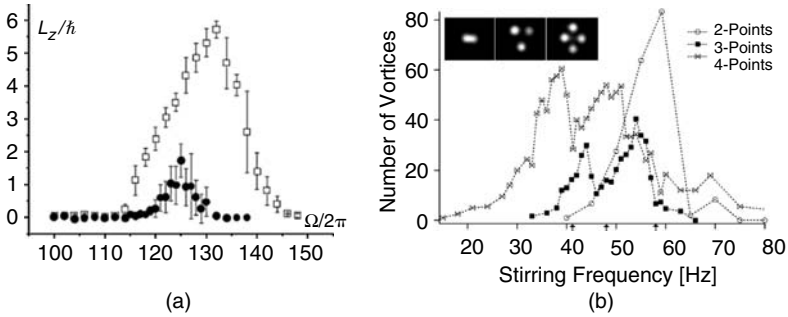
FIGURE 3   Dependence of the vortex number (angular momentum per atom) on the rotation frequency. (a) Result of the ENS group (Chevy et al., 2000, 2001). The parameter values are $N = 2.5 \times 10^5$, $\omega_\perp = 2\pi \times 172$ Hz and an anisotropic parameter ϵ (black dots: $\epsilon = 0.01$, white square: $\epsilon = 0.02$). The angular momentum was measured by the surface wave spectroscopic technique described in Section 4.2.2. With increasing Ω, the value of the angular momentum has a peak at $\Omega \simeq \omega_\perp/\sqrt{2} = 122$ Hz, a resonance frequency of the quadrupole mode. The width of this peak structure increases as the trapping potential becomes more anisotropic. (b) Result of the MIT group (Raman et al., 2001). The parameter values are $N \sim 10^7$ and $\omega_\perp = 2\pi \times 86$ Hz. The arrows below the graph show the positions of the surface mode resonance $\omega_\perp/\sqrt{\ell}$. The inset shows 2-, 3-, and 4-point potentials produced by a laser beam. Source: Chevy et al. (2001) and Raman et al. (2001). Reprinted with permission from American Physical Society (APS).

$\ell = 2$ is resonantly excited at $\Omega = \omega_\perp/\sqrt{2} \simeq 0.707\omega_\perp$. A theoretical study has revealed that when the quadrupole mode is resonantly excited, an imaginary component appears in frequencies of fluctuations with high multipolarities (Sinha and Castin, 2001). This indicates that dynamic instability can trigger vortex nucleation even at zero temperature. This scheme is supported further by the experiment of the MIT group (Raman et al., 2001), where surface modes with higher multipolarities ($\ell = 3, 4$) were resonantly excited using multiple laser beam spots, where the largest number of vortices were generated at frequencies close to the expected values $\Omega = \omega_\perp/\sqrt{\ell}$, as seen in Figure 3b.

Another mechanism to produce vortex nucleation is formulated by considering elliptically-deformed stationary states of a BEC in a rotating elliptical trap. The stationary solutions can be obtained in the TF limit by solving the superfluid hydrodynamic equations (Recati et al., 2001). At low rotation rates, only one stationary solution is found ('normal branch'). However, at higher rotation rates, $\Omega > \omega_\perp/\sqrt{2}$ specifically, a bifurcation of the solutions occurs and up to three stationary solutions appear, with two solutions in an 'overcritical branch' and one normal branch solution. Above Ω of the bifurcation point, one or more of the solutions become dynamically unstable for fluctuations with high

multipolarities (Sinha and Castin, 2001), which leads to vortex formation (Parker et al., 2006). Madison et al. (2001) followed these stationary states experimentally by adiabatically introducing trap ellipticity and rotation. They observed vortex nucleation in the expected dynamically unstable region.

An overview on the problem of vortex nucleation in a trapped BEC can be seen in the review paper (Ghosh, 2004).

Formation Dynamics of a Vortex Lattice Madison et al. (2001) directly observed nonlinear processes such as vortex nucleation and lattice formation in a rotating condensate. The left panel of Figure 4 depicts the time development of the condensate ellipticity $\alpha = \Omega(R_X^2 - R_Y^2)/(R_X^2 + R_Y^2)$, where $R_{X,Y}$ is the TF radius measured from the image. By suddenly turning on the rotation of the potential, the initially axisymmetric condensate undergoes a collective quadrupole oscillation in which the condensate deforms elliptically. This oscillation continues for a few hundred milliseconds with gradually decreasing amplitude. Then, the axial symmetry of the condensate suddenly recovers and concurrently the vortices enter the condensate from its surface, eventually settling into a lattice configuration.

This observation has been well reproduced by a simulation of the GP equation in 2D (Kasamatsu et al., 2003; Tsubota et al., 2002) and 3D (Kasamatsu et al., 2005a) space. The results shown in the right panel of
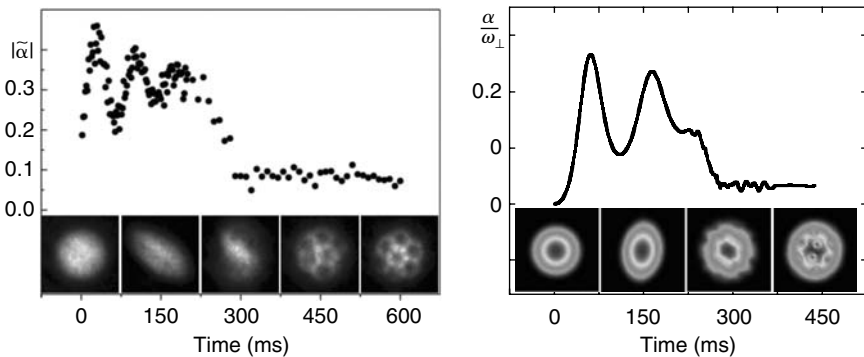
FIGURE 4   Left: measurement of the time dependence of α (see text) when the stirring anisotropy is turned on rapidly from $\epsilon = 0$ to $\epsilon = 0.025$ in 20 ms and $\Omega = 0.7$ and held constant for 300 ms. Five images taken at intervals of 150 ms show the transverse profile of the elliptic state and reveal the nucleation and ordering of the vortex lattice. Right: comparing numerical simulation of the 3D GP equation with phenomenological dissipation ($\gamma = 0.03$) and the experimentally relevant parameters. The density profile in the bottom panels is integrated along the z-axis.
Source: Madison et al. (2001). Reprinted with permission from APS.

Figure 4 were obtained by a 3D simulation with the parameters of the ENS group experiment. The simulation result shows that after a few hundred milliseconds, the boundary surface of the condensate becomes unstable and generates ripples that propagate along the surface, identified as invisible 'ghost' vortices in the low-density surface region. The ripples develop into vortex cores, which enter the condensate. In these simulations, a dissipation term was introduced phenomenologically by rewriting the time derivative term of the GP equation (Equation (12)) as $(i - \gamma)\partial/\partial t$, which caused the lattice configuration to settle. Other works have simulated vortex lattice formation using dissipation derived from the microscopic approach, such as quantum kinetic theory (Penckwitt, 2002) or the classical field formalism (Lobo, 2004). Long numerical propagation of the energy-conserving GP equation can cause crystallisation of a lattice through the vortex-phonon interaction (Parker, 2005)

Vortex Nucleation by a Moving Object   Vortices can also be nucleated in BECs by a moving localised potential. Numerical simulations of the GP equation for a 2D uniform condensate flow around a circular hard-walled potential show that vortex–antivortex pairs nucleate when the flow velocity exceed a critical value (Frisch et al., 1992). In trapped BECs, a similar situation can be realised experimentally using a narrow blue detuned laser potential, being studied theoretically (Crescimanno et al., 2000; Jackson et al., 1998). In experiments by the MIT group, a repulsive laser beam was oscillated in an elongated condensate to study the dissipationless flow of a Bose gas (Onofrio et al., 2000; Raman et al., 1999). Although vortices were not observed directly, the measurement of condensate heating and drag above a critical velocity was consistent with the nucleation of vortices (Jackson et al., 2000). Focused laser beams moving in a circular path around the trap centre can also stir the condensate by nucleating vortices (Caradoc-Davies et al., 1999, 2000; Lundh et al., 2003). This scheme was used in the experiment detailed in Raman et al., 2001 where vortices were generated at lower stirring frequencies than the critical value given by surface mode instability.

3.3 Phase Engineering

Atom optics techniques allow the controlled creation of vortices by imprinting a spatial phase pattern of the condensate wave function. Several ideas for the creation of vortices by this technique have been proposed theoretically, based on the coherent control of the time evolution of the wave function, instead of mechanical rotation (Andrelczyk et al., 2001; Damski et al., 2001; Dum et al., 1998; Kapale and Dowling, 2005; Marzlin

et al., 1997; Marzlin and Zhang, 1998; Möttönen et al., 2003; Nakahara et al., 2000; Nandi et al., 2004; Williams and Holland, 1999).

3.3.1 Phase-Imprinting Method

The first observation of a quantised vortex in an atomic gas BEC was achieved in a two-component BEC consisting of ^{87}Rb atoms with hyperfine spin states $|F = 1, m_F = -1\rangle \equiv |1\rangle$ and $|F = 2, m_F = 1\rangle \equiv |2\rangle$ (Matthews et al., 1999a), which were confined simultaneously in almost identical magnetic potentials. Since the scattering lengths between atoms of $|1\rangle$ and $|1\rangle$, $|2\rangle$ and $|2\rangle$, and $|1\rangle$ and $|2\rangle$ are all different, the two states are not equivalent, and the two-component condensate is characterised by two-component order parameters.

In this experiment, condensed atoms are initially trapped in one state, say the $|1\rangle$ state. Then, a two-photon microwave field is applied, inducing coherent Rabi transitions of atomic populations between the $|1\rangle$ state and the $|2\rangle$ state. For a homogenous system in which both components have uniform phases, interconversion takes place at the same rate everywhere. However, the time variation of the spatially inhomogeneous potential changes the nature of the interconversion. This is a key point of the phase-imprinting method for vortex creation.

The underlying physics can be understood by considering a corotating frame with an off-centred perturbation potential at the rotation frequency Ω'. In this frame, the energy of a vortex with one unit of angular momentum is shifted by $\hbar\Omega'$ relative to its value in the laboratory frame. When this energy shift is compensated for by the sum of the detuning energy of an applied microwave field and the small chemical potential difference between the vortex and nonvortex states, a resonant transfer of population can occur. Experimentally, the rotating perturbation is created by a laser beam with a spatially inhomogeneous profile, rotating around the initial nonrotating component, say $|1\rangle$. By adjusting the detuning and Ω', the $|2\rangle$ component is resonantly transferred to a state with unit angular momentum by precisely controlling the time when the coupling drive is turned off (Williams and Holland, 1999). This procedure results in a 'composite' vortex, where the $|2\rangle$ component has a vortex at the centre, whereas the nonrotating $|1\rangle$ component occupies the center and works as a *pinning* potential that stabilises the vortex core (Kasamatsu et al., 2005b).

As shown in Section 2.4, a far-off-resonant laser beam can create an external potential $V_{\text{las}}(\mathbf{r})$ in the condensate. By directly applying a laser pulse with an inhomogeneous intensity to the condensate, the condensate phase can be modulated. This can be easily understood by observing the evolution of the phase by inserting the form $\Psi(\mathbf{r}, t) = |\Psi(\mathbf{r}, t)|e^{i\theta(\mathbf{r},t)}$ into Equation (3). When the laser intensity is much stronger than the other terms and the duration of the pulse τ is sufficiently short, the evolution of the phase is governed by $\theta(\mathbf{r}, t) = -\hbar^{-1}\int_0^\tau dt V_{\text{las}}(\mathbf{r}, t)$. Since the

potential amplitude of V_{las} is proportional to the laser intensity, a suitable spatial variation of the intensity can imprint the phase into the condensate (Andrelczyk et al., 2001). This phase-imprinting technique has been used to create a *dark soliton* (Burger et al., 1999; Denschlag et al., 2000), which is a topological excitation with a complete density dip across which the phase changes by π. It is known that a dark soliton in a dimensional space larger than 2D experiences dynamical instability called 'snake instability'. This instability causes the decay of the dark solitons into a form of a *vortex ring* (Anderson et al., 2001; Dutton et al., 2001).

3.3.2 Topological Vortex Formation

Leanhardt et al. (2002, 2003) used a method called 'topological phase imprinting' (Isoshima et al., 2000; Nakahara et al., 2000; Ogawa et al., 2002) to create a vortex in a trapped BEC. In this experiment, ^{23}Na condensates were prepared in either a lower, $|F, m_F\rangle = |1, -1\rangle$, or upper, $|2, +2\rangle$, hyperfine state and confined in a Ioffe–Pritchard magnetic trap, described by $\mathbf{B} = B'(x\hat{x} - y\hat{y}) + B_z\hat{z}$. A vortex was created by adiabatically inverting the axial bias field B_z along the trap axis.

   To interpret the mechanism, consider an alkali atom with a hyperfine-spin $|F| = 1$. The order parameter has three components $\Psi_{\pm 1}$ and Ψ_0, corresponding to with $F_z = \pm 1, 0$. The basis vectors in this representation are $\{|\pm\rangle, |0\rangle\}$. We introduce another set of basis vectors $|x\rangle, |y\rangle$ and $|z\rangle$, which are defined by $F_x|x\rangle = F_y|y\rangle = F_z|z\rangle = 0$. These vectors are related to the previous vectors as $|\pm 1\rangle = \mp(1/\sqrt{2})\left(|x\rangle \pm i|y\rangle\right)$ and $|0\rangle = |z\rangle$. When the z-axis is taken parallel to the uniform magnetic field, the order parameter of the weak field seeking state takes the form $\Psi_{-1} = \psi$ and $\Psi_0 = \Psi_1 = 0$ or in vectorial form as $\Psi = (\psi/\sqrt{2})\left(\hat{x} - i\hat{y}\right)$. When the magnetic field points in the direction $\hat{\mathbf{B}} = (\sin\beta\cos\alpha, \sin\beta\sin\alpha, \cos\beta)$, a rotational transformation with respect to the Euler angle (α, β, γ) gives $\Psi = (\psi/\sqrt{2})e^{i\gamma}(\hat{\mathbf{m}} + i\hat{\mathbf{n}})$, where $\hat{\mathbf{m}} = (\cos\beta\cos\alpha, \cos\beta\sin\alpha, -\sin\beta)$ and $\hat{\mathbf{n}} = (\sin\alpha, -\cos\alpha, 0)$. The unit vector $\hat{\mathbf{l}} = \hat{\mathbf{m}} \times \hat{\mathbf{n}} = (\cos\alpha\sin\beta, -\sin\alpha\sin\beta, -\cos\beta)$ is the direction of the spin polarisation. The three real vectors $\{\hat{\mathbf{l}}, \hat{\mathbf{m}}, \hat{\mathbf{n}}\}$ form a triad, analogous to the order parameter of the orbital part of superfluid ^{3}He. The same amplitudes in the basis $\{|0\rangle, |\pm\rangle\}$ are $\Psi_1 = (\psi/2)(1 - \cos\beta)e^{-i\alpha+i\gamma}$, $\Psi_0 = -(\psi/\sqrt{2})\sin\beta e^{i\gamma}$ and $\Psi_{-1} = (\psi/2)(1 + \cos\beta)e^{i\alpha+i\gamma}$.

   When the field B_z is strong compared to the quadrupole field, the trapped condensate has an order parameter $\Psi = (\psi/\sqrt{2})(\hat{x} - i\hat{y})$ without vorticity. This configuration corresponds to $\beta = 0$ and $\gamma = -\alpha = \phi$, where ϕ is the azimuthal angle. Then, B_z is adiabatically decreased, where the adiabatic condition is required for atoms to remain in the weak field seeking state so that $\hat{\mathbf{l}}$ is always antiparallel to $\mathbf{B}$. In the final step, the external field B_z is gradually increased in the opposite $(-z)$ direction. Then, the

Î-vector points so that $\beta = \pi$. Substituting these angles into $\Psi_{\pm 1}$ and Ψ_0, we obtain $\Psi_{-1} = \Psi_0 = 0$ and $\Psi_1 = \psi e^{2i\phi}$, which corresponds to a vortex with winding number $q = 2$. This result can be reinterpreted in terms of Berry's phase (Leanhardt et al., 2002; Ogawa et al., 2002) (which is why it is called 'topological phase imprinting'). When the hyperfine spin is F in general, we obtain a vortex with a winding number $2F$ since Ψ_{-F} and Ψ_F have phases $F(\alpha + \gamma)$ and $F(-\alpha + \gamma)$, respectively (Kumakura et al., 2006; Shin et al., 2004).

When the bias field vanishes during the inversion ($B_z = 0$), a spin texture known as cross disgyration appears in the Ioffe–Pritchard trap. Here, the angle β increases from 0 to $\pi/2$ and γ and $-\alpha$ are identified with ϕ, where the Î-vector aligns with a hyperbolic distribution around the singularity at the centre. This texture has a nonvanishing vorticity n when $\gamma = n\phi$. This spin texture has been observed as a coreless vortex composed of three-component order parameters $\Psi_{\pm 1,0}$ of a spinor BEC (Leanhardt et al., 2003).

3.3.3 Stimulated Raman Process

Some papers proposed generating vortices in a BEC using stimulated Raman processes with configurations of optical fields that have orbital angular momentum (OAM) (Dum et al., 1998; Kapale and Dowling, 2005; Marzlin et al., 1997; Marzlin and Zhang, 1998; Nandi et al., 2004). A light beam with a phase singularity, such as a Laguerre-Gaussian (LG) beam, has a well-defined OAM along its propagation axis. The set of LG mode

$$\text{LG}_p^l(r, \phi) = \sqrt{\frac{2p}{\pi(|l| + p)}} \frac{1}{w_0} \left(\frac{\sqrt{2}r}{w_0} \right)^{|l|} L_r^{|l|} \left(\frac{2r^2}{w_0^2} \right) e^{-r^2/w_0^2 + il\phi} \qquad (13)$$

defines a possible basis set to describe paraxial laser beams, where w_0 is the beam width, l the winding number and p the number of radial nodes for radius $r > 0$. Each photon in the LG_p^l mode carries OAM $l\hbar$ along its direction of propagation.

A group at NIST (Anderson et al., 2006; Ryu et al., 2007) used a two-photon stimulated Raman process with a Gaussian laser beam propagating along $+x$ and a LG_0^1 beam, carrying $\hbar$ of OAM, propagating along $-x$. Interference of counter-propagating Gaussian beams generates a moving sinusoidal optical dipole potential, which can give a directed linear momentum (LM) to Bose-condensed atoms via Bragg diffraction. The potential generated by interference of the counter propagating LG_0^1 and Gaussian beams is not sinusoidal but corkscrew-like due to the radial intensity profile and the helical phase of the LG_0^1 beam. Diffraction off this corkscrew potential produces a vortex state with a centre of mass motion,

where atoms that absorb a photon from one beam and simuletedly emit a photon into the other beam acquire both LM and OAM difference of the beams, which in this case was $2\hbar k$ (k the photon wavevector) and $\hbar$, respectively.

They generated vortices of higher charge by transferring to each atom the angular momentum from several LG_0^1 photons (Anderson et al., 2006; Ryu et al., 2007). This experiment directly demonstrated that the OAM of a photon is transferred coherently to an atom in quantised units of $\hbar$. In some situations, it might be desirable to generate rotational states with no net LM. This could be accomplished by using an initial Bragg diffraction pulse to put atoms in a nonzero LM state from which they could subsequently be transferred to a rotational state with zero LM.

4. A SINGLE VORTEX IN AN ATOMIC BEC

In this section, we concentrate on the problem of a single vortex state in a trapped BEC. As described in Section 3.1, vortex stability is ensured by the rotation of the system. Studying the motion of a vortex line is the first step towards understanding superfluid hydrodynamics in such a system. Trapped BECs are mesoscopic systems in the sense that the healing length is not significantly smaller than the sample size. Thus, vortex dynamics have noticeable effects on the collective excitation of the condensate, in contrast to the case for traditional superfluid helium systems.

4.1 Equilibrium Properties

The solution of the GP equation shows that a vortex has a core with a size of the order of the healing length ξ, in which the condensate density is zero. When $\mathbf{\Omega} = \Omega\hat{\mathbf{z}}$, vortices are identified by a density dip in the transverse density distribution (in the xy plane). TOF observations by the ENS group (Madison et al., 2000), however, show that the density is not completely zero in the dip. This result implies that the vortex line is not necessarily straight because the condensate density along the z-axis (rotation axis) is integrated for the transverse image. Surprisingly, such vortex bending remains stationary in the ground state of a cigar-shaped condensate (Aftalion and Jerrard, 2002; Aftalion and Danaila, 2003; García-Ripoll and Perez-Garcia, 2001; Modugno et al., 2003).

Evidence of vortex bending in the ground state was observed by the ENS group (Rosenbusch et al., 2002). They prepared a single vortex state slightly above Ω_c and equilibrated it for a sufficient long time. In the TOF measurements, two imaging beams were aligned along the y and z directions and probed the atom distribution simultaneously (Figure 5a). The transverse image in Figure 5b shows the vortex line, corresponding to the
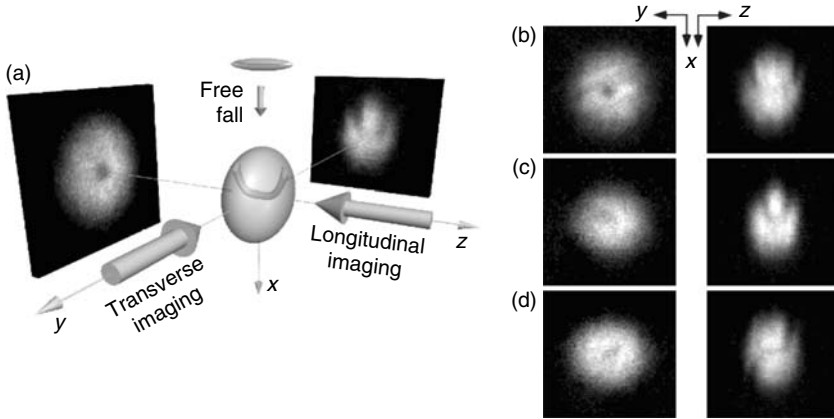
FIGURE 5 (a) Schematic of the imaging method of a vortex line. Two beams image the atom cloud simultaneously along the longitudinal (z) and transverse (y) directions of the initial cigar. In (b)–(d), the left column shows the 'longitudinal' view along z, representing the atom distribution in the xy plane. The right column depicts the 'transverse' view along the y direction, representing the atom distribution in the xz plane. The images were taken after equilibration times of (b) 4 s, (c) 7.5 s, (d) and 5 s. In the atom distribution of the transverse image, the ellipticity is inverted with respect to the initial cigar form, caused by transverse expansion during the TOF.
Source: Rosenbusch et al. (2002). Reprinted with permission from APS.

lower atom density; it is not straight and has the shape of a wide 'U'. Figure 5c shows the decay of a U vortex for which the angular momentum has decreased significantly compared with Figure 5b. In the longitudinal view, we can see a vortex off-centre. In the transverse view, a narrow U can be seen.

This result is supported by theoretical analysis based on the 3D GP equation with experimentally appropriate parameters (Aftalion and Jerrard, 2002; Aftalion and Danaila, 2003; García-Ripoll and Perez-Garcia, 2001; Modugno et al., 2003), where the ground state with a rotation $\boldsymbol{\Omega} = \Omega\hat{\mathbf{z}}$ was calculated by minimising the energy functional in Equation (11). The central vortex is generally bent if the trap aspect ratio $\lambda = \omega_z/\omega_\perp$ is much less than unity. A simple physical picture of the bending can be gained by viewing a cigar-shaped condensate as a series of 2D sheets at various z (Modugno et al., 2003). For each sheet, there is a corresponding 2D vortex stability problem with a critical frequency $\Omega_c^{2D}(z)$ (see Section 3.1), above which a centred vortex is the stable solution. Since the effective 2D chemical potential is $\mu_{2D}(z) = \mu - m\omega_z^2 z^2/2$, the radius of the 2D condensate at z becomes $R_\perp^2(z) = 2\mu_{2D}(z)/m\omega_\perp^2 = R_\perp^2(0) - \lambda^2 z^2$. Thus, $\Omega_c^{2D}(z) \propto R_\perp$ is a decreasing function from $z = 0$ to $|z| = R_z$. For a given rotation frequency Ω, the vortex line minimising the total energy is well centred

for $|z| < z_c$ and is strongly bent for $|z| > z_c$, where $\Omega_c^{2D}(z_c) = \Omega$. This bending is a symmetry-breaking effect, which does not depend on the presence of rotating anisotropy and which occurs even in a completely axisymmetric system (García-Ripoll and Perez-Garcia, 2001). A precursor of this bending effect can be found in the excitation spectrum of a condensate with a centred straight vortex (Feder, 2001a; Svidzinsky and Fetter, 2000b), in which negative-energy modes localised at the core (so-called 'anomalous modes') appear with increasing λ. As these modes grow, the central vortex is pushed outward. This indicates that the bending instability needs a dissipation mechanism and that it takes a long time at low temperatures.

Figure 5d shows a vortex line in the shape of an 'S', which can be regarded as a U vortex with a half part rotated by 180°. An S single vortex can also be found by numerical simulation as the stationary state of an elongated condensate for a given rotation frequency (Aftalion and Danaila, 2003), having an energy higher than that of the U vortex (Komineas et al., 2005).

4.2 Dynamical Properties

4.2.1 Precession and Decay of an Off-Centred Vortex

Precession of a vortex core off-centre in a condensate is a simple example of vortex motion. Core precession can be described in terms of a Magnus force effect. A net force on a quantised vortex core creates a pressure imbalance resulting in core motion perpendicular to both the force and the vortex quantisation axis. In the case of trapped BECs, these net forces can be caused by either condensate density gradients (Jackson et al., 1999; McGee and Holland, 2001; Svidzinsky and Fetter, 2000a,b) or drag due to thermal atoms (Fedichev and Shlyapnikov, 1999). The former may be thought of as a sort of effective buoyancy. Typically, the total buoyancy force is towards the condensate surface, and the net effect is a precession of the core around the condensate axis via the Magnus effect. The latter causes radial drag and spiraling of the core towards the condensate surface due to energy dissipation and damping processes.

Core precession has been investigated in detail by the JILA group (Anderson et al., 2000). Starting with a composite vortex created by the phase-engineering method of Section 3.3, they selectively removed components filling the vortex core with resonant light pressure. In the limit of complete removal, a single-component vortex state with a bare core can be obtained. The vortex was off-centre because of the instability of the formation process. The precession frequency was determined from the vortex position taken directly from the density profile. The vortex core precessed in the same direction as the vortex fluid flow around the core. The obtained

result of 1.8 Hz agrees well with analytical results based on the Magnus force picture (Svidzinsky and Fetter, 2000a,b) and more precise numerical simulations (Feder, 2001a; Jackson et al., 1999; McGee and Holland, 2001).

In some results, the vortex core disappeared from the observed images during the time evolution. However, these were not associated with the decay of vortices because there was no evidence of radial spiral motion due to energy dissipation, which could be caused by the thermal drag (Fedichev and Shlyapnikov, 1999) or the sound radiation from a moving vortex (Lundh and Ao, 2000; Parker et al., 2004). Subsequently, an experiment using the surface wave spectroscopic technique revealed that vortices were actually present for a long time in the condensate (Haljan et al., 2001). The main cause of the disappearance was the tilting motion of a vortex, the lowest odd-order normal mode of a single vortex state, which is sensitive to small trap anisotropy (Svidzinsky and Fetter, 2000b).

4.2.2 Vortex Dynamics Coupled With Collective Modes

Vortex dynamics are greatly affected by the overall collective motion of the condensate because of the mesoscopic nature of the system. Here, we detail several interesting results of coupled dynamics. The determination of the frequency of the collective modes allows precise measurement of the angular momentum carried by the quantised vortices.

Transverse Quadrupole Mode   The collective modes of a trapped condensate can be classified by expressing the density fluctuations in terms of polynomials of degree in the cartesian coordinates $(x_1, x_2, x_3) = (x, y, z)$. The quadrupole modes are characterised by a density fluctuation with a polynomial of second order, for example, $\delta n = \sum p_{ij} x_i x_j$, which gives six normal modes. In an axisymmetric harmonic potential, linear combinations of the diagonal components p_{xx}, p_{yy}, and p_{zz} describe three normal modes: one transverse mode with $m_z = 2$ and two radial-breathing modes with $m_z = 0$, where m_z is the projected angular momentum on the symmetry axis. The remaining three normal modes are associated with the off-diagonal components p_{xy}, p_{yz} and p_{zx}, which are scissors modes (Guery-Odelin and Stringari, 1999; Marago et al., 2000).

The first study was done for the excitation of two transverse quadrupole modes with $m_z = \pm 2$ (Chevy et al., 2000). When a vortex is present in a condensate, the frequencies of the $m_z = \pm 2$ quadrupole modes increase by $\omega_+ - \omega_- = 2\langle L_z \rangle / mN \langle x^2 + y^2 \rangle$ because of broken rotational symmetry (Zambelli and Stringari, 1998), where $\langle \ \rangle$ stands for the average within the condensate. The increase causes precession of the eigenaxes of the quadrupole mode at an angular frequency $\dot{\theta} = (\omega_+ - \omega_-)/2|m_z|$. By measuring the angular velocity of this precession, we can determine

the mean angular momentum $\langle L_z \rangle$ of the condensate. This spectroscopic method has also been used to characterise the tilting motion of a vortex (Haljan et al., 2001) and the winding number of a single vortex (Leanhardt et al., 2002).

Excitation of the transverse quadrupole mode yields further interesting vortex dynamics. The ENS group observed that when the superposition of the $m_z = \pm2$ quadrupole modes are excited with equal amplitudes, the oscillation of the $m_z = -2$ mode decays faster than that of the $m_z = +2$ mode (Bretin et al., 2003). A possible physical origin of this phenomenon is that the $m_z = -2$ mode decays to Kelvin modes through a nonlinear Beliaev process. This is supported by theoretical analysis based on the BdG equation (Mizushima et al., 2003). Kelvin modes correspond to long-wavelength helical traveling waves along a vortex line with a dispersion relation $\omega_K \simeq (\hbar k^2/2m) \ln(1/k\xi)$ ($k\xi \ll 1$). According to the Kelvin–Helmoltz theorem, the Kelvin modes rotate always in the sense opposite to the vortex velocity field. Consequently, the angular momentum of a quantum of a Kelvin mode associated with a singly-quantised vortex is $-\hbar$. Because of the negative angular momentum with respect to the vortex winding number, this mechanism is effective only for the $m_z = -2$ mode. From the energy $\omega_{-2} = 2\omega_K$ and angular momentum conservation, an excitation of the quadrupole mode $m_z = -2$ can decay to a pair of Kelvin-waves with wave vectors k and $-k$, while angular momentum conservation forbids the decay of the $m_z = +2$ mode.

Gyroscope Motion   What happens when the other quadrupole modes are excited in a condensate with a vortex? The Oxford group studied the response of a condensate with a vortex when the xz or yz scissors modes are excited (Hodby et al., 2003). Similar to the case of transverse quadruople modes, in the presence of the vortex, the plane of oscillation of a scissors mode precesses slowly around the z axis. In polar coordinates, the scissors oscillation is in the θ direction and the precession is in the ϕ direction, as shown schematically in Figure 6. This can be regarded as a kind of gyroscope motion of the vortex line (Stringari, 2001).

The relationship between the precession rate and $\langle L_z \rangle$ can be derived by considering the scissors mode as an equal superposition of two counter-rotating $m_z = \pm1$ modes. These modes represent a condensate tilted by a small angle from the horizontal plane rotating around the z axis at the frequency of the scissors oscillation, $\omega_\pm = \omega_{sc}$. The symmetry and degeneracy of these modes are also broken by the axial angular momentum $\langle L_z \rangle$. By applying a similar argument as that for transverse quadrupole modes (Stringari, 2001), the precession rate is related to the frequency splitting, $\omega_+ - \omega_- = \langle L_z \rangle / mN \langle x^2 + z^2 \rangle$, allowing the angular momentum $\langle L_z \rangle$ to be determined.
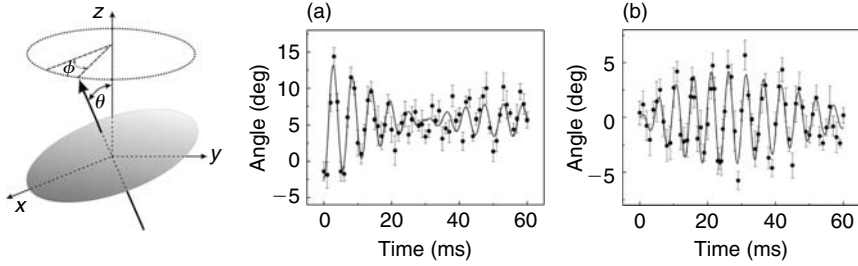
FIGURE 6   Left: schematic picture of gyroscope motion of the experiment of Hodby et al. (2003). The scissors mode involves a fast oscillation of the small angle θ between the condensate normal axis and the z axis. When a vortex is present, the plane of this oscillation (initially the xz plane with $\phi = 0$) slowly precesses through angle ϕ about the z axis. Right: data of the evolution of the tilt angle θ projected onto the xz plane when the scissors mode is initially excited (a) in the xz plane and (b) in the yz plane. *Source:* Hodby et al. (2003). Reprinted with permission from APS.

The precession associated with gyroscope motion can be seen in the results of Figure 6a and b, corresponding to a slowly varying oscillation component. The pattern of increase and decrease of the amplitude is exchanged between (a) and (b), with different directions of the excitation. This is a clear evidence of a slow precession along the ϕ direction. The results also show that the motion of the vortex core exactly follows the axis of the condensate. These observations can be well reproduced by direct numerical simulations of the 3D GP equation (Nilsen et al., 2003). From the precession rate, the measured angular momentum per particle associated with a vortex line was found to be $1.07\,\hbar \pm 0.18\,\hbar$.

4.2.3 Splitting of a Multiply Quantised Vortex

The energy cost to create a $q > 1$ vortex is less favourable than q single-quantised vortices, as seen in Equation (10). This raises an interesting question as to what happens when such an unstable vortex is created. As it happens, topological phase imprinting, shown in Section 3.3.2, can be used to create an unstable vortex.

The stability characteristics of a multiply quantised vortex in a trapped BEC exhibit an interesting interaction dependence because of the finite-size effect (Pu et al., 1999). BdG analysis for a cylindrical system reveals complex eigenvalue modes, which implies that a multiply quantised vortex is dynamically unstable. For a vortex with a winding number q, angular momentum conservation leads to constraints on the normal mode functions $u_j(\mathbf{r}) = u_j(r)e^{i(k_j+q)\theta}$ and $v_j(\mathbf{r}) = v_j(r)e^{i(k_j-q)\theta}$, where k_j denotes the angular momentum quantum number of the mode. For $q = 2$, there are alternating stable and unstable regions with respect to the interaction parameter $an_z = a \int |\Psi|^2 \mathrm{d}x\mathrm{d}y$; the first and second regions appear for

$0 < an_z < 3$ and $11.4 < an_z < 16$. Numerical simulations demonstrate that when a system is in an unstable region, a doubly quantised vortex decays into two singly quantised vortices (Möttönen et al., 2003).

An experiment by the MIT group studied the splitting process of a doubly quantised vortex and its characteristic timescale as a function of $an_{z=0}$ (Shin et al., 2004). The results show that a doubly quantised vortex decays, but that the lifetime increases monotonically with $an_{z=0}$, showing no periodic behaviour. This is contrary to the above theoretical prediction. Recent numerical studies of 3D GP equations reveal this mysterious observation, emphasising that the detailed dynamical behaviour of a vortex along the entire z-axis is relevant for characterising the splitting process in an elongated condensate (Huhtamäki et al., 2006a; Mateo, 2006).

The trigger for splitting instability is likely to be gravitational sag during the formation process with a reversing axial bias field B_z (Huhtamäki et al., 2006a). In experiments, absorption images were restricted to a 30-μm thick central slice of the condensate to increase the visibility of the vortex cores. The experimental results in Figure 7a shows that the fastest decay occurs at $an_z \simeq 1.5$, consistent with the BdG and numerical analysis. As the particle number increases, the first instability region ($0 < an_z < 3$) moves progressively away from the central slice towards
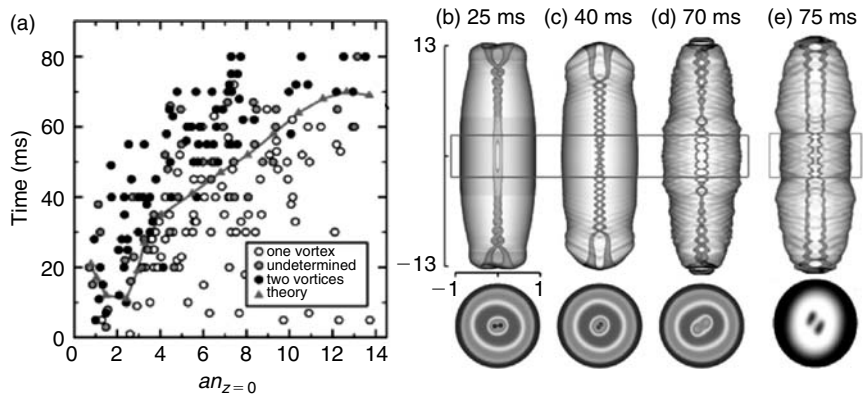
FIGURE 7 Splitting process of a doubly quantised vortex. (a) Experimental data combined with theoretically predicted splitting times as a function of $an_{z=0}$ for a 4% quadrupolar perturbation acting during 0.3 ms. The splitting is identified by the number of visible vortex cores from the density profile of the axial absorption images taken from a 30-μm thick central slice of the condensate. (b)–(e): time evolution of the splitting process for $an_{z=0} = 13.75$, obtained by a 3D simulation of the GP equation. The shaded zones in (b) indicate the instability regions. The corresponding axial absorption images of the central slice are also shown at the bottom of the figure. The lengths are in units of 6.05 μm.

Source: Mateo (2006). Reprinted with permission from APS.

the edges of the condensate because of the trapping potential. As a consequence, the splitting instability of the vortex core has to propagate from those regions to the centre. This process is responsible for the monotonic increase in the lifetime for $an_z > 3$. According to the theory, a second minimum is expected about $an_{z=0} \simeq 13.75$. Even though no such minimum occurs, a change in the slope of the predicted curve at $an_{z=0} \simeq 13.75$ is seen as $an_{z=0}$ enters the second instability region (Huhtamäki et al., 2006a; Mateo, 2006). Figures 7b–e show the time evolution of the splitting process for $an_{z=0} = 13.75$. The first and second instability regions correspond to the shaded zones in Figure 7b. This clearly shows that at $t = 25$ ms, the splitting process has already begun in both the edges and the centre of the condensate. The different precession frequency along different z slices causes interwinding of two single-quantised vortices. However, the two vortex cores near the central slice still overlap (Figure 7c) and thus cannot be experimentally resolved until much longer times. At $t \approx 70$ ms (Figure 7d), the vortex cores begin to disentangle so that they can be unambiguously resolved at $t = 75$ ms (Figure 7e). Thus, there is no contradiction with the theoretical prediction.

The physical origin of the periodic appearance of the unstable region is anomalous modes with negative eigenvalues. When the eigenvalue of positive-energy modes coincides with the absolute value of the eigenvalue of negative-energy modes, a complex eigenvalue mode are produced through mutual annihilation of these two excitations (Jackson et al., 2005; Kawaguchi and Ohmi, 2004; Lundh, 2006; Skryabin, 2000); the total angular momentum of these excitations is also vanished. Since the an_z dependence of the negative-energy eigenvalues is very different from that of positive-energy ones, the above matching condition can be satisfied in sequence with increasing an_z, which results in the periodic appearance of the complex-eigenvalue modes. Thus, splitting instability of a multiply quantised vortex can be suppressed for a particular trap asymmetry and interaction strength because the collective excitations depend strongly on the character of the trapping potential (Huhtamäki et al., 2006b). It has also been predicted that multiply quantised vortices can be stabilised by introducing a suitable localised pinning potential (Simula et al., 2002a) or simply connected geometry such as quartic confinement (Lundh, 2002). Very recently, splitting dynamics of a quadruply quantised ($q = 4$) vortex was reported (Isoshima et al., 2007).

5. A LATTICE OF QUANTISED VORTICES IN AN ATOMIC BEC

We now address the issue of a rapidly rotating BEC where many vortices have been nucleated and arranged into a regular triangular lattice (Abo-Shaeer et al., 2001; Coddington et al., 2004). We first present a discussion of the equilibrium properties of a rapidly rotating condensate

and then present the basic theoretical background for its description. The equilibrium properties of vortex lattices in a trapped BEC have been extensively studied by the JILA group (Coddington et al., 2004; Schweikhard et al., 2004a). We next discuss the collective dynamics of an assembly of vortices in a trapped BEC. Finally, we discuss an unconventional vortex phase which occurs in the presence of an externally applied potential created by laser beams.

5.1 Equilibrium Properties

For very large Ω, the rotation of the superfluid mimics a rigid body rotation with $\nabla \times \mathbf{v}_s = 2\mathbf{\Omega}$ by forming a vortex lattice. Using the fact that the vorticity is given by the form $\nabla \times \mathbf{v}_s = \kappa \delta^{(2)}(\mathbf{r}_\perp)\hat{\mathbf{z}}$, we find that the average vorticity per unit area is given by $\nabla \times \mathbf{v}_s = \kappa n_v \hat{\mathbf{z}}$, where n_v is the number of vortices per unit area. Hence, the density of the vortices is related to the rotation frequency Ω as $n_v = 2\Omega/\kappa$ (Feynman et al., 1955). This relation can be used to estimate the maximum possible number of vortices in a given area as a function of Ω. As shown below, the properties of a vortex lattice can be characterised by the nearest-neighbour lattice spacing $\sim b = (\hbar/m\Omega)^{1/2}$, defined by the area per vortex $n_v^{-1} = \pi b^2$, and by the radius of each vortex core $\sim \xi$.

Note that the GP energy functional of Equation (11) in a rotating frame can be rewritten as

$$E' = \int d\mathbf{r} \left(\frac{\hbar^2}{2m} \left| \left(-i\nabla - \frac{m}{\hbar}\mathbf{\Omega} \times \mathbf{r}\right)\Psi \right|^2 + V_{\text{eff}}|\Psi|^2 + \frac{g}{2}|\Psi|^4 \right), \quad (14)$$

where $V_{\text{eff}} = m(\omega_\perp^2 - \Omega^2)r^2/2 + m\omega_z^2 z^2/2$ is the effective trapping potential combined with the centrifugal potential; the rotation effectively softens the radial potential and vanishes at $\Omega = \omega_\perp$. Because the first term in Equation (14) reads $\hbar^2(\nabla|\Psi|)^2/2m + m(\mathbf{v}_s - \mathbf{\Omega} \times \mathbf{r})^2|\Psi|^2/2$, it can be neglected in the TF limit and the rigid body rotation limit $\mathbf{v}_s = \mathbf{\Omega} \times \mathbf{r}$. Then, the TF radius is given by $R_\perp(\Omega) = R_\perp/[1 - (\Omega/\omega_\perp)^2]^{3/10}$ with $R_\perp$ for nonrotating condensate and an aspect ratio of $\lambda_{\text{rb}} = R_\perp(\Omega)/R_z = \lambda/[1 - (\Omega/\omega_\perp)^2]^{1/2}$. Thus, measuring λ_{rb} will give the rotation rate of the condensate (Haljan et al., 2001; Raman et al., 2001). Also, in the high rotation limit $\Omega \to \omega_\perp$, the condensate flattens out and reaches an interesting quasi-2D regime; current experiments have reached $\Omega/\omega_\perp \approx 0.995$ (Coddington et al., 2004).

Abrikosov triangular lattice of quantised vortices have been observed experimentally, as shown in Figure 2. Direct imaging allows a detailed investigation of the nature of a vortex lattice in an inhomogeneous superfluid. Here, we summarise the salient results and theoretical interpretations of these observations.

5.1.1 Lattice Inhomogeneity

Experimental observations (Abo-Shaeer et al., 2001; Engels et al., 2002) and numerical simulation of the 3D GP equation (Feder, 2001b) have revealed that for a finite-size trapped BEC, the vortex density in a lattice is lower than the rigid body estimate and the lattice is remarkably regular. Sheehy and Radzihovsky (2004a,b) explained these points analytically in the TF limit; they derived a small, radial-position-dependent, inhomogeneity-induced correction term to the vortex density as

$$n_v(r) = \frac{2\Omega}{\kappa} - \frac{1}{2\pi} \frac{R_\perp(\Omega)^2}{(R_\perp(\Omega)^2 - r^2)^2} \ln \frac{e^{-1}\kappa}{2\pi\Omega\xi^2}. \tag{15}$$

This result indicates that the vortex density is always lower than the rigid body estimate of the first term in Equation (15). Also, the vortex density is higher in regions where the condensate density is most uniform, that is, the central part of a harmonically trapped gas. However, the position-dependent correction is small (n_v changes less than a few % over a region in which the atom density varies by 35%), which seemingly causes regularity of the lattice. These results have been confirmed by a detailed experimental study (Coddington et al., 2004). It should be also noted that inhomogeneity in the area density of vortices can also be derived in the limit of the lowest Landau level (LLL) (Aftalion et al., 2005; Baym et al., 2007; Cooper et al., 2004; Watanabe et al., 2004), as explained below.

5.1.2 Attainment of the LLL Regime

Note that the first term in Equation (14) can be identified as the Hamiltonian $H_L = (-i\hbar\nabla - e\mathbf{A}/c)^2/2m$ of a charge $-e$ particle moving in the xy plane under a magnetic field $B\hat{z}$ with a vector potential $\mathbf{A} = (mc/e)\mathbf{\Omega} \times \mathbf{r}$. If the interaction is neglected ($g = 0$), the eigenvalues of the Hamiltonian of Equation (14) forms Landau levels as $\epsilon_{n,m}/\hbar = \omega_\perp + n(\omega_\perp + \Omega) + m(\omega_\perp - \Omega)$, where n is the Landau level index and m labels the degenerate states within a Landau level. The lowest energy states of two adjacent Landau levels are separated by $\hbar(\omega_\perp + \Omega)$, whereas the distance between two adjacent states in a given Landau level is $\hbar(\omega_\perp - \Omega)$; when $\Omega = \omega_\perp$, all states in a given Landau level are degenerate. Physically, this corresponds to the case where the centrifugal force exactly balances the trapping force in the x-y plane and only the Coriolis force remains. The system is then invariant under translation and hence has macroscopic degeneracy. This formal analogy has led to the prediction that quantum Hall-like properties would emerge in rapidly rotating BECs (Cazalilla et al., 2005; Chang et al., 2005;

Cooper et al., 2001; Ho, 2001; Morris and Feder, 2006; Regnault and Jolicoeur, 2003, 2004; Rezayi et al., 2005; Sinova et al., 2002; Viefers et al., 2000).

Interaction effects mix different (m, n) states. Because the density $\bar{n}$ of the system drops as $\Omega \to \omega_\perp$, the interaction energy $\sim g\bar{n}$ can become small compared with the Landau level separation $2\hbar\omega_\perp$. In this limit, particles should condense into the LLL with $n = 0$. Then, the system enters the 'mean field' quantum Hall regime, where the wave function can be described by only the LLL orbitals with the form $\Psi_{\text{LLL}} = A \prod_j (z - z_j) e^{-r^2/2a_{\text{ho}}^2}$, where $z = x + iy$, z_j is the positions of vortices (zeros), and A is a normalisation constant. The minimisation of Equation (14) using the ansatz Ψ_{LLL} is a useful theoretical prescription to tackle the properties of rapidly rotating BECs (Aftalion et al., 2005, 2006; Cooper et al., 2004; Cozzini et al., 2006; Sonin, 2005b; Watanabe et al., 2004).

Schweikhard et al. (2004a) created rapidly rotating BECs by spinning condensates to $\Omega/\omega_\perp > 0.99$. When the condensate enters the LLL regime, characteristic equilibrium properties appear, as described below.

Global Structure   In the LLL limit, the radial condensate density profile with uniform vortex distribution has been predicted to change from a parabolic TF profile to a Gaussian profile as Ω is increased (Ho, 2001). However, no signs of such crossover have been found in experiments; even when the dynamics were restricted to the LLL, the density profile remained a parabolic TF profile as $\Omega \to \omega_\perp$ (Coddington et al., 2004; Schweikhard et al., 2004a). This result can be seen qualitatively from the energy minimisation under the LLL limit with nonuniform vortex density (Aftalion et al., 2005; Cooper et al., 2004; Watanabe et al., 2004). As long as the total number of vortices is much larger than unity ($N_v \gg 1$), the energy in the LLL regime is given by

$$E' = \Omega N + \int d\mathbf{r} \left[(\omega_\perp - \Omega)\frac{r^2}{a_{\text{ho}}^2} n(\mathbf{r}) + \frac{bg}{2} n(\mathbf{r})^2 \right] \qquad (16)$$

plus terms involving the trapping potential in the z-direction. Here, $n(\mathbf{r}) = \langle |\Psi_{\text{LLL}}|^2 \rangle$ is the coarse grain-averaged density profile in order to smooth the rapid variations at the vortex cores. Then, the interaction parameter g is renormalised to bg, where $b = \langle |\Psi_{\text{LLL}}|^4 \rangle / \langle |\Psi_{\text{LLL}}|^2 \rangle^2$ is the Abrikosov parameter. The energy (Equation (16)) is then minimised by the TF profile, $n(r) = [\mu - \Omega - (\omega_\perp - \Omega)r^2/a_{\text{ho}}^2]/bg$.

Since the energy (Equation (16)) depends only on the smoothed density, the vortices adjust their locations so that the smoothed density becomes an inverted parabola. In the LLL regime, the relation between the condensate density $n(\mathbf{r})$ and the mean vortex density $n_v(\mathbf{r}) = \sum_j \delta(\mathbf{r} - \mathbf{r}_j)$ is given by

$4^{-1}\nabla^2 \ln n(\mathbf{r}) = -a_{\text{ho}}^{-2} + \pi n_v(\mathbf{r})$ (Aftalion et al., 2005; Ho, 2001). If the density profile is Gaussian, the vortex density is constant. However, for a TF profile,

$$n_v(r) = \frac{2\Omega}{\kappa} - \frac{1}{\pi R_{\perp}^2} \frac{1}{\left(1 - r^2/R_{\perp}^2\right)^2}. \tag{17}$$

This result is similar to Equation (15) in the low rotation regime, where the coefficient of the second term is different. Since the second term is smaller than the first, as $\sim a_{\text{ho}}^2/R_{\perp}^2 \simeq N_v^{-1}$, the density of the vortex lattice is basically uniform, consistent with the argument in Section 5.1.1. Turning the argument around, very small distortions of the vortex lattice from perfect triangular can result in large changes in the global density distribution such that the TF form is energetically favoured rather than the Gaussian.

Vortex Core Structure and Fractional Area Another interesting characteristic of the LLL is that the vortex core is of the same size as the distance $b = (\hbar/m\Omega)^{1/2}$ between adjacent vortices. The radius of a single vortex core is of order $\xi = 1/\sqrt{8\pi na}$ so that a vortex core would begin to overlap the next at $\xi \sim b$. This gives an upper-critical rotation frequency $\Omega_{c1} \sim 8\pi na\hbar/m \sim 10^3 - 10^5$ rad/s, which is an experimentally accessible rate. However, there is no phase transition associated with vortex cores overlapping in a rotating condensate. Rather, vortex cores begin to shrink as the intervortex spacing becomes comparable to the healing length ξ, and eventually the core radius scales with the intervortex spacing (Baym, 2004b; Fischer and Baym, 2003; Watanabe et al., 2006).

Figure 8 shows the measured fractional area, defined as $\mathcal{A} = r_v^2/b^2 = n_v\pi r_v^2$, as a function of the inverse of the LLL parameter $\Gamma_{\text{LLL}} = \mu/2\hbar\Omega$ (Coddington et al., 2004; Schweikhard et al., 2004a). The linear rise of $\mathcal{A}$ at small Ω occurs because the core size remains constant, while n_v increases linearly with Ω. Explicitly, the core radius was estimated numerically as $r_v = 1.94\xi$ (Schweikhard et al., 2004a), and $n_v = m\Omega/\pi\hbar$ by neglecting the effect of inhomogeneity. These values yield $\mathcal{A} = 1.34\Gamma_{\text{LLL}}^{-1}$, shown by the dashed line in Figure 8, where $n = 0.7n_{\text{peak}}$ and $\mu = gn_{\text{peak}}$ were used for the estimation. The flattening of $\mathcal{A}$ with increasing Ω is a consequence of the vortex radius scaling with the intervortex spacing. The upper dotted line shows the upper limit $\mathcal{A} = 0.225$ obtained by using the oscillator p-state structure $|\Psi_{\text{core}}(r)|^2 \sim [(r/b)\exp(-r^2/2b^2)]^2$ as the profile of a vortex core in the LLL limit, where b is regarded as the radius of the (cylindrical) Wigner–Seitz cell around a given vortex. The data in Figure 8 show the expected initial linear rise, with the predicted scaling of the core radius with intervortex spacing. More detailed theoretical studies
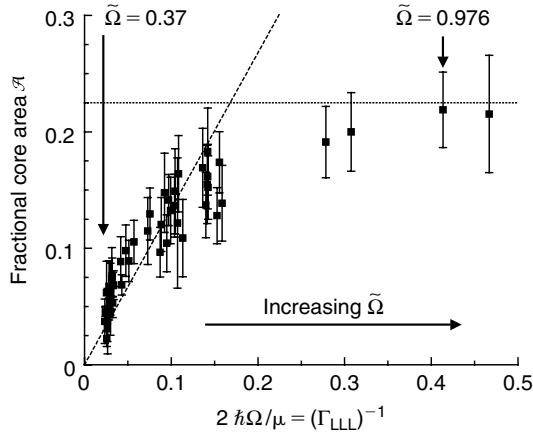
FIGURE 8 Fraction of the condensate surface area occupied by vortex cores $\mathcal{A}$ (see text) versus the inverse of the LLL parameter Γ_{LLL}^{-1}, measured after condensate expansion. The data clearly show a saturation of $\mathcal{A}$ as $\Omega/\omega_\perp \to 1$. The dashed line represents the prediction for the preexpansion value in the case of a low rotation rate. The dotted line shows the results for a saturated value of $\mathcal{A}$ in the LLL limit. *Source:* Schweikhard et al. (2004a). Reprinted with permission from APS.

which treat the core structure explicitly obtain excellent agreement with the experimental results (Cozzini et al., 2006; Watanabe et al., 2006).

5.2 Collective Dynamics of a Vortex Lattice

5.2.1 Vortex Lattice Dynamics Coupled With Collective Modes

As shown in Section 4.2.2, vortex states undergo interesting responses to excitation of the transverse quadrupole modes with $m_z = \pm 2$. Similar studies have been made for rapidly rotating BECs. In this case, the dispersion relation of the quadrupole modes is given by $\omega_{\pm 2} = \sqrt{2\omega_\perp^2 - \Omega^2} \pm \Omega$ (Cozzini et al., 2003), which has been measured experimentally (Haljan et al., 2001). When $\Omega \to \omega_\perp$, we have $\omega_{+2} \to 2\omega_\perp$ and $\omega_{-2} \to 0$, reflecting the tendency of the system to become unstable against quadrupole deformation. Excitation of the quadrupole mode for $\Omega \to \omega_\perp$ induces large deformations of the condensate and nonequilibruim dynamics of vortex lattices (Engels et al., 2002). Interestingly, when the $m_z = -2$ mode was excited, a vortex lattice was distorted to form a one-dimensional set of closely spaced vortices. This observation was explained by the fact that vortices should follow the stream line of the background quadrupole velocity field (Cozzini et al., 2003; Mueller and Ho, 2003). In contrast, excitation of an $m_z = +2$ mode dissolved the regular lattice, where the

vortex lines were randomly arranged in the x-y plane but were still strictly parallel along the z-axis.

As stated in Section 5.1, a centrifugal force distorts the cloud into an extremely oblate shape, and thus the rotating cloud approaches the quasi-2D regime. Excitation of an axial breathing mode ($m_z = 0$) has been used to confirm the 2D signature of a rapidly rotating BEC (Schweikhard et al., 2004a). For a BEC in the axial TF regime, an axial breathing frequency $\omega_B = \sqrt{3}\omega_z$ has been predicted in the limit $\Omega/\omega_\perp \to 1$ (Cozzini et al., 2003), whereas $\omega_B = 2\omega_z$ is expected for a noninteracting gas, expected for $\mu < \hbar\omega_z$. Schweikhard et al. (2004a) observed a crossover of ω_B from $\sqrt{3}\omega_z$ to $2\omega_z$ with increasing Ω ($\mu \sim 3\hbar\omega_z$). Also, excitation of the scissors mode in a condensate with a vortex lattice induces a collective tilting mode of the vortex array (the lowest-energy Kelvin-wave of the lattice) (Smith et al., 2004), referred to as an anomalous scissors mode (Chevy and Stringari, 2003).

5.2.2 Transverse Oscillation of a Vortex Lattice: Tkachenko Mode

The dynamics of vortex lattices itself raises many interesting problems. It should be possible to propagate collective waves in a transverse direction to the vortex lattice in the superfluid, called Tkachenko (TK) modes. For an incompressible superfluid, the dispersion law is given by $\omega_{TK}(k) = \sqrt{\hbar\Omega/4mk}$. The TK modes of a vortex lattice in a trapped BEC have been analysed theoretically (Baksmaty et al., 2004; Baym, 2003, 2004a; Cozzini et al., 2004; Gifford and Baym, 2004; Mizushima et al., 2004; Sonin, 2005a,b) and observed experimentally (Coddington et al., 2003).

Experimentally, TK modes have been excited by the selective removal of atoms at the centre of a condensate with a resonant focused laser beam or by the insertion of a red detuned optical potential at the centre to draw atoms into the middle of the condensate. The former method has also been used to create long-lived vortex aggregates (Engels et al, 2003). In the experiment, the TK modes were identified by the sinusoidal displacement of the vortex cores with the origin at the centre of the condensate; see Figure 9a. TK modes can be classified by the quantum number (n, m), associated with radial and angular nodes, in a presumed quasi-2D geometry.

To explain the observed frequency of the TK mode $\omega_{(n,m)}$, the effects of compressibility should be taken into account. According to the elasto-hydrodynamic approach developed by Baym (2003), the TK frequency is described by the compressional modulus C_1 and shear modulus C_2 of the vortex lattice, included in the elastic energy

$$E_{el} = \int d\mathbf{r} \left\{ 2C_1(\nabla \cdot \epsilon)^2 + C_2 \left[\left(\frac{\partial \epsilon_x}{\partial x} - \frac{\partial \epsilon_y}{\partial y} \right)^2 + \left(\frac{\partial \epsilon_x}{\partial y} + \frac{\partial \epsilon_y}{\partial x} \right)^2 \right] \right\},$$

(18)
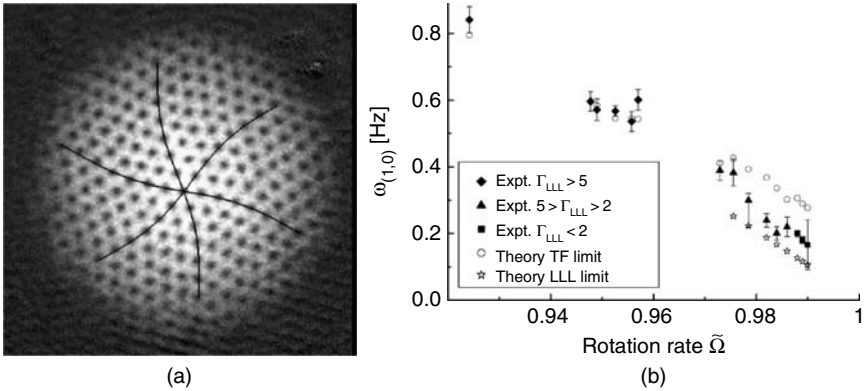
FIGURE 9 (a) TK mode $(n, m) = (1, 0)$ at $N = 1.5 \times 10^5$ and $\Omega = 0.989\omega_\perp$, fitted by sine fits. (b) Comparison of measured TK mode frequency $\omega_{(1,0)}$ (solid symbols) versus the theoretical value (Baym, 2003), using the vortex lattice shear modulus C_2^{TF} in the TF limit (circles) and C_2^{LLL} in the LLL regime (stars). Note that both N and Γ_{LLL} decrease as $\tilde{\Omega} = \Omega/\omega_\perp$ increases. For $\Gamma_{LLL} \simeq 3$ (reached at $N = 7.8 \times 10^5$ and $\tilde{\Omega} \simeq 0.978$), the data cross over from the TF to the LLL prediction.
Source: Schweikhard et al. (2004a). Reprinted with permission from APS.

where $\epsilon(\mathbf{r}, t)$ is the continuum displacement field of the vortices from their home positions. In the incompressible TF regime, $C_2 = -C_1 = n\hbar\Omega/8$. Then, the upper branch of the energy spectrum follows the dispersion law $\omega_+^2 = 4\Omega^2 + c^2 k^2$ with sound velocity $c = \sqrt{gn/m}$, being the standard inertial mode of a rotating fluid and having a gap at $k = 0$. Conversely, the low frequency branch corresponds to the TK mode and has

$$\omega_-^2 = \frac{\hbar\Omega}{4m} \frac{c^2 k^4}{4\Omega^2 + c^2 k^2}. \tag{19}$$

For large k, this reproduces the original TK frequency ω_{TK}, while for small k it exhibits the quadratic behaviour $\omega_- \simeq \sqrt{\hbar/16m\Omega}\, ck^2$. The transition between k^2 and k dependence occurs at $k \sim \Omega/c > R_\perp^{-1}$. This suggests that the effects of compressibility, characterising the k^2 dependence, play a crucial role in the TK mode. Thus, this regime is distinguished from the usual incompressible TF regime as the 'soft' TF regime. When the finite compressibility is included, the observed values of $\omega_{(1,0)}$ are well explained (Baym, 2003; Cozzini et al., 2004; Sonin, 2005a). First-principle simulations based on the GP formalism also agree excellently with the experimental data (Baksmaty et al., 2004; Mizushima et al., 2004).

In the LLL limit, corrections to the elastic shear modulus C_2 of the vortex lattice are important; with increasing Ω, its value eventually reaches

$C_2^{\text{LLL}} \simeq (81/80\pi^4)mc^2n$ (Baym, 2003). Using this value, Schweikhard et al. (2004a) compared the measured $\omega_{(1,0)}$ with the theoretical prediction, finding a crossover of $\omega_{(1,0)}$ from the TF results to the LLL results as shown in Figure 9b. However, more detailed theoretical analysis in the LLL limit revealed that the value of the shear modulus is estimated as $0.1027mnc^2$, which is a factor of 10 larger than $(81/80\pi^4)mnc^2$ (Cozzini et al., 2006; Sinova et al., 2002; Sonin, 2005b). This indicates that even though the equilibrium properties in the experiment are consistent with the LLL picture, the data of the TK frequency are still far from the LLL limit. One possible explanation of this discrepancy is an underestimate of the rotation rate from the aspect ratio of the cloud due to the defocus of the imaging camera or the breakdown of the TF theory (Watanabe, 2007).

5.3 Vortices in an Anharmonic Potential

For a rotating condensate with a frequency Ω in a harmonic potential $(1/2)m\omega_\perp^2 r^2$, the centrifugal potential cancels the confinement, thus preventing a BEC from rotating at Ω beyond $\omega_\perp$. This restriction can be avoided by introducing an additional quartic potential so that the combined trapping potential in the xy plane becomes $V_{\text{ex}}(r) = (1/2)m\omega_\perp^2 (r^2 + \lambda r^4/a_{\text{ho}}^2)$, where the dimensionless parameter λ characterises the relative strength of the quartic potential. The properties of a rotating condensate in an anharmonic potential have recently attracted a lot of theoretical attention (Aftalion and Danaila, 2004; Bargi et al., 2006; Danaila, 2005; Fetter, 2001b; Fetter et al., 2005; Fischer and Baym, 2003; Fu and Zaremba, 2006; Jackson, 2004a,b; Kasamatsu, 2002a; Kavoulakis and Baym, 2003; Kim and Fetter, 2005; Lundh, 2002).

The vortex phases in an anharmonic trap are quite different from those in a harmonic trap since it is possible to rotate the system arbitrarily fast. The predicted phase diagram of the vortex states as a function of interparticle interaction strength versus rotation rate is shown in Figure 10. For small Ω, the equilibrium state is the usual vortex lattice state. As Ω increases, the vortices begin to merge in the central region and the centrifugal force pushes the particles towards the edge of the trap. This results in a new vortex state consisting of a uniform lattice (multiple circular arrays of vortices) with a central density hole. The central hole becomes larger with increasing Ω, and the condensate forms an annular structure with a single circular array of vortices. A further increase of Ω stabilises a *giant vortex*, where all vortices are concentrated in the single hole (Fischer and Baym, 2003).

A combined harmonic-plus-quartic potential was formulated by the ENS group by superimposing a blue detuned laser with the Gaussian profile (Bretin et al., 2003). Since the waist w of the beam propagating along the z-axis is larger than the condensate radius, the potential created by the
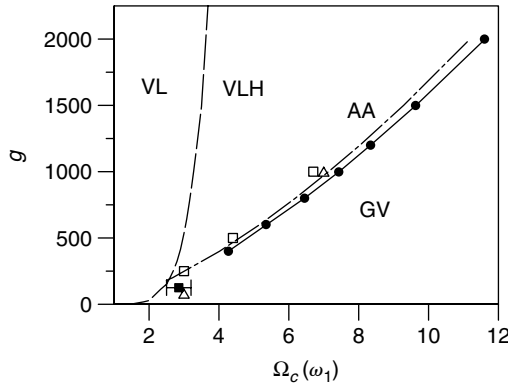
FIGURE 10 Phase diagram of the vortex state with an additional quartic potential for $\lambda = 1/2$ as a function of interparticle interaction strength ($g = 4\pi n_z a$) versus rotation rate ($\Omega_c = \Omega$). The dashed curve denotes the onset of a central density hole (VLH) in the uniform vortex lattice state (VL), obtained by TF analysis as $\Omega_h^2 = 1 + 2\sqrt{\lambda}(3\sqrt{\lambda}g/2\pi)^{1/3}$ (Fetter et al., 2005). The dashed-dotted curve and the solid points (•) joined by solid lines show the phase boundary Ω_c between the annular condensate with a circular array of vortices (AA) and the giant vortex (GV) state, which are determined by two different analytical methods (Fu and Zaremba, 2006). The open triangles ($\triangle$) are the values of Ω_c determined by the GP solution (Fetter et al., 2005), and the open squares ($\square$) are the results using an improved variational approach (Kim and Fetter, 2005). The filled square ($\blacksquare$) with error bars gives the approximate bounds on Ω_c determined numerically for $g = 125$ (Kasamatsu, 2002a). For a weakly interacting limit $g \sim 10$, a much richer structure was revealed (Jackson, 2004a,b). *Source:* Fu and Zaremba (2006). Reprinted with permission from APS.

laser $U_0 \exp(-2r^2/w^2)$ can be written as $U(r) \simeq U_0(1 - 2r^2/w^2 + 2r^4/w^4)$. The second term leads to a reduction of the transverse trapping frequency $\omega_\perp$ and the third term provides the desired quartic confinement, giving $\omega_\perp/2\pi = 65\,\text{Hz}$ and $\lambda \simeq 10^{-3}$ for $V_{\text{ex}}(r)$. Figure 11 shows experimental images of the condensate density as the rotation frequency Ω is increased (Bretin et al., 2003). For $\Omega < \omega_\perp$, the vortex lattice is clearly visible. When $\Omega > \omega_\perp$, however, the vortices becomes gradually difficult to observe and the images become less clear for $\Omega = 1.05\omega_\perp$ ($= 2\pi \times 68\,\text{Hz}$), which suggests a transition into a new vortex phase.

Despite the visibility of the cores, the angular momentum of the condensate monotonically increased, confirmed by the measurement of R_{TF} and surface wave spectroscopy. Hence, the most plausible explanation for this mysterious observation is that the vortex lines are still present but strongly bent when $\Omega > \omega_\perp$. This bending may occur due to the finite temperature effect on the fragile vortex lattice at a high rotation rate; numerical simulations of the 3D GP equation show that when looking for the ground state of the system using imaginary time evolution of the GP equation,

(a)

$\Omega/2\pi = 62$ 64   65   66   67   68

(b)
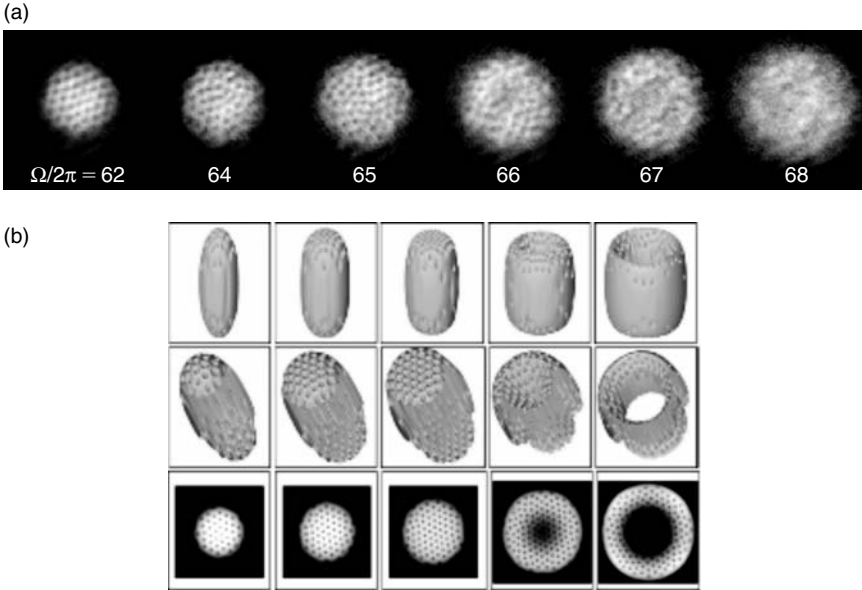
FIGURE 11   (a) Density profiles of a rapidly rotating condensate in a quadratic plus quartic potential for various stirring frequencies $\Omega/2\pi$. For these data, $\omega_\perp/2\pi = 65\,\text{Hz}$. (b) Ground state structure obtained by numerical simulations with a parameter corresponding to the experiment of (Bretin et al., 2003). The rotation frequency is $\Omega/2\pi = 60, 64, 66, 70.6, 73\,\text{Hz}$ (respectively, $\Omega/\omega_\perp = 0.92, 0.98, 1.01, 1.08, 1.11$) from left to right, where $\Omega/2\pi = 70.6\text{Hz}$ corresponds to Ω_h. The first two rows show 3D views of the vortex lattice as isosurfaces of low atomic density. In the bottom row, the density distribution is integrated along the z-axis.
Source: Bretin et al. (2003) and Danaila (2005). Reprinted with permission from APS.

much longer imaginary times were required to reach a well-ordered vortex lattice for $\Omega > \omega_\perp$ than for $\Omega < \omega_\perp$. Compared with the numerical results shown in the bottom in Figure 11, the condensate should still have an ordered visible lattice even for $\Omega \geq \omega_\perp$. To observe the density hole at the centre, it is necessary to rotate at a slightly faster rate than the upper frequency used in this experiment.

5.4 Vortex Pinning in an Optical Lattice

Rotating BECs combined with an optical lattice are an interesting system, which has two competing length scales, vortex separation and the periodicity of the optical lattice. The structure of the vortex lattice is strongly dependent on the externally applied optical lattice. Various vortex phases appear depending on the number of vortices per pinning centre, that is, the filling factor. The JILA group formulated a rotating optical lattice using a rotating mask (Tung et al., 2006). Such a rotating optical lattice provides
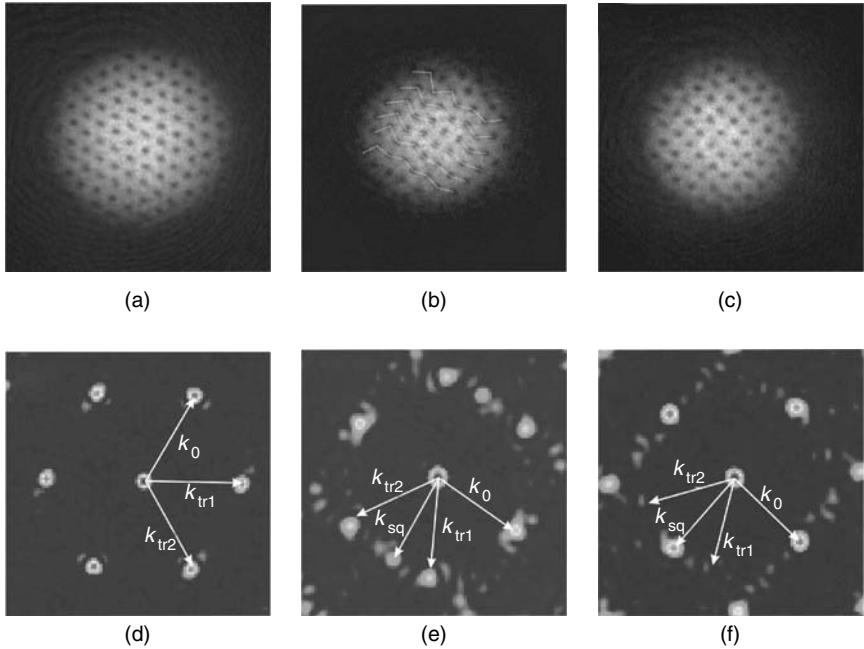
FIGURE 12 Images of rotating condensates pinned to a corotating optical lattice at $\Omega = 0.866\omega_\perp$ with pinning strength $U_{pin}/\mu =$ (a) 0.049, (b) 0.084, (c) 0.143, showing the structural crossover of the vortex lattice. (a)–(c) show absorption images of the vortex lattices after expansion. (d)–(f) are the Fourier transforms of the images in (a)–(c). k_0 is taken by convention to be the strongest peak; k_{tr1}, k_{sq} and k_{tr2} are at 60°, 90° and 120°, respectively, from k_0.
Source: Tung et al. (2006). Reprinted with permission from APS.

a periodic pinning potential which is static in the corresponding rotating frame. The authors have observed a structural crossover from a triangular to a square lattice by increasing the potential amplitude of the optical lattice, as shown in Figure 12. These observations are consistent with theoretical studies (Pu et al., 2005; Reijnders and Duine, 2004). The rotating optical lattice provides new phenomena in vortex physics for rotating bosons, such as the realisation of a driven vortex system in a periodic array (Kasamatsu and Tsubota, 2006) or strongly correlated phases in rotating bosons (Bhat et al., 2006).

6. OTHER TOPICS AND FUTURE STUDIES

In this section, we discuss other intriguing problems associated with quantised vortices in atomic BECs. Since many theoretical works have predicted

novel properties of vortices under a variety of situations, it is impossible to refer to all studies in this section. We thus select some important issues that have been highlighted in the ultracold atom community or are likely to be investigated in experiments in the near future.

6.1 A Vortex in an Attractively Interacting BEC

Although we have dealt primarily with vortices in repulsively interacting BECs, vortices in attractively interacting BECs characterised by a negative s-wave scattering length $a < 0$ have also received theoretical interest. A homogenous BEC with $a < 0$ is never stable due to self-focusing collapse, but a BEC in a confining potential can remain stable as long as the number of condensed atoms N lies below a critical value $N_c \sim a_{\text{ho}}/|a|$ (Bradley et al., 1995). This is because the self-focusing can be balanced by the kinetic energy (quantum pressure), which tends to defocus the wave function.

Since a central vortex state reduces the peak density, it may help stabilisation of a trapped condensate with $a < 0$ in the sense that it can contain a larger number of atoms by suppressing self-focusing. However, for $\Omega < \omega_\perp$, excitation of a vortex in a harmonically trapped BEC with $a < 0$ is prohibited by the centre of mass motion, which is the lowest energy state for a given angular momentum (Wilkin et al., 1998). Some authors have proposed that the use of an anharmonic confinement can support a stable vortex phase as well as regimes of centre of mass motion (Collin et al., 2005; Ghosh, 2004; Kavoulakis et al., 2004; Lundh, 2004). The vortex state in this system can be regarded as a ring bright soliton with nonzero winding number (Carr and Clark, 2006), showing interesting splitting dynamics dominated by the dynamical instability of the quadrupole mode (Saito and Ueda, 2002).

6.2 Vortices in Dipolar Condensates

BECs of chromium atoms have recently been created (Griesmaier et al., 2005), exhibiting a larger magnetic dipole moment ($\mu_d = 6\mu_B$; μ_B is the Bohr magneton) than those of typical alkali atoms ($\mu_d \simeq \mu_B$). This opens the door for studying the effect of anisotropic long-range interactions in BECs. The interaction potential between two magnetic dipoles $\mu_d \hat{\mathbf{e}}$ separated by $\mathbf{r}$ is given by $V_{dd}(\mathbf{r}) = (\mu_0 \mu_d^2/4\pi)(1 - 3\cos^2\theta)/r^3$, where μ_0 is the vacuum magnetic permeability and $\hat{\mathbf{e}} \cdot \hat{\mathbf{r}} = \cos\theta$. Such dipole–dipole interactions contribute to the GP equation as a nonlocal mean-field potential as $i\hbar\partial\psi/\partial t = [-\hbar^2\nabla^2/2m + V_{\text{ex}} + g|\psi|^2 + \int d\mathbf{r}' V_{dd}(\mathbf{r}' - \mathbf{r})|\psi(\mathbf{r}')|^2]\psi$. Since the scattering length can be tuned to zero by a Feshbach resonance technique,

we can obtain novel quantum *ferrofluids* dominated by the dipole–dipole interaction (Lahaye et al., 2007).

The principal effect of V_{dd} on the equilibrium properties of a condensate is to cause distortion of its aspect ratio so that it is elongated along the direction of the dipoles. This feature affects the stability of a vortex in a dipolar BEC; the thermodynamic critical rotation frequency Ω_c decreases for a condensate in a pancake-shaped trap ($\omega_\perp < \omega_z$), while it increases a cigar-shaped trap ($\omega_\perp < \omega_z$), compared to that of a conventional BEC (Section 3.1) (O'Dell and Eberlein, 2007). Interestingly, the critical frequency Ω_c can become larger than the onset of the dynamical instability of a rotating condensate (see Section 3.2.2). This is an intriguing regime where a rotating dipolar BEC is dynamically unstable but vortices will not enter (Bijnen et al., 2007). Numerical simulations show that the structure of vortices has a crater-like shape for $\hat{\mathbf{e}} \parallel \hat{\mathbf{z}}$ and has an elliptical shape for $\hat{\mathbf{e}} \perp \hat{\mathbf{z}}$ (Pu et al., 1999). Rapidly rotating dipolar BECs possess a rich variety of vortex phases characterised by different symmetries of the lattice structure (Cooper et al., 2005; Komineas and Cooper, 2007; Zhang and Zhai, 2005).

6.3 Melting State of Vortex Lattices: Beyond the LLL Regime

At sufficiently high rotation rates, a vortex lattice should melt via quantum fluctuations (Sinova et al., 2002) and the system should then begin to enter a strongly-correlated vortex liquid phase. Exact diagonalisation studies for small number of bosons have revealed that the ground states exhibit strong analogy with the physics of electronic fractional quantum Hall states (Cooper et al., 2001; Ghosh and Baskaran, 2004; Paredes et al., 2002; Regnault and Jolicoeur, 2003, 2004; Viefers et al., 2000); for specific filling factors $\nu = N/N_v$, that is, the ratio of the total number and the vortex number, the ground state possesses incompressibility characterised by the energy gap. For example, at angular momentum $L_z = N(N - 1)$, where $N_v = 2N$, the exact ground state is an N-particle fully symmetric Laughlin wave function adopted for bosons: $\Psi(\mathbf{r}_1, \mathbf{r}_2, \ldots, \mathbf{r}_N) \sim \prod_{j \neq k}(z_j - z_k)^2 e^{-\Sigma_l r_l^2/2a_{ho}^2}$ with $z_j = x_j + iy_j$.

The conditions for the formation of these states have been expressed as $\nu \leq \mathcal{O}(1)$. It can be seen that an unrealistically high rotation is necessary to satisfy the condition; observed filling factors are always greater than 100 (Schweikhard et al., 2004a), which are still deeply within the mean-field GP regime. To overcome this difficulty, insertion of a 1D optical lattice along the z-direction has been proposed to enhance the quantum fluctuations of the vortices (Martikainen and Stoof, 2003; Snoek and Stoof, 2006). Then, the optical lattice divides the condensate into pancake fractions coupled

by a tunneling process between near neighbours, and N in a single pancake is greatly reduced. Achieving this regime experimentally remains an important challenge.

6.4 Spontaneous Vortex Generation Associated With Phase Transitions

In 2D systems with continuous symmetry, true long-range order is destroyed by thermal fluctuations at any finite temperature. For 2D Bose systems, a quasi-condensate can be formed with a correlation decaying algebraically in space, where superfluidity is still expected below a certain critical temperature. This 2D phase transition is closely connected with the emergence of thermally activated vortex–antivortex pairs, known as the Berezinskii–Kosterlitz–Thouless (BKT) phase transition occurring at $T = T_{BKT}$ (Berezinskii, 1972; Kosterlitz and Thouless, 1973). For $T < T_{BKT}$, isolated free vortices are absent; vortices always exist only in the form of bound pairs formed by two vortices with opposite circulations. The contribution of these vortex pairs to the decay of the correlation is negligible, and the algebraic decay is dominated by phonons. For $T > T_{BKT}$, the free vortices form a disordered gas of phase defects and give rise to an exponential decay of the correlation.

Recently, the BKT transition was observed experimentally in ultracold atomic gases (Hadzibabic et al., 2006, 2007; Krüger, 2007; Schweikhard et al., 2007). In the ENS experiment, a 1D optical lattice was applied to an elongated condensate, splitting the 3D condensate into an array of independent quasi-2D BECs (Hadzibabic et al., 2006). The interference technique revealed the temperature dependence of an exponent of the first-order correlation function of the fluctuating 2D bosonic field (Polkovnikov et al., 2006). A universal jump in the superfluid density characteristic of the BKT transition was identified by observing the sudden change of the exponent, where the finite-size effect causes a finite-width crossover rather than a sharp transition. Surprisingly, the microscopic origin of this transition, that is, whether or not it is a BKT type transition, was directly clarified from the image of the interference of the two 2D condensates. If isolated free vortices are present in either of two condensates, the interference fringes exhibit dislocations. Such a dislocation has been observed in the high-T region of the crossover, supported by the theory using classical field simulations (Simula and Blakie, 2006).

In contrast, the JILA group inserted a 2D optical lattice into a condensate to create 2D bosonic Josephson junction arrays (Schweikhard et al., 2007). Each condensate was localised at a site j. Each had an individual phase θ_j and was separated by a potential barrier from the nearest neighbours. This system can be mapped to the XY model, $H = -J \sum_{\langle j,j' \rangle} \cos(\theta_j - \theta_{j'})$, where J denotes the tunneling coupling and the sum

is restricted within nearest neighbours (Trombettoni et al., 2005). The XY model is expected to exhibit a BKT transition at $T_{BKT} \simeq J$ from free-energy considerations. Direct imaging of vortex cores and the systematic determination of J revealed evidence for a gradual increase in the number of isolated free vortices at $T \geq J$, consistent with the BKT crossover picture.

A related work is vortex formation by merging three uncorrelated BECs that are initially separated by a triple well potential (Scherer et al., 2007). Depending on the relative phases between the condensates and merging rate, vortices formed stochastically without applying rotation. This situation is useful to clarify the mechanism of spontaneous vortex generation through the Kibble-Zurek mechanism (Kibble, 1976; Zurek, 1985) during rapid phase transition (Kasamatsu, 2002b; Leggett, 1998).

6.5 Skyrmions in Multicomponent BECs

Another important issue in vortex physics is to elucidate the vortex phases in multicomponent (spinor) BECs. Multicomponent order parameters allow the formation of various unconventional topological defects with complex properties that arise from interactions between different order parameter components. Since it is possible to load and cool atoms in more than one hyperfine spin state or more than one atomic element in the same trap, multicomponent condensates can be realised experimentally. Such systems offer an ideal testing ground for the study of unconventional topological defects; similar structures appear in other condensed matter systems such as superfluid ^{3}He and unconventional superconductors, and theories in high-energy physics and cosmology. A few experimental works have investigated the properties of composite vortices in spinor BECs (Leanhardt et al., 2003; Sadler, 2006; Schweikhard, 2004b). A review of this topic is presented by Kasamatsu et al. (2005b) and references therein.

6.6 Vortices in Fermion Condensates

Quantum degenerate Fermi gases provide a remarkable opportunity to study strongly interacting fermions. In contrast to other Fermi systems, such as superconductors, neutron stars or the quark–gluon plasma, these gases have low densities, and their interactions can be precisely controlled over a wide range by using a Feshbach resonance technique. For small and negative values of the scattering length a, the equation of state approaches the limit of a noninteracting Fermion gas, while for small and positive values, the system behaves as bosons of tightly bound molecules. Therefore, we can study the crossover from a BEC of molecules to a Bardeen–Cooper–Schrieffer (BCS) superfluid of loosely-bound Cooper pairs when an external magnetic field is varied across a Feshbach resonance. Recent topics in this rapidly growing field are presented in the comprehensive review paper (Giorgini et al., 2007).

Decisive evidence for fermion superfluidity was obtained from obser-
vations of long-lived vortex lattices in a strongly-interacting rotating
Fermion gas (Zwierlein et al., 2005). Rotation was applied to an ultra-
cold gas of ^{6}Li atoms in $|F = 1/2, m_F = \pm 1/2\rangle$, in a similar way as for
conventional BECs (see Section 3.2.1), with magnetic fields covering the
entire BEC–BCS crossover region. A crucial problem was detecting the
vortex cores in the BCS limit because a sufficient density depletion at
the vortex core could not be expected (Nygaard et al., 2003). In the exper-
iment, the visibility of the vortex cores was increased by a rapid sweep of
the magnetic field from the BCS to the BEC side during ballistic expan-
sion of the TOF measurement. These measurements strongly support the
existence of vortices before the expansion even on the BCS side of the
resonance.

The most striking aspect of this experiment is that it opens up the possi-
bility of studying vortex physics in a strongly-coupled fermion superfluid
in a systematically controlled way. In the strong-coupling limit $|a| \to \infty$
at the resonance, called a unitarity limit, the Fermi gas exhibits universal
behaviour. Along this line, several microscopic calculations of the vortex
structure, based on the BdG formalism, have been carried out (Bulgac and
Yu, 2003; Chien et al., 2006; Machida and Koyama, 2005; Machida et al.,
2006; Sensarma et al., 2006). More detailed studies may provide useful pre-
dictions of the mysterious vortex properties in high-T_c superconductors,
and eventually those in room-temperature superconductors.

7. CONCLUSION

Quantised vortices in atomic BECs constitute an active research field,
which has drawn the continuous attention of researchers in related fields
such as superconductors, mesoscopic systems, nonlinear optics, atomic
nuclei and cosmology, as well as superfluid helium. Quantised vortices in
rotating condensates have provided conclusive evidence for superfluidity
because they are a direct consequence of the existence of a macroscopic
wave function that describes the superfluid. The direct imaging of the vor-
tex cores and lines helps us understand the fundamentals of superfluid
dynamics. Especially, the inhomogeneous effect caused by a confining
potential yields new features in both a slowly rotating regime and a rapidly
rotating one, not found in a bulk superfluid system. The observed phenom-
ena are consistent with the prediction of the GP equation without fitting
parameters.

Finally, this volume addresses mainly the topics of *quantum turbulence*.
The feasibility of generating quantum turbulence in a trapped BEC is
discussed by one of the authors (Kobayashi and Tsubota, 2007).

ACKNOWLEDGEMENTS

REFERENCES

Abo-Shaeer, J. R., Raman, C., Vogels, J. M. and Ketterle, W. (2001). *Science*, 292, 476.

Aftalion, A. and Jerrard, R. L. (2002). *Physical Review A*, 66, 023611.

Aftalion, A. and Danaila, I. (2003). *Physical Review A*, 68, 023603.

Aftalion, A. and Danaila, I. (2004). *Physical Review A*, 69, 033608.

Aftalion, A., Blanc, X. and Dalibard, J. (2005). *Physical Review A*, 71, 023611.

Aftalion, A., Blanc, X. and Nier, F. (2006). *Physical Review A*, 73, 011601.

Anderson, M. H., Ensher, J. R., Matthews, M. R., Wieman, C. E. and Cornell, E. A. (1995). *Science*, 269, 198.

Anderson, B. P., Haljan, P. C., Wieman, C. E. and Cornell, E. A. (2000). *Physical Review Letters*, 85, 2857.

Anderson, B. P., Haljan, P. C., Regal, C. A., Feder, D. L., Collins, L. A., Clark, C. W. and Cornell, E. A. (2001). *Physical Review Letters*, 86, 2926.

Anderson, M. F., Ryu, C., Cladé, P., Natarajan, V., Vaziri, A., Helmerson, K. and Phillips, W. D. (2006). *Physical Review Letters*, 97, 170406.

Andrelczyk, G., Brewczyk, M., Dobrek, L., Gajda, M. and Lewenstein, M. (2001). *Physical Review A*, 64, 043601.

Andrews, M. R., Mewes, M.-O., van Druten, N. J., Durfee, D. S., Kurn, D. M. and Ketterle, W. (1996). *Science*, 273, 84.

Anglin, J. R. (2001). *Physical Review Letters*, 87, 240401.

Baksmaty, L. O., Woo, S. J., Choi, S. and Bigelow, N. P. (2004). *Physical Review Letters*, 92, 160405.

Bargi, S., Kavoulakis, G. M. and Reimann, S. M. (2006). *Physical Review A*, 73, 033613.

Barrett, M. D., Sauer, J. A. and Chapman, M. S. (2001). *Physical Review Letters*, 87, 010404.

Baym, G. and Pethick, C. J. (1995). *Physical Review Letters*, 76, 6.

Baym, G. (2003). *Physical Review Letters*, 91, 110402.

Baym, G. (2004a). *Physical Review A*, 69, 043618.

Baym, G. and Pethick, C. J. (2004b). *Physical Review A*, 69, 043619.

Baym, G., Pethick, C. J., Gifford, S. A. and Watanabe, G. (2007). *Physical Review A*, 75, 013602.

Berezinskii, V. L. (1972). *Soviet Physics: Journal of Experimental and Theoretical Physics*, 34, 610.

Bhat, R., Holland, M. J. and Carr, L. D. (2006). *Physical Review Letters*, 96, 060405.

van Bijnen, R. M. W., O'Dell, D. H. J., Parker, N. G. and Martin, A. M. (2007). *Physical Review Letters*, 98, 150401.

Bradley, C. C., Sackett, C. A., Tollett, J. J. and Hulet, R. G. (1995). *Physical Review Letters*, 75, 1687.

Bretin, V., Rosenbusch, P., Chevy, F., Shlyapnikov, G. V. and Dalibard, J. (2003). *Physical Review Letters*, 90, 100403.

Bretin, V., Stock, S., Seurin, Y. and Dalibard, J. (2004). *Physical Review Letters*, 92, 050403.

Bulgac, A. and Yu, Y. (2003). *Physical Review Letters*, 91, 190404.

Burger, S., Bongs, K., Dettmer, S., Ertmer, W., Sengstock, K., Sanpera, A., Shlyapnikov, G. V. and Lewenstein, M. (1999). *Physical Review Letters*, 83, 5198.

Butts, D. A. and Rokhsar, D. S. (1999). *Nature*, 397, 327.

Caradoc-Davies, B. M., Ballagh, R. J. and Burnett, K. (1999). *Physical Review Letters*, 83, 895.

Caradoc-Davies, B. M., Ballagh, R. J. and Blakie, P. B. (2000). *Physical Review A*, 62, 011602.

Carr, L. D. and Clark, C. W. (2006). *Physical Review Letters*, 97, 010403.

Cazalilla, M. A., Barberán, N. and Cooper, N. R. (2005). *Physical Review B*, 71, 121303(R).

Chang, M.-S., Hamley, C. D., Barrett, M. D., Sauer, J. A., Fortier, K. M., Zhang, W., You, L. and Chapman, M. S. (2004). *Physical Review Letters*, 92, 140403.

Chang, C.-C., Regnault, N., Jolicoeur, T. and Jain, J. K. (2005). *Physical Review A*, 72, 013611.

Chevy, F., Madison, K. W. and Dalibard, J. (2000). *Physical Review Letters*, 85, 2223.

Chevy, F., Madison, K. W., Bretin, V. and Dalibard, J. (2001). *Comptes Rendus De l'Académie Des Sciences Paris*, IV, 663.

Chevy, F. and Stringari, S. (2003). *Physical Review A*, 68, 053601.

Chien, C. C., He, Y., Chen, Q. and Levin, K. (2006). *Physical Review A*, 73, 041603(R).

Coddington, I., Engels, P., Schweikhard, V. and Cornell, E. A. (2003). *Physical Review Letters*, 91, 100402.

Coddington, I., Haljan, P. C., Engels, P., Schweikhard, V., Tung, S. and Cornell, E. A. (2004). *Physical Review A*, 70, 063607.

Collin, A., Lundh, E. and Suominen, K.-A. (2005). *Physical Review A*, 71, 023613.

Cooper, N. R., Wilkin, N. K. and Gunn, J. M. F. (2001). *Physical Review Letters*, 87, 120405.

Cooper, N. R., Komineas, S. and Read, N. (2004). *Physical Review A*, 70, 033604.

Cooper, N. R., Rezayi, E. H. and Simon, S. H. (2005). *Physical Review Letters*, 95, 200402.

Cozzini, M. and Stringari, S. (2003). *Physical Review A*, 67, 041602(R).

Cozzini, M., Pitaevskii, L. P. and Stringari, S. (2004). *Physical Review Letters*, 92, 220401.

Cozzini, M., Stringari, S. and Tozzo, C. (2006). *Physical Review A*, 73, 023615.

Crescimanno, M., Koay, C. G., Peterson, R. and Walsworth, R. (2000). *Physical Review A*, 62, 063612.

Cornell, E. A. and Wieman, C. E. (2002). *Reviews of Modern Physics*, 74, 875.

Cornish, S. L., Claussen, N. R., Roberts, J. L., Cornell, E. A. and Wieman, C. E. (2000). *Physical Review Letters*, 85, 1795.

Dalfovo, F. and Stringari, S. (2000). *Physical Review A*, 63, 011601.

Damski, B., Karkuszewski, Z. P., Sacha, K. and Zakrzewski, J. (2001). *Physical Review A*, 65, 013604.

Danaila, I. (2005). *Physical Review A*, 72, 013605.

Davis, K. B., Mewes, M.-O., Andrews, M. R., van Druten, N. J., Durfee, D. S., Kurn, D. M. and Ketterle, W. (1995). *Physical Review Letters*, 75, 3969.

Denschlag, J., Simsarian, J. E., Feder, D. L., Clark, C. W., Collins, L. A., Cubizolles, J., Deng, L., Hagley, E. W., Helmerson, K., Reinhardt, W. P., Rolston, S. L., Schneider, B. I. and Phillips, W. D. (2000). *Science*, 287, 97.

Donnelly, R. J. (1991). *Quantized Vortices in Helium II*. Cambridge University Press, Cambridge.

Dos Santos, F. P., Léonard, J., Wang, J., Barrelet, C. J., Perales, F., Rasel, E., Unnikrishnan, C. S., Leduc, M. and Cohen-Tannoudji, C. (2001). *Physical Review Letters*, 86, 3459.

Dum, R., Cirac, J. I., Lewenstein, M. and Zoller, P. (1998). *Physical Review Letters*, 80, 2972.

Dutton, Z., Budde, M., Slowe, C. and Hau, L. V. (2001). *Science*, 293, 663.

Engels, P., Coddington, I., Haljan, P. C. and Cornell, E. A. (2002). *Physical Review Letters*, 89, 100403.

Engels, P., Coddington, I., Haljan, P. C., Schweikhard, V. and Cornell, E. A. (2003). *Physical Review Letters*, 90, 170405.

Feder, D. L., Clark, C. W. and Schneider, B. I. (1999a). *Physical Review Letters*, 82, 4956.

Feder, D. L., Clark, C. W. and Schneider, B. I. (1999b). *Physical Review A*, 61, 011601(R).

Feder, D. L., Svidzinsky, A. A., Fetter, A. L. and Clark, C. W. (2001a). *Physical Review Letters*, 86, 564.

Feder, D. L. and Clark, C. W. (2001b). *Physical Review Letters*, 87, 190401.

Feder, D. L. (2004). *Physical Review Letters*, 93, 200406.

Fedichev, P. O. and Shlyapnikov, G. V. (1999). *Physical Review A*, 60, R1779.

Fetter, A. L. and Svidzinsky, A. A. (2001a). *Journal of Physics Condensed Matter*, 13, R135.

Fetter, A. L. (2001b). *Physical Review A*, 64, 063608.

Fetter, A. L., Jackson, B. and Stringari, S. (2005). *Physical Review A*, 71, 013605.

Feynman, R. P. (1955). in edited by Gorter, C. J. (ed.), *Progress in Low Temperature Physics*, vol. 1, ch. 2, North-Holland Publications, Amsterdam.

Fischer, U. R. and Baym, G. (2003). *Physical Review Letters*, 90, 140402.

Fried, D. G., Killian, T. C., Willimann, L., Landhuis, D., Moss, S. C., Kleppner, D. and Greytak, T. J. (1998). *Physical Review Letters*, 81, 3811.

Frisch, T., Pomeaum, Y. and Rica, S. (1992). *Physical Review Letters*, 69, 1644.

Fu, H. and Zaremba, E. (2006). *Physical Review A*, 73, 013614.

Garcia-Ripoll, J. J. and Perez-Garcia, V. M. (2001). *Physical Review A*, 64, 053611.

Gifford, S. A. and Baym, G. (2004). *Physical Review A*, 70, 033602.

Giorgini, S., Pitaevskii, L. P. and Stringari, S. (2007). arXiv:0706.3360.

Ghosh, S. (2004). *Phase Transition*, 77, 625.

Ghosh, T. K. and Baskaran, G. (2004). *Physical Review A*, 69, 023603.

Ghosh, T. K. (2004). *Physical Review A*, 69, 043606.

Griesmaier, A., Werner, J., Hansler, S., Stuhler, J. and Phau, T. (2005). *Physical Review Letters*, 94, 160401.

Guery-Odelin, D. and Stringari, S. (1999). *Physical Review Letters*, 83, 4452.

Hadzibabic, Z., Kruger, P., Cheneau, M., Battelier, B. and Dalibard, J. (2006). *Nature (London)*, 441, 1118.

Hadzibabic, Z., Kruger, P., Cheneau, M., Rath, S. P. and Dalibard, J. (2007). arXiv:0712.1265.

Haljan, P. C., Anderson, B. P., Coddington, I. and Cornell, E. A. (2001). *Physical Review Letters*, 86, 2922.

Hall, D. S., Matthews, M. R., Ensher, J. R., Wieman, C. E. and Cornell, E. A. (1998). *Physical Review Letters*, 81, 1539.

Ho, T. L. (1998). *Physical Review Letters*, 81, 742.

Ho, T. L. (2001). *Physical Review Letters*, 87, 060403.

Hodby, E., Hechenblaikner, G., Hopkins, S. A., Marago, O. M. and Foot, C. J. (2002). *Physical Review Letters*, 88, 010405.

Hodby, E., Hopkins, S. A., Hechenblaikner, G., Smith, N. L. and Foot, C. J. (2003). *Physical Review Letters*, 91, 090403.

Huhtamaki, J. A. M., Mottonen, M., Isoshima, T., Pietila, V. and Virtanen, S. M. M. (2006a). *Physical Review Letters*, 97, 110406.

Huhtamaki, J. A. M., Mottonen, M. and Virtanen, S. M. M. (2006b). *Physical Review A*, 74, 063619.

Inouye, S., Andrews, M. R., Stenger, J., Miesner, H.-J., Stamper-Kurn, D. M. and Ketterle, W. (1998). *Nature (London)*, 392, 151.

Inouye, S., Gupta, S., Rosenband, T., Chikkatur, A. P., Gorlitz, A., Gustavson, T. L., Leanhardt, A. E., Pritchard, D. E. and Ketterle, W. (2001). *Physical Review Letters*, 87, 080402.

Isoshima, T. and Machida, K. (1999). *Physical Review A*, 60, 3313.

Isoshima, T., Nakahara, M., Ohmi, T. and Machida, K. (2000). *Physical Review A*, 61, 063610.

Isoshima, T., Okano, M., Yasuda, H., Kasa, K., Huhtamaki, J. A. M., Kumakura, M. and Takahashi, Y. (2007). *Physical Review Letters*, 99, 200403.

Jackson, A. D., Kavoulakis, G. M. and Lundh, E. (2004a). *Physical Review A*, 69, 053619.

Jackson, A. D. and Kavoulakis, G. M. (2004b). *Physical Review A*, 70, 023601.

Jackson, A. D., Kavoulakis, G. M. and Lundh, E. (2005). *Physical Review A*, 72, 053617.

Jackson, B., McCann, J. F. and Adams, C. S. (1998). *Physical Review Letters*, 80, 3903.

Jackson, B., McCann, J. F. and Adams, C. S. (1999). *Physical Review A*, 61, 013604.

Jackson, B., McCann, J. F. and Adams, C. S. (2000). *Physical Review A*, 61, 051603(R).

Kapale, K. T. and Dowling, J. P. (2005). *Physical Review Letters*, 95, 173601.

Kasamatsu, K., Tsubota, M. and Ueda, M. (2002a). *Physical Review A*, 66, 053606.

Kasamatsu, K. and Tsubota, M. (2002b). *Journal of Low Temperature Physics*, 126, 315.

Kasamatsu, K., Tsubota, M. and Ueda, M. (2003). *Physical Review A*, 67, 033610.

Kasamatsu, K., Machida, M., Sasa, N. and Tsubota, M. (2005a). *Physical Review A*, 71, 063616.

Kasamatsu, K., Tsubota, M. and Ueda, M. (2005b). *International Journal of Modern Physics B*, 19, 1835.

Kasamatsu, K. and Tsubota, M. (2006). *Physical Review Letters*, 97, 240404.

Kavoulakis, G. M. and Baym, G. (2003). *New Journal of Physics*, 5, 51.

Kavoulakis, G. M., Jackson, A. D. and Baym, G. (2004). *Physical Review A*, 70, 043603.

Kawaguchi, Y. and Ohmi, T. (2004). *Physical Review A*, 70, 043610.

Ketterle, W. (2002). *Reviews of Modern Physics*, 74, 1131.

Kibble, T. W. B. (1976). *Journal of Physics A*, 9, 1387.

Kim, J. and Fetter, A. L. (2005). *Physical Review A*, 72, 023619.

Kobayashi, M. and Tsubota, M. (2007). *Physical Review A*, 76, 045603.

Komineas, S., Cooper, N. R. and Papanicolaou, N. (2005). *Physical Review A*, 72, 053624.

Komineas, S. and Cooper, N. R. (2007). *Physical Review A*, 75, 023623.

Kosterlitz, J. M. and Thouless, D. J. (1973). *Journal of Physics C*, 6, 1181.

Krüger, P., Hadzibabic, Z. and Dalibard, J. (2007). *Physical Review Letters*, 99, 040402.

Kumakura, M., Hirotani, T., Okano, M., Takahashi, Y. and Yabuzaki, T. (2006). *Physical Review A*, 73, 063605.

Kuwamoto, T., Araki, K., Eno, T. and Hirano, T. (2004). *Physical Review A*, 69, 063604.

Lahaye, T., Koch, T., Frohlich, B., Fattori, M., Metz, J., Griesmaier, A., Giovanazzi, S. and Pfau, T. (2007). *Nature (London)*, 448, 676.

Leanhardt, A. E., Gorlitz, A., Chikkatur, A. P., Kielpinski, D., Shin, Y., Pritchard, D. E. and Ketterle, W. (2002). *Physical Review Letters*, 89, 190403.

Leanhardt, A. E., Shin, Y., Kielpinski, D., Pritchard, D. E. and Ketterle, W. (2003). *Physical Review Letters*, 90, 140403.

Leggett, A. J. (1998). *Journal of Low Temperature Physics*, 110, 719.

Leggett, A. J. (2001). *Reviews of Modern Physics*, 73, 307.

Lobo, C., Sinatra, A. and Castin, Y. (2004). *Physical Review Letters*, 92, 020403.

Lundh, E., Pethick, C. J. and Smith, H. (1997). *Physical Review A*, 55, 2126.

Lundh, E. and Ao, P. (2000). *Physical Review A*, 61, 063612.

Lundh, E. (2002). *Physical Review A*, 65, 043604.

Lundh, E., Martikainen, J.-P. and Suominen, K.-A. (2003). *Physical Review A*, 67, 063604.

Lundh, E., Collin, A. and Suominen, K.-A. (2004). *Physical Review Letters*, 92, 070401.

Lundh, E. and Nilsen, H. M. (2006). *Physical Review A*, 74, 063620.

Machida, M. and Koyama, T. (2005). *Physical Review Letters*, 94, 140401.

Machida, M., Ohashi, Y. and Koyama, T. (2006). *Physical Review A*, 74, 023621.

Madison, K. W., Chevy, F., Wohlleben, W. and Dalibard, J. (2000). *Physical Review Letters*, 84, 806.

Madison, K. W., Chevy, F., Bretin, V. and Dalibard, J. (2001). *Physical Review Letters*, 86, 4443.

Marago, O. M., Hopkins, S. A., Arlt, J., Hodby, E., Hechenblaikner, G. and Foot, C. J. (2000). *Physical Review Letters*, 84, 2056.

Martikainen, J.-P. and Stoof, H. T. C. (2003). *Physical Review Letters*, 91, 240403.

Marzlin, K.-P., Zhang, W. and Wright, E. M. (1997). *Physical Review Letters*, 79, 4728.

Marzlin, K.-P. and Zhang, W. (1998). *Physical Review A*, 57, 4761.

Matthews, M. R., Anderson, B. P., Haljan, P. C., Hall, D. S., Wieman, C. E. and Cornell, E. A. (1999a). *Physical Review Letters*, 83, 2498.

McGee, S. A. and Holland, M. J. (2001). *Physical Review A*, 63, 043608.

Mizushima, T., Ichioka, M. and Machida, K. (2003). *Physical Review Letters*, 90, 180401.

Mizushima, T., Kawaguchi, Y., Machida, K., Ohmi, T., Isoshima, T. and Salomaa, M. M. (2004). *Physical Review Letters*, 92, 060407.

Modugno, G., Ferrari, G., Roati, G., Brecha, R. J., Simoni, A. and Inguscio, M. (2001). *Science*, 294, 1320.

Modugno, M., Pricoupenko, L. and Castin, Y. (2003). *The European Physical Journal D*, 22, 235.

Morris, A. G. and Feder, D. L. (2006). *Physical Review A*, 74, 033605.

Mottonen, M., Mizushima, T., Isoshima, T., Salomaa, M. M. and Machida, K. (2003). *Physical Review A*, 68, 023611.

Mottonen, M., Pietila, V. and Virtanen, S. M. M. (2007). *Physical Review Letters*, 99, 250406.

Mueller, E. J. and Ho, T. L. (2003). *Physical Review A*, 67, 063602.

Mateo, A. M. and Delgado, V. (2006). *Physical Review Letters*, 97, 180409.

Nakahara, M., Isoshima, T., Machida, K., Ogawa, S.-I. and Ohmi, T. (2000). *Physica B*, 284–288, 17.

Nandi, G., Walser, R. and Schleich, W. P. (2004). *Physical Review A*, 69, 063606.

Nilsen, H. M., McPeake, D. and McCann, J. F. (2003). *Journal of Physics B*, 36, 1703.

Nygaard, N., Bruun, G. M., Clark, C. W. and Feder, D. L. (2003). *Physical Review Letters*, 90, 210402.

O'Dell, D. H. J. and Eberlein, C. (2007). *Physical Review A*, 75, 013604.

Ogawa, S.-I., Mottonen, M., Nakahara, M., Ohmi, T. and Shimada, H. (2002). *Physical Review A*, 66, 013617.

Ohmi, T. and Machida, K. (1998). *Journal of Physics Society of Japan*, 67, 1822.

Onofrio, R., Raman, C., Vogels, J. M., Abo-Shaeer, J. R., Chikkatur, A. P. and Ketterle, W. (2000). *Physical Review Letters*, 85, 2228.

Paredes, B., Zoller, P. and Cirac, J. I. (2002). *Physical Review A*, 66, 033609.

Parker, N. G., Proukakis, N. P., Barenghi, C. F. and Adams, C. S. (2004). *Physical Review Letters*, 92, 160403.

Parker, N. G. and Adams, C. S. (2005). *Physical Review Letters*, 95, 145301.

Parker, N. G., van Bijnen, R. M. W. and Adams, C. S. (2006). *Physical Review A*, 73, 061603(R).

Penckwitt, A. A., Ballagh, R. J. and Gardiner, C. W. (2002). *Physical Review Letters*, 89, 260402.

Pethick, C. J. and Smith, H. (2002). *Bose-Einstein Condensation in Dilute Gases*. Cambridge University Press, Cambridge.

Pitaevskii, L. and Stringari, S. (2003). *Bose-Einstein Condensation*. Oxford University Press, Oxford.

Polkovnikov, A., Altman, E. and Demler, E. (2006). *Proceedings of the National Academy of Sciences of the United States of America*, 103, 6125.

Pu, H., Law, C. K., Eberly, J. H. and Bigelow, N. P. (1999). *Physical Review A*, 59, 1533.

Pu, H., Baksmaty, L. O., Yi, S. and Bigelow, N. P. (2005). *Physical Review Letters*, 94, 190401.

Raman, C., Köhl, M., Onofrio, R., Durfee, D. S., Kuklewicz, C. E., Hadzibabic, Z. and Ketterle, W. (1999). *Physical Review Letters*, 83, 2502.

Raman, C., Abo-Shaeer, J. R., Vogels, J. M., Xu, K. and Ketterle, W. (2001). *Physical Review Letters*, 87, 210402.

Recati, A., Zambelli, F. and Stringari, S. (2001). *Physical Review Letters*, 86, 377.

Regnault, N. and Jolicoeur, Th. (2003). *Physical Review Letters*, 91, 030402.

Regnault, N. and Jolicoeur, Th. (2004). *Physical Review B*, 69, 235309.

Reijnders, J. W. and Duine, R. A. (2004). *Physical Review Letters*, 93, 060401.

Rezayi, E. H., Read, N. and Cooper, N. R. (2005). *Physical Review Letters*, 95, 160404.

Roati, G., Zaccanti, M., D'Errico, C., Catani, J., Modugno, M., Simoni, A., Inguscio, M. and Modugno, G. (2007). *Physical Review Letters*, 99, 010403.

Robert, A., Sirjean, O., Browaeys, A., Poupard, J., Nowak, S., Boiron, D., Westbrook, C. I. and Aspect, A. (2001). *Science*, 292, 461.

Rosenbusch, P., Bretin, V. and Dalibard, J. (2002). *Physical Review Letters*, 89, 200403.

Ryu, C., Anderson, M. F., Cladé, P., Natarajan, V., Helmerson, K. and Phillips, W. D. (2007). *Physical Review Letters*, 99, 260401.

Saito, H. and Ueda, M. (2002). *Physical Review Letters*, 89, 190402.

Sadler, L. E., Higbie, J. M., Leslie, S. R., Vengalattore, M. and Stamper-Kurn, D. M. (2006). *Nature (London)*, 443, 312.

Scherer, D. R., Weiler, C. N., Neely, T. W. and Anderson, B. P. (2007). *Physical Review Letters*, 98, 110402.

Schmaljohann, H., Erhard, M., Kronjäger, J., Kottke, M., van Staa, S., Cacciapuoti, L., Arlt, J. J., Bongs, K. and Sengstock, K. (2004). *Physical Review Letters*, 92, 040402.

Schweikhard, V., Coddington, I., Engels, P., Mogendorff, V. P. and Cornell, E. A. (2004a). *Physical Review Letters*, 92, 040404.

Schweikhard, V., Coddington, I., Engels, P., Tung, S. and Cornell, E. A. (2004b). *Physical Review Letters*, 93, 210403.

Schweikhard, V., Tung, S. and Cornell, E. A. (2007). *Physical Review Letters*, 99, 030401.

Sensarma, R., Randeria, M. and Ho, T. L. (2006). *Physical Review Letters*, 96, 090403.

Sheehy, D. E. and Radzihovsky, L. (2004a). *Physical Review A*, 70, 051602(R).

Sheehy, D. E. and Radzihovsky, L. (2004b). *Physical Review A*, 70, 063620.

Shin, Y., Saba, M., Vengalattore, M., Pasquini, T. A., Sanner, C., Leanhardt, A. E., Prentiss, M., Pritchard, D. E. and Ketterle, W. (2004). *Physical Review Letters*, 93, 160406.

Simula, T. P., Virtanen, S. M. M. and Salomaa, M. M. (2002a). *Physical Review A*, 65, 033614.

Simula, T. P., Virtanen, S. M. M. and Salomaa, M. M. (2002b). *Physical Review A*, 66, 035601.

Simula, T. P. and Blakie, P. B. (2006). *Physical Review Letters*, 96, 020404.

Sinha, S. and Castin, Y. (2001). *Physical Review Letters*, 87, 190402.

Sinova, J., Hanna, C. B. and MacDonald, A. H. (2002). *Physical Review Letters*, 89, 030403.

Skryabin, D. V. (2000). *Physical Review A*, 63, 013612.

Smith, N. L., Heathcote, W. H., Krueger, J. M. and Foot, C. J. (2004). *Physical Review Letters*, 93, 080406.

Snoek, M. and Stoof, H. T. C. (2006). *Physical Review Letters*, 96, 230402.

Sonin, E. B. (2005a). *Physical Review A*, 71, 011603(R).

Sonin, E. B. (2005b). *Physical Review A*, 72, 021606(R).

Stenger, J., Inouye, S., Stamper-Kurn, D. M., Miesner, H.-J., Chikkatur, A. P. and Ketterle, W. (1998). *Nature (London)*, 396, 345.

Stringari, S. (1996). *Physical Review Letters*, 77, 2360.

Stringari, S. (2001). *Physical Review Letters*, 86, 4725.

Svidzinsky, A. A. and Fetter, A. L. (2000a). *Physical Review Letters*, 84, 5919.

Svidzinsky, A. A. and Fetter, A. L. (2000b). *Physical Review A*, 62, 063617.

Takasu, Y., Maki, K., Komori, K., Takano, T., Honda, K., Kumakura, M., Yabuzaki, T. and Takahashi, Y. (2003). *Physical Review Letters*, 91, 040404.

Trombettoni, A., Smerzi, A. and Sodano, P. (2005). *New Journal of Physics*, 7, 57.

Tsubota, M., Kasamatsu, K. and Ueda, M. (2002). *Physical Review A*, 65, 023603.

Tung, S., Schweikhard, V. and Cornell, E. A. (2006). *Physical Review Letters*, 97, 240402.

Viefers, S., Hansson, T. H. and Reimann, S. M. (2000). *Physical Review A*, 62, 053604.

Volovik, G. E. (2003). *The Universe in a Helium Droplet*. Oxford University Press, Oxford.

Watanabe, G., Baym, G. and Pethick, C. J. (2004). *Physical Review Letters*, 93, 190401.

Watanabe, G., Gifford, S. A., Baym, G. and Pethick, C. J. (2006). *Physical Review A*, 74, 063621.

Watanabe, G. (2007). *Physical Review A*, 76, 031601(R).

Weber, T., Herbig, J., Mark, M., Nägerl, H.-C. and Grimm, R. (2003). *Science*, 299, 232.

Wilkin, N. K., Gunn, J. M. F. and Smith, R. A. (1998). *Physical Review Letters*, 80, 2266.

Williams, J. E. and Holland, M. J. (1999). *Nature (London)*, 401, 568.

Williams, J. E., Zaremba, E., Jackson, B., Nikuni, T. and Griffin, A. (2002). *Physical Review Letters*, 88, 070401.

Yarmchuk, E. J., Gordon, M. J. V. and Packard, R. E. (1979). *Physical Review Letters*, 43, 214.

Yi, S. and Pu, H. (2006). *Physical Review A*, 73, 061602(R).

Zambelli, F. and Stringari, S. (1998). *Physical Review Letters*, 81, 1754.

Zhang, J. and Zhai, H. (2005). *Physical Review Letters*, 95, 200403.

Zurek, W. H. (1985). *Nature (London)*, 317, 505.

Zwierlein, M. W., Abo-Shaeer, J. R., Schirotzek, A., Schunck, C. H. and Ketterle, W. (2005). *Nature (London)*, 435, 1047.

This page intentionally left blank

AUTHOR INDEX

This page intentionally left blank

SUBJECT INDEX

A
AB interface, 57, 62, 76
AB interface, shear-flow instability, 76
Andreev reflection, 152, 154, 157, 163, 167, 173–175, 202
Andreev scattering, 149–153, 162, 186, 192, 225

B
Baker pH technique, 212
Bernoulli force, 203, 205
Biot–Savart expression, 13
Biot–Savart integral, 68
Boltzmann distribution, 152
Bose-Einstein condensation, 2, 149, 352, 354
bottle-neck effect, 9
boundary frequency, 314, 320, 322, 323
boundary velocity, superfluid, 68
Brownian motion, 272–274

C
capillary turbulence, 323–326, 330
capillary turbulence, decay of, 314, 323–326, 334–340, 342, 344, 345
capillary turbulence, formation, 327
capillary turbulence, homogeneous, 310, 312
capillary turbulence, local model of, 340–344
capillary turbulence, quasiadiabatic decay of, 314
capillary turbulence, stationary spectrum of, 330
capillary turbulence, theoretical background, 310–315
capillary waves, 306, 311
classical–quantum crossover, 36–38
classical turbulence, 148, 149, 177, 189, 190, 197, 199, 248, 255, 256
coarse-grained hydrodynamics, 96
coherence length, 3
cold atoms, 357
condensate, 149, 151, 152, 156, 169
correlation function, 319, 320
cosmological analogues, 148, 173

counterflow, 248, 250, 255, 261, 277, 279–293, 295, 299, 300
counterflow, in rotation, 56
counterflow jet, 251, 271, 291–293
counterflow, NMR signature, 60
counterflow, peak, 57, 60
counterflow, thermal, 114
critical velocity, 158, 159, 160, 162, 175
critical velocity, shear flow instability, 77
critical velocity, for vortex formation, 49, 62
cross-over length scale, 107

D
decay of capillary turbulence, 314, 323–326, 334–340, 342, 344, 345, 347
decay of quantum turbulence, 148
dispersion curve, 149, 150, 152, 156
dissipation in vortex motion, 75, 99
drag crisis, 206

E
energy cascade, 74, 100
energy cascade, bottleneck, 96, 107
energy cascade, Kelvin-wave, 75, 96, 107, 113, 135, 140
energy cascade, Kolmogorov/ Richardson, 107, 112
energy cascade, warm, 108
energy-containing range, 5
energy flux, 99, 107, 115, 128
Euler's equation, 148
evolution of turbulence, 148, 149, 188
excitation wind, 167

F
Fermi surface, 152
field emission, 121
flow visualisation, 248–251, 271, 276, 279
fluid surface, 328–332
Fourier transformation, 317

G
Glaberson instability, 64
gravity-capillary wave turbulence, 307